

Advanced Series on Ocean Engineering — Volume 11

OCEAN SURFACE WAVES: THEIR PHYSICS AND PREDICTION



Stanisław R. Massel

World Scientific

OCEAN SURFACE WAVES: THEIR PHYSICS AND PREDICTION

ADVANCED SERIES ON OCEAN ENGINEERING

Series Editor-in-Chief

Philip L- F Liu (*Cornell University*)

- Vol. 1** The Applied Dynamics of Ocean Surface Waves
by Chiang C Mei (MIT)
- Vol. 2** Water Wave Mechanics for Engineers and Scientists
by Robert G Dean (Univ. Florida) *and Robert A Dalrymple*
(Univ. Delaware)
- Vol. 3** Mechanics of Coastal Sediment Transport
by Jørgen Fredsøe and Rolf Deigaard (Tech. Univ. Denmark)
- Vol. 4** Coastal Bottom Boundary Layers and Sediment Transport
by Peter Nielsen (Univ. Queensland)
- Vol. 5** Numerical Modeling of Ocean Dynamics
by Zygmunt Kowalik (Univ. Alaska) *and T S Murty* (Inst. Ocean Science, BC)
- Vol. 6** Kalman Filter Method in the Analysis of Vibrations Due to Water Waves
by Piotr Wilde and Andrzej Kozakiewicz (Inst. Hydroengineering, Polish
Academy of Sciences)
- Vol. 7** Physical Models and Laboratory Techniques in Coastal Engineering
by Steven A. Hughes (Coastal Engineering Research Center, USA)
- Vol. 8** Ocean Disposal of Wastewater
by Ian R Wood (Univ. Canterbury), *Robert G Bell* (National Institute of Water
& Atmospheric Research, New Zealand) *and David L Wilkinson* (Univ.
New South Wales)
- Vol. 9** Offshore Structure Modeling
by Subrata K. Chakrabarti (Chicago Bridge & Iron Technical
Services Co., USA)
- Vol. 10** Water Waves Generated by Underwater Explosion
by Bernard Le Méhauté and Shen Wang (Univ. Miami)
- Vol. 11** Ocean Surface Waves; Their Physics and Prediction
by Stanislaw R Massel (Australian Inst. of Marine Sci)

Forthcoming titles:

Water Waves Propagation Over Uneven Bottoms

by Maarten W Dingemans (Delft Hydraulics)

Tsunami Run-up

by Philip L- F Liu (Cornell Univ.), *Costas Synolakis* (Univ. Southern California),
Harry Yeh (Univ. Washington) *and Nobu Shuto* (Tohoku Univ.)

Advanced Series on Ocean Engineering — Volume 11

OCEAN SURFACE WAVES: THEIR PHYSICS AND PREDICTION

Stanisław R. Massel

Australian Institute of Marine Science
Australia

 **World Scientific**

NEW JERSEY • LONDON • SINGAPORE • BEIJING • SHANGHAI • HONG KONG • TAIPEI • CHENNAI

Published by

World Scientific Publishing Co. Pte. Ltd.

5 Toh Tuck Link, Singapore 596224

USA office: 27 Warren Street, Suite 401-402, Hackensack, NJ 07601

UK office: 57 Shelton Street, Covent Garden, London WC2H 9HE

Library of Congress Cataloging-in-Publication Data

Massel, Stanislaw R.

Ocean surface wave : their physics and prediction / Stanislaw R.

Massel.

p. cm. -- (Advanced series on ocean engineering : v. 11)

Includes bibliographical references and indexes.

ISBN 9810216866 -- ISBN 9810221096 (pbk)

1. Ocean waves. I. Title. II. Series.

GC211.2.M37 1996

551.47'02--dc20

95-18642

CIP

British Library Cataloguing-in-Publication Data

A catalogue record for this book is available from the British Library.

First published 1996

Reprinted 1998, 2005

Copyright © 1996 by World Scientific Publishing Co. Pte. Ltd.

All rights reserved. This book, or parts thereof, may not be reproduced in any form or by any means, electronic or mechanical, including photocopying, recording or any information storage and retrieval system now known or to be invented, without written permission from the Publisher.

For photocopying of material in this volume, please pay a copying fee through the Copyright Clearance Center, Inc., 222 Rosewood Drive, Danvers, MA 01923, USA. In this case permission to photocopy is not required from the publisher.

Printed in Singapore by Utopia Press Pte Ltd

**To my wife Barbara
and children
Andrzej, Magdalena and Bartosz**

This page is intentionally left blank

Preface

Surface waves are one of the most obvious phenomena, almost constantly present on the surface of any water basin, such as ponds, lakes, rivers, artificial reservoirs, seas and oceans. The first studies on waves concentrated on the ideal, regular wave forms and resulted in a formulation of basic principles of surface wave mechanics. Regular waves can be considered only as a very crude approximation to real ocean waves. Modern marine science and ocean engineering practice need a more realistic representation of the ocean surface.

In the 1940s and '50s substantial progress in the theory of random functions and mathematical statistics provided powerful mathematical tools for a description of ocean waves as random phenomena. The first results of such studies were summarized by Kinsman in his book published thirty years ago.

Recent advances in instrument design and in data handling have allowed sampling of the ocean at rates and on scales hitherto inaccessible. Widespread use of high-speed computers has provided theoreticians with powerful tools and has made possible great improvement in the analysis of experimental data.

In the last three decades, numerous fundamental results were achieved and documented in hundreds of papers, distributed in many journals. However, at the same time, only a few books dedicated totally or partly to wind-induced waves were published. Several books on wind waves were also published in Russia, but due to the language barrier, these books are almost totally unknown among the Western scientific community. All published books fall into two distinct groups: those oriented towards classic oceanography, and those of an engineering nature. However, at the present time, the gap between oceanography, and coastal and ocean engineering, is becoming narrower in the sense that the discoveries in oceanography are transmitted almost immediately to practical applications in marine engineering.

The philosophy of the close link between ocean physics and ocean engineering is adopted in this book, which offers a very comprehensive and updated discussion of the fundamental scientific concepts of ocean wave mechanics and their practical applications. It is hoped that the very broad picture of ocean waves, given in the book, may provide some inspiration to new efforts and new solutions.

The book has two main objectives. The first is to provide a comprehensive review of the present understanding of the physics of ocean waves and their statistical and spectral description. The second objective is to provide a basic description of the

prediction models which can be used in ocean and coastal engineering, and in applied oceanography.

In order to achieve both of these objectives, the evolution of the scientific efforts in ocean wave physics during the last forty years is reviewed. Stochastic and probabilistic terminology is introduced, and the basic statistical and spectral properties of ocean waves are developed and discussed in detail.

Moreover, the book deals with practical prediction methods for waves in deep ocean and coastal zones, in island archipelagos and coral reefs. Simple as well as very sophisticated methods are presented. The long-term evaluation of ocean wave parameters for design purposes are given and measurement techniques, including satellite applications and methods of wave data processing, are discussed.

This book is intended as a handbook for professionals and researchers in the areas of ocean and coastal engineering, physical oceanography, applied physics and as a useful book for graduate students in these fields. It should help bridge the gap between general texts on mathematical statistics and random processes and more descriptive texts on ocean engineering and oceanography.

The reader is assumed to have a working knowledge of calculus, and the analysis of the time series as well. A basic knowledge of hydrodynamic concepts would be helpful, although those subjects are reviewed shortly in the initial chapters of the book.

While the fundamental concepts of ocean wave physics are given in great detail, some advanced topics are only overviewed. However, an index and many cross references are provided in order to make the book more efficient as a handbook. The book's structure can be summarized as follows:

Chapter 1 discusses the basic assumptions and approaches to the description of ocean waves. The fundamentals of time series and spectra are discussed in detail.

Chapter 2 provides a brief description of the airflow over the ocean surface. This is followed by a presentation of the basic wave generation models. In particular, the various implementations to the classical Phillips-Miles model are considered. The spectral representations of wave energy balance, which are extensively used in the following chapters, are also discussed.

In **Chapter 3** emphasis is placed on the various representation of ocean wave spectra and their usefulness for engineering and oceanographic applications.

In **Chapter 4** a comprehensive and updated overview of the statistical properties of ocean waves is given. Topics include probability distributions for all surface wave parameters, as well as wave-induced velocities and pressure. For the particular ocean region (deep water, shallow water, surf zone etc.), corresponding wave statistics are identified.

Chapter 5 deals with wave prediction methods in deep water. First, the basic physical processes responsible for wave behaviour in the deep ocean are discussed. Topics include atmospheric forcing, nonlinear interactions between spectral components and wave energy dissipation. This is followed by a presentation of various

forecasting methods. Besides the sophisticated prediction methods of first, second and third generation models, more simple empirical methods are also discussed.

Chapter 6 deals with ocean waves in finite water depth. The basic physical processes involved in wave motion include wave refraction, diffraction, reflection, non-linear interactions and wave energy dissipation. As in **Chapter 5**, wave prediction methods are treated extensively.

Wave mechanics and wave forecasting techniques for island archipelagoes and coral reefs are still rather poorly known. **Chapter 7** presents the basic methods for the evaluation of wind-induced waves in such environments. Emphasis is placed on the transformation, scattering and dissipation processes at islands and coral reefs.

Chapter 8 focuses on the prediction of design wave parameters using long-term statistics principles. First, the available visual observations and instrumental data are reviewed, and then the probability densities for extreme values are discussed. Some information on the 'geography' of extreme waves is also given.

Chapter 9 overviews wave measurement techniques and methods for wave data processing. Satellite wave detection techniques, as well as the more traditional techniques (wave staffs, wave buoys etc.), are discussed.

A large list of references, symbols and notation, as well as subject and author indexes are included in the book. For convenience, the titles of non-English papers are given in the original transcript, as well as in the English translation.

I apologize for the inevitable errors which may occur in this book, despite my efforts to eliminate them. Please bring these errors to my attention.

I would like to express my thanks to the Australian Institute of Marine Science for support during the preparation of this book. I also wish to acknowledge the stimulating discussions provided by many colleagues and members of the staff of the Institute. Thanks are also due to Christine Cansfield-Smith for accurate proof-reading, and to Bartosz Massel and Steve Clarke who worked on the figures.

I thank Dr Tom Hardy (JCU) and Dr Derek Burrage (AIMS) for their review of chapters and invaluable suggestions.

I am especially grateful to my wife, Barbara, for her accurate and patient word processing, and for her support during the writing.

Townsville, August 1995

Stanislaw R. Massel

This page is intentionally left blank

Contents

1	Introduction	1
1.1	Waves in the ocean and their significance	1
1.2	Basic assumptions on seawater and wave motion	3
1.2.1	Continuous fluid and water particle concept	3
1.2.2	Properties of seawater and its motion	4
1.3	Methods of description of random waves	6
1.3.1	A brief orientation	6
1.3.2	Basic definitions and concepts of time series analysis	8
1.3.3	Fundamentals of spectral description of ocean waves	10
1.3.3.1	Deterministic description of wave train	10
1.3.3.2	Second-order stochastic process	13
1.3.3.3	Wiener-Khinchine Theorem	15
1.3.3.4	Cross-spectral density function	19
2	Generation of Waves by Wind	21
2.1	Introduction	21
2.2	Airflow over sea surface	23
2.2.1	Atmospheric boundary layer above water	23
2.2.2	Similarity laws for drag coefficient C_x and roughness length z_0	26
2.2.3	Practical applications	29
2.3	Similarity laws for wind-induced waves	33
2.4	Wave generation models	36
2.4.1	Jeffreys' mechanism of wave generation	36
2.4.2	Basic results of the Phillips-Miles model	38
2.4.3	Resonance type model in water of finite depth	43
2.4.4	Resonance type model with dissipation	47
2.4.5	Inclusion of fluctuation of tangential stresses	50
2.4.6	Inclusion of airflow turbulence in the Miles' model	52
2.4.7	Effect of wind-generated waves on airflow	53
2.4.8	Wind-current coupling in gravity-capillary wave generation model	55
2.5	Wave energy balance in spectral form	57

3	Spectral Properties of Ocean Waves	63
3.1	Introduction	63
3.2	Frequency spectra of ocean waves	64
3.2.1	Spectral moments and spectral width	64
3.2.2	Spectrum shape	69
3.2.2.1	Saturation range	69
3.2.2.2	Typical frequency spectra	79
3.2.3	Higher order spectra	92
3.2.4	Dispersion relation for ocean waves	95
3.3	Directional spectral functions	99
4	Statistical Properties of Ocean Waves	109
4.1	Introduction	109
4.2	Surface displacement	110
4.2.1	Probability distribution of surface displacement	110
4.2.2	Distribution of nonlinear wave surface displacements	114
4.2.3	Extreme surface displacements	118
4.2.3.1	Probability distribution for positive and negative maxima	118
4.2.3.2	Structure of extreme waves	124
4.2.4	Influence of wave breaking on probability distribution of surface displacement in deep water	127
4.2.5	Probability distribution of surface displacement in finite water depth	131
4.3	Wave height	136
4.3.1	Probability distribution of wave height for a narrow-band spectrum	136
4.3.2	Influence of wave nonlinearity on wave height distribution	142
4.3.2.1	Modification of the Rayleigh distribution	142
4.3.2.2	Crest-to-trough wave height distribution	145
4.3.2.3	Probability distribution of large wave heights	148
4.3.2.4	Influence of second order nonlinearities	150
4.3.3	Influence of wave breaking on wave height distribution in deep water	153
4.3.4	Probability distribution of extreme wave height	155
4.3.5	Probability distribution of wave height in finite water depth	160
4.3.6	Probability distribution of wave height in a surf zone	164
4.4	Wave period	172
4.4.1	Joint distribution of wave heights and periods	172
4.4.2	Probability distribution of wave period	176
4.5	Wave orbital velocities and pressure	180
4.5.1	Probability distribution of orbital velocities and pressure	180

4.5.2	Influence of intermittence effect on probability distribution of orbital velocities and pressure near water level	188
4.6	Wave group statistics	192
4.6.1	Level-crossing problem	194
4.6.2	Markov chain representation	198
5	Prediction of Ocean Waves in Deep Water	201
5.1	Introduction	201
5.2	Basic wave processes in deep water	202
5.2.1	Atmospheric forcing	203
5.2.2	Nonlinear interaction between wave components	209
5.2.2.1	Evaluation of nonlinear energy transfer	209
5.2.2.2	Parameterization of nonlinear energy transfer	214
5.2.2.3	Nonlinear coupling between swell and wind waves	216
5.2.3	Energy dissipation due to white capping	218
5.2.4	Energy balance for fully-developed and growing seas	220
5.3	Wave prediction models	222
5.3.1	Wave models based on energy transfer equation	223
5.3.1.1	First generation wave models	223
5.3.1.2	Second generation wave models	225
5.3.1.3	Third generation wave models	231
5.3.2	Empirical prediction models	235
5.3.2.1	Fetch- and time-limited wave growth	235
5.3.2.2	JONSWAP prediction graphs	237
5.3.2.3	SPM prediction graphs	239
5.3.2.4	SMB prediction graphs	241
5.3.2.5	Donelan method	241
5.3.2.6	Krylov method	243
5.3.2.7	Comparison of empirical prediction methods	251
6	Prediction of Ocean Waves in Shallow Water	255
6.1	Introduction	255
6.2	Basic wave processes in shallow water	256
6.2.1	Wave refraction due to bottom shoaling	256
6.2.2	Refraction by currents in a shoaling water depth	264
6.2.2.1	Propagation of random waves in an inhomogeneous region	264
6.2.2.2	Influence of uniform current on a saturation range spectrum	269
6.2.3	Combined refraction and diffraction	271
6.2.4	Reflection of ocean waves	275
6.2.5	Nonlinear interaction between spectral wave components	284

6.2.5.1	Narrow-band spectrum approximation	284
6.2.5.2	Stokes' perturbation technique	285
6.2.6	The largest wave height in water of constant depth	291
6.2.6.1	Experimental data	291
6.2.6.2	Regular waves	292
6.2.6.3	Irregular waves	303
6.2.7	Wave energy dissipation at sea bottom	306
6.2.7.1	A brief orientation	306
6.2.8	Energy dissipation due to bottom friction	306
6.2.9	Energy dissipation due to bottom permeability	308
6.2.9.1	Energy dissipation due to soft mud	311
6.2.10	Energy dissipation due to wave breaking	315
6.2.10.1	Periodic bore approach	316
6.2.10.2	Energy flux difference model	321
6.2.10.3	Local water depth model	322
6.2.10.4	Surface roller concept	323
6.3	Wave prediction models	324
6.3.1	Models based on energy transfer equation	324
6.3.1.1	First generation wave models	324
6.3.1.2	Second generation wave models	325
6.3.1.3	Third generation wave models	327
6.3.1.4	Wave prediction in very shallow water	328
6.3.2	Empirical prediction models	330
6.3.2.1	SPM prediction method	330
6.3.2.2	Krylov prediction method	334
7	Waves at Islands and Coral Reefs	337
7.1	Introduction	337
7.2	Propagation of waves over steep bottom slopes	337
7.2.1	Geometrical optics and mild-slope approximations	337
7.2.2	Application of extended refraction-diffraction equation	339
7.2.2.1	Non-breaking waves	339
7.2.2.2	Breaking waves	343
7.2.2.3	Wave set-down and set-up	345
7.2.2.4	Numerical examples and comparison with experiments	346
7.3	Maximum wave height on shoal (reef) flat	350
7.4	Sheltering of surface waves by islands	352
7.4.1	A brief orientation	352
7.4.2	Scattering of waves by an isolated steep conical island	352
7.4.2.1	Pure refraction solution	354
7.4.2.2	Refraction-diffraction solution with dissipation	355
7.4.3	Scattering of waves by a group of islands	357

7.5	Prediction of waves on island (reef) archipelagoes	358
7.6	Interaction of waves with coral reef bottoms	359
7.6.1	Forces on coral	360
7.6.2	Velocity field around coral	366
7.6.3	Probability of coral dislodgement or persistence	367
8	Long-Term Statistics for Ocean Surface Waves	369
8.1	Introduction	369
8.2	Visual observations of wave heights	369
8.3	Visual observations versus instrumental data	372
8.4	Visual observations of wave periods	373
8.5	Long-term distributions of wave heights	374
8.5.1	The initial probability distribution is unknown	375
8.5.2	Probability distributions of extreme waves	381
8.6	Estimation of distribution parameters	386
8.7	Goodness of fit tests and confidence intervals	386
8.8	Design wave selection	387
8.9	Geography of waves	388
8.9.1	A brief orientation	388
8.9.2	Atlantic Ocean	390
8.9.3	Pacific Ocean	391
8.9.4	Indian Ocean	392
8.9.5	Examples of wave climate in various seas	394
9	Measurement, Simulation and Data Processing	395
9.1	Introduction	395
9.2	A single point wave data	395
9.2.1	Measurement techniques	395
9.2.1.1	Laboratory wave measurement	395
9.2.1.2	Field wave measurements	398
9.2.2	Determination of spectral characteristics of surface waves	399
9.2.2.1	Data sampling	399
9.2.2.2	Standardization of data, trend removal and filtering	401
9.2.2.3	Calculation of frequency spectra	402
9.2.3	Calculation of statistical characteristics of waves	406
9.3	Measurement of wave directionality	407
9.3.1	Measurement techniques	407
9.3.2	Determination of directional wave spectra	408
9.3.2.1	Fourier Expansion Method	408
9.3.2.2	Maximum Entropy Method	411
9.3.2.3	Maximum Likelihood Method	416
9.3.2.4	Comparison of various analytical techniques	417

9.4 Remote sensing techniques	418
9.4.1 A brief orientation	418
9.4.2 Application of satellite altimetry	419
9.4.3 Application of satellite Synthetic Aperture Radar	420
9.5 Numerical simulation techniques	421
9.5.1 Time domain simulation with a random-phase structure	422
9.5.2 Frequency domain simulation by a random-phase structure	423
10 References	427
Symbols and Notation	467
Author index	475
Subject index	485

Chapter 1

Introduction

1.1 Waves in the ocean and their significance

Ocean water is permanently subjected to the external forces of nature, which dictate what types of waves can be induced in the ocean. The most obvious cause of surface waves is an action of wind. The ancient Greeks were well aware of interaction between the atmosphere and sea surface. Aristotle (384-322 BC) realized that wind acting on the sea surface plays a very important role in the development of waves. Pliny (AD 23-79) observed that oil poured upon waves calms them. From the time of Aristotle to the Renaissance of science in the 'Golden Age of Discovery' in the late fifteenth century, very little progress was made towards an understanding of the generation and growth of waves. It was not until well into the nineteenth and twentieth centuries that more fundamental knowledge of what caused waves and how they behaved was accumulated.

In general, five basic types of ocean waves can be distinguished: sound, capillary, gravity, internal and planetary waves. Sound waves are due to water compressibility, which is, in fact, very small. Gravity forces, acting on water particles displaced from equilibrium at the ocean surface or at an internal geopotential surface in a stratified fluid, induce gravity waves (surface or internal). At the contact surface between air and water, the combination of the turbulent wind and surface tension gives rise to short, high frequency capillary waves. On the other hand, very slow, large-scale planetary or Rossby waves are induced by the variation of the equilibrium potential vorticity, due to changes in depth or latitude. All of the above wave types can occur together, producing more complicated patterns of oscillations.

The frequency range associated with external forces is very wide and ocean surface response occupies an extraordinary broad range of wave lengths and periods, from capillary waves, with periods of less than a second, through wind-induced waves and swell with periods of the order of a few seconds, to tidal oscillations with periods of the order of several hours and days. In Fig. 1.1 and in Table 1.1, the schematic representation of energy contained in the surface waves, and the physical mechanisms

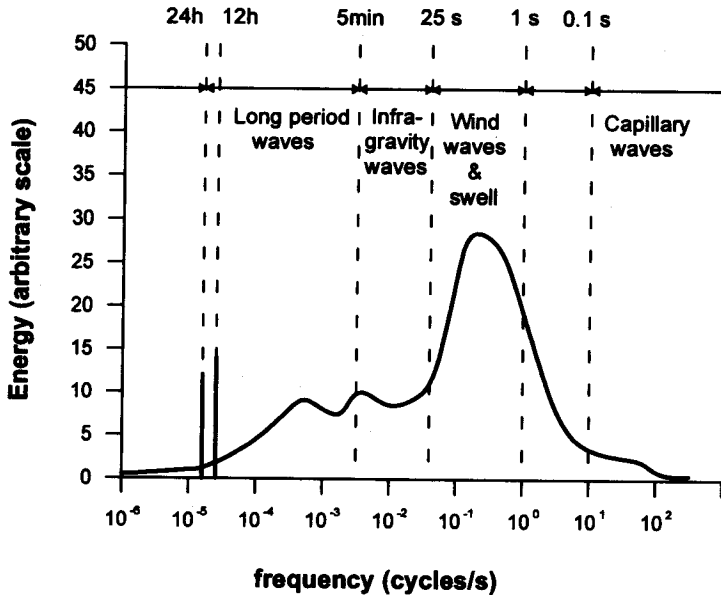


Figure 1.1: Schematic distribution of wave energy in frequencies.

generating these waves, are listed. The Figure gives some impression of the relative importance of various kinds of surface oscillations, but does not necessarily reflect the actual energy content.

For engineering activity in the sea, gravity waves are of the greatest importance, as the influence of wind-induced waves on engineering structures is most sensible and hostile. Marine structures must be designed to sustain the forces and velocities induced by these waves. A thorough understanding of the interaction of waves with offshore structures has now become a vital factor in the safe and economical design of such structures. The calculation procedures needed to establish the structural loading generally involve the following steps in which knowledge on the surface waves is essential: a) establishing the wave climate in the vicinity of a structure, b) estimating design wave conditions for the structure, and c) selecting and applying a wave theory to determine the hydrodynamic loading on the structure.

The role of waves in coastal marine environment can not be overestimated. Waves approaching the shoreline break and dissipate their energy on beaches. Storm and cyclone waves impose large forces on natural coastal and man made structures. Long-

Table 1.1: Waves, physical mechanisms, and periods.

Wave type	Physical mechanism	Periods
Capillary waves	Surface tension	$< 10^{-1}$ s
Wind waves	Wind shear, gravity	< 15 s
Swell	Wind waves	< 30 s
Surf beat	Wave groups	1 – 5 min
Seiche	Wind variation	2 – 40 min
Harbour resonance	Surf beat	2 – 40 min
Tsunami	Earthquake	10 min - 2 h
Storm surges	Wind stresses and atmospheric pressure variation	1 – 3 days
Tides	Gravitational action of the moon and sun, earth rotation	12 – 24 h

shore currents transport sediments and create areas of erosion and accumulation. Knowledge of wave motion and the sediment budget provides the key to the proper selection of protecting structures and methods of shoreline stabilization. Our present understanding of these processes is still not adequate to develop effective management plans or engineering designs which are today subjected to very stringent requirements to minimize their impact on the environment.

Other types of ocean waves which either play a smaller role in ocean and coastal engineering or may have been treated in other books are not included here. In particular, for a systematic review of planetary waves, tides and storm surges, internal waves and coastal trapped waves I refer the reader to the books by Phillips (1977), LeBlond and Mysak (1978), Pedlosky (1979), Efimov (1985), and Monin and Krasitskii (1985).

1.2 Basic assumptions on seawater and wave motion

1.2.1 Continuous fluid and water particle concept

Prior to introducing the basic concepts on fluids and fluid motion, we will adopt the rectangular coordinate system $O(x, y, z)$ or $O(x_i, z)$; $i = 1, 2$. The origin of the system is at the mean sea surface. The axes x and y are horizontal. The z axis is directed opposite to the force of gravity.

One of the most important physical principles of hydrodynamics is that the fluid is *continuous*. By continuous fluid in continuous motion, we mean that the velocity

\vec{u} is everywhere finite and continuous while its space derivatives of the first order are finite (but not necessarily continuous). Thus, any closed surface S which moves with the fluid, permanently and completely separates the fluid matter inside S from that outside. The fluid can be treated as continuous when the flow past an obstacle of the dimension A which is much larger than the average free path of the molecule l_0 (for water $l_0 \approx 3 \cdot 10^{-10}m$). The rate $\left(\frac{l_0}{A}\right)$ is known as the Knudsen number (**Kn**). If:

$$\mathbf{Kn} = \frac{l_0}{A} < 0.01, \quad (1.1)$$

the fluid can be treated as continuous (Puzyrewski and Sawicki, 1987).

With regard to continuous fluid, we can define a *fluid particle* as consisting of the fluid contained within an infinitesimal volume, that is to say, a volume whose size may be considered so small that for the particular purpose in hand its linear dimensions are negligible. We can then treat a fluid particle as a geometrical point.

1.2.2 Properties of seawater and its motion

In general, the equation of motion for the fluid particle depends on the physical properties of the fluid and motion itself. In order to render the subject amenable to exact mathematical treatment, we examine some physical and chemical properties of seawater and simplifying assumptions on the medium and its motion, i.e.:

(a) *water is an inviscid fluid*

An inviscid fluid is a continuous fluid which can exert no shearing stress. However, real fluids do have viscosity which creates stresses and additional dissipations within the fluid. Thus:

$$\vec{\tau} = \mu \frac{d\vec{u}}{d\vec{n}}, \quad (1.2)$$

where $\vec{\tau}$ is tangential stress, $\vec{u} = (u, v, w)$ is fluid velocity vector, \vec{n} denotes vector normal to vector \vec{u} , and μ is coefficient of viscosity of the fluid. Sometimes for convenience, we will represent the vector \vec{u} as $\vec{u} = (u_i, w; i = 1, 2)$; therefore $u_1 = u, u_2 = v$. Thus, for the inviscid fluid:

$$\vec{\tau} = 0 \quad \text{or} \quad \mu = 0 \quad \text{when} \quad \vec{u} \neq \vec{0}, \quad (1.3)$$

in which $\vec{0} = (0, 0, 0)$. To justify the identity (1.3), we adopt the differential length scale L in which the velocity varies in magnitude by U . The ratio $\mathbf{Re} = \frac{\rho U L}{\mu}$ (the Reynolds number) represents the relative magnitudes of the inertial and viscous terms. In many oceanic motions, the Reynolds number is very large. Thus, the viscous influence is often quite negligible over most of the field of motion. The viscous forces

are important only in narrow regions of the flow, where the local inertial and viscous forces are comparable. In the ocean, the interfacial layer between the air and the water, as well as the bottom boundary layer are such regions. The thickness δ of the surface boundary layer is of the order $\delta \approx \left(\frac{2\nu}{\omega}\right)^{\frac{1}{2}}$, where ω is a wave frequency, and ν is kinematic coefficient of viscosity (for water $\nu \approx 1.2 \cdot 10^{-6} m^2 s^{-1}$). For typical ocean wave frequencies, the thickness $\delta \sim 0.001 m$. For the boundary layer near the natural sea bottom, the eddy viscosity is much higher ($\sim 100\nu$). The thickness of the boundary layer is then about $0.1 m$, which is still quite small. Therefore, the boundary layer regions are but a very small fraction of a fluid volume, and the influence of the molecular viscosity on the wave motion can be neglected.

(b) *water is an incompressible fluid*

The compressibility of water is rather small and the Young's modulus is of order $E \approx 3.05 \cdot 10^8 N m^{-2}$ (Dera, 1992). As the typical velocity of seawater is much smaller than the speed of sound, the very small water compressibility has no influence on water motion. Therefore, the equation of continuity for the homogeneous incompressible fluid becomes (Milne-Thomson, 1960):

$$\text{div } \vec{u} = \nabla \cdot \vec{u} = \frac{\partial u}{\partial x} + \frac{\partial v}{\partial y} + \frac{\partial w}{\partial z}, \quad (1.4)$$

where:

$$\nabla = \frac{\partial}{\partial x} \vec{i} + \frac{\partial}{\partial y} \vec{j} + \frac{\partial}{\partial z} \vec{k}. \quad (1.5)$$

In general, vector \vec{u} represents the sum of the current and wave velocities.

(c) *seawater salinity and density*

Seawater is not a pure water. It contains salts, dissolved organic substances, and mineral and organic suspended matter. The relatively constant composition of the main constituents of sea salt has made it possible to introduce a single parameter defining the salt concentration in seawater. This is known as salinity (S). The salinity of ocean water is close to 35 parts/million. In semi-closed seas, where evaporation exceeds precipitation, the salinity may be higher than in the oceans (for example, 42 parts/million in the Red Sea). On the other hand, in cold, semi-closed seas, like the Baltic, the salinity is very low due to inflowing rivers (7-8 parts/million).

The density of seawater is usually derived from the International Equation of State for Sea Water (Dera, 1992). This equation is valid for salinity S from 0 to 42 parts/million, temperature T from -2 to $40^\circ C$ and of pressure p from 0 to 1000 bars. For example, for $S = 0, T = 5, p = 0$ (atmospheric pressure), the density $\rho = 999.966 kg \cdot m^{-3}$, while for $S = 35, T = 25, p = 0$, the density $\rho = 1023.343 kg \cdot m^{-3}$.

The density of seawater and its distribution in the water column determines the hydrostatic stability of water masses and influences sound propagation and turbulence. However, the influence of density on surface waves is negligible, except perhaps for the stage of wave generation under wind action (see Chapter 2).

(d) *motion is irrotational*

This means that the individual elementary particles of the fluid do not rotate. The mathematical expression of this is:

$$\text{rot } \vec{u} = \text{curl } \vec{u} = \nabla \times \vec{u} = \vec{0}, \quad (1.6)$$

When the vorticity is different from zero, the motion is defined as *rotational*. As indicated above, in many oceanic motions the influence of the viscous terms is quite negligible. In this event, the Lagrange theorem (Kochin et al., 1963) indicates that if, at some initial instant, the vorticity vanishes everywhere in the field of flow, the motion is irrotational. This remains so in the absence of viscous effects. The consequence of Eq. (1.6) is that the velocity \vec{u} can be represented as the gradient of a scalar function, the velocity potential Φ :

$$\vec{u} = \nabla \Phi; \quad (1.7)$$

then, in virtue of the continuity equation (1.4), the potential Φ obeys the Laplace equation:

$$\text{div}(\nabla \Phi) \equiv \nabla^2 \Phi = \frac{\partial^2 \Phi}{\partial x^2} + \frac{\partial^2 \Phi}{\partial y^2} + \frac{\partial^2 \Phi}{\partial z^2}. \quad (1.8)$$

1.3 Methods of description of random waves

1.3.1 A brief orientation

In looking at ocean surface waves one notices both their randomness and their quasi-regularity. The wave profile changes constantly with time and in a random fashion. Consequently, the properties of waves are not readily defined on a wave-by-wave basis.

As the fundamental property of surface waves, induced by wind, is their irregularity, the prediction of wave parameters can be achieved only through stochastic analysis of the sea surface, which span three basic domains: time, frequency, and probability (see Fig. 1.2).

In the time domain, the auto or cross-correlation functions are evaluated from measured wave records. The autocorrelation function is a measure of the connection between the two values $\eta(t)$ and $\eta(t + \tau)$ of the random variable η . From the time series of a given quantity, i.e. surface elevation, orbital velocity or pressure, the first statistical moments can be calculated in the straightforward manner. An interesting

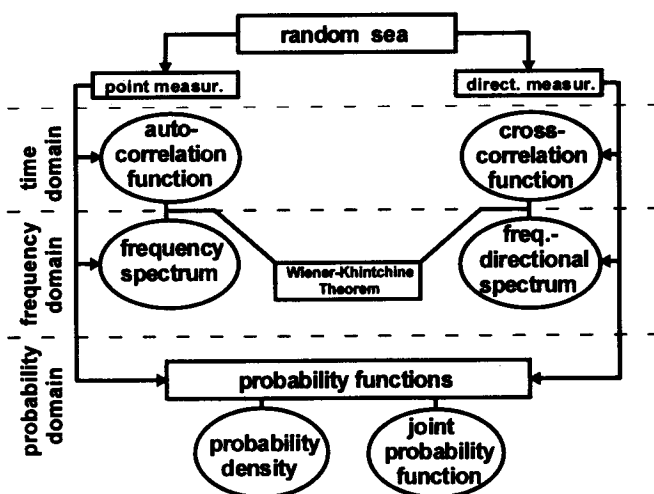


Figure 1.2: Methods of processing of random wave data.

application of the time domain approach for the evaluation of maxima of surface displacements is discussed in Section 4.2.3.

Frequency analysis deals mainly with an evaluation of the distribution of wave energy (potential or kinetic) among various frequencies and directions. There are two main methods for the development of frequency spectrum. The traditional method is based on the Fourier Transform of the correlation function. The theoretical background of this transformation is provided by the Wiener-Khinchine theorem. The transformation of the autocorrelation function gives the spectral density function of the particular variable, and the transformation of cross-correlation function results in cross-spectral density function, which is a complex function. The real part of the cross-spectral function is called the co-spectrum and the imaginary part is called the quadrature spectrum. A more general spectral representation of surface waves is obtained when the frequency, as well the directional energy distribution, is taken into account. The resulting spectrum is called the frequency-directional spectrum.

The second method is based on the straightforward transferring of the time series into its Fourier components. This technique, known as Fast Fourier Transform (FFT), was first introduced in a new form by Cooley and Tukey (1965). It reduces the number of calculations from a number proportional to n^2 (n is a number of samples) to a number approximately proportional to $n \log n$ and has revolutionized the spectral analysis of time series.

If waves are propagating in an inhomogeneous medium, the wave spectrum varies in time and space. This is mainly due to the interaction of waves with the wind field

over the sea, varying currents and water depth. The slow evolution of spectral energy is described by the radiative transfer equation (or transport equation or the kinetic equation).

In the probability domain, the particular wave parameters, e.g. ordinate of surface displacement at a given time, wave amplitude, wave height, wave period, etc. are considered as elementary random events. The probability approach is easy to understand when we are dealing with digitized data. The digitized data of a particular parameter form a set of random realizations of a random variable, when the time sequence of the parameter is exterminated. The final results in this approach are expressed in terms of probability density functions, distribution functions and statistical moments.

The simplest statistics are obtain when one assumes that the observed wave field is a result of a linear superposition of a large number of dynamically independent waves. This is the basis of the Gaussian model, in which two first moments are sufficient for the complete statistical description of the wave field. However, in the real ocean, due to nonlinear interaction between spectral harmonics and energy dissipation processes, a substantial departure from the Gaussian model is observed. Ocean waves should be treated in many cases as examples of the non-Gaussian stochastic processes.

1.3.2 Basic definitions and concepts of time series analysis

Let us begin with an ensemble of k wave records $\{\zeta_k(t)\}$ taken under identical macroscopic conditions, i.e.: position on the ocean surface, water depth, mean wind velocity, air-sea temperature, etc. Even under identical conditions, we cannot expect that these wave records will be identical or even closely similar in detail. The family $\{\zeta_k(t)\}$ represents k realizations of the stochastic process $\zeta(t)$. For a given k , $\zeta(t)$ is a function of time t , while when $t = t_1$, $\zeta_k(t)$ is a random variable.

Stochastic processes may belong to one of three categories: a) stationary and ergodic, b) stationary, and c) non-stationary.

Random process (or random function) is stationary in the wide sense if:

$$E[\zeta(t)] = \bar{\zeta} = \text{const}, \quad (1.9)$$

$$K(t_1, t_2) = K(t_1 - t_2) = E[\zeta(t_1) \zeta(t_2)] = K(\tau), \quad \tau = t_1 - t_2, \quad (1.10)$$

in which $E[\]$ denotes the mean of ζ and $K(\)$ is an autocorrelation function. Strictly, a random process is stationary if all statistical moments are translationally invariant. These two definitions of stationarity coincide when ζ is a Gaussian, in which case all the statistics of ζ are completely determined by the first and second moments. This strict definition is often relaxed and stationarity in wide sense is assumed.

In general, using the ensemble of wave records $\{\zeta_k(t)\}$, we can develop any function of ζ , say F , to give $F\{\zeta_k(t)\}$. To be more specific, we select time $t = t_1$ in the family

$\{\zeta_k(t)\}$. When F is the ζ value itself, then averaging $F\{\zeta_k(t_1)\}$ over k results in the ensemble mean of the process at $t = t_1$, i.e.:

$$E[F\{\zeta_k(t_1)\}]_k = E[\zeta_k(t_1)]_k = \lim_{N \rightarrow \infty} \frac{\sum_{k=1}^N \zeta_k(t_1)}{N}. \quad (1.11)$$

The condition $N \rightarrow \infty$ is only conceptual since in practice N is always finite.

When $F\{\zeta_k(t_1)\} \equiv [\zeta_k(t_1)]^2$, then averaging $F\{\zeta_k(t_1)\}$ over k leads to the variance at $t = t_1$:

$$E[F\{\zeta_k(t_1)\}]_k = E\{[\zeta_k(t_1)]^2\}_k = \lim_{N \rightarrow \infty} \frac{\sum_{k=1}^N [\zeta_k(t_1)]^2}{N}. \quad (1.12)$$

Let us now define F as:

$$F\{\zeta_k(t_1)\} = \begin{cases} 1 & \text{if } a < \zeta_k(t_1) \leq b \\ 0 & \text{otherwise} \end{cases} \quad (1.13)$$

Averaging over the ensemble $E[F\{\zeta_k(t_1)\}]_k$ can be interpreted as the ensemble probability that $\zeta_k(t_1)$ falls on the interval from a to b at $t = t_1$.

Repetition of the above averaging for the different times helps us to obtain the different numerical values for the statistics. However, the repeated observations technique which provides us with an ensemble of k wave records can be attained in laboratory wave tanks, but is inapplicable to observations of wave phenomena in field experiments. To overcome these difficulties, the ergodic theorem is usually invoked. This allows the ensemble averages to be replaced with time averages.

The ergodic theorem states that (Kinsman, 1965):

if $\zeta(t)$ is an ergodic stationary random function, then the statistics obtained by ensemble averages at a given time $t = t_$ are identical to the corresponding statistics computed by the time averaging for any given realization $k = k_*$.*

Hence, the ergodic stationary process should satisfy the following equality:

$$\begin{aligned} E[F\{\zeta_k(t = t_*)\}]_k &= \lim_{N \rightarrow \infty} \frac{\sum_{k=1}^N F\{\zeta_k(t = t_*)\}}{N} = E[F\{\zeta_{k=k_*}(t)\}]_t = \\ &= \lim_{T \rightarrow \infty} \frac{1}{2T} \int_{-T}^T F\{\zeta_{k=k_*}(t)\} dt. \end{aligned} \quad (1.14)$$

We can say that, while stationary processes are a limited subset of random processes, ergodic processes in their turn are an even more limited subset of stationary processes.

The significance of the ergodic theorem is that it enables us to develop the statistics of the process $\zeta(t)$ using one, sufficiently long realization. However, it is never possible to demonstrate ergodicity for ocean waves since experiments cannot be exactly repeated in the ocean as they can in the laboratory.

It can be shown that for a stationary wave process $\zeta(t)$ to be ergodic it is sufficient that its autocorrelation function $K(\tau)$ satisfies the following condition (Tikhonov, 1966):

$$K(\tau) = 0 \quad \text{at} \quad \tau \rightarrow \infty. \quad (1.15)$$

Let us now demonstrate the applicability of the ergodic theorem and condition (1.15) for a simple process. We assume that we have an ensemble of records of a process $\{\zeta_k(t)\} = z_k$. This means, that for a particular k , the process $\zeta_k(t)$ is constant and equal z_k . It is clear that process is stationary. For any chosen time t , any statistic, for example the mean, calculated across the ensemble gives the same number. However, when any single record $\zeta_{k=k_*}(t)$ is chosen at random and its time average calculated (Kinsman, 1965):

$$E[\zeta_{k=k_*}(t)]_t = \lim_{T \rightarrow \infty} \frac{1}{2T} \int_{-T}^T \zeta_{k=k_*}(t) dt, \quad (1.16)$$

then, it is obvious that:

$$E[\zeta_k(t = t_*)]_k \neq E[\zeta_{k=k_*}(t)]_t. \quad (1.17)$$

Hence, this extremely simple process is stationary, but not ergodic. The condition (1.15) is clearly not satisfied as:

$$K(\tau) = E[\zeta_{k=k_*}(t) \zeta_{k=k_*}(t + \tau)] = \lim_{T \rightarrow \infty} \frac{1}{2T} \int_{-T}^T z_{k_*}^2 dt = z_{k_*}^2. \quad (1.18)$$

In the following we assume that the ergodic property holds for the stochastic process discussed in this text. Therefore, a single record $\zeta(t)$ will be used instead of an ensemble of records $\{\zeta_k(t)\}$.

1.3.3 Fundamentals of spectral description of ocean waves

1.3.3.1 Deterministic description of wave train

Let us begin with the deterministic description of a wave train observed at some point $P(x, y)$. The deterministic description is a natural starting point for the development of random models which will be given later. The profile of a wave traveling at an angle Θ to the x axis may be presented as:

$$\zeta(x, y, t) = a \cos[k(x \cos \Theta + y \sin \Theta) - \omega t + \varphi], \quad (1.19)$$

in which h is a water depth, φ is a phase shift and k is a wave number related to wave frequency ω by the dispersion relation:

$$\omega^2 = gk \tanh(kh), \quad (1.20)$$

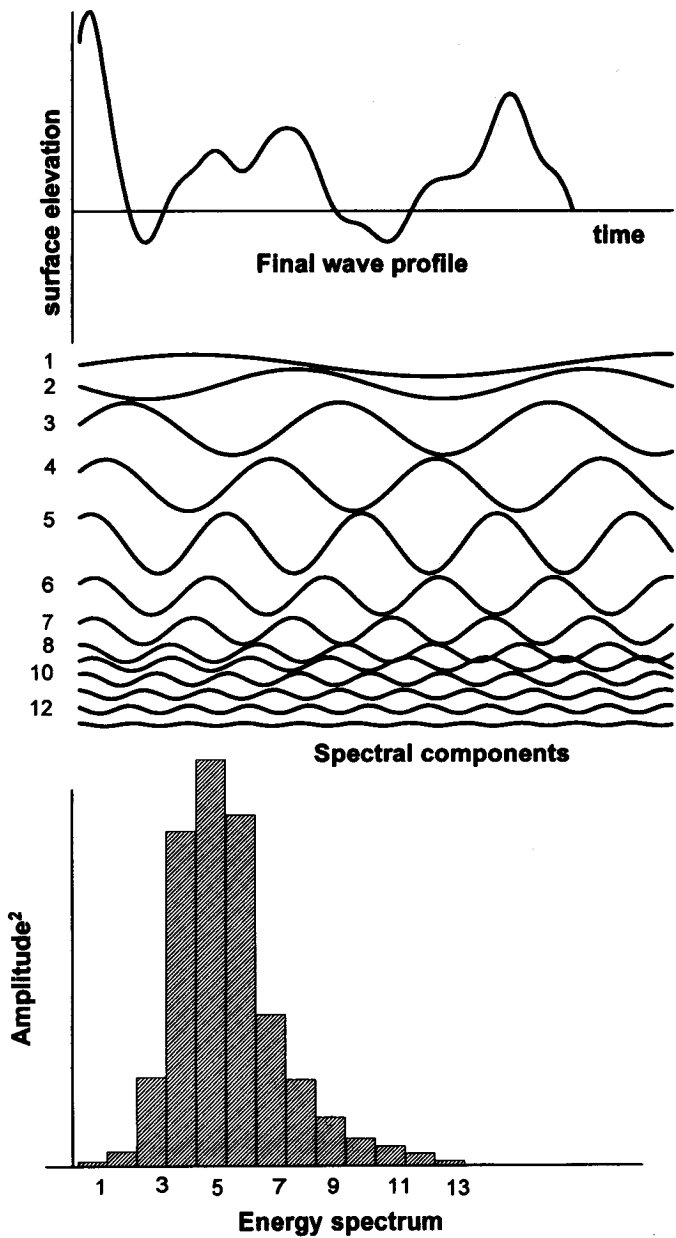


Figure 1.3: Superposition of spectral components and resulting spectrum.

The simplest and the most natural representation of the confused sea surface would be the linear superposition of many wave harmonics traveling in various directions.

A simple illustration of such a superposition is given in Fig. 1.3, where 13 elementary components sum to form a final wave profile. Thus, using Eq. (1.19), the wave profile may be written as:

$$\zeta(x, y, t) = \sum_{l=1}^{l=N} a_l \cos [k_l(x \cos \Theta_l + y \sin \Theta_l) - \omega_l t + \varphi_l]. \quad (1.21)$$

The direction Θ_l and phase φ_l cover the range $-\pi, \pi$, and wave amplitudes and frequencies are from the range $0 \leq a_l \leq \infty$ and $0 \leq \omega_l \leq \infty$.

The integral version of this would be:

$$\zeta(x, y, t) = 2 \int_0^\infty \int_{-\pi}^\pi a(\omega, \Theta) \cos [k(x \cos \Theta + y \sin \Theta) - \omega t + \varphi] d\omega d\Theta, \quad (1.22)$$

under the assumption that (Borgman, 1972):

$$a(\omega, \Theta) = \frac{1}{2} \sum_{l=1}^N a_l \delta(\omega - \omega_l) \delta(\Theta - \Theta_l), \quad (1.23)$$

where $\delta(\)$ denotes Dirac delta function (Lighthill, 1975).

Using Euler's identity:

$$\cos \alpha = \frac{1}{2} [\exp(i\alpha) + \exp(-i\alpha)], \quad (1.24)$$

we rewrite Eq. (1.22) in the form:

$$\zeta(x, y, t) = \int_{-\infty}^\infty \int_{-\pi}^\pi a(\omega, \Theta) \exp [i\varphi(\omega, \Theta)] \exp [ik(x \cos \Theta + y \sin \Theta) - \omega t] d\omega d\Theta. \quad (1.25)$$

Let us define the cumulative function:

$$A(\omega, \Theta) = \int_{-\infty}^\omega \int_{-\pi}^\Theta a(\omega', \Theta') \exp [i\varphi(\omega', \Theta')] d\omega' d\Theta'. \quad (1.26)$$

Then, Eq. (1.25) becomes:

$$\zeta(x, y, t) = \int_{-\infty}^\infty \int_{-\pi}^\pi \exp [i(\vec{k} \cdot \vec{x} - \omega t)] dA(\omega, \Theta), \quad (1.27)$$

where $dA(\omega\Theta)$ is a differential element in the two-dimensional space (ω, Θ) , \vec{k} is a two-dimensional vector $(k \cos \Theta, k \sin \Theta)$ and \vec{x} is the vector (x, y) .

For later convenience it will be useful to express Eq. (1.27) as a Fourier transform in three dimensions, (x, y, t) . Thus, we define:

$$u = k \cos \Theta, \quad v = k \sin \Theta, \quad w = -\omega, \quad (1.28)$$

and

$$\hat{A}(u, v, w) = \int_{-\infty}^u \int_{-\infty}^v \int_{-\infty}^w \hat{a}(u', v', w') dw' dv' du', \quad (1.29)$$

in which:

$$\hat{a}(u, v, w) = A(\omega, \Theta) \delta \left[|\omega| - (gk \tanh(kh))^{1/2} \right]. \quad (1.30)$$

Using Eq. (1.28), the Eq. (1.27) may be rewritten as:

$$\zeta(x, y, t) = \int_{-\infty}^{\infty} \int_{-\infty}^{\infty} \int_{-\infty}^{\infty} \exp[i(ux + vy + wt)] d\hat{A}(u, v, w). \quad (1.31)$$

Due to the restriction Eq. (1.30) imposed on frequency ω and wave number k , a triple integral in Eq. (1.31) is in fact a double integral only.

The advantage of the integral representation (1.31) is that it makes application of the technique of Fourier integrals possible. This means that for given measurements of $\zeta(x, y, t)$ over the (x, y, t) space, the function $\hat{a}(u, v, w)$ can be computed in principle by an inverse Fourier transform. It can be seen from Eq. (1.30) that $\hat{a}(u, v, w)$ has nonzero values only when (u, v, w) satisfy the dispersion relation (1.20).

1.3.3.2 Second-order stochastic process

The representation (1.31) is quite general but still a deterministic one. We will use it now for evaluation of the random wave model. We assume that $\zeta(t)$ is a stationary ergodic process satisfying the conditions (1.9) and (1.10). Without losing generality we can say that $\bar{\zeta} = 0$. Under the above assumptions there exists stochastic process $\tilde{A}(u, v, w)$, such that the process $\zeta(x, y, t)$ has the representation (Yaglom, 1962):

$$\zeta(x, y, t) = \int_{-\infty}^{\infty} \int_{-\infty}^{\infty} \int_{-\infty}^{\infty} \exp[i(ux + vy + wt)] d\tilde{A}(u, v, w). \quad (1.32)$$

A three-dimensional stochastic process $\tilde{A}(u, v, w)$ possesses uncorrelated increments which means that differences $[\tilde{A}(u'', v'', w'') - \tilde{A}(u', v', w')]$ for (u'', v'', w'') and (u', v', w') within a given cube in (u, v, w) space are uncorrelated with differences within any other non-overlapping cube.

The integrals (1.31) and (1.32) look similar, but they are significantly different. The former representation is a deterministic integral, while the latter is a representation of random function and should be defined by probabilistic limits.

The general representation given by Eq. (1.32) depends only on the assumption that process $\zeta(x, y, t)$ is ergodic and conditions (1.9) and (1.10) are valid. It also is important to note that this representation exists without assuming that the sea surface is composed of a superposition of linear waves. If we assume for a moment that linear theory is approximately correct, we should impose a restriction on wave number k and wave frequency ω expressed by the dispersion relation:

$$w^2 = \omega^2 = g(u^2 + v^2)^{1/2} \tanh \left[(u^2 + v^2)^{1/2} h \right]. \quad (1.33)$$

The $d\tilde{A}(u, v, w)$ is zero whenever the above relation is not satisfied. Now, the parameters (u, v, w) can be replaced by the two parameters (ω, Θ) , or alternatively by $\vec{k} = (u, v)$. Thus, Eq. (1.32) becomes the Fourier-Stieltjes integral representation in space (ω, Θ) or (k_x, k_y) :

$$\zeta(x, y, t) = \int_{-\infty}^{\infty} \int_{-\pi}^{\pi} \exp[i(\vec{k} \cdot \vec{x} - \omega t)] d\tilde{A}(\omega, \Theta), \quad (1.34)$$

or:

$$\zeta(x, y, t) = \int_{-\infty}^{\infty} \int_{-\infty}^{\infty} \exp[i(\vec{k} \cdot \vec{x} - \omega t)] dB(\vec{k}). \quad (1.35)$$

The models implied by Eqs. (1.34) and (1.35) permit both random phases and random amplitudes.

By definition, the cross-correlation function $K(X, Y, \tau)$ is:

$$\begin{aligned} K(X, Y, \tau) &= E[\zeta(x, y, t) \zeta^*(x + X, y + Y, t + \tau)] = \\ &= \int_{-\infty}^{\infty} \int_{-\infty}^{\infty} \int_{-\pi}^{\pi} \int_{-\pi}^{\pi} E\{\exp[i(ux + vy) - i\omega t] \cdot \\ &\quad \exp[-i[u'(x + X) + v'(y + Y)] + i\omega'(t + \tau)] \cdot \\ &\quad dA(\omega, \Theta) dA^*(\omega', \Theta')\}, \end{aligned} \quad (1.36)$$

in which $(*)$ denotes the conjugate of the complex variable. The $dA(\omega, \Theta) = d\tilde{A}(\omega, \Theta)$ and $dA^*(\omega', \Theta') = d\tilde{A}^*(\omega', \Theta')$ and these are uncorrelated unless $u = u', v = v'$ and $\omega = \omega'$. Using the fact that variance of $\zeta(x, y, t)$ is finite, it can be shown that (Yaglom, 1962):

$$E[dA(\omega, \Theta) dA^*(\omega', \Theta')] = \hat{S}(\omega, \Theta) \delta(\omega - \omega') \delta(\Theta - \Theta') d\omega d\omega' d\Theta d\Theta', \quad (1.37)$$

in which $\hat{S}(\omega, \Theta)$ is a two-dimensional spectral density function of surface waves. Using Eq. (1.37) and the known relation (Lighthill, 1975):

$$\int_{-\infty}^{\infty} f(y) \delta(x - y) dy = f(x), \quad (1.38)$$

we obtain from Eq. (1.36):

$$\begin{aligned} K(X, Y, \tau) &= \int_{-\infty}^{\infty} \int_{-\pi}^{\pi} \exp[i(uX + vY + \omega\tau)] \hat{S}(\omega, \Theta) d\omega d\Theta = \\ &= \int_{-\infty}^{\infty} \int_{-\pi}^{\pi} \exp[i(\vec{k} \cdot \vec{X} + \omega\tau)] \hat{S}(\omega, \Theta) d\omega d\Theta, \end{aligned} \quad (1.39)$$

where $\vec{X} = (X, Y)$.

In a similar way, from Eq. (1.35) we have:

$$K(X, Y, \tau) = \int_{-\infty}^{\infty} \int_{-\infty}^{\infty} \exp[i(\vec{k} \cdot \vec{X} + \omega\tau)] \hat{\Psi}(\vec{k}) dk_x dk_y, \quad (1.40)$$

in which $\hat{\Psi}(\vec{k})$ is a wave number spectrum.

1.3.3.3 Wiener-Khinchine Theorem

Let us now consider wave observation at a single point $P(x, y)$; thus $X = Y = 0$. Expression (1.39) becomes the autocorrelation function:

$$K(\tau) = \int_{-\infty}^{\infty} \int_{-\pi}^{\pi} \hat{S}(\omega, \Theta) e^{i\omega\tau} d\omega d\Theta, \quad (1.41)$$

or:

$$K(\tau) = \int_{-\infty}^{\infty} \tilde{S}(\omega) e^{i\omega\tau} d\omega, \quad (1.42)$$

in which:

$$\tilde{S}(\omega) = \int_{-\pi}^{\pi} \hat{S}(\omega, \Theta) d\Theta. \quad (1.43)$$

The $\tilde{S}(\omega)$ is a frequency spectral density function or frequency spectrum of the ocean surface. It represents the distribution of wave energy in the frequency domain. Hence, the variance of surface waves is:

$$E[\zeta^2] = \sigma_{\zeta}^2 = K(0) = \int_{-\infty}^{\infty} \int_{-\pi}^{\pi} \hat{S}(\omega, \Theta) d\omega d\Theta = \int_{-\infty}^{\infty} \tilde{S}(\omega) d\omega. \quad (1.44)$$

By taking the inverse Fourier transform, we have:

$$\tilde{S}(\omega) = \frac{1}{2\pi} \int_{-\infty}^{\infty} K(\tau) e^{-i\omega\tau} d\tau. \quad (1.45)$$

Sometimes the function $\tilde{S}(\omega)$ is called the symmetric function, as $\tilde{S}(\omega) = \tilde{S}(-\omega)$. This spectrum is usually used in theoretical considerations.

In experimental practice, the so called non-symmetric spectrum $S(\omega)$ is used. It can be seen from Eqs. (1.42) and (1.45) that for ergodic stationary real random process $\zeta(t)$ with zero mean, the spectral density function $\tilde{S}(\omega)$ and the autocorrelation function $K(\tau)$ are a Fourier transform pair. This is called *the Wiener-Khinchine Theorem*, which was proved independently by Wiener in the United States and Khinchine in the Soviet Union in the early 1930s.

A few specific examples of autocorrelation functions $K(\tau)$ and spectral density functions $\tilde{S}(\omega)$ are given in Tables 1.2 and 1.3. For most processes, $K(\tau) \rightarrow 0$. The decay time which characterize this behaviour is often called correlation scale. For example, from Table 1.2 follows that a Markov process has the autocorrelation function as:

$$K(\tau) = K_0 \exp\left(-\frac{|\tau|}{\tau_0}\right), \quad (1.46)$$

in which τ_0 is the correlation scale. Hence, $\tau = \tau_0$ when $\frac{K(\tau_0)}{K_0} = e^{-1} \approx 0.368$.

Taking the limit $\tau_0 \rightarrow 0$ in Eq. (1.46) gives the autocorrelation of a white noise random process (see Table 1.2).

Table 1.2: Autocorrelation functions.

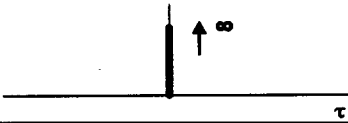
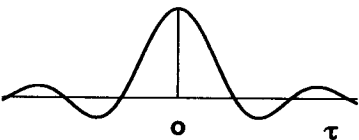
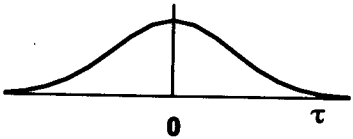
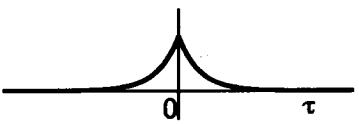
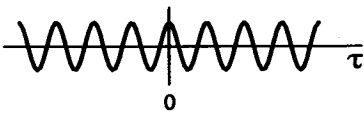
Process	$K(\tau) = \int_{-\infty}^{\infty} \tilde{S}(\omega) e^{i\omega\tau} d\omega$	
	Analytical expression	Graphical representation
White noise	$K_0 \delta(\tau)$	
Finite-band white noise	$K_0 \frac{\sin\left(\frac{\tau}{\tau_0}\right)}{\frac{\tau}{\tau_0}}$	
Gaussian	$K_0 \exp(-\alpha\tau^2)$	
Markov	$K_0 \exp\left(-\frac{ \tau }{\tau_0}\right)$	
Cosinusoidal signal with random phase	$K_0 \cos(\omega_0\tau)$	

Table 1.3: Spectral density functions.

$\tilde{S}(\omega) = \frac{1}{2\pi} \int_{-\infty}^{\infty} K(\tau) e^{-i\omega\tau} d\tau$	
Analytical expression	Graphical representation
$\frac{K_0}{\pi}$	
$K_0\tau_0$ for $ \omega \leq \tau_0^{-1}$ 0 for $ \omega > \tau_0^{-1}$	
$\frac{K_0}{\sqrt{\pi\alpha}} \exp\left(-\frac{\omega^2}{4\alpha}\right)$	
$\frac{2K_0}{\pi} \frac{\tau_0}{1 + (\omega\tau_0)^2}$	
$K_0 [\delta(\omega - \omega_0) + \delta(\omega + \omega_0)]$	

The autocorrelation function $K(\tau)$ for surface elevation $\zeta(t)$ is a real and even function, i.e. $K(\tau) = K(-\tau)$. Therefore, the spectral density $\tilde{S}(\omega)$ is also a real and even function, and Eqs. (1.42) and (1.45) can be written as follows:

$$K(\tau) = \int_{-\infty}^{\infty} \tilde{S}(\omega) e^{i\omega\tau} d\omega = 2 \int_0^{\infty} \tilde{S}(\omega) \cos(\omega\tau) d\omega, \quad (1.47)$$

and

$$\tilde{S}(\omega) = \frac{1}{2\pi} \int_{-\infty}^{\infty} K(\tau) e^{-i\omega\tau} d\tau = \frac{1}{\pi} \int_0^{\infty} K(\tau) \cos(\omega\tau) d\tau. \quad (1.48)$$

We define non-symmetric spectrum $S(\omega)$ as:

$$S(\omega) = 2\tilde{S}(\omega). \quad (1.49)$$

Therefore, Eqs. (1.47) and (1.48) take the form:

$$K(\tau) = \int_0^{\infty} S(\omega) \cos(\omega\tau) d\omega, \quad (1.50)$$

and

$$S(\omega) = \frac{2}{\pi} \int_0^{\infty} K(\tau) \cos(\omega\tau) d\tau. \quad (1.51)$$

The Eqs. (1.50) and (1.51) are frequently used in the applications.

Let us consider now the wave number spectrum $\hat{\Psi}(\vec{k})$. From Eq. (1.40) we have:

$$K(\tau) = \int_{-\infty}^{\infty} \int_{-\infty}^{\infty} e^{i\omega\tau} \hat{\Psi}(\vec{k}) dk_x dk_y = \int_0^{\infty} \int_{-\pi}^{\pi} e^{i\omega\tau} \Psi(k, \Theta) k dk d\Theta, \quad (1.52)$$

in which $k = |\vec{k}|$ and $X = Y = 0$.

In deep water, the dispersion relation (1.20) becomes $\omega^2 = gk$ and $k dk = 2 \frac{\omega^3}{g^2} d\omega$. After substituting this into Eq. (1.52) we obtain:

$$K(\tau) = \int_{-\infty}^{\infty} \int_{-\pi}^{\pi} e^{i\omega\tau} \left\{ \frac{2\omega^3}{g^2} \Psi(k, \Theta) \Big|_{k=\frac{\omega^2}{g}} \right\} d\omega d\Theta. \quad (1.53)$$

Now Eq. (1.53) can be compared with Eq. (1.41), i.e.:

$$\hat{S}(\omega, \Theta) = \frac{2\omega^3}{g^2} \Psi(k, \Theta), \quad (1.54)$$

and

$$S(\omega) = \frac{2\omega^3}{g^2} \int_{-\pi}^{\pi} \Psi(k, \Theta) d\Theta. \quad (1.55)$$

Thus, the frequency spectrum $S(\omega)$ represents an integral over the wave number spectrum $\Psi(k, \Theta)$ for all directions Θ , when k is constant and equals ω^2/g .

1.3.3.4 Cross-spectral density function

The above definitions can be immediately extended to a set of two random processes, simultaneously recorded at the same point or at two different points. As an example, we will first consider the surface elevation $\zeta(t)$ and the horizontal component of orbital velocity $u(t)$ recorded at point $P(0,0)$. Using the linear wave theory we express velocity $u(t)$ as corresponding to surface elevation $\zeta(t)$, given by Eq. (1.34), i.e.:

$$u(0,0,t) = \int_{-\infty}^{\infty} \int_{-\pi}^{\pi} \frac{gk \cos \Theta}{\omega} \frac{\cosh k(z+h)}{\cosh kh} \exp(-i\omega t) d\tilde{A}(\omega, \Theta), \quad (1.56)$$

in which z is a level at which velocity u is recorded.

The cross-correlation function $K_{\zeta u}(\tau)$ takes the form:

$$K_{\zeta u}(\tau) = E[\zeta(t)u(t+\tau)] = \int_{-\infty}^{\infty} \int_{-\infty}^{\infty} \int_{-\pi}^{\pi} \int_{-\pi}^{\pi} \frac{gk' \cos \Theta'}{\omega'} E\{\exp[i(\omega' - \omega) + i\omega'\tau]\} E\{dA(\omega, \Theta)dA^*(\omega', \Theta')\}.$$

$$E\{\exp[i(\omega' - \omega) + i\omega'\tau]\} E\{dA(\omega, \Theta)dA^*(\omega', \Theta')\}. \quad (1.57)$$

Using similar arguments to the above we can rewrite Eq. (1.57) as:

$$K_{\zeta u}(\tau) = \int_{-\infty}^{\infty} \left\{ \int_{-\pi}^{\pi} \frac{gk \cos \Theta}{\omega} \hat{S}(\omega, \Theta) d\Theta \right\} e^{i\omega\tau} d\omega. \quad (1.58)$$

Defining $S_{\zeta u}(\omega)$ as:

$$S_{\zeta u}(\omega) = \int_{-\pi}^{\pi} \frac{gk \cos \Theta}{\omega} \hat{S}(\omega, \Theta) d\Theta, \quad (1.59)$$

the Wiener-Khinchine theorem yields:

$$K_{\zeta u}(\tau) = \int_{-\infty}^{\infty} S_{\zeta u}(\omega) e^{i\omega\tau} d\omega, \quad (1.60)$$

and

$$S_{\zeta u}(\omega) = \frac{1}{2\pi} \int_{-\infty}^{\infty} K_{\zeta u}(\tau) e^{-i\omega\tau} d\tau. \quad (1.61)$$

In general $S_{\zeta u}(\omega)$ is a complex function, i.e.:

$$S_{\zeta u}(\omega) = C_{\zeta u}(\omega) + i Q_{\zeta u}(\omega), \quad (1.62)$$

in which the real part $C_{\zeta u}(\omega)$ is referred to as the *co-spectrum*, while the imaginary part $Q_{\zeta u}(\omega)$ is referred to as the *quadrature spectrum*. The amplitude spectrum of $S_{\zeta u}(\omega)$ becomes:

$$S_{\zeta u}(\omega) = \sqrt{[C_{\zeta u}(\omega)]^2 + [Q_{\zeta u}(\omega)]^2}, \quad (1.63)$$

and the phase spectrum is given by:

$$\varphi(\omega) = \tan^{-1} \left\{ \frac{Q_{\zeta u}(\omega)}{C_{\zeta u}(\omega)} \right\}^{1/2}. \quad (1.64)$$

The various properties of the co- and quadrature spectra can be found elsewhere (for example, Bendat and Piersol, 1986; Ochi, 1990)

The two-dimensional spectrum of surface waves $\hat{S}(\omega, \Theta)$ is commonly represented as a product of a frequency spectrum $S(\omega)$ and directional spreading function $D(\Theta; \omega)$, i.e.:

$$\hat{S}(\omega, \Theta) = S(\omega) D(\Theta; \omega). \quad (1.65)$$

Function $D(\Theta; \omega)$ will be discussed in detail in Section 3.3.

After substituting Eq. (1.65) into Eq. (1.58) and using Eq. (1.62), we obtain:

$$\left. \begin{aligned} C_{\zeta u}(\omega) &= \frac{gk}{\omega} S(\omega) \int_{-\pi}^{\pi} D(\Theta; \omega) \cos \Theta d\Theta \\ Q_{\zeta u}(\omega) &= 0 \end{aligned} \right\}. \quad (1.66)$$

The vanishing of the quadrature spectrum $Q_{\zeta u}(\omega)$ is a consequence of the assumption that sea surface oscillation $\zeta(t)$ and wave-induced horizontal velocity $u(t)$ are given in the same point and that there is no time delay between them.

We now consider the case when surface elevation is simultaneously recorded in two points, i.e. point $P(x, y,)$ and $P_1(x + X, y + Y)$. Eq. (1.39) for cross-correlation function yields:

$$K(X, Y, \tau) = \int_{-\infty}^{\infty} \int_{-\pi}^{\pi} \exp \{ ikd \cos(\theta - \theta_0) + i\omega\tau \} \hat{S}(\omega, \theta) d\omega d\theta, \quad (1.67)$$

in which $d = \sqrt{X^2 + Y^2}$ and $\tan^{-1}\theta_0 = \frac{Y}{X}$. Now the Wiener-Khinchine theorem yields:

$$\hat{S}(\omega, \theta; d, \theta_0) = \int_{-\pi}^{\pi} \exp [ikd \cos(\theta - \theta_0)] \hat{S}(\omega, \theta) d\omega d\theta. \quad (1.68)$$

Using the identity (Abramowitz and Stegun, 1975):

$$\exp [ikd \cos(\theta - \theta_0)] = \sum_{m=0}^{\infty} \epsilon_m i^m J_m(kd) \cos m(\theta - \theta_0), \quad (1.69)$$

($\epsilon_0 = 1$ and $\epsilon_m = 2$ ($m \geq 1$); $J_m(x)$ is a first kind of Bessel function of m order) and separating the real and imaginary parts we obtain co-spectrum $C(\omega; d, \theta_0)$ and quadrature spectrum $Q(\omega; d, \theta_0)$ in the form:

$$C(\omega; d, \theta_0) = J_0(kd) + 2 \sum_{m=1}^{\infty} (-1)^m J_{2m}(kd) \cos [2m(\theta - \theta_0)], \quad (1.70)$$

and

$$Q(\omega; d, \theta_0) = 2 \sum_{m=0}^{\infty} (-1)^m J_{2m+1}(kd) \cos [(2m+1)(\theta - \theta_0)]. \quad (1.71)$$

Chapter 2

Generation of Waves by Wind

2.1 Introduction

At the initial stage of wave generation, the turbulent fluctuations of the atmospheric pressure induce small waves, of almost regular form, called capillary waves. These waves are usually unstable and attenuate, due to surface tension, when the wind calms. When wind velocity increases, waves grow and gravity forces are sufficient to support the wave motion. Wave growth is not infinite; when waves reach their limiting steepness (about $1/7$ in deep water), they break in the form of white caps or spilling or plunging breakers (Massel, 1989; Banner and Peregrine, 1993).

Knowledge on the mechanisms of generation, interaction and decay of ocean waves has been accumulated during the last 70 years. However, modern understanding of the dynamic processes involved has developed only within the last 40 years. The starting points of contemporary wave generation models are the pressure fluctuations and variations in shear stresses at the water surface, associated with the airflow over the waves. Hence, prior to a discussion of particular wave generation models, basic information on physics of the air boundary layer above the sea surface and on the similarity laws for wind-induced waves will be provided.

The key technique of the analysis of the air boundary layer is the formulation of the similarity laws for drag coefficient C_z and roughness length z_0 . Although the initial set of defining parameters comprises many variables, substantial simplifications are possible for some typical atmospheric flows, such as the smooth wind flow over sea surfaces, and fully rough flow. Furthermore, as was shown by Kitaigorodskii (1962), the similarity approach can also be applied to provide the first insight into a problem of an evolution of the wind wave spectra in time and space. Pierson and Moskowitz (1964) and Hasselmann et al. (1973) successfully used the Kitaigorodskii (1962) similarity arguments to analyse experimental data from their field experiments in the Atlantic Ocean and the North Sea, respectively.

The second purpose of this Chapter is to discuss the present wave generation models. In spite of the clear connection between wind and waves, and a long history

of theoretical efforts, only in the 1950s and 60s was a basic understanding of the mechanisms of wind-wave generation acquired. In 1956 Ursell, in his review of actual wind-wave generation theories, concluded that all available theories were grossly inadequate to account for observations (Ursell, 1956). One year later, the independent and complementary works of Phillips (1957) and Miles (1957) provided the cornerstones on which now rests our theoretical understanding of wind-wave generation.

Phillips' model of wind-wave generation is based on the assumption that the atmospheric turbulent pressure fluctuations are undisturbed by the waves and are advected over the sea surface at some velocity U related to the wind speed. Phillips showed that resonance is possible between the advected pressure and those waves which travel at the right speed to keep the forcing.

The resonance mechanism accounts for the excitation and initial growth of waves on an undisturbed water surface. However, it is too weak to support the continued growth of wind waves. Once waves have appeared on the sea surface, their presence modifies the air flow. This effect may be analyzed through linear stability for the coupled air-water motion. Miles (1957) used the simplest inviscid form of the stability theory, i.e. Rayleigh's equation in the air and Laplace's equation in the water with suitable matching and boundary conditions. In this idealized model, the turbulence does not participate explicitly in the momentum transfer to the sea surface, which is entirely through pressure forces. The resulting wave number spectrum of the surface waves is growing much rapidly in time than in the case of the Phillips resonance mechanism.

Instead of discussing the Phillips and Miles solutions separately, in Section 2.4.2 we discuss the extended wave generation theory in which Phillips' resonance mechanism is combined with Miles' shear flow approach. The comparison with experiments showed that the Phillips' theory accounts reasonably well for the initial wave growth. However, the major portion of the spectral development occurs due to Miles' mechanism. The experimental results are in agreement with Miles' theory by an order of magnitude, although the theory still predicts energy transfer rates that are smaller than measured values.

The Phillips-Miles theory was (and still is) reviewed and supplemented by many authors (Kinsman, 1965; Krasitskii, 1980; Krasitskii and Zaslavskii, 1978; Riley et al., 1982; Krylov et al., 1986; Jacobs, 1987; Janssen, 1989, 1991; Chalikov and Makin, 1991; Komen et al., 1994; and others). Some of these extensions and improvements will be given in this Chapter to better clarify physical processes involved in the generation of waves by wind.

In particular, we will show that water depth and molecular viscosity have a negligible effect on the resonance type mechanism. However, the discussion gives an opportunity to develop the relations for the minimum gravity wave phase and length. It was also demonstrated that inclusion of the wave-turbulence interaction provides an additional mechanism for energy transfer from wind to waves.

Furthermore, the analysis is presented to estimate the impact of wind-generated

waves on airflow. This impact, expressed in terms of wave-induced stress at the sea surface depends on the wave age. It becomes a considerable part of the total stress for the 'young' sea and is negligible for an 'old' sea.

In Miles' laminar wave generation model, a linear-logarithmic flow in air is assumed and water is at rest, i.e. the wind-induced current is neglected. Numerical analysis, given in Section 2.4.8, indicates that the influence of the current profile on the wave growth is not negligible.

The remaining Section 2.5 introduces the spectral representation of the wave energy balance which is extensively used in the following Chapters.

2.2 Airflow over sea surface

2.2.1 Atmospheric boundary layer above water

The atmosphere-ocean system acts as a coupled thermodynamic system, in which the response of one fluid to the forcing imposed by the other, leads to a change in the interfacial conditions and to the exchange rates. We are not concerned here with the general description of the coupled ocean-atmosphere interaction, but rather with the dynamics of the thin surface boundary layer [$O(10m)$].

The surface boundary layer is treated as a layer of constant vertical fluxes of momentum, heat and humidity. The idea of constant fluxes is based on the analysis of the mean horizontal momentum equation:

$$\frac{\partial \vec{U}_h}{\partial t} + (\vec{U} \cdot \nabla_h) \vec{U}_h = f_c \vec{U}_h \times \vec{k} - \frac{1}{\rho_a} \nabla_h p + \frac{1}{\rho_a} \frac{\partial \vec{\tau}_h}{\partial z}, \quad (2.1)$$

in which \vec{U} is a mean wind velocity vector, \vec{U}_h is its horizontal component, f_c is the Coriolis parameter ($f_c = 1.454 \cdot 10^{-4} \sin \varphi$, where φ is a latitude), \vec{k} is a vertical unit vector, ∇_h is the horizontal gradient operator:

$$\nabla_h = \frac{\partial}{\partial x} \vec{i} + \frac{\partial}{\partial y} \vec{j}, \quad (2.2)$$

and $\vec{\tau}_h$ is the horizontal stress vector, ρ_a is air density, and p is pressure.

Under the steady-state and horizontally homogeneous conditions, the left-hand side of Eq. (2.1) vanishes leaving a balance between the Coriolis term, the horizontal pressure gradient, and the vertical stress gradient as:

$$-f_c \vec{U}_h \times \vec{k} + \frac{1}{\rho_a} \nabla_h p = \frac{1}{\rho_a} \frac{\partial \vec{\tau}_h}{\partial z}. \quad (2.3)$$

Integrating Eq. (2.3) from $z = 0$ (water surface) to some height h_p gives:

$$\int_0^{h_p} \left[-f_c \vec{U}_h \times \vec{k} + \frac{1}{\rho_a} \nabla_h p \right] dz = \frac{1}{\rho_a} [(\vec{\tau}_h)_{h_p} - (\vec{\tau}_h)_0]. \quad (2.4)$$

If h_p is selected sufficiently small, the influence of the integral on the left-hand side of Eq. (2.4) can be neglected, if compared with $(\bar{\tau}_h)_0/\rho_a$. Thus, for neutral stratification we obtain:

$$(\bar{\tau}_h)_{h_p} \approx (\bar{\tau}_h)_0 \approx \text{const}, \quad (2.5)$$

with accuracy 10–20% in the layer $h_p \approx 10 - 50$ m (Kitaigorodskii, 1970).

At the water surface, the stress $|(\bar{\tau}_h)_0| = \tau_0$ is usually represented as:

$$\frac{\tau_0}{\rho_a} = u_*^2 = \nu_a \frac{\partial U}{\partial z} - \overline{u'w'} = \text{const}, \quad (2.6)$$

in which ν_a is the kinematic viscosity of air, U is a mean horizontal wind velocity (subscript h was omitted for convenience), u' and w' are the horizontal and vertical components of random velocity fluctuations, respectively. The over bar indicates averaging in time.

In a very thin sublayer (~ 1 mm), adjacent to the surface, turbulence is suppressed and the term $\left(\nu_a \frac{\partial U}{\partial z}\right)$ in Eq. (2.6) dominates. Hence, the velocity profile becomes linear:

$$U \sim \frac{u_*^2}{\nu_a} z. \quad (2.7)$$

On the other hand, within the turbulent sublayer far from the surface, the tangential stress is equal to the momentum flux:

$$\tau = -\rho_a \overline{u'w'}. \quad (2.8)$$

The description of constant stress layer for stationary and homogeneous conditions is based on the Monin-Obukhov similarity theory (Monin and Yaglom, 1965). In this theory, the following scales for velocity and temperatures play an important role:

$$u_* = \left(\frac{\tau}{\rho_a}\right)^{1/2}, \quad (2.9)$$

and

$$T_* = -\frac{q_\Theta}{\kappa c_p \rho_a u_*}. \quad (2.10)$$

Using Eqs. (2.9) and (2.10), the scale of length L results:

$$L = -\frac{c_p \rho_a u_*^3 \Theta}{\kappa q_\Theta}, \quad (2.11)$$

where c_p is a specific heat at constant pressure, Θ is the absolute temperature, q_Θ is a vertical heat flux, u_* is a friction velocity, and $\kappa = 0.4$ is a Karman constant.

According to the Monin-Obukhov similarity hypothesis, the non-dimensional characteristics obtained from velocity measurements using a scale u_* , temperature measurements using a scale T , and length measurements using a scale L , should be functions of non-dimensional parameter $\zeta = z/L$ only. Parameter ζ represents a local criterion of the hydrostatic stability. If $\zeta < 0$, heat flux is directed from the ocean surface to the atmosphere and stratification is unstable; for $\zeta > 0$, heat flux is directed towards the sea surface and stratification is stable. For $\zeta = 0$, stratification is neutral, when buoyancy effects can be neglected.

The similarity arguments provide the following expression for the vertical velocity gradient in the constant stress layer:

$$\frac{\partial U(z)}{\partial z} = \frac{u_*}{\kappa z} \phi_u(\zeta), \quad (2.12)$$

in which $\phi_u(\zeta)$ is a universal function. Function $\phi_u(\zeta)$ must be determined empirically from the flux profile relation (2.12). For the neutral stratification, $\phi_u(0) = 1$ and integration of Eq. (2.12) from $z = z_0$ to z , yields the known logarithmic profile for wind velocity:

$$U(z) = \frac{u_*}{\kappa} \ln \left(\frac{z}{z_0} \right), \quad (2.13)$$

where z_0 is the vertical origin of the velocity profile or roughness length. The length z_0 will be discussed in the next Section.

When stratification is not stable, the velocity profile takes the form (Donelan, 1990):

$$U(z) = \frac{u_*}{\kappa} \left[\ln \left(\frac{z}{z_0} \right) - \psi_u(\zeta) \right], \quad (2.14)$$

in which:

$$\psi_u(\zeta) = \int_{\zeta_0}^{\zeta} \frac{1 - \phi_u(\zeta)}{\zeta} d\zeta. \quad (2.15)$$

The motion of surface waves contaminates the logarithmic vertical profile of wind velocity and wave components are observed in the spectrum of wind velocity. Assuming that wind flows smoothly over the low-frequency wave components, Kitaigorodskii and Volkov (Kitaigorodskii, 1970) argued that the modified profile of mean wind velocity should be expressed as:

$$U(z) = \frac{u_*}{\kappa} \left[\ln \left(\frac{z}{z_0} \right) - \frac{1}{2} \left(\frac{\sigma_\zeta}{z} e^{-k_p z} \right)^2 \right], \quad (2.16)$$

and the variance of random velocity fluctuations becomes:

$$\sigma_{u'}^2 = \overline{u'^2} = \sigma_{u_0}^2 + \frac{u_*^2}{\kappa} \left[\left(\frac{\sigma_\zeta}{z} e^{-k_p z} \right)^2 + \frac{1}{2} \left(\frac{\sigma_\zeta}{z} e^{-k_p z} \right)^4 \right], \quad (2.17)$$

in which k_p is a wave number corresponding to peak frequency ω_p , σ_ζ is a standard deviation of surface elevation, and $\sigma_{u_0}^2$ is a variance of downwind velocity fluctuations in a logarithmic layer without surface waves.

In the neutrally stratified boundary layer, the corrections due to surface waves are not substantial and the observed velocity profile becomes logarithmic, starting from a few centimeters above water surface.

2.2.2 Similarity laws for drag coefficient C_z and roughness length z_0

Consider the wind blowing from land over the sea surface characterized by uniform roughness. The convenient expression of this roughness is a drag coefficient C_z , usually written as:

$$C_z = \frac{\tau_0}{\rho_a U^2(z)} = \left(\frac{u_*}{U(z)} \right)^2. \quad (2.18)$$

In routine meteorological observations, wind speed is measured at the anemometer height $z = 10$ m above mean sea surface, i.e. $U(10) \equiv U_{10}$ and $C_z = C_{10}$. In general, the experimental data on the drag coefficient C_z show a large scatter, typically from $3 \cdot 10^{-4}$ to $5 \cdot 10^{-3}$, and functional dependence on wind speed is not well pronounced. Garratt (1977), in his comprehensive review of drag coefficients over oceans and continents, suggested that in the velocity range $4 < U < 21$ m/s, C_{10} can be approximated by a power law relation:

$$C_{10} \approx 0.51 \cdot 10^{-3} U^{0.46}, \quad (2.19)$$

or by a linear form:

$$C_{10} \approx (a + bU) \cdot 10^{-3}, \quad (2.20)$$

in which $a = 0.75$ and $b = 0.067$. The values of a and b , reported by other authors, vary as $0 < a < 1.18$ and $0.016 < b < 0.100$ (Krylov et al., 1986). Wu (1982) has shown that formula (2.20) with $a = 0.8$ and $b = 0.065$ closely fits the data throughout the entire wind velocity range, even for hurricane winds.

Substituting Eq. (2.18) into (2.13) we obtain the relationship between drag coefficient C_z and roughness length z_0 in the form:

$$C_z = \kappa^2 \left[\ln \left(\frac{z}{z_0} \right) \right]^{-2}. \quad (2.21)$$

In two extreme marine atmospheric conditions, i.e. for smooth flow and fully rough flow, the roughness length takes simple form. For smooth flow, when roughness elements are buried within the viscous sublayer and the outer flow remains unperturbed

by these elements, the length z_0 depends solely on the friction velocity u_* and kinematic viscosity ν_a :

$$z_0 = m \frac{\nu_a}{u_*}, \quad (2.22)$$

in which m is a constant ($m \approx 0.11$).

With increasing u_* , the viscous sublayer decreases and roughness elements begin to interact with the outer turbulent flow, thus causing some additional form drag. In the case of seas near to full development, when the flow is fully aerodynamically rough, the roughness length is proportional to the height of roughness elements ($z_0 \sim h_0$) and most of the stress is supported by short gravity waves. In this case, the z_0 length is given by the Charnock's formula:

$$z_0 = m \frac{u_*^2}{g}. \quad (2.23)$$

The coefficient m varies from $0.3 \cdot 10^{-2}$ to $8.0 \cdot 10^{-2}$. Garratt (1977) gives $m = 1.44 \cdot 10^{-2}$.

More precise and systematic insight into the dependence of C_{10} and z_0 on hydro-meteorological conditions may be obtained using the similarity approach. The set of defining parameters comprises: wind fetch X , wind velocity $U(z)$ at z level above mean sea surface, friction velocity u_* , water depth h , Monin-Obukhov length L (see Eq. 2.11), kinematic viscosity of air and water, ν_a and ν_w , air and water densities ρ_a and ρ_w , and gravitational acceleration g . Using these parameters, the following non-dimensional expression for C_z can be formulated (Krylov et al., 1986):

$$C_z = \left[\frac{u_*}{U(z)} \right]^2 = F_1 \left(\mathbf{Re}_z, \mathbf{Re}_x, \mathbf{Re}_h, \mathbf{Fr}, \zeta, \frac{\nu_a}{\nu_w}, \frac{\rho_a}{\rho_w} \right), \quad (2.24)$$

in which $\mathbf{Re}_z = \frac{u_* z}{\nu_a}$ is a 'vertical' Reynolds number, $\mathbf{Re}_x = \frac{u_* X}{\nu_a}$ is a 'horizontal' Reynolds number, $\mathbf{Re}_h = \frac{u_* h}{\nu_a}$ is a Reynolds number related to water depth, $\mathbf{Fr} = \frac{u_*}{\sqrt{gz}}$ is a Froude number, and $\zeta = \frac{z}{L}$ is a stratification parameter.

Assuming that $\frac{\rho_a}{\rho_w}$ and $\frac{\nu_a}{\nu_w}$ are constants, Eq. (2.24) simplifies as:

$$C_z = F_2(\mathbf{Re}_z, \mathbf{Re}_x, \mathbf{Re}_h, \mathbf{Fr}, \zeta). \quad (2.25)$$

Further simplification applies for deep and shallow waters, i.e.:

$$C_z = F_3(\mathbf{Re}_z, \mathbf{Re}_x, \mathbf{Fr}, \zeta) \quad - \quad \text{for deep water}, \quad (2.26)$$

and

$$C_z = F_4(\mathbf{Re}_z, \mathbf{Re}_h, \mathbf{Fr}, \zeta) \quad - \quad \text{for shallow water}. \quad (2.27)$$

For small Reynolds numbers \mathbf{Re}_x (close to the shore line or in the initial stage of wave generation), the roughness of the sea surface due to waves is not present or is buried within the viscous sublayer. Therefore, the airflow can be classified as a smooth flow over the sea surface and the drag coefficient in the deep sea depends on \mathbf{Re}_x and ζ only:

$$C_z = F_5(\mathbf{Re}_x, \zeta), \quad (2.28)$$

for $0 < \mathbf{Re}_x < (\mathbf{Re}_x)_{cr}$. The critical Reynolds number $(\mathbf{Re}_x)_{cr}$ corresponds to the stage when the viscous sublayer thins and the roughness elements begin to interact directly with the turbulent outer flow.

For large Reynolds numbers \mathbf{Re}_x , the drag coefficient is no longer dependent on wind fetch X and kinematic viscosity ν_a . Therefore, Eq. (2.26) becomes:

$$C_z = F_6(\mathbf{Fr}, \zeta). \quad (2.29)$$

The similarity laws for roughness length z_0 are simpler than for parameter C_z as the lengths z and L are excluded from the set of defining parameters (Krylov et al., 1986):

$$\tilde{z}_0 = \Pi_1(\tilde{u}_*, \mathbf{Re}_x, \mathbf{Re}_h), \quad (2.30)$$

where $\tilde{z}_0 = \frac{gz_0}{u_*^2}$ is non-dimensional roughness length, and $\tilde{u}_* = \frac{u_*}{\sqrt[3]{g\nu_a}}$ is non-dimensional friction velocity.

Some simplifications of the relation (2.30) can be derived for deep and shallow waters, i.e.:

$$\tilde{z}_0 = \Pi_2(\tilde{u}_*, \mathbf{Re}_x) \quad - \quad \text{for deep water}, \quad (2.31)$$

and

$$\tilde{z}_0 = \Pi_3(\tilde{u}_*, \mathbf{Re}_h) \quad - \quad \text{for shallow water}. \quad (2.32)$$

Moreover, for smooth flow over the sea surface we write:

$$\tilde{z}_0 = \Pi_4(\tilde{u}_*), \quad (2.33)$$

or:

$$z_0 = \frac{u_*^2}{g} \Pi_4(\tilde{u}_*). \quad (2.34)$$

For a smooth flow z_0 should not depend on g , but on ν_a and u_* , i.e.:

$$\frac{u_*^2}{g} \Pi_4\left(\frac{u_*}{\sqrt[3]{g\nu_a}}\right) \rightarrow m \frac{\nu_a}{u_*}, \quad (2.35)$$

or:

$$\Pi_4\left(\frac{u_*}{\sqrt[3]{g\nu_a}}\right) \rightarrow m \frac{\nu_a g}{u_*^3} = m \left(\frac{u_*}{\sqrt[3]{g\nu_a}}\right)^{-3}. \quad (2.36)$$

Thus, Eq. (2.33) yields:

$$\tilde{z}_0 = m \tilde{u}_*^{-3}, \quad (2.37)$$

while from Eq. (2.34) we obtain:

$$m = \frac{u_* z_0}{\nu_a} = \mathbf{Re}_{z_0}, \quad (2.38)$$

in which \mathbf{Re}_{z_0} is a roughness Reynolds number.

In the inertial interval for large wind fetch and deep sea, length \tilde{z}_0 becomes:

$$\tilde{z}_0 = \frac{gz_0}{u_*^2} = m, \quad (2.39)$$

where m is a constant. Eq. (2.39) is identical with Charnock's formula (2.23).

2.2.3 Practical applications

We now apply the formulated similarity laws to the analysis of experimental data on C_z and z_0 . In the smooth flow stage, the laboratory experiments by Kunishi (1963) indicate that constant m in Eq. (2.37) is equal 0.11, i.e.:

$$z_0 = 0.11 \frac{\nu_a}{u_*} \quad \text{for } u_* < 2(\nu_a g)^{1/3}. \quad (2.40)$$

However, Krylov et al. (1986) field data suggest that $m = 0.46$. Substituting Eq. (2.40) into Eq. (2.21) gives:

$$C_z = \kappa^2 \left[\ln \left(\frac{zu_*}{0.11\nu_a} \right) \right]^{-2}, \quad (2.41)$$

or

$$C_z = [2.5 \ln (\mathbf{Re}_z) + 5.52]^{-2}. \quad (2.42)$$

In the case of seas near to full development, most of the stress is supported by short gravity waves and the influence of the viscous sublayer can be neglected. A comparison of laboratory experiments (when $\mathbf{Re}_x > 6 \cdot 10^5$ and $u_* > 0.6$ m/s) with Eq. (2.39) is given in Fig. 2.1, from which a value of $m = 0.021$ was found. The drag coefficient, as determined by Eq. (2.29) for neutral stratification, becomes:

$$C_z = \kappa^2 \left[\ln \left(\frac{gz}{mu_*^2} \right) \right]^{-2}, \quad (2.43)$$

or

$$C_z = \left[2.5 \ln \left(\frac{1}{\mathbf{Fr}^2} \right) + 9.66 \right]^{-2}. \quad (2.44)$$

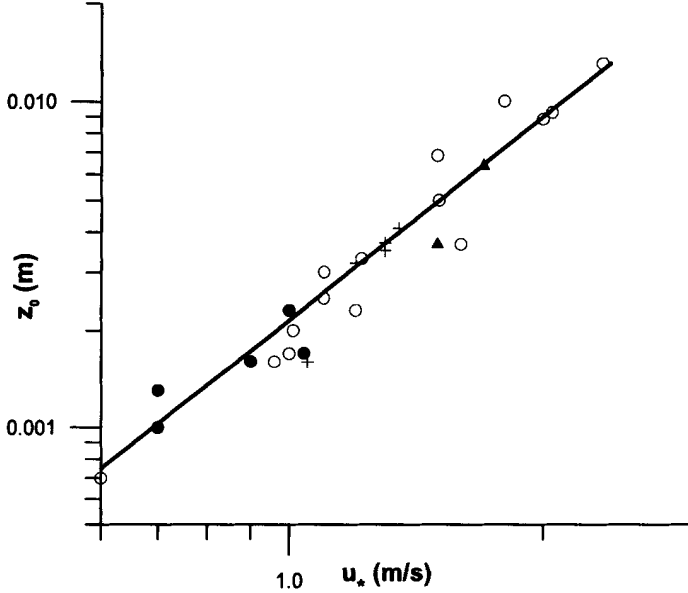


Figure 2.1: Roughness length z_0 versus friction velocity u_* . Data from Krylov et al. (1986). The solid line corresponds to Charnock's formula with $m = 0.021$.

Eq. (2.44) is compared with various field data in Fig. 2.2. Wind velocity varies from 5 m/s to 53 m/s. The critical Reynolds number Re_x , from which the similarity law (2.39) satisfies, is approximately equal $\text{Re}_x \approx 10^{10}$.

In the transitional regime, with increasing friction velocity u_* , the roughness length z_0 also increases to reach the fully aerodynamically rough stage, as discussed above. The laboratory experimental data indicate that relationship (2.31) takes then the simple form (Krylov et al., 1986):

$$\tilde{z}_0 = m \text{Re}_x. \quad (2.45)$$

The coefficient m for neutral stratification is equal 10^{-7} for $\tilde{u}_* < 9.8$ and $6.0 \cdot 10^{-8}$ for $\tilde{u}_* > 9.8$. The relationship (2.45) is also satisfied in the field experiments with coefficient $m = (2.04 \pm 0.65) \cdot 10^{-12}$ and for $\tilde{u}_* > 10$. For the drag coefficient we obtain:

$$C_z = \left\{ 2.5 \left[\ln \left(\frac{1}{\text{Fr}^2} \right) - \ln (\text{Re}_x) + 1.69 \right] \right\}^{-2}. \quad (2.46)$$

When waves propagate in water of finite depth, the roughness length should be determined from Eq. (2.30). Using the data of Mitsuyasu et al. (1971) and Snyder (1974),

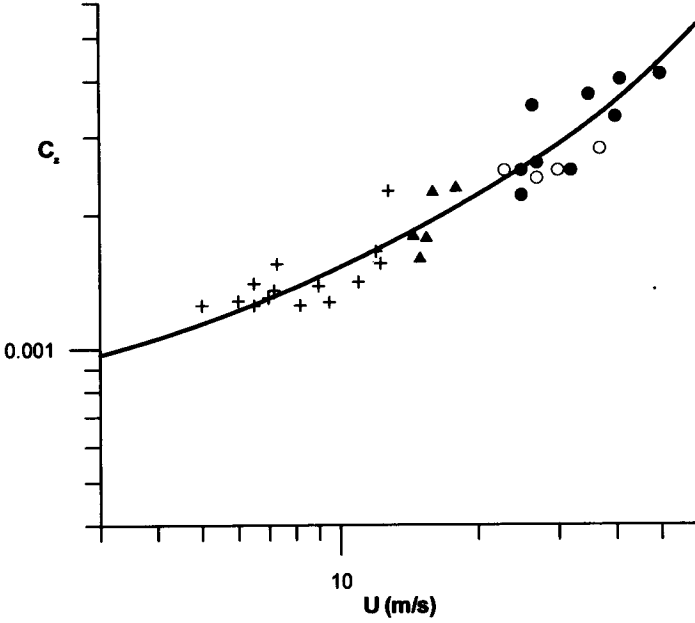


Figure 2.2: Comparison of Eq.(2.44) with field data (after Strekalov and Krivitskii, 1983).

Krivitskii and Strekalov (1985) found that:

$$\tilde{z}_0 = 8.65 \cdot 10^{-5} \frac{\text{Re}_x}{\text{Re}_h}, \quad (2.47)$$

and

$$C_z = \left\{ 2.5 \left[\ln \left(\frac{1}{\text{Fr}^2} \right) + \ln \left(\frac{\text{Re}_h}{\text{Re}_x} \right) + 4.05 \right] \right\}^{-2}. \quad (2.48)$$

In the similarity laws developed above, the roughness length z_0 and drag coefficient C_z are not directly dependent on wave parameters. This dependence is only through the friction velocity u_* , wind fetch X , and water depth h . Therefore, it would be desirable to complete the similarity laws by procedures which account for direct wave contribution to the surface roughness.

Kitaigorodskii (1970) suggests including the mobility of the roughness elements (say surface waves) into similarity laws in the form:

$$\frac{U(z)}{u_*} = \frac{1}{\kappa} \ln \left(\frac{z}{a \exp(-k_p C / u_*)} \right). \quad (2.49)$$

Thus:

$$z_0 \approx a \exp \left(-\frac{k_p C}{u_*} \right), \quad (2.50)$$

in which a is a wave amplitude, k_p is a wave number corresponding to the peak frequency and C is a phase velocity. Including the additional effect of varying steepness across the spectrum yields another formula for z_0 :

$$z_0 \approx 0.3 \sigma_\zeta \exp \left(-\frac{k_p C}{u_*} \right), \quad (2.51)$$

where σ_ζ is a standard deviation of the surface waves.

For fully rough flow, the roughness length z_0 can be parameterized by the simple regression equation (Donelan, 1990):

$$\frac{z_0}{\sigma_\zeta} = A \left(\frac{U_{10}}{C} \right)^B, \quad (2.52)$$

in which $A = 5.53 \cdot 10^{-4}$ and $B = 2.66$ for field data and $9.76 \cdot 10^{-6}$ and 3.48 for laboratory data, respectively.

Hsu (1974) modified Charnock's formula (2.23) to allow m to be a function of the wave steepness and obtained:

$$z_0 = \frac{1}{2\pi} \left(\frac{\sqrt{gH}}{C} \right)^2 \frac{u_*^2}{g}, \quad (2.53)$$

in which H is a wave height. In fact, the coefficient $m = \frac{1}{2\pi} \left(\frac{\sqrt{gH}}{C} \right)^2 = \frac{1}{2\pi} \left(\frac{C^2}{g} \right)$ is

proportional to the wave steepness. For neutral stratification a corresponding drag coefficient C_z (see Eq. (2.29)) becomes:

$$C_z = \frac{1}{6.25} \left\{ \ln \left(\frac{1}{Fr^2} \right) + \ln \left[2\pi \left(\frac{C}{\sqrt{gH}} \right)^2 \right] \right\}^{-2}. \quad (2.54)$$

Hsu's result appears to be in agreement with various field and laboratory data. However, his prediction of the roughness at full development is somewhat larger than that given by Charnock's formula (2.23).

There is some experimental evidence on the wave age dependence of the drag coefficient C_z . The wave age parameter is a practical indicator of the stage of development of the wind sea. A 'young' sea, when $\frac{U_{10}}{C} \geq 1$ (or when $\frac{C}{u_*} \leq 10$), refers to a sea state where waves have just been generated by wind. An 'old' sea, when $\frac{U_{10}}{C} \leq 1$, (or when $\frac{C}{u_*} \geq 10$), corresponds to a saturated sea. Donelan (1982) showed that the drag coefficient of airflow over a young sea is about 50% larger than the drag coefficient over an old sea. The theoretical explanation of the wave age dependence of the drag coefficient was given by Janssen (1989). His model is discussed in Section 2.4.7.

2.3 Similarity laws for wind-induced waves

The atmosphere-ocean system is a coupled thermodynamic system in which the response of one fluid to the forcing imposed by the other leads to substantial changes of the interfacial (for instance, sea surface) conditions. The solution of the boundary value problem for the sea surface and prediction of surface wave growth is still a very demanding task due to the complexity of atmospheric forcing, evolution and dissipation processes.

In such circumstances, similarity and dimensional methods provide at least the first insight into a problem. Historically, the first attempt to apply some universal relationships for heights and periods of wind waves was suggested by Sverdrup and Munk (1947). They developed graphs for dependence of non-dimensional significant wave height $\frac{gH_s}{U^2}$ and non-dimensional phase velocity $\frac{C}{U}$ on non-dimensional fetch $\frac{gX}{U^2}$ and non-dimensional wind duration $\frac{gt}{U}$. Kitaigorodskii (1962, 1970) was the first to apply similarity principles and dimensional analysis to study the evolution of the wind wave spectra in time and space.

We consider first the wave train generated by constant wind blowing over an unlimited sea surface. The statistical characteristics of such waves depend on the wind duration t , but not the fetch X . According to Kitaigorodskii, the full set of parameters determining the frequency spectrum $S(\omega)$ of surface waves is:

$$S(\omega) = F(\rho_a, \rho_w, \nu_a, \nu_w, \gamma, g, U_\infty, f_c, t, \omega), \quad (2.55)$$

in which ρ_a and ρ_w are densities of air and water, respectively; ν_a and ν_w are kinematic viscosities of air and water, respectively; γ is the ratio of surface tension to water density; U_∞ is a mean wind velocity at the upper limit of the atmospheric boundary layer, independent of time t and vertical coordinate z , and f_c is the Coriolis parameter.

For the effective application of the similarity theory, the number of non-dimensional combinations of parameters listed in Eq. (2.55) should be relatively small. Therefore, we assume additionally that:

1. Wave motion is irrotational and the influence of molecular viscosity ν_w can be neglected.
2. Only the gravitational part of the spectrum $S(\omega)$ is considered; the influence of surface tension is neglected and frequency ω is restricted to the range

$$\omega \ll \omega_\gamma = \left(\frac{4g^3}{\gamma} \right)^{1/4}. \quad (2.56)$$

3. Nonlinear interactions between spectral components are neglected.

4. The energy transfer from the wind to the sea surface is only due to the atmospheric boundary layer adhering to the sea surface. As the characteristic height of the boundary layer is $h_p = U_\infty/f_c$ and wave number k satisfies the relation $kh_p \gg 1$, we obtain the following condition for wave frequency ω :

$$\omega \gg \left(\frac{g f_c}{U_\infty} \right)^{1/2}. \quad (2.57)$$

Assuming that Eq. (2.57) is satisfied, the Coriolis parameter f_c can be omitted in the set of parameters in Eq. (2.55).

5. In fact, the first and second assumptions imply that the main part of wind energy is transferred to waves by the normal stresses. Moreover, we assume that high-frequency wave components, when $\omega \gg \omega_\gamma$, play a negligible role in the distribution of these stresses along the sea surface. This is probably not true for the initial stage of wave generation, when the capillary waves are generated first on the previously calm sea surface. However, by neglecting the initial stage of wave generation, i.e., $t > t_i(\omega)$, we can neglect the parameters ν_a and γ in Eq. (2.55).
6. The influence of molecular air viscosity is important only at the initial stage of wave growth. Then the viscous sublayer may redistribute the wind stresses, which are responsible for energy transfer to surface gravity waves for $\omega \ll \omega_\gamma$. However, following Phillips (1957) and Miles (1962) we can neglect this mechanism (and also parameter ν_a) from consideration, assuming that:

$$\omega \ll \left(\frac{g U_\infty}{\nu_a} \right)^{1/2}. \quad (2.58)$$

Considering that the ratio of air and water densities is a constant, Eq. (2.55) finally becomes:

$$S(\omega) = F(\omega, g, U_\infty, t) \quad \text{at} \quad \begin{cases} \omega \ll \omega_\gamma \\ t \gg t_i(\omega) \end{cases}, \quad (2.59)$$

or

$$\frac{S(\omega)g^3}{U_\infty^5} = \varphi \left(\frac{\omega U_\infty}{g}, \frac{gt}{U_\infty} \right) \quad \text{at} \quad \begin{cases} \frac{\omega U_\infty}{g} \ll \left(\frac{4U_\infty^4}{g\gamma} \right)^{1/4} \\ \frac{gt}{U_\infty} \gg \frac{gt_i(\omega)}{U_\infty} \end{cases}. \quad (2.60)$$

In the above formulas, the mean wind velocity U_∞ at the upper limit of the boundary layer is still unknown. The wind velocity U is usually measured at some standard level

(z) above mean sea surface (for example $z = 10$ m). Using the relationships given in Section 2.2 we can replace unknown velocity U_∞ by the friction velocity u_* and subsequently use the relationship $u_*^2 = C_z U^2$ to parameterize the non-dimensional spectra (2.59) and (2.60) in terms of velocity U .

Using the same arguments, the similarity law for a fetch limited condition and multi-directional sea becomes:

$$\frac{\hat{S}(\omega, \Theta) g^3}{U^5} = \varphi \left(\frac{\omega U}{g}, \Theta, \frac{gt}{U}, \frac{gX}{U^2}, \frac{gh}{U^2} \right). \quad (2.61)$$

In the case of a fully-developed unidirectional sea in deep water, i.e. when $\frac{gt}{U} \rightarrow \infty$, $\frac{gh}{U^2} \rightarrow \infty$, and $\frac{gX}{U^2} \rightarrow \infty$, the non-dimensional spectrum depends only on the non-dimensional wind velocity:

$$\frac{S(\omega) g^3}{U^5} = \varphi \left(\frac{\omega U}{g} \right). \quad (2.62)$$

Pierson and Moskowitz (1964) applied Kitaigorodskii's similarity law for a fully-developed sea and found that the function φ can be written as:

$$\varphi \left(\frac{\omega U}{g} \right) = 8.10 \cdot 10^{-3} \left(\frac{\omega U}{g} \right)^{-5} \exp \left[-0.74 \left(\frac{\omega U}{g} \right)^{-4} \right]. \quad (2.63)$$

After substitution into Eq. (2.62) we obtain the popular form of the Pierson-Moskowitz spectrum:

$$S(\omega) = 8.10 \cdot 10^{-3} g^2 \omega^{-5} \exp \left[-0.74 \left(\frac{\omega U}{g} \right)^{-4} \right]. \quad (2.64)$$

The Pierson-Moskowitz spectrum is discussed in detail in Section 3.2.2.2.

The similarity scaling can also be applied to the characteristic wave parameters. For example, for significant wave height H_s and peak frequency ω_p we obtain:

$$\frac{gH_s}{U^2} \left(\frac{\omega_p U}{g} \right) = f \left(\frac{gX}{U^2}, \frac{gt}{U}, \frac{gh}{U^2} \right). \quad (2.65)$$

These results are commonly presented in terms of the fetch-limited or duration-limited graphs. If $\frac{gt}{U}$ is sufficiently large so as not to influence H_s and ω_p , but rather it is gX/U^2 that controls them, then we have fetch-limited waves, i.e.:

$$\left. \begin{aligned} \frac{gH_s}{U^2} &= f_1 \left(\frac{gX}{U^2}, \frac{gh}{U^2} \right) \\ \frac{\omega_p U}{g} &= f_2 \left(\frac{gX}{U^2}, \frac{gh}{U^2} \right) \end{aligned} \right\}. \quad (2.66)$$

Conversely, for the duration-limited case we obtain:

$$\left. \begin{aligned} \frac{gH_s}{U^2} &= f_3 \left(\frac{gt}{U}, \frac{gh}{U^2} \right) \\ \frac{\omega_p U}{g} &= f_4 \left(\frac{gt}{U}, \frac{gh}{U^2} \right) \end{aligned} \right\} \quad (2.67)$$

In order to attain the fetch-limited condition, a certain time t_{min} is needed, where $\frac{gt_{min}}{U} = f \left(\frac{gX}{U^2} \right)$; for $t < t_{min}$, duration-limited waves are observed. When both the fetch and duration are sufficiently large for H_s and ω_p to reach limiting values, they will become dependent only upon the wind speed U and the condition of a fully developed sea will exist.

In the shallow-water limit case, when the wind wave growth is fully controlled by water depth we have:

$$\left. \begin{aligned} \frac{gH_s}{U^2} &= f_5 \left(\frac{gh}{U^2} \right) \\ \frac{\omega_p U}{g} &= f_6 \left(\frac{gh}{U^2} \right) \end{aligned} \right\} \quad (2.68)$$

The specific forms of the functions f, f_1, \dots, f_6 , for appropriate wave generation conditions, will be given in Chapters 5 and 6.

2.4 Wave generation models

As the wind blowing over the water surface is random, the resulting waves also are random. Historically, many approaches have been utilized to describe the basic mechanism of the transfer of wind energy to surface waves. Some of these approaches today only possess historical value, others are still utilized in engineering and oceanographic practice.

2.4.1 Jeffreys' mechanism of wave generation

In one of the first attempts, Jeffreys (1925) postulated that when a wind blows, the normal wind tension at the sea surface can be expressed as a sum of two terms, one being a constant reference to atmospheric pressure (p) and the other to the wind pressure (Δp), which will be different over different parts of the wave surface, i.e.:

$$p_n = -p - \Delta p, \quad (2.69)$$

in which:

$$\Delta p = s\rho_a(U - C)^2 \frac{\partial \zeta}{\partial x}, \quad (2.70)$$

where ζ is a sea surface elevation and s is called a sheltering coefficient, since it is a measure of the resistance of the wave form to the airflow. The coefficient s can also be treated as a measure of a back reaction of the waves on the wind. Therefore, the average rate of wind energy transmitted to the sinusoidal sea surface $\zeta = a \cos(kx - \omega t)$ by normal pressure is:

$$R_w = \frac{1}{L} \int_0^L p_n w(0) dx, \quad (2.71)$$

where $w(0)$ is a vertical component of orbital velocity at the sea surface ($z \approx 0$). Assuming small amplitude wave theory, for deep water we have (Massel, 1989):

$$w(0) = a\omega \sin(kx - \omega t) = akC \sin(kx - \omega t). \quad (2.72)$$

Hence, from Eqs. (2.71) and (2.72) we obtain for $U > C$:

$$R_w = \frac{1}{2} s \rho_a (U - C)^2 k^2 a^2 C. \quad (2.73)$$

If $C > U$, the relative wind is against the direction of wave travel and Δp is 180 degrees out of phase with slope,

$$R_w = -\frac{1}{2} s \rho_a (U - C)^2 k^2 a^2 C. \quad (2.74)$$

Assuming now that the normal energy flux R_w is the only important mechanism for wave growth, we can say that the necessary requirement for this growth is $R_w > R_d$, where R_d is the viscous dissipation, i.e. $R_d = 2\mu k^3 a^2 C^2$ (μ is a dynamic viscosity of water; $\mu \sim 1.3 \cdot 10^{-2}$ g cm⁻¹ s⁻¹ at 10° C). Thus, Jeffreys' criterion for growth of surface waves in deep water is:

$$s \rho_a (U - C)^2 C > 4\mu g. \quad (2.75)$$

The relation (2.75) depends on the value of the empirical sheltering coefficient s , which was estimated by Jeffreys as $s \approx 0.27$. The resulting limiting wind velocity to generate waves is $U \approx 1.1$ m/s. Laboratory experiments on solid wave models appear to give values of the pressure difference much smaller than Jeffreys required to account for the rate of wave growth that he had observed. Some improvement of Jeffreys' solution was to include the effect of the tangential stresses as suggested by Sverdrup and Munk (1947). Instead of Eq. (2.75) we should write (Kinsman, 1965):

$$\pm s \rho_a (U - C)^2 + 2c_r \rho_a U^2 C > 4\mu g, \quad (2.76)$$

in which c_r is a resistance coefficient ($c_r \approx 2.6 \cdot 10^{-3}$). This criterion does not require the wind to be faster than the waves for growth to be possible. However, tangential stresses should also generate currents. Therefore, wave motion becomes rotational. In order to keep the wave motion irrotational, Sverdrup and Munk postulated that all mechanical energy transferred from wind to water is used for wave generation, not for currents.

2.4.2 Basic results of the Phillips-Miles model

The discrepancies in early attempts to formulate a theory of wave generation gave great stimulus to the search for new alternatives. First of all, it became obvious that new theories should take into account the random character of wave motion and wind fluctuations above the sea surface.

In natural flows the wind is always turbulent. The pressure differences at the wave surface are therefore available to initiate and support wave motion. Wind energy is transmitted to the water either by pressure fluctuations or by tangential stresses. As was mentioned above, these forcing mechanisms result in two different kinds of wave motion. Pressure fluctuations yield an irrotational response to water surface, while tangential stress forcing induces a wave motion possessing some vorticity.

It will be shown later that if the pressure fluctuations in the wind are in random phase with the surface waves, the wave growth will be linear. However, when the pressure fluctuations maintain some fixed phase relation to the surface waves, this growth can be exponential.

Let us first consider in some detail stresses over the wave surface. Under the assumption of an irrotational motion, the surface elevation can be expressed in a form of the Fourier-Stieltjes integral:

$$\zeta(\vec{x}, t) = \int_{\vec{k}} dA(\vec{k}, t) e^{i\vec{k} \cdot \vec{x}}. \quad (2.77)$$

In deep water, the corresponding velocity potential $\Phi(\vec{x}, z, t)$ satisfying Laplace's equation

$$\nabla^2 \Phi = \left(\frac{\partial^2}{\partial x^2} + \frac{\partial^2}{\partial y^2} + \frac{\partial^2}{\partial z^2} \right) \Phi, \quad (2.78)$$

and the kinematic boundary condition become:

$$\Phi(\vec{x}, z, t) = \int_{\vec{k}} \frac{dA_t(\vec{k}, t)}{k} e^{kz} e^{i\vec{k} \cdot \vec{x}}. \quad (2.79)$$

Subscript (t) denotes differentiation in time. We define now the pressure distribution over the sea surface as a sum of two spectral components:

$$dP(\vec{k}, t) = d\bar{P}(\vec{k}, t) + dP'(\vec{k}, t), \quad (2.80)$$

in which $d\bar{P}(\vec{k}, t)$ is a pressure associated (or correlated) with the wave form and $dP'(\vec{k}, t)$ is a pressure resulting from turbulent eddies.

It can be shown that only wave-induced pressure $d\bar{P}(\vec{k}, t)$ components, which are in phase with the wave slope, contribute to the energy flux to waves (Miles, 1957):

$$d\bar{P}(\vec{k}, t) = (\nu_1 + i\mu_1) \rho_w C^2 k dA(\vec{k}), \quad (2.81)$$

in which $kdA(\vec{k})$ is the local slope of the wave, $(\nu_1 + i\mu_1)$ is a dimensionless coupling coefficient.

A similar specification can be used for shear stress variations at the water surface, i.e.:

$$d\tau(\vec{k}, t) = d\bar{\tau}(\vec{k}, t) + d\tau'(\vec{k}, t), \quad (2.82)$$

in which $d\bar{\tau}(\vec{k}, t)$ represents the wave-induced variations in shear stress and $d\tau'(\vec{k}, t)$ is the randomly varying component associated with atmospheric turbulence.

The first part of the shear stress takes the form (when the wave slope is small):

$$d\bar{\tau}(\vec{k}, t) = (\nu_2 + i\mu_2) \rho_w C^2 kdA(\vec{k}). \quad (2.83)$$

Longuet-Higgins (1969b) showed that the tangential stress applied at the free surface is dynamically equivalent to a normal pressure fluctuation of the same magnitude, lagging $\pi/2$ in phase behind the tangential stress. Thus, a tangential stress in phase with the wave elevation is equivalent to a pressure in phase with the wave slope.

The Fourier component of the effective normal surface stress $d\sigma_e$ is a sum of the directly induced stresses (2.81) and (2.83), and random contributions $dP'(\vec{k}, t)$ and $d\tau'(\vec{k}, t)$, i.e.:

$$d\sigma_e(\vec{k}, t) = (\nu + i\mu) \rho_w C^2 kdA(\vec{k}) + d\Pi(\vec{k}, t), \quad (2.84)$$

in which $\nu = \nu_1 - \mu_2$, $\mu = \mu_1 + \nu_2$ and $d\Pi(\vec{k}, t) = dP'(\vec{k}, t) + id\tau'(\vec{k}, t)$. The turbulent stresses Π provide energy input over a wide spectral range while the wave-induced stresses provide rather a selective input to certain components only.

Two basic wave generation models were published by Phillips (1957) and Miles (1957, 1962) in which the above stresses were taken into account separately. In Phillips' model, the resonance mechanism between the free surface waves and the turbulent pressure fluctuations $dP'(\vec{k}, t)$ was considered. Turbulent fluctuations of tangential stresses $d\tau'(\vec{k}, t)$, and all correlated stresses $d\bar{P}(\vec{k}, t)$ and $d\bar{\tau}(\vec{k}, t)$ were neglected. Phillips' theory results in a linear growth of the wave spectrum in time.

Miles' approach was based on an analysis of the stability mechanism of the interface of two fluids (air and water), with different densities and speeds, and with some gradient of air density in the boundary layer. Airflow was assumed to be inviscid and turbulence did not play a role, except in maintaining the shear flow (quasi-laminar approach). A possible mechanism for the generation of water waves is the resonant interaction of waves with the wave-induced pressure fluctuations. All turbulent stresses (dP' in our notation) are omitted, while normal stresses $d\bar{P}$, correlated with wave slope, are retained. The resulting wave growth of the wave spectrum becomes exponential in time.

Following Phillips (1977), we combine both approaches in one linear theory of wave generation. Anticipating that shear stresses play a minor role in air-sea interaction,

it can be assumed that the motion beneath the surface boundary layer is irrotational and the velocity potential $\Phi(\vec{x}, z, t)$ exists (see Eq. (2.79)).

The linearized dynamic free surface boundary condition becomes:

$$\frac{\partial \Phi}{\partial t} + g\zeta + \frac{p}{\rho_w} = 0 \quad \text{at } z = 0. \quad (2.85)$$

Substituting Eqs. (2.77) and (2.79) into Eq. (2.85), and using Eq. (2.84) leads to an equation for the spectral amplitude $dA(\vec{k}, t)$:

$$dA_{tt}(\vec{k}, t) + [gk + (\nu + i\mu)k^2 C^2] dA(\vec{k}, t) = \frac{k}{-\rho_w} d\Pi(\vec{k}, t), \quad (2.86)$$

or

$$dA_{tt}(\vec{k}, t) + \Omega^2 dA(\vec{k}, t) = -\frac{k}{\rho_w} d\Pi(\vec{k}, t), \quad (2.87)$$

in which:

$$\Omega^2 = \omega^2 (1 + \nu + i\mu). \quad (2.88)$$

As both $|\nu|$ and $|\mu|$ are small quantities, frequency $\Omega \approx \omega (1 + \frac{1}{2}i\mu)$.

The solution to Eq. (2.87), subject to the initial zero conditions is:

$$dA(\vec{k}, t) = -\frac{k}{\rho_w \Omega} \int_0^t d\Pi(\tau) \sin[\Omega(t - \tau)] d\tau. \quad (2.89)$$

To this approximation, the wave frequency (the real part of Ω) is unchanged by the atmospheric transfer. The imaginary part of Ω , proportional to the part of the induced normal stresses that are in phase with the wave slope, determines the development of the wave spectral density in time.

To evaluate the wave spectrum $\hat{\Psi}(\vec{k}, t)$ we first need to develop an autocorrelation function of the turbulent stresses:

$$\begin{aligned} K_{\Pi\Pi}(\vec{k}, \tau) &= E[d\Pi(k, t) d\Pi(k, t + \tau)] = E[dP' dP'^*] + E[d\tau' d\tau'^*] + \\ &+ i \{ E[d\tau dP'^*] - E[d\tau^* dP'] \}, \end{aligned} \quad (2.90)$$

in which E is a symbol of statistical averaging and $(*)$ denotes the complex conjugate.

Fluctuations of the mean square turbulent pressure are usually about one hundred times the shear stress fluctuations, as are the spectral ranges. Therefore, it is reasonable to assume that the first term in Eq. (2.90) is dominant. If the turbulent stress is stationary in time, Eq. (2.89) yields the following expression for the surface displacement spectrum:

$$\hat{\Psi}(\vec{k}, t) = \frac{\pi \Psi_a(\vec{k}, \omega) \sinh(\mu \omega t)}{\rho_w^2 C^2 \mu \omega}, \quad (2.91)$$

in which $\Psi_a(\vec{k}, \omega)$ is the wave number-frequency spectrum of the atmospheric turbulent stresses $d\Pi(\vec{k}, t)$.

When the wind duration t is small compared with $(\mu\omega)^{-1}$, Eq. (2.91) becomes:

$$\hat{\Psi}(\vec{k}, t) = \frac{\pi \Psi_a(\vec{k}, \omega)}{\rho_w^2 C^2} t. \quad (2.92)$$

The wave spectrum increases linearly with time under the influence of the turbulent stress fluctuations only. As the fluctuation pattern is connected with some advection velocity \vec{U} (for instance, mean wind velocity), the spectral density $\Psi_a(\vec{k}, \omega)$ has a maximum at $\omega = \vec{k} \cdot \vec{U}$. Thus, a response spectrum $\hat{\Psi}(\vec{k}, t)$ is a maximum when $\omega \approx (gk)^{1/2} = \vec{k} \cdot \vec{U}$. The dominant frequency of the advected stress fluctuations is equal to the frequency of free surface waves, having the same wave number. This resonance mechanism was first described by Phillips (1957).

Extending the condition $\mu\omega t \ll 1$ for all the wave components at a given frequency ω (or a given scalar wave number k), wave growth will be maximum at the angles $(\phi - \theta)$ for which:

$$\omega = \vec{k} \cdot \vec{U} = kU \cos(\phi - \theta), \quad (2.93)$$

where ϕ is the wind direction and θ is the direction of wave propagation.

In particular, for gravity waves in deep water when $(\omega^2 = gk)$ we obtain:

$$\phi - \theta = \cos^{-1}\left(\frac{C}{U}\right) = \cos^{-1}\left(\frac{g}{\omega U}\right) = \cos^{-1}\left[\left(\frac{g}{kU^2}\right)^{1/2}\right]. \quad (2.94)$$

When the scalar wave number $k = \frac{g}{U^2}$, an angle $(\phi - \theta) = 0$ and wave energy spectrum is the greatest for components propagating in the direction of the wind ($\theta = \phi$).

For $k > \frac{g}{U^2}$, the angles satisfy a condition $-\frac{\pi}{2} < \phi - \theta < \frac{\pi}{2}$. The initial growth of shorter waves is anticipated at angles $\pm(\phi - \theta)$ to the wind direction, and the directional distribution becomes bi-modal. The resulting pattern of the sea surface takes a rhomboidal shape (see for example a photograph in Kinsman (1965)).

As $\mu\omega t$ increases, the induced stress on the growing waves becomes important and a 'feedback' system develops. The wave growth is now very rapid and for times $\mu\omega t \geq 1$, $\sinh(\mu\omega t) \approx \frac{1}{2} \exp(\mu\omega t)$. Thus, the wave number spectrum (2.91) takes the form:

$$\hat{\Psi}(\vec{k}, t) = \frac{\pi \Psi_a(\vec{k}, \omega)}{2\rho_w^2 C^2 \mu\omega} \exp(\mu\omega t). \quad (2.95)$$

Eq. (2.95) involves both forcing mechanisms, i.e. turbulent stress $d\Pi$ and normal stress components $d\bar{P}$ in phase with wave slope. As will be shown in Section 5.2, Eq. (2.95) is a solution of the differential equation:

$$\frac{\partial \hat{\Psi}}{\partial t} = \mu \omega \hat{\Psi}, \quad (2.96)$$

in which turbulent stresses do not appear. The rate of growth is totally dependent on the incident stresses acting at the free surface and it is directly proportional to the coupling coefficient μ which is the rate of energy growth per radian.

Miles (1957, 1959) showed that the coefficient μ is given by:

$$\mu \omega = -\pi \frac{\rho_a}{\rho_w} C(k) |\chi_c|^2 \frac{W_c''}{|W_c'|}, \quad (2.97)$$

in which the subscript c refers to evaluation at the critical height z_c defined by $W(z) = U(z) - C = 0$, where $U(z)$ is the wind profile. It is clear from Eq. (2.97) that wave growth is possible only when $W_c'' < 0$. The quantity χ is a normalized vertical component of the wave-induced air velocity ($= w/w(0)$) satisfying Rayleigh's equation (Miles, 1957):

$$\left\{ \begin{aligned} & \left[W \left(\frac{\partial^2}{\partial z^2} - k^2 \right) - W'' \right] \chi = 0 \\ & \chi(0) = 1, \quad \chi(\infty) \rightarrow 0 \end{aligned} \right\}. \quad (2.98)$$

The primes denote differentiation against the vertical coordinate z .

The growth parameter μ may be also represented as:

$$\mu = \beta \left(\frac{\rho_a}{\rho_w} \right) \left(\frac{U_1}{C} \right)^2, \quad (2.99)$$

where β is a dimensionless pressure coefficient used by Miles, and $U_1 = u_*/\kappa$ is a reference speed. Miles (1959) found that β was a function of two dimensionless parameters, C/U_1 and $\Omega = g z_0/U_1^2$. The parameter C/U_1 may be thought of as a dimensionless wave speed, and the parameter Ω as a dimensionless roughness. Growth rate, β , decreases or increases with increasing roughness, Ω , depending on the value of Ω . For $0 < \Omega < 0.006$ the wave growth increases, whereas for $\Omega > 0.006$ the wave growth rate decreases.

Using field experiments by Snyder et al. (1981), Hasselmann et al. (1985) showed an order of magnitude agreement with Miles' theory, although the theory still predicts energy transfer rates that are smaller than measured values. Experimental results on coupling coefficient μ , and their comparison with Miles' theory, will be discussed in more detail in Section 5.2.

Since the energy of a particular component first grows linearly in time and later the growth becomes exponential, there must be a transition zone in which it changes

from one mode of growth to another. Phillips and Katz (1961) found that for ocean waves with phase speed near the wind speed, the time for transition is rather long ($\sim 10^4 \cdot T$, in which T is wave period of the wave component). This suggests that these components are generated linearly entirely by resonance with pressure fluctuations.

For wave components with $C/U \ll 1$, transition occurs much sooner, so that components with short wavelengths generally experience an exponential growth. Exponential growth can not continue indefinitely, and after some time the nonlinearities and other processes not included in the model place a limit on the growth of the waves.

The transition time for wave components propagating in water of finite depth is shorter than in deep water (Zaslavskii and Krasitskii, 1976). This time depends on the angle of propagation of the particular component with respect to the wind direction. The components propagating closer to the wind direction more rapidly transform to the stage of exponential growth. Thus, spectral components with the same frequency, but with a large angle, may still be in the stage of linear resonance growth.

The magnitude of the resulting wave spectrum at the resonance peak can also be expressed in terms of the frequency spectrum rather than in the wave number spectrum (Phillips, 1966), i.e.:

$$S(\omega) \approx 240 \left(\frac{\rho_a}{\rho_w} \right)^2 \frac{u_*^4 \sinh(\mu\omega t)}{g^2 \mu\omega}. \quad (2.100)$$

2.4.3 Resonance type model in water of finite depth

In the original Phillips-Miles wave generation model the water depth was not explicitly included. Therefore, it will be instructive to analyze in brief the influence of the water depth on the wave growth rate. Let us thus consider the linear potential water motion induced by uniform turbulent pressure fluctuations over the free surface. The velocity potential $\Phi(x, y, z, t)$ should satisfy the Laplace equation (2.78) and boundary conditions at the surface ($z = 0$):

$$\frac{\partial \zeta}{\partial t} = \frac{\partial \Phi}{\partial z}, \quad (2.101)$$

$$\frac{\partial \Phi}{\partial t} + g\zeta - \frac{T}{\rho_w} \left(\frac{\partial^2 \zeta}{\partial x^2} + \frac{\partial^2 \zeta}{\partial y^2} \right) = -\frac{1}{\rho_w} p_a(\vec{x}, t), \quad (2.102)$$

and at the bottom ($z = -h$):

$$\frac{\partial \Phi}{\partial z} = 0, \quad (2.103)$$

in which T is the surface tension.

We express, the velocity potential Φ in a form of the Fourier-Stieltjes integral:

$$\Phi(x, y, z, t) = \int_{\vec{k}} \exp(i\vec{k}\vec{x}) \frac{\cosh k(z+h)}{k \sinh kh} dA_t(\vec{k}, t), \quad (2.104)$$

in which subscript t denotes a differentiation in time. The corresponding surface elevation $\zeta(\vec{x}, t)$ is given by Eq. (2.77).

In a similar way we express the random pressure fluctuation $p_a(\vec{x}, t)$, i.e.:

$$p_a(\vec{x}, t) = \int_{\vec{k}} dP(\vec{k}, t) \exp(i\vec{k}\vec{x}). \quad (2.105)$$

Substitution of Eqs. (2.77), (2.104) and (2.105) into Eq. (2.102) leads to the following equation for the spectral amplitude:

$$\frac{dA_t(\vec{k}, t)}{k \tanh(kh)} + \left(g + \frac{Tk^2}{\rho_w}\right) dA(\vec{k}, t) = -\frac{1}{\rho_w} dP(\vec{x}, t), \quad (2.106)$$

or

$$dA_t(\vec{k}, t) + \omega^2 dA(\vec{k}, t) = -\frac{k \tanh kh}{\rho_w} dP(\vec{x}, t), \quad (2.107)$$

in which:

$$\omega^2 = \left(gk + \frac{Tk^3}{\rho_w}\right) \tanh(kh). \quad (2.108)$$

The solution to Eq. (2.107) subject to the initial conditions:

$$dA(\vec{k}, 0) = dA_t(\vec{k}, 0) = 0, \quad (2.109)$$

is (Krylov et al., 1976):

$$dA(\vec{k}, t) = \frac{ik \tanh kh}{2\rho_w \omega} \int_0^t dP(\vec{k}, \tau) \{\exp[i\omega(t-\tau)] - \exp[-i\omega(t-\tau)]\} d\tau. \quad (2.110)$$

Thus, the sea surface at time t depends on the history of evolution of pressure fluctuations since $t = 0$.

A more detailed expression for the amplitude $dA(\vec{k}, t)$ requires parameterization of the pressure fluctuations $dP(\vec{k}, \tau)$. Following Phillips (1957) we assume that the eddies in a turbulent wind are rigidly advected by the mean motion of the wind. The pressure itself slowly evolves in time, since the turbulent eddies interact. The characteristic time $t_{cr}(\vec{k})$, during which eddies maintain their existence, may be expected to be much greater than the apparent period of a fluctuation observed at a fixed point, i.e. $t_{cr}(\vec{k}) \gg \frac{L}{U} \sim \frac{1}{kU}$. Therefore, the pressure field changes will be much slower if the observation is made from a point travelling at the mean wind speed.

Let us consider wave generation for $t < t_{cr}$, when the pressure field is advected over the water as a rigid body, i.e.:

$$p_a(\vec{x}, t) = p(\vec{x} - \vec{U}t), \quad (2.111)$$

in which \vec{U} is a mean wind velocity. Using Eqs. (2.105) and (2.111) gives:

$$dP(\vec{k}, \tau) = dP(\vec{k}, 0) \exp(i\vec{k}\vec{U}\tau). \quad (2.112)$$

Substituting Eq. (2.112) into Eq. (2.110) yields:

$$\begin{aligned} dA(\vec{k}, t) = & \frac{ik \tanh(kh) dP(\vec{k}, 0)}{2\rho_w \omega} \left\{ \exp(i\omega t) \int_0^t \exp[i(\vec{k}\vec{U} - \omega)\tau] d\tau - \right. \\ & \left. - \exp(-i\omega t) \int_0^t \exp[i(\vec{k}\vec{U} + \omega)\tau] d\tau \right\}. \end{aligned} \quad (2.113)$$

The integrations in Eq. (2.113) depend on the relationship between ω^2 and $(\vec{k}\vec{U})^2$. When $\omega^2 \neq (\vec{k} \cdot \vec{U})^2$, Eq. (2.113) yields the oscillating type solution with finite amplitude while for $\omega = \vec{k} \cdot \vec{U}$ we obtain:

$$dA(\vec{k}, t) = \frac{ik \tanh(kh) dP(\vec{k}, 0)}{2\rho_w \omega} \left[\exp(i\omega t) - \frac{1}{\omega t} \sin(\omega t) \right] t. \quad (2.114)$$

For ωt sufficiently large, wave amplitude $dA(\vec{k}, t)$ will grow linearly in time. Thus, the necessary condition is:

$$\vec{k} \cdot \vec{U} = \omega = \left(gk + \frac{Tk^3}{\rho_w} \right)^{1/2} \tanh^{1/2}(kh), \quad (2.115)$$

or

$$U \cos \alpha = \left(\frac{g}{k} + \frac{Tk}{\rho_w} \right)^{1/2} \tanh^{1/2}(kh) = C(k), \quad (2.116)$$

in which α is an angle between wind and resonantly growing waves.

Eq. (2.116) indicates that resonance appears between the advection velocity of the pressure field and those free waves for which phase velocity is equal $U \cos \alpha$. In wave number space (k_x, k_y) resonance condition (2.116) can be written as:

$$\frac{T}{\rho_w g} (k_x^2 + k_y^2) - \left[\frac{U^2}{g} \coth(\sqrt{k_x^2 + k_y^2} h) \right] \frac{k_x^2}{\sqrt{k_x^2 + k_y^2}} + 1 = 0, \quad (2.117)$$

in which $k_x = k \cos \alpha$, $k_y = k \sin \alpha$.

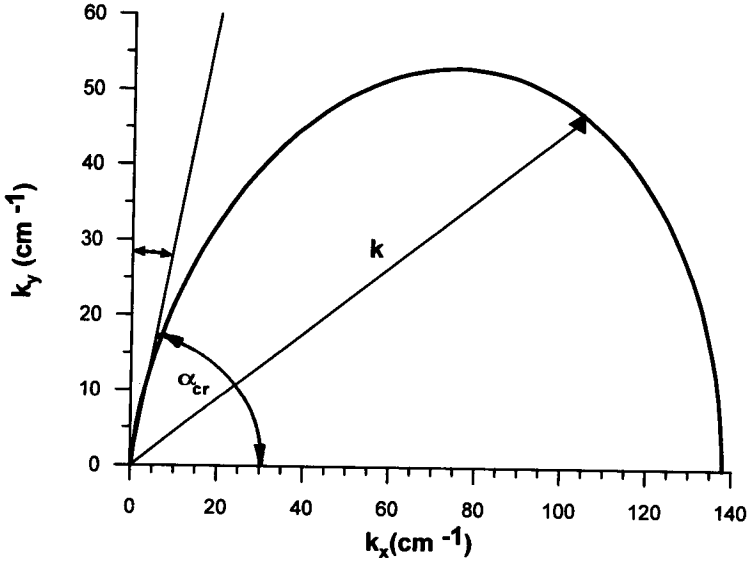


Figure 2.3: The locus of resonance wave number for $U = 1\text{m/s}$ and $h = 100\text{ m}$.

The locus of resonant wave numbers for $U = 1\text{m/s}$ and water depth $h = 100\text{m}$ is given in Fig. 2.3. The k_x axis corresponds to the wind direction.

For angle $\alpha < \alpha_{cr}$, the radius from the origin intersects the resonant curve twice. The intersection point closer to the origin determines the resonant wave number for gravity waves, while the intersection point with the greater wave number corresponds to the capillary waves. The tangent to the curve determines the critical angle α_{cr} .

In Fig. 2.3, a first intersection of resonant curve with k_x axis is very close to the origin ($k_x = 0.0982\text{cm}^{-1}$) and is not distinguishable in the Figure. The second intersection corresponds to $k_x = 137.98\text{ cm}^{-1}$.

At $\alpha = \alpha_{cr}$, both wave numbers coalesce into a single point. To find the corresponding wave number k we rewrite Eq. (2.117) as:

$$\frac{T}{\rho_w g} k^2 - \left[\frac{U^2}{g} \coth(kh) \cos^2 \alpha \right] k + 1 = 0. \quad (2.118)$$

At $\alpha = \alpha_{cr}$, Eq. (2.118) should have one double root. Hence:

$$k_{cr} = \sqrt{\frac{\rho_w g}{T}} \approx 3.68\text{cm}^{-1}, \quad (2.119)$$

and

$$\alpha_{cr} = \cos^{-1} \left\{ \frac{4gT \tanh(kh)}{\rho_w U^4} \right\}^{1/4}. \quad (2.120)$$

For the example illustrated in Fig. 2.3, angle $\alpha_{cr} \approx 76.7^\circ$.

The wave number k_{cr} corresponds to the minimum value of phase velocity of gravity waves C_{min} and minimum gravity wavelength L_{min} :

$$L_{min} = \frac{2\pi}{k_{cr}} \approx 1.7 \text{ cm}. \quad (2.121)$$

For all practical water depths h , the wave number $kh \gg 1.0$ and $\tanh(kh) \approx 1.0$; hence:

$$\alpha_{cr} = \cos^{-1} \left\{ \frac{4gT}{\rho_w U^4} \right\}^{1/4}. \quad (2.122)$$

The influence of water depth on resonant wave numbers is negligible. In Fig. 2.3, the resonant curves for water depths $h = 0.15$ m (not shown) or $h = 100$ m are practically the same as for infinite water depth.

The resonance theory of Phillips (1957) suggests that the amplitude of waves moving at the angle α_{cr} to the mean wind direction is greater than for any angle $\alpha < \alpha_{cr}$. Therefore, for limited time of wind action, when turbulent pressure fluctuations contain components with length scales equal to the length of surface waves, a rhomboid pattern of small waves intersecting under the angles $\pm \alpha_{cr}$ is created.

When the time of wind action is much greater than time of evolution of pressure fluctuations t_{cr} , the pressure field cannot be considered as advected as a rigid pattern across the water, and the assumption (2.112) is no longer valid. A more realistic assumption is to consider the pressure fluctuation as a uniform random field with frequency-wave number spectrum $\Psi_a(\vec{k}, \omega)$. Using Eq. (2.110) we obtain the extension of Phillips' result (2.92) in the form:

$$\hat{\Psi}(\vec{k}, t) = \frac{\pi \tanh^2(kh)}{\rho_w^2 C^2} \Psi_a(\vec{k}, \omega) t. \quad (2.123)$$

2.4.4 Resonance type model with dissipation

Phillips' original linear model does not include dissipation processes. However, the dissipation mechanisms due to molecular viscosity, white capping and other forms of wave breaking, are always present in the wave field. However, wave breaking is a nonlinear phenomenon, and in the linear model can be included only approximately.

In the following we consider the irrotational wave motion on the surface of the deep ocean with energy dissipation. At time $t = 0$ the turbulent pressure field $p(\vec{x}, t)$ appears over the initially calm sea surface. The corresponding boundary value problem

for the velocity potential $\Phi(\vec{x}, z, t)$, satisfying the Laplace equation, can be formulated as follows:

$$\left. \begin{aligned} \frac{\partial \Phi}{\partial t} + 2\beta\Phi + g\zeta &= -\frac{p_a}{\rho_w} \\ \frac{\partial \zeta}{\partial t} &= \frac{\partial \Phi}{\partial z} \end{aligned} \right\} \text{ at } z = 0, \quad (2.124)$$

and

$$\frac{\partial \Phi}{\partial z} \rightarrow 0 \text{ at } z \rightarrow -\infty. \quad (2.125)$$

The small positive parameter β is an attenuation coefficient, due to dissipation, which will be specified later.

We assume now that pressure fluctuations are random, but stationary in time and uniform in space (x, y) . Therefore, $p_a(\vec{x}, t)$ can be represented in the form of double Fourier-Stieltjes integral:

$$p(\vec{x}, t) = \int_{\vec{k}} \int_{\omega} \exp[i(\vec{k} \cdot \vec{x} - \omega t)] dP(\vec{k}, \omega). \quad (2.126)$$

If $\Psi_a(\vec{k}, \omega)$ is a wave number-frequency spectrum of the atmospheric pressure fluctuations, then we can write (Phillips, 1977):

$$E[dP(\vec{k}, \omega) dP^*(\vec{k}', \omega')] = \Psi_a(\vec{k}, \omega) d\vec{k} d\omega \delta(\vec{k} - \vec{k}') \delta(\omega - \omega'), \quad (2.127)$$

where $\delta(\cdot)$ denotes the Dirac delta function (Lighthill, 1975).

Under an action of pressure fluctuations $p(\vec{x}, t)$, the sea surface ordinates will evolve in time and wave field will be non-stationary. Thus:

$$\zeta(\vec{x}, t) = \int_{\vec{k}} \int_{\omega} \exp[i(\vec{k} \cdot \vec{x} - \omega t)] dA(\vec{k}, \omega, t), \quad (2.128)$$

where $dA(\vec{k}, \omega, t)$ is a slowly changing function of time.

The wave number-frequency spectrum of the surface fluctuations $\tilde{\Psi}(\vec{k}, \omega, t)$ is represented in similar way as spectrum $\Psi_a(\vec{k}, \omega)$, i.e.:

$$E[dA(\vec{k}, \omega, t) dA^*(\vec{k}', \omega', t)] = \tilde{\Psi}(\vec{k}, \omega, t) d\vec{k} d\omega \delta(\vec{k} - \vec{k}') \delta(\omega - \omega'). \quad (2.129)$$

The velocity potential Φ satisfying Laplace's equation and the kinematic boundary condition takes the form:

$$\Phi(\vec{x}, z, t) = \int_{\vec{k}} \int_{\omega} k^{-1} \exp[kz + i(\vec{k} \cdot \vec{x} - \omega t)] (dA_t - i\omega dA). \quad (2.130)$$

After substitution of Eqs. (2.126), (2.128) and (2.130) into the dynamic boundary condition (first relation in Eq. (2.124)) we obtain:

$$dA_{tt} + 2(\beta - i\omega) dA_t + \left[(gk - 2i\beta\omega) - \omega^2 \right] dA = -\frac{k dP}{\rho_w}. \quad (2.131)$$

Using the Laplace transform technique and applying the zero boundary conditions:

$$dA(\vec{k}, \omega, 0) = dA_t(\vec{k}, \omega, 0) = 0,$$

yields the solution of Eq. (2.131) in the form:

$$dA(\vec{k}, \omega, t) = \frac{dP\omega_0^2}{\rho_w g \omega_\beta} \int_0^t \exp[(\beta - i\omega)(\tau - t)] \sin[\omega_\beta(\tau - t)] d\tau, \quad (2.132)$$

where $\omega_0^2 = gk$, $\omega_\beta^2 = \omega_0^2 - \beta^2 = gk - \beta^2$. The frequency ω_0 is an intrinsic frequency of water surface oscillations.

Using the technique described in the Section 1.3.3 we obtain the wave number-frequency spectrum for surface oscillations in the form (Krylov et al., 1986):

$$\bar{\Psi}(\vec{k}, \omega, t) = \Psi_1(\vec{k}, \omega) \left\{ 1 + \frac{1}{2} \left(1 + \frac{\omega^2}{\omega_0^2} \right) e^{-2\beta t} - \left(1 + \frac{\omega}{\omega_0} \right) \cos(\Delta\omega t) e^{-\beta t} \right\}, \quad (2.133)$$

in which $\Delta\omega = \omega_\beta - \omega$ and $\Psi_1(\vec{k}, \omega)$ is a corresponding spectrum for the stationary stage, i.e. for $t \rightarrow \infty$

$$\Psi_1(\vec{k}, \omega) = \frac{\Psi_a(\vec{k}, \omega)}{\rho_w^2 g^2 \left[\left(1 - \frac{\omega^2}{\omega_0^2} \right)^2 + \left(\frac{2\beta\omega}{\omega_0^2} \right)^2 \right]}. \quad (2.134)$$

Under the assumption that $\beta \ll 1$, Eq. (2.133) can be integrated with respect to ω to get an approximation of the wave number spectrum $\hat{\Psi}(\vec{k}, t)$ as:

$$\hat{\Psi}(\vec{k}, t) \simeq \frac{\pi \Psi_a(\vec{k}, \omega)}{2\rho_w^2 \beta C^2} (1 - e^{-2\beta t}). \quad (2.135)$$

When the dissipation effects are negligible, Eq. (2.135) becomes:

$$\hat{\Psi}(\vec{k}, t) \simeq \frac{\pi \Psi_a(\vec{k}, \omega)}{\rho_w^2 C^2} t. \quad (2.136)$$

Equation (2.136) agrees with Phillips' result (2.92). From Eq. (2.135) it follows that, the spectral components do not grow infinitely in time, but rather approach some stationary stage when wave number spectrum becomes:

$$\hat{\Psi}(\vec{k}, t \rightarrow \infty) \approx \frac{\pi \Psi_a(\vec{k}, \omega)}{2\rho_w^2 \beta C^2}. \quad (2.137)$$

The attenuation coefficient β due to molecular viscosity only can be represented as:

$$\beta = 2\nu_w k^2. \quad (2.138)$$

Let us assume now that formula (2.138) can also be used for the turbulent motion when the kinematic coefficient of molecular viscosity ν_w is replaced by the kinematic coefficient of turbulent viscosity ν_T .

The coefficient ν_T depends on wind velocity U . Laboratory data by Kononkova (1969) gives the ν_T value in the range from $6 \cdot 10^{-4} \text{ cm}^2/\text{s}$ to $758 \cdot 10^{-4} \text{ cm}^2/\text{s}$ for wind velocity U varying from 6m/s to 20m/s. Assuming that $k \approx \frac{g}{U^2}$, it can be shown that the attenuation coefficient β varies from $4.1 \cdot 10^{-4} \text{ s}^{-1}$ for wind velocity $U = 4\text{m/s}$ to $0.95 \cdot 10^{-4} \text{ s}^{-1}$ for $U = 20\text{m/s}$. Kononkova's data indicate also, that non-dimensional attenuation coefficient $\frac{\beta_T U}{g}$ is equal to $1.88 \cdot 10^{-4}$ for all wind velocities under consideration. Thus, for turbulent motion we can write:

$$\beta_T \approx 1.88 \cdot 10^{-4} \frac{g}{U}. \quad (2.139)$$

The coefficient β_T is still a very small quantity which justifies the approximation used for developing of Eq. (2.135).

2.4.5 Inclusion of fluctuation of tangential stresses

The analysis given above follows the traditional approach in which only the spectrum of pressure fluctuations is taken into account and wave motion is linear and irrotational. The fluctuations of tangential stresses are totally neglected. However, in a real situation a turbulent wind induces both the normal and tangential stresses at the sea surface. Following Krasitskii (1980), we briefly present the possible way to include the tangential stress in the analysis.

The linearized equations of water motion and boundary conditions can be summarized as follows:

$$\left. \begin{aligned} \frac{\partial u_i^{(w)}}{\partial t} &= -\frac{1}{\rho_w} \frac{\partial p^{(w)}}{\partial x_i} + \nu_w \nabla^2 u_i - g \delta_{i3} \\ \frac{\partial u_i^{(w)}}{\partial x_i} &= 0 \end{aligned} \right\}, \quad (2.140)$$

$$\left. \begin{aligned} (p^{(w)} - p^{(a)}) n_i &= (\sigma_{ij}^{(w)} - \sigma_{ij}^{(a)}) n_j - T n_i \nabla_h^2 \zeta \\ \frac{\partial \zeta}{\partial t} &= u_3^{(w)} \end{aligned} \right\} \text{ for } z = 0, \quad (2.141)$$

in which superscripts (w) and (a) denote water and atmospheric components, respectively; $i, j = 1, 2, 3$; $x_1 = x, x_2 = y$ and axis $x_3 = z$ (directed upwards). The symbol

∇^2 is the three-dimensional Laplace operator (2.78) and ∇_h^2 is the two-dimensional Laplace operator in the horizontal plane:

$$\nabla_h^2 = \frac{\partial^2}{\partial x_1^2} + \frac{\partial^2}{\partial x_2^2} = \frac{\partial^2}{\partial x^2} + \frac{\partial^2}{\partial y^2}; \quad (2.142)$$

$\sigma_{ij} = \rho\nu \left(\frac{\partial u_i}{\partial x_j} + \frac{\partial u_j}{\partial x_i} \right)$ is a viscous stress tensor; $\vec{n} = (0, 0, 1)$ is a unit vector. At $z \rightarrow -\infty$, the velocities $u_i \rightarrow 0$. At $t = 0$, the turbulent wind starts to blow over an initially calm sea surface.

The resulting velocity field in water and in air, and the water pressure are represented in the form of two components, i.e. mean value and turbulent fluctuations. After averaging the equations (2.140) and (2.141) we obtain a system of equations for the fluctuating components of water and air motion. Solving this set of equations, and using the boundary conditions at the air-water interface, yields the relation of the wave spectrum and spectrum of the atmospheric forcing in a form identical to Eq. (2.135), i.e.:

$$\Psi(\vec{k}, t) = \frac{\pi \Psi_a(\vec{k}, \omega)}{2\rho^2 \beta C^2} (1 - e^{-2\beta t}), \quad (2.143)$$

with the spectrum of the atmospheric forcing as (Krasitskii, 1980):

$$\Psi_a(\vec{k}, \omega) = \Psi_p(\vec{k}, \omega) + \frac{k_i k_j}{k^2} \Psi_{ij}^{(t)}(\vec{k}, \omega) + \frac{k_i}{k} \Psi_i^{(in)}(\vec{k}, \omega), \quad (2.144)$$

where $\Psi_p(\vec{k}, \omega)$ denotes the spectrum of the atmospheric pressure as in Phillips' model, $\Psi_{ij}^{(t)}(\vec{k}, \omega)$ is a spectrum of components related to fluctuations of tangential stresses, and $\Psi_i^{(in)}(\vec{k}, \omega)$ is a spectrum resulting from the interaction between normal and tangential stresses. We present these spectra in Fourier integral form, i.e.:

$$\Psi_p(\vec{k}, \omega) = \frac{1}{2\pi} \int K_p(\vec{k}, \tau) \exp(i\omega\tau) d\tau, \quad (2.145)$$

$$\Psi_{ij}^{(t)}(\vec{k}, \omega) = \frac{1}{2\pi} \int \Pi_{ij}(\vec{k}, \tau) \exp(i\omega\tau) d\tau, \quad (2.146)$$

and:

$$\Psi_i^{(in)}(\vec{k}, \omega) = \frac{1}{2\pi} \int 2\Im \left\{ f_i(\vec{k}, \tau) \exp(i\omega\tau) \right\} d\tau, \quad (2.147)$$

where:

$$K_p(\vec{k}, \tau) \delta(\vec{k} - \vec{k}') = E \left[p_{\vec{k}}(t) p_{\vec{k}'}^*(t + \tau) \right], \quad (2.148)$$

$$\Pi_{ij}(\vec{k}, \tau) \delta(\vec{k} - \vec{k}') = E \left[\tau_i(t, \vec{k}) \tau_j^*(t + \tau, \vec{k}') \right], \quad (2.149)$$

and:

$$f_i(\vec{k}, \tau) \delta(\vec{k} - \vec{k}') = E \left[p_{\vec{k}}(t) \tau_i^*(t + \tau, \vec{k}') \right]. \quad (2.150)$$

The $\tau_i(t)$ in Eq. (2.149) denotes the components of tangential turbulent stresses, i.e.:

$$\tau_i(t) = \rho_a \nu_a \frac{\partial u_i}{\partial x_3}. \quad (2.151)$$

When the tangential stresses and interaction between normal and tangential stresses are neglected, Eq. (2.135) is obtained. However, due to the lack of experimental data, it is difficult at present to assess the impact of the tangential stress components on the wave spectrum.

2.4.6 Inclusion of airflow turbulence in the Miles' model

Miles' theory of wave generation is a well-argued mathematical theory within the assumptions made that airflow is inviscid and the turbulence plays no role except in setting up the shear flow. When applying this theory to the field situation where the airflow is inevitably turbulent, the mean shear flow velocity $U(z)$ and the wave-perturbation velocity resulting from Miles' theory give the total mean of the turbulent airflow over a wave surface (Riley et al., 1982). According to this idea, the mean velocity and pressure should be presented as:

$$\left. \begin{aligned} \bar{u} &= U(z) + u_w \\ \bar{v} &= v_w \\ \bar{p} &= p_w + p_T \end{aligned} \right\}, \quad (2.152)$$

where the wave-induced velocity components u_w and v_w and the pressure p_w are given by Miles' theory. Riley et al. (1982) showed that the part of surface pressure p_T , due to interaction of the airflow turbulence with waves, has the form:

$$p_T|_{z=0} = \rho \frac{u_*^2}{\kappa^2} k \zeta (\alpha_T + i\beta_T), \quad (2.153)$$

where:

$$\alpha_T = -\kappa \left[\sqrt{\left(\frac{k\nu}{u_*} \right)^2 + (2kl_0)^2} - \frac{k\nu}{u_*} \right] \left[2.4 \phi(\xi) + \Im \left(\frac{d\phi}{d\xi} \right) \right]_{\xi=0}, \quad (2.154)$$

$$\beta_T = -\kappa \left[\sqrt{\left(\frac{k\nu}{u_*} \right)^2 + (2kl_0)^2} - \frac{k\nu}{u_*} \right] \Re \left(\frac{d\phi}{d\xi} \right)_{\xi=0}, \quad (2.155)$$

in which \Re and \Im denote the real and imaginary part of a complex function, respectively. The first component of surface pressure $\rho \frac{u_*^2}{\kappa} k \zeta \alpha_T$ represents the pressure which is in phase with the wave elevation, while the second component $\rho \frac{u_*^2}{\kappa} k \zeta \beta_T$ denotes the surface pressure in quadrature with surface elevation. The function $\phi(\xi)$, where $\xi = kz$, is a solution of Miles' equation $\phi'' - \left[1 + \left(\frac{w'}{w}\right)\right] \phi = 0$, in which $w(\xi) = \frac{U - C}{u_*}$. Prime denotes a differentiation with respect to z .

The symbol l_0 is the mixing length at the surface. It accounts for the turbulent mixing which occurs right at the surface in rough flow when the turbulent stresses are directly related to the roughness elements. For smooth flow, $l_0 = 0$, hence $\alpha_T = \beta_T = 0$, and the wave-turbulence interaction has no effect on the surface pressure.

In the transition region, when $0.14 < \frac{z_0 u_*}{\nu} < 2.2$, the mixing length increases rapidly to a maximum and decreases again more slowly.

In the rough region, when $\frac{z_0 u_*}{\nu} > 2.2$, the mixing length is proportional to the roughness length z_0 . It can be shown that $\beta_T = 2\kappa^2 = 0.32$. Thus, the wave-turbulence interaction provides an additional mechanism for energy transfer from wind to waves. The energy input from wind to waves, travelling with the wind, increases by about 10% for aerodynamically rough flow.

Numerical calculations also indicate that the flux due to surface turbulent stresses is about 5% of the energy flux due to the pressure field (Chalikov and Makin, 1991). However, the extended theory predicts a growth rate which is still a factor of 2-3, too small when compared with experiment.

2.4.7 Effect of wind-generated waves on airflow

As was shown in Section 2.2, the drag coefficient C_z depends strongly on the wave age. This dependence is a manifestation of the coupling mechanism between wind and waves. In comparison with airflow over a flat plate, the airflow over surface gravity waves feels an additional stress due to the presence of the waves. This is referred as wave-induced stress τ_w :

$$\tau_w(z) = \rho_w \int_0^{k(z)} \omega \frac{\partial}{\partial t} \phi|_{wind} dk. \quad (2.156)$$

The ratio of wave-induced stress τ_w to the total stress τ ($\tau = \rho_a u_*^2$), depends strongly on the wave age. The wave-induced stress τ_w is large for a young sea (say $\frac{C}{u_*} \approx 5$) and rather small for an old sea (say $\frac{C}{u_*} \approx 30$). In other words, the airflow over a young sea corresponds to the flow over a rough sea surface with a higher value of the drag coefficient and strong coupling of the wind and surface gravity waves.

The rate of change of the wind profile in time, which induces the influence of waves on the airflow, is governed by the equation (Janssen, 1989):

$$\frac{\partial U}{\partial t} = \nu \frac{\partial^2 U}{\partial z^2} + \frac{1}{\rho_a} \frac{\partial \tau_{turb}}{\partial z}, \quad (2.157)$$

in which $\nu = \nu_a + \mathcal{D}_w$, and wave diffusion coefficient \mathcal{D}_w is proportional to the wave spectrum $\hat{\Psi}(k)$:

$$\mathcal{D}_w = \frac{\pi C^2 k^2 |\chi|^2}{|C - C_g|} \hat{\Psi}(k), \quad (2.158)$$

where χ is a solution of Rayleigh's equation (2.98), and C_g is a group velocity.

Equation (2.157) suggests that the effect of waves on the wind profile is similar to the effect of molecular viscosity, and accordingly, the turbulent stresses in Eq. (2.157) are modelled by the mixing-length approach in which:

$$\tau_{turb} = \rho_a l^2 \left| \frac{\partial U}{\partial z} \right| \frac{\partial U}{\partial z}, \quad (2.159)$$

where $l = \kappa z$.

The two mechanisms on the right-hand side of Eq. (2.157) have a different impact in the wind profile; namely the air turbulence attempts to maintain a logarithmic wind profile while the viscosity and surface waves try to maintain a linear wind profile.

The total stress for a steady-state solution are a summation of the wave-induced, turbulent, and viscous stresses:

$$\tau_{total} = \tau_w + \tau_{turb} + \tau_{visc}, \quad (2.160)$$

in which τ_w and τ_{turb} are given by Eqs. (2.156) and (2.159), respectively, and viscous stresses take the form:

$$\tau_{visc} = \rho_a \nu_a \frac{\partial U}{\partial z}. \quad (2.161)$$

Numerical calculations showed that for a young sea ($C/u_* = 5$) the wave-induced stress becomes a considerable part of the total stress ($\sim 95\%$) at the sea surface, where $gz/u_* \approx 0.02$, while the turbulent stress is only a small portion of total stress. For an old sea, the surface stress is dominated by the turbulent stress related to the very short gravity and capillary waves. The wave-induced stresses at the sea surface are smaller, being only 30% of the total stress. The contribution of viscous stresses at the sea surface is quite small. This result agrees with Miles (1965) who considered only fully developed sea spectra and found that the effect of the gravity waves on wind profile is very small.

For a given phase speed, the coupling coefficient μ (as well as the wave growth rate) is larger for an old sea than for a young sea. For a young sea the resonance between wave and airflow occurs at a larger height rather than for an older, smooth

sea. In this wind speed range the wind profile is logarithmic and $W''/W' \approx \frac{1}{z_c}$ in Eq. (2.97). For fixed phase velocity this quantity is smaller for a young sea. At the same time, the wave-induced air velocity increases. The resulting reduction of the growth rate for a young sea is a combination of these two competing mechanisms.

2.4.8 Wind-current coupling in gravity-capillary wave generation model

In recent years, remote sensing techniques have become more and more popular for detecting the sea surface (see Chapter 9). Formation of radar image of the surface strongly depends on the processes transferring energy and momentum from the wind to the waves. For example, the amount of microwave radar backscatter is dominant at the Bragg wave length of the order of 4–40 cm. These wave lengths correspond to the early stage of wave generation. In Section 2.4.2 we briefly described basic models of wave generation. Miles' laminar model, whereby the air motion, modulated by the vertical motion of the water, leads to a resonant coupling between the surface motion and the horizontal variations in the pressure field. A linear-logarithmic flow in air is assumed and water is at rest, i.e. the wind-induced current is neglected. This means that these two flows do not satisfy the equation for continuity of shearing stress at the boundary of two fluids.

Physically, the growth of waves on the interface of water and air can be seen as the perturbation of the equilibrium consisting of a plane interface and uniform basic flow $U(z)$ in air and water (see Fig. 2.4). When wind sets in, after a few seconds, the upper layer of the water starts to drift with the wind. These flows are both strongly sheared near the interface and unstable and ripples soon start to appear.

Assuming that gravity is the only body force present, and turbulence and other nonlinear features are negligibly small, we can view the growing surface waves as perturbations on the shear current. The wave dynamics is then described by the appropriate Orr-Sommerfeld equation. Let $\zeta(x, t)$ be a displacement of the interface from equilibrium and the perturbation velocity components be $u(x, z, t)$ and $w(x, z, t)$. A perturbation stream function $\psi(x, z, t)$ takes the form (Valenzuela, 1976; Gastel et al., 1985):

$$\psi(x, z, t) = \phi(z) \exp [ik(x - Ct)], \quad (2.162)$$

with the surface elevation expressed in the wave-like form:

$$\zeta(x, t) = \zeta_0 \exp [ik(x - Ct)]. \quad (2.163)$$

The resulting Orr-Sommerfeld equation for ϕ in air and in water becomes (Valenzuela, 1976):

$$i\nu_a (\phi_a^{IV} - 2k^2 \phi_a'' + k^4 \phi_a) + k [(U - C) (\phi_a'' - k^2 \phi_a) - U_a'' \phi_a] = 0, \quad (2.164)$$

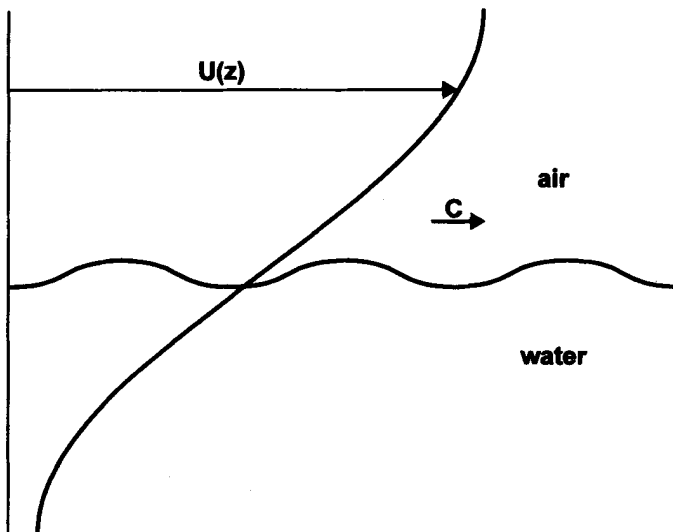


Figure 2.4: Interface of air and water flows.

and

$$i\nu_w (\phi_w^{IV} - 2k^2\phi_w'' + k^4\phi_w) + k [(U - C)(\phi_w'' - k^2\phi_w) - U_w''\phi_w] = 0. \quad (2.165)$$

The primes denote the differentiation against z .

At the surface, the discontinuity in normal pressure is balanced by surface tension. Moreover, the tangential stresses must be continuous. The resulting boundary conditions, for normal stresses are applied at the sea surface but are referred to $z = 0$, i.e.:

$$\left(p_a(z) - 2\mu_a \frac{\partial w_a}{\partial z} \right) - \left(p_w(z) - 2\mu_w \frac{\partial w_w}{\partial z} \right) = T \frac{\partial^2 \zeta}{\partial x^2} \quad \text{at } z = 0, \quad (2.166)$$

in which subscripts a and w denote the quantities in air and in water, respectively, and T is surface tension.

The continuity in tangential stresses can be expressed as:

$$\mu_a \left(\frac{\partial w_a}{\partial x} + \frac{\partial u_a}{\partial z} + \zeta \frac{\partial^2 U_a}{\partial z^2} \right) = \mu_w \left(\frac{\partial w_w}{\partial x} + \frac{\partial u_w}{\partial z} + \zeta \frac{\partial^2 U_w}{\partial z^2} \right) \quad \text{at } z = 0. \quad (2.167)$$

Finally, the continuity of first-order velocity components at the free surface requires that:

$$\left. \begin{aligned} w_a &= w_w \\ u_a + \zeta \frac{\partial U_a}{\partial z} &= u_w + \zeta \frac{\partial U_w}{\partial z} \end{aligned} \right\} \text{ at } z = 0. \quad (2.168)$$

In general in the air, the linear-logarithmic profile is used, while in the water various profiles are adopted. Valenzuela (1976) assumes a linear-logarithmic profile while, Kawai (1979) uses an error-function-line profile, and Gastel et al. (1985) apply an exponential profile. It should be noted that Miles (1962) took simply $U(z) = 0$ in water.

The numerical solutions of the boundary value problem (2.162) – (2.168) indicate that the growth rate of the initial wavelets is very sensitive to the wind speed and wind profile. Moreover, changes in the shape of the wind profile, even above the critical height, can change the growth rate by a factor of more than three (Gastel et al., 1985). The influence of the current profile in water layer on the growth was found to be less dramatic, but still significant. For example, when the current was uniformly set to zero the growth rates were about 15% lower than when an exponential velocity profile was used. It was found that the phase velocity is more sensitive to the wind-induced current than to the wind itself. Good agreement of numerical models can be obtained when the value of the current at the surface is known *a priori*.

The influence of some contaminants at the surface on wave generation and growth was examined recently by Creamer and Wright (1992). They found that the main effect of adding surfactants to the surface is a large reduction in the growth rate of wind-generated waves due to the presence of film material. However, this reduction is mostly related to the change in the wave number of the maximally growing waves rather than to the actual attenuation due to the film itself.

2.5 Wave energy balance in spectral form

Wave generation models provide the linkage between spectrum of air pressure fluctuations $\Psi_a(\vec{k}, \omega)$ and the wave number spectrum of surface oscillations $\hat{\Psi}(\vec{k}, \vec{x}, t)$ in a simpler case when waves propagate in deep water or in water of finite but constant depth. Generally, when water depth changes in space, and island or artificial obstacles are present, the wind generated waves will undergo several other processes such as refraction, diffraction and dissipation due to bottom friction, white capping and breaking in the surf zone.

Taking into account the random character of wave motion, it seems that the most appropriate method of evaluation of waves, in time and space are the spectral methods. Resulting functions of these methods, i.e. the spectral densities $S(\omega, \Theta)$ or $\hat{\Psi}(\vec{k})$, provide the distribution of wave energy in the frequency or wave number space.

In order to develop an energy balance equation we assume for a moment that the dispersion relation does not depend on time, but is rather a slowly changing function of space coordinates. It can also depend on local properties such as water depth, current velocity or ambient density current, i.e.:

$$\omega = \Omega \left[\vec{k}, f(\vec{x}, h, \vec{U}, \rho, \dots) \right]. \quad (2.169)$$

If the medium itself is moving with velocity \vec{U} , the frequency of waves passing a field point is:

$$\omega = \Omega(\vec{k}, \vec{x}) = \sigma + \vec{k} \cdot \vec{U} = [gk \tanh(kh)]^{1/2} + \vec{k} \cdot \vec{U}. \quad (2.170)$$

Usually the quantity ω is called the observed or apparent frequency, while σ is the intrinsic frequency whose functional dependence on \vec{k} is known as a classical dispersion relation:

$$\sigma^2 = gk \tanh(kh). \quad (2.171)$$

It is well known that the number of wave crests passing a given point per unit time is determined by the kinematical conservation equation (Massel, 1989):

$$\frac{\partial \vec{k}}{\partial t} + \nabla_{\vec{k}} \omega = 0, \quad \frac{\partial k_i}{\partial x_j} - \frac{\partial k_j}{\partial x_i} = 0, \quad i, j = 1, 2. \quad (2.172)$$

Substituting Eq. (2.169) into Eq. (2.172) gives:

$$\frac{\partial k_i}{\partial t} + C_{g_j}(\vec{x}, \vec{k}, t) \frac{\partial k_j}{\partial x_i} = - \frac{\partial \Omega}{\partial x_i}, \quad (2.173)$$

in which $C_{g_j} = \frac{\partial \Omega}{\partial k_j}$ is a group velocity.

Eq. (2.173) can be rewritten as:

$$\frac{dk_i}{dt} = - \frac{\partial \Omega}{\partial x_i} \quad \text{and} \quad \frac{dx_i}{dt} = \frac{\partial \Omega}{\partial k_i}. \quad (2.174)$$

Equations (2.174) are identical to the Hamilton equations in mechanics. The vectors \vec{x} should be interpreted as coordinates and vectors \vec{k} represent the momenta, and the frequency $\Omega(\vec{k}, \vec{x}, t)$ is taken to be the Hamiltonian (Whitham, 1974; Massel, 1989).

For free surface waves, the mean densities of potential and kinetic energy are equal. Therefore, $2\hat{\Psi}(\vec{k}, \vec{x}, t)$ is a mean spectral density of total wave energy in the unit volume $d\vec{k} \cdot d\vec{x}$ in phase space (\vec{k}, \vec{x}) at a given time t . According to Liouville's theorem, this energy should be conservative during volume evolution:

$$\frac{d\hat{\Psi}}{dt} = \frac{\partial \hat{\Psi}}{\partial t} + \frac{\partial x_i}{\partial t} \frac{\partial \hat{\Psi}}{\partial x_i} + \frac{\partial k_i}{\partial x_i} \frac{\partial \hat{\Psi}}{\partial k_i} = 0, \quad (2.175)$$

or

$$\frac{\partial \hat{\Psi}}{\partial t} + \frac{\partial \Omega}{\partial k_i} \frac{\partial \hat{\Psi}}{\partial x_i} - \frac{\partial \Omega}{\partial x_i} \frac{\partial \hat{\Psi}}{\partial k_i} = 0, \quad (2.176)$$

when Eq. (2.174) is used.

If the wave field is subjected to processes of generation, dissipation, nonlinear interaction between spectral components and other possible interactions with atmospheric boundary layer and various ocean movements (currents, internal waves, etc.), Eq. (2.176) should be supplemented by a source - sink term at the right-hand side, i.e.:

$$\frac{\partial \hat{\Psi}}{\partial t} + \frac{\partial \Omega}{\partial k_i} \frac{\partial \hat{\Psi}}{\partial x_i} - \frac{\partial \Omega}{\partial x_i} \frac{\partial \hat{\Psi}}{\partial k_i} = Q(\vec{k}, \vec{x}, t), \quad (2.177)$$

in which $Q = \sum_i Q_i$.

The first term at the left-hand side of Eq. (2.177) expresses the local evolution of the spectrum in time, while the second term represents the evolution of the spectrum for the horizontally non-homogeneous wave field. This term shows that energy is transported at the group velocity. The third term reflects the effects of refraction and shoaling due to a non-horizontal bottom or due to current. The spectral energy balance equation is also known as the radiative transfer equation or the transport equation. In particular, an analogy between the sea and a kinetic gas, which explains the name kinetic equation, is used by Russian oceanographers.

In engineering and oceanographic practice the two-dimensional spectrum $\hat{S}(\omega, \theta; \vec{x}, t)$ is frequently used, rather than the wave number spectrum $\hat{\Psi}(\vec{k}; \vec{x}, t)$. To evaluate spectrum $\hat{S}(\omega, \theta; \vec{x}, t)$, we adopt the following variables transformation:

$$k_1 = \chi(\omega, \vec{x}) \cos \theta, \quad k_2 = \chi(\omega, \vec{x}) \sin \theta, \quad (2.178)$$

where function $\chi(\omega, \vec{x}) = k$ is a solution of the dispersion relation:

$$\omega^2 = gk \tanh(kh). \quad (2.179)$$

Hunt (1979) found an approximate solution of this dispersion relation in Pade' approximant form (accurate to 0.1% for all frequency range) as:

$$(kh)^2 = \left(\frac{\omega^2 h}{g} \right)^2 + \frac{\frac{\omega^2 h}{g}}{1 + \sum_{n=1}^{\infty} d_n \left(\frac{\omega^2 h}{g} \right)^n}, \quad (2.180)$$

in which:

$d_1 = 0.6666666667$, $d_2 = 0.3555555556$, $d_3 = 0.1608465608$, $d_4 = 0.0632098765$, $d_5 = 0.0217540484$ and $d_6 = 0.0065407983$. Variables transformation (2.178) yields:

$$\hat{\Psi}(\vec{k}; \vec{x}, t) = J \hat{S}(\omega, \theta; \vec{x}, t) = f(\omega, \theta; \vec{x}, t), \quad (2.181)$$

in which J is a Jacobian of the transformation, i.e.:

$$J = \frac{\partial(\omega, \theta)}{\partial(k_1, k_2)} = \left[\frac{\partial(k_1, k_2)}{\partial(\omega, \theta)} \right]^{-1} \quad (2.182)$$

Thus:

$$J = \left\{ \begin{vmatrix} \frac{\partial \chi}{\partial \omega} \cos \theta, & -\chi \sin \theta \\ \frac{\partial \chi}{\partial \omega} \sin \theta, & -\chi \cos \theta \end{vmatrix} \right\}^{-1} = \frac{C_g}{\chi} \quad (2.183)$$

After substituting Eq. (2.181) into Eq. (2.177) we obtain (Krasitskii, 1974):

$$\begin{aligned} \frac{\partial f}{\partial t} + C_g \cos \theta \frac{\partial f}{\partial x} + C_g \sin \theta \frac{\partial f}{\partial y} + C_g \left(\cos \theta \frac{\partial \ln \chi}{\partial y} - \sin \theta \frac{\partial \ln \chi}{\partial x} \right) \frac{\partial f}{\partial \theta} = \\ = \frac{C_g}{\chi} \hat{Q}(\omega, \theta, \vec{x}, t). \end{aligned} \quad (2.184)$$

As $C = \frac{\omega}{\chi} = \frac{\omega}{k}$, we can rewrite Eq. (2.184) as follows:

$$\begin{aligned} \frac{\partial}{\partial t}(CC_g \hat{S}) + C_g \cos \theta \frac{\partial}{\partial x}(CC_g \hat{S}) + C_g \sin \theta \frac{\partial}{\partial y}(CC_g \hat{S}) + \\ + \frac{C_g}{C} \left[\sin \theta \frac{\partial C}{\partial x} - \cos \theta \frac{\partial C}{\partial y} \right] \frac{\partial}{\partial \theta}(CC_g \hat{S}) = CC_g \hat{Q}(\omega, \theta, \vec{x}, t), \end{aligned} \quad (2.185)$$

in which $\hat{Q} = \sum_i \hat{Q}_i$. Some solutions of Eq. (2.184) (or (2.185)) will be discussed in Chapters 5 and 6.

Equations (2.184) and (2.185) can apply for a dispersion relation not depending on time, when an ambient current is uniform in space. If waves propagate on a non-stationary and non-uniform current $\vec{U}(\vec{x}, t)$, the intrinsic frequency σ may vary in space and time. In such a case, the spectral energy density will not be conserved. Bretherton and Garrett (1969) showed that the quantity called wave action density

$N = \frac{\hat{\Psi}(\vec{k}; \vec{x}, t)}{\sigma}$ is conserved in a moving medium. Therefore, instead of Eq. (2.177), we apply a more general principle of conservation of wave action density N in the form:

$$\frac{\partial N}{\partial t} + \frac{\partial \Omega}{\partial k_i} \frac{\partial N}{\partial x_i} - \frac{\partial \Omega}{\partial x_i} \frac{\partial N}{\partial k_i} = \frac{Q}{\sigma}. \quad (2.186)$$

In order to illustrate the relationship between wave action density N and energy density $\hat{\Psi}$ let us consider the simplest example of a steady unidirectional wave train

in deep water on a variable current $U(x)$ (source term $Q \equiv 0$). Then, Eq. (2.186) reduces to:

$$\frac{\partial}{\partial x} \left[\hat{\Psi} \left(\frac{U + C_g}{\sigma} \right) \right] = 0. \quad (2.187)$$

For gravity waves in deep water $\sigma = g/C$ and $C_g = \frac{1}{2}C$. Thus:

$$\hat{\Psi} \left(U + \frac{1}{2}C \right) C = \text{const} = \frac{1}{2} \hat{\Psi}_0 C_0^2. \quad (2.188)$$

Although the flux of wave action is constant, the flux of wave energy is not. For example, as C decreases in an adverse current, the energy flux of the wave motion increases because of the work done by 'radiation stress' (Longuet-Higgins and Stewart, 1964; Massel, 1989).

The basic difficulty in solving Eq. (2.177) or (2.186) is an evaluation of the function Q . In general, Q is a function of wave number \vec{k} and a functional of $\hat{\Psi}$, i.e. $Q = Q[\vec{k}, \hat{\Psi}]$. Function Q can also be dependent on other parameters which are functions of \vec{x} and t (for example, wind velocity).

One of the basic components of function Q is a term which describes the nonlinear interactions between wave components. In general, nonlinear interactions in the wave field are weak as the evolution time of the wave field is much greater than the characteristic wave period and the evolution in space is much greater than the characteristic wavelength. However, in some regions and at some times, the interactions may be quite strong. For example, strong interactions are induced by wave breaking.

The theory of nonlinear weak interactions for wind-induced waves was first formulated by Hasselmann (1962, 1968). Assuming that:

$$\frac{1}{k} \frac{\partial \hat{\Psi}}{\partial k_i} \ll 1 \quad \text{and} \quad \frac{1}{\omega} \frac{\partial \hat{\Psi}}{\partial t} \ll 1, \quad (2.189)$$

with the accuracy of the second approximation in interaction equations, Hasselmann evaluated the general form of function Q as (Hasselmann, 1968; Willebrand, 1975):

$$Q(\vec{k}) = \sum_{i=1}^{i=9} Q_i, \quad (2.190)$$

in which

$$Q_1 = \alpha, \quad (2.191)$$

$$Q_2 = \beta \hat{\Psi}(\vec{k}), \quad (2.192)$$

$$Q_3 = \hat{\Psi}(\vec{k}) \int \hat{\gamma}(\vec{k}, \vec{k}') \hat{\Psi}(\vec{k}') d\vec{k}', \quad (2.193)$$

$$Q_4 = -\delta \hat{\Psi}(\vec{k}) + \int \epsilon(\vec{k}, \vec{k}') \hat{\Psi}(\vec{k}') d\vec{k}', \quad (2.194)$$

$$Q_5 = \int [T_1 \hat{\Psi}(\vec{k}') \hat{\Psi}(\vec{k}'') \hat{\Psi}(\vec{k} - \vec{k}' - \vec{k}'') - T_2 \hat{\Psi}(\vec{k}) \hat{\Psi}(\vec{k}') \hat{\Psi}(\vec{k}'')] d\vec{k}' d\vec{k}'', \quad (2.195)$$

$$Q_6 = -\nu_{ij} k_i k_j \hat{\Psi}(\vec{k}), \quad (2.196)$$

$$Q_7 = -\hat{\gamma} \hat{\Psi}(\vec{k}). \quad (2.197)$$

The coefficients $\alpha, \beta, \delta, \epsilon, \hat{\gamma}$ depend on the properties of the interacting fields. Similar expressions for \hat{Q} in Eq. (2.185) are obtained after appropriate variables transformation.

The term Q_1 describes energy flux due to turbulent fluctuations of surface pressure (Phillips' mechanism). Term Q_2 corresponds to Miles' coupling mechanism between the wave field and the mean boundary layer flow. The term Q_3 is a nonlinear correction of Miles' theory and Q_4 is responsible for interaction of the wave motion with atmospheric turbulence. The term Q_5 expresses nonlinear interaction between spectral components, while Q_6 represents the energy changes due to interaction of waves with the mean current. The term Q_7 expresses the energy changes due to interaction of waves with turbulence in the water layer. The two other components of source function Q (Q_8 and Q_9) describe the strong nonlinearities. The term Q_8 is related to energy dissipation due to bottom friction and Q_9 represents the dissipation of wave energy due to wave breaking.

Further discussion of the particular Q_i components and their importance for wave prediction models is given in Chapters 5 and 6.

Chapter 3

Spectral Properties of Ocean Waves

3.1 Introduction

In this Chapter we apply the basic properties of spectral analysis of the time series, introduced in Chapter 1, to interpret the spectra of ocean surface waves. In general, the resulting shape of the frequency spectrum depends on the external wave generation conditions (wind speed, wind fetch and duration, water depth, swell presence, and storm stage) as well as on internal mechanisms in the wave field (nonlinear interaction between wave components, energy dissipation due to wave breaking or bottom friction). However, the spectrum shape is not arbitrary and some fundamental properties of energy distribution apply for all spectra.

The wave spectral energy reaches its maximum at frequency $\omega = \omega_p$ and decreases for both lower and higher frequencies. Usually the decreasing at the low-frequency range is faster than that for the high-frequency band. The lowest frequency for the wind-induced gravity waves is estimated at approximately 0.03 Hz (0.2 rad/s). Energy at frequencies lower than this value is for surf beat, seiches or tides (Massel, 1989).

The highest frequency of wind-induced gravity waves corresponds to the minimum phase velocity of 23 cm/s at a minimum wavelength of 1.7 cm (in clean water at 20°C). Thus, the highest frequency is 13.6 Hz (85 rad/s). For higher frequencies, the restoring force is predominantly the result of surface tension, which is typical for capillary waves. The limiting frequencies given above are theoretical approximations. In practice we consider a much smaller frequency band of gravity, wind-induced waves.

Furthermore, spectra often show regularity, such as power-law regions, where $S(\omega) \sim \omega^{-n}$ for some power n . A good example of such regularities is provided by the saturation range (or equilibrium range) in the wave spectrum, when a spectrum shows ω^{-5} (or ω^{-4}) dependence. The saturation range expresses some equilibrium between energy loss, mainly due to breaking, and the same rate of energy acquired by waves from the wind.

To include the most energetic part of the spectrum, a variety of power functions multiplied by some exponential functions have been proposed. This variety of the spectra is mostly a result of various experimental time series which are the base for spectrum formulation and which reflect various wave generation conditions.

The spectrum provides a complete description of the ocean waves only when they are considered as a linear superposition of many elementary sinusoidal components. However, especially in shallow waters, ocean waves show increasingly sharper peaks and shallower troughs, caused by the harmonic components generation and their interactions. Presence of the harmonic components can be seen in ocean spectrum as additional peaks, usually in its high frequency range.

This information is not sufficient for a detection of the interacting frequency combinations which cause such peaks. To obtain the 'map' of interacting frequencies, a higher order spectral analysis is needed. In Section 3.2.3, the bispectrum is formulated and its usefulness is discussed. The bispectrum is a Fourier transform of the two-dimensional autocorrelation function and represents a contribution of three Fourier components to the third moment $E[\zeta^3]$.

Finally, in Section 3.3 the directional energy spreading is described. Due to the complicated energy transfer from the atmosphere to the sea, the resulting surface waves are multidirectional. Only part of wave energy is aligned with the wind direction. Because of the limitation of observational methods, a knowledge on the directional spreading is relatively poor compared to the frequency spectrum. In this Section we give a review of the present representations of the directional properties of ocean waves, namely the cosine-power models, wrapped-around the Gaussian model, von Mises model, hyperbolic type model, and double peak spreading model.

3.2 Frequency spectra of ocean waves

3.2.1 Spectral moments and spectral width

In Fig. 3.1, a typical frequency wave spectrum and corresponding autocorrelation function are shown. The normalized autocorrelation function $K(\tau)/\sigma_\zeta^2$ starts at unity for zero lag, $\tau = 0$. Using a definition of the correlation scale (see Eq. 1.46) we can recognize that in our case $\tau_0 \approx 7s$. In Table 1.2 has been shown that the autocorrelation function $K(\tau)$ of a cosinusoidal signal with random phase is given as:

$$\frac{K(\tau)}{K_0} = \cos(\omega_0\tau) = \cos\left(\frac{2\pi\tau}{T_0}\right), \quad (3.1)$$

in which T_0 is a period of signal. Function $K(\tau)$ vanishes for $\tau_1 = T_0/4$. Assuming that most of wave energy is concentrated around the peak frequency $\omega_p = 2\pi/T_0$, it is then natural to associate the first zero crossing of function $K(\tau)$, at $\tau = \tau_1$, with the dominant period of the process. Thus, the peak frequency $\omega_p = 2\pi/4\tau_1$.

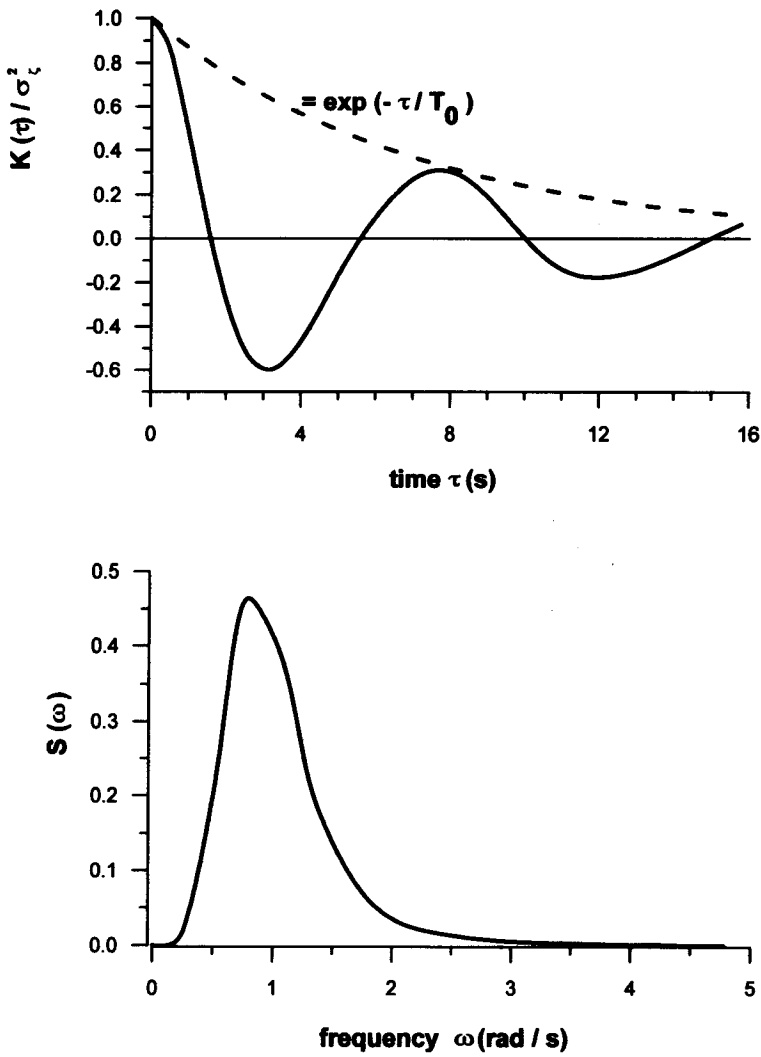


Figure 3.1: Autocorrelation function $K(\tau)$ and spectral density function $S(\omega)$.

In Fig. 3.1, $\tau_1 \simeq 1.7s$, corresponding to peak frequency $\omega_p = 2\pi/(4 \cdot 1.7) = 0.92$ rad/s. A glance at the spectrum in Fig. 3.1 shows a peak at $\omega_p \approx 0.85$ rad/s, which is close to the approximated value of 0.92 rad/s.

The function $S(\omega)$ represents a distribution of wave energy in the frequency domain. Thus:

$$\int_0^\infty S(\omega) d\omega = \sigma_\zeta^2 = m_0. \quad (3.2)$$

The variance σ_ζ^2 is also called the zero-moment of the spectrum. In general, the spectral moments m_r are defined as:

$$m_r = \int_0^\infty \omega^r S(\omega) d\omega. \quad (3.3)$$

The few first moments are of special importance for the spectral description of ocean waves. The first moment m_1 determines the mean wave frequency and mean wave period, i.e.:

$$\bar{\omega} = \frac{m_1}{m_0} \quad \text{and} \quad \bar{T} = \frac{2\pi}{\bar{\omega}} = 2\pi \frac{m_0}{m_1}. \quad (3.4)$$

An alternative estimate of the mean frequency (period) also exists. It is called the average frequency of up-crossing of the mean level $\bar{\omega}_0$ (and average period \bar{T}_0):

$$\bar{\omega}_0 = \sqrt{\frac{m_2}{m_0}} \quad \text{and} \quad \bar{T}_0 = \frac{2\pi}{\bar{\omega}_0} = 2\pi \sqrt{\frac{m_0}{m_2}}. \quad (3.5)$$

If determined in this way, $\bar{\omega}_0$ has the property that the curve $\zeta = a_{rms} \cos(\bar{\omega}_0 t)$ has the same number of zero-crossings per unit time as the record with spectrum $S(\omega)$ (Rice, 1944). The a_{rms} denotes the root mean square wave amplitude. More details on the statistics of wave period are given in Chapter 4.

As well as moments m_r , the central spectral moments \tilde{m}_r are also used. They are defined as:

$$\tilde{m}_r = \int_0^\infty (\omega - \bar{\omega})^r S(\omega) d\omega. \quad (3.6)$$

Thus:

$$\tilde{m}_0 = m_0, \quad \tilde{m}_1 = m_1 - \bar{\omega} m_0 = 0, \quad \tilde{m}_2 = m_2 - \frac{m_1^2}{m_0}. \quad (3.7)$$

The central moment \tilde{m}_2 is a measure of concentration of the spectral wave energy around frequency $\bar{\omega}$.

When we normalize \tilde{m}_2 in Eq. (3.7) by product $(\bar{\omega}^2 m_0)$, we obtain non-dimensional parameter ν^2 as:

$$\nu^2 = \frac{\tilde{m}_2}{\bar{\omega}^2 m_0} = \frac{m_0 m_2}{m_1^2} - 1. \quad (3.8)$$

Parameter ν^2 is a convenient, lower-order quantity which is a measure of the spectral width. Equation (3.8) clearly indicates that when all wave energy is concentrated in the one frequency $\omega = \bar{\omega}$, then $\nu^2 \rightarrow 0$. When wave energy is broadly distributed among frequencies, then ν^2 increases. In typical storm conditions, the spectral width parameter ν is approximately equal to 0.3.

Typical wave profiles, corresponding to narrow- and wide-spectra are shown in Fig. 3.2. It is seen that waves of a narrow spectrum have almost the same frequency but gradually varying amplitudes. The upper and lower envelopes coincide exactly with crests and troughs, and form a pair of symmetrical curves with respect to mean value. In such a case, the positive and negative maximum excursions of the wave surface are equal to each other, and equal to wave amplitude (for more discussion on wave amplitude see Section 4.3). In the case of a wide spectrum, waves of many frequencies are present and these ride on each other to produce local maxima as readily below mean sea level as above it.

Another measure of spectral width appears when developing the statistics of wave amplitude (see Section 4.3). Parameter ϵ^2 was first defined by Cartwright and Longuet-Higgins (1956) as:

$$\epsilon^2 = \frac{1}{2m_0m_4} \int_0^\infty \int_0^\infty S(\omega_1)S(\omega_2) (\omega_1^2 - \omega_2^2)^2 d\omega_1 d\omega_2, \quad (3.9)$$

or

$$\epsilon^2 = \frac{m_0m_4 - m_2^2}{m_0m_4}. \quad (3.10)$$

It follows that:

$$0 < \epsilon^2 \leq 1.$$

When the wave spectrum $S(\omega)$ is extremely narrow, say $S(\omega) = \sigma_\zeta^2 \delta(\omega - \omega_p)$, then $\epsilon^2 \rightarrow 0$.

Let us assume that spectrum $S(\omega)$ takes a form:

$$S(\omega) = \begin{cases} S_0 & , \quad \omega < n\omega_p \\ 0 & , \quad \omega \geq n\omega_p \end{cases}, \quad (3.11)$$

in which ω_p is some characteristic frequency and n is some positive number. Then, using Eq. (3.10) we obtain:

$$\epsilon^2 = \frac{4}{9}. \quad (3.12)$$

It should be noted that ϵ^2 value is independent of the frequency band $n\omega_p$.

Finally, we apply definition (3.9) to a spectrum with two peaks:

$$S(\omega) = \sigma_\zeta^2 \alpha \delta(\omega - \omega_a) + \sigma_\zeta^2 (1 - \alpha) \delta(\omega - \omega_b). \quad (3.13)$$

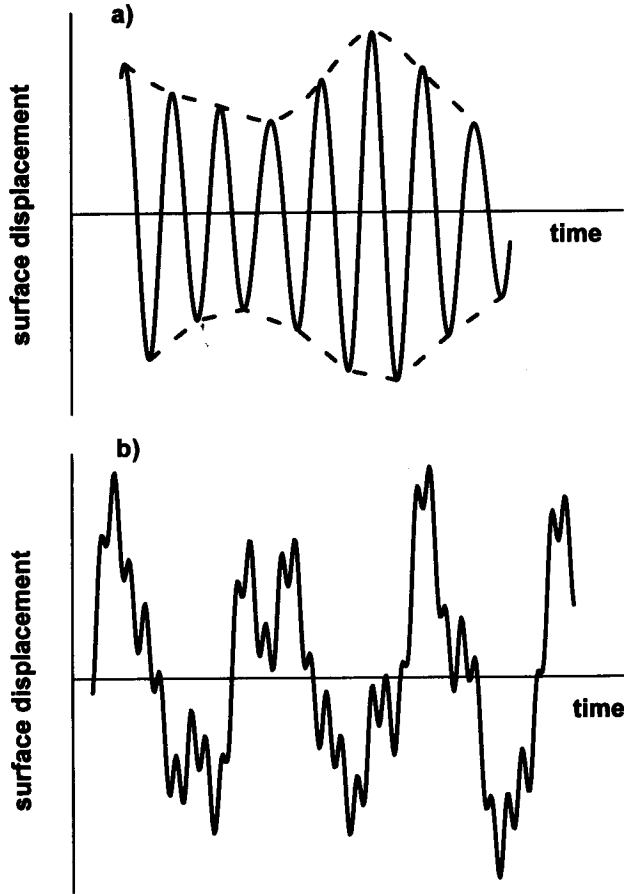


Figure 3.2: Time history of surface displacement: a) narrow spectrum and b) wide spectrum.

The calculation gives:

$$\epsilon^2 = \frac{\alpha(1-\alpha)(\omega_a^4 + \omega_b^4) - 4\alpha(1-\alpha)\omega_a^2\omega_b^2}{\alpha\omega_a^4 + (1-\alpha)\omega_b^4}. \quad (3.14)$$

Assuming that $\frac{\omega_a}{\omega_b} \rightarrow 0$ and $\omega_a \neq 0$ yields $\epsilon^2 = \alpha$. Thus, ϵ^2 can be as near to unity as is the α value.

3.2.2 Spectrum shape

3.2.2.1 Saturation range

The growth of waves under the influence of wind is not infinite. The energy supplied by the wind is balanced by wave interactions which transfer energy from a given frequency band to other frequencies, and by energy dissipation. In deep water, the dissipation frequently takes the form of 'white caps' of scale smaller than the wavelength. White caps occur when two wave crests are superimposed or when shorter waves ride over the crest of longer ones.

Another form of the limitation of wave growth is related to the formation of capillary waves just in front of sharp primary wave crests. These capillary waves extract energy from primary waves of high curvature (Phillips, 1977). We also note that the surface drift layer produced by wind stress enhances wave breaking at a greatly reduced wave amplitude. More information on wave breaking in deep and shallow water is given in Chapters 5 and 6. Here we only point to the fact that each of these mechanisms places an upper limit on the growth of waves by the extraction of energy at a critical condition.

The occurrence of any such mechanism is an indication of a stage of saturation of wave components, in which a balance between energy supplied by wind and that lost by dissipation is achieved. Therefore, the saturation range should be exclusively described by local physical parameters that govern the extreme configuration of waves, i.e. gravitational acceleration (g), friction velocity of the wind over the wave surface (u_*), and local frequency (ω). Phillips (1958), using dimensional arguments, found that:

$$S(\omega) = f\left(\frac{\omega u_*}{g}\right) g^2 \omega^{-5}. \quad (3.15)$$

When the surface drift is unimportant, i.e. $\frac{\omega u_*}{g} \ll 2$ ($u_* = \left(\frac{\tau}{\rho_a}\right)^{1/2}$, τ is mean tangential stress), Eq. (3.15) yields:

$$S(\omega) = \alpha g^2 \omega^{-5} \quad \left(\omega_p \ll \omega \ll \frac{2g}{u_*}\right), \quad (3.16)$$

in which α is a constant ($\alpha = 1.23 \cdot 10^{-2}$).

The wave number spectrum $\hat{\Psi}(\vec{k})$, corresponding to spectrum (3.16), takes the form:

$$\hat{\Psi}(\vec{k}) = f(\theta) k^{-4} \quad \left(k_p \ll k \ll \frac{2g}{u_*^2}\right), \quad (3.17)$$

in which the angle θ specifies the direction of the wave number vector \vec{k} and $f(\theta)$ is the undetermined coefficient function. Results of field experiments on the wave

number spectrum for the wavelength range of 0.2 - 1.6 m were presented by Banner et al. (1989). They found that the spectrum $\hat{\Psi}(\vec{k})$ can be approximated as:

$$\hat{\Psi}(\vec{k}) = 0.3 \cdot 10^{-4} k^{-4}, \quad (3.18)$$

for $(u_*^2 k/g) = 10^{-2}$, when $k = |\vec{k}|$ is expressed in cycles/meter.

Phillips' constant α and energy loss by wave breaking

Longuet-Higgins (1969a) derived a semi-theoretical estimate of the relationship between α and energy loss assuming that wave breaking occurs whenever the vertical acceleration at the crest approaches $\left(-\frac{1}{2}g\right)$. If for a moment we use a linear expression for surface waves:

$$\zeta = a \cos(kx - \omega t), \quad (3.19)$$

it follows that the breaking condition is:

$$a\omega^2 = \frac{1}{2}g. \quad (3.20)$$

In the more general case of a narrow spectrum, the distribution of wave amplitude a is a Rayleigh distribution (see Chapter 4):

$$f(a) = \frac{2a}{a_{rms}^2} \exp\left[-\frac{a^2}{a_{rms}^2}\right], \quad (3.21)$$

in which a_{rms} is a root-mean-square amplitude.

Let us assume that all waves of amplitude greater than the critical amplitude a_0 will break; using Eq. (3.20) we have:

$$a_0 \bar{\omega}_0^2 = \frac{1}{2}g, \quad (3.22)$$

in which $\bar{\omega}_0$ is given by Eq. (3.5). The mean loss of energy per average period $\bar{T}_0 = \frac{2\pi}{\bar{\omega}_0}$ is:

$$\int_{a_0}^{\infty} \frac{1}{2}g(a^2 - a_0^2) f(a) da = E \exp(-E_0/E), \quad (3.23)$$

where:

$$E = \rho_w g \bar{\zeta}^2 = \rho_w g \int_0^{\infty} S(\omega) d\omega = \rho_w g m_0, \quad (3.24)$$

and

$$E_0 = \frac{1}{2} \rho_w g a_0^2 = \frac{1}{8} \rho_w g^3 (\bar{\omega}_0)^{-4}. \quad (3.25)$$

Therefore, the proportion (r) of energy lost per mean wave cycle is:

$$r = \exp \left[-\frac{E_0}{E} \right] = \exp \left[-\frac{1}{8} \frac{g^2}{m_0 \bar{\omega}_0^4} \right]. \quad (3.26)$$

Using representation (3.16) with sharp low-frequency cut-off at $\omega = \omega_p$, we obtain:

$$r = \exp \left(-\frac{1}{8\alpha} \right), \quad (3.27)$$

which is independent of ω_p .

To estimate the proportion r of wave energy lost due to white capping per average period, we consider the rate of working of wind W in the form:

$$W \sim \tau u_* = \rho_a u_*^3, \quad (3.28)$$

where the wind stress τ is:

$$\tau = \rho_a u_*^2 \approx C_{10} \rho_a U^2, \quad (3.29)$$

in which a drag coefficient $C_{10} \sim 1.5 \cdot 10^{-3}$.

From Eqs. (3.28) and (3.29) we obtain:

$$W = C_{10}^{3/2} \rho_a U^3. \quad (3.30)$$

The energy input per wave period becomes:

$$WT \approx 2\pi C_{10}^{3/2} \rho_a U^3 (\bar{\omega}_0)^{-1}, \quad (3.31)$$

Under saturation conditions this energy input is equal to the loss by wave breaking. Thus:

$$r \sim \frac{WT}{E}, \quad (3.32)$$

or

$$r \sim 1600 C_{10}^{3/2} \left(\frac{\rho_a}{\rho_w} \right). \quad (3.33)$$

With the values $C_{10} = 1.5 \cdot 10^{-3}$, $\frac{\rho_a}{\rho_w} = 1.3 \cdot 10^{-3}$, for a well-developed sea, we obtain:

$$r \sim 1.0 \cdot 10^{-4}. \quad (3.34)$$

Finally, from Eq. (3.27) the saturation range constant $\alpha \sim 1.35 \cdot 10^{-2}$. This value of α falls within the range of the experimentally determined values of α .

Dependence of α on external growth conditions

As more accurate and extensive measurements have become available, it has become more evident that the idea of a saturated upper limit to the spectrum is no

longer tenable. The constant (α) implied in Eq. (3.16) appeared to be a function of fetch, or wave age rather than an absolute constant. In particular, Eqs. (3.31) and (3.32) indicate that the coefficient (r) is proportional to T/E . As the variation of period T under different wind conditions is generally less pronounced than the variation of energy E , it might be expected that coefficient (r) will decrease with non-dimensional fetch (gX/U^2) or non-dimensional wind duration or wave age (gt/U). In fact, this tendency was observed by Hasselmann et al. (1973) during the JONSWAP experiment, i.e.:

$$\alpha = 0.076 \left(\frac{gX}{U^2} \right)^{-0.22}, \quad (3.35)$$

in which X is a wind fetch.

In general, the hypotheses of similarity for ocean waves (Kitaigorodskii, 1962) give the following representation of the energy spectrum:

$$S(\omega) = f(\omega, X, t, U, g). \quad (3.36)$$

In the same way we assume that variance σ_ζ^2 and peak frequency ω_p are:

$$\left. \begin{aligned} \sigma_\zeta^2 &= f_\sigma(X, t, U, g) \\ \omega_p &= f_\omega(X, t, U, g) \end{aligned} \right\}. \quad (3.37)$$

Using Eq. (3.37) we rewrite Eq. (3.36) in the form:

$$S(\omega) = f_1(\omega, g, \sigma_\zeta, \omega_p), \quad (3.38)$$

or in the non-dimensional form (Krylov et al., 1986):

$$S(\omega) = f_2 \left(\frac{\omega}{\omega_p}, \delta \right) g^2 \omega^{-5}, \quad (3.39)$$

in which $\delta = \frac{\sigma_\zeta \omega_p^2}{g}$ is a characteristic slope in deep water.

In saturation range of the spectrum $S \approx \omega^{-5}$. Then, $f_2 \left(\frac{\omega}{\omega_p}, \delta \right) \rightarrow f_2(\delta)$ for $\frac{\omega}{\omega_p} \gg 1$. The simplest approximation of function f_2 is:

$$f_2 \left(\frac{\omega}{\omega_p}, \delta \right) = \begin{cases} f_2(\delta) & \text{for } \frac{\omega}{\omega_p} \geq b \\ 0 & \text{for } \frac{\omega}{\omega_p} < b \end{cases}, \quad (3.40)$$

in which b is obtained from a normalization condition:

$$\sigma_\zeta^2 = \int_0^\infty S(\omega) d\omega. \quad (3.41)$$

As the spectral function $S(\omega)$ decreases more rapidly in the low- than in the high-frequency range, b should be ≈ 1 . Thus, from Eqs. (3.39), (3.40) and (3.41) we obtain:

$$f_2(\delta) = 4b^4 \left(\frac{\sigma_c \omega_p^2}{g} \right)^2 = 4b^4 \delta^2. \quad (3.42)$$

Substitution into Eq. (3.39) yields:

$$S(\omega) = 4b^4 \delta^2 g^2 \omega^{-5} \quad \text{for} \quad \frac{\omega}{\omega_p} \gg 1. \quad (3.43)$$

Spectrum (3.43) can be compared with Phillips' form (3.16); hence:

$$\alpha = 4b^4 \delta^2. \quad (3.44)$$

Therefore, parameter α appears to be a function of the characteristic slope δ (say it is a function of external growth conditions: X, t and U). However, it should be pointed out that the result (3.44) is valid under the assumption that b is independent on the external growth conditions. Some experimental evidence for relationship (3.44) is given in Section 3.2.2.2.

Zaslavskii and Zakharov' representation

The fact that the coefficient α is not absolutely constant means that the expression (3.16) cannot be treated as a 'hard limiting' spectral form and an existence of the saturation range is doubtful. On the other hand, the question arises as to whether it is possible to approximate the frequency spectrum for $\omega \gg \omega_p$ in a form:

$$\tilde{S}(\tilde{\omega}) = \alpha_0 f\left(\frac{\tilde{\omega}}{\tilde{\omega}_p}\right) \tilde{\omega}^{-n_0}, \quad (3.45)$$

in which α_0 and n_0 will be absolute constants. In Eq. (3.45) $\tilde{\omega}$ and \tilde{S} denote $\tilde{\omega} = \frac{\omega U}{g}$,

$$\tilde{\omega}_p = \frac{\omega_p U}{g}, \quad \tilde{S} = \frac{S g^3}{U^5} \quad \text{and}$$

$$f\left(\frac{\tilde{\omega}}{\tilde{\omega}_p}\right) = \begin{cases} 1 & \text{for } \tilde{\omega} \geq \tilde{\omega}_p \\ 0 & \text{for } \tilde{\omega} < \tilde{\omega}_p. \end{cases} \quad (3.46)$$

Zaslavskii (1982) showed that if $n_0 = 11/3 = 3.67$, the coefficient $\alpha_0 = 3.4 \cdot 10^{-3}$ is constant and does not depend on the wave growth. Thus, we finally have:

$$\tilde{S}(\tilde{\omega}) = \alpha_0 \tilde{\omega}^{-11/3}. \quad (3.47)$$

In other words, changing the power of the frequency from (-5) to $(-11/3)$ compensates for the dependence of the parameter α on a non-dimensional fetch.

Approximation (3.47) was confirmed theoretically by Zaslavskii and Zakharov (1982). Their theory is based on the concept of Kolmogorov's spectra in which a fundamental role is given to the wave action density N satisfying the radiative transfer equation in the form:

$$\frac{\partial N}{\partial t} + \frac{\partial \Omega}{\partial k_i} \frac{\partial N}{\partial x_i} - \frac{\partial \Omega}{\partial x_i} \frac{\partial N}{\partial k_i} = I_k + P_k^+ - P_k^-, \quad (3.48)$$

in which I_k expresses the nonlinear interaction between spectral components, and P_k^+ and P_k^- are total spectral sources and sinks. If the energy input and energy dissipation bands are sufficiently separated in the wave number space, dimensional analysis yields the frequency spectrum in the form:

$$S(\omega) = g^2 \omega^{-5} \phi(\omega, p, g), \quad (3.49)$$

where $p = \frac{dN}{dt}$ is the flux of the wave action and

$$\phi(\omega, p, g) = 2\beta_z p^{1/3} g^{-2/3} \omega^{4/3} H_1\left(\frac{\omega}{\omega_p}\right). \quad (3.50)$$

The H_1 is a 'smudged' Heaviside's function such that $H_1(\frac{\omega}{\omega_p}) \rightarrow 0$ for $\frac{\omega}{\omega_p} \ll 1$ and $H_1(\frac{\omega}{\omega_p}) \rightarrow 1$ for $\frac{\omega}{\omega_p} \gg 1$. This reflects energy accumulation in the vicinity of the spectral maximum. Using Eq. (3.50) in Eq. (3.49) for $\omega \geq \omega_p$ yields the non-dimensional form of the spectrum as:

$$\tilde{S}(\tilde{\omega}) = 2\beta_z \tilde{p}^{1/3} \tilde{\omega}^{-11/3}, \quad (3.51)$$

where $\tilde{\omega} = \frac{\omega U}{g}$, $\tilde{p} = \frac{pg^2}{U^4}$, $\tilde{S} = \frac{Sg^3}{U^5}$, and $\beta_z \approx 0.83$.

The normalized wave action flux \tilde{p} determines all mechanisms of interaction of waves with wind and drift current. In the weak-turbulence theory of the wind-induced waves, the wave action flux \tilde{p} should not be dependent on the wave growth, i.e. $\tilde{p}(\tilde{\omega}_p) \approx \text{const.}$ This is related to the assumption that the Kolmogorov type spectrum (3.51) induces a constant value of the flux \tilde{p} over the spectrum. In practice, energy input by the wind and dissipation do not appear to be sufficiently separated in frequency to allow Zaslavskii and Zakharov's arguments to be applied rigorously. However, the concept is quite helpful to understand why the one-dimensional spectra tend to be fairly close to a ω^{-4} power law when observed two-dimensional spectra are far from isotropic.

The experimental data on wave action flux are not numerous. We use here the data collected during the International Coastal Experiment 'Kamchiya' which was

undertaken on the Bulgarian coast of the Black Sea in 1977–1979 (Antsyferov et al., 1990). For \tilde{p} it was found that (Belberova et al., 1990):

$$\tilde{p}(\tilde{X}) \approx 1.4 \cdot 10^{-8} \tilde{X}^{-0.12}, \quad \tilde{X} = \frac{gX}{U^2}, \quad (3.52)$$

and

$$\tilde{p}(\tilde{\omega}_p) \approx 4.4 \cdot 10^{-8} \tilde{\omega}_p^{0.46}. \quad (3.53)$$

Using Eq. (3.53) in Eq. (3.51) yields:

$$\tilde{S}(\tilde{\omega}) \approx \beta_z \tilde{\omega}_p^{-0.15} \tilde{\omega}^{-11/3}, \quad (3.54)$$

where $\beta_z = 2.63 \cdot 10^{-3}$.

The approximation (3.52) indicates that wave action flux is only slowly changing with non-dimensional fetch. This means that the experimental data support the theoretical assumption of an almost constant value of wave action flux which is necessary for the existence of Kolmogorov's type of spectrum (3.51).

Toba's representation

In 1973 Toba empirically found that the best approximation to his wind-tunnel data was a spectral density function in the form (Toba, 1973):

$$S(\omega) = \beta u_* g \omega^{-4}, \quad (3.55)$$

in which $\beta = 0.02$, using the laboratory data.

This representation was confirmed by the field observations of Kawai et al. (1977), Donelan et al. (1985) and others. Phillips (1985) re-examined the idea for the equilibrium range using the more detailed description of the balance of the spectral density of wave action:

$$\frac{\partial N}{\partial t} + (C_g + \vec{U}) \cdot \nabla N = -\nabla_k \cdot \vec{T}(\vec{k}) + S_{in} - D, \quad (3.56)$$

where an action spectral density N is defined as:

$$N(\vec{k}) = \frac{g}{\omega} \hat{\Psi}(\vec{k}), \quad (3.57)$$

and ω is the intrinsic frequency, i.e. $\omega^2 = gk$ in deep water. On the right-hand side of Eq. (3.56), $\vec{T}(\vec{k})$ represents the net spectral flux of action through the wave number \vec{k} by resonant wave-wave interactions. The S_{in} is an energy input from the wind and D is a loss of energy by breaking.

Assuming that all three of these processes are important in the equilibrium range, the frequency spectrum is found to be of form (3.55) and the corresponding wave number spectrum is:

$$\hat{\Psi}(\vec{k}) = B D(\theta) u_* g^{-1/2} k^{-7/2}. \quad (3.58)$$

A similar result has been obtained by Kitaigorodskii (1983) who assumed the existence of the Kolmogorov type equilibrium range in wind generated waves in which energy input from wind occurs at the energy-containing frequencies, while the dissipation is restricted to much larger frequencies.

Liu (1989), examining over 2200 well-developed storm wave spectra recorded in the Great Lakes, concluded that most of the exponents lie in the -3.5 to -5.5 range. For practical applications, a representation of ω^{-4} is perhaps a useful approximation for fully-developed cases.

Finite water depth

The water depth does not appear explicitly in any of the above mentioned spectra. However, the representation (3.17) is consistent with the occurrence of sharp spikes among waves of much larger amplitude, independently of water depth. Such spikes approximate Dirac δ -function, the Fourier transform of which is flat at all frequencies (see for example relationships for white noise in Tables 1.2 and 1.3). In similar way, if a function $f(x, y,)$ has discontinuities in slope, then its Fourier transform is proportional to k^{-2} at large k and the mean square of the Fourier transform will be proportional to k^{-4} (Lighthill, 1975).

Thus, let us assume that shapes of the equilibrium spatial wave spectra will be identical for both deep and shallow seas, i.e. (Kitaigorodskii et al., 1975):

$$\hat{\Psi}(\vec{k}) = B(g, h) D(\theta) k^{-4}, \quad (3.59)$$

and

$$F(k) = \int_{|\vec{k}|=k} \hat{\Psi}(\vec{k}) d\vec{k} = \int_{-\pi}^{\pi} \Psi(k, \theta) k d\theta = B k^{-3}, \quad (3.60)$$

in which $\vec{k} = (k \cos \theta, k \sin \theta)$, θ is a direction of wave propagation. Directional spreading function D satisfies the normalization condition:

$$\int_{-\pi}^{\pi} D(\theta) d\theta = 1. \quad (3.61)$$

The relation between the frequency spectrum $S(\omega)$ and wave number spectrum $F(k)$ has the form:

$$S(\omega) = F(k)|_{k=k(\omega)} \frac{\partial k}{\partial \omega}. \quad (3.62)$$

Using the dispersion relation:

$$\omega_*^2 = \frac{\omega^2 h}{g} = k h \tanh(k h) \quad \text{and} \quad k h = f_0(\omega_*^2), \quad (3.63)$$

we obtain:

$$\omega_*^2 = f_0 \tanh(f_0), \quad (3.64)$$

or

$$f = f_0 \omega_*^{-2}, \quad 1 = f \tanh(\omega_*^2 f) \quad \text{and} \quad k = \frac{\omega^2}{g} f. \quad (3.65)$$

Now the derivative $\frac{\partial k}{\partial \omega}$ can be calculated as:

$$\frac{\partial k}{\partial \omega} = \frac{2\omega}{g} f \left[1 + \frac{2\omega_*^2 f}{\sinh(2\omega_*^2 f)} \right]^{-1}. \quad (3.66)$$

After substituting Eq. (3.66) into Eq. (3.62) and comparing with Eq. (3.16) we obtain:

$$S(\omega) = \alpha g^2 \omega^{-5} r(\omega_*), \quad (3.67)$$

in which $\alpha = 2B$ and

$$r(\omega_*) = f^{-2} \left[1 + \frac{2\omega_*^2 f}{\sinh(2\omega_*^2 f)} \right]^{-1}. \quad (3.68)$$

The function $r(\omega_*)$ is shown in Fig. 3.3. When $\omega_* \rightarrow \infty$ (deep water), $r(\omega_*) \rightarrow 1$ and Eq. (3.67) is equivalent to Eq. (3.16). In shallow water, when $\omega_* \rightarrow 0$ and $r(\omega_*) \rightarrow \frac{1}{2}\omega_*^2$, from Eq. (3.67) we obtain:

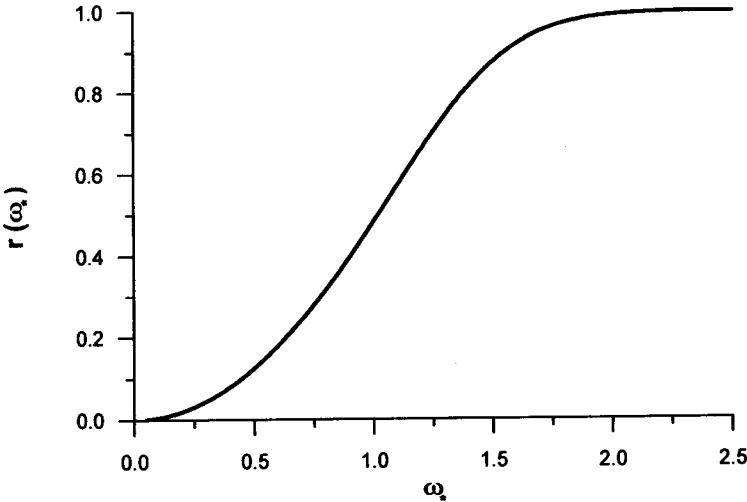


Figure 3.3: Function $r(\omega_*)$.

$$S(\omega) = \frac{1}{2} \alpha g h \omega^{-3}. \quad (3.69)$$

Using similar arguments, we obtain the following extension of Toba's spectrum (3.55) for arbitrary water depth:

$$S(\omega) = \beta u_* g \omega^{-4} r_T(\omega_*), \quad (3.70)$$

where:

$$r_T(\omega_*) = f^{-3/2} \left[1 + \frac{2\omega_*^2 f}{\sinh(2\omega_*^2 f)} \right]^{-1}. \quad (3.71)$$

It can be verified that $r_T(\omega_*) \rightarrow 1$ when $\omega_* \rightarrow \infty$ (deep water), while for $\omega_* \rightarrow 0$ (shallow water), $r_T(\omega_*) \rightarrow \frac{1}{2}\omega_*^{3/2}$, and Eq. (3.70) gives:

$$S(\omega) = \frac{1}{2} \beta u_* h \omega^{-2}. \quad (3.72)$$

Influence of surface drift

In the saturation range concept it is assumed that a specific balance of wave energy exists within a restricted frequency band. However, one might anticipate that the properties of waves in the saturation range depend on the nature of waves outside that range. In particular, Kitaigorodskii et al. (1975) examined the influence of the gravitational and advective effects generated by long waves. They concluded that these effects are of secondary importance.

Another mechanism which may have influence on the saturation range is the surface drift. The surface wind drift reduces the maximum wave elevation ζ by a factor $\left(1 - \frac{q}{C}\right)^2$, where q is the magnitude of the surface drift at the point where the wave profile crosses the mean water level and C is the wave speed. If wind speed $U = 10$ m/s, the mean surface wind drift is approximately $U \approx 0.3$ m/s, and the surface waves have the length $L = 0.3$ m; the corresponding phase speed $C \approx 0.7$ m/s. Therefore, the maximum unbroken wave elevation is only 0.3 times the Stokes limiting irrotational wave elevation (Banner and Phillips, 1974).

If a short wave is riding over a long wave, there is a nonlinear augmentation of the surface drift near the long wave crests. Short waves, superimposed on the longer ones, experience augmented drift in these regions. This mechanism reduces the maximum amplitude that the short waves can attain when they are at the point of incipient breaking. The reduction of wave amplitude is given by Phillips and Banner (1974) as:

$$r = \left(\frac{g}{g'} \right) \frac{(C_c - q_c)^2}{(C_0 - q_0)^2}, \quad (3.73)$$

in which r is a ratio of the maximum amplitude to what it would be in the absence of the long waves, C_0 is the short wave speed at the point where the surface displacement of the long wave is zero, $C_c = C_0(1 - \alpha_b)$ is the phase speed of the short wave at the crest of the swell (α_b is a long wave slope), q_0 is a surface drift, q_c is the augmented value of the drift at the crest of the swell, and g' is the apparent gravitational acceleration of the short wave swept over the long wave crest. Good agreement of experimental data with Eq. (3.73) was noted.

3.2.2.2 Typical frequency spectra

Spectral forms discussed so far are restricted to the saturation range only, when $\omega > \omega_p$. To include the most energetic part of the spectrum, a variety of power functions multiplied by exponential functions have been proposed. A general form of the spectral density function is:

$$S(\omega) = A\omega^{-p} \exp \left[-B\omega^{-q} \right], \quad (3.74)$$

in which A, B, p and q are free parameters. Thus, the spectral moments defined by Eq. (3.3) become:

$$m_r = AB^{(r-p+1)/q} \left(\frac{1}{q} \right) \Gamma \left(\frac{p-r-1}{q} \right), \quad (3.75)$$

in which $\Gamma()$ is a gamma function (Abramowitz, Stegun, 1975).

The Pierson-Moskowitz spectrum

Probably the most popular spectrum among all proposed forms is that proposed by Pierson and Moskowitz (1964), who, using the field data and theoretical discoveries of Phillips (1958) and Kitaigorodskii (1962), showed that:

$$S(\omega) = \alpha g^2 \omega^{-5} \exp \left[-B \left(\frac{g}{\omega U} \right)^4 \right], \quad (3.76)$$

where $\alpha = 8.1 \cdot 10^{-3}$, $B = 0.74$ and U is a wind speed at an elevation of 19.5 m above the sea surface. The shape of the wave spectrum is controlled by a single parameter – wind speed U . The spectrum of Eq. (3.76) was proposed for fully-developed sea, when phase speed is equal to wind speed. The experimental spectra given by Pierson and Moskowitz yield:

$$\frac{U\omega_p}{g} = \text{const} = 0.879 \quad \text{and} \quad \frac{U\omega_p}{2\pi g} = \frac{Uf_p}{g} = 0.13. \quad (3.77)$$

After substitution into Eq. (3.76) we obtain:

$$S(\omega) = \alpha g^2 \omega^{-5} \exp \left[-\frac{5}{4} \left(\frac{\omega}{\omega_p} \right)^{-4} \right]. \quad (3.78)$$

Some mathematical problems arise when calculating the spectral fourth moment using Eq. (3.78). This moment, which physically denotes the mean-squared acceleration measured at a Eulerian point, is unbounded. To remedy this shortcoming, a cutoff frequency is usually imposed, i.e.:

$$m_4 = \int_0^{\omega_c} S(\omega) d\omega, \quad (3.79)$$

in which $\omega_c = n\omega_p$ and n is taken as $n > 3$.

We now show how the spectrum (3.78) can be obtained without invoking the similarity hypothesis. Krylov (1966) showed that the probability distribution function for wave period is:

$$F(T) = \exp \left[-\Gamma^4 \left(\frac{5}{4} \right) \left(\frac{T}{\bar{T}} \right)^4 \right], \quad (3.80)$$

in which \bar{T} is a mean period.

Thus, the probability density function $f(T)$ takes the form:

$$f(T) = -\frac{dF}{dT} = 4\Gamma^4 \left(\frac{5}{4} \right) \frac{1}{\bar{T}} \left(\frac{T}{\bar{T}} \right)^3 \exp \left[-\Gamma^4 \left(\frac{5}{4} \right) \left(\frac{T}{\bar{T}} \right)^4 \right]. \quad (3.81)$$

The wave period and wave frequency are functionally dependent. Hence:

$$f(T)dT = f(\omega)d\omega, \quad (3.82)$$

and the resulting probability density function $f(\omega)$ becomes:

$$f(\omega) = \frac{dF(\omega)}{d\omega} = 4\Gamma^4 \left(\frac{5}{4} \right) \bar{\omega}^4 \omega^{-5} \exp \left[-\Gamma^4 \left(\frac{5}{4} \right) \left(\frac{\omega}{\bar{\omega}} \right)^4 \right]. \quad (3.83)$$

For narrow-band processes the probability density function can be interpreted as a frequency spectrum, normalized on variance (Krylov et al, 1986), i.e.:

$$f(\omega) = \frac{S(\omega)}{\sigma_\xi^2}. \quad (3.84)$$

In particular, the peak frequency ω_p is given by condition $\frac{dS(\omega)}{d\omega} = 0$, i.e.:

$$\omega_p = \left(\frac{4}{5} \right)^{1/4} \Gamma \left(\frac{5}{4} \right) \bar{\omega}. \quad (3.85)$$

After substitution Eq. (3.85) into Eq. (3.84) we obtain:

$$S(\omega) = \alpha g^2 \omega^{-5} \exp \left[-\frac{5}{4} \left(\frac{\omega}{\omega_p} \right)^4 \right], \quad (3.86)$$

in which:

$$\alpha = 5 \left(\frac{\omega_p^2 \sigma_\zeta}{g} \right)^2. \quad (3.87)$$

Equation (3.86) is identical with the Pierson-Moskowitz spectrum (3.78). It was obtained without any assumptions on the limiting sea stage and without applying the similarity laws. The forms (3.78) and (3.86) are numerically equivalent when $\frac{\omega_p^2 \sigma_\zeta}{g} \simeq 0.04$. Assuming that the significant wave height $H_s \approx 4\sigma_\zeta$, this condition

yields $\frac{H_s}{L_p} \approx 0.025$. Such values are commonly observed for sufficiently large non-

dimensional fetches $\frac{gX}{U^2}$ and they are still much smaller than the limited slope ($\sim 1/7$).

It should be noted that the Pierson-Moskowitz spectrum does not necessarily correspond to a fully-developed sea. In fact, Hasselmann et al. (1976) found, after careful examinations of the Pierson-Moskowitz experimental spectra, that only part of these spectra corresponds to a fully-developed sea.

The JONSWAP spectrum and its modifications

The JONSWAP spectrum extends the Pierson-Moskowitz spectrum to include fetch-limited seas. This spectrum is based on an extensive wave measurement program (Joint North Sea Wave Project) carried out in 1968 and 1969 in the North Sea. The JONSWAP spectrum, after publication in 1973, received almost instant recognition and became very well known in international literature. The resulting spectral model takes the form (Hasselmann et al., 1973):

$$S(\omega) = \alpha g^2 \omega^{-5} \exp \left[-\frac{5}{4} \left(\frac{\omega}{\omega_p} \right)^{-4} \right] \gamma^\delta, \quad (3.88)$$

in which:

$$\delta = \exp \left[-\frac{(\omega - \omega_p)^2}{2\sigma_0^2 \omega_p^2} \right]. \quad (3.89)$$

Spectrum (3.88) contains five parameters, i.e. α, γ, ω_p and $\sigma_0 = \sigma'_0$ for $\omega \leq \omega_p$ and $\sigma_0 = \sigma''_0$ for $\omega > \omega_p$ which should be known *a priori*. The term γ^δ is a peak enhancement factor, added to the Pierson-Moskowitz spectrum, to represent a narrow, more peaked spectrum which is typical for a growing sea. The γ parameter describes the degree of peakedness and σ_0 parameter describes the width of the peak region.

The mean JONSWAP spectrum yields $\gamma = 3.3$, $\sigma'_0 = 0.07$ and $\sigma''_0 = 0.09$, while α and ω_p are given by:

$$\alpha = 0.076 \left(\frac{gX}{U^2} \right)^{-0.22}, \quad (3.90)$$

and

$$\omega_p = 7\pi \left(\frac{g}{U} \right) \left(\frac{gX}{U^2} \right)^{-0.33} \quad (3.91)$$

For the non-dimensional total wave energy \mathcal{E} we have:

$$\mathcal{E} = \frac{m_0 g^2}{U^4} = 1.6 \cdot 10^{-7} \left(\frac{gX}{U^2} \right) \quad (3.92)$$

Equations (3.91) and (3.92) demonstrate that the peak frequency ω_p decreases and total energy increases with non-dimensional fetch (Fig. 3.4).

Using the two non-dimensional parameters $\xi = \frac{gX}{U^2}$, $\nu = \frac{\omega_p U}{2\pi g}$, Eqs. (3.90), (3.91) and (3.92) can be rewritten as:

$$\left. \begin{aligned} \xi &= 44.534 \nu^{-3.03} \\ \alpha &= 0.076 \xi^{-0.22} = 0.033 \nu^{0.67} \\ \mathcal{E} &= 1.6 \cdot 10^{-7} \cdot \xi = 7.13 \cdot 10^{-6} \cdot \nu^{-3.03} \end{aligned} \right\} \quad (3.93)$$

On the other hand, the integration of Eq. (3.88), using $\gamma = 3.3$ and two first relations (3.93) yields:

$$\mathcal{E} = 0.99 \cdot 10^{-7} \xi^{1.1} \quad (3.94)$$

This result is inconsistent with the third relation in Eq. (3.93). Hasselmann et al. (1976) attempted to regularize this discrepancy and developed slightly modified relationships for α , ξ and \mathcal{E} using a number of theoretical arguments. Eventually they obtained:

$$\left. \begin{aligned} \xi &= 32.438 \nu^{-3.03} \\ \alpha &= 0.0662 \xi^{-0.2} = 0.033 \nu^{0.67} \\ \mathcal{E} &= 1.63 \cdot 10^{-7} \xi = 5.30 \cdot 10^{-6} \nu^{-3.33} \end{aligned} \right\} \quad (3.95)$$

In principle, the JONSWAP spectrum should asymptotically approach the Pierson-Moskowitz spectrum for large fetch, i.e. as $\nu \rightarrow 0.13$, $\alpha \rightarrow 8.1 \cdot 10^{-3}$ and $\gamma \rightarrow 1.0$. In fact, the JONSWAP and other fetch-limited spectra showed no marked tendency of decreasing of γ toward 1 with increasing fetch.

Hasselmann et al. (1976) reanalysed the Pierson-Moskowitz spectral set using the same parameter-fitting scheme as applied to the JONSWAP spectra and found that a little more than half the spectra contained multiple peaks. After excluding these data from analysis, the remaining spectra yielded a mean peak-enhancement factor $\gamma = 1.4$, which is considerably higher than 1. This result indicates that a transition to the fully-developed spectrum occurs in the very final stages of development.

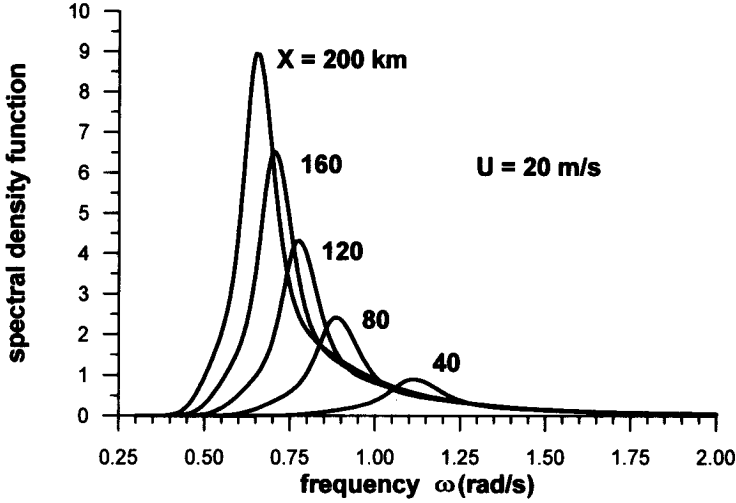


Figure 3.4: Evolution of the JONSWAP spectrum with fetch.

An independent data set to that of Hasselmann et al. (1976) gives $\gamma = 1.7$ at the Pierson-Moskowitz limit (Mitsuyasu et al., 1980). Allowing σ'_0 and σ''_0 to vary, but still assuming that the Pierson-Moskowitz form is correct, Lewis and Allos (1990) found:

$$\gamma = 17.54 \xi^{-0.284} = 5.87 \nu^{0.86}. \quad (3.96)$$

However, the large scatter of the JONSWAP data did not suggest a clear trend for γ .

In the previous Section several arguments were presented for the revision of the original Phillips' equilibrium range law ω^{-5} by replacing it with Toba's law ω^{-4} . As the JONSWAP spectrum also comprises the Phillips' saturation range formulation at high frequency, modification of the JONSWAP spectrum is desirable to establish whether Toba's formulation fits the data better.

Revision by Battjes et al. (1987) showed that in the high-frequency band, the difference in goodness-of-fit between ω^{-4} and ω^{-5} laws is statistically significant at a level of confidence of 99.9% and the wave spectrum can be better approximated by a ω^{-4} tail.

The energy scale parameter β (see Eq. (3.55)) was found to be virtually independent on the wave development factor $\left(\frac{\omega U}{g}\right)$. The value of β varies from 0.06 in laboratory experiments to 0.13 for field data. According to Donelan et al. (1985) the parameter β is a function of $\frac{\omega U}{g}$ i.e. $\beta \approx 0.068 \left(\frac{\omega U}{g}\right)^{-0.45}$. A modified JONSWAP

spectrum, which includes Toba's formulation of the saturation range, was proposed by Donelan et al. (1985) in the form:

$$S(\omega) = \beta g^2 \omega_p^{-1} \omega^{-4} \exp \left[- \left(\frac{\omega}{\omega_p} \right)^{-4} \right] \gamma^\delta, \quad (3.97)$$

in which:

$$\beta = 0.006 \nu^{0.55} \quad \text{for} \quad 0.83 < \nu < 5.0, \quad (3.98)$$

$$\gamma = \begin{cases} 6.489 + 6 \log \nu & \text{for} \quad 1.0 \leq \nu < 5 \\ 1.7 & \text{for} \quad 0.83 < \nu < 1 \end{cases} \quad (3.99)$$

$$\mathcal{E} = 0.00274 \nu^{-3.3}, \quad (3.100)$$

$$\sigma_0 = 0.08 + 0.32 \nu^{-3}. \quad (3.101)$$

When ν decreases (peak frequency shifts to lower frequencies), both β and γ decrease and σ_0 remains relatively constant until near full development, when it increases rapidly. The γ parameter does not reach a value of 1.0 at the full development limit, but it is close to 1.7.

In Fig. 3.5 the Pierson-Moskowitz spectrum, the JONSWAP spectrum and the Donelan spectrum are compared for two different regimes. The first figure illustrates fetch limited conditions when fetch $X = 25$ km and wind velocity $U = 10$ m/s. The resulting peak frequency and wave development parameters are $\omega_p = 1.64$ rad/s, and $\nu = \frac{\omega_p U}{g} = \frac{U}{C} = 1.673$ (C is a phase velocity in deep sea). The second figure presents the spectra for a fully-developed sea ($X = 200$ km, $U = 10$ m/s, $\omega_p = 0.862$ rad/s and $\nu = 0.879$). The Pierson-Moskowitz spectrum applies only for the fully-developed case. On the other hand, the JONSWAP spectrum, extrapolated to the fully-developed limit, retains its enhanced peak, which is in contrast to a much broader fully-developed spectrum. The Donelan et al. form shows a good agreement with the JONSWAP spectrum in the fetch-limited stage and it also reflects the basic features of the fully developed sea spectrum.

The relationships (3.98) - (3.101) fully determine the spectrum (3.97). For engineering purposes it would be more suitable to present these relationships in terms of the significant wave height (H_s) and peak period (T_p), which are commonly used in design practice. Houmb and Overvik (1976) already showed that this principle is possible for the JONSWAP spectrum. Using this idea, Young (1992) obtained the following relationships for the Donelan et al. (1985) spectrum:

$$\beta = 200 g^{-1.571} m_0^{0.786} T_p^{-3.143}, \quad (3.102)$$

$$\gamma = 6.489 + 6 \log \left[2.649 \cdot 10^7 g^{-2.857} m_0^{1.429} T_p^{-5.714} \right], \quad (3.103)$$

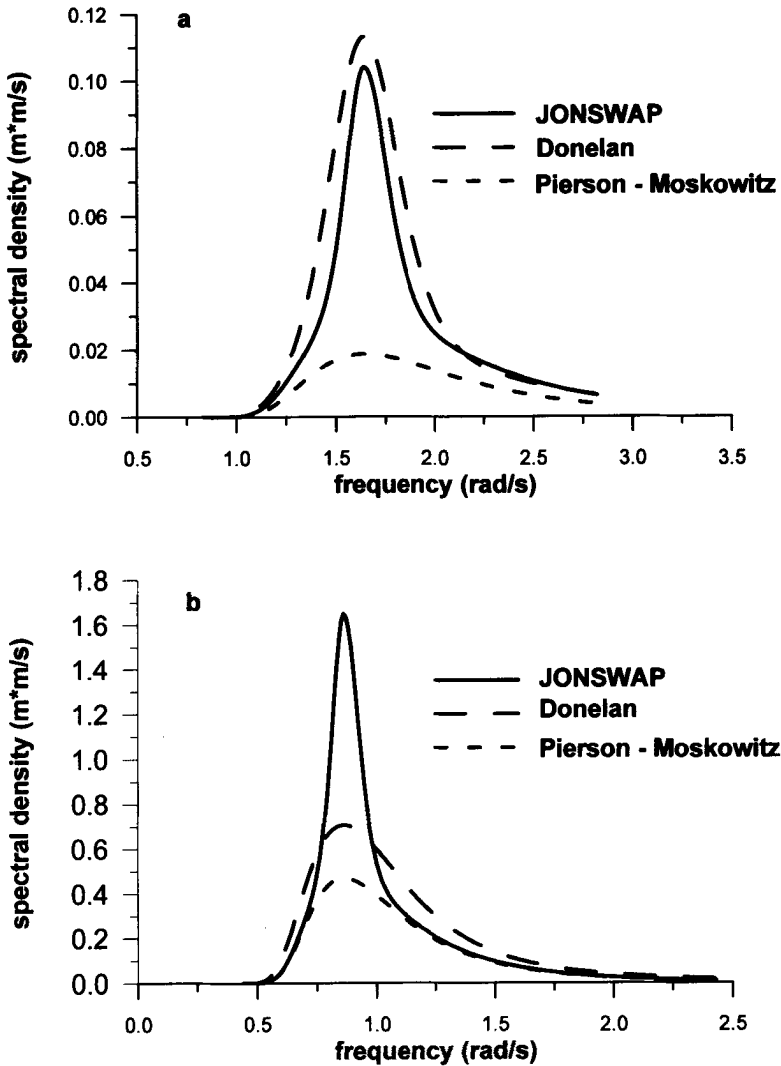


Figure 3.5: Comparison of the Pierson-Moskowitz, the JONSWAP and the Donelan et. al. spectra: a) fetch limited conditions and b) fully developed sea.

$$\sigma_0 = 0.08 + 6.940 \cdot 10^{-26} g^{8.571} m_0^{-4.287} T_p^{17.142}, \quad (3.104)$$

in which $m_0 = \frac{H_s^2}{16}$ and m_0 is given by Eq. (3.2).

The Wallops spectrum

The proposed spectral model is based on the laboratory data collected in the wind-wave channel at the NASA Wallop Center (Huang et al., 1981). The basic form of the two-parameter spectrum is:

$$S(\omega) = \beta g^2 \omega_p^{-5} \left(\frac{\omega}{\omega_p} \right)^{-m} \exp \left[-\frac{m}{4} \left(\frac{\omega}{\omega_p} \right)^{-4} \right], \quad (3.105)$$

in which β and m are functions of the significant slope sl :

$$sl = \frac{\sigma_\zeta}{L_p}, \quad (3.106)$$

where σ_ζ is the standard deviation of the surface elevation, and L_p , ω_p are the wavelength and frequency of the waves at the spectral peak.

Reasoning that the asymptotic form of the energy range of the spectrum could not be higher than for the strong nonlinear scenario when the higher harmonics are present, they obtained for m (Huang et al., 1981, 1983a):

– deep water

$$m = \left\lceil \frac{\log \left(\sqrt{2\pi} sl \right)^2}{\log 2} \right\rceil, \quad (3.107)$$

– intermediate and shallow water

$$m = \left\lceil \frac{\log \left(2\pi^2 (sl)^2 \coth^2(k_p h) \left[1 + \frac{3}{2 \sinh^2 k_p h} \right]^2 \right)}{\log 2} \right\rceil \quad \text{for } 1 < k_p h. \quad (3.108)$$

Furthermore, using the definition of the spectral moments (3.3), it can be shown that:

$$\beta = \frac{(2\pi sl)^2 m^{(m-1)/4}}{4^{(m-5)/4}} \cdot \frac{1}{\Gamma\left(\frac{m-1}{4}\right)}. \quad (3.109)$$

Thus, the whole spectrum is totally determined by two-parameters based on the sea state rather than the wind, i.e. significant wave slope (sl) and the peak frequency (ω_p).

The Krylov spectrum

Krylov (1966) starts from the general form (3.74) in which A, B, p and q are free parameters. Utilizing two moments m_0 and m_2 , Eq. (3.75) is solved first for A and B :

$$A = \frac{\left[\Gamma\left(\frac{p-1}{q}\right) \right]^{\frac{p-3}{2}}}{\left[\Gamma\left(\frac{p-3}{q}\right) \right]^{\frac{p-1}{2}}} q m_0 (\bar{\omega}_0)^{(p-1)}, \quad (3.110)$$

$$B = \left(\frac{\Gamma\left(\frac{p-1}{q}\right)}{\Gamma\left(\frac{p-3}{q}\right)} \right)^{q/2} (\bar{\omega}_0)^q, \quad (3.111)$$

in which $\bar{\omega}_0 = \left(\frac{m_2}{m_0} \right)^{1/2}$. Then, based on observations of nearly fully-developed sea states, Krylov (1966) found that $p \approx 7$ and $q \approx 4$, i.e.:

$$A = \pi m_0 (\bar{\omega}_0)^6; \quad \text{and} \quad B = \frac{\pi}{4} (\bar{\omega}_0)^4. \quad (3.112)$$

After substitution into Eq. (3.74) Krylov's spectrum becomes:

$$S(\omega) = \frac{\pi m_0}{\bar{\omega}_0} \left(\frac{\omega}{\bar{\omega}_0} \right)^{-7} \exp \left[-\frac{\pi}{4} \left(\frac{\omega}{\bar{\omega}_0} \right)^{-4} \right]. \quad (3.113)$$

The Davidan spectrum

Davidan et al. (1985) utilized a similar approach to Krylov. The coefficients A and B in Eq. (3.74) were determined using the first spectral moment (m_0) and the peak frequency (ω_p). Hence, A and B become:

$$A = q m_0 \frac{B^{(p-1)/q}}{\Gamma\left(\frac{p-1}{q}\right)}; \quad B = \left(\frac{p}{q} \right) \omega_p^q. \quad (3.114)$$

They assumed further that $p = q + 1$. Therefore, the only parameter to be determined is q . They found experimentally that q depends on the stage of wave growth and the typical q values vary from 5 to 6. They finally selected $q = 5.5$; hence the Davidan et al. spectrum takes the form:

$$S(\omega) = \frac{6.5 m_0}{\omega_p} \left(\frac{\omega}{\omega_p} \right)^{-6.5} \exp \left[-1.18 \left(\frac{\omega}{\omega_p} \right)^{-5.5} \right]. \quad (3.115)$$

Multipeak spectra

Observed ocean wave spectra sometimes possess a very complicated pattern where more than one peak in the frequency spectrum is observed. Various mechanisms can be responsible for such behaviour. The obvious one is the superposition of various wave systems approaching the observation point. For example, as well as locally generated waves, the swell from other remote generating areas can be recorded at a given point.

In a finite water depth or in a shallow water zone, the nonlinear interaction mechanisms manifest themselves in the form of additional peaks at higher harmonic of main frequency. The most common are spectra with double peaks; one in the lower frequency part, the other in the higher frequency part. The percentage of occurrence of double-peaked spectra is about 22% for the North Atlantic and 16% for the North Sea (Soares, 1984, 1991). For the fetch limited locations (for example, in the Norwegian Coast), double-peaked spectra occur only in 11% of the cases. The percentage of occurrence depends on the significant wave height. It is higher for low sea states and lower for stormy seas.

Multipeak spectra cannot be represented by the previous models. The simplest way to represent the entire spectral shape is to decompose the spectrum into two parts: the main energetic component and the high-frequency component. Strekalov and Massel (1971) proposed such a decomposition in the non-dimensional form (see Fig. 3.6):

$$\tilde{S}\left(\frac{\omega}{\omega_p}\right) = \tilde{S}_e\left(\frac{\omega}{\omega_p}\right) + \tilde{S}_h\left(\frac{\omega}{\omega_p}\right), \quad (3.116)$$

in which:

$$\tilde{S}_e\left(\frac{\omega}{\omega_p}\right) = A \exp\left[-B\left(\frac{\omega}{\omega_p} - 1\right)^2\right], \quad (3.117)$$

$$\tilde{S}_h\left(\frac{\omega}{\omega_p}\right) = C\left(\frac{\omega}{\omega_p}\right)^{-n} \exp\left[-7.987\left(\frac{\omega}{\omega_p}\right)^{-m}\right]. \quad (3.118)$$

The spectrum components $\tilde{S}_e\left(\frac{\omega}{\omega_p}\right)$ and $\tilde{S}_h\left(\frac{\omega}{\omega_p}\right)$ are normalized using peak frequency ω_p and variance σ_ζ^2 . The free parameters are: $A = 1.835$, $B = 22.222$, $C = 4.211$, $n = 5$, and $m = 8$. These values of the free parameters were based on the experimental data from the Kaspiyan Sea, and wind speed $7 \leq U \leq 15$ m/s, and fetch $100 < X < 300$ km. The ratio $\frac{\omega_p}{\omega}$ was assumed to be constant and equal to 0.8.

Extended verification of the form (3.116) was recently reported by Krylov et al. (1986). They collected the experimental results from various sources: Ewing (1971),

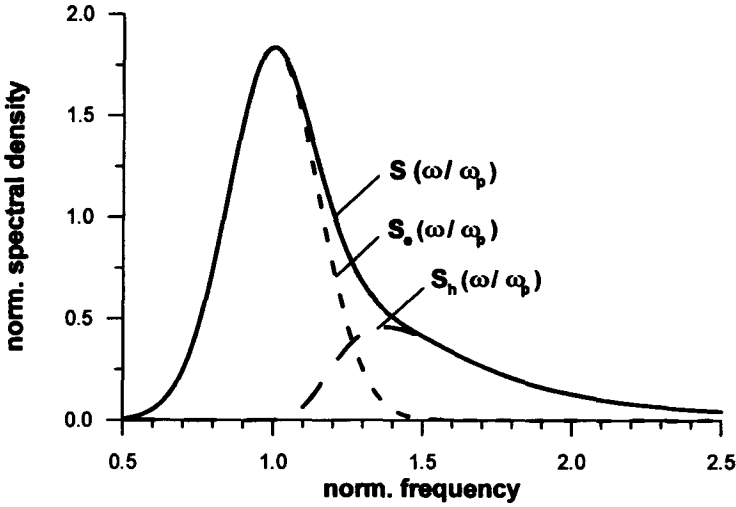


Figure 3.6: Two-component spectrum by Strekalov and Massel (1971).

Hasselmann et al. (1973), Krylov et al. (1976), Davidan et al. (1978), Kostichkova and Polyakov (1980), Mitsuyasu et al. (1980), and Antsyferov et al. (1990). All experimental spectra (about 200) were subjected to careful verification and normalization (see Krylov et al. (1986) for details). The averaged experimental spectrum is given in Fig. 3.7. The mean value of $\frac{S(\omega_p)\omega_p}{\sigma_\zeta^2} \approx 1.80$ for all spectra. Moreover, the small secondary peak is observed at $\frac{\omega}{\omega_p} \approx 1.35$. The comparison of the experimental averaged spectrum with the Strekalov–Massel spectrum shows a good agreement. In particular, the maximum value of $\frac{S(\omega_p)\omega_p}{\sigma_\zeta^2} = 1.835$ is very close to the experimental value of 1.80. It is recommended that the spectrum (3.116) be used for the non-dimensional fetch range $10^2 \leq \frac{gX}{U^2} \leq 10^4$.

Krylov et al. (1986) supplemented the spectrum (3.116) by an additional approximation in the low-frequency band when $0 \leq \omega \leq \omega_{min}$. The frequency ω_{min} is a frequency corresponding to a minimum of the spectrum, located on the low-frequency side of the energetic part of the spectrum. In this frequency range, the spectral density is approximately defined only by airflow within the boundary layer. The experimental data (Phillips, 1977) suggest that the frequency spectrum of turbulent atmospheric pressure fluctuations can be expressed as:

$$S_p(\omega) \approx \alpha_1 \rho_a^2 u_*^4 \omega^{-1}, \quad (3.119)$$

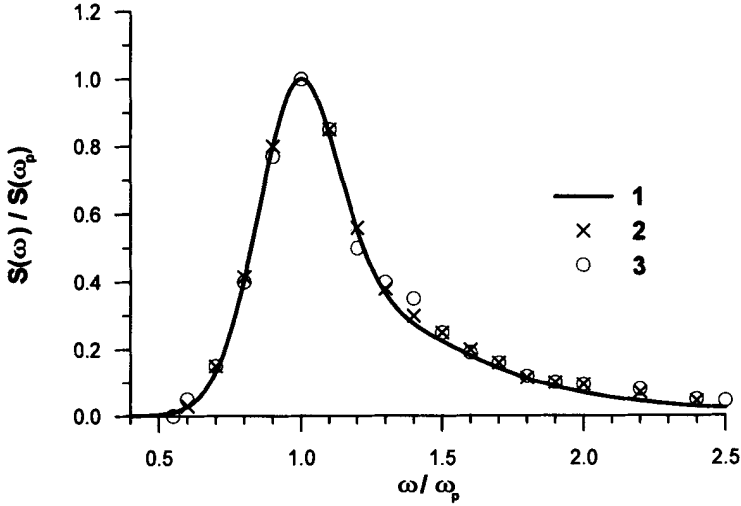


Figure 3.7: Comparison of the Strelkov and Massel spectrum (1) with mean experimental spectrum (2) and averaged spectrum proposed by various authors (3).

in which α_1 is a constant.

On the other hand, the analysis given in Chapter 2 indicates that:

$$S_{\zeta}(\omega) \approx \frac{S_p(\omega)}{\rho_w^2 g^2}. \quad (3.120)$$

Therefore:

$$S(\omega) \approx \frac{u_*^4}{g^2} \omega^{-1}. \quad (3.121)$$

In Fig. 3.8, the energetic part of the spectrum (3.116) and its supplementing by spectrum (3.121) are shown. Within the frequency range $0.1 < \frac{\omega}{\omega_p} < 0.4$, the experimental data (laboratory data and field data from the Baltic Sea) satisfactorily agree with approximation (3.121).

Ochi and Hubble (1976) proposed another approximation for multipeak spectra. They represented each spectrum component in the form of a three-parameter formula:

$$S(\omega) = \frac{\left(\frac{4\lambda+1}{4}\omega_p^4\right)^\lambda}{4\Gamma(\lambda)} \frac{H_s^2}{\omega^{4\lambda+1}} \exp \left[- \left(\frac{4\lambda+1}{4} \right) \left(\frac{\omega_p}{\omega} \right)^4 \right], \quad (3.122)$$

where H_s is a significant wave height and λ is a spectrum shape parameter. For $\lambda = 1$, Eq. (3.122) is reduced to a spectrum of type (3.74).

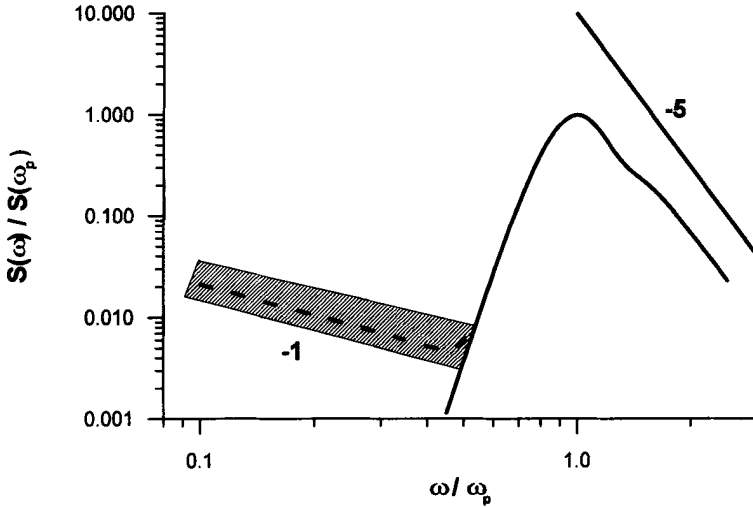


Figure 3.8: Strekalov-Massel spectrum (—), supplemented by Strekalov's low-frequency approximation (---). Shadow area indicates the scattered experimental data.

By combining two sets of (3.122) spectra, one representing the low-frequency component and the other the high-frequency component, they finally obtained the following six-parameter spectral representation:

$$S(\omega) = \sum_{j=1}^2 \frac{[(4\lambda_j + 1)\omega_{pj}^4/4]^{\lambda_j}}{4\Gamma(\lambda_j)} \frac{H_{sj}^2}{\omega^{4\lambda_j+1}} \exp \left[- \left(\frac{4\lambda_j + 1}{4} \right) \left(\frac{\omega_{pj}}{\omega} \right)^4 \right], \quad (3.123)$$

in which $j = 1$ and 2 represents the lower and higher frequency components, respectively. The parameters of spectrum (3.123) should be determined numerically to best fit the observed spectra.

The TMA spectrum

The extension of Kitaigorodskii et al. (1975), similarity scaling (see Section 3.2.2.1) to the entire spectrum, gives in principle the possibility of developing a finite water depth form of the wave spectrum. An application of this scaling to the JONSWAP spectrum is (Bouws et al., 1985):

$$S(\omega, h) = S_J(\omega) r(\omega_*), \quad (3.124)$$

where $S_J(\omega)$ is the JONSWAP form of Eq. (3.88), and $r(\omega_*)$ is given by Eq. (3.68). The extension of the Kitaigorodskii et al. (1975) scaling across the entire spectrum

does not mean that the wave breaking mechanism dominates the entire spectrum. The proposed form (3.124) is useful representation of spectral distribution of energy in finite water depth. The hypothesis of a similarity of spectral shape was successfully tested with three extensive field data sets (TEXEL, MARSEN, and ARSLOE experiments).

The swell spectrum

All spectra discussed above provide a description of the developing and (or) a fully-developed sea. When wind speed decreases, waves start to attenuate. They become free waves rather than forced ones. Attenuation does not act simultaneously on the whole frequency range. The weakening wind is still capable of supporting the energy balance in the high-frequency part of the spectrum, while the low-frequency waves become similar to free surface waves. At the same time, the energy in saturation range reduces and the influence of non-linear effects decline. Davidan (1969) proposed the swell spectrum in the form:

$$S(\omega) = 6m_0\omega_p^{-1} \left(\frac{\omega}{\omega_p}\right)^{-6} \exp \left[-1.2 \left(\frac{\omega}{\omega_p}\right)^{-5} \right]. \quad (3.125)$$

The form (3.125) agrees well with experiments for swell when $\frac{\bar{H}}{gT^2} \leq 0.00125$.

3.2.3 Higher order spectra

It is generally accepted that nonlinearities in deep water are weak. The observed wave field can be envisioned as consisting of many independent pure sinusoidal components, and the resulting probability density function becomes Gaussian distribution.

However, in a shallow water zone, the departure of the observed probability density from a Gaussian distribution cannot be neglected (see Chapter 4). Surface elevation, wave-induced pressure, and orbital velocity time series show increasingly sharper peaks and shallower troughs, caused by higher harmonic generation and their interaction as waves approach the surf zone. The stochastic properties of such processes can no longer be expressed by the first two statistical moments. The third (or higher moments) may be required to adequately describe the stochastic processes. Here, the third moment will be evaluated from the two-dimensional spectral density function, called bispectrum.

Bispectral analysis was first carried out by Hasselmann et al. (1963) to study the nonlinear interactions of ocean waves. Since then, the analysis has been applied in many diverse fields, such as fluid turbulence, wave generation mechanism, internal wave interactions, plasma studies, ship rolling motion, economic time series, etc.

Let us define the two-dimensional autocorrelation function $K_{\zeta\zeta}^{(2)}(\tau_1, \tau_2)$ in a similar way to the one-dimensional function:

$$K_{\zeta\zeta}^{(2)}(\tau_1, \tau_2) = E[\zeta(t) \zeta(t + \tau_1) \zeta(t + \tau_2)]. \quad (3.126)$$

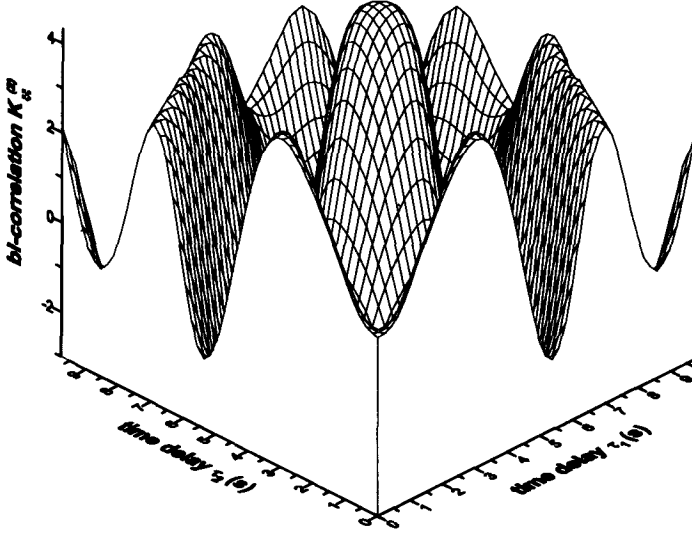


Figure 3.9: Two-dimensional autocorrelation function $K_{\zeta\zeta}^{(2)}$.

Thus, the two-dimensional autocorrelation function is evaluated by shifting the time history of $\zeta(t)$ by the time τ_1 and τ_2 , and then averaging the product $\zeta(t)\zeta(t+\tau_1)\zeta(t+\tau_2)$. An example of autocorrelation function $K_{\zeta\zeta}^{(2)}(\tau_1, \tau_2)$ is shown in Fig. 3.9. It should be noted that the function $K_{\zeta\zeta}^{(2)}(\tau_1, \tau_2)$ possesses the following symmetry relationships (Ochi, 1990):

$$\begin{aligned}
 K_{\zeta\zeta}^{(2)}(\tau_1, \tau_2) &= K_{\zeta\zeta}^{(2)}(\tau_2, \tau_1) = \\
 &= K_{\zeta\zeta}^{(2)}(-\tau_2, \tau_1 - \tau_2) = K_{\zeta\zeta}^{(2)}(\tau_1 - \tau_2, -\tau_2) = . \\
 &= K_{\zeta\zeta}^{(2)}(-\tau_1, \tau_2 - \tau_1) = K_{\zeta\zeta}^{(2)}(\tau_2 - \tau_1, -\tau_1)
 \end{aligned} \tag{3.127}$$

Applying the Wiener-Khinchine theorem to the two-dimensional autocorrelation function $K_{\zeta\zeta}^{(2)}(\tau_1, \tau_2)$ we obtain the bispectrum in the form:

$$B(\omega_1, \omega_2) = \left(\frac{1}{2\pi}\right)^2 \int_{-\infty}^{\infty} \int_{-\infty}^{\infty} K_{\zeta\zeta}^{(2)}(\tau_1, \tau_2) \exp[-i(\omega_1\tau_1 + \omega_2\tau_2)] d\tau_1 d\tau_2. \tag{3.128}$$

It was shown in Eq. (3.127) that there are six two-dimensional autocorrelation functions for a given τ_1 and τ_2 . Therefore, there also are six bispectra for a given ω_1 and ω_2 , having the same value, i.e.:

$$\begin{aligned}
 B(\omega_1, \omega_2) &= B(\omega_2, \omega_1) = B(\omega_1, -\omega_1 - \omega_2) = \\
 &= B(-\omega_1 - \omega_2, \omega_1) = B(\omega_2, -\omega_1 - \omega_2) = B(-\omega_1 - \omega_2, \omega_1),
 \end{aligned} \tag{3.129}$$

and

$$B(\omega_1, \omega_2) = B^*(-\omega_1, -\omega_2), \tag{3.130}$$

where the asterisk denotes the complex conjugate. Because of these symmetries, it is sufficient to evaluate the bispectrum only in the domain defined by $0 \leq \omega_2 < \omega_1 \leq |\omega_1 + \omega_2|$.

Using the representation of the sea surface in terms of the Fourier-Stieltjes integral we can write the following relationship:

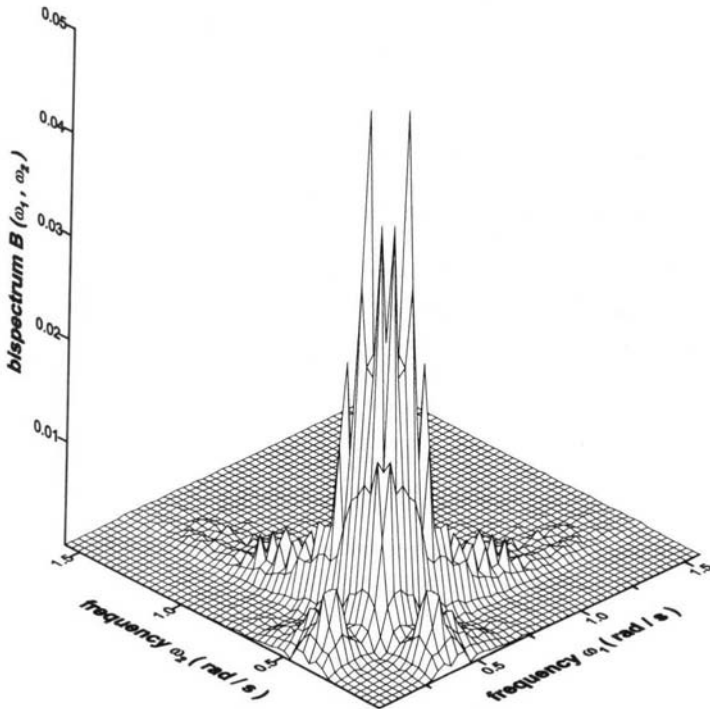


Figure 3.10: Bispectrum function $B(\omega_1, \omega_2)$.

$$dA(\omega_1) dA(\omega_2) dA(\omega_3) = \begin{cases} B(\omega_1, \omega_2) d\omega_1 d\omega_2 & \text{for } \omega_1 + \omega_2 + \omega_3 = 0 \\ 0 & \text{for } \omega_1 + \omega_2 + \omega_3 \neq 0 \end{cases} \quad (3.131)$$

Thus, integrating the real part of the bispectrum yields an estimate of skewness which is proportional to the third moment $E[\zeta^3]$. Prior to the work of Masuda and Kuo (1981) no physical interpretation had been attached to the imaginary part of the bispectrum. However, they showed that the imaginary part of the bispectrum is related to the vertical asymmetry of the waves. Moreover, Elgar and Guza (1985) related the imaginary part of the bispectrum to a measure of the skewness of the temporal derivative of a time series.

The Fast Fourier Transform offers an alternative method of calculating the bispectrum directly from recorded data (see, for example, Liu and Green, 1978; Kim and Powers, 1979 and Chapter 9).

In Fig. 3.10 an example of a bispectrum is shown. This bispectrum was calculated by the FFT method from wave data recorded in shallow water.

3.2.4 Dispersion relation for ocean waves

In an evaluation of spectral representation of ocean waves, the unique relationship between the wave number k and the frequency ω (see Eq. (1.20)) was frequently used. This relationship, known as the dispersion relation, results from linearized equations of motion, satisfying the surface boundary condition (Massel, 1989). Laboratory and theoretical studies indicate that the deviation of the dispersion relation from Eq. (1.20) only amounts to a few percent at most. As a result, it has also been widely used for ocean waves.

There are at least a few reasons for which the dispersion relation should not be satisfied exactly in the random wave field. The dispersion relation (1.20) is restricted to small amplitude waves only. Even for regular waves, the influence of finite amplitude in deep water, up to a third order of accuracy, yields (Wehausen and Laitone, 1960):

$$\omega^2 = gk \left[1 + (ka)^2 \right]. \quad (3.132)$$

For the limiting steepness ($ka \approx 0.4$), Eq. (3.132) gives $\omega^2 \approx 1.16gk$.

In a shallow water case when $kh \rightarrow 0$, the corresponding dispersion relation for nonlinear waves becomes:

$$\omega^2 = \sqrt{gh}k \left[1 + \frac{1}{2} \left(\frac{a}{h} \right) \right], \quad (3.133)$$

and for $\frac{a}{h} \approx 0.4$ we obtain $\omega^2 \approx 1.2\sqrt{gh}k$.

Other reasons for the possible deviation of the observed dispersion relation from Eq. (1.20) are nonlinear interactions between elementary wave components. Since there are infinitely many components of waves in the ocean, there will be infinitely

many possible combinations for interaction to occur. To preserve algebraic simplicity, suppose that two wave trains with frequencies ω_1 and ω_2 , and wave numbers k_1 and k_2 are propagating in the same direction. Nonlinear interaction produces bounded second-order components of the frequencies $\omega_1 \pm \omega_2$ and wave numbers $k_1 \pm k_2$. It can be seen that for these components, the dispersion relation (1.20) is not satisfied as:

$$(\omega_1 \pm \omega_2)^2 \neq g(k_1 \pm k_2) \tanh[(k_1 \pm k_2)h]. \quad (3.134)$$

Moreover, a higher order nonlinear mechanism generates waves of frequencies and wave numbers $\omega_1 \pm 2\omega_2$, $k_1 \pm 2k_2$ etc., as discussed by Phillips (1960b) and Longuet-Higgins (1962).

If the water itself is moving with velocity \bar{U} , the observed frequency is related to the wave number \vec{k} by:

$$\omega = [gk \tanh(kh)]^{1/2} + \vec{k} \cdot \bar{U}, \quad (3.135)$$

in which $\vec{k} = (k \cos \theta, k \sin \theta)$, $k = |\vec{k}|$, and θ is a direction of wave propagation.

The relationship (3.135) can be extended to the nonlinear case as (Willebrand, 1975):

$$\omega = \vec{k} \cdot \bar{U} + (\tanh kh)^{1/2} \left\{ 1 + \int_{\vec{k}'} Q(\vec{k}, \vec{k}') \Psi(\vec{k}') d\vec{k}' \right\}, \quad (3.136)$$

in which $Q(\vec{k}, \vec{k}')$ is a source function.

A wide range of frequencies and amplitudes co-exist in a typical wind wave field. This means, for example, that short waves propagate under the influence of additional acceleration due to large-scale components. The corresponding dispersion relation takes the form:

$$\omega^2 = (g + a)k \tanh(kh), \quad (3.137)$$

in which a is an acceleration induced by low-frequency components.

In natural field conditions all mechanisms, mentioned above, act simultaneously with various intensities. Thus, the classical dispersion relation is only an approximation to the 'true' dispersion relation. Let us provide some insight into the 'true' dispersion relation for random sea.

Huang and Tung (1976) developed a correction to the linear dispersion relation using a complete system of nonlinear equations up to a third-order approximation. They found that a mean deviation of the dispersion relation from the linear formula in deep water ($\omega^2 = gk$) is:

$$g - \frac{\omega^2}{|\vec{k}|} = - \int_{\vec{k}_1} \int_{\omega_1} f(\vec{k}, \omega; \vec{k}_1, \omega_1) \bar{\Psi}(\vec{k}_1, \omega_1) d\vec{k}_1 d\omega_1, \quad (3.138)$$

in which $\tilde{\Psi}(\vec{k}_1, \omega_1)$ is a frequency-wave number spectrum and:

$$\begin{aligned}
 f = & \frac{\omega^2}{|\vec{k}|} \left\{ \frac{1}{2} (\vec{k} + 2\vec{k}_1) \cdot \vec{k} - \frac{\vec{k} \cdot (\vec{k} - \vec{k}_1) (\vec{k} - \vec{k}_1) \cdot \vec{k}}{|\vec{k}| |\vec{k} - \vec{k}_1|} \right\} + \\
 & + \frac{(\vec{k} + \vec{k}_1) \cdot \vec{k}}{|\vec{k}|} \omega(\omega + \omega_1) - \frac{1}{2} \omega^2 |\vec{k}| - \frac{1}{2} \left(1 - \frac{\vec{k} \cdot \vec{k}_1}{|\vec{k}| |\vec{k}_1|} \right) \\
 & \cdot (|\vec{k}| + |\vec{k}_1|) \omega \omega_1 + \frac{1}{2} \left(1 - \frac{(\vec{k} - \vec{k}_1) \cdot \vec{k}_1}{|\vec{k} - \vec{k}_1| |\vec{k}_1|} \right) \frac{(\vec{k} - \vec{k}_1) \cdot \vec{k}}{|\vec{k}|} \omega \omega_1.
 \end{aligned} \quad (3.139)$$

If we neglect all the nonlinear terms, we immediately recover the linear approximation $\omega^2 = gk$.

For waves propagating in the same direction, Eq. (3.138) becomes:

$$g - \frac{\omega^2}{k} = -2\omega \int_0^\infty \int_0^\infty k_1 \omega_1 \hat{S}(k_1, \omega_1) dk_1 d\omega_1. \quad (3.140)$$

To compute the mean deviation of the dispersion relation from the linear formula, the wave number-frequency spectrum $\tilde{\Psi}(\vec{k}, \omega)$ is required. Because of measurement

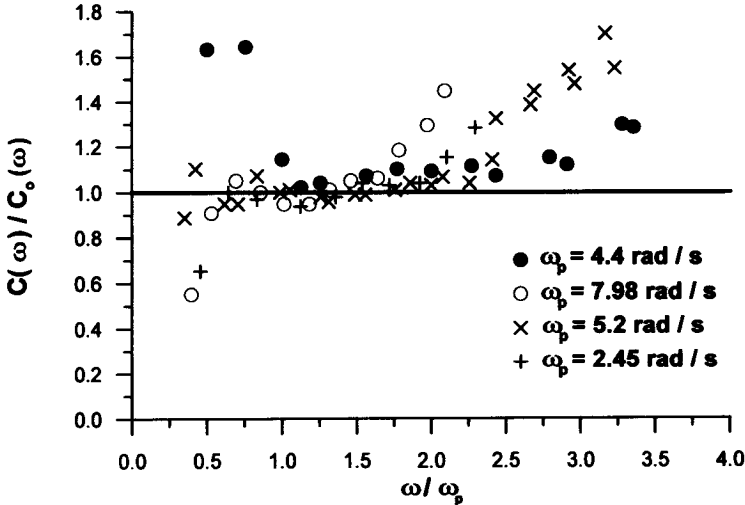


Figure 3.11: Normalized phase speed as a function of normalized frequency.

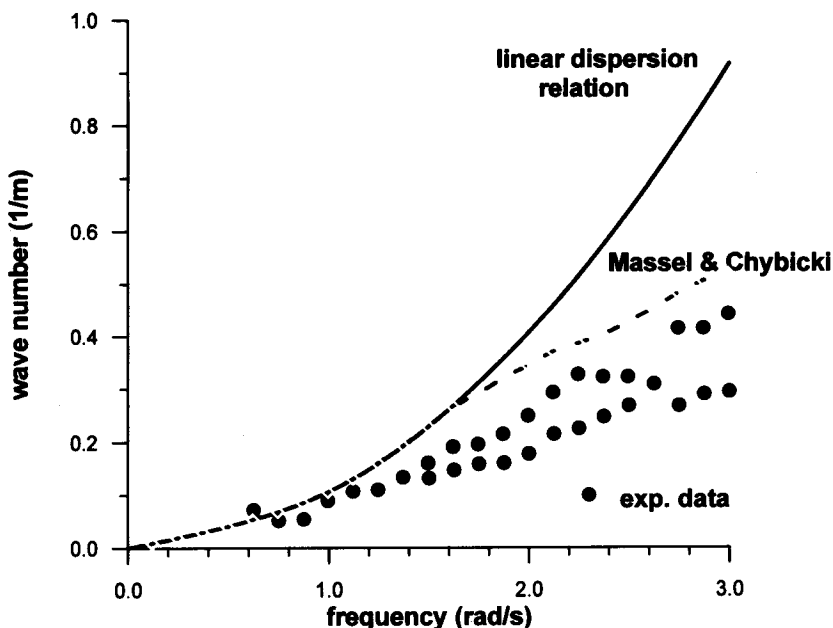


Figure 3.12: Comparison of experimental and theoretical dispersion relation

difficulties, this spectrum is not directly available. However, it may be related to the directional frequency spectrum $\hat{S}(\omega, \Theta)$ or wave number spectrum $\hat{\Psi}(\vec{k})$. Numerical results by Huang and Tung (1977) showed that the dispersion relation varies both as a function of the directional energy distribution and the direction of wave component propagation. In particular, the deviation from the linear approximation increases as the energy spreading decreases. The results of Huang and Tung have been extended to the case of finite water depth by Massel and Chybicki (1983).

Experimental data on the dispersion relation are very limited. Ramamonjiarisoa and Coantic (1976) found in their large tunnel experiments that wave components at frequencies greater than peak frequency do not propagate as freely travelling waves, but are bound as harmonics of the dominant waves. Their phase velocity was nearly constant, corresponding to the velocity of mean components close to the spectral peak.

In the experiments performed by Bendykowska and Werner (1989) the random waves of the JONSWAP spectrum ($\gamma = 1$ and $\gamma = 6$) were reproduced by a programmable wave generator. Four probes with a spatial separation 0.10 m in the

down-channel direction recorded surface displacements simultaneously in constant water depth of $h = 0.2$ m. In Fig. 3.11, the experimental phase speed (C), normalized by the linear one (C_0) as a function of frequency, is presented. In the range of $\omega \geq 1.5\omega_p$ (ω_p is a spectrum peak frequency), phase speed is greater than that resulting from the linear theory. The discrepancy increases with the frequency. This phenomenon was also confirmed by field experiments. Efimov et al. (1972) observed a good agreement with the linear dispersion relation in deep water for frequencies $\omega \leq 2\omega_p$. When $\omega > 2\omega_p$, the ratio of the experimental wave number and the linear one is equal to approximately 0.87. Hence, the phase velocity is about 15% higher than in the linear one.

Results of experiments in the Bulgarian coastal zone of the Black Sea in water depth $h = 18$ m are shown in Figure 3.12. (Massel, 1980; Massel and Chybicki, 1983). The experimental data start to deviate from the linear dispersion curve for frequencies greater than $1.5\omega_p$. During the experiments, peak frequency $\omega_p \approx 1.0$ rad/s and significant wave height $H_s \approx 2.0$ m. In the same figure, the nonlinear dispersion relation, calculated by Massel and Chybicki (1983), is shown for comparison. In the calculations the unidirectional wave train was adopted, i.e. $D(\Theta; \omega) \approx \delta(\Theta - \Theta_0)$.

3.3 Directional spectral functions

The most widely used and accepted method of studying wind generated waves is an examination of the spectra at a single point. However, single point measurements are not sufficient to describe the full nature of wind-induced surface waves. Due to complicated energy transfer from the atmosphere to the sea and due to wave-wave interactions the resulting surface waves are multidirectional. Only part of the wave energy is aligned with the wind direction. More specifically, wave energy associated with the frequencies $\omega \approx \omega_p$ is primarily propagated in the direction of the wind, whereas wave energy associated with lower or higher frequencies is distributed over a range of directions. Wave multidirectionality is also a result of the superposition at a given point of various wave trains, which may be generated by different remote atmospheric forcing systems.

Directional spreading is a fundamental property of a random wave field and is a key element for understanding the ocean wave mechanics, as well as generation, propagation and breaking. Information about the directional distribution of wave energy is required for the proper prediction of various oceanographic and geomorphological phenomena in shallow and in deep waters. For example, sediment transport in the coastal zone is induced mainly by a longshore current and the intensity of this current depends strongly on the direction of waves at the breaking line (Massel, 1989). The effectiveness of coastal and offshore structures depends on their orientation to incoming waves. Moreover, the forces induced by waves on the structures are a function of the directional distribution of wave energy (Sarpkaya and Isaacson, 1981; Wiegell, 1982).

Due to a limitation of the observational methods, knowledge on the directional spectrum is relatively poor compared to the frequency spectrum. The basic approach to the two-dimensional spectrum $\hat{S}(\omega, \Theta)$ is to multiply the frequency spectrum $S(\omega)$ by an empirically determined directional spreading function D (see Eq. (1.65)). A more general expression for \hat{S} , that includes a variety of commonly used directional spreading representations, can be written as (Niedzwecki and Whatley, 1991):

$$\hat{S}(\omega, \Theta) = S(\omega) D(\Theta; \omega, p_1, p_2, \dots), \quad (3.141)$$

in which p_1, p_2, \dots represent the various parameters associated with the various directional spreading functions.

There are four basic forms of the directional spreading function: the cosine-power function, exponential function, exponential series, and hyperbolic function.

The cosine-power models

Historically, the first attempt to model directional energy spreading was suggested by Pierson et al. (1955) in the form of the cosine type function (Fig. 3.13):

$$D(\Theta) = \frac{2}{\pi} \cos^2 \Theta, \quad -\frac{\pi}{2} \leq \Theta \leq \frac{\pi}{2}. \quad (3.142)$$

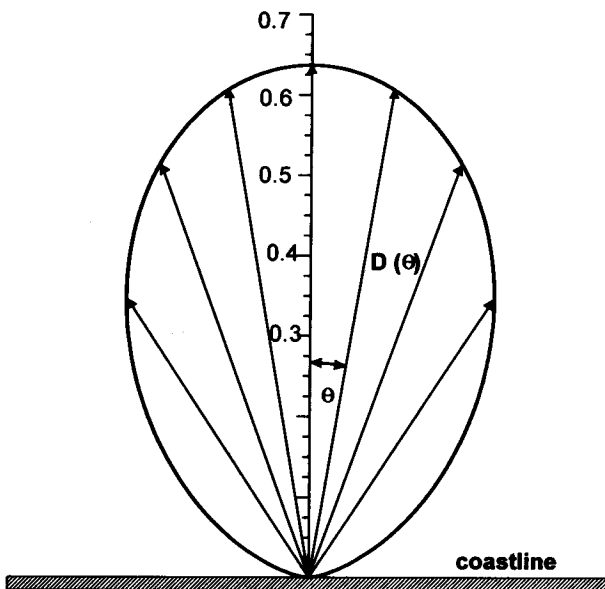


Figure 3.13: Directional spreading function (3.142).

From Eq. (3.142) it follows that in the sector - wind direction $\pm 5^\circ$ - only 11% of wave energy is propagated. In a direction normal to wind direction, waves do not propagate. This directional spreading function is not realistic because it gives the same directional divergence of all frequency components.

On the basis of a field study with the pitch-and-roll buoy, Longuet-Higgins et al. (1961b) proposed a more elaborate form of the cosine type spreading function as:

$$D(\Theta; s) = \frac{2^{2s-1}}{\pi} \frac{\Gamma^2(s+1)}{\Gamma(2s+1)} \cos^{2s} \left(\frac{\Theta - \Theta_0}{2} \right), \quad -\pi \leq \Theta \leq \pi, \quad (3.143)$$

or:

$$D(\Theta; s) = \frac{1}{\sqrt{\pi}} \frac{\Gamma \left(1 + \frac{s_1}{2} \right)}{\Gamma \left[\frac{(1+s_1)}{2} \right]} \cos^{2s_1} (\Theta - \Theta_0), \quad -\frac{\pi}{2} \leq \Theta \leq \frac{\pi}{2}, \quad (3.144)$$

in which Θ_0 is the main peak frequency direction, s and s_1 are the empirical functions of $\left(\frac{U}{C} \right)$ and $\Gamma(\cdot)$ is a gamma function (Abramowitz and Stegun, 1975).

Various representations have been proposed in the past for s or (s_1) . All of them show the wave frequency dependent nature of the directional spreading function D . For example, Krylov et al. (1966) found that:

$$D(\Theta; \omega) = 2^{1.8/\omega_*} \frac{\Gamma \left[2 \left(\frac{1.8}{\omega_*} + 1 \right) \right]}{\Gamma^2 \left(\frac{1.8}{\omega_*} + 1 \right)} [\cos (\Theta - \Theta_0)]^{1.8/\omega_*}, \quad (3.145)$$

in which $\omega_* = \frac{\omega}{\bar{\omega}}$. Hence, the low-frequency components ($\omega \ll \bar{\omega}$) possess a very narrow directional spreading, concentrated around direction Θ_0 , while the high-frequency components ($\omega > \bar{\omega}$) are spread in a wider directional band. In the vicinity of the spectral maximum ($\omega_* \approx 0.8$), the directional spreading function $D \sim \cos^2 \Theta$.

In most of the experiments, the characteristic asymmetry in frequency dependence of parameter s was observed. The parameter s reaches its maximum value for peak frequency and decreases both for lower and higher frequencies. The decreasing trends are different, and more rapid decrease is observed in the low-frequency range. Using the cloverleaf buoy data, Mitsuyasu et al. (1975) suggest the following dependence for s in Eq. (3.143):

$$\frac{s}{s_p} = \begin{cases} \left(\frac{\tilde{\omega}}{\tilde{\omega}_p} \right)^5 & \text{for } \tilde{\omega} \leq \tilde{\omega}_p \\ \left(\frac{\tilde{\omega}}{\tilde{\omega}_p} \right)^{-2.5} & \text{for } \tilde{\omega} \geq \tilde{\omega}_p, \end{cases} \quad (3.146)$$

where $\tilde{\omega} = \frac{\omega U}{g}$, $\tilde{\omega}_p = \frac{\omega_p U}{g}$, and $s_p = 11.5 \tilde{\omega}_p^{-2.5}$.

The asymmetry mentioned above is clearly reflected in the values of powers (5 and 2.5). It should be noted that parameter s increases when ω_p decreases. Hence, the directional distribution becomes narrower with the development of waves.

Similar dependence of parameter s on the wave frequency was found during the JONSWAP experiment (Hasselmann et al., 1980). They defined parameter s as follows:

$$s = s_p \left(\frac{\omega}{\omega_p} \right)^\mu, \quad (3.147)$$

in which:

$$\left. \begin{aligned} s_p &= 6.97 \pm 0.83 \\ \mu &= 4.06 \pm 0.22 \end{aligned} \right\} \text{ for } \omega < \omega_p, \quad (3.148)$$

and

$$\left. \begin{aligned} s_p &= 9.77 \pm 0.43 \\ \mu &= -(2.33 \pm 0.06) - (1.45 \pm 0.45) \left(\frac{U}{C} - 1.17 \right) \end{aligned} \right\} \text{ for } \omega \geq \omega_p. \quad (3.149)$$

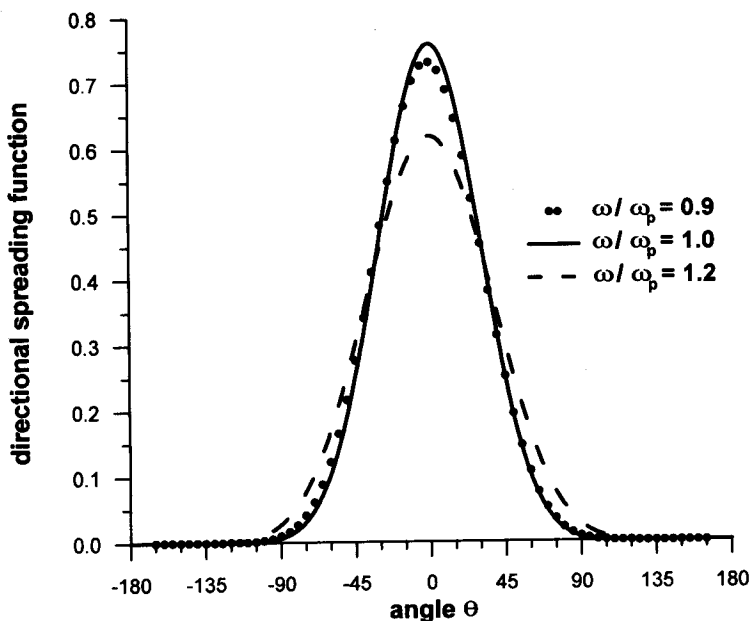


Figure 3.14: Directional spreading function according to Hasselmann et al. (1980).

The above formulas are valid for a developing sea, i.e. when $1 \leq \frac{U}{C} \leq 1.5$.

The directional spreading (3.143) with the Hasselmann et al. parameterization of power s is shown in Fig. 3.14 for three different frequencies, i.e. $\frac{\omega}{\omega_p} = 0.8; 1.0; 1.8$.

For low-frequency components ($\omega < \omega_p$), directional spreading is determined by the ratio $\left(\frac{\omega}{\omega_p}\right)$ only. In the frequency band $\omega \geq \omega_p$, this spreading also depends on the ratio of wind velocity and wave phase velocity (wave age). When waves mature, the directional spreading narrows (see also Davidan et al., 1985). At the spectral peak, the parameter $s = 9.77$ is a much higher value than $s = 2$, suggested by the earlier estimations (Pierson et al. 1955; Krylov et al., 1966).

The parameterization (3.148), proposed by Hasselmann et al. (1980), is based on the assumption that the spectral shape for $\omega \leq \omega_p$ is governed by nonlinear interactions when we should expect dependence of s on the ratio $\left(\frac{\omega}{\omega_p}\right)$. However, in a high-frequency range ($\omega > \omega_p$), the spectrum shape also depends on input from the wind. Hasselmann et al. (1980) showed that this dependence is rather weak and the scaling of s on $\left(\frac{\omega}{\omega_p}\right)$ is more important, i.e. the spreading parameter s for $\omega \geq \omega_p$ finally takes the form as given in Eq. (3.149).

One can now ask whether the saturation range of the two-dimensional spectrum $S(\omega, \Theta)$ exists in a similar way to the saturation range in the frequency spectrum. Davidan et al. (1985) reported some field observations which showed that within the low-frequency range, where the isolines of $S(\omega, \Theta)$ spectrum have been changed along the wave growth, while the isolines associated with the higher frequencies (saturation range) remained unchanged. Therefore, the directional spreading in the saturation range does not depend on the stage of wave growth, but only on the wave frequency.

The role of the directional spreading of energy has long been recognized to be useful for the design of offshore structures. However, mathematical models which use a separation of variables to isolate the frequency and directional components are still used. Only recently, Niedzwecki and Whatley (1991) used the modified cosine-power type model (Eq. (3.143)), in which $s = s(\omega)$ and $\Theta_0 = \Theta_0(\omega)$, and field data of Forristall et al. (1978), to estimate the frequency dependence of directional spreading parameters, with special emphasis on their application in the design of offshore structures.

The wrapped-around Gaussian model

The wrapped-around Gaussian model is an exponential model, based on a normal

distribution. It can be expressed as (Mardia, 1972):

$$\begin{aligned}
 D(\Theta; \Theta_0, \omega, \sigma, n, q) &= \sum_{n=1}^{\infty} \frac{\exp\left(-\frac{n^2 \sigma^2}{2}\right)}{\pi} \cos[n(\Theta - \Theta_0)] = \\
 &= \sum_{-q}^q \frac{\exp\left[-\frac{(\Theta - \Theta_0 - 2\pi q)^2}{2\sigma^2}\right]}{\sqrt{2\pi}\sigma}, \tag{3.150}
 \end{aligned}$$

in which σ is a circular standard deviation in radians. The first formula is the best if $\sigma > \pi$, while the second is better if $\sigma < \pi$.

Unlike the cosine-power spreading function, the tails of the wrapped-around Gaussian model do not decrease to zero at $\Theta = \pi$ or $-\pi$, when σ is greater than 1. They are wrapped back into the interval which is the source of their name. There are two parameters in the wrapped-around Gaussian model which need to be specified, i.e. the number of terms $n(q)$, used in the series approximation, and the circular standard deviation σ . Briggs et al. (1987) suggest that including five terms ($n = q = 5$) gives generally adequate results. It can be shown that after proper selection of standard deviation σ , the resulting directional spread of energy is very similar to that of cosine-power spreading (Niedzwecki and Whatley, 1991).

For offshore engineering applications, Berge and Penzien (1974) argue that $\sigma = 0.6$ is a fairly good estimation.

The von Mises formula

Von Mises proposed the directional spreading function $D(\Theta; \omega)$ in the form:

$$D(\Theta; \omega_0, c) = \frac{1}{2\pi I_0(c)} \exp[c \cos(\Theta - \Theta_0)], \tag{3.151}$$

in which I_0 is a modified Bessel function of zero order (Abramowitz and Stegun, 1975):

$$I_0(c) = \frac{1}{2\pi} \int_0^{2\pi} \exp(c \cos \Theta) d\Theta = \sum_{r=0}^{\infty} \frac{1}{(r!)^2} \left(\frac{c}{2}\right)^{2r}. \tag{3.152}$$

Parameter c serves as a measure of concentration around mean direction Θ_0 . A reasonable value of c in terms of parameter s (see Eq. (3.143)) is:

$$2 \cos^{-1} \left(1 - \frac{\log 2}{c}\right) = 4 \cos^{-1} \left[\left(\frac{1}{2}\right)^{1/2s}\right]. \tag{3.153}$$

When $c = 0$, the directional spreading is constant and all waves are coming uniformly from all directions. As c increases, the spreading becomes narrower.

The hyperbolic type model

The parameterization of spreading function (3.143) was mainly based on the data obtained from pitch-roll buoys. Donelan et al. (1985) found that directional spread-

ing formulation based on buoy data did poorly when compared to data from wave staff array. This led them to propose a directional spreading function in the form of a hyperbolic function, i.e. $\sim \cosh^{-2}(\beta\Theta)$. An envelope soliton group propagating around the main wave direction is described by a hyperbolic secant. Therefore, the distribution of wave energy in the direction transverse to the mean wave direction behaves like $\cosh^{-2}(\beta\Theta)$. Assuming now that the wave field consists of mainly (envelope) soliton groups, they suggest that the directional distribution of waves observed at a given point about the main wave direction must follow approximately a $\cosh^{-2}(\beta\Theta)$. The $\cosh^{-2}(\beta\Theta)$ distribution extends beyond $\pm\frac{1}{2}\pi$, but values of β are generally larger than 1.2, so that at $\pm\pi/2$, the spreading function is less than 9% of its peak value. Less than 5% of the energy is outside the range $-\frac{1}{2}\pi < \Theta < \frac{1}{2}\pi$. Using the dependence of β on $\frac{\omega}{\omega_p}$ given by Donelan et al. (1985), the directional spreading function takes the form (Fig. 3.15):

$$D(\Theta; \omega) = \frac{1}{2}\beta \cosh^{-2} [\beta(\Theta - \Theta_0)], \quad (3.154)$$

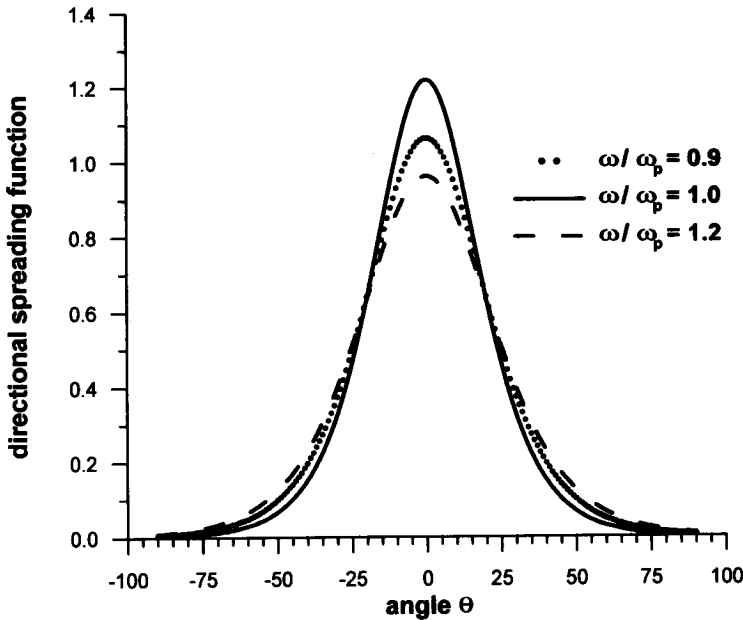


Figure 3.15: Directional spreading function according to Donelan et al. (1985).

in which:

$$\beta = \begin{cases} 2.61 \left(\frac{\omega}{\omega_p} \right)^{1.3} & \text{for } 0.56 < \frac{\omega}{\omega_p} < 0.95 \\ 2.28 \left(\frac{\omega}{\omega_p} \right)^{-1.3} & \text{for } 0.95 < \frac{\omega}{\omega_p} < 1.60 \\ 1.24 & \text{otherwise.} \end{cases} \quad (3.155)$$

The β dependence on $\left(\frac{\omega}{\omega_p} \right)$ only, which is valid for $1 < \frac{U}{C} < 4$ and $0.8 < \frac{\omega}{\omega_p} < 1.6$, confirms the Hasselmann et al. (1980) conclusion that nonlinear interactions are more important than direct wind input. In particular, it should be noted that the angular spreading of wave energy is the smallest at a frequency about 5% less than the peak frequency ω_p . Therefore, the narrowest spreading occurs on the forward face of the frequency spectrum where the spectrum shape is determined predominantly by the energy transfer due to nonlinear wave-wave interaction.

Banner (1990) using the high-frequency stereo photography found that the assumption $\beta = \text{constant}$ for $\omega/\omega_p > 1.6$ is unreasonable. He proposed a formulation for β beyond $1.6\omega_p$, which when combined with Eq. (3.155) gives:

$$\beta = \begin{cases} 2.61 \left(\frac{\omega}{\omega_p} \right)^{1.3} & \text{for } 0.56 < \frac{\omega}{\omega_p} < 0.95 \\ 2.28 \left(\frac{\omega}{\omega_p} \right)^{-1.3} & \text{for } 0.95 < \frac{\omega}{\omega_p} < 1.60 \\ 10^y & \text{for } \frac{\omega}{\omega_p} > 1.6, \end{cases} \quad (3.156)$$

in which:

$$y = -0.4 + 0.8393 \exp \left[-0.567 \ln \left(\frac{\omega}{\omega_p} \right)^2 \right]. \quad (3.157)$$

The double peak spreading model

In order to determine the best spreading function more precise data and a better theoretical understanding is needed rather than simply adjusting the form or coefficients of the predetermined functions. One theoretical explanation of the directional spectrum formation was published recently by Zakharov and Shrira (1990). They showed qualitatively that formation of narrow angular spreading can be described by the mechanism of scattering of wind waves by the wind-induced current. This mechanism contributes to radiative transfer equation for the wave action spectral density

$N_{\vec{k}}$ which is proportional to $N_{\vec{k}}^2$ and to the small parameter of the ratio of the wind drift velocity to the phase velocity of wind waves.

The scattering mechanism causes the angular redistribution of the wave action but does not influence directly the wave number module spectrum. When waves propagate with the wind-induced current, the directional spreading function narrows. For waves propagated against the current, the spreading function is wider. The initial directional spreading $D(\Theta)$ evolves in time into a bi-modal directional distribution.

There are a number of published data sets which provide some support for the bi-modal distribution, not necessary for Zakharov and Shrira explanation (Holthuijsen, 1983; Jähne and Riemer, 1983; Young et al., 1995). Young et al. (1995) showed experimentally that a frequencies of approximately twice of peak frequency, the uni-modal spreading becomes bi-modal. The bi-modal sidelobes continue to separate with increasing frequency and become larger in magnitude.

Numerical techniques to model directional spreading on the base of experimental data are discussed in Chapter 9.

This page is intentionally left blank

Chapter 4

Statistical Properties of Ocean Waves

4.1 Introduction

Frequency spectra characterize the temporal dependencies of wave phenomena. A number of other statistical distributions of ocean waves are found useful. For example, a statistics of extreme waves plays a key role in determining the design wave height for offshore and coastal structures. In the statistical approach a temporal sequence of the particular wave parameters, such as: surface displacement, wave height, wave period, etc., is disregarded. These parameters are considered as random variables which possess some statistical characteristics.

In this Chapter, classical statistics of the Gaussian processes, as well as new statistical distributions are discussed. They include the distributions of surface displacement and wave height of nonlinear waves, breaking waves in deep and shallow waters, and others.

In Section 4.2.3 the intriguing question of how big a wave can be is addressed. More specifically, the recently discovered distribution of sea surface in the vicinity of the extreme crest is discussed. It was shown that the expected spatial configuration of extreme waves is approximately proportional to the two-dimensional spatial autocorrelation function of the wave field as a whole.

It is widely acknowledged that the Rayleigh distribution does not reflect a measured distribution of large wave heights. The Rayleigh distribution overpredicts the probabilities of the higher waves in a record. In Section 4.3.4 numerous reasons for the causes of the observed overprediction have been suggested and discussed in detail.

The distributions of orbital velocities and pressure are of interest to oceanographers and coastal engineers. The velocities and pressure are forcing factors for determination of the sediment transport and forces on the sea bottom and man-made structures. In particular, the wave motion at the point situated near the free surface (for example, in the area between the wave trough and wave crest) is the most

energetic. It should be expected that velocity or pressure in such an area has a non-Gaussian distribution even for the surface displacement $\zeta(t)$ which has the Gaussian distribution. It was shown that the probability density function for velocity (or pressure) in such an intermittent flow depends strongly on the elevation of the observation point with respect to mean water level.

In the final Section 4.6, wave grouping phenomenon is discussed in detail.

4.2 Surface displacement

4.2.1 Probability distribution of surface displacement

Consider a point $P(x, y)$ at the sea surface in deep water. Using one of the various measurement methods (described in Chapter 9), the vertical oscillations of the sea surface are recorded at point P . As an illustration, the time series recorded by a Wave Rider Buoy, at water depth 50 m, is shown in Fig. 4.1. As was the case in Chapter 3, in the simplest model of ocean waves, the sea surface elevation $\zeta(\vec{x}, t)$ is treated as a summation of contributions of a large number of elementary waves of various frequencies ω_m and directions Θ_n ($-\pi \leq \Theta_n \leq \pi$), superimposed in random fashion, i.e.:

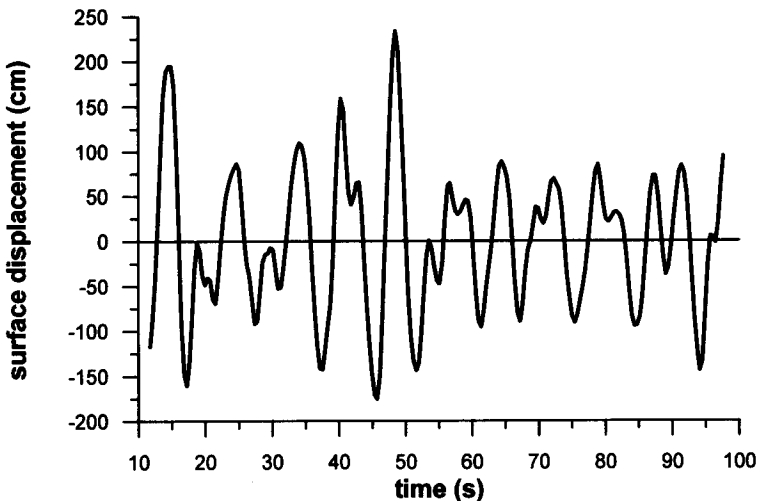


Figure 4.1: Sea surface displacement $\zeta(t)$.

$$\zeta(\vec{x}, t) = \sum_{m=1}^M \sum_{n=1}^N \zeta_{mn}(\vec{x}, t), \quad (4.1)$$

where:

$$\zeta_{mn}(\vec{x}, t) = a_{mn} \cos [k_m (x \cos \Theta_n + y \sin \Theta_n) - \omega_m t + \epsilon_{mn}]. \quad (4.2)$$

The wave number k_m is related to a wave frequency ω_m by the linear dispersion relation:

$$\omega_m^2 = g k_m \tanh(k_m h). \quad (4.3)$$

The phase ϵ_{mn} is assumed to be a random variable distributed uniformly in the interval $-\pi, \pi$. The amplitude a_{mn} is a random variable related to the two-dimensional spectrum $\hat{S}(\omega, \Theta)$ by $a_{mn} = \sqrt{2 \hat{S}(\omega, \Theta) \Delta \omega_m \Delta \Theta_n}$. Note that when $M \rightarrow \infty$ and $N \rightarrow \infty$, the representation (4.1) is equivalent to the Fourier-Stieltjes integral representation (1.27).

Let us assume now that particular contributions $\zeta_1, \zeta_2, \zeta_3, \dots, \zeta_N$ are statistically independent random variables having the same distribution with a mean value $\bar{\zeta}/N$ and variance $\sigma_{\bar{\zeta}}^2/N$, where N is large. This means physically that we neglect all nonlinear interactions between wave components. Therefore, the Central Limit Theorem (Ochi, 1990) yields the conclusion that observed sea surface displacement $\zeta(t)$ is normally distributed with mean $\bar{\zeta}$ and variance $\sigma_{\bar{\zeta}}^2$, while the probability density function $f(\zeta)$ takes the form:

$$f(\zeta) = \frac{1}{\sqrt{2\pi} \sigma_{\bar{\zeta}}} \exp \left[-\frac{(\zeta - \bar{\zeta})^2}{2\sigma_{\bar{\zeta}}^2} \right]. \quad (4.4)$$

The mean and variance are the first and second central moments μ_1 and μ_2 , respectively:

$$\mu_1 = \bar{\zeta} = E[\zeta] = \int_{-\infty}^{\infty} \zeta f(\zeta) d\zeta, \quad (4.5)$$

$$\mu_2 = \sigma_{\bar{\zeta}}^2 = E[(\zeta - \bar{\zeta})^2] = E[\zeta^2] - \bar{\zeta}^2 = \int_{-\infty}^{\infty} (\zeta - \bar{\zeta})^2 f(\zeta) d\zeta. \quad (4.6)$$

The estimation of parameters $\bar{\zeta}$ and $\sigma_{\bar{\zeta}}^2$ from observed data is discussed in Chapter 9. The variance of sea surface oscillation can also be defined as a zero-moment of the frequency spectrum $S(\omega)$, i.e.:

$$\text{var}[\zeta] = m_0 = \int_0^{\infty} S(\omega) d\omega. \quad (4.7)$$

In the following, both notations will be used, while the symbol $\sigma_{\bar{\zeta}}^2$ is reserved for general discussion as well as for the situation where variance is defined from the

probability density function, as in Eq. (4.6), or from experimental data. The symbol m_0 will be used when variance is given by Eq. (4.7).

In the following we will also use the standardized Gaussian probability density function:

$$f(\xi) = \frac{1}{\sqrt{2\pi}} \exp\left(-\frac{1}{2}\xi^2\right), \quad (4.8)$$

which is obtained from Eq. (4.4) by transformation of variables:

$$\xi = \frac{\zeta - \bar{\zeta}}{\sigma_\zeta}, \quad (4.9)$$

and

$$f(\xi) = f[g(\xi)] \left| \frac{dg(\xi)}{d\xi} \right| \quad \text{and} \quad g(\xi) = \sigma_\zeta \xi + \bar{\zeta}. \quad (4.10)$$

It can be shown that all odd numbered central moments of the Gaussian random variable are equal to zero, while even numbered moments are:

$$\mu_{2n} = 1 \cdot 3 \cdot 5 \cdots (2n - 1) \sigma_\zeta^{2n}, \quad (4.11)$$

where:

$$\mu_n = \int_{-\infty}^{\infty} (\zeta - \bar{\zeta})^n f(\zeta) d\zeta. \quad (4.12)$$

The distribution (4.8) usually is abbreviated as $N(0, 1)$, as the two first moments of the standardized probability density function are 0 and 1, respectively. In general, the moments of the standardized Gaussian probability density function (4.8) may be written as:

$$\hat{m}_n = \int_{-\infty}^{\infty} \xi^n f(\xi) d\xi. \quad (4.13)$$

Thus:

$$\hat{m}_n = \begin{cases} 1 \cdot 3 \cdot 5 \cdots (n - 1) & \text{for even numbered moments} \\ 0 & \text{for odd numbered moments,} \end{cases} \quad (4.14)$$

and:

$$\hat{m}_n = \frac{\mu_n}{\sigma_\zeta^n}. \quad (4.15)$$

In Fig. 4.2 the probability density function of the surface displacement calculated from wave measurements is compared with a Gaussian distribution of the same variance. The distribution is only approximately Gaussian, however, a small asymmetry and

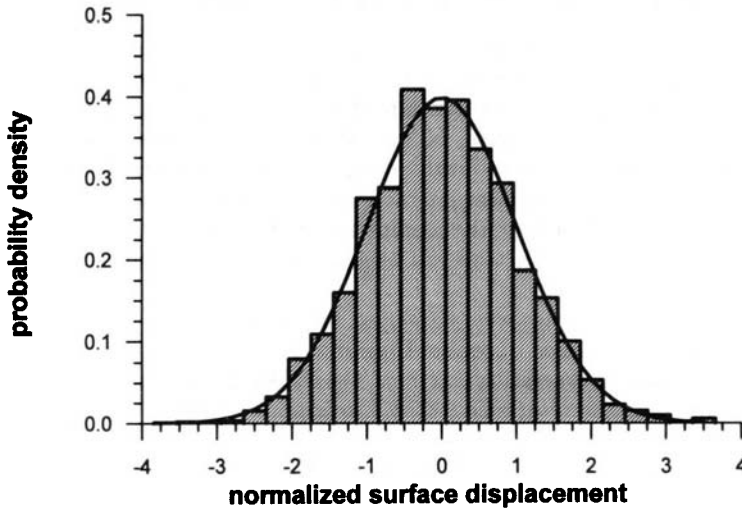


Figure 4.2: Comparison of an experimental probability density distribution with Gaussian distribution (—).

different peakedness are observed. These discrepancies are usually expressed in terms of the skewness γ_1 and kurtosis γ_2 :

$$\gamma_1 = \frac{\mu_3}{\sigma_\zeta^3} = \hat{m}_3, \quad (4.16)$$

$$\gamma_2 = \frac{\mu_4}{\sigma_\zeta^4} - 3 = \hat{m}_4 - 3. \quad (4.17)$$

Skewness and kurtosis are quantities of a higher order and are related to nonlinearities in the wave field. The skewness is a statistical measure of the vertical asymmetry of the sea surface exemplified by the sharp crests and rounded troughs of gravity waves. The kurtosis represents a degree of peakedness of the distribution when the normal distribution is taken as a reference. When $\gamma_1 = \gamma_2 = 0$, the random variable is normally distributed.

In most cases, the probability density function $f(\zeta)$, for sea surface displacements, has a positive skewness. This means that the mode of the distribution is located at a value smaller than the mean. Figure 4.2, in which γ_1 is very small ($\gamma_1 = 0.0982$) and positive, demonstrates such a situation. The positive value of kurtosis γ_2 corresponds to distribution with a peak sharper than the normal distribution (in Fig. 4.2 the $\gamma_2 = 0.068$).

4.2.2 Distribution of nonlinear wave surface displacements

Although in most cases the probability distribution of surface displacement ζ is very close to Gaussian, it is evident that a departure from a Gaussian distribution may become apparent when the higher wave field and higher order of approximation are considered. For example, in water of finite depth, wave profiles have higher, more peaked crests and higher, longer troughs, compared with deepwater waves (see Section 4.2.5). In such cases the nonlinear interactions between particular wave components cannot be neglected. Therefore, the conditions of the Central Limit Theorem will not be satisfied, skewness and kurtosis will have non-zero values, and the wave process will not be Gaussian.

Two different approaches were developed for the probability density function of the non-Gaussian processes. Longuet-Higgins (1963) derived the $f(\zeta)$ function by applying the cumulant generating function. The resulting probability density function of a standardized random variable ξ takes the form:

$$f(\xi) = \frac{1}{\sqrt{2\pi}} \exp\left(-\frac{1}{2}\xi^2\right) \left\{ 1 + \frac{\hat{m}_3}{3!} H_3(\xi) + \frac{\hat{m}_4 - 3}{4!} H_4(\xi) + \right. \\ \left. + \frac{\hat{m}_5 - 10\hat{m}_3}{120} H_5(\xi) + \dots \right\}, \quad (4.18)$$

in which $H(\)$ are the Hermite polynomials:

$$\left. \begin{aligned} H_3(z) &= z^3 - 3z \\ H_4(z) &= z^4 - 6z^2 + 3 \\ H_5(z) &= z^5 - 10z^3 + 15z \\ H_6(z) &= z^6 - 15z^4 + 45z^2 - 15 \end{aligned} \right\}, \quad (4.19)$$

\hat{m}_n is the n th moment of the standardized random variable ξ given by Eq. (4.13). The probability density function (4.18) can also be derived by using the concept of orthogonal polynomials:

$$f(\xi) = \frac{1}{\sqrt{2\pi}} \exp\left(-\frac{1}{2}\xi^2\right) \left\{ 1 + \frac{\gamma_1}{3!} H_3(\xi) + \frac{\gamma_2}{4!} H_4(\xi) + \right. \\ \left. + \frac{\hat{m}_5 - 10\gamma_1}{120} H_5(\xi) + \frac{\hat{m}_6 - 15\hat{m}_4 + 30}{720} H_6(\xi) + \dots \right\}. \quad (4.20)$$

This is called the Gram-Charlier series of Type A. Despite the fact that, in many cases, series Eq. (4.20) represents the probability density function of surface elevation well, it has certain drawbacks. For some range of displacement, the Gram-Charlier approximation gives negative density values (especially for steep waves), for which is obviously not physically acceptable. Moreover, skewness and kurtosis, as well as

higher moments, must be known *a priori*. Although Longuet-Higgins (1963) developed the formulas for γ_1 and γ_2 in terms of a convolution integral of the wave spectrum, the amount of computation, especially for kurtosis γ_2 , is very large. Therefore, estimation of γ_1 and γ_2 through convolution integrals is not used in ocean engineering and oceanography.

An alternative approach to modelling the probability density function for a nonlinear wave train is based on the technique of transformation of random variables used by Huang et al. (1983b). Suppose first that nonlinear waves with a narrow-band spectrum can be presented in the form of the Stokes expansion to the third order (Stokes, 1847):

$$\zeta(\bar{x}, t) = \frac{1}{2}a^2k + a \cos \chi + \frac{a^2k}{2} \cos 2\chi + \frac{3a^3k^2}{8} \cos 3\chi + \dots, \quad (4.21)$$

where a is the local wave amplitude, k is a fixed wave number, and χ is a phase function:

$$\chi = k(x \cos \Theta + y \sin \Theta - \omega t + \epsilon). \quad (4.22)$$

By linear theory, the Rayleigh distribution describes the wave amplitude a (see Section 4.3.1), and the phase shift ϵ is uniformly distributed in the interval $(-\pi, \pi)$. Therefore, the variables:

$$\zeta_1 = a \cos \chi, \quad \zeta_2 = a \sin \chi, \quad (4.23)$$

are normally distributed with the zero mean. Introducing the normalized variables Z_1 and Z_2 :

$$Z_1 = \frac{a}{(\overline{a^2}/2)^{1/2}} \cos \chi, \quad Z_2 = \frac{a}{(\overline{a^2}/2)^{1/2}} \sin \chi, \quad (4.24)$$

we obtain their joint probability distribution as:

$$f(Z_1, Z_2) = \frac{1}{2\pi} \exp \left\{ -\frac{1}{2} (Z_1^2 + Z_2^2) \right\}. \quad (4.25)$$

Using a perturbation scheme it can be shown that a variance of variable ζ is (to the second order):

$$\sigma_\zeta^2 = \frac{\overline{a^2}}{2} (1 + \overline{a^2}k^2). \quad (4.26)$$

It may be verified that the normalized surface displacement takes the form:

$$\xi = \frac{\zeta - \bar{\zeta}}{\sigma_\zeta} = \frac{Z_1}{\psi} + \frac{k\sigma_\zeta}{\psi^2} Z_1^2 + \frac{3(k\sigma_\zeta)^2}{8\psi^3} (Z_1^3 - 3Z_1Z_2^2) - \sigma_\zeta k, \quad (4.27)$$

in which:

$$\psi = \frac{\sigma_\zeta}{\left(\frac{g^2}{2}\right)^{1/2}} = 1 + (\sigma_\zeta k)^2. \quad (4.28)$$

Let $\eta = Z_2$ be an auxiliary random variable. Given the joint probability distribution $f(Z_1, Z_2)$ and the functional relationship of Z_1, Z_2 to the variables ξ, η , the variable transformation gives (Papoulis, 1965):

$$f(Z_1, Z_2)dZ_1dZ_2 = f[Z_1(\xi, \eta), Z_2(\xi, \eta)] J \left(\frac{Z_1, Z_2}{\xi, \eta} \right) d\xi d\eta, \quad (4.29)$$

in which $J(\dots)$ is the Jacobian of the variable transformation. To calculate the Jacobian, Eq. (4.27) is inverted. This can be achieved by successive approximation. To the third order, function Z_1 is:

$$Z_1 = \psi \xi - \psi (\xi^2 - 1) \sigma_\zeta k + \psi \left(\frac{13}{8} \xi^3 - 2\xi \right) \sigma_\zeta^2 k^2 + \frac{9}{8} \frac{\xi \eta^2}{\psi} \sigma_\zeta^2 k^2. \quad (4.30)$$

Now the Jacobian becomes:

$$J = \begin{pmatrix} \frac{\partial Z_1}{\partial \xi}, & \frac{\partial Z_1}{\partial \eta} \\ \frac{\partial Z_2}{\partial \xi}, & \frac{\partial Z_2}{\partial \eta} \end{pmatrix} = \psi \left[1 - 2k\sigma_\zeta \xi + \sigma_\zeta^2 k^2 \left(\frac{39}{8} \xi^2 - 2 \right) \right] + \frac{9}{8} (k\sigma_\zeta)^2 \frac{\eta^2}{\psi}. \quad (4.31)$$

Substituting Eqs. (4.30) and (4.31) into Eq. (4.29) and integrating with respect to η , we finally obtain the probability density distribution for the nonlinear wave profile ζ :

$$f(\xi) = \frac{1}{(2\pi)^{1/2}} \exp \left(-\frac{1}{2} A \right) \left[\frac{B}{C^{1/2}} + \frac{9}{8} \frac{(k\sigma_\zeta)^2}{\psi} \frac{1}{C^{3/2}} \right], \quad (4.32)$$

where:

$$A = \psi^2 \left[\xi - k\sigma_\zeta (\xi^2 - 1) + \sigma_\zeta^2 k^2 \left(\frac{13}{8} \xi^3 - 2\xi \right) \right]^2, \quad (4.33)$$

$$B = \psi \left[1 - 2\sigma_\zeta k \xi + \sigma_\zeta^2 k^2 \left(\frac{39}{8} \xi^2 - 2 \right) \right], \quad (4.34)$$

$$C = 1 + \frac{9}{4} (k\sigma_\zeta)^2 \xi^2. \quad (4.35)$$

It should be noted that for the estimation of $f(\xi)$ only second moments are required. The probability density function $f(\xi)$ is always non-negative and depends on one parameter $k\sigma_\zeta$ only:

$$k\sigma_\zeta = 2\pi \frac{\sigma_\zeta}{L} = 2\pi(sl), \quad (4.36)$$

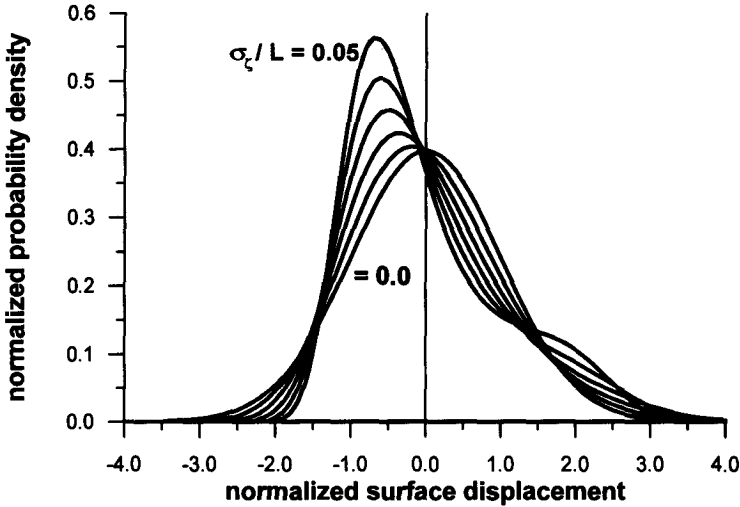


Figure 4.3: Probability density function based on third-order Stokes wave model for significant slopes ranging from 0 to 0.05 at a step of 0.01.

where L is the wavelength of the wave corresponding to the peak of the spectrum, and (sl) is the significant slope. Function $f(\xi)$ is shown in Fig. 4.3 for significant slopes ranging from 0 to 0.05, in steps of 0.01. The probability density function becomes more positively skewed as the significant slope increases. It is also noted that at high slopes (sl) there is a hump between $\xi = 1$ and 2.

The relationship between surface skewness and surface slope strongly depends on the wave spectrum shape, while a simple relationship between skewness γ_1 and surface slope (sl) does not exist. Only in a case of an extremely narrow spectrum, when all energy is concentrated around the peak frequency ω_p , this relationship (Srokosz and Longuet-Higgins, 1986) is:

$$\gamma_1 = 6\pi \frac{\sigma_\zeta}{L}. \quad (4.37)$$

The same authors showed that if spectrum $S(\omega)$ has a special form:

$$S(\omega) = \begin{cases} \alpha \omega^{-n}, & \omega > \omega_p, \\ 0, & \omega < \omega_p, \end{cases} \quad n > 3, \quad (4.38)$$

then:

$$\gamma_1 = \frac{6(n-1)}{n-2} \pi \left(\frac{\sigma_\zeta}{L} \right). \quad (4.39)$$

When $n = 5$ (the Phillips' spectrum) we obtain $\gamma_1 = 8\pi \left(\frac{\sigma_\zeta}{L} \right)$ while for $n = 4$ (the Toba's spectrum) we obtain $\gamma_1 = 9\pi \left(\frac{\sigma_\zeta}{L} \right)$.

4.2.3 Extreme surface displacements

4.2.3.1 Probability distribution for positive and negative maxima

In a rough sea, under specific conditions, extreme wave events are generated. The nonlinear interactions, current influence and diffraction mechanisms probably are the major factors in creating so called 'freak waves' (Peregrine, 1990a) – see also Chapter 8. At many times big waves have influenced the imagination of poets and painters, while also frightening sailors. In book five of Homer's *The Odyssey* such a description of an extreme wave can be found:

... Poseidon, shaker of the earth, drove on a great wave, that was terrible and rough, and it curled over and broke down upon him, and scatters it abroad in every direction...

How big can a wave be, or more precisely: what is the probability of very high sea surface elevations?

For a random process with an arbitrary spectrum we can define positive and negative maxima as well as positive and negative minima (see Fig. 4.4). The problem of expected number of maxima and their probability distribution has been discussed in many papers, e.g. Rice (1944), Cartwright and Longuet-Higgins (1956), and in books, e.g. Middleton (1960), Tikhonov (1966) and Ochi (1990).

Let us consider time t at which surface displacement $\zeta(t)$ has a local positive maximum, i.e. $\zeta(t_0) = \zeta_{max}$. The behavior of function $\zeta(t)$, and the first and second derivatives in time, $\dot{\zeta}(t)$ and $\ddot{\zeta}(t)$ in the vicinity of $t = t_0$, is shown schematically in Fig. 4.5. The probability that in a small time interval $(t_0 < t < t_0 + \Delta t)$, the local maximum of surface displacement (of value in the range $(\zeta_0, \zeta_0 - \Delta\zeta)$) exists, is given by:

$$dP = f_3 \left[\zeta(t_0), \dot{\zeta}(t_0), \ddot{\zeta}(t_0) \right] \tilde{\Delta}\zeta \left(-\Delta\dot{\zeta} \right) \Delta\ddot{\zeta}, \quad (4.40)$$

in which the Gaussian process is assumed and the three-dimensional probability density f_3 is (Tikhonov, 1966):

$$f_3 \left(\zeta_{max}, \dot{\zeta}, \ddot{\zeta} \right) = \frac{1}{(2\pi)^{3/2} \sqrt{\tilde{\Delta} m_2}} \cdot \exp \left\{ -\frac{1}{2\tilde{\Delta}} \left[m_4 \zeta_{max}^2 + 2m_2 \zeta_{max} \ddot{\zeta} + m_0 \ddot{\zeta}^2 \right] - \frac{1}{2m_2} \dot{\zeta}^2 \right\}; \quad (4.41)$$

m_n is the m th moment of the spectral density function $S(\omega)$:

$$m_n = \int_0^\infty \omega^n S(\omega) d\omega, \quad (4.42)$$

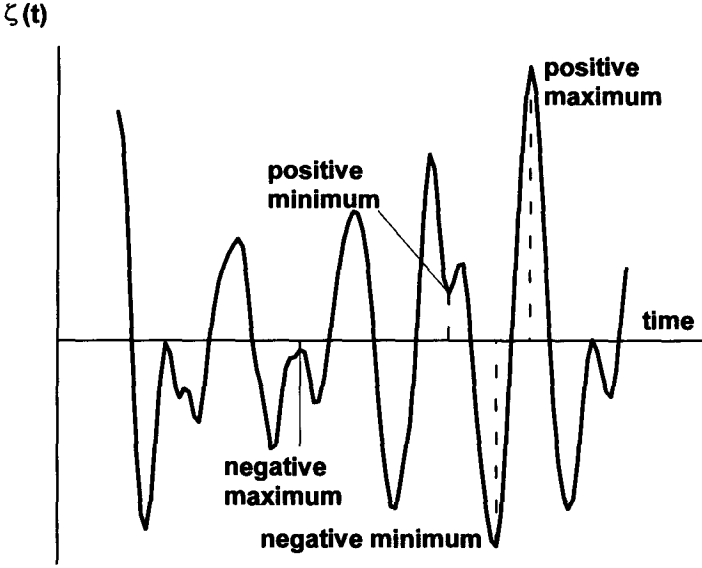


Figure 4.4: Definition of positive and negative maxima and minima.

and

$$\bar{\Delta} = m_0 m_4 - m_2^2. \quad (4.43)$$

For a sufficiently small time interval Δt , close to time t_0 , $\Delta \zeta \approx \ddot{\zeta} \Delta t$ and Eq. (4.40) becomes:

$$dP = -\Delta t f_3(\zeta_{max}, 0, \ddot{\zeta}) \ddot{\zeta} \Delta \zeta \Delta \ddot{\zeta}. \quad (4.44)$$

Integrating Eq. (4.44) with respect to acceleration $\ddot{\zeta}$ from $-\infty$ to 0, we obtain the probability $P_1(\zeta, t)$ that a maximum of ζ is situated in an elementary area ($\Delta \zeta \Delta t$):

$$P_1(\zeta, t) = -\Delta t \Delta \zeta \int_{-\infty}^0 f_3(\zeta_{max}, 0, \ddot{\zeta}) \ddot{\zeta} d\ddot{\zeta}. \quad (4.45)$$

As the surface displacement $\zeta(t)$ is assumed to be continuous, we should expect only one maximum (or minimum) for a sufficiently small time interval $t_0 \leq t \leq t_0 + \Delta t$. Therefore, the expected number of maxima with height ζ in the time interval Δt becomes:

$$N_+(\zeta, t) = 1 \cdot P_1(\zeta, t) + 0 \cdot P_0(\zeta, t) = P_1(\zeta, t), \quad (4.46)$$

in which $P_0(\zeta, t)$ is a probability that within interval $(t_0 \leq t \leq t_0 + \Delta t)$ a maximum does not exist.

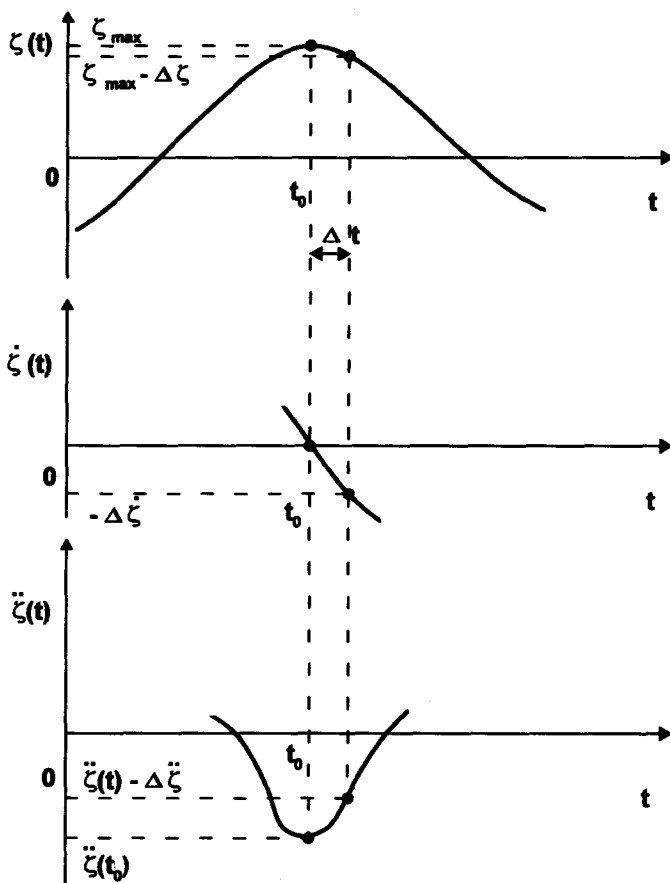


Figure 4.5: Surface elevation and two derivatives at a local maximum.

Using Eq. (4.46) in Eq. (4.45), the average number of maxima in the interval $(\zeta - \Delta\zeta, \zeta)$, in unit time becomes:

$$N_+(\zeta) = -\Delta\zeta \int_{-\infty}^0 f_3(\zeta_{max}, 0, \ddot{\zeta}) |\dot{\zeta}| d\ddot{\zeta}. \quad (4.47)$$

The average number of positive maxima in unit time, independent of their value, can be obtained by an integration of Eq. (4.47), with respect to all possible ζ values, from 0 to ∞ . Hence:

$$N_+ = - \int_0^\infty d\zeta \int_{-\infty}^0 f_3(\zeta_{max}, 0, \ddot{\zeta}) |\dot{\zeta}| d\ddot{\zeta}. \quad (4.48)$$

Finally, the probability density for extreme positive crests can be found as a ratio of numbers $N_+(\zeta)$ and N_+ :

$$f_{\max}(\zeta_{\max}) \Delta\zeta = \frac{N_+(\zeta)}{N_+}. \quad (4.49)$$

Thus:

$$f_{\max}(\zeta_{\max}) = \frac{\int_{-\infty}^0 f_3(\zeta_{\max}, 0, \ddot{\zeta}) |\ddot{\zeta}| d\ddot{\zeta}}{\int_0^{\infty} d\zeta \int_{-\infty}^0 f_3(\zeta_{\max}, 0, \ddot{\zeta}) |\ddot{\zeta}| d\ddot{\zeta}}, \quad 0 \leq \zeta < \infty. \quad (4.50)$$

After substituting Eq. (4.41) into Eq. (4.50) and using the non-dimensional value $\xi = \zeta_{\max}/\sqrt{m_0}$, we obtain:

$$f_{\max}(\xi) = \frac{2}{1 + \sqrt{1 - \epsilon^2}} \left\{ \frac{\epsilon}{\sqrt{2\pi}} e^{-\xi^2/2\epsilon^2} + \sqrt{1 - \epsilon^2} \xi e^{-\xi^2/2} \Phi\left(\frac{\sqrt{1 - \epsilon^2}}{\epsilon} \xi\right) \right\}, \quad (4.51)$$

in which ϵ is called the bandwidth parameter (Cartwright and Longuet-Higgins, 1956; also see Section 3.2 for more discussion):

$$\epsilon^2 = \frac{\bar{\Delta}}{m_0 m_A} = 1 - \frac{m_2^2}{m_0 m_A}; \quad (4.52)$$

$\Phi(z)$ is a cumulative distribution function of the standardized normal probability density (Abramowitz and Stegun, 1975):

$$\Phi(z) = \frac{1}{\sqrt{2\pi}} \int_{-\infty}^z e^{-t^2/2} dt = \frac{1}{2} \left[1 + \operatorname{erf}\left(\frac{z}{\sqrt{2}}\right) \right], \quad (4.53)$$

where the error function has the form:

$$\operatorname{erf}(z) = \frac{2}{\sqrt{\pi}} \int_0^z \exp(-t^2) dt. \quad (4.54)$$

In two special cases, the probability density function $f_{\max}(\xi)$ simplifies considerably. Value $\epsilon = 0$ corresponds to a narrow-band random process (see Section 3.2) and Eq. (4.51) yields:

$$f_{\max}(\xi) = \xi e^{-\xi^2/2}, \quad (4.55)$$

which is the Rayleigh probability density function (see Section 4.3.1).

If $\epsilon = 1$, the sea surface displacement represents the wide-band process and Eq. (4.51) becomes:

$$f_{\max}(\xi) = \sqrt{\frac{2}{\pi}} e^{\xi^2/2}, \quad (4.56)$$

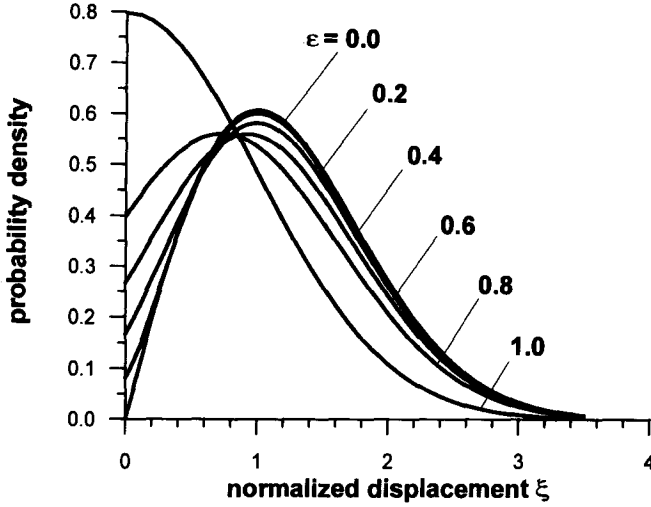


Figure 4.6: Probability density function of positive maxima as a function of parameter ϵ .

which is a truncated normal distribution. The probability density function $f_{max}(\xi)$, for various values of ϵ , is shown in Fig. 4.6.

The probability density function of all extreme crests (positive and negative) can be obtained in a similar manner. It is sufficient to change the range of integration in the denominator in Eq. (4.50) as follows:

$$f_{max}(\zeta) = \frac{\int_{-\infty}^0 f_3(\zeta, 0, \ddot{\zeta}) |\ddot{\zeta}| d\ddot{\zeta}}{\int_{-\infty}^{\infty} d\zeta \int_{-\infty}^0 f_3(\zeta, 0, \ddot{\zeta}) |\ddot{\zeta}| d\ddot{\zeta}}, \quad -\infty < \zeta < \infty. \quad (4.57)$$

After integration of Eq. (4.57), the non-dimensional probability density function for extreme crests of sea surface, independent of crests sign, becomes (Cartwright and Longuet-Higgins, 1956):

$$f_{max}(\xi) = \frac{\epsilon}{\sqrt{2\pi}} e^{-\xi^2/2\epsilon^2} + \sqrt{1-\epsilon^2} \xi e^{-\xi^2/2} \Phi\left(\frac{\sqrt{1-\epsilon^2}}{\epsilon} \xi\right), \quad -\infty < \xi < \infty. \quad (4.58)$$

For a narrow-band process, Eq. (4.58) simplifies to the Rayleigh probability density function (4.55), while for a wide-band process we obtain a normal probability density function (4.8), i.e.:

$$f_{max}(\xi) = \frac{1}{\sqrt{2\pi}} e^{-\xi^2/2}. \quad (4.59)$$

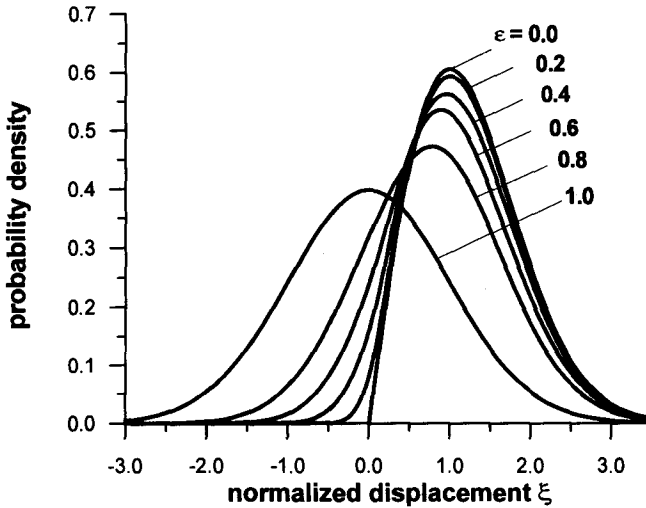


Figure 4.7: Probability density function of positive and negative maxima as a function of parameter ϵ .

The function (4.58) is illustrated in Fig. 4.7 for various values of ϵ . Integrating Eq. (4.51) or (4.58), with respect to ξ , gives the corresponding probability distribution function $F(\xi)$, i.e.:

$$F(\xi_0) = Pr \{ \xi < \xi_0 \}. \quad (4.60)$$

In Fig. 4.8, the probability distribution function for sea surface maxima (positive and negative) is shown for three particular values of bandwidth parameter ϵ : 0, 0.4, and 1.0. The value $\epsilon = 0.4$ is frequently observed in storm waves; the values $\epsilon = 0$ and $\epsilon = 1$ correspond to the narrow-band and wide-band processes, respectively. From Fig. 4.8 it follows that the probability of existence of the negative extreme wave crest ($\xi \leq 0$) is equal to 50% for $\epsilon = 1$, 4% for $\epsilon = 0.4$ and 0% for $\epsilon = 0$. On the other hand, the probability that the wave crest will be higher than $2\sqrt{m_0}$, is equal to 3%, 12% and 14% for bandwidth parameter ϵ equal to 1, 0.4, and 0, respectively. Thus, for a narrow-band process, the chances for higher positive crests are greater than for a wide-band process, which is as expected. The probability that wave crests fall below $-2\sqrt{m_0}$ is practically zero for wave processes with $\epsilon = 0.4$ and $\epsilon = 0$. Only for the wide-band process ($\epsilon = 1$), is the probability again equal to 3%, as the probability density function is symmetric with respect to $\xi = 0$.

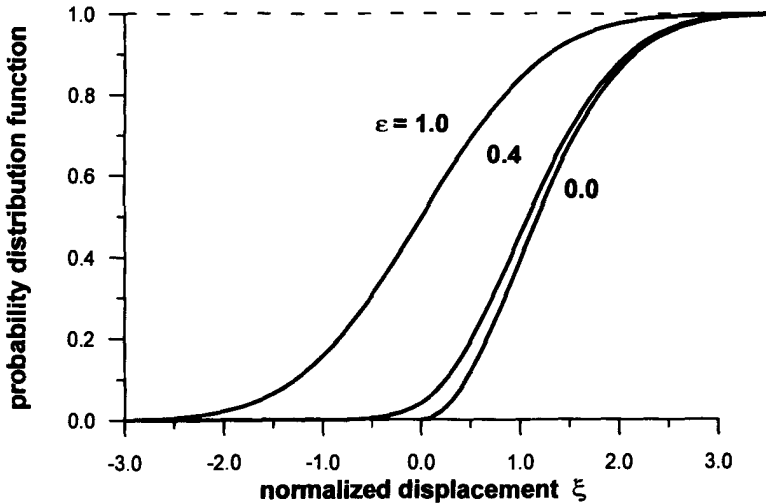


Figure 4.8: Probability distribution function for positive and negative maxima for $\epsilon = 0, 0.4, 1$.

4.2.3.2 Structure of extreme waves

The formulas (4.51) and (4.58) determine the probability of occurrence of extreme wave crests of a given height and at a given location. This probability depends on the sea severity described by variance m_0 , and on the bandwidth parameter ϵ . Obviously close to the maximum crest the surface displacements satisfy the condition $\zeta < \zeta_{max}$, and as the distance in space and time from the maxima increases, so the mean value of ζ decreases. At a large distance from an extreme crest, the expected position of the free surface approaches the mean water level, $\bar{\zeta}$, with variance equal to that of the overall wave field.

We cannot predict where or when in a random sea, extreme crests or troughs will appear, but we can predict what their expected configuration will be when they do occur. Let us assume first, that at point $P(\vec{x})$ and at time t , the sea surface elevation is very large, say $\zeta(\vec{x}, t) > \gamma\sigma_\zeta$, where γ is large. The question is what is the expected distribution of ζ in the vicinity of point P and what is the standard deviation about this expected value. This problem was first formulated by Boccotti (1981, 1989). A simple solution to the problem was published recently by Phillips et al. (1993a, 1993b). This method will be outlined in the following. Let $\zeta_1 = \zeta(\vec{x}, t)$ and $\zeta_2 = \zeta(\vec{x} + \vec{r}, t + \tau)$. The conditional probability density of ζ_2 under the condition

that $\zeta_1 \geq \gamma \sigma_\zeta$ is:

$$f(\zeta_2 | \zeta_1 \geq \gamma \sigma_\zeta) = \frac{f(\zeta_2, \zeta_1 \geq \gamma \sigma_\zeta)}{f(\zeta_1 \geq \gamma \sigma_\zeta)}. \quad (4.61)$$

Using the two-point probability density function for a zero mean Gaussian field with variance σ_ζ as (Ochi, 1990):

$$f(\zeta_1, \zeta_2) = \frac{1}{2\pi\sigma_\zeta^2\sqrt{1-\rho^2}} \exp\left\{-\frac{\zeta_1^2 - 2\rho\zeta_1\zeta_2 + \zeta_2^2}{2\sigma_\zeta^2(1-\rho^2)}\right\}, \quad (4.62)$$

in which $\rho = \rho(\vec{r}, \tau)$ is the correlation function between ζ_1 and ζ_2 , the numerator on the right hand side of Eq. 4.61 can be written in the form:

$$f(\zeta_2, \zeta_1 \geq \gamma \sigma_\zeta) = \int_{\gamma \sigma_\zeta}^{\infty} f(\zeta_1, \zeta_2) d\zeta_1 = \frac{\exp(-\zeta_2^2/2\sigma_\zeta^2)}{\sqrt{2}\pi\sigma_\zeta} \int_{u_0}^{\infty} e^{-u^2} du, \quad (4.63)$$

where:

$$u_0 = \frac{\gamma \sigma_\zeta - \rho \zeta_2}{\sigma_\zeta [2(1-\rho^2)]^{1/2}}. \quad (4.64)$$

In a similar way the denominator in Eq. (4.61) becomes:

$$f(\zeta_1 \geq \gamma \sigma_\zeta) = \frac{1}{\sqrt{2\pi}\sigma_\zeta} \int_{\gamma \sigma_\zeta}^{\infty} \exp\left(-\frac{\zeta_1^2}{2\sigma_\zeta^2}\right) d\zeta_1. \quad (4.65)$$

After substituting $z = \frac{\zeta_1}{\sqrt{2}\sigma_\zeta}$, Eq. (4.65) becomes:

$$f(\zeta_1 \geq \gamma \sigma_\zeta) = \frac{1}{2} \operatorname{erfc}\left(\frac{\gamma}{\sqrt{2}}\right), \quad (4.66)$$

where (Abramowitz and Stegun, 1975):

$$\operatorname{erfc}(z) = \frac{2}{\sqrt{\pi}} \int_z^{\infty} e^{-t^2} dt = 1 - \operatorname{erf}(z), \quad (4.67)$$

where $\operatorname{erf}(z)$ is given in Eq. (4.54). For a sufficiently large γ , the value of function $\operatorname{erfc}(z)$ can be represented by its asymptotic expansion and Eq. (4.66) becomes (Phillips et al., 1993a):

$$f(\zeta_1 \geq \gamma \sigma_\zeta) = \frac{1}{\sqrt{2\pi}\gamma} e^{-\gamma^2/2} g(\gamma), \quad (4.68)$$

in which:

$$g(\gamma) \approx 1 - \gamma^2 + \frac{3}{\gamma^4} - \frac{5}{\gamma^6} + \dots \quad (4.69)$$

For γ enclosed in the most important range (2, 3), $g(\gamma)$ decreases from 0.86 to 0.92. Using Eqs. (4.62) and (4.68) in Eq. (4.61) yields:

$$f(\zeta_2 | \zeta_1 \geq \gamma\sigma_\zeta) = \frac{1}{\sqrt{\pi}\sigma_\zeta} \frac{\gamma e^{\frac{1}{2}\gamma^2}}{g(\gamma)} \exp\left(-\frac{\zeta_2^2}{2\sigma_\zeta^2}\right) \int_{u_0}^{\infty} e^{-u^2} du. \quad (4.70)$$

Thus, the expected value of $\zeta_2 = \zeta(\vec{x} + \vec{r}, t + \tau)$ under the condition that $\zeta_1 = \zeta(\vec{x}, t) \geq \gamma\sigma_\zeta$ can be written as:

$$E[\zeta_2] = \int_{-\infty}^{\infty} \zeta_2 f(\zeta_2 | \zeta_1 \geq \gamma\sigma_\zeta) d\zeta_2. \quad (4.71)$$

The integration can be performed by parts to give:

$$E[\zeta_2] = \frac{\gamma\sigma_\zeta\rho}{g(\gamma)}. \quad (4.72)$$

When $\vec{r} = 0$ and $t = 0$, the autocorrelation function is unity; thus:

$$E[\gamma_1] = \frac{\gamma\sigma_\zeta}{g(\gamma)}. \quad (4.73)$$

Dividing Eq. (4.72) by Eq. (4.73) we obtain the expected profile of the surface displacement surrounding an extreme crest as:

$$\frac{\bar{\zeta}(\vec{x} + \vec{r}, t + \tau)}{\bar{\zeta}(\vec{x}, t) |_{\zeta > \gamma\sigma_\zeta}} = \rho(\vec{r}, \tau). \quad (4.74)$$

Thus, the expected spatial configuration of extreme waves is approximately proportional to the two-dimensional spatial autocorrelation function of the wave field as a whole.

The variance of different realizations about the mean can be presented as:

$$\begin{aligned} \text{var } \zeta_2 &= E[(\zeta_2 - E(\zeta_2))^2] = E[\zeta_2^2] - (E[\zeta_2])^2 = \\ &= \sigma_\zeta^2 \left(\frac{\gamma^2 \rho^2}{g(\gamma)} + 1 \right) - \left(\frac{\gamma\sigma_\zeta\rho}{g(\gamma)} \right)^2 = \sigma_\zeta^2 \left(1 - \frac{\gamma^2 \rho^2}{g^2(\gamma)} (1 - g(\gamma)) \right). \end{aligned} \quad (4.75)$$

Using the asymptotic expansion (4.69), Eq. (4.75) becomes:

$$\text{var } \zeta_2 \approx \sigma_\zeta^2 [1 - \rho^2 (1 - \gamma^{-2})] \quad \text{for } \gamma \gg 1. \quad (4.76)$$

Near the crests of extreme waves, where $\rho \approx 1$, the variance $\approx (\sigma_\zeta/\gamma)^2$; thus for $\gamma \gg 1$ the variance about the expected profile is very small. With the increasing distance \vec{r} or time τ from the crest, the variance increases, but always remains less than or equal to σ_ζ^2 . The Eq. 4.74 was compared with buoy data obtained during the Surface Wave Dynamics Experiment (SWADE) and the agreement was found to be remarkably good (Phillips et al., 1993a). Further verification was provided by examination of scanning radar altimeter measurements in four different sea states: a unimodal mature wave field, a short fetch, wind generated sea crossing swell, a very broad directional spectrum, and a fetch limited wind sea with opposing swell (Phillips et al., 1993b).

4.2.4 Influence of wave breaking on probability distribution of surface displacement in deep water

The energy flow from the atmosphere to the ocean generates an aerodynamically rough sea surface. If the energy flow is sufficiently intensive, in some points the surface waves will lose their stability and eventually break in the form of whitecaps of various scales. Breaking is a very localized and non-stationary phenomenon.

White capping is a strongly nonlinear process, which involves an instability of the surface waves with space and time scales several orders of magnitude smaller than those associated with gravity wave motion. White caps are usually formed at or near the crests of the larger waves and occur in groups with successive crests breaking downwind of one another.

Although there are widespread occurrences of breaking processes in the ocean, the present knowledge of wave breaking mechanisms is still incomplete. A very comprehensive review of the present state of research on wave breaking is given by Banner and Peregrine (1993). One of the most puzzling question is the selection of the appropriate breaking criterion. Longuet-Higgins (1973), Banner and Phillips (1974), and Phillips and Banner (1974) suggest that wave breaking is the property of short waves riding on long waves on a mean drift current. A set of simple criteria of the limiting form of wave motion were established by Stokes more than one hundred years ago (Stokes 1847, 1880). According to Stokes, the necessary criteria to start an individual wave breaking are:

- a) the particle velocity of fluid at the wave crest equals the phase velocity,
- b) the crest of the wave attains a sharp point with an angle of 120° ,
- c) the ratio of wave height to wavelength is approximately $1/7$,
- d) the particle acceleration at the crest of the wave equals to $0.5g$.

The above criteria for breaking of regular waves in deep water have been addressed from various viewpoints in a series of papers by Longuet-Higgins (1969a, 1974, 1976a), Cokelet (1977a), and others. However, for irregular waves we apply the Snyder and Kennedy (1983a,b) hypothesis which states that the stability of the gravity wave flow is controlled by the level of some 'threshold' variable defined on the surface of the fluid. The vertical acceleration was selected as such a variable. Longuet-Higgins (1985) has distinguished two different vertical accelerations depending on the measurement procedure, i.e. the *apparent* acceleration measured by a fixed vertical probe, and the *real* acceleration of the fluid particles, as measured by a small, free-floating buoy.

In limiting regular waves, the crest attains a sharp point with an angle of 120° and the particle acceleration at the crest is equal to $0.5g$. However, near limiting waves have rounded crests with a very small radius of curvature. It was shown (Longuet-Higgins and Fox, 1977) that the local crest profile of such waves approaches a self-similar form.

Furthermore, the maximum surface slope can exceed the 30° slope of the limiting wave, ultimately reaching a value of about 30.38° . The vertical acceleration at the crest is not $0.5g$ but equals approximately $0.389g$ (Williams, 1985).

To estimate the probability of wave breaking of irregular waves we modify slightly the acceleration criterion, assuming that the downward acceleration at the wave crests (where the breaking is the most likely to appear) has to be greater or equal to αg (α is a positive constant) to consider these crests to be breaking.

Assuming that the breaking occurs only at the sea surface crests we can use the probability density function (4.58), introducing the condition that acceleration $|\ddot{\zeta}| > \alpha g$. This means that the integral in Eq. (4.57) should be taken in the range $(-\infty, -\alpha g)$. Using this approach, Srokosz (1986) showed that the probability density for a breaking wave crest of elevation ξ , above the mean water level, becomes:

$$f_{max}(\xi; |\ddot{\zeta}| > \alpha g) = \frac{1}{\sqrt{2\pi}} \left\{ \epsilon \exp \left[-\frac{1}{2}\gamma^2 - \frac{1}{2\epsilon^2}(\xi - \sqrt{1 - \epsilon^2}\gamma)^2 \right] + \sqrt{1 - \epsilon^2} \xi \exp \left(-\frac{1}{2}\xi^2 \right) \int_u^\infty \exp \left(-\frac{1}{2}x^2 \right) dx \right\}, \quad (4.77)$$

in which:

$$\xi = \frac{\zeta}{\sqrt{m_0}},$$

$$\gamma = \frac{\alpha g}{\sqrt{m_4}},$$

$$u = \frac{1}{\epsilon} \left(\gamma - \sqrt{1 - \epsilon^2} \xi \right).$$

The probability density $f_{max}(\xi; |\ddot{\zeta}| > \alpha g)$ is shown in Fig. 4.9 as a function of the non-dimensional moment $m_4/\alpha^2 g^2$. The α and ϵ values were taken as 0.4 and 0.6, respectively. For comparison, the probability density (4.58) is shown for the same value of $\epsilon = 0.6$. Equation (4.58) corresponds to a value of $\alpha = 0$ ($m_4/\alpha^2 g^2 = \infty$) and implies that all the crests are breaking. To obtain the probability F_{br} , that a crest of any height will break, Srokosz (1986) integrated Eq. (4.77) over all crests and obtained:

$$F_{br} = \int_{-\infty}^{\infty} f_{max}(\xi; |\ddot{\zeta}| > \alpha g) = \exp \left[-\frac{\alpha^2 g^2}{2m_4} \right]. \quad (4.78)$$

Note that probability F_{br} is independent of any assumption about the spectrum width. However, it depends strongly on the shape of the spectrum, because of the fourth moment of the spectrum. As the probability of breaking increases significantly with an increase in the fourth moment of the spectrum, breaking is very sensitive to the existence of high-frequency energy. When $m_4 \rightarrow \infty$, $F_{br} \rightarrow 1$; thus all wave crests

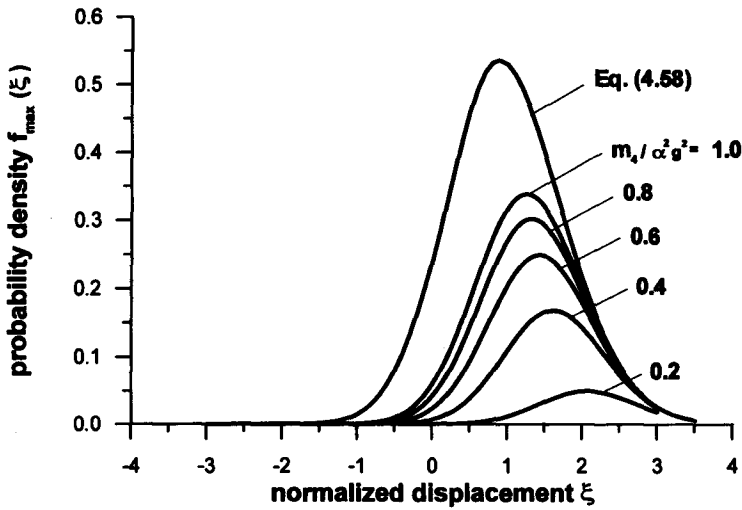


Figure 4.9: Probability density function of wave crests that are breaking when acceleration is greater than αg .

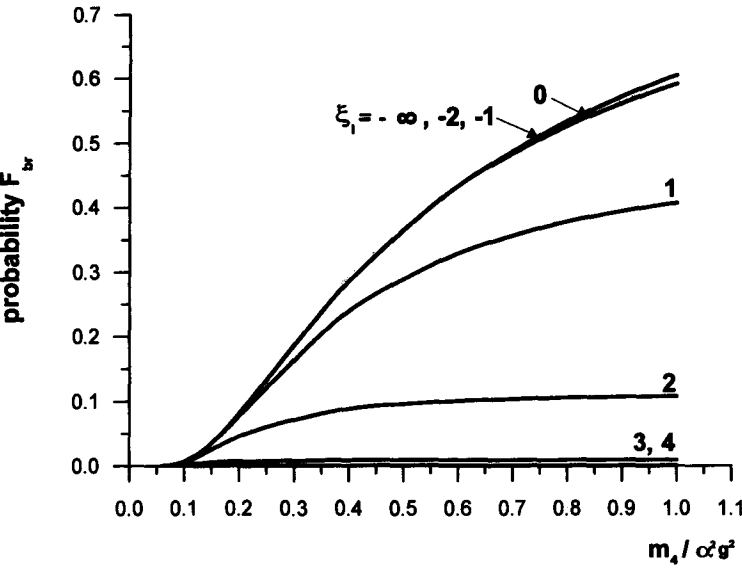


Figure 4.10: Probability of breaking F_{br} plotted against $\frac{m_4}{\alpha^2 g^2}$.

can be broken. For small waves $m_4 \rightarrow 0$ and $F_{br} \rightarrow 0$. The probability F_{br} is shown in Fig. 4.10 (upper envelope $\zeta_1 = -\infty$) as a function of the dimensionless fourth moment $m_4/\alpha^2 g^2$. This graph is in very good agreement with Ochi and Tsai's results (1983; their Figure 9). They evaluated the probability of breaking using the joint distribution of wave height and period given by Cavanie et al. (1976), and a breaking criterion based on wave steepness:

$$H \gg 0.020g T^2.$$

It should be noted that Eq. (4.78) is a probability of wave breaking at a given point, irrespective of crest height. In engineering applications, however, we require the probability that a wave crest is above height ζ_l and also breaking. This probability can be derived by changing the lower limit of integration in Eq. (4.78) from $-\infty$ to ξ_l (Greenhow, 1989):

$$\begin{aligned} F_{br}(\xi \geq \xi_l) &= \int_{\xi_l}^{\infty} f_{max}(\xi; |\ddot{\xi}| > \alpha g) d\xi = \frac{1}{2} \exp\left(-\frac{1}{2}\gamma^2\right) \operatorname{erfc}\left[\frac{\xi_l - \gamma(1 - \epsilon^2)^{1/2}}{\sqrt{2}\epsilon}\right] \\ &+ \frac{(1 - \epsilon^2)^{1/2}}{2} \exp\left(-\frac{1}{2}\xi_l^2\right) \operatorname{erfc}\left[\frac{\gamma - \sqrt{1 - \epsilon^2}\xi_l}{\sqrt{2}\epsilon}\right], \end{aligned} \quad (4.79)$$

in which $\xi_l = \zeta_l/\sqrt{m_0}$.

Note that as $\xi_l \rightarrow -\infty$, the Srokosz result (4.78) is obtained. Probability $F_{br}(\xi \geq \xi_l)$ is illustrated in Fig. 4.10 as a function of non-dimensional moment $m_4/\alpha^2 g^2$ and crest levels $\xi_l = \zeta_l/\sqrt{m_0}$. An upper envelope (when $\xi_l = -\infty$) corresponds to the Srokosz's solution. Probability F_{br} is an increasing function of moment m_4 . However, it decreases when the wave crest level increases. This means that the chance that a very high and breaking wave crest will occur is very small. For example, for $m_4/\alpha^2 g^2 = 0.6$, when all wave crests are taken into account, a probability F_{br} is equal to 43.4%, but the probability that breaking crests will be higher than $2\sqrt{m_0}$ is only 10.1%. Moreover, the probability of breaking F_{br} for non-dimensional crests elevations $\xi_l = -\infty, -3, -2, -1, 0$ is practically the same for a given value of $m_4/\alpha^2 g^2$. This probability decreases drastically when $\xi_l \geq 0$.

It should be pointed out that this approach differs from the probability studied by Snyder and Kennedy (1983a,b) who estimated the fraction β of the sea surface covered by breaking waves as:

$$\beta = 1 - \Phi\left(\frac{\alpha g}{\sqrt{m_4}}\right), \quad (4.80)$$

in which $\Phi(z)$ is defined in Eq. (4.53). The β represents the probability that breaking will occur at a point on the surface, chosen at random. It can be shown that as $m_4 \rightarrow \infty$, the probability $\beta \rightarrow 1/2$; thus, half the sea surface can be covered by broken waves.

The fundamental difficulty in applying the above theories is the estimation of moment m_4 . The evaluation of m_4 from some spectral formulas requires the assumption of a cutoff frequency. Moreover, experimental data obtained from wave rider buoys cannot be used for the estimation of m_4 as the buoys cannot properly respond to the short waves (see Chapter 9). Radar altimeter measurements seem to offer a feasible alternative for detection of short surface waves. More discussion of remote sensing techniques for surface waves applications can be found in Chapter 9.

4.2.5 Probability distribution of surface displacement in finite water depth

Shallow water waves have many specific properties which distinguish them from deep water waves. As waves travel into shallower water, their dynamics becomes progressively more nonlinear and dissipative. Coastal waves have a definite excess of high crests and shallower troughs in contrast to those of deep water waves. Moreover, in coastal areas additional asymmetry, with respect to a vertical line passing through the crest, also exists. Therefore, in general, surface waves in shallow water cannot be classified as a Gaussian process, and the probability density (4.4) is not valid, except for very small waves.

The observed departure from the Gaussian distribution can still be expressed in terms of the Gram-Charlier series (4.20). Figure 4.11 illustrates such an approximation for a wave record taken in the shallow water of the South Baltic ($h = 3\text{m}$). The skewness and kurtosis coefficients were estimated, using experimental data, as $\gamma_1 = 1.153$ and $\gamma_2 = 1.542$ (Massel, 1973). Note that values of both coefficients are much higher than those for deep water conditions (compare Fig. 4.2). More examples of application of the Gram-Charlier series techniques can be found elsewhere (Bitner, 1980; Ochi and Wang, 1984). The calculations showed that the skewness parameter γ_1 is the dominant parameter affecting the non-Gaussian characteristics of coastal waters. To simplify the evaluation of the probability distribution, Ochi and Wang (1984) represented the parameter γ_1 as a function of water depth and sea severity, expressed in terms of significant wave height H_s . Using the ARSLOE data they got:

$$\gamma_1 = 1.16 \exp(-0.42h)H_s^p, \quad (4.81)$$

where $p = 0.74h^{0.59}$. Water depth and significant wave height should be given in meters. The parameter γ_2 can be evaluated as a function of γ_1 :

$$\gamma_2 = \begin{cases} -0.15 + 1.10(\gamma_1 - 0.2)^{1.17} & \text{for } 0.2 < \gamma_1 < 0.5 \\ -0.15 + 1.10(\gamma_1 - 0.2)^{1.17} + 1.48(\gamma_1 - 0.5)^{1.47} & \text{for } \gamma_1 > 0.5. \end{cases} \quad (4.82)$$

Another set of data collected in the coastal zone of the Baltic Sea provides the following relationship for γ_1 and γ_2 (Cieřlikiewicz and Thai, 1991):

$$\gamma_1 = 5.73 \exp \left[1.81 \ln \left(\frac{H_s}{h} \right) \right], \quad (4.83)$$

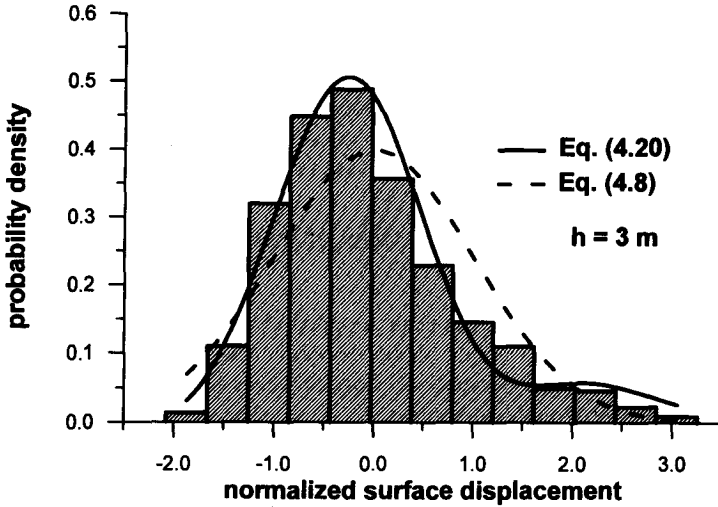


Figure 4.11: Comparison of Gaussian distribution (4.8) and Gram-Charlier distribution (4.20) with the experimental data.

and

$$\gamma_2 = 1.59 \exp[1.70 \ln(\gamma_1)] - 3.05. \quad (4.84)$$

As in the case of deep water, the major drawback of the Gram-Charlier series approximation is the lack of a simple method to parameterize the skewness and kurtosis coefficients in terms of the spectrum. Moreover, the form of the probability density distribution is assumed *a priori*.

Let us now formulate in a different way the problem of evaluating the unknown probability density function for a given set of data. Suppose we have *a priori* knowledge of some characteristics of the probability density function. For instance, certain moments are already known. Thus, the problem is reduced to the choice of distribution which is (in some sense) the best estimate of the population distribution based on these known characteristics. In general, there is a variety of distributions which may satisfy these constraints. To find such a probability density function for surface elevation we use the principle of maximum entropy. This approach will also be used later (see Section 9.3.2), for determining directional spreading.

The definition of entropy of a system was first given by Boltzman as a measure of our degree of ignorance as to its true state. Shannon (1948a,b) developed a mathematical theory of entropy and applied it to the field of communication. The Shannon

entropy functional $I[f]$, which is a measure of uncertainty associated with the probability density $f(\zeta)$, in describing a random variable ζ is defined as:

$$I[f] = - \int_{-\infty}^{\infty} f(\zeta) \ln [f(\zeta)] d\zeta. \quad (4.85)$$

Let us now assume that the mean surface elevation $\bar{\zeta} = 0$ and the moments σ_{ζ}^2 , μ_3 and μ_4 are known. As usual, the probability density function $f(\zeta)$ is a positive function for every ζ and it is normalized to unity:

$$\int_{-\infty}^{\infty} f(\zeta) d\zeta = 1. \quad (4.86)$$

According to Jaynes (1982), the minimally prejudiced assignment of probabilities is that which maximizes the entropy functional $I[f]$ subject to the given information (i.e. values of moments and normalization (4.86)). The entropy functional I can be maximized by the method of Lagrange multipliers. This introduces parameters $1 - a_0, a_1, \dots, a_4$ such that variations in a functional of $f(\zeta)$ will vanish. As a result we obtain (Cieřlikiewicz, 1990):

$$f(\zeta) = A^{-1} \exp \left\{ - \sum_{i=1}^4 a_i \zeta^i \right\}, \quad (4.87)$$

in which $A^{-1} = \exp(-1 - a_0)$. To determine the Lagrange multipliers we use known moments and normalization (4.86), i.e.:

$$\begin{cases} G_0 = A, & G_1 = 0, & G_2 = A\sigma_{\zeta}^2, \\ G_3 = A\mu_3, & G_4 = A\mu_4, \end{cases} \quad (4.88)$$

where:

$$G_n = \int_{-\infty}^{\infty} \zeta^n \exp \left\{ - \sum_{i=1}^4 a_i \zeta^i \right\} d\zeta. \quad (4.89)$$

Equations (4.88) form a system of five nonlinear equations for unknown coefficients a_0, a_1, \dots, a_4 . One can prove that only three equations of system (4.88) are independent. Thus, we obtain:

$$\begin{cases} G_0 = A, & G_1 = 0, \\ G_2 - \frac{\sigma_{\zeta}^2}{\mu_3} G_3 = 0. \end{cases} \quad (4.90)$$

Therefore, two relations between the unknown quantities $A, \alpha_1, \dots, \alpha_4$ should exist. They are:

$$\begin{cases} \alpha_1 G_0 + 2\alpha_0 G_1 + 3\alpha_3 G_2 + 4\alpha_4 G_3 & = 0 \\ G_0 - \alpha_1 G_1 - 2\alpha_2 G_2 - 3\alpha_3 G_3 - 4\alpha_4 G_4 & = 0. \end{cases} \quad (4.91)$$

In Fig. 4.12 a comparison of the probability density function, obtained by the maximum entropy method with experimental data of Ochi and Wang (1984), is shown. The Gram-Charlier solution and Gaussian distribution are given as well. The agreement of the maximum entropy solution with experimental data is remarkable. It should be noted that the Gram-Charlier series provide very small negative values of the probability density function close to ~ -2 m. Both methods described above give reasonably accurate mathematical expressions for the probability density function approximating the experimental function. However, in both cases, knowledge of the statistical moments (up to the 4th moment) is required.

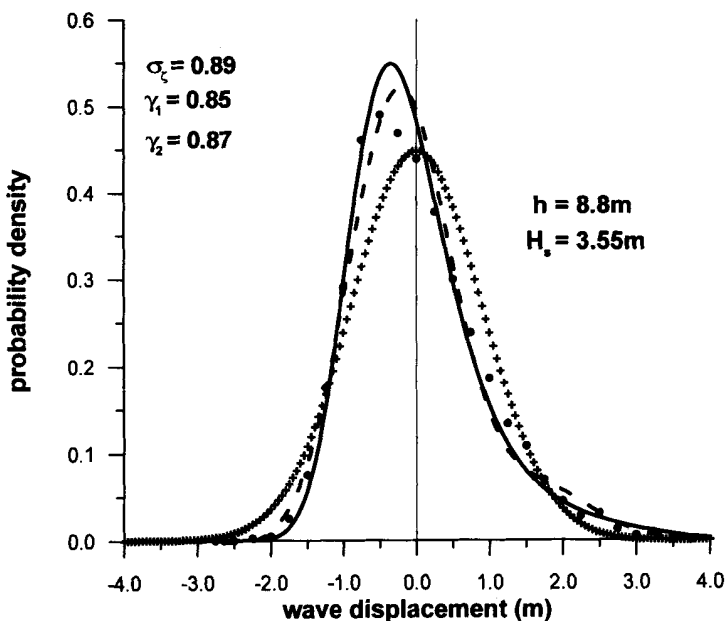


Figure 4.12: Comparison of various probability density distribution functions for surface displacement in finite water depth: ——— max. entropy method; - - - Gram-Charlier series; + + + Gaussian distr.; • • • experimental data by Ochi and Wang (1984).

An alternative method of modelling can be based on an extension of the Huang et al. (1983b) method, to finite water depth. The procedure of derivation is similar to that given in Section 4.2.2. Thus, for completeness, only the final results are given:

$$f(\xi) = \frac{1}{(2\pi)^{1/2}} \exp \left[-\frac{1}{2} A^2 \right] \left\{ B \left(\frac{1}{C^{1/2}} - \frac{3}{2} \frac{(k\sigma_\zeta)^2}{\psi^2} \frac{D^2}{C^{5/2}} \right) - \frac{(k\sigma_\zeta)^2 E}{\psi} \frac{1}{C^{3/2}} \right\}, \quad (4.92)$$

where:

$$\xi = \frac{\zeta - \bar{\zeta}}{\sigma_\zeta}, \quad (4.93)$$

$$A = \psi \left\{ \xi - k\sigma_\zeta \left[(F_0 + F_1) \xi^2 - F_0 \right] + (k\sigma_\zeta)^2 \left[2(F_0 + F_1)^2 \xi^3 - \frac{3}{8} F_2 \xi^3 - 2F_0 (F_0 + F_1) \xi \right] \right\}, \quad (4.94)$$

$$B = \left\{ 1 - 2k\sigma_\zeta (F_0 + F_1) \xi + (k\sigma_\zeta)^2 \left[6(F_0 + F_1)^2 - \frac{9}{8} F_2 \right] \xi^2 - 2(k\sigma_\zeta)^2 F_0 (F_0 + F_1) \right\} \psi, \quad (4.95)$$

$$C = 1 + 2(k\sigma_\zeta) AD, \quad (4.96)$$

$$D = F_1 - k\sigma_\zeta \left(2F_0 F_1 + 2F_1 - \frac{9}{8} F_2 \right) \xi, \quad (4.97)$$

$$E = 2F_1 (F_0 + F_1) - \frac{9}{8} F_2, \quad (4.98)$$

$$\psi = \left[1 + (k\sigma_\zeta)^2 F_0 F_3 \right]^{1/2}, \quad (4.99)$$

$$F_0 = \coth(kh), \quad F_1 = \frac{3}{4} \frac{\coth(kh)}{\sinh^2(kh)}, \quad (4.100)$$

$$F_2 = 1 + \frac{3}{\sinh^3(kh)} + \frac{3}{\sinh^4(kh)} + \frac{9}{8 \sinh^6(kh)}, \quad (4.101)$$

$$F_3 = 1 + \left(1 + \frac{3}{2 \sinh^2(kh)} \right)^2. \quad (4.102)$$

A comparison of the probability function 4.92) with the experimental data of Bitner (1980) is shown in Huang et al. (1983b). Although the presented agreement cannot be treated as a definite proof of the model (4.92), the comparison indicates that it does offer a viable alternative to the computation of the probability function in finite water depth.

4.3 Wave height

4.3.1 Probability distribution of wave height for a narrow-band spectrum

Besides the probability distribution for local sea surface deviations from mean water level, random wave process is frequently characterized by amplitude statistics. Amplitude distributions are widespread in physics and electronics. However, for surface ocean waves, the wave height probability is also frequently used. Both these statistical characteristics will be discussed below.

Wave amplitude can be detected in the simplest way under the assumption of narrow-band spectrum, in which the positive and negative maximum excursions are equal to each other, and equal to wave amplitude. However, this is not usually the case for real ocean surface waves. A typical record of ocean waves for a non-narrow-band spectrum is given in Fig. 4.13. It is clear that the envelopes of the process are not symmetrical curves. Therefore, the positive and negative amplitudes are different. In order to overcome this uncertainty, in physical oceanography and ocean engineering, the crest-to-trough excursion is used and wave height is defined as a sum of the two values of the upper and lower amplitudes. Only for a narrow-band spectrum, is the wave height equal to twice the upper (or lower) amplitude.

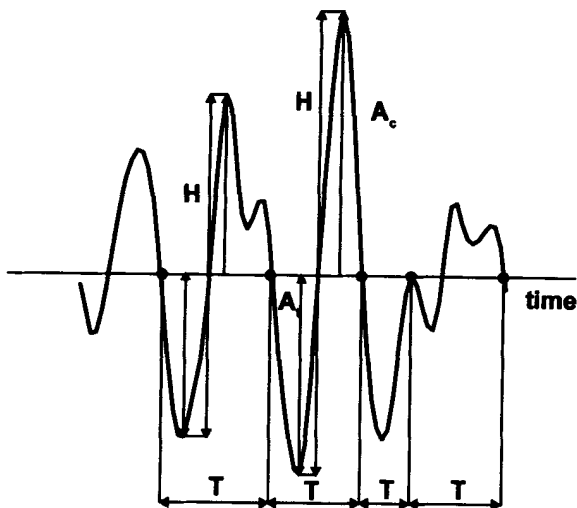


Figure 4.13: Definition of zero-downcrossing waves.

It should be noted that the definition of an individual wave height depends entirely on the choice of the trough occurring before or after the crest. In the following, we will adopt the recommendations of the International Association for Hydraulic Research Working Group (IAHR, 1989). Thus, a wave height is defined as zero-down-crossing wave height and the wave trough occurs before the wave crest (Fig. 4.13).

Consider the unidirectional wave motion of a narrow-band frequency spectrum at a given point $P(0, 0)$:

$$\zeta(t) = \sum_{i=1}^{\infty} a_i \cos(\omega_i t - \epsilon_i). \quad (4.103)$$

Using a frequency ω_p , which corresponds to the spectrum peak, we can rewrite Eq. (4.103) as:

$$\zeta(t) = A_c(t) \cos(\omega_p t) - A_s(t) \sin(\omega_p t), \quad (4.104)$$

in which:

$$\left. \begin{aligned} A_c(t) &= \sum_{i=1}^{\infty} a_i \cos[(\omega_i - \omega_p)t - \epsilon_i] \\ A_s(t) &= \sum_{i=1}^{\infty} a_i \sin[(\omega_i - \omega_p)t - \epsilon_i] \end{aligned} \right\} \quad (4.105)$$

Because of the narrowness of the process, the amplitudes $A_c(t)$ and $A_s(t)$ are very slowly varying functions of time. Let us rewrite Eq. (4.104) in terms of wave amplitude $A(t)$ and phase $\varphi(t)$, i.e.:

$$\zeta(t) = A(t) \cos[\omega_p t + \varphi(t)], \quad (4.106)$$

where:

$$A(t) = \sqrt{A_c^2(t) + A_s^2(t)}, \quad (4.107)$$

$$\varphi(t) = \tan^{-1}[A_s(t)/A_c(t)], \quad (4.108)$$

and

$$A_c(t) = A(t) \cos \varphi(t), \quad A_s(t) = A(t) \sin \varphi(t). \quad (4.109)$$

It should be noted that, in the case of a narrow-band spectrum, the amplitude A is equal to the amplitude of the wave envelope, which varies slowly in time. In virtue of the Central Limit Theorem, A_c and A_s are Gaussian processes with mean value equal to zero and variance σ_ζ^2 as:

$$E[A_c^2] = E[A_s^2] = E[\zeta^2] = \sigma_\zeta^2. \quad (4.110)$$

It can be shown that $E[A_c A_s] = 0$. Thus, ζ_c and ζ_s are independent variables and the two-dimensional probability density function becomes:

$$f_2(A_c, A_s) = f(A_c) f(A_s) = \frac{1}{2\pi\sigma_\zeta^2} \exp\left[-\frac{A_c^2 + A_s^2}{2\sigma_\zeta^2}\right]. \quad (4.111)$$

Using Eq. (4.111) and the Jacobian of the variable transformation $J = \frac{\partial(A_c, A_s)}{\partial(A, \varphi)} = A$, we represent f_2 as a function of variables A and φ , i.e.:

$$f_2(A, \varphi) = f[A_c(A, \varphi), A_s(A, \varphi)] J = \frac{A}{2\pi\sigma_\zeta^2} \exp\left(-\frac{A^2}{2\sigma_\zeta^2}\right). \quad (4.112)$$

Finally, the one-dimensional probability densities for amplitude A and phase φ are obtained through integration of Eq. (4.112), with respect to phase φ and amplitude A , respectively:

$$f(A) = \int_{-\pi}^{\pi} f_2(A, \varphi) d\varphi = \frac{A}{\sigma_\zeta^2} \exp\left(-\frac{A^2}{2\sigma_\zeta^2}\right), \quad (4.113)$$

and

$$f(\varphi) = \frac{1}{2\pi} \int_0^\infty \frac{A}{\sigma_\zeta^2} \exp\left(-\frac{A^2}{2\sigma_\zeta^2}\right) dA = \frac{1}{2\pi}. \quad (4.114)$$

Equation (4.113) represents the well-known Rayleigh distribution for wave amplitude. Result (4.114) indicates that for a narrow-band process, the phase is uniformly distributed in the range $(-\pi, \pi)$.

For later convenience, we calculate the moments of wave amplitude:

$$E[A^m] = \overline{A^m} = \int_0^\infty \frac{A^{m+1}}{\sigma_\zeta^2} \exp\left(-\frac{A^2}{2\sigma_\zeta^2}\right) dA = (2\sigma_\zeta^2)^{m/2} \Gamma\left(1 + \frac{m}{2}\right), \quad (4.115)$$

in which $\Gamma(\cdot)$ is a Gamma function (Abramowitz and Stegun, 1975). In particular, for $m = 2$ we have:

$$\sigma_\zeta^2 = \frac{1}{2} E[A^2] = \frac{1}{2} \overline{A^2}. \quad (4.116)$$

Therefore, the Rayleigh distribution takes the form:

$$f(A) = \frac{A}{\sigma_\zeta^2} \exp\left(-\frac{A^2}{2\sigma_\zeta^2}\right) = \frac{2A}{\overline{A^2}} \exp\left(-\frac{A^2}{\overline{A^2}}\right). \quad (4.117)$$

As was mentioned above, in physical oceanography and ocean engineering, the wave height H is preferred to wave amplitude A . The assumption of a narrow-band spectrum leads to the conclusion that $H \approx 2A$. The transformation of variable A to H in Eq. (4.113) gives the Rayleigh distribution in terms of wave height H :

$$f(H) = \frac{H}{4\sigma_\zeta^2} \exp\left(-\frac{H^2}{8\sigma_\zeta^2}\right), \quad (4.118)$$

or:

$$f(\xi) = \frac{1}{4}\xi \exp\left(-\frac{1}{8}\xi^2\right), \quad (4.119)$$

in which $\xi = \frac{H}{\sigma_\zeta}$.

Similarly to Eq. (4.115), the moments of wave height can be presented as:

$$E[H^m] = \overline{H^m} = 2^{3m/2} \sigma_\zeta^m \Gamma\left(1 + \frac{m}{2}\right). \quad (4.120)$$

In particular, the mean wave height \bar{H} and the root-mean-square wave height H_{rms} are obtained from Eq. 4.120, if $m = 1$ and $m = 2$, respectively:

$$\bar{H} = \sqrt{2\pi} \sigma_\zeta, \quad H_{rms} = 2\sqrt{2} \sigma_\zeta = \frac{2}{\sqrt{\pi}} \bar{H}. \quad (4.121)$$

Using Eq. (4.121), the distribution (4.118) can be rewritten as:

$$f(H) = \frac{2H}{H_{rms}^2} \exp\left(-\frac{H^2}{H_{rms}^2}\right), \quad (4.122)$$

or

$$f(\xi) = 2\xi \exp(-\xi^2), \quad (4.123)$$

in which $\xi = \frac{H}{H_{rms}}$, and

$$f(H) = \frac{\pi}{2} \frac{H}{\bar{H}^2} \exp\left[-\frac{\pi}{4} \left(\frac{H}{\bar{H}}\right)^2\right]. \quad (4.124)$$

The Rayleigh distribution (4.119) is compared with experimental data recorded during a few hours of a tropical storm in the Coral Sea (see Fig. 4.14). It should be noted that the wave height is normalized by the standard deviation $\sqrt{m_0}$ calculated from the spectrum. Two other distributions are shown in the same Figure. Their origin and properties are described in next Section.

Although various wave height relations based on the Rayleigh distribution can be found elsewhere (for example, Massel, 1989), here we only discuss one specific wave height frequently used in oceanographic and ocean engineering practice namely, the significant wave height H_s . The concept of the significant wave was introduced by Sverdrup and Munk (1947). They defined wave height H_s as the average of the highest one-third of wave heights. This wave height is close to the mean wave height estimated by human eye. Assuming a narrow-band wave spectrum, we first calculate the threshold wave height H^* which has the probability of exceedance of $\frac{1}{3}$ which corresponds to value $H^* = \frac{H}{\sigma_\zeta} \approx 3.0$ (see Fig. 4.15). Using Eq. (4.122) we have:

$$Pr\{H > H^*\} = \int_{H^*}^{\infty} \frac{2H}{H_{rms}^2} \exp\left[-\left(\frac{H}{H_{rms}}\right)^2\right] dH = \frac{1}{3}, \quad (4.125)$$

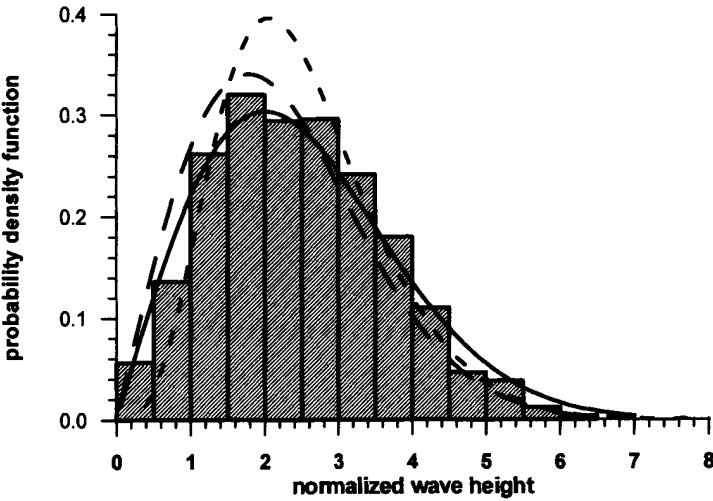


Figure 4.14: Comparison of various probability density functions for wave height with experimental data: ——— Rayleigh distr.; - - - modified Rayleigh distribution; - . - crest-to-trough distribution.

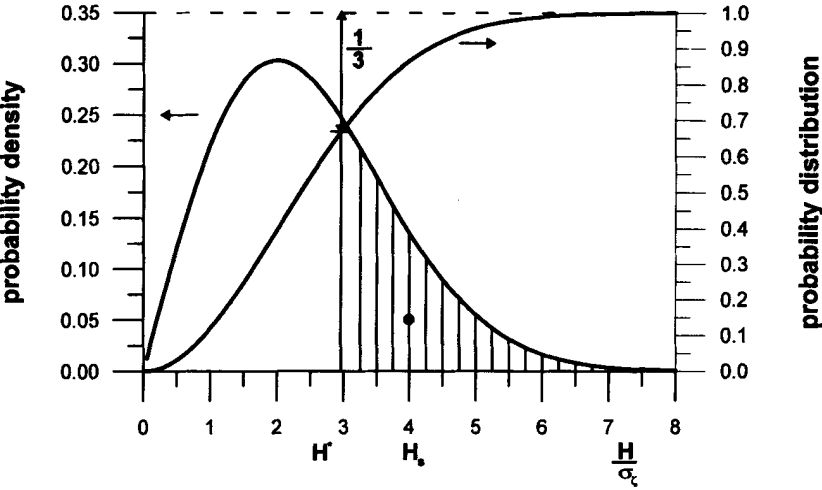


Figure 4.15: Determination of significant wave height H_s .

or:

$$\int_{H^*}^{\infty} d \left\{ \exp \left[- \left(\frac{H}{H_{rms}} \right)^2 \right] \right\} = \frac{1}{3}. \quad (4.126)$$

Thus:

$$H^* = \sqrt{\ln 3} H_{rms} = 1.048 H_{rms}. \quad (4.127)$$

According to definition, the significant wave height corresponds to the center of gravity of the shaded area in Fig. 4.15. The balance of moments with respect to the origin yields:

$$\frac{1}{3} H_s = \int_{H^*}^{\infty} H f(H) dH, \quad (4.128)$$

or:

$$H_s = \left\{ \frac{3\sqrt{\pi}}{2} \operatorname{erfc}(\sqrt{\ln 3}) + \sqrt{\ln 3} \right\} H_{rms} \approx 1.416 H_{rms}, \quad (4.129)$$

where the complementary error function $\operatorname{erfc}(z)$ is given by Eq. (4.67).

Using the second relation of (4.121), the significant wave height can be expressed as:

$$H_s = 1.416 H_{rms} = 4.004 \sigma_{\zeta}. \quad (4.130)$$

The development of various reliable digital data recording and analysis techniques (see Chapter 9) over the last 20 years has led to a fundamental change in the way significant wave height is estimated. Except for H_s , being the mean of the highest one-third of wave height, significant wave height is commonly estimated from gauge records using relation (4.130) when standard deviation is calculated from the frequency spectrum $S(\omega)$. This significant wave height is usually noted as H_{m0} , i.e.:

$$H_{m0} = 4.004 \sqrt{m_0}. \quad (4.131)$$

In other words, H_{m0} is an energy based significant wave height, determined as four times the square root of the area contained under the energy spectrum $S(\omega)$ (IAHR, 1989). H_{m0} is approximately equal to H_s except when water depth is small (see Section 4.2.5) or waves are very steep. In situations where H_{m0} is equal to H_s , either can be used. However, when H_{m0} differs from H_s , it cannot be used directly to estimate wave height statistics.

The formula (4.125) can be generalized to evaluate the average of the highest $1/N$ th wave heights $\bar{H}_{1/N}$, based on the Rayleigh distribution, i.e.:

$$\bar{H}_{1/N} = \left[\frac{N\sqrt{\pi}}{2} \operatorname{erfc}(\sqrt{\ln N}) + \sqrt{\ln N} \right] H_{rms}. \quad (4.132)$$

In Table 4.1 the values of $\bar{H}_{1/N}$ are listed for selected values of N .

Table 4.1: Characteristic wave heights based on the Rayleigh distribution.

N	$\bar{H}_{1/N}/H_{rms}$	$\bar{H}_{1/N}/\bar{H}$	$\bar{H}_{1/N}/\sigma_\zeta^2$	Remarks
500	2.680	3.023	7.580	Highest 1/100th wave
200	2.503	2.823	7.078	
100	2.359	2.662	6.671	
50	2.206	2.488	6.239	
25	2.042	2.303	5.775	
10	1.800	2.030	5.090	
5	1.591	1.795	4.499	Significant wave
3	1.416	1.597	4.004	
1	0.886	1.000	2.505	Mean wave

4.3.2 Influence of wave nonlinearity on wave height distribution

4.3.2.1 Modification of the Rayleigh distribution

All statistical characteristics of wave height discussed in the previous Section are based on the assumption that the probability distribution of surface displacement $\zeta(t)$ is Gaussian. In fact, as was shown in Section 4.2.2, the probability distribution of ζ is only approximately Gaussian, having some skewness and kurtosis. The non-Gaussian profile is asymmetric with respect to the mean water surface. Usually the crests are sharper and narrower, and the troughs are shallower and longer. Thus, quadratic and higher-order interactions between component waves exist, and the resulting surface displacement is not a Gaussian process.

In this Section we examine the influence of the wave field non-linearities on the statistics of wave heights. In general, the departure from a Gaussian process of surface displacement is not very large and surface displacement $\zeta(t)$ can be treated as a quasi-Gaussian. Thus, it is useful to explore first the application of the Gram-Charlier series approach to wave height distribution. The narrow-band wave process can be represented as a harmonic signal with randomly modulated amplitude and phase, which are slowly varying in time (see Eq. (4.106)):

$$\zeta(t) = A(t) \cos [\omega_p t + \varphi(t)], \quad (4.133)$$

where amplitude $A(t)$ is given by Eq. (4.107). It is quite acceptable to assume that surface displacement $\zeta(t)$ is differentiable in time:

$$\frac{d\zeta(t)}{dt} = \dot{\zeta}(t) \approx -A(t) \omega_p \sin [\omega_p t + \varphi(t)], \quad (4.134)$$

in which we neglected the time derivatives of slowly varying amplitude $A(t)$ and phase $\varphi(t)$. Using Eq. (4.107) we rewrite Eq. (4.134) as:

$$\frac{\dot{\zeta}(t)}{\omega_p} = -A_c(t) \sin(\omega_p t) - A_s(t) \cos(\omega_p t). \quad (4.135)$$

Solving Eqs. (4.104) and (4.135), with respect to $A_c(t)$ and $A_s(t)$, gives:

$$\left. \begin{aligned} A_c(t) &= \zeta(t) \cos(\omega_p t) - \frac{\dot{\zeta}(t)}{\omega_p} \sin(\omega_p t) \\ A_s(t) &= -\frac{\dot{\zeta}(t)}{\omega_p} \cos(\omega_p t) - \zeta(t) \sin(\omega_p t) \end{aligned} \right\}. \quad (4.136)$$

Thus, amplitude $A(t)$ becomes (Tikhonov, 1966):

$$A(t) = \sqrt{\zeta^2(t) + \left(\frac{\dot{\zeta}(t)}{\omega_p}\right)^2}. \quad (4.137)$$

If process $\zeta(t)$ is Gaussian, the derivative $\dot{\zeta}(t)$ is also Gaussian. By virtue of the linearity of Eq. (4.136), $A_c(t)$ and $A_s(t)$ will be Gaussian too.

The joint probability density function $f_2(A_c, A_s)$ can be obtained by using the two-dimensional Hermite polynomials (Kuznetsov et al., 1960). Then, transforming the function $f_2(A_c, A_s)$ to the joint probability density function of amplitude and phase $f_2(A, \varphi)$ and integrating it against φ , yields the probability density function for wave amplitude (Bitner, 1978, 1980). Provided that the peak-to-trough wave height H is approximately equal to the double amplitude, Bitner obtained the probability density function $f(H)$ as:

$$\begin{aligned} f(H) &= \frac{H}{4\sigma_\zeta^2} \exp\left[-\frac{H^2}{8\sigma_\zeta^2}\right] \left\{ 1 + \left[\frac{H^4}{1024\sigma_\zeta^4} (b_{40} + b_{04} + 2b_{22}) - \right. \right. \\ &\quad \left. \left. - \frac{H^2}{32\sigma_\zeta^2} (b_{40} + b_{04} + 2b_{22}) + \frac{1}{8} (b_{40} + b_{04} + 2b_{22}) \right] \right\}, \end{aligned} \quad (4.138)$$

in which:

$$b_{40} = \overline{\xi_c^4} - 3, \quad b_{04} = \overline{\xi_s^4}, \quad b_{22} = \overline{\xi_c^2 \xi_s^2} - 1, \quad (4.139)$$

$$\xi_c = \frac{A_c(t) - \overline{A_c(t)}}{\sigma_\zeta}, \quad \xi_s = \frac{A_s(t) - \overline{A_s(t)}}{\sigma_\zeta}. \quad (4.140)$$

In particular, mean wave height \bar{H} is:

$$\bar{H} = \sqrt{2\pi}\sigma_\zeta \left[1 - \frac{1}{64} (b_{40} + b_{04} + 2b_{22}) \right]. \quad (4.141)$$

However, no suitable parameterization technique is available for evaluation of the coefficients b_{40} , b_{04} and b_{22} . Bitner (1980) determined these coefficients numerically using experimental data.

In general, in deep water, the corrections in the mean wave height \bar{H} , due to coefficients b_{40} , b_{04} , and b_{22} are not significant. This conclusion is in agreement with the Longuet-Higgins (1980) suggestion that the Rayleigh distribution for non-Gaussian random waves is still applicable when the root-mean-square wave height in Eq. (4.122) is properly chosen. Particularly, he used the probability density function $f(H)$ in the form:

$$f(H) = \frac{2H}{H_{rms}^2} \exp \left[-\frac{H^2}{H_{rms}^2} \right], \quad (4.142)$$

where:

$$H_{rms}^2 = 8\sigma_\zeta^2 \left[1 - \left(\frac{\pi^2}{8} - \frac{1}{2} \right) \nu^2 \right] < 8\sigma_\zeta^2, \quad (4.143)$$

in which ν is the lower-order bandwidth parameter. From curve-fitting the Forristall (1978) data from the Gulf of Mexico, Longuet-Higgins obtained $H_{rms} = 1.85 \sqrt{2}\sigma_\zeta < 2\sqrt{2}\sigma_\zeta$.

A simple argument that the denominator in Eq. (4.142) should be smaller than $8\sigma_\zeta^2$ was given by Vinje (1989). Assuming that a wave train is a superposition of a carrier wave with slowly varying amplitude A , frequency Ω and phase φ , and a small random perturbation $\zeta_1(t)$, we obtain:

$$\zeta(t) = A(\epsilon t) \cos [\Omega(\epsilon t) + \varphi(\epsilon t)] + \zeta_1(t), \quad (4.144)$$

in which ϵ is a small parameter. It should be expected that the maxima and minima of the surface elevation $\zeta(t)$ approximately coincides with the maxima and minima of the carrier wave. Therefore, the wave height H is simply the difference of the surface elevations at t -time (wave crest) and $t = t_{max} + \frac{\pi}{\Omega}$ (wave trough). To determine the probability distribution for H we define the Gaussian process $X(t)$ as:

$$X(t) = \zeta(t) - \zeta \left(t + \frac{\pi}{\Omega} \right). \quad (4.145)$$

Now wave height H can be considered as the maximum of the process $X(t)$. The wave height H will have approximately the Rayleigh distribution with the root-mean-square value H_{rms} :

$$H_{rms} = 4 \left[K_\zeta(0) - K_\zeta \left(\frac{\pi}{\Omega} \right) \right], \quad (4.146)$$

where $K_\zeta(\tau)$ is the autocorrelation function of $\zeta(t)$. For narrow-banded processes, the value $K_\zeta \left(\frac{\pi}{\Omega} \right)$ corresponds approximately to the minimum of $K_\zeta(\tau)$; so $K_\zeta \left(\frac{\pi}{\Omega} \right) \approx [K_\zeta(\tau)]_{min}$. Finally, the probability density distribution function $f(H)$ becomes:

$$f(H) = \frac{H}{2\sigma_\zeta^2(1 - r_{min})} \exp \left[-\frac{H^2}{4\sigma_\zeta^2(1 - r_{min})} \right], \quad (4.147)$$

where r_{\min} denotes the global minimum of the normalized autocorrelation function $r_{\min} = [K_{\zeta}(\tau)]_{\min}/K_{\zeta}(0)$. For the very narrow-banded process $r_{\min} \rightarrow -1$ and the probability density function (4.147) becomes identical with the Rayleigh distribution function (4.118).

The distribution (4.147) was also obtained by Naess (1985a). In his derivation, the normalized autocorrelation function r_{\min} was calculated at the time as $\tau = \frac{T_p}{2}$, where T_p denotes the period corresponding to the spectrum peak frequency.

It should be noted that Longuet-Higgins value of $H_{rms} = 1.85\sqrt{2}\sigma_{\zeta}$ corresponds to $r_{\min} = -0.711$. Using the autocorrelation function $K(\tau)$, corresponding to the Pierson-Moskowitz spectrum, results in $r_{\min} = -0.653$. A similar calculation for the JONSWAP spectrum gives -0.73 and -0.8 , for peakedness $\gamma = 3.3$ and $\gamma = 7.0$, respectively.

The probability distribution function (4.147) was shown in Fig. 4.14. The minimum r_{\min} of the normalized autocorrelation function was calculated using the experimental data ($r_{\min} = -0.59$). Thus, the denominator in Eq. (4.147) is $4\sigma_{\zeta}^2(1 - r_{\min}) = 6.36\sigma_{\zeta}^2$. Note that for the same experimental data, the Longuet-Higgins formula (4.143) gives the value $7.19\sigma_{\zeta}^2$.

4.3.2.2 Crest-to-trough wave height distribution

The Rayleigh distribution and its modifications were evaluated under the assumption that upper and lower wave envelopes coincide with crests and troughs. This is essentially relevant to the narrow-banded spectrum when the envelopes vary slowly in time (see Fig. 3.2). When the spectrum is non-narrow banded, the envelopes are not the symmetric curves with respect to mean value. Therefore, it may be more appropriate to consider the wave height as the sum of the highest-crest (A_c) and the lowest-trough (A_t) amplitudes in a zero-upcrossing wave, i.e.:

$$H = A_c(t) + A_t(t + \tau). \quad (4.148)$$

Both amplitudes are separated by the time interval τ . We expect that time τ is approximately equal to $\bar{T}/2$, where \bar{T} is a mean wave period. The probability density function of two normalized amplitudes $A_1^{(+)}$ and $A_2^{(-)}$ separated by time τ was given by Rice (1945) (also see Massel, 1985; Ochi, 1990):

$$f_2(\xi_1, \xi_2 | \tau) = \frac{\xi_1 \xi_2}{1 - r_0^2} I_0 \left(\frac{\xi_1 \xi_2 r_0}{1 - r_0^2} \right) \exp \left[-\frac{\xi_1^2 + \xi_2^2}{2(1 - r_0^2)} \right], \quad (4.149)$$

in which:

$$\xi_1 = \frac{A_t(t)}{\sqrt{m_0}}, \quad \xi_2 = \frac{A_c(t + \tau)}{\sqrt{m_0}}, \quad (4.150)$$

$r_0(\tau)$ is a correlation coefficient between wave amplitudes (strictly speaking between squares of the amplitudes), separated by time interval τ and

$$r_0^2(\tau) = \rho_0^2(\tau) + \lambda_0^2(\tau), \quad (4.151)$$

in which:

$$\rho_0(\tau) = \frac{1}{m_0} \int_0^\infty S(\omega) \cos [(\omega - \bar{\omega}) \tau] d\omega, \quad (4.152)$$

$$\lambda_0(\tau) = \frac{1}{m_0} \int_0^\infty S(\omega) \sin [(\omega - \bar{\omega}) \tau] d\omega. \quad (4.153)$$

The $I_0(\)$ is a modified Bessel function of zero order (Abramowitz and Stegun, 1975).

Note that for any frequency spectrum $S(\omega)$, which is symmetric with respect to frequency $\bar{\omega}$, the coefficient $\lambda_0(\tau) = 0$ for all τ .

Let us assume that spectrum $S(\omega)$ is extremely narrow ($\nu \rightarrow 0$), i.e.:

$$S(\omega) = m_0 \delta(\omega - \bar{\omega}), \quad (4.154)$$

in which $\delta(\)$ is the delta function. Substituting Eq. (4.154) into Eqs. (4.152) and (4.153) we obtain $\rho_0(\tau) = 1$ and $\lambda_0(\tau) = 0$; thus, $r_0 = 1$. It can be shown that the same result can be obtained when assuming $|\tau| \rightarrow 0$ for an arbitrary spectrum.

When $r_0 \rightarrow 1$, because of the high correlation between ξ_1 and ξ_2 , the two-dimensional probability density function $f_2(\xi_1, \xi_2; \tau)$ takes the form (Middleton, 1960):

$$f_2(\xi_1, \xi_2; \tau) \rightarrow f(\xi_1) \delta(\xi_1 - \xi_2), \quad (4.155)$$

which corresponds to the Rayleigh distribution when $r_0 \rightarrow 1$ ($\nu \rightarrow 0$). For other extreme cases, when $\tau \rightarrow \infty$, the correlation coefficient $r_0 \rightarrow 0$, and so:

$$f_2(\xi_1, \xi_2 | \tau) = f(\xi_1) f(\xi_2). \quad (4.156)$$

Thus, amplitudes ξ_1 and ξ_2 are statistically independent.

Let us normalize the wave height in Eq. (4.149) using variance m_0 ; then:

$$\xi = \xi_1 + \xi_2 \quad \text{and} \quad \xi_1 = \xi - \xi_2, \quad (4.157)$$

where $\xi = H/\sqrt{m_0}$; the ξ_1 and ξ_2 are given by the Eq. (4.150).

The probability density function for ξ takes a form of the convolution integral (Tayfun, 1981b):

$$f(\xi | \tau) = \int_0^\xi f_2(\xi - \xi_2, \xi_2; \tau) d\xi_2, \quad (4.158)$$

in which $\tau = T/2$, where T is a wave period. Allowing the wave period T to take all possible values from 0 to ∞ , the probability density function of crest-to-trough wave height becomes:

$$f(\xi) = \int_0^\infty \int_0^\xi f(T) f_2\left(\xi - \xi_2, \xi_2; \tau = \frac{T}{2}\right) d\xi_2 dT, \quad (4.159)$$

in which $f(T)$ is a probability density function of the wave period.

Calculation of the probability density function in (4.159) is complicated. To simplify the problem, Tayfun (1981b) assumed that the spectrum is sufficiently narrow and is concentrated around the mean frequency $\bar{\omega}$. Then, the probability density function of the wave period has non-zero values around the mean period \bar{T} only, and Eq. (4.159) becomes:

$$f(\xi) = \int_0^\xi f_2 \left(\xi - \xi_2, \xi_2; \tau = \frac{\bar{T}}{2} \right) d\xi_2. \quad (4.160)$$

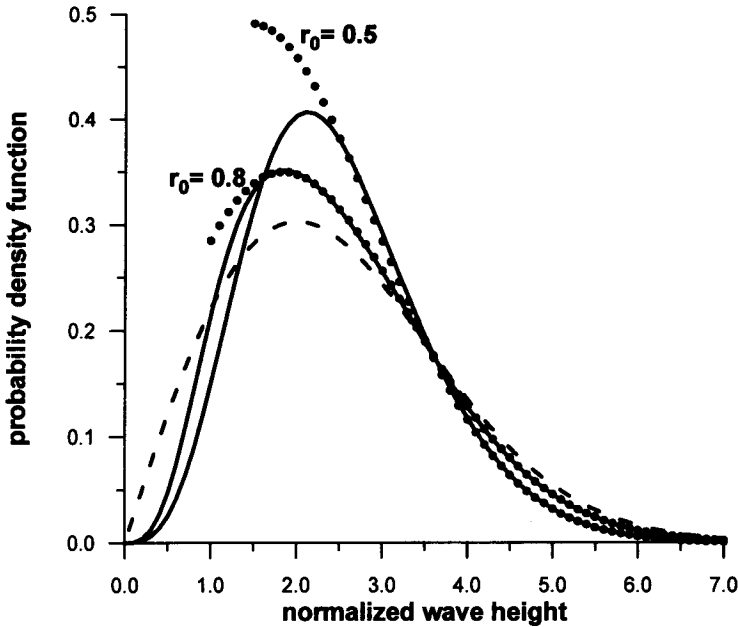


Figure 4.16: Comparison of various theoretical probability density functions for large wave heights: - - - Rayleigh distribution; ——— crest-to-trough distribution for $r_0 = 0.5$ and $r_0 = 0.8$; •••• Tayfun's distribution for large wave heights for $r_0 = 0.5$ and $r_0 = 0.8$.

Substitution of Eq. (4.149) into Eq. (4.160) gives:

$$f(\xi) = \frac{1}{1-r_0^2} \int_0^\xi (\xi-x) x I_0 \left[\frac{(\xi-x) x r_0}{1-r_0^2} \right] \exp \left[-\frac{(\xi-x)^2 + x^2}{2(1-r_0^2)} \right] dx. \quad (4.161)$$

The first two moments of distribution (4.161) are:

$$E[\xi] = \sqrt{2\pi}, \quad (4.162)$$

and

$$E[\xi^2] = 4 \left[1 + \frac{\pi}{4} \left(1 + \mu + \frac{\mu^2}{4} + \frac{\mu^3}{4} + \frac{\mu^4}{64} + \dots \right) \right], \quad (4.163)$$

in which $\mu = r_0^2/4$. Thus, the mean wave height is identical with that resulting from the Rayleigh distribution. Moreover, the series representation (4.163) of the normalized root-mean-square wave height for $r_0 \rightarrow 1$ ($\nu \rightarrow 0$) gives $E[\xi^2] = 8$, which is also the Rayleigh limit. When $0 \leq r_0 \leq 1$, Eq. (4.163) gives $2.672 \leq \frac{H_{rms}}{\sigma_\xi} \leq 2\sqrt{2}$; this means that the root-mean-square value of zero-crossing wave heights predicted by Eq. (4.161) is smaller than that given by the classical Rayleigh distribution.

The distribution (4.161) is illustrated in Fig. 4.16 for $r_0 = 0.5$ and $r_0 = 0.8$. The Rayleigh distribution is included for comparison. Both distributions resulting from Eq. (4.161) predict lower probabilities for small and high waves. On the other hand, the wave heights close to the mean, i.e. when $\xi = \sqrt{2\pi} \approx 2.5$, are more likely to occur according to Eq. (4.161) than according to the Rayleigh function. The smaller r_0 value produces the higher probability of occurrence of such waves.

Comparison of the distribution (4.161) with experimental data is also shown in Fig. 4.14. Experimental data in this Figure corresponds to the correlation coefficient r_0 in the range $0.57 \leq r_0 \leq 0.60$ (mean value $r_0 \approx 0.58$ was used in calculation) and band-width parameter ν in the range $0.36 \leq \nu \leq 0.38$.

4.3.2.3 Probability distribution of large wave heights

A probability distribution of large wave heights is of special interest for ocean engineers. However, the application of distribution (4.161) is impeded by the necessity of numerical integration which requires evaluation of the Bessel function I_0 . When we restrict our attention to the higher waves, say for $\xi \geq E[\xi] = \sqrt{2\pi}$ and use the asymptotic expansion of the Bessel function $I_0(\cdot)$ for larger values, the probability density function $f(\xi)$ can be presented in the much simpler closed form (Tayfun, 1990):

$$f(\xi) = \frac{\xi}{2[r_0(1+r_0)]^{1/2}} \left(1 + \frac{1-r_0^2}{4r_0\xi^2} \right) \exp \left[-\frac{\xi^2}{4(1+r_0)} \right]. \quad (4.164)$$

A typical comparison of Eq. (4.164) with exact distribution (4.161) is shown in Fig. 4.16 for $r_0 = 0.5$ and $r_0 = 0.8$. For normalized wave height $\xi \geq \sqrt{2\pi} \sim 2.5$, both distributions (4.161) and (4.164) are almost the same.

It should be noted that the significant wave height calculated on the base of Eq. (4.164) is smaller than the classical value $4.004\sqrt{m_0}$ for all practical values of r_0 ($0.5 \leq r_0 \leq 1.0$). In particular, for $r_0 = 0.5$ the significant wave height is equal to $3.75\sqrt{m_0}$ and then approaches almost linearly to $4.004\sqrt{m_0}$ for $r_0 = 1$.

The corresponding probability of exceedance of a given value ξ , when $\xi \geq E[\xi]$ is:

$$F_1(\xi) = \int_{\xi}^{\infty} f(\xi) d\xi = \left(1 + \frac{1 - r_0^2}{4r_0\xi^2}\right) \left(\frac{1 + r_0^2}{2r_0}\right)^{1/2} \exp\left[-\frac{\xi^2}{4(1 + r_0)}\right]. \quad (4.165)$$

The function $F_1(\xi)$ for $r_0 = 0.5$ and 0.8 is illustrated in Fig. 4.17. For comparison, Rayleigh distribution, which represents the limit $r_0 \rightarrow 1$, was added. A good agreement was found when comparing the asymptotic probability of exceedance (4.165) with experimental data (Forristall, 1978) and numerical simulation (Forristall, 1984; Osborne, 1982).

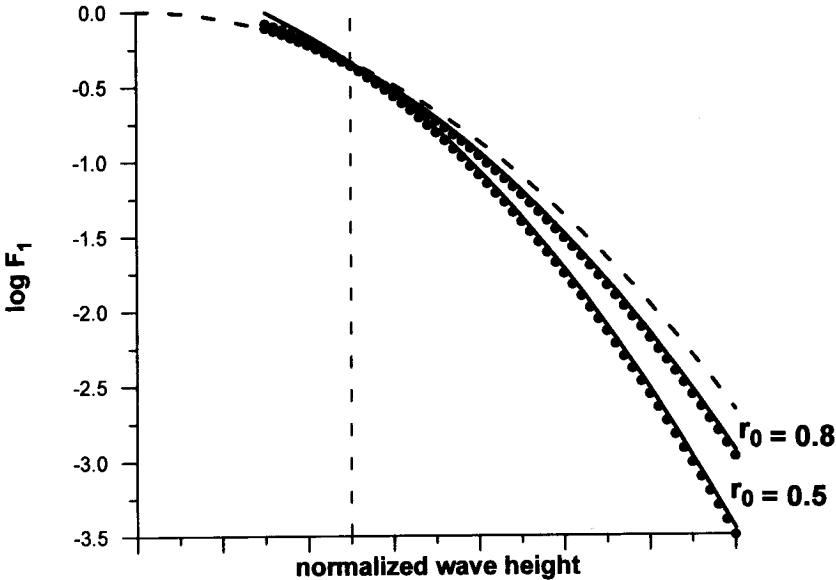


Figure 4.17: Probability of exceedance a given normalized wave height: - - - Rayleigh distribution; ——— crest-to-trough distribution for $r_0 = 0.5$ and $r_0 = 0.8$; ●●● distribution for large wave heights.

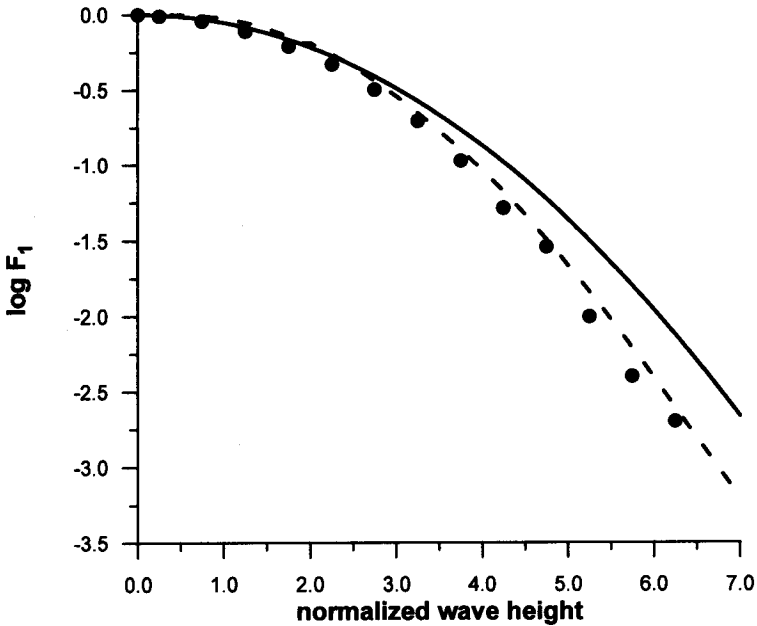


Figure 4.18: Comparison of various probabilities of exceedance with experimental data: ——— Rayleigh distribution; - - - modified Rayleigh distribution; • • • • experimental data.

A reliable estimation of the probability exceedance of high waves is fundamental in the design of structures and in the planning of operational and maintenance activities. Many experiments in the field, as well as simulation exercises, indicate that the Rayleigh distribution overpredicts the probability of the highest waves, and hence errors grow towards the low probability tail of the distribution. This can be seen in Fig. 4.18, in which the Rayleigh distribution is compared with the modified distribution (4.147), and with the experimental data from the Coral Sea.

4.3.2.4 Influence of second order nonlinearities

As yet, we have considered various approximations of the probability density function $f(H)$ without any straightforward relation to the nonlinearity of the wave process itself. In order to estimate the influence of nonlinearity in the wave process we assume that the nonlinear surface displacement is given by:

$$\zeta(t) = \zeta_1(t) + \zeta_2(t) = A_1 \cos \phi_1 + \frac{1}{2} A_1^2 \bar{k} \cos 2\phi_1, \quad (4.166)$$

in which $\phi_1 = \omega t + \varphi$; $\zeta_1(t)$ is a linear Gaussian process, $\zeta_2(t)$ is a second-order nonlinear correction, and $k = \frac{\omega^2}{g}$ is the wave number in deep water. Because of approximation (4.166), the analysis is restricted to wave trains of small steepness $\alpha = k(2\sigma_\zeta^2)^{1/2}$; so it is correct to $O(\alpha)$. The statistics of amplitude A_1 and φ can be evaluated using the component process approach. The component process $\eta(t)$ is given by the Hilbert transform of $\zeta(t)$, i.e. (Tikhonov, 1966; Tayfun and Lo, 1989):

$$\eta(t) = \frac{1}{\pi} \int_{-\infty}^{\infty} \frac{\zeta(\tau)}{t - \tau} d\tau. \quad (4.167)$$

After substituting Eq. (4.166) into Eq. (4.167) we obtain:

$$\eta(t) = -A_1 \sin \phi_1 - \frac{1}{2} A_1^2 \bar{k} \sin 2\phi_1. \quad (4.168)$$

The complex nonlinear process can now be defined as:

$$W = \zeta(t) + i\eta(t) = A \exp(i\psi), \quad (4.169)$$

such that:

$$A = A_1 + \frac{1}{2} A_1^2 \bar{k} \cos \phi_1, \quad (4.170)$$

$$\tan \psi = \left[1 + \frac{1}{2} A_1 \bar{k} \sec(\phi_1) \right] \tan \phi_1. \quad (4.171)$$

The joint probability density of A and ψ follows from the standard transformation:

$$f_2(A, \psi) = |J| f_2(A_1, \phi_1), \quad (4.172)$$

in which:

$$f_2(A, \phi) = f(A_1) f(\phi_1). \quad (4.173)$$

Probability densities $f(A_1)$ and $f(\phi_1)$ are given by Eqs. (4.113) and (4.114), respectively. Therefore, the Jacobian transformation yields:

$$J = \frac{\partial(A_1, \phi_1)}{\partial(A, \psi)} = 1 - \frac{3}{2} A k \cos \psi. \quad (4.174)$$

After substitution of Eqs. (4.173) into Eq. (4.172) and integration, we obtain the marginal distributions of A and ψ as:

$$f(A) = \frac{A}{\sigma_\zeta^2} \exp\left(-\frac{A^2}{2\sigma_\zeta^2}\right), \quad (4.175)$$

and

$$f(\psi) = \frac{1}{2\pi} \left(1 - \frac{\sqrt{\pi}}{4} \alpha \cos \psi\right). \quad (4.176)$$

Thus, A and ψ are no longer independent. The envelope is Rayleigh distributed to $O(\alpha)$. Although the surface profile itself is asymmetric with crests $(A_1 + \frac{1}{2}A_1^2k)$ and troughs $(-A_1 + \frac{1}{2}A_1^2k)$, the envelopes $\pm A$ are symmetric and the difference between a wave crest and an adjacent trough is then given by $H = 2A_1$. Hence, the nonlinearities do not appear to affect the distribution of zero-crossing wave heights.

The result (4.176) indicates that the probability density of phase ψ is not uniform; it has a maximum at $\psi = \pi$ and minima at $\psi = 0, 2\pi$. The comparison with the data from hurricane *Camille*, given in Tayfun and Lo's paper (1989), shows a satisfactory agreement with their theoretical result (4.176).

It should be noted that because the envelopes $\pm A$ are symmetric, they cannot be used to describe the nonlinear crest or trough statistics. However, a similar perturbation technique may be applied to obtain approximate probability density functions of the peaks and troughs of the second order Stokes waves:

$$\zeta = a \cos \phi + a^2 k \cos^2 \phi, \quad (4.177)$$

in which a is amplitude and ϕ is a phase $\phi = kx - \omega t + \epsilon$. The peaks of the wave profile are given by:

$$\zeta_c = a + a^2 k, \quad (4.178)$$

or in non-dimensional form:

$$\xi_c = \alpha + \alpha^2 \sigma_\zeta k, \quad (4.179)$$

in which $\xi_c = \zeta_c / \sigma_\zeta$ and $\alpha = a / \sigma_\zeta$. Using the method of the transformation of random variables we obtain the probability density function of ξ_c as (Tung and Huang, 1985):

$$f(\xi_c) = \frac{-1 + (1 + 4\xi_c \sigma_\zeta k)^{1/2}}{2\sigma_\zeta k (1 + 4\xi_c \sigma_\zeta k)^{1/2}} \cdot \exp\left\{-\frac{1}{8\sigma_\zeta^2 k^2} \left[-1 + (1 + 4\xi_c \sigma_\zeta k)^{1/2}\right]^2\right\}. \quad (4.180)$$

The function (4.180) is shown in Fig. 4.19 for $\sigma_\zeta k = 0.10$. The Rayleigh distribution was plotted in this Figure to demonstrate the effect of nonlinearity of wave motion on the probability density function.

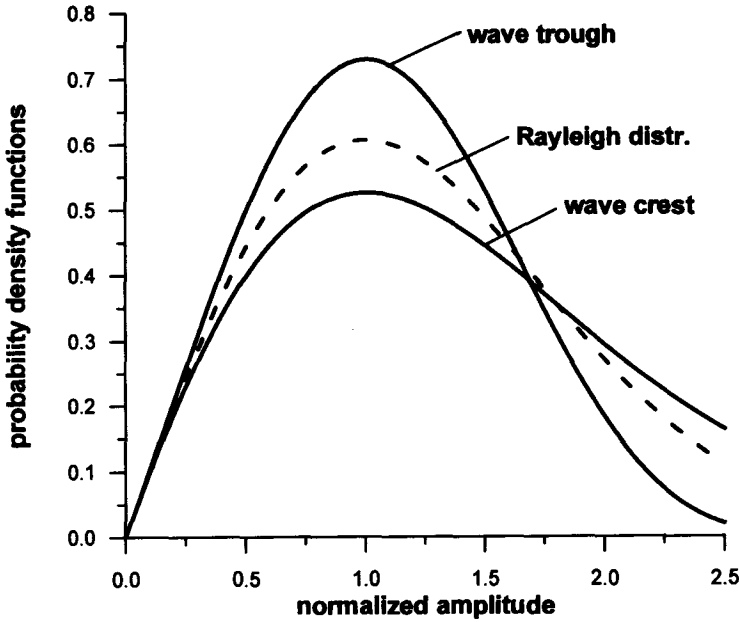


Figure 4.19: Probability density function for crests and troughs of nonlinear waves.

The probability density function of the troughs of $\zeta(t)$ may be obtained in a similar way to produce the final result as:

$$f(\xi_t) = \frac{1 - (1 - 4\xi_t\sigma_\zeta k)^{1/2}}{2\sigma_\zeta k(1 - 4\xi_t\sigma_\zeta k)^{1/2}} \cdot \exp \left\{ -\frac{1}{8\sigma_\zeta^2 k^2} \left[1 - (1 - 4\xi_t\sigma_\zeta k)^{1/2} \right]^2 \right\}, \quad (4.181)$$

in which $\xi = \frac{|\zeta_t|}{\sigma_\zeta}$ and ζ_t is an ordinate of wave trough.

Function $f(\xi_t)$ is also plotted in Fig. 4.19. Nonlinear waves have a higher probability of occurrence of high crest values than linear waves and lower probability of occurrence of high trough values.

4.3.3 Influence of wave breaking on wave height distribution in deep water

Although the probability densities of wave height do not put any limits on wave height, it is quite obvious that some waves will reach limiting height or steepness and

will break. Wave breaking will reduce the probability of extreme wave height. In Section 4.2.4, the probability that breaking will occur at the crest of a wave, at a given point on the sea surface, was estimated using the acceleration criterion. The most commonly known breaking criterion is that the wave height should exceed 14.2 percentage of the Stokes limiting wavelength, i.e.:

$$H \geq 0.142L = 0.027gT^2. \quad (4.182)$$

Dean (1968) gave a value of 0.033 for the constant in Eq. (4.182) based on the stream function representation of nonlinear regular waves, while the observations by Ochi and Tsai (1983) showed that in random waves the following relationship may be adopted as a breaking criterion:

$$H \geq 0.020gT^2. \quad (4.183)$$

Thus, the probability that a particular wave is breaking (or the percent of breaking waves in a given record) may be defined as:

$$P_{br} = P \left\{ H \geq \alpha g T^2 \right\}. \quad (4.184)$$

When wave height and wave period are considered independent random variables and when wave height and the square of the wave period are Rayleigh distributed, the probability P_{br} becomes (Nath and Ramsey, 1976):

$$P_{br} = \frac{\chi^2}{\chi^2 + 1}, \quad (4.185)$$

where:

$$\chi = \frac{H_{rms}}{\alpha g T_{rms}^2}, \quad (4.186)$$

T_{rms}^2 is the root-mean-square value of T^2 .

However, the assumption on the wave height and period independence is rather unrealistic. Wave height and wave period are clearly correlated to some extent. Thus, in general,

$$f_2(H, T) \neq f(H) f(T), \quad (4.187)$$

in which $f_2(H, T)$ is a two-dimensional probability density function of H and T , and $f(H)$ and $f(T)$ are probability density functions of H and T , correspondingly. A detailed discussion of function $f(H, T)$ and $f(T)$ is left to Section 4.4. However, to assess the probability of wave breaking in the wave field in which some correlation between H and T exists, we use the distribution $f(H, T)$ proposed by Longuet-Higgins (1983). After normalization we obtain (see also Eq. (4.253)):

$$f_2(\xi, \tau) = C_L \left(\frac{\xi}{\tau} \right)^2 \exp \left\{ -\frac{\xi^2}{8} \left[1 + \frac{1}{\nu^2} \left(1 - \frac{1}{\tau} \right)^2 \right] \right\}, \quad (4.188)$$

where C_L is a function of parameter ν and is given by Eq. (4.254); $\xi = H/\sqrt{m_0}$ and $\tau = T/\bar{T}$.

Now the probability of breaking waves takes the form:

$$P_{br} = \int_0^\infty \int_{\beta\tau^2}^\infty f_2(\xi, \tau) d\xi d\tau, \quad (4.189)$$

and

$$\beta = \alpha \frac{g\bar{T}^2}{\sqrt{m_0}} = 4\pi^2 \alpha \left(\frac{gm_0^{3/2}}{m_1^2} \right). \quad (4.190)$$

It should be noted that quantity:

$$\beta^{-1} = \frac{1}{\alpha} \frac{\sqrt{m_0}}{g\bar{T}^2} = 1.266 \frac{m_1^2}{gm_0^{3/2}}, \quad (4.191)$$

is proportional to the wave steepness.

In contrast to Eq. (4.78), probability of breaking depends itself on the spectrum width. However, its dependence on the spectrum shape manifests through the spectral moments of lower orders. Thus, this probability is not so sensitive to the high-frequency range of spectrum.

Another approach to the breaking-limited wave height distribution, based on the characteristic function method, was described by Tayfun (1981a).

4.3.4 Probability distribution of extreme wave height

Design wave criteria for coastal and offshore structures are based on occurrence probabilities of extreme wave conditions. For example, the classical Rayleigh probability density distribution (4.118) decreases exponentially as the wave height becomes large. The maximum wave height H_{max} in a sample depends fundamentally on the number of waves N in the sample. Because the sampling of waves is random, the maximum wave height is a random variable too, with its own probability density $f_{H_{max}}(H_{max})$. Assuming that the occurrence of wave height is an independent event and that the wave spectrum is narrow-banded, Longuet-Higgins (1952) showed that:

$$f_{H_{max}}(H_{max}) = N f_H(H_{max}) [F_H(H_{max})]^{N-1}, \quad (4.192)$$

and:

$$F_{H_{max}}(H_{max}) = [F_H(H_{max})]^N, \quad (4.193)$$

where $f_H(H_{max})$ is the probability density distribution of individual wave height, and $F_H(H_{max})$ is a cumulative distribution. Using Eq. (4.122) for $f_H(H)$ and normalizing with H_{rms} we obtain:

$$f_{\rho_{max}}(\rho_{max}) = N f_\rho(\rho_{max}) [F_\rho(\rho_{max})]^{N-1}, \quad (4.194)$$

in which $\rho = H/H_{rms}$, $\rho_{max} = H_{max}/H_{rms}$, and:

$$f_{\rho}(\rho_{max}) = 2\rho_{max} \exp(-\rho_{max}^2), \quad F_{\rho}(\rho_{max}) = 1 - \exp(-\rho_{max}^2). \quad (4.195)$$

The normalized mean extreme wave heights (\bar{H}_{max}/H_{rms}) and the most probable extreme wave heights (\tilde{H}_{max}/H_{rms}) for various sample sizes are listed in the second columns of Tables 4.2 and 4.3.

Table 4.2: Normalized mean maximum wave heights

N	Rayleigh distr.	Rayleigh modif.	Crest-to-trough distr.	Markov chain	Finite depth	
					$\bar{H}/h = 0.25$	$\bar{H}/h = 0.5$
200	2.41	2.22	2.24	2.37	2.02	1.65
1800	2.83	2.61	2.61	2.82	2.27	1.79
3600	2.95	2.73	2.75	2.94	2.35	1.82
5000	3.01	2.78	2.81	3.00	2.38	1.84
10000	3.13	2.88	2.91	3.11	2.45	1.88
20000	3.24	2.98	3.01	3.22	2.51	1.98
50000	3.38	3.11	3.14	3.35	2.59	1.95
100000	3.48	3.20	3.24	3.45	2.65	1.98

Table 4.3: Normalized the most probable maximum wave heights

N	Rayleigh distr.	Rayleigh modif.	Crest-to-trough distr.	Markov chain	Finite depth	
					$\bar{H}/h = 0.25$	$\bar{H}/h = 0.5$
200	2.32	2.16	2.18	2.29	1.96	1.64
1800	2.76	2.52	2.57	2.74	2.24	1.76
3600	2.88	2.64	2.68	2.86	2.32	1.80
5000	2.92	2.72	2.74	2.92	2.34	1.83
10000	3.04	2.80	2.84	3.04	2.40	1.84
20000	3.16	2.92	2.94	3.16	2.48	1.88
50000	3.30	3.04	3.08	3.30	2.56	1.92
100000	3.40	3.12	3.17	3.40	2.60	1.96

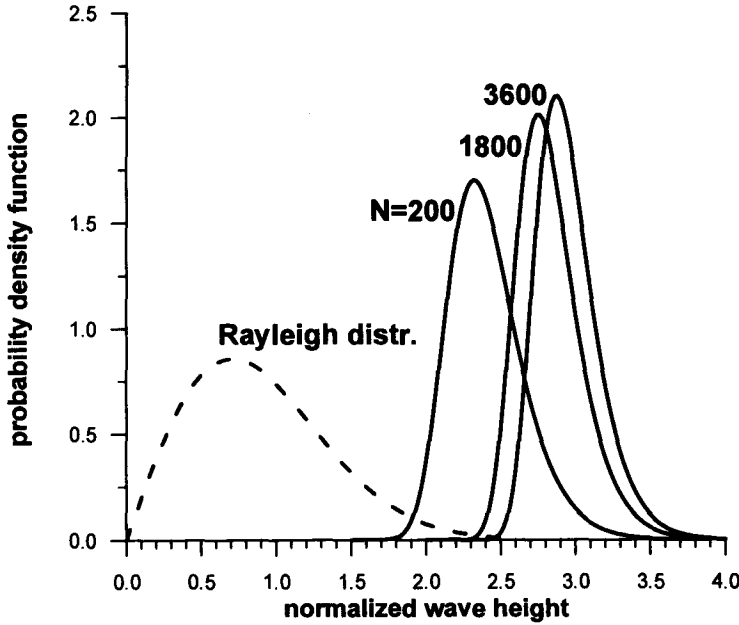


Figure 4.20: Probability density function of extreme wave heights for three sample sizes. The Rayleigh distribution is given for comparison.

In Fig. 4.20 the functions $f_{\rho}(\rho)$ and $f_{\rho_{max}}(\rho_{max})$ for three sample sizes ($N = 200$, 1800 and 3600) are shown. For large ρ_{max} , the calculation of the most probable value of ρ_{max} simplifies considerably. Hence:

$$F_{\rho_{max}}(\rho_{max}) \frac{df_{\rho_{max}}}{d\rho_{max}} + (N - 1) [f_{\rho_{max}}]^2 = 0, \quad (4.196)$$

or:

$$\exp(-\rho^2) = \frac{1 - 2\rho_{max}^2}{1 - 2N\rho_{max}^2}. \quad (4.197)$$

When $\rho_{max} \gg 1$, Eq. (4.197) yields:

$$\exp(\rho^2) = N, \quad (4.198)$$

or:

$$\tilde{H}_{max} = \sqrt{\ln N} H_{rms} + O(\ln N)^{-3/2}. \quad (4.199)$$

Closer approximations to ρ_{max} can be found by applying Newton's method starting with a value given by Eq. (4.199).

It is widely acknowledged that the Rayleigh distribution does not reflect a measured distribution of the more extreme waves from field data. Equation (4.122) overpredicts the probabilities of the higher waves in a record, and the error increases toward the low-probability tail of the distribution (see Fig. 4.18). Numerous reasons for the observed overprediction have been suggested (Forristall, 1978; Longuet-Higgins, 1980; Tayfun, 1981b; Naess, 1985b; Myrhaug and Kjeldsen, 1986). Statistical estimates of extreme wave heights, that are based on the Rayleigh distribution, will be even less likely to follow field observations. For example, Myrhaug and Kjeldsen (1986) analyzed statistically about 25,000 single storm waves recorded on the Norwegian continental shelf. The measured extreme wave heights were smaller than those calculated from the Rayleigh distribution. Sobey et al. (1990) also compared the highest wave heights H_{max} in a standard 20 minutes record from tropical Cyclone *Victor* with those computed from Eq. (4.194). The Cyclone *Victor* data show a systematic overprediction of order 10% by the Rayleigh distribution. The probable causes of the observed discrepancy between measured and calculated extreme wave heights are likely to be: finite spectral width, correlation between successive wave maxima, nonlinearity of profile and asymmetry of crest and trough of the extreme waves, limited water depth, wave breaking, errors associated with instrumentation, and others. In the following we examine some of these causes in detail.

In Section 4.3.2 it was shown that finite spectral width can be incorporated into the Rayleigh distribution with properly chosen root-mean-square wave height (see Eq. (4.143)). The mean and the most probable normalized extreme wave heights for various sample sizes, based on the modified Rayleigh distribution (4.142), are shown in the third column of Tables 4.2 and 4.3. The value $\nu = 0.45$ was used in calculations. A comparison of the second and third columns suggests that finite spectral width reduces the highest wave in a sample.

Strictly speaking, the above analysis of the extreme wave heights is valid only for random sampling. However, when the bandwidth of the spectrum goes to zero, there must be some correlation between members of the sample. Thus, waves with a narrow-band spectrum cannot be treated as independent. There are several ways of including the correlation of neighboring maxima of a Gaussian process $\zeta(t)$. In fact, in Section 4.3.2 we applied the correlation between adjacent wave crest and trough, and developed the probability density function of the crest-to-trough excursion (4.159). Using Eq. (4.161) in Eq. (4.194), the mean maximum wave heights and the most probable maximum wave heights were calculated and listed in the fourth column in Tables 4.2 and 4.3. For numerical calculation, the JONSWAP spectrum with peak frequency $\omega_p = 0.8$ rad/s and correlation coefficient $r_0 = 0.73$ was applied. Again, the smaller value of normalized mean and the most probable maximum wave heights were obtained when compared with the Rayleigh distribution.

Another way to include the correlation of particular sample elements is to impose the Markov chain conditions on the sequence A_1, A_2, \dots, A_N of maxima (Naess, 1984). This means that correlation exists only between neighboring maxima and is zero for further maxima. Epstein (1949) showed that a cumulative distribution function of the largest A value among N consecutive maxima of the Gaussian process $\zeta(t)$ can be presented as:

$$F_{A_{\max}}(A) = \text{Prob}(A_1 \leq A, \dots, A_N \leq A) = \frac{[F_{A_1, A_2}(A, A)]^{N-1}}{F_{A_1}(A)}, \quad (4.200)$$

where:

$$F_{A_1}(A) = \text{Prob}(A_1 \leq A) = 1 - \exp\left(-\frac{1}{2} \frac{A^2}{\sigma_\zeta^2}\right), \quad (4.201)$$

and

$$\begin{aligned} F_{A_1, A_2}(A, A) &= \text{Prob}(A_1 \leq A, A_2 \leq A) = \\ &= 1 - 2 \exp\left(-\frac{A^2}{2\sigma_\zeta^2}\right) + \exp\left\{\frac{-A^2}{[1 + r(\bar{T})] \sigma_\zeta^2}\right\}, \end{aligned} \quad (4.202)$$

in which $r(t) = R(t)/R(0)$ is a normalized autocorrelation function and \bar{T} is a mean wave period. For a sufficiently narrow spectrum it is reasonable to assume that correlation has the same effect on the joint distribution of successive wave heights as it has on the joint distribution of successive maxima. Thus, after changing variables in Eq. (4.200) we obtain:

$$\begin{aligned} F_{\rho_{\max}}(\rho_{\max}) &= 2\rho_{\max} \frac{(N-1)(1-2\eta_1+\eta_2)^{N-2}}{(1-\eta_1)^{N-1}} \cdot \\ &\cdot \left[2(1-\eta_1) \left(\eta_1 - \frac{\eta_2}{1+r(\bar{T})} \right) - \frac{N-2}{N-1} \eta_1 (1-2\eta_1+\eta_2) \right], \end{aligned} \quad (4.203)$$

in which $\rho_{\max} = \frac{H_{\max}}{H_{rms}}$ and:

$$\eta_1(\rho_{\max}) = \exp(-\rho_{\max}^2), \quad \eta_2(\rho_{\max}) = \exp\left(-\frac{2\rho_{\max}^2}{1+r(\bar{T})}\right). \quad (4.204)$$

Using Eq. (4.203), the mean and the most probable extreme wave heights in a given sample have been calculated. The results of such calculations for the mean JONSWAP spectrum ($\gamma = 3.3$) with $r(\bar{T}) \approx 0.5$ are listed in the fifth columns of Tables 4.2 and 4.3. The Markov chain correlation results in extreme values which are smaller than those predicted by the classical Rayleigh distribution. However, the difference is rather small ($\approx 1 \div 2\%$).

The influence of water depth on the probability density function of wave height will be discussed in the next Section. Here we only conclude that in shallow water areas the extreme wave heights are also smaller (see the sixth and seventh columns in Tables 4.2 and 4.3).

An inspection of Tables 4.2 and 4.3 shows that all examined mechanisms provide values of extreme wave heights smaller than those resulting from the Rayleigh distribution. The differences in the mean and in the most probable wave heights usually are small; less than 10%. However, in the case of limited water depth, extreme wave heights are much smaller.

In a real situation of severe sea, many mechanisms mentioned above superimpose and contribute to the final result, which is difficult to predict. The extreme values resulting from the Rayleigh distribution can be regarded as an upper limit of other theoretically predicted or experimentally observed values. The asymptotic distributions of extreme values, when $N \rightarrow \infty$, will be discussed in Chapter 8.

4.3.5 Probability distribution of wave height in finite water depth

In Section 4.2.5 it was shown that the probability distribution of the surface displacement ζ in finite water depth, and especially in shallow water areas, is not Gaussian. The sea bottom imposes extra constraints on wave motion, which departs further from the simple linear superposition model. Although the sea surface is very asymmetric about the still water level and the vertical lines passing through the wave crests, the influence of the nonlinear motion is not so strong. This conclusion is in agreement with Thornton and Guza's experimental data (1983), which showed that wave height, even within the surf zone, is reasonably well described by the Rayleigh distribution, which contradicts the findings of Bitner (1978, 1980) under similar conditions. Bitner used the distribution (4.138) based on two-dimensional Hermite polynomials. The agreement with experiments is not particularly good, perhaps because of data sparsity and possible breaking over the underwater bars.

Basically we can use the Rayleigh distribution or its modifications given in Section 4.3.2, to describe the wave height distribution in finite water depth. However, none of these distributions explicitly contain the water depth as a parameter, for they were developed mostly for deep water.

Glukhovskiy (1966) has developed an extension of the Rayleigh distribution for finite water depth in the form:

$$f(H) = \frac{b}{\bar{H}} \left(\frac{H}{\bar{H}} \right)^{\frac{1+n}{1-n}} \exp \left[-a \left(\frac{H}{\bar{H}} \right)^{\frac{2}{1-n}} \right], \quad (4.205)$$

in which:

$$a = \frac{\pi}{4 \left(1 + \frac{n}{\sqrt{2\pi}} \right)}; \quad b = \frac{2a}{1-n}. \quad (4.206)$$

The coefficient n is a ratio of mean wave height and water depth and ranges from 0 to 0.5. When $n = 0$ (deep water), the Glukhovskiy distribution coincides with the Rayleigh distribution (4.124). The upper limit, $n = 0.5$, corresponds to the offshore limit of the surf zone when the probability density function becomes:

$$f(H) = \frac{4a_1}{\bar{H}} \left(\frac{H}{\bar{H}} \right)^3 \exp \left[-a_1 \left(\frac{H}{\bar{H}} \right)^4 \right], \quad (4.207)$$

$$\text{where: } a_1 = \frac{(2\pi)^{3/2}}{4(1 + 2\sqrt{2\pi})} \approx 0.654.$$

Let us now normalize the probability distribution (4.205) using the root-mean-square wave height H_{rms} . Hence, we have:

$$H_{rms}^2 = \int_0^\infty H^2 f(H) dH, \quad (4.208)$$

or:

$$H_{rms} = \gamma \bar{H}, \quad (4.209)$$

where:

$$\gamma = \left\{ b \int_0^\infty x^{\frac{3-n}{1-n}} \exp \left(-a x^{\frac{2}{1-n}} \right) dx \right\}^{1/2}, \quad (4.210)$$

or:

$$\gamma = \left\{ b \int_0^\infty x^{\alpha+1} \exp(-a x^\alpha) dx \right\}^{1/2}, \quad (4.211)$$

in which $\alpha = \frac{1}{1-n}$. After integrating in Eq. (4.208) we obtain (Gradshteyn and Ryzhik, 1980):

$$\gamma = \left[\frac{b}{\alpha} a^{-(1+\frac{2}{\alpha})} \Gamma \left(1 + \frac{2}{\alpha} \right) \right]^{1/2}, \quad (4.212)$$

in which $\Gamma(\cdot)$ is a gamma function. For $n = 0$, $\gamma = \frac{2}{\sqrt{\pi}} \approx 1.1284$, while for $n = 0.5$ Eq. (4.212) yields $\gamma \approx 1.047$.

Substituting Eqs. (4.209) and (4.212) into Eq. (4.205) gives the probability density function for normalized wave height $\xi = \frac{H}{H_{rms}}$ in the form:

$$f(\xi) = b\gamma^\alpha \xi^{\alpha-1} \exp[-a\gamma^\alpha \xi^\alpha]. \quad (4.213)$$

The probability density function $f(\xi)$ is given in Fig. 4.21 for parameter n varying from 0 to 0.5 at a step of 0.1. In two limiting cases the function (4.213) simplifies:

for $n = 0$ (deep water):

$$f(\xi) = 2\xi \exp(-\xi^2), \quad (4.214)$$

and for $n = 0.5$ (offshore of surf zone):

$$f(\xi) = \pi a_1 \xi^3 \exp\left(-\frac{\pi a_1}{4} \xi^4\right), \quad (4.215)$$

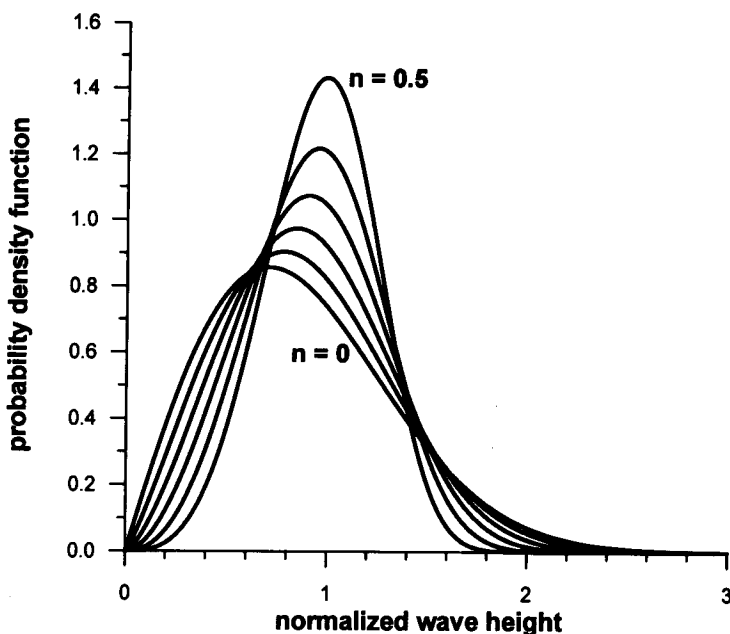


Figure 4.21: The Glukhovskiy's probability density function for n ranging from 0 to 0.5 at a step 0.1.

Table 4.4: Characteristic wave heights for Glukhovskiy's distribution

n	H_{rms}/\bar{H}	H_s/H_{rms}	H_s/\bar{H}
0.0	1.1284	1.4213	1.601
0.1	1.1127	1.4067	1.565
0.2	1.0961	1.3730	1.505
0.3	1.0792	1.3530	1.460
0.4	1.0625	1.3174	1.400
0.5	1.0465	1.2572	1.316

or:

$$f(\xi) = 2.055\xi^3 \exp(-0.514\xi^4). \quad (4.216)$$

The distribution is thus, more symmetric and narrow if the water depth decreases. Moreover, the most probable wave height shifts towards higher values. In Table 4.4, some characteristic wave heights are listed for parameter n varying from 0 to 0.5. All ratios, namely $\left(\frac{H_{rms}}{\bar{H}}\right)$, $\left(\frac{\bar{H}_s}{H_{rms}}\right)$ and $\left(\frac{H_s}{\bar{H}}\right)$ decrease with n (i.e. as waves approach the surf zone). Due to narrowing of the probability density $f(\xi)$, the dependence of the characteristic values on parameter n also weakens.

The normalized mean and the most probable maximum wave height based on the Glukhovskiy distribution are included in Tables 4.2 and 4.3 for $n = 0.25$ and $n = 0.5$.

In fact the Glukhovskiy distribution is very similar to another distribution which is frequently used in engineering and oceanography, i.e. the Weibull distribution (Massel, 1989; Ochi, 1990) developed on empirical grounds:

$$f(\xi) = \frac{\alpha}{\beta} \xi^{\alpha-1} \exp\left(-\frac{\xi^\alpha}{\beta}\right), \quad (4.217)$$

where ξ is normalized wave height; α and β are the distribution parameters. If $\xi = H/\sigma_\zeta$, $\alpha = 2$, and $\beta = 8$, Eq. (4.217) is identical with the Rayleigh distribution (4.119). The distribution (4.217) is frequently used for fitting experimental data. For example, Forristall (1978), on the basis of deep water data from the Gulf of Mexico, estimated the coefficients α and β as 2.13 and 8.42, respectively. The best fit of shallow water data ($h = 7.5$ m) from the Baltic Sea provides α and β values of 1.995 and 6.684.

More details on shallow water wave statistics can be found in other papers (Massel, 1985, 1989; Massel and Robakiewicz, 1986; Massel et al., 1990).

4.3.6 Probability distribution of wave height in a surf zone

Prediction of wave climate in the surf zone of natural beaches presents many challenges, mostly due to the complicated process of energy dissipation and the variability of parameters of waves approaching the shoreline. The prediction of spectral energy variation in a surf zone is discussed in Chapter 6. In this Section we concentrate on prediction of the transformation of the probability density function $f(H)$ across the surf zone, starting with a known $f(H)$ function at some offshore location.

Deep water wave heights are first transformed into shallow water using the shoaling theory in which all energy losses are neglected. The near shore unbroken wave height distribution is calculated using the local Rayleigh distribution:

$$f(H) = \frac{2H}{(K_s H_{rmsi})^2} \exp \left[- \left(\frac{H}{K_s H_{rmsi}} \right)^2 \right], \quad (4.218)$$

where K_s is a shoaling coefficient and H_{rmsi} is the deep water root-mean-square wave height.

Eventually, the waves reach such shallow water that they start to break, with the largest waves breaking farthest offshore. Attempts to model the transformation of probability density are complicated by the existence of both breaking and non-breaking waves at any location in the surf zone. In the first models, the wave breaking is simulated by truncating the tail of the Rayleigh distribution (4.218) using various breaking criteria. The broken waves are required to have the same height H_b and their representation in the probability domain is the Dirac delta function at H_b (Collins, 1970; Battjes, 1972a). Collins used the linear shoaling theory and the breaking criterion after Le Mehaute and Koh (1967), i.e.:

$$\frac{H_b}{H_{rms0}} = 0.76 \beta^{1/7} \left(\frac{H_{rms0}}{L_0} \right)^{-1/4}, \quad (4.219)$$

in which β is a bottom slope and L_0 is a deep water wavelength, while Battjes applied the breaking criterion based on the Miche (1944) formula:

$$H_b = \frac{0.88}{k} \tanh \left(\frac{\gamma}{0.88} kh \right). \quad (4.220)$$

In shallow water ($kh \rightarrow 0$), Eq. (4.220) is simplified as:

$$H_b = \gamma h, \quad (4.221)$$

where γ is a proportionality coefficient at incipient breaking.

Kuo and Kuo (1974) eliminated the delta function type spike in the Collins distribution, redistributing the area under the spike across the range of heights in proportion to the probability of unbroken waves at each height, i.e.:

$$f(H) = \begin{cases} f_0(H) \left[\int_0^{H_b} f_0(H) dH \right]^{-1}, & 0 \leq H \leq H_b \\ 0, & H > H_b. \end{cases} \quad (4.222)$$

However, the sharp cutoff at H_b is still nonphysical.

In the Goda (1975) model, instead of the sharp cutoff, a more gradual (linear) attenuation of wave height distribution $f(H)$ across the upper range of heights, before normalization, was assumed. Goda applied a breaker criterion based on laboratory data which takes into account bottom slope and wave steepness in deep water H_d/H_0 , i.e.:

$$\frac{H_b}{H_0} = A \frac{L_0}{H_0} \left\{ 1 - \exp \left[-1.5 \frac{h}{L_0} (1 + K\beta^s) \right] \right\}, \quad (4.223)$$

in which β is a bottom slope, $A = (0.12 \div 0.18)$, $K = 15$ and $s = \frac{4}{3}$.

Seelig (1980) used the Goda theory to calculate the maximum wave heights and critical water depth. He defined the H_{smax} value as the peak value of significant wave height and the H_{1max} value, which is the average of the highest 1% of the waves, as the height with an exceedance probability of approximately $\frac{1}{260}$. The Goda model predicts that the peak value of H_1 occurs just seaward of H_{smax} . The peak wave heights decrease as the wave steepness increases and the beach slope becomes flatter (Seelig, 1980; Massel, 1989).

In a more sophisticated approach, Battjes and Janssen (1978) also used the probability distribution shape of Collins (1970), but applied the energy flux balance to calculate the wave height rather than the transformation of the $f(H)$ function. Their model will be considered in Chapter 6.

Modification of the Rayleigh distribution

To describe the random nature of wave height in the surf zone Thornton and Guza (1983) adopted the unmodified Rayleigh distribution, with the contribution of the breaking waves population defined by an empirical constant based on the locally measured H_{rms} value. A weighting of the Rayleigh distribution for all waves is assumed in the form:

$$f_{br}(H) = W(H)f(H), \quad (4.224)$$

in which $f(H)$ is the Rayleigh distribution (4.218) and the weighting function $W(H) \leq 1$. Distribution $f_{br}(H)$ is a subset of the distribution $f(H)$ for all waves, breaking and non-breaking. This means that the area under the distribution is equal to the percentage of breaking waves, i.e.:

$$A_{br} = \int_0^\infty f_{br}(H) dH, \quad (4.225)$$

in which $0 \leq A_{br} \leq 1$.

The simplest hypothesis is that the waves break in proportion to the distribution for all waves:

$$W(H) = A_b = \left(\frac{H_{rms}}{\gamma h} \right)^n. \quad (4.226)$$

As A_b is constant, the likelihood of a wave breaking is independent of its height. However, observations indicate that the largest waves are more likely to break and a greater proportion of the larger waves contribute to the breaking wave distribution. This is reflected in a modified weighting function $W(H)$ as:

$$W(H) = \left(\frac{H_{rms}}{\gamma h} \right)^n \left\{ 1 - \exp \left[- \left(\frac{H}{\gamma h} \right)^2 \right] \right\} \leq 1. \quad (4.227)$$

A comparison of Eq. (4.224), using Eq. (4.226) with $n = 2$ and 4, and Eq. (4.227) ($n = 2$) with the field measurements showed that only a small percentage of waves are predicted to break until about $\frac{H_{rms}}{\gamma h} \approx \frac{1}{2}$. After that, the waves quickly reach saturation, when all waves are breaking, i.e. $\frac{H_{rms}}{\gamma h} \approx 1$. The best fit to observations, made at Soldiers Beach in California, was obtained for $n = 4$ in Eq. (4.226) or Eq. (4.227).

A common feature of all the models mentioned above is that the basic shape for the probability distribution $f(H)$ is assumed *a priori*. Then, a single characteristic wave height (root-mean-square or significant values), representing the distribution, is transformed using the linear wave theory. Thus, the transformation of individual waves, which determines the transformation of the $f(H)$ function, is not treated in these models.

Transformation of probability distribution

The field measurements of Ebersole and Hughes (1987) and Antsyferov et al. (1990) showed that the basic shape of the distribution $f(H)$ changes significantly across the surf zone. The most recent models of transformation of the probability density function $f(H)$ across the surf zone are based on the assumption that in that zone random waves behave as a collection of individual regular waves (Dally, 1990). At a location well seaward of the surf zone, it is assumed that the Rayleigh distribution is valid. Thus:

$$f_{in}(H_i) = \frac{2H_i}{H_{rmsi}} \exp \left[- \left(\frac{H_i}{H_{rmsi}} \right)^2 \right], \quad (4.228)$$

where subscript (*in*) denotes the initial probability distribution.

The local distribution in shoaling water, as defined by Eq. (4.218), can be found by applying some wave transformation theories. The simplest one is the linear shallow water theory. The resulting shoaling for a planar beach is given by Green's law (Massel, 1989):

$$\frac{H}{H_i} = \left(\frac{h}{h_i} \right)^{-1/4}. \quad (4.229)$$

After a standard transformation of variables, i.e.:

$$f_{sh}(H; h) = f_{in}(H_i) \left| \frac{\partial H_i}{\partial H} \right|, \quad (4.230)$$

Eq. (4.228) yields (Dally, 1990):

$$f_{sh}(H; h) = \left(\frac{2H}{H_{rmsi}^2} \right) \left(\frac{h}{h_i} \right)^{1/2} \exp \left[- \left(\frac{H_i}{H_{rmsi}} \right)^2 \left(\frac{h}{h_i} \right)^{1/2} \right], \quad (4.231)$$

and after normalization, Eq. (4.231) becomes:

$$f_{sh}(\xi) = 2\xi \tilde{h}^{1/2} \exp \left[-\tilde{h}^{1/2} \xi^2 \right] \quad \text{for } \xi < \frac{\gamma h_b}{H_{rmsi}}, \quad (4.232)$$

in which $\xi = \frac{H}{H_{rmsi}}$ and $\tilde{h} = \frac{h}{h_i}$.

The distribution (4.232) is valid for unbroken waves. Therefore, it must be truncated at the wave height $\xi_b = \frac{\gamma h_b}{H_{rmsi}} = \gamma \tilde{h} \left(\frac{H_{rmsi}}{h_i} \right)^{-1}$, i.e. at the highest unbroken wave that occurs at the local water depth.

The incipient breaking coefficient γ depends on deep water wave steepness as well as beach slope. Any of several available empirical formulas would be appropriate, but following Dally (1990) we express γ as follows:

$$\gamma = b(\beta) - 0.0827 a(\beta) \chi_0^{4/5}, \quad (4.233)$$

where:

$$a(\beta) = 43.8 [1.0 - \exp(-19\beta)], \quad (4.234)$$

$$b(\beta) = \frac{1.56}{1.0 - \exp(-19.5\beta)}, \quad (4.235)$$

in which β is a bottom slope and χ_0 is deep water steepness, equal to $\frac{H_0}{L_0}$, where H_0 and L_0 are deepwater height and wave length, respectively.

The distribution (4.232) is illustrated in Fig. 4.22 for $\tilde{h} = 0.1, 0.3$ and 0.5 . The incipient breaking coefficient $\gamma = 0.93$ for $\beta = 1/20$ and deep water steepness $\chi_0 = 0.05$. The value $\frac{H_{rmsi}}{h_i}$ was assumed to be equal to 0.2 .

As waves start to break, the turbulent dissipation of wave energy is the dominant dissipation mechanism, and breaking processes dominate wave transformation. However, in contrast to monochromatic waves, there is no well-defined breakpoint for random waves. Because of the randomness of waves, the occurrence of breaking at a fixed location is itself a random process characterized by the probability density

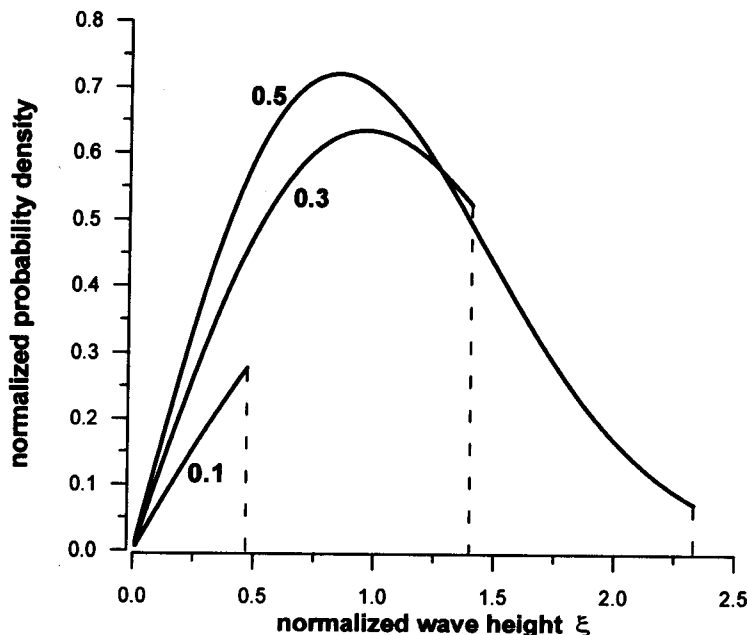


Figure 4.22: Probability density function for shoaling waves versus non-dimensional wave height $\tilde{h} = 0.1, 0.3, 0.5$.

function of water depth h_b , at which incipient breaking is attained. Applying Green's law (4.229) for a planar beach we can write:

$$H_i = H_b \left(\frac{h_b}{h_i} \right)^{1/4} = \gamma h_b^{5/4} h_i^{-1/4}, \quad (4.236)$$

and

$$f_{hb}(h_b) = f(H_i) \left| \frac{\partial H_i}{\partial h_b} \right|. \quad (4.237)$$

Hence:

$$f_{hb}(\tilde{h}_b) = \frac{5}{2} \gamma^2 \left(\frac{H_{rmsi}}{h_i} \right)^{-2} (\tilde{h}_b)^{3/2} \exp \left[-\gamma^2 \left(\frac{H_{rmsi}}{h_i} \right)^{-2} (\tilde{h}_b)^{5/2} \right], \quad (4.238)$$

in which $\tilde{h}_b = \frac{h_b}{h_i}$.

The resulting most probable depth, at which the incipient breaking is attained, is given by:

$$\left(\frac{h_b}{h_i} \right)_{most \ prob.} = \left[\frac{3}{5\gamma^2} \left(\frac{H_{rmsi}}{h_i} \right)^2 \right]^{2/5}. \quad (4.239)$$

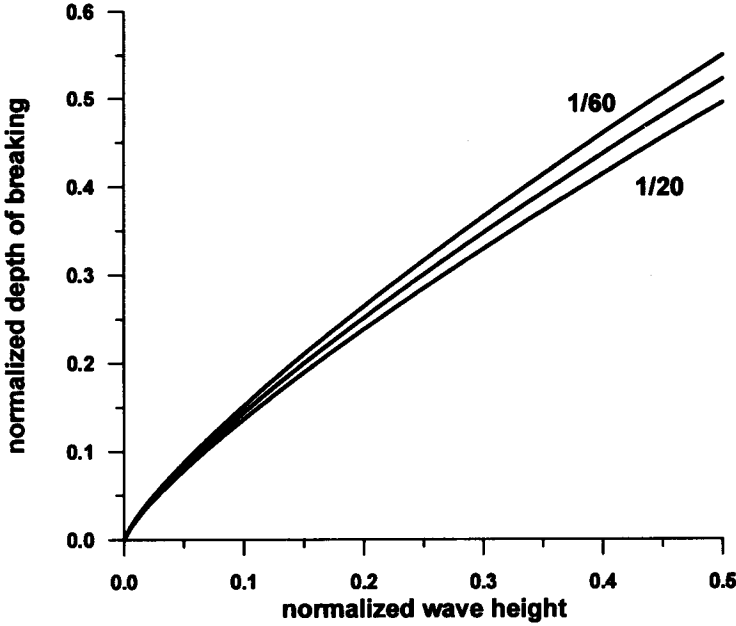


Figure 4.23: The most probable water depth at which the incipient breaking is attained.

Eq. (4.239) is presented in Fig. 4.23 as a function of $\left(\frac{H_{rmsi}}{h_i}\right)$ for three different bottom slopes 1/20, 1/30 and 1/60. The deep water steepness was assumed as 0.05.

Let us now evaluate the contribution of broken waves to the probability density function $f(H)$ at particular points in the surf zone. Under the assumption that, in the surf zone, random waves behave as a collection of individual regular waves, the transformation from water depth h_b to wave height H , provides the portion of the probability density $f(H)$ due to broken waves as:

$$f_{br}(H) = f_{h_b}(\tilde{h}_b) \left| \frac{\partial \tilde{h}_b}{\partial H} \right| = f_{h_b}(\tilde{h}_b) \left(\frac{\partial \tilde{h}_b}{\partial \xi} \right) \frac{1}{H_{rmsi}}. \quad (4.240)$$

According to Dally's et al. (1985) analytical solution, the attenuation of regular wave heights on a planar beach is given by:

$$\frac{H}{h_b} = \left[\left(\gamma^2 + \alpha_* \right) \left(\frac{h}{h_b} \right)^{\left(\frac{K}{\beta} - \frac{1}{2} \right)} - \alpha_* \left(\frac{h}{h_b} \right)^2 \right]^{1/2}, \quad (4.241)$$

where:

$$\alpha_* = \frac{\left(\frac{K}{\beta}\right) \Gamma^2}{\left(\frac{5}{2} - \frac{K}{\beta}\right)}. \quad (4.242)$$

The recommended coefficients are $K = 0.17$ and $\Gamma = 0.5$. Note that for lower values of γ and steeper slopes, the decay profiles are convex in shape. When $\alpha_* = -\gamma^2$, the profiles are linear, otherwise they are concave.

Solving Eq. (4.241) for h_b we obtain:

$$\tilde{h}_b = \tilde{h} F^r(\xi), \quad (4.243)$$

where:

$$F(\xi) = \left[\frac{\xi^2 \left(\frac{H_{rmsi}}{h_i} \right)^2 \tilde{h}^{-2} + \alpha_*}{\gamma^2 + \alpha_*} \right], \quad (4.244)$$

and

$$r = \left(\frac{5}{2} - \frac{K}{\beta} \right)^{-1}. \quad (4.245)$$

After differentiation of Eq. (4.243) against ξ and substitution into Eq. (4.240), we obtain a portion of the probability density function due to broken waves in the form:

$$f_{br}(\xi)_{br} = \frac{5\gamma^2}{\gamma^2 + \alpha_*} r \tilde{h}^{1/2} F^{\frac{5}{2}r-1} \exp \left\{ -\gamma^2 \left(\frac{H_{rmsi}}{h_i} \right)^{-2} \tilde{h}^{5/2} F^{5r/2} \right\}, \quad (4.246)$$

for

$$\xi_b \leq \xi \leq \frac{H_{rmsi}}{h_i} \leq \xi_{bm}, \quad (4.247)$$

in which ξ_{bm} is the highest normalized non-breaking wave height.

The closed form of the probability density function facilitates the calculation of the proportion of waves that are breaking, i.e.:

$$N_{br} = 1 - \int_0^{\xi_b} f_{sh}(\xi) d\xi. \quad (4.248)$$

After substituting Eq. (4.232) into Eq. (4.248) and integrating, we obtain:

$$N_{br} = \exp \left[-\tilde{h}^{1/2} \xi_b \right], \quad (4.249)$$

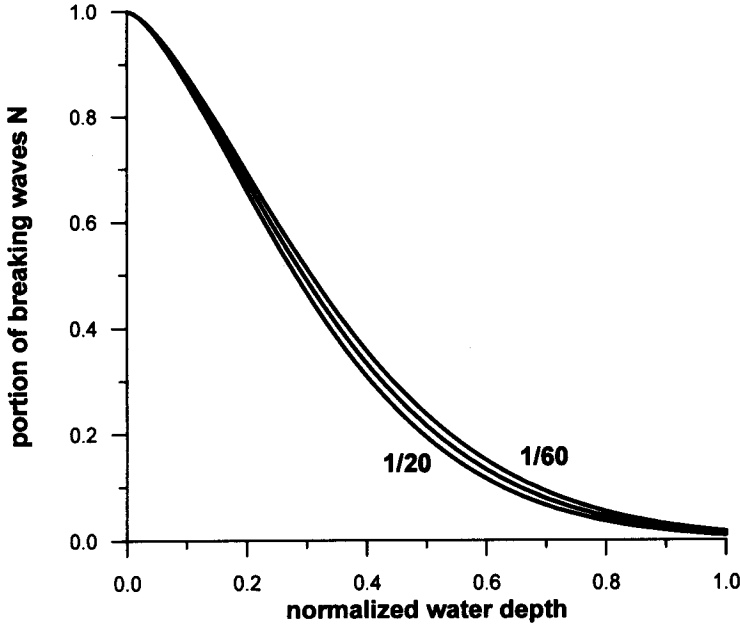


Figure 4.24: Portion of breaking waves N_{br} for three different slopes.

where $\xi_b = \frac{\gamma h}{H_{rmsi}} = \gamma \tilde{h} \left(\frac{H_{rmsi}}{h_i} \right)^{-1}$. Thus, Eq. (4.249) yields:

$$N_{br} = \exp \left[-\gamma \left(\frac{H_{rmsi}}{h_i} \right)^{-1} \tilde{h}^{3/2} \right]. \quad (4.250)$$

The portion N_{br} of breaking waves N_{br} is shown in Fig. 4.24 for three different slopes (1/20, 1/30, 1/60) and for $H_{rmsi}/h_i = 0.2$.

The characteristic wave heights, i.e. the dimensionless average wave height $\bar{\xi} = \frac{\bar{H}}{H_{rmsi}}$ and the dimensionless root-mean-square wave height $\xi_{rms} = \frac{H_{rms}}{H_{rmsi}}$ can be calculated by numerical integration of the probability density function, i.e.:

$$\bar{\xi} = \int_0^{\xi_b} \xi f_{sh}(\xi) d\xi + \int_{\xi_b}^{\xi_{bm}} \xi f_{br}(\xi) d\xi, \quad (4.251)$$

and

$$\xi_{rms} = \int_0^{\xi_b} \xi^2 f_{sh}(\xi) d\xi + \int_{\xi_b}^{\xi_{bm}} \xi^2 f_{br}(\xi) d\xi. \quad (4.252)$$

Comparisons of the solution with field experiments (for example, DUCK'85) demonstrates the model's ability to reproduce changes in shape of the histogram within the surf zone. The greatest effect on the shape of the probability density function is due to breaking intensity and bottom slope.

4.4 Wave period

In contrast to wave height distributions, limited attention has been directed to the distribution of wave periods and the joint distribution of wave height and period. However, a knowledge of these distributions is of interest to oceanographers and engineers. The design of structures in the marine environment, and their construction and maintenance require a reliable estimate of the probability distribution of wave periods and joint distributions of periods and wave heights. These distributions are also used to evaluate other distributions, such as the joint distribution of wave height and wave slope which are related to wave breaking and the occurrence of whitecapping.

In the next Section, the distribution of wave period is developed as a marginal distribution of the joint probability distribution of wave height and period.

4.4.1 Joint distribution of wave heights and periods

The papers by Rice (1944, 1945), on Gaussian random noise, provide the basis for all the existing joint probability distributions of heights and periods. The joint distributions of wave heights and periods vary depending on the assumptions adopted and techniques used.

Longuet-Higgins (1975, 1983) defined a wave period as the time interval between successive zero-upcrossings, and the corresponding wave height as the difference between the maximum and minimum within the time interval. The distributions are applicable to a narrow spectrum when the bandwidth parameter $\nu^2 \leq 0.36$. Longuet-Higgins' (1983) joint distribution (which is a modification of his version from 1975), for non-dimensional variables $\xi = H/\sqrt{m_0}$ and $\tau = T/\bar{T}$ (\bar{T} is a spectral mean period associated with mean frequency, i.e. $\bar{T} = 2\pi m_0/m_1$), takes the form:

$$f_2(\xi, \tau) = C_L \left(\frac{\xi}{\tau} \right)^2 \exp \left\{ -\frac{\xi^2}{8} \left[1 + \frac{1}{\nu^2} \left(1 - \frac{1}{\tau} \right)^2 \right] \right\}, \quad (4.253)$$

where:

$$C_L = \frac{1}{4\sqrt{2\pi\nu} \left[1 + (1 + \nu^2)^{-1/2} \right]}, \quad (4.254)$$

and the bandwidth parameter ν is given by Eq. (3.8).

The contours of $f_2(\xi, \tau)$ for $\nu = 0.2$ and $\nu = 0.6$ are plotted in Fig. 4.25. For

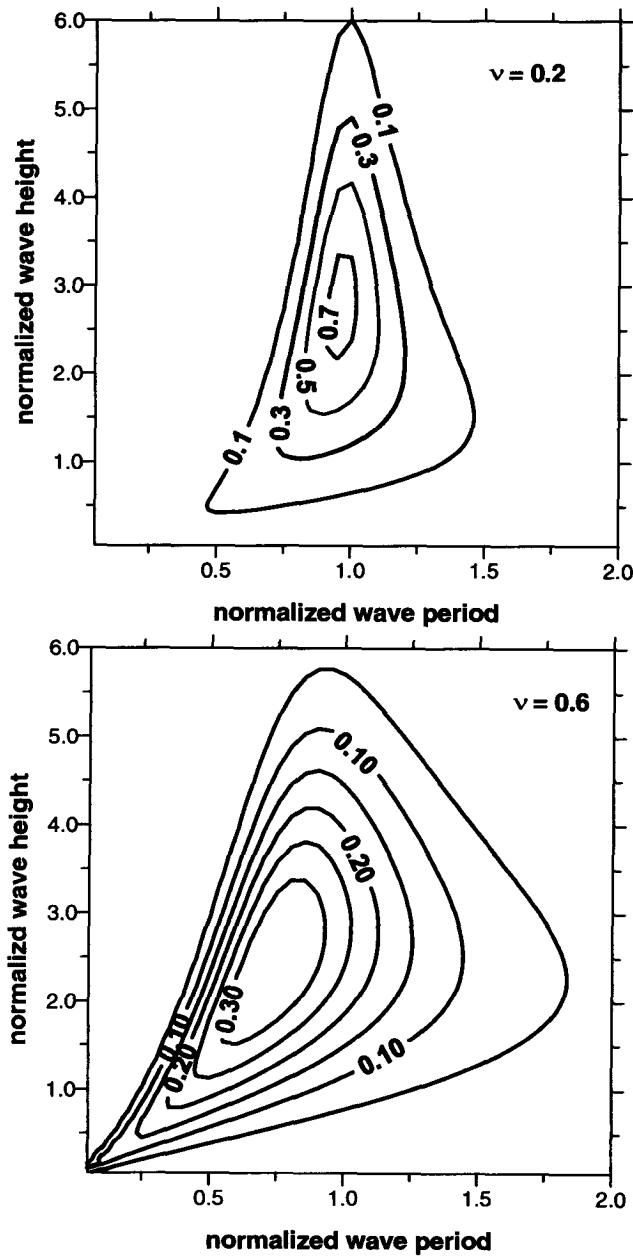


Figure 4.25: Contours of probability density $f_2(\xi, \tau)$ for $\nu = 0.2$ and 0.6 .

small ν the distribution is symmetric with respect to $\tau = 1$. In the limit as $\nu \rightarrow 0$, Eq. (4.253) reduces to:

$$f_2(\xi, \tau) = \frac{1}{8\sqrt{2\pi\nu}} \xi^2 \exp \left\{ -\frac{\xi^2}{8} \left[1 + \left(\frac{\tau-1}{\nu} \right)^2 \right] \right\}, \quad (4.255)$$

which is the joint distribution proposed by Longuet-Higgins (1975). When ν value increases, the density shows asymmetry with respect to τ . We note that the position of the maximum of $f_2(\xi, \tau)$ is given by:

$$\xi = \frac{2\sqrt{2}}{\sqrt{1+\nu^2}}, \quad \tau = \frac{1}{1+\nu^2}, \quad (4.256)$$

and the value of $f_2(\xi, \tau)$ at this point is:

$$[f_2(\xi, \tau)]_{max} = \frac{8C_L}{e} (1+\nu^2), \quad (4.257)$$

in which $e = 2.71828$. Therefore, the most probable pair of wave height and period is $(H = 2.773\sqrt{m_0}, T = 0.961\bar{T})$ for $\nu = 0.2$ and $(H = 2.425\sqrt{m_0}, T = 0.735\bar{T})$ for $\nu = 0.6$.

Cavanie et al. (1976) proposed the joint distribution which is based on the triple probability density $f_3(\zeta, \dot{\zeta}, \ddot{\zeta})$. After transformation of variables, this distribution becomes:

$$f_2(\xi, \tau) = C_{CA} \frac{\xi^2}{\tau^5} \exp \left\{ -\frac{\xi^2}{8\epsilon^2\tau^4} \left[\left(\tau^2 - \left(\frac{1-\epsilon^2}{1+\nu^2} \right) \right)^2 + \beta^2 \left(\frac{1-\epsilon^2}{1+\nu^2} \right) \right] \right\}, \quad (4.258)$$

in which $C_{CA} = \frac{1}{4} (1-\epsilon^2) (2\pi)^{-1/2} \epsilon^{-1} \alpha^{-1} (1+\nu^2)^{-2}$, $\alpha = [1 + (1-\epsilon^2)^{1/2}]/2$ and $\beta = \epsilon/(1-\epsilon^2)^{1/2}$. The distribution depends on two spectral bandwidth parameters ν and ϵ . However, after changing the scaling for the period, it can be shown that the distribution is in fact dependent only on parameter ϵ , as was given in the original paper by Cavanie et al. (1976). The representation of the joint distribution in the form (4.258) facilitates the comparison with the Longuet-Higgins distribution, as in both distributions, (4.253) and (4.258), the wave period is scaled in the same way.

Srokosz and Challenor (1987) examined the applicability of the joint distributions (4.253) and (4.258) using approximately stationary but continuous record sequences of duration up to 12 hr from the wave rider buoy off the Scilly Isles ($49^\circ 55'N, 6^\circ 37'W$). The comparison suggests that in the narrow-band case, the Longuet-Higgins distribution adequately represents the joint distribution of zero-upcrossing height and period, while Cavanie's distribution does the same for the joint distribution of crest-to-trough height and period.

It should be mentioned that the most accurate representation of the distribution of crest-to-trough height and period was obtained using Lindgren's distribution (Lindgren and Rychlik, 1982). This distribution is based on properties of a normal

process near a local maximum. Wave height is defined using the wave crest-to-trough definition (used by Cavanie et al. (1976)). However, the wave period is defined by the time between a maximum and the succeeding minimum, i.e. it is approximately one half of the period used by Cavanie et al. Lindgren's distribution depends not just on the two parameters ν and ϵ but on the entire covariance function and its first four derivatives, which should be estimated from the spectrum obtained from the data. Due to the extensive computation involved, Lindgren's distribution is too complex to use for engineering design purposes.

It should be noted that Memos (1994) recently developed a set of differential equations for the probability density function of wave height and period particularly suitable for wide-band spectra.

When comparing any theoretical distribution with the field observations, the long data records with sufficient resolution are needed. The standard 20 min wave record, which typically contains a little over 100 waves, is clearly insufficient. On the other hand, a much longer record introduces concerns regarding the stationarity and homogeneity of the data.

In order to overcome these difficulties and uncertainties, a third type of the joint probability density distribution can be considered, i.e. joint distribution predicted from random simulation (Sobey, 1992a). The theoretical basis of this methodology is the Gaussian random wave model of an irregular sea state. The method avoids an adoption of compromising assumptions on wave amplitudes and periods. Using this methodology it has been showed that the spectral shape appears to dominate the detail of predicted joint distributions. For JONSWAP spectra, a distinct bimodal structure of the joint distribution is observed. While the wave height distributions for JONSWAP spectra differ little from the Rayleigh distribution, the period distributions are strongly sensitive to spectral shape.

The application of Longuet-Higgins (1983) joint distribution to the shoaling region was considered by Doering and Donelan (1993) using laboratory data collected on 1/40 and 1/20 planar beach slopes. Comparison between the data and Longuet-Higgins (1983) joint distribution indicates that it gives a reasonable fit provided $h/L > 0.1$ (L is a wavelength corresponding to spectral peak frequency). However, the observed distribution is shifted slightly in both height and period. This shift is correlated with the spectral width parameter ν . The parameter ν was found to be strongly correlated with Ursell parameter U_r :

$$U_r = \frac{3}{4} \frac{ak}{(kh)^3}. \quad (4.259)$$

The parameterization of ν using Ursell parameter U_r is of considerable practical importance because it provides a simple method for predicting the joint distribution of wave heights and periods in a shoaling region by adopting the deep water distribution of Longuet-Higgins (1983).

4.4.2 Probability distribution of wave period

The probability density function of period T , regardless of wave height H , is found by integrating $f_2(\xi, \tau)$ with respect to ξ over $0 < \xi < \infty$. Using the Longuet-Higgins distribution (4.253) we obtain:

$$f(\tau) = \frac{4\sqrt{2\pi}C_L}{\tau^2} \left[1 + \frac{1}{\nu^2} \left(1 - \frac{1}{\tau} \right)^2 \right]^{-3/2}. \quad (4.260)$$

Function (4.260) is shown in Fig. 4.26 for some representative values of ν .

The distribution is asymmetric in accordance with observations. It depends on the three lowest moments m_0, m_1, m_2 of the spectral density function (through spectral width parameter ν). The mode of the distribution decreases with ν as:

$$\tau_m = \frac{2}{\sqrt{9 + 8\nu^2} - 1}. \quad (4.261)$$

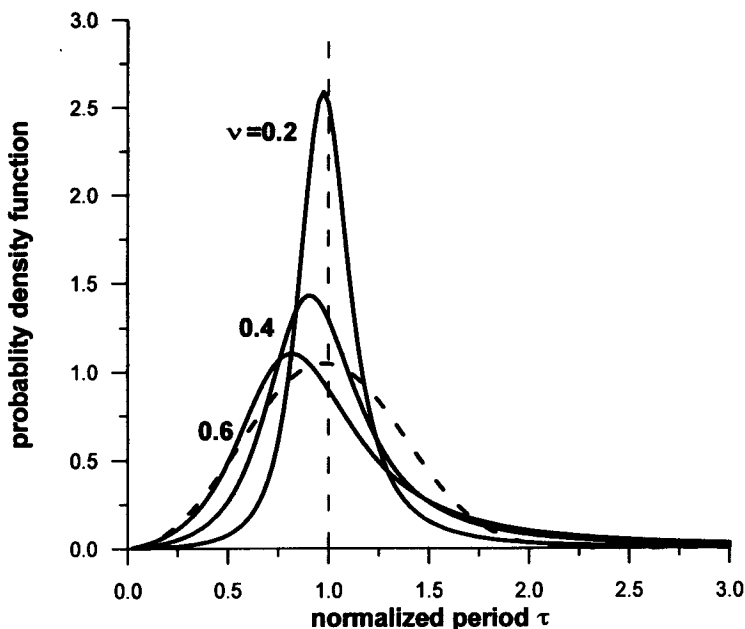


Figure 4.26: Probability density function of wave period for $\nu = 0.2, 0.4$ and 0.6 (—); distribution according to Davidan et al., 1985 (---).

Note that the mean of the distribution is theoretically infinite, since for large values of τ the density $f(\tau)$ behaves like τ^{-2} . However, using the exact value of the average frequency of up-crossings of the mean level, it can be found that mean zero-crossing wave period \bar{T}_0 is:

$$\bar{T}_0 = \frac{\bar{T}}{\sqrt{1 + \nu^2}} = 2\pi \sqrt{\frac{m_0}{m_2}}, \quad (4.262)$$

in which:

$$\bar{T} = 2\pi \frac{m_0}{m_1}, \quad (4.263)$$

is the mean wave period. For comparison, in Figure 4.26 the empirical distribution proposed by Davidan et al. (1978, 1985) was shown:

$$f(\tau) = 3A \tau^2 \exp(-A\tau^3), \quad (4.264)$$

in which $A = \Gamma^3\left(\frac{4}{3}\right) \approx 0.712$. The distribution based on the large set of data, is included in the Russian oceanographic tables.

Eq. (4.260) is a probability density function of wave period, regardless of wave height. If wave height is given, the probability distribution function of associated periods is the conditional density function $f(\tau/\xi)$:

$$f(\tau | \xi) = \frac{f_2(\xi, \tau)}{f(\xi)}. \quad (4.265)$$

After substituting Eq. (4.253) we obtain:

$$f(\tau | \xi) = \frac{\xi}{2\sqrt{2\pi}\nu\tau^2 \Phi\left(\frac{\xi}{2\nu}\right)} \exp\left[-\frac{\xi^2}{8\nu^2}\left(1 - \frac{1}{\tau}\right)^2\right], \quad (4.266)$$

in which $\Phi(z)$ is given by Eq. (4.53).

The most probable wave period, associated with a given wave height, results from the condition $\partial f/\partial \tau = 0$, i.e.:

$$\tau_m = \frac{2}{1 + \sqrt{1 + \frac{32\nu^2}{\xi^2}}}. \quad (4.267)$$

For large ξ , the most probable wave period asymptotically approaches the value $\tau = 1$ ($T = \bar{T}$). On the other hand, for small ξ we have $\tau \approx \xi/2\sqrt{2}\nu$.

The conditional probability density of wave period associated with large wave heights ($\xi > \sqrt{2\pi}$) was derived by Tayfun (1993), assuming that $0 < \tau < 2$; i.e.:

$$f(\tau | \xi) = C_1 \exp\left[-\frac{1}{2}\left(\frac{\tau - \tau_m}{\sigma_{\tau|\xi}}\right)^2\right], \quad (4.268)$$

in which:

$$\tau_m = 1 + \frac{\nu^2}{(1 + \nu^2)^{3/2}}, \quad (4.269)$$

$$\sigma_{\tau|\xi} = \frac{2\nu}{\xi} \frac{1}{1 + \nu^2}, \quad (4.270)$$

for large ξ . Coefficient C_1 results from normalization:

$$\int_0^2 f(\tau | \xi) d\tau = 1. \quad (4.271)$$

The distribution (4.268) compares well with simulated data (Tayfun, 1993).

Combining Eqs. (4.164) and (4.268), the joint probability density distribution of large wave heights and associated periods (for $\xi > \sqrt{2\pi}$, $0 < \tau < 2$) takes the form:

$$f_2(\xi, \tau) \approx C \left(1 + \frac{1 - r_0^2}{4r_0\xi^2} \right) \exp \left\{ -\frac{1}{2} \left[\frac{\xi^2}{2(1 + r_0)} + \left(\frac{\tau - \tau_m}{\sigma_{\tau|\xi}} \right)^2 \right] \right\}, \quad (4.272)$$

in which:

$$C = \frac{1}{2[4\pi r_0(1 + r_0)]^{1/2} \sigma_{\tau|\xi}}. \quad (4.273)$$

In contrast to Eq. (4.253), the distribution (4.272) depends on the bandwidth parameter ν and r_0 as well. The distribution (4.272) compares favourably with the experimental data of Srokosz and Challenor (1987).

In the conventional zero-downcrossing analysis the period (T) of a given wave is a summation of the time $T^{(-)}$, when the wave profile is under mean water level ($\zeta < \bar{\zeta}$) and time $T^{(+)}$, when the wave profile is above mean water level ($\zeta > \bar{\zeta}$). For the narrow-band process, $\bar{T}^{(+)} \approx \bar{T}^{(-)}$. However, in a rough sea, the wave profile becomes asymmetric with sharper crests and shallower troughs. The time during which the sea surface is above mean sea level, is usually shorter than that for which the sea surface is below mean sea level. Such time asymmetry is related to a positive value of the skewness coefficient. To distinguish the mean time $T^{(+)}$ and $T^{(-)}$, we represent the total mean wave period \bar{T} in the form:

$$\bar{T} = \overline{T^{(+)}} + \overline{T^{(-)}}, \quad (4.274)$$

in which (Sveshnikov, 1965; Massel, 1973):

$$\overline{T^{(+)}} = \frac{\int_0^\infty f(\zeta) d\zeta}{\int_0^\infty v f_2(0, v) dv}, \quad (4.275)$$

and

$$\overline{T^{(-)}} = \frac{-\int_{-\infty}^0 f(\zeta) d\zeta}{\int_{-\infty}^0 v f_2(0, v) dv}, \quad (4.276)$$

in which ζ is the displacement of the sea surface, and v is the rate of change of displacement ζ with respect to time, i.e. $v(t) = d\zeta/dt$.

Let us define the two non-dimensional variables:

$$\eta_1 = \frac{\zeta - \bar{\zeta}}{\sigma_\zeta}, \quad \eta_2 = \frac{v}{\sigma_v}, \quad (4.277)$$

where $\sigma_u = d\zeta/dt$.

At a given time, these two variables are uncorrelated. Using this fact and presenting the joint probability density function $f_2(\eta_1, \eta_2)$ in the form of two-dimensional Hermite polynomials (Kuznetsov et al., 1960) we obtain:

$$\begin{aligned} f_2(\zeta, v) = & \frac{1}{2\pi \sigma_\zeta \sigma_v} \exp\left(-\frac{1}{2} \frac{v^2}{\sigma_v^2}\right) \left\{ 1 + \frac{1}{3!} \left[d_{03} \left(\frac{v^3}{\sigma_v^3} - 3 \frac{v}{\sigma_v} \right) - 3d_{21} \frac{v}{\sigma_v} \right] + \right. \\ & \left. + \frac{1}{4!} \left[3d_{40} + d_{04} \left(\frac{v^4}{\sigma_v^4} - 6 \frac{v^2}{\sigma_v^2} + 3 \right) + 6d_{22} \left(1 - \frac{v^2}{\sigma_v^2} \right) \right] \right\}. \end{aligned} \quad (4.278)$$

After substituting Eq. (4.278) into Eq. (4.274) we obtain (Massel, 1973):

$$\begin{aligned} \bar{T} = & \sqrt{2\pi} \frac{\sigma_\zeta}{\sigma_v} \left\{ \frac{\sqrt{\frac{\pi}{2}} - \frac{1}{6}d_{30}}{1 - \frac{\sqrt{2\pi}}{4}d_{21} - \frac{1}{4}d_{22} + \frac{1}{8}d_{40} - \frac{1}{25}d_{04}} + \right. \\ & \left. + \frac{\sqrt{\frac{\pi}{2}} + \frac{1}{6}d_{30}}{1 + \frac{\sqrt{2\pi}}{4}d_{21} - \frac{1}{4}d_{22} + \frac{1}{8}d_{40} - \frac{1}{25}d_{04}} \right\}, \end{aligned} \quad (4.279)$$

where:

$$\begin{aligned} d_{21} &= E \left[\eta_1^2(t) \eta_2(t) \right]; \quad d_{22} = E \left[\eta_1^2(t) \eta_2^2(t) \right] - 1; \\ d_{40} &= E \left[\eta_1^4(t) \right] - 3; \quad d_{04} = E \left[\eta_2^4(t) \right] - 3; \quad d_{30} = E \left[\eta_1^3(t) \right]. \end{aligned} \quad (4.280)$$

When $\zeta(t)$ is a normal process, all coefficients in Eq. (4.280) are equal zero and Eq. (4.279) becomes:

$$\bar{T} = 2\pi \frac{\sigma_\zeta}{\sigma_v} = 2\pi \sqrt{\frac{m_0}{m_2}}. \quad (4.281)$$

Comparison of the theoretical wave periods $\overline{T^{(+)}}$ and $\overline{T^{(-)}}$ with experimental data is given by Massel (1973) and Bitner (1980).

4.5 Wave orbital velocities and pressure

4.5.1 Probability distribution of orbital velocities and pressure

Examining the distribution of surface elevation we assume that the observed time series are the result of linear superposition of many sinusoidal wave components (see Eq. (4.1)). However, nonlinear interaction between these components or wave breaking could induce small deviations from linearity (see Sections 4.2.2 and 4.2.4), at least in deep water. Using an analogy to surface elevation, it is reasonable to assume that fluid particle velocity and pressure are also the result of linear superposition of elementary components. Hence, the expressions for orbital velocities and pressure can be summarized as follows:

$$u(x, y, z, t) = \frac{\partial \phi}{\partial x} = \Re \int_{-\infty}^{\infty} \int_{-\pi}^{\pi} \frac{gk \cos \Theta}{\omega} \frac{\cosh k(z+h)}{\cosh kh} \exp [ik(x \cos \Theta + y \sin \Theta) - \omega t] dA(\omega, \Theta), \quad (4.282)$$

$$v(x, y, z, t) = \frac{\partial \phi}{\partial y} = \Re \int_{-\infty}^{\infty} \int_{-\pi}^{\pi} \frac{gk \sin \Theta}{\omega} \frac{\cosh k(z+h)}{\cosh kh} \exp [ik(x \cos \Theta + y \sin \Theta) - i\omega t] dA(\omega, \Theta), \quad (4.283)$$

$$w(x, y, z, t) = \frac{\partial \phi}{\partial z} = \Re \int_{-\infty}^0 \int_{-\pi}^{\pi} \frac{-igk}{\omega} \frac{\sinh k(z+h)}{\cosh kh} \exp [ik(x \cos \Theta + y \sin \Theta) - i\omega t] dA(\omega, \Theta), \quad (4.284)$$

$$p(x, y, z, t) = \rho g \Re \int_{-\infty}^{\infty} \int_{-\pi}^{\pi} \frac{\cosh k(z+h)}{\cosh kh} \exp [ik(x \cos \Theta + y \sin \Theta) - i\omega t] dA(\omega, \Theta), \quad (4.285)$$

in which ϕ is a velocity potential and

$$\overline{dA(\omega, \Theta) dA^*(\omega_1, \Theta_1)} = \frac{1}{2} \hat{S}(\omega, \Theta) \delta(\omega - \omega_1) \delta(\Theta - \Theta_1) d\omega d\omega_1 d\Theta d\Theta_1, \quad (4.286)$$

where $\hat{S}(\omega, \Theta)$ is a directional frequency spectrum, $\delta(\cdot)$ is a delta function, $(*)$ denotes the complex conjugate value, and \Re is a real part of the complex function.

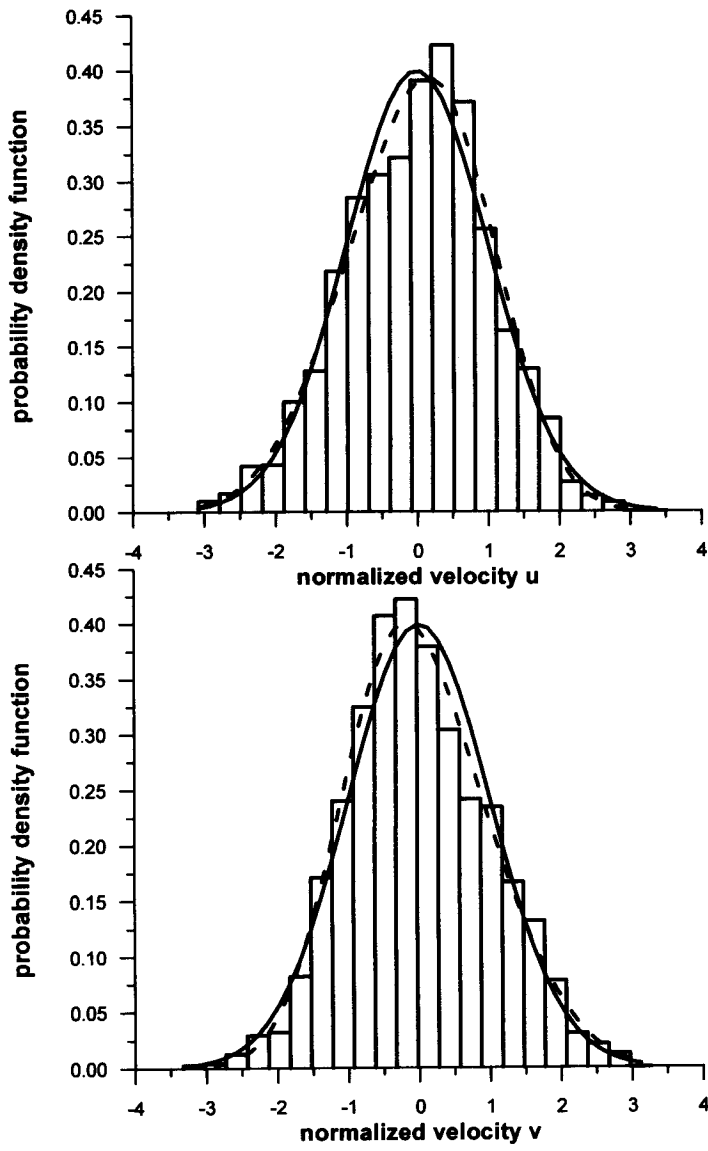


Figure 4.27: Probability density functions for orbital velocities: ——— Gaussian distribution; - - - Gram-Charlier series; bars denote experimental data.

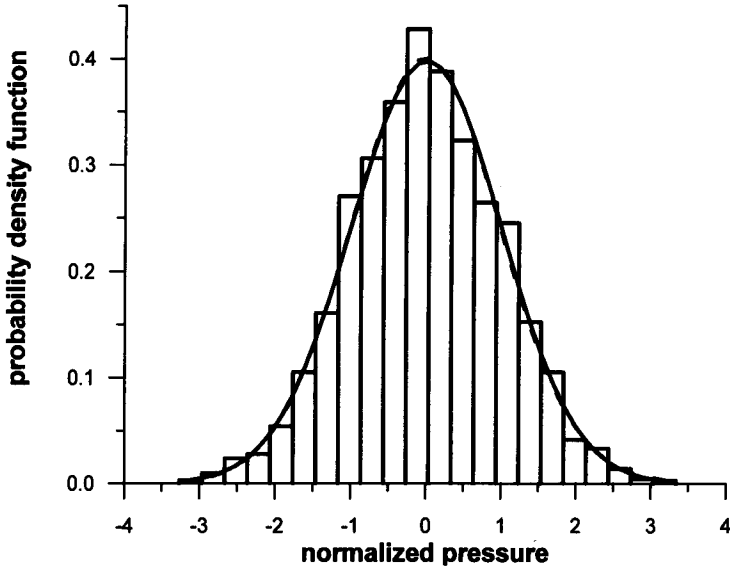


Figure 4.28: Probability density function for dynamic pressure: ——— Gaussian distribution; - - - Gram-Charlier series; bars denote experimental data.

Thus, it can be reasonably assumed that u, v, w and p follow a Gaussian probability distribution with zero mean and variances $\sigma_u^2, \sigma_v^2, \sigma_w^2$ and σ_p^2 . By making use of the autocorrelation functions definition, we obtain the following expressions for variances:

$$\sigma_u^2 = \frac{1}{2} \int_{-\infty}^{\infty} \int_{-\pi}^{\pi} \left(\frac{gk \cos \Theta}{\omega} \right)^2 \frac{\cosh^2 k(z+h)}{\cosh^2 kh} \hat{S}(\omega, \Theta) d\Theta d\omega, \quad (4.287)$$

$$\sigma_v^2 = \frac{1}{2} \int_{-\infty}^{\infty} \int_{-\pi}^{\pi} \left(\frac{gk \sin \Theta}{\omega} \right)^2 \frac{\cosh^2 k(z+h)}{\cosh^2 kh} \hat{S}(\omega, \Theta) d\Theta d\omega, \quad (4.288)$$

$$\sigma_w^2 = \frac{1}{2} \int_{-\infty}^{\infty} \left(\frac{gk}{\omega} \right)^2 \frac{\sinh^2 k(z+h)}{\cosh^2 kh} S(\omega) d\omega, \quad (4.289)$$

$$\sigma_p^2 = \frac{(\rho g)^2}{2} \int_{-\infty}^{\infty} \frac{\cosh^2 k(z+h)}{\cosh^2 kh} S(\omega) d\omega. \quad (4.290)$$

Figures 4.27 and 4.28 show examples of the comparison of an experimental distribution with a Gaussian distribution and the Gram-Charlier distribution (4.20). The experimental data were recorded in a coastal zone at water depth ~ 6.5 m and 0.4 m

above an almost horizontal bottom. The experimental distributions follow the Gaussian distribution very closely. The skewness coefficients γ_1 are -0.18 , 0.21 and 0.05 for u , v and p , respectively, while the corresponding kurtosis coefficients are -0.16 , -0.03 and 0.07 . In this case, the Gram-Charlier distribution does not give any substantial improvement.

This agrees with the observations of Sultan and Hughes (1993). They reported that the Gram-Charlier distribution was less effective than the plain Gaussian distribution in fitting their wave flume velocity data.

Bottom velocity

The kinematics of wave motion at two boundaries, namely: the sea surface and sea bottom, are of special interest for engineering and oceanographic practice. Let us first consider the bottom velocities. Accurate representation of bottom orbital velocities, occurring under given sea conditions, are necessary to model wave effects on sediment transport in shallow waters. Bottom velocity also controls bottom friction and energy dissipation over a large sea.

We assume the sea surface spectrum as:

$$\hat{S}(\omega, \Theta) = S(\omega) D(\Theta), \quad (4.291)$$

in which directional spreading $D(\Theta)$ is given by Eq. (3.143). The frequency spectrum $S(\omega)$ is represented in the form of the Pierson-Moskowitz spectrum or JONSWAP spectrum. Following Chakrabarti (1986) and Soulsby (1987) we write both spectra in unified form:

$$S(\omega) = B \left(\frac{H_s}{4} \right)^2 \frac{\omega_p}{\omega^5} \exp \left[-\frac{5}{4} \left(\frac{\omega}{\omega_p} \right)^{-4} \right] \gamma^\delta, \quad (4.292)$$

where H_s is a significant wave height, ω_p is a peak frequency, and $\gamma = 3.3$, while δ is given by Eq. (3.89). The B value for the Pierson-Moskowitz spectrum is equal to 5, while for the JONSWAP it is 3.29.

After substitution of Eqs. (3.143) and (4.292) into Eq. (4.287) we obtain:

$$\frac{\sigma_u}{H_s \sqrt{\frac{g}{h}}} = \frac{1}{4} \sqrt{A_\omega \left(\frac{\omega_p^2 h}{g} \right)} \sqrt{A_\Theta(\Theta_0)}, \quad (4.293)$$

where:

$$A_\omega = \int_0^\infty \frac{B}{2} \left(\frac{x}{x_p} \right)^{-2} \sinh^{-2}[kh(x)] \exp \left[-\frac{5}{4} \left(\frac{x}{x_p} \right)^{-2} \right] \gamma^\delta dx, \quad (4.294)$$

$$A_\Theta(\Theta_0) = \int_{-\pi}^\pi \cos^2 \Theta D(\Theta) d\Theta, \quad (4.295)$$

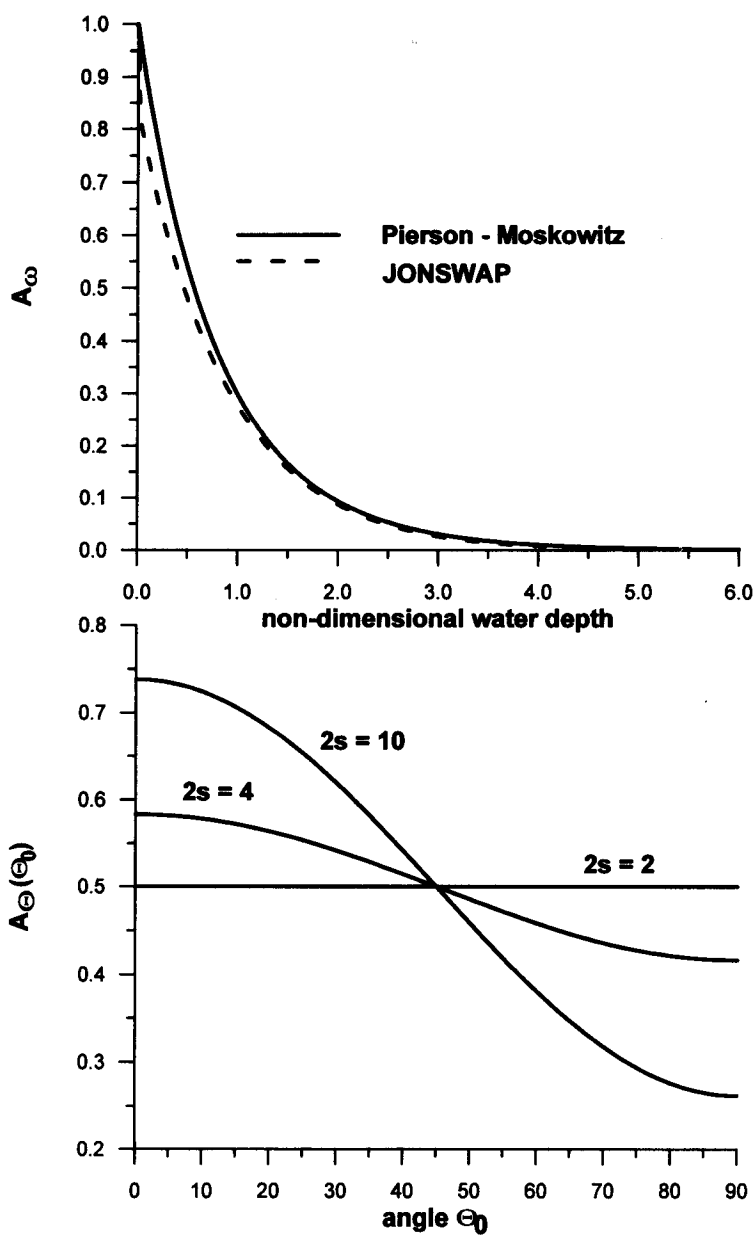


Figure 4.29: Functions $A_\omega\left(\frac{\omega^2 h}{g}\right)$ and $A_\Theta(\Theta_0)$.

$$\text{and } x_p = \frac{\omega_p^2 h}{g}, \quad x = \frac{\omega^2 h}{g}.$$

The parameters A_ω and A_Θ are shown in Fig. 4.29. Both spectral models give almost the same results for A_ω . For small values of $\frac{\omega_p^2 h}{g}$ (long waves), the parameter A_ω tends to 1, while for large values of $\frac{\omega_p^2 h}{g}$ (short waves), it tends to zero. The value A_ω for the JONSWAP spectrum is slightly smaller than for the Pierson-Moskowitz spectrum.

The parameter A_Θ is shown for three different spreading parameters: $2s = 2, 4$ and 10 , and is concentrated around value of $\frac{1}{2}$. The departure from $\frac{1}{2}$ increases with the narrowness of the directional spreading (higher values of s).

Let us now consider an equivalent monochromatic wave which can be used as a substitute for the full spectrum under the condition that the frequency of the surface wave is ω_p . The height H_e of the equivalent regular wave can be determined from the requirement that the variance of the bottom velocity and mean wave direction Θ_0 of the spectrum are the same as those of the monochromatic wave.

Thus, from linear wave theory we have:

$$u(t) = \frac{g H_e k_p \cos \Theta_0}{2 \omega_p} \frac{1}{\cosh(k_p h)} \cos(\omega_p t), \quad (4.296)$$

and:

$$\sigma_u^2 = \frac{1}{2} \left\{ \frac{g H_e k_p \cos \Theta_0}{2 \omega_p} \frac{1}{\cosh(k_p h)} \right\}^2, \quad (4.297)$$

or:

$$\frac{\sigma_u}{H_s \sqrt{\frac{g}{h}}} = \frac{1}{2\sqrt{2}} \left(\frac{\omega_p^2 h}{g} \right)^{1/2} \frac{\cos \Theta_0}{\sinh(k_p h)} \frac{H_e}{H_s}. \quad (4.298)$$

Combining Eqs. (4.293) and (4.298) gives:

$$\frac{H_e}{H_s} = \frac{1}{\sqrt{2}} \frac{\sqrt{A_\omega} \sinh(k_p h)}{\sqrt{\frac{\omega_p^2 h}{g}}} \frac{\sqrt{A_\Theta}}{\cos \Theta_0}. \quad (4.299)$$

The correction coefficient (4.299) is a product of the correction due to frequency distribution and to directional spreading. The ratio H_e/H_s is shown in Fig. 4.30 as a function of normalized depth $\omega_p^2 h/g$. The JONSWAP spectrum and the directional spreading (3.143) were used with $2s = 4$.

The curves in Fig. 4.30 correspond to the three different angles $\Theta_0 = 0^\circ, 30^\circ$ and 60° . As an illustration let us consider a sea with a significant wave height $H_s = 5$ m, peak frequency $\omega_p = 0.628$ ($T_p = 10$ s), and water depth $h = 15$ m; thus, $\omega_p^2 h/g = 0.6$. The height of the monochromatic wave, which produces the same variance of bottom velocity u as the JONSWAP spectrum, is $H_e = 0.44H_s$, $0.51H_s$, and $0.89H_s$ for

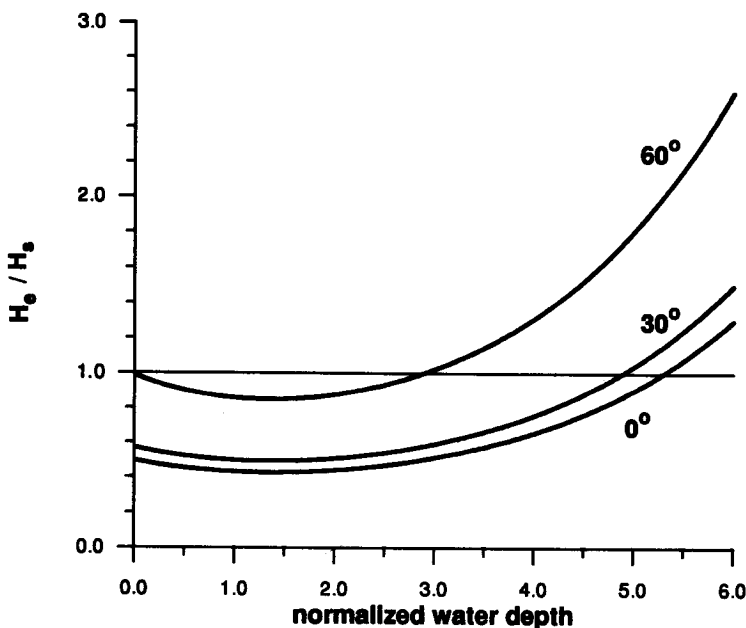


Figure 4.30: Functions $\frac{H_e}{H_s} = f\left(\frac{\omega^2 h}{g}\right)$ for three mean wave directions.

$\Theta_0 = 0^\circ, 30^\circ$ and 60° , respectively. The frequency of the monochromatic wave is ω_p and the direction of propagation is $\Theta = \Theta_0$.

It should be noted that the peak of the bottom orbital velocity spectrum $S_u(\omega)$ occurs at a smaller value of ω than the peak of the elevation spectrum $S_\zeta(\omega)$ because of frequency dependence of the attenuation with depth. However, as was shown by Soulsby (1987), the velocity peak frequency is very close to ω_p for $\frac{\omega_p^2 h}{g} \leq \sqrt{\frac{\pi}{2}} \approx 1.25$, i.e. for shallow water waves and intermediate water depth waves, if a JONSWAP spectrum is used. The difference in the peak frequencies is greater for the Pierson-Moskowitz spectrum.

Velocity close to sea surface

The flow field near the free surface is particularly important in engineering calculations of wave-induced forces on coastal and offshore structures. The usual basis for such calculations is the Morison equation (Morison et al., 1950), in which the resulting force is a summation of the components due to drag and inertia of the fluid. The first component is proportional to fluid speed squared while the second to local

acceleration. Therefore, the calculated drag force is especially sensitive to errors in speed estimates in regions of high flow speed, namely: near and above the mean water level.

The velocity potential, based on the linear wave theory, does not satisfy the kinematic and dynamic free surface boundary conditions exactly. However, the errors in both free boundary conditions do not strongly influence the prediction of wave kinematics at mid-depth and near the bottom. Sultan and Hughes (1993) have shown that linear wave theory predicts the variance of water particle velocity at these levels within 10% accuracy. Unfortunately, this is not the case for velocity near the sea surface.

The application of linear theory in this area leads to considerable overestimation of velocity and pressure because the hyperbolic quotients in Eqs. (4.282) - (4.285) become exceptionally large for high frequencies.

Alternate methods have been proposed in the past for the evaluation of velocities above the mean water level. Instead of looking for the global solution, these methods developed to represent the local behaviour of irregular waves. One form of local approximation is the so called stretching method by Wheeler (1969), based on the following transformation of the vertical coordinate:

$$z = \frac{(z' - \zeta)}{\zeta + h}, \quad (4.300)$$

in which z' is the desired location of velocity evaluation, and ζ is a local surface elevation. Thus, the surface velocities in a stretched system are equivalent to those at the mean water level of an unstretched system. The elevation z never exceeds the mean water level, which is in full agreement with linear wave theory.

In the Forristall (1982) modification of the linear theory, a linear variation of velocity above the mean water level is assumed. The linear theory is used up to mean water level and subsequent values are extrapolated upward using the vertical gradient of velocity at the mean water level, i.e.:

$$u(x, y, z, t) = u(x, y, 0, t) + \frac{\partial u(x, y, 0, t)}{\partial z} z. \quad (4.301)$$

It is evident that error associated with this method is proportional to the size of z . Another method was suggested by Lo and Dean (1986). They obtained a modified stretching factor of the form $\cos kh / \cosh k(\zeta + h)$ with appropriate changing of the dispersion relation.

However, it is clear that none of the above modifications, which involve the distortion of the vertical coordinate, satisfy the Laplace equation. Donelan et al. (1992) developed a method based on the linear superposition of a sum of freely propagating wave trains which does satisfy the Laplace equation. They assumed that shorter waves ride on longer ones, so the mean surface seen by a particular wave component is given by the linear superposition of all the longer wave components and has the

surface velocity commensurate with that. The addition of successively shorter wave components alters the surface elevation and changes the flow field in accordance with linear theory which is applied to the new component. A step-by-step procedure for computing the flow field compares well with laboratory data.

More appropriate local methods for approximating irregular wave kinematics are those which do not compromise the requirements of satisfying both the field equation and bottom and free surface boundary conditions.

The basis of such methods is the representation of the velocity potential function within each local window in the form of Fourier series (Sobey, 1992b,c) or power series (Fenton, 1986). The Fourier series approximation of the velocity potential shows:

$$\Phi(x, z, t) = \sum_{j=1}^M A_j \frac{\cosh jk(z+h)}{\cosh kjh} \sin j(kx - \omega t). \quad (4.302)$$

This is more suitable for deeper water where the vertical variation tends to be exponential. On the other hand, a truncated polynomial series for the complex velocity potential is:

$$\Phi(X, z) + i\Psi(X, z) = \sum_{j=0}^M \frac{A_j}{j+1} [X + i(h+z)]^{j+1}. \quad (4.303)$$

This would be the most appropriate in shallow water where the polynomial variation in the vertical is similar to that of cnoidal wave theory.

Within each moving window, the velocity potentials (4.302) and (4.303) satisfy the field equation and bottom boundary condition exactly. The coefficients A_j are determined numerically to best fit the kinematic and dynamic free surface boundary conditions. Comparison with hurricane *Camille* data showed that the free surface boundary condition errors are sharply reduced by the local Fourier approximation (4.302), in comparison with the Wheeler stretching method and simple linear superposition method.

4.5.2 Influence of intermittence effect on probability distribution of orbital velocities and pressure near water level

Let us assume now that an ideal current meter or pressure sensor is situated at level z , between the troughs and crests of incoming waves (see Fig. 4.31). The sensors record signals of whose duration depends on sensor elevation with respect to the mean water level. For example, a point at mean water level remains submerged for 50% of the total observation time, while a point at an elevation of $\sigma\zeta$ above mean water level remains submerged for only 15.9% of time. For real sensors, the changes of velocities (or pressure) from a zero to a non-zero value, due to sensor inertia, are not so abrupt as that shown in Fig. 4.31, but in our analysis we assume ideal sensors with zero inertia.

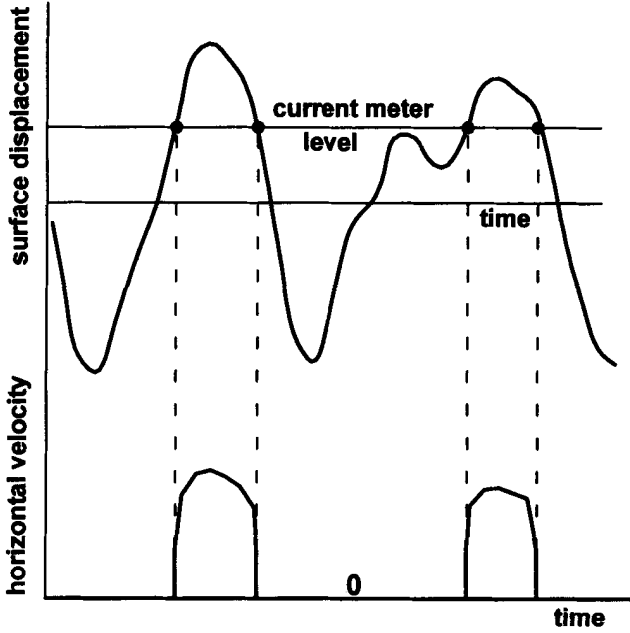


Figure 4.31: Intermittency effect on orbital velocity.

Thus, the measured horizontal velocity $u_m(t)$ can be represented as:

$$u_m(x, y, z, t) = \begin{cases} u(x, y, z, t) & \text{for } z \leq \zeta(x, y, t) \\ 0 & \text{for } z > \zeta(x, y, t). \end{cases} \quad (4.304)$$

Similar expressions can be derived for v and w velocity components, and pressure p . In the following we will concentrate our attention on the u variable only; for other variables final results will be given.

The probability density for wave velocities in intermittent flow, derived by Tung (1975) under the condition that surface elevation $\zeta(t)$ has a Gaussian distribution, and the zero mean Gaussian joint probability density function of surface elevation and horizontal component of orbital velocity u , takes the form:

$$f_2(\zeta, u) = \frac{1}{2\pi\sigma_\zeta\sigma_u\sqrt{\tilde{\Delta}}} \exp \left\{ -\frac{1}{2\tilde{\Delta}} \left[\frac{\zeta^2}{\sigma_\zeta^2} + \frac{u^2}{\sigma_u^2} - \frac{2r\zeta u}{\sigma_\zeta\sigma_u} \right] \right\}, \quad (4.305)$$

where $\tilde{\Delta} = 1 - r^2$; r is a correlation coefficient between ζ and u .

Cieřlikiewicz (1985), and Cieřlikiewicz and Gudmestad (1993) extended Tung's approach to nonlinear random waves, assuming that the probability densities for surface displacement $\zeta(t)$ and velocity $u(t)$ are represented in the form of the Gram-Charlier series.

Using the theorem of total probability, the probability density function for measured velocity $u_m(z)$ takes the form:

$$f_{um}(u; z) = \delta(u) P[\zeta < z] + f_{um|\zeta > z}(u) P[\zeta > z], \quad (4.306)$$

where:

$$f_{um|\zeta > z}(u) = \frac{\int_z^\infty f_2(\zeta, u) d\zeta}{P[\zeta \geq z]}, \quad (4.307)$$

and $P[\]$ denotes the probability of the event shown in bracket $[\]$.

A comparison of function (4.306) with experimental data (Anastasiou et al., 1982; Cieřlikiewicz and Gudmestad, 1993) showed that the influence of the nonlinearities of the wave motion on measured velocities is very small and velocities are mainly dependent on the intermittence of the flow field. So, in the following we will give final formulas for that case only. The results for the combined effect of intermittence and nonlinearity are given by Cieřlikiewicz and Gudmestad (1993). Therefore, an evaluation of functions in Eq. (4.306) for intermittent flow yields (Tung, 1975; Cieřlikiewicz and Gudmestad, 1993):

$$f_{um}(u; z) = [1 - Q(\tilde{z})] \delta(u) + \frac{1}{\sigma_u(z)} Z(\tilde{u}) Q[\xi(\tilde{z}, \tilde{u}; r)], \quad (4.308)$$

in which:

$$\tilde{z} = \frac{z}{\sigma_\zeta}, \quad \tilde{u} = \frac{u}{\sigma_u}, \quad \xi = \frac{\tilde{z} - r\tilde{u}}{\sqrt{\Delta}},$$

and:

$$Z(\gamma) = \frac{1}{\sqrt{2\pi}} e^{-\frac{\gamma^2}{2}} \quad Q(\gamma) = \int_\gamma^\infty Z(z) dz. \quad (4.309)$$

Expressions similar to Eq. (4.308) may be derived for velocity v and pressure p . While $f_{um}(u; z)$ describes a non-zero mean, skewed process, $f_{vm}(v; z)$ describes a zero mean unskewed process.

The two first moments of distribution (4.308) are:

$$E[u_m(z)] = r\sigma_u Z\left(\frac{z}{\sigma_\zeta}\right), \quad (4.310)$$

and:

$$E[u_m^2(z)] = \sigma_u^2 Q\left(\frac{z}{\sigma_\zeta}\right) + \sigma_u^2 r^2 \left(\frac{z}{\sigma_\zeta}\right) Z\left(\frac{z}{\sigma_\zeta}\right). \quad (4.311)$$

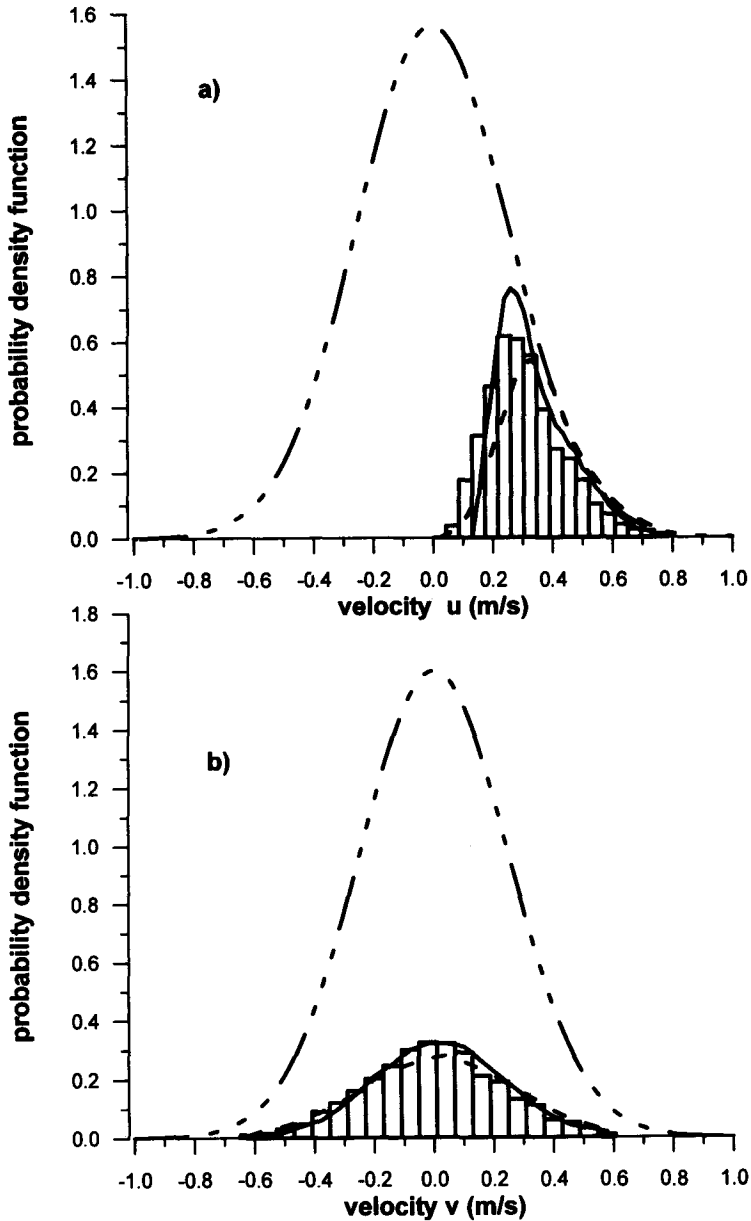


Figure 4.32: Comparison of probability density functions for orbital velocities when the intermittency effects are included: ——— intermittency and nonlinearity effects are included; - - - only intermittency effect is included; Gaussian distribution; bars denote experimental data.

When $z \rightarrow -\infty$, $E[u_m] \rightarrow 0$, $E[u_m^2] = \sigma_u^2$, and $\sigma_{um}^2 = \sigma_u^2$. Thus, the intermittence effect ceases for points located far below the free surface.

In Fig. 4.32, the probability density functions for velocities u and v are compared with laboratory experimental data (Cieřlikiewicz and Gudmestad, 1994b). The irregular wave train with target JONSWAP spectrum ($\gamma = 3.0$) was generated in a tank of 1.8 m deep. Significant wave height $H_s = 0.21$ m and peak period $T_p = 1.8$ s were adopted. The velocities were measured at level $z = 0.05$ m above mean water level. The comparison shows a good agreement of the theory with the experiment. Horizontal velocity u is highly skewed, while vertical velocity v is not. In both Figures the theoretical result which involves the intermittence effect and nonlinearity of the wave process, is shown too. The influence of nonlinearity is especially pronounced for velocity close to the mean velocity. In each case, the Gaussian distribution is totally irrelevant to the observations.

Examination of the vertical profile of the mean value and standard deviation indicates that the effect due to wave nonlinearity is negligible. The non-zero positive mean velocity is observed only in the vicinity of mean water level. The observed discrepancy between predictions and experiment are due to the existence of the return current in the wave flume. This problem was treated by Cieřlikiewicz and Gudmestad (1994a). They argued that the mean flux is distributed in the region between wave trough and wave crest, rather than only being associated with the free surface (Starr, 1947; Phillips, 1960a).

The influence of the intermittence effect on the wave pressure at the vertical wall was discussed by Cieřlikiewicz and Massel (1988).

4.6 Wave group statistics

It is a well known fact that the heights of wind-generated waves are not uniform; they occur in successive groups of higher or lower waves. The existence of wave groups has been known to sea-farming men for a long time. Out of their experience has come the popular but mistaken notion that 'every' seventh (or ninth) wave is the highest, or an old Icelandic saying that *large waves seldom come alone*.

Interest in wave grouping is stimulated by the fact that wave groups often cause serious problems for the safety of marine systems. In particular, when the periods of individual waves in the group are close to the marine system's natural motion period, resonance may occur which, in turn, can induce capsizing of ships or damage marine structures.

Other examples of the influence of wave grouping are long-period oscillations and large forces in the mooring lines of moored vessels, and irregular oscillations of the mean water level near the shoreline which are within a period of several minutes.

Prior to describing the statistical properties of wave groups, we consider the simple case of wave groups in a regular wave train. Using the linear superposition principle

for regular waves propagating in the positive x direction, we obtain:

$$\zeta(x, t) = \sum_n A_n \cos(\omega_n t - k_n x + \varphi_n), \quad (4.312)$$

where frequencies ω_n are not the integer multiples of any fundamental frequency. Squaring Eq. (4.312) and separating the result into two parts yields:

$$\zeta^2(x, t) = \frac{1}{2}P^2(x, t) + \frac{1}{2}G^2(x, t), \quad (4.313)$$

in which:

$$P^2(x, t) = \sum_{n,m} A_n A_m \cos [(\omega_n + \omega_m)t - (k_n + k_m)x + (\varphi_n + \varphi_m)], \quad (4.314)$$

and

$$G^2(x, t) = \sum_{n,m} A_n A_m \cos [(\omega_n - \omega_m)t - (k_n - k_m)x + (\varphi_n - \varphi_m)]. \quad (4.315)$$

Each component wave in Eq. (4.314) oscillates with frequency $(\omega_n + \omega_m)$ and propagates approximately with the phase velocity. The second part of Eq. (4.313) represents a sum of component waves of frequency $(\omega_n - \omega_m)$ and velocity C_g :

$$C_g = \frac{\omega_n - \omega_m}{k_n - k_m} = \frac{\Delta\omega}{\Delta k}. \quad (4.316)$$

For a relatively narrow spectrum, with peak frequency ω_p and spectral bandwidth $\Delta\omega$, respectively, the number of waves in a group is roughly equal to:

$$n \sim \frac{\omega_p}{\Delta\omega}. \quad (4.317)$$

For irregular random waves, the number of waves in a group and the recurrence interval between successive wave groups are random variables. Several studies of the stochastic analysis of wave groups in random seas may be categorized according to the following approaches. In the first approach, wave groups are considered as a level-crossing problem, associated with the envelope of a random process. The second approach is based on the assumption that a sequence of wave heights is a Markov chain, wherein the transition probability is derived from the two-dimensional Rayleigh distribution. Finally, in the third approach, the general probability density function of the time duration, associated with the envelope exceeding a given level, is considered.

4.6.1 Level-crossing problem

Consider a sufficiently narrow-band record which obeys a Gaussian distribution (4.4). The envelope of such a record is a function slowly varying in time, and the envelope amplitude is very close to the amplitude of individual waves. The probability density of the amplitude A of an envelope is given by Eq. (4.113).

The velocity of changing the envelope amplitude in time, i.e. dA/dt is a random variable statistically independent to the amplitude A . The probability density of $\frac{dA}{dt} = \dot{A}$ is a Gaussian one, i.e.:

$$f(\dot{A}) = (2\pi\tilde{m}_2)^{-\frac{1}{2}} \exp \left[-\frac{\dot{A}^2}{2\tilde{m}_2} \right], \quad (4.318)$$

in which \tilde{m}_2 denotes the second moment of spectral density $S(\omega)$ about mean:

$$\tilde{m}_2 = m_2 - m_1^2/m_0;$$

and spectral moments are given by Eq. (3.3).

The number of up-crossings of a given level, per unit time by the wave envelope is:

$$N_A = \int_0^\infty f(A) f(\dot{A}) \dot{A} d\dot{A} = \left(\frac{\tilde{m}_2}{2\pi} \right)^{1/2} f(A). \quad (4.319)$$

It is clear that the number N is a maximum when $f(A)$ is a maximum, i.e. when $A = (m_0)^{1/2}$. Hence, (Longuet-Higgins, 1984):

$$N_{max} = (2\pi e)^{-1/2} \left(\frac{\tilde{m}_2}{m_0} \right)^{1/2}. \quad (4.320)$$

Let us now define the time interval between successive groups t_2 (or total run) as a time between the exceedance of level A by a group of waves to the next exceedance of the same level by the succeeding group of waves. Hence, time t_2 would be:

$$t_2 = \frac{T_0}{T_0 N_A} = \frac{1}{N_A}. \quad (4.321)$$

Time t_2 is approximately equal to the time interval between the peak of one wave group and the peak of the next wave group. It is clear that t_2 depends upon the arbitrary level A . Moreover, assuming a narrow wave spectrum, the mean number of waves in a total run t_2 becomes:

$$\bar{N}_t = \frac{1}{\sqrt{2\pi}} \frac{\sqrt{1+\nu^2}}{\nu} \frac{\sqrt{m_0}}{A} \exp \left[-\frac{A^2}{2m_0} \right]. \quad (4.322)$$

For example, when critical level A is taken as the mean wave amplitude $A = \sqrt{\frac{1}{2}\pi} \sqrt{m_0}$, we have $\bar{N}_t = 2.4$ for $\nu = 0.30$. When $A = 2\sqrt{m_0}$, which is close to the significant wave amplitude, $\bar{N}_t = 5.1$.

Now we consider the run of high waves $N_h(A)$ as a sequence of waves the heights of which exceed a particular level A . The proportion of time during which level A is exceeded is:

$$q(A) = \int_A^\infty f(A) dA = \exp \left[-\frac{A^2}{2m_0} \right]. \quad (4.323)$$

Hence, the mean run of high waves \bar{N}_h would be:

$$\bar{N}_h = \frac{q(A)}{N_A}, \quad (4.324)$$

or:

$$\bar{N}_h = \frac{1}{\sqrt{2\pi}} \frac{\sqrt{1+\nu^2}}{\nu} \frac{\sqrt{m_0}}{A}. \quad (4.325)$$

Thus, \bar{N}_h varies simply like A^{-1} . When $\nu = 0.3$ and $A = \sqrt{\frac{1}{2}\pi} \sqrt{m_0}$, or $A = 2\sqrt{m_0}$, Eq. (4.325) gives $\bar{N}_h = 1.1$ and 0.7 , respectively. Care must be taken when interpreting the results for \bar{N}_t , especially when the \bar{N}_t and \bar{N}_h are very small and fractional. The envelope method can identify wave groups of small duration, while a wave crest may or may not be present during the interval. However, the fractional number of waves is still a measure of the probability of a wave crest exceeding the given level in that interval.

So far only the mean values \bar{N}_t and \bar{N}_h have been given. In general, the statistical distributions $f(N_t)$ and (N_h) are difficult to determine. Under the assumption that the wave spectrum is narrow and the successive up-crossings are uncorrelated, the probability density $f(N_t)$ would be approximately:

$$f(N_t) \approx \bar{N}_t \exp \left\{ -\frac{N_t}{\bar{N}_t} \right\}. \quad (4.326)$$

As the high run N_h is in some proportion to the corresponding total run N_t , we can also say that:

$$f(N_h) \approx \bar{N}_h \exp \left\{ -\frac{N_h}{\bar{N}_h} \right\}. \quad (4.327)$$

A more rigorous approach to determine $f(N_t)$ and $f(N_h)$ was undertaken by Kuznetsov et al. (1954), and Ochi and Sahinoglu (1989). Kuznetsov et al. considered the probability density function for crossings of some chosen level by the wave envelope $A(t)$, using the theory of multi-dimensional characteristic functions and multi-dimensional Hermite's polynomials.

Ochi and Sahinoglu (1989) derived the probability density function of the time duration, associated with the envelope exceeding level A . Subsequently, this probability density function was modified so that it is only concerned with the time interval

during which two or more wave crests are present. This condition is required for the existence of a wave group.

To evaluate the mean number of up-crossings \bar{N}_A and mean run of high waves \bar{N}_h , the amplitude of the envelope should first be calculated. To calculate the wave envelope function of a given time series $\zeta(t)$ we need both the surface elevation $\zeta(t)$ and its Hilbert transform $\eta(t)$ (see Eq. (4.167)):

$$A(t) = \pm (\zeta^2(t) + \eta^2(t))^{1/2}. \quad (4.328)$$

For moderately long records it is more practical to use Fourier analysis to calculate $\eta(t)$ (Longuet-Higgins, 1984). Hence, $\zeta(t)$ and $\eta(t)$ become:

$$\left. \begin{aligned} \zeta(t) &= 2 \sum_{n_{\min}}^{n_{\max}} [a_n \cos(n\omega t) + b_n \sin(n\omega t)] \\ \eta(t) &= 2 \sum_{n_{\min}}^{n_{\max}} [a_n \sin(n\omega t) - b_n \cos(n\omega t)] \end{aligned} \right\}, \quad (4.329)$$

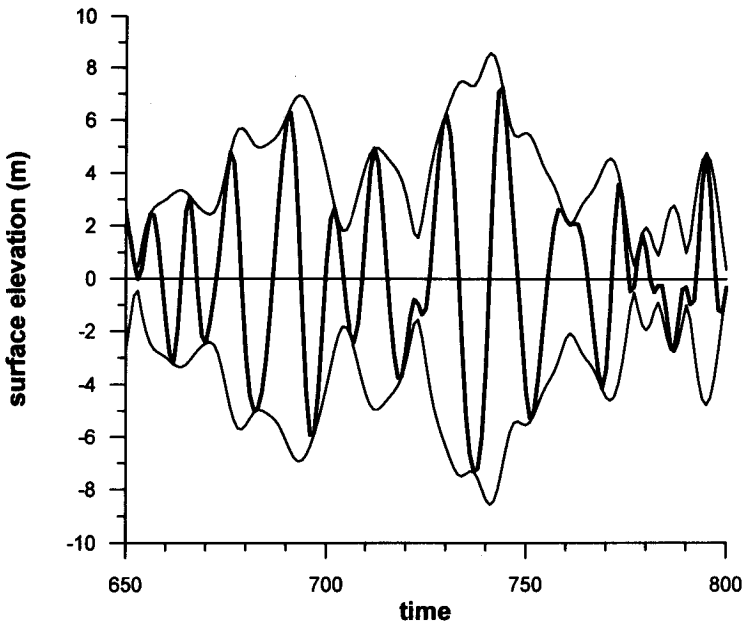


Figure 4.33: Section of filtered record and its envelope.

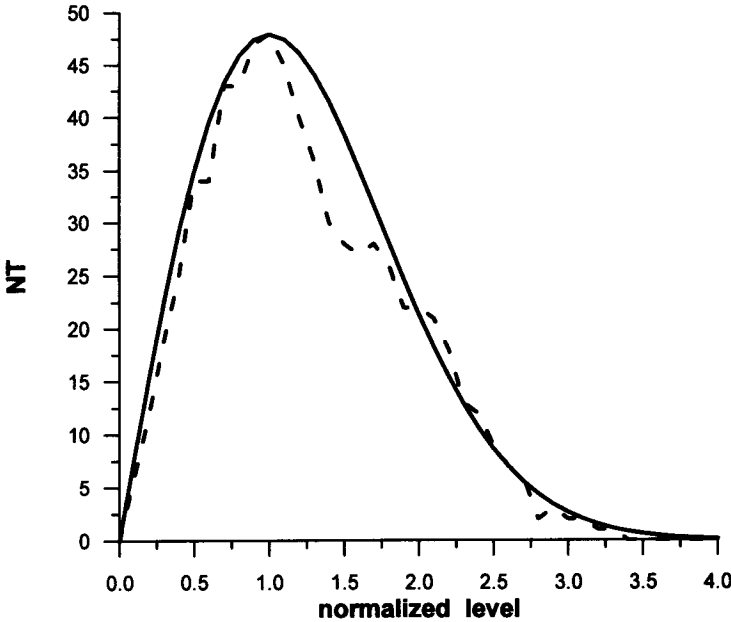


Figure 4.34: Total number of up-crossings by the envelope function: — Longuet-Higgins' solution; - - experimental data.

in which $1 \leq n_{\min} < n_{\max} < \frac{1}{2}M$, $M = \frac{T_0}{\Delta t}$, $\omega = \frac{2\pi}{M}$, and T_0 is the length of a record.

Usually some reduction in the upper limit ($n_{\max} \leq \frac{1}{2}M$) may be desirable to avoid the aliasing of energy from frequencies higher than the Nyquist frequency and the filtering of low frequencies is needed, mainly to exclude unwanted measurement effects.

Figure 4.33 shows a section of filtered record $\zeta(t)$ and envelope function $\pm A(t)$, based on data taken in the South Pacific (Steedman, 1993). The spectrum has a single dominant peak at about $\omega = 0.419$ rad/s. In calculation, the lower and upper cutoff frequencies at $n_{\min} = 15$ and $n_{\max} = 200$, respectively, were used.

The corresponding total number of up-crossings $N_A T_0$ of a given level A by the envelope function throughout the record is shown in Fig. 4.34. The level A was normalized by the standard deviation $\sqrt{m_0}$. The empirical points agree reasonably with the theoretical curve (4.319), but the $N_A T_0$ theoretical values for levels $1.0 < \frac{A}{\sqrt{m_0}} < 1.5$ are somewhat greater than the observed values.

4.6.2 Markov chain representation

We now consider the sequence of wave-heights as a Markov chain. The following derivation of probabilities of total run and high run is mainly due to Longuet-Higgins (1984). Let us choose a critical wave-height to be equal to H^* . Given that a certain wave height H_1 exceeds H^* , we denote by f_+ the probability that the next wave height H_2 also exceeds H^* . For a high run of length j , the first wave height and next $(j-1)$ wave heights must exceed H^* , and the one after must not exceed H^* . Hence, the probability of such an event is:

$$f(N_{h,j}^{(d)}) = f_+^{(j-1)}(1-f_+), \quad (4.330)$$

and the mean length of high runs is given by:

$$\bar{N}_h^{(d)} = \sum_1^\infty j f(N_{h,j}^{(d)}) = \frac{1}{1-f_+}. \quad (4.331)$$

The superscripts (d) in Eqs. (4.330) and (4.331) are added to stress that we are dealing with discrete waves, identified by their heights, in contrast with the continuous approach used in the previous Section.

To derive the probability of distribution for total runs we assume that in a total run of length j , the first i waves, say, will be a high run of length i , and the remaining $(j-i)$ waves will be a low run of length $(j-i)$. The probability of such an event is:

$$f(N_{t,j}^{(d)}) = (1-f_+)(1-f_-) \frac{f_+^{j-1} - f_-^{j-1}}{f_+ - f_-}, \quad n \geq 2, \quad (4.332)$$

and the mean total run is:

$$\bar{N}_t^{(d)} = \sum_2^\infty j f(N_{t,j}^{(d)}) = \frac{1}{1-f_+} + \frac{1}{1-f_-}. \quad (4.333)$$

Let us now assume that wave heights H_1 and H_2 are given approximately by $H_1 = 2A_1$ and $H_2 = 2A_2$. Using this assumption, Kimura (1989) showed that the unknown probabilities f_+ and f_- can be expressed through a two-dimensional Rayleigh distribution as:

$$\left. \begin{aligned} f_+ &= \int_{A^*}^\infty \int_{A^*}^\infty f(A_1, A_2) dA_1 dA_2 / \int_0^\infty \int_{A^*}^\infty f(A_1, A_2) dA_1 dA_2 \\ f_- &= \int_0^{A^*} \int_0^{A^*} f(A_1, A_2) dA_1 dA_2 / \int_0^\infty \int_0^{A^*} f(A_1, A_2) dA_1 dA_2 \end{aligned} \right\}, \quad (4.334)$$

in which $A^* = \frac{1}{2}H^*$.

When correlation coefficient r_0 (see Eq. (4.151)) is equal to 0, then:

$$f_+ = \exp\left(-\frac{1}{2}\xi^2\right), \quad f_- = 1 - \exp\left(-\frac{1}{2}\xi^2\right), \quad (4.335)$$

where $\xi = \frac{A}{\sqrt{m_0}}$.

For a more general case when $r_0 \neq 0$, we obtain:

$$\left. \begin{aligned} 1 - f_+ &\approx 1 - \exp\left(-\frac{1}{2}\xi^2\right)(1 - r_0^2)^{1/2} \\ 1 - f_- &\approx \exp\left(-\frac{1}{2}\xi^2\right)(1 - r_0^2)^{1/2} \end{aligned} \right\}. \quad (4.336)$$

For a narrow spectrum we can replace the trigonometric terms in Eqs. (4.152) and (4.153) by the first term in their power series and obtain:

$$\begin{aligned} 1 - r_0^2 &\approx \frac{\bar{m}_2}{m_0} \left(\frac{2\pi}{\bar{\omega}}\right)^2 = 4\pi^2 \left(\frac{m_2}{m_0} - \frac{m_1^2}{m_0^2}\right) \left(\frac{m_0}{m_1}\right)^2 = \\ &= 4\pi^2 \left(\frac{m_2 m_0}{m_1^2} - 1\right) = 4\pi^2 \nu^2. \end{aligned} \quad (4.337)$$

Substituting Eq. (4.337) into Eq. (4.336) we get:

$$\left. \begin{aligned} 1 - f_+ &\approx 2\pi\nu \left[1 - \exp\left(-\frac{1}{2}\xi^2\right)\right] \\ 1 - f_- &\approx 2\pi\nu \exp\left(-\frac{1}{2}\xi^2\right) \end{aligned} \right\}. \quad (4.338)$$

Hence, Eqs. (4.331) and (4.333) yield:

$$\left. \begin{aligned} \bar{N}_h^{(d)} &= \frac{1}{2\pi\nu} \frac{\exp\left(\frac{1}{2}\xi^2\right)}{\exp\left(\frac{1}{2}\xi^2\right) - 1} \\ \bar{N}_t^{(d)} &= \frac{1}{2\pi\nu} \frac{\exp\left(\xi^2\right)}{\exp\left(\frac{1}{2}\xi^2\right) - 1} \end{aligned} \right\}. \quad (4.339)$$

To compare the mean values \bar{N}_h and \bar{N}_t , resulting from the level-crossing method, with those of Eq. (4.339), we note that both methods predict \bar{N}_h values inversely proportional to ν . Moreover, if we neglect for a moment ν^2 in Eqs. (4.322) and (4.325), we obtain:

$$\left. \begin{aligned} \bar{N}_h &= \frac{1}{\sqrt{2\pi}} \frac{1}{\nu\xi} \\ \bar{N}_t &= \frac{1}{\sqrt{2\pi}} \frac{1}{\nu\xi} \exp\left(\frac{1}{2}\xi^2\right) \end{aligned} \right\}, \quad (4.340)$$

in which $\xi = \frac{A}{\sqrt{m_0}}$.

Although the functional dependence on ξ in Eqs. (4.339) and (4.340) is quite different, a numerical comparison shows that mean values of total and high runs are very similar. In particular, those mean values evaluated at three different levels ($H^* = H_{mode}$, H_{mean} and $H_{1/3}$) agree to within 10%.

It appears that the level-crossing method (or Gaussian noise theory) is more closely related to the wave spectrum, and is valid asymptotically as $\nu \rightarrow 0$. The Markov chain approach can be useful for an intermediate range of ν which corresponds to typical spectra of wind waves (see, for example, La Thi Cang, 1987a,b). Moreover, the Gaussian theory is strictly applicable to linear surface waves only. For a nonlinear wave train, when the harmonic components are dependent, the Markov theory can still be applied with some caution.

Chapter 5

Prediction of Ocean Waves in Deep Water

5.1 Introduction

This Chapter deals with prediction methods in a deep water. Firstly, the most important physical processes responsible for wave behaviour in a deep ocean, such as atmospheric transfer, nonlinear wave-wave interaction, and energy dissipation, are discussed. All these processes are expressed in source-sink terms for the energy balance equation introduced in Chapter 2.

Secondly, the energy balance equation is used to describe various wave prediction models, usually classified as the models of first, second and third generation . In the first generation models, each energy component is evaluated independently of the other. Therefore, nonlinear interactions are not taken into account. Energy dissipation is modelled simply by establishing the limiting form of a saturation spectrum. Besides some success in the forecasting of wave field, there was some doubt as to whether the first generation models really represent correctly the complete energy balance.

Extensive field and laboratory experimental studies provided a lot of new information which led to a restructuring of the prediction procedures and resulted in the second generation wave models. In contrast to the first generation, in the second generation models the nonlinear interaction term is included in various ways. There are three basic types of second generation wave models, namely: discrete spectral models, parametric models, and hybrid models.

Numerical simulation studies in the mid-1980s demonstrated that the first and second generation wave models cannot be applied for some extreme situations. At the same time, new numerical improvements in the computation of the Boltzmann-type integral provided a powerful tool to overcome the numerical difficulties of the second generation wave models. These improvements were used in the third generation model developed by the WAMDI group (the Wave Model Development and Implementation

group). The final report on those efforts was recently published by Komen et al. (1994).

The final Sections of this Chapter deal with simple prediction techniques based on the dimensional analysis. These empirical prediction models are very useful when a quick estimation of wave climate is needed and when more sophisticated numerical models are not available. All of the most popular empirical models, i.e. JONSWAP, SMB, SPM are discussed. Moreover, the Krylov method, which was developed in the Soviet Union and which is unknown in Western literature, is described in some detail.

5.2 Basic wave processes in deep water

In Chapter 2 we discussed a basic energy balance equation in the spectral form. This equation describes an evolution of the energy spectrum in space and time. The particular form of this equation depends on atmospheric forcing and bathymetry. In this Section we assume that the sea is deep enough to neglect the sea bottom influence on wave propagation. Hence, we suppose that the water depth approximately satisfies the following relation:

$$h > \frac{L_p}{2}, \quad (5.1)$$

in which L_p corresponds to the peak frequency ω_p , i.e.:

$$L_p = \frac{2\pi g}{\omega_p^2} = \frac{gT_p^2}{2\pi}. \quad (5.2)$$

The source function Q in energy balance equation (2.177) represents at least nine different processes. In the following we will discuss the most important ones, which are usually used in prediction procedures for the deep water case, namely: atmospheric transfer, nonlinear wave-wave interaction, and energy dissipation.

Thus, the general radiative-transfer equations (2.177), or (2.184) and (2.185) simplify as follows:

$$\frac{\partial \hat{\Psi}}{\partial t} + \frac{\partial \Omega}{\partial k_i} \frac{\partial \hat{\Psi}}{\partial x_i} = (Q_1 + Q_2) + Q_5 + Q_7, \quad (5.3)$$

$$\frac{\partial f}{\partial t} + C_g \cos \Theta \frac{\partial f}{\partial x} + C_g \sin \Theta \frac{\partial f}{\partial y} = \frac{C_g}{\chi} [(\hat{Q}_1 + \hat{Q}_2) + \hat{Q}_5 + \hat{Q}_7], \quad (5.4)$$

and

$$\begin{aligned} \frac{\partial}{\partial t} (CC_g \hat{S}) + C_g \cos \Theta \frac{\partial}{\partial x} (CC_g \hat{S}) + C_g \sin \Theta \frac{\partial}{\partial y} (CC_g \hat{S}) = \\ = CC_g [(\hat{Q}_1 + \hat{Q}_2) + \hat{Q}_5 + \hat{Q}_7]. \end{aligned} \quad (5.5)$$

5.2.1 Atmospheric forcing

The relationship between the wave number spectrum of surface waves and wave number frequency spectrum of the turbulent atmospheric pressure at the water surface is given by Eq. (2.91), i.e.:

$$\hat{\Psi}(\vec{k}, \vec{x}, t) = \frac{\pi \Psi_a(\vec{k}, \omega)}{\rho_w^2 C^2} \frac{\sinh(\mu \omega t)}{\mu \omega}. \quad (5.6)$$

For initial time ($t \ll 1/\mu\omega$) Eq. (5.6) describes linear growth in the wave spectrum:

$$\hat{\Psi}(\vec{k}, \vec{x}, t) = \frac{\pi \Psi_a(\vec{k}, \omega)}{\rho_w^2 C^2} t. \quad (5.7)$$

We assume now that waves are generated in deep water and only the local term in the left-hand side of Eq. (5.3) is retained. The source term is restricted to a generation process only at $t \ll 1/\mu\omega$. Therefore, we obtain:

$$\frac{\partial \hat{\Psi}}{\partial t} = \frac{\pi \Psi_a(\vec{k}, \omega)}{\rho_w^2 C^2}, \quad (5.8)$$

or in terms of frequency-direction spectrum $\hat{S}(\omega, \Theta, \vec{x}, t)$:

$$\frac{\partial \hat{S}}{\partial t} = \frac{\pi \omega \Psi_a(\vec{k}, \omega)}{\rho_w^2 C^3 C_g}. \quad (5.9)$$

Comparing the right-hand side of Eq. (5.8) with Eq. (2.191) yields:

$$Q_1 = Q_{in}^{(P)} = \alpha = \frac{\pi \Psi_a(\vec{k}, \omega)}{\rho_w^2 C^2}, \quad (5.10)$$

while Eqs. (2.185) and (5.9) give:

$$\frac{\partial \hat{S}(\omega, \Theta)}{\partial t} = \hat{Q}_1, \quad (5.11)$$

where:

$$\hat{Q}_1 = \hat{Q}_{in}^{(P)} = \frac{\pi \omega \Psi_a(\vec{k}, \omega)}{\rho_w^2 C^3 C_g}. \quad (5.12)$$

For large time ($t \gg 1/\mu\omega$), when $\sinh(\mu\omega t) \approx \frac{1}{2} \exp(\mu\omega t)$, the resulting wave number spectrum in Eq. (5.6) takes the form:

$$\hat{\Psi}(\vec{k}, \vec{x}, t) = \frac{\pi \Pi(\vec{k}, \omega)}{2 \rho_w^2 C^2 \mu \omega} e^{\mu \omega t}. \quad (5.13)$$

Thus:

$$\frac{\partial \hat{\Psi}}{\partial t} = \frac{\pi \Pi(\vec{k}, \omega)}{2\rho_w^2 C^2} e^{\mu\omega t}, \quad (5.14)$$

or:

$$\frac{\partial \hat{\Psi}}{\partial t} = \mu\omega \hat{\Psi}(\vec{k}, t). \quad (5.15)$$

Comparing Eq. (5.15) with Eq. (2.192) we have:

$$Q_2 = Q_{in}^{(M)} = \beta \hat{\Psi}(\vec{k}, \vec{x}, t) = \mu\omega \hat{\Psi}(\vec{k}, \vec{x}, t), \quad (5.16)$$

and

$$\hat{Q}_2 = \hat{Q}_{in}^{(M)} = \mu\omega \hat{S}(\omega, \Theta). \quad (5.17)$$

The source term $Q_{in}^{(P)}$, corresponding to the Phillips resonant mechanism, is responsible for an initial excitation of the sea. The numerical implementation of this term requires knowledge of the $\Psi_a(\vec{k}, \omega)$ spectrum, details of which are not readily available. In early field experiments (Barnett, and Wilkerson, 1967) the $Q_{in}^{(P)}$ predictions were too small. It is now a well-accepted opinion that the linear generation term $Q_{in}^{(P)}$ plays some role in the initiation of the wave field, while its influence on further wave field evolution is negligible.

This is demonstrated in Eq. (5.15) which describes the continuing development of the wave field. Atmospheric turbulence does not appear in this expression. The rate of growth of the spectral density at the particular wave number \vec{k} is directly proportional to the existing spectral density at the same wave number. The coefficient of proportionality μ (coupling coefficient) represents that part of the induced normal stresses at the water surface which are in phase with the wave slope (see Chapter 2). Moreover, Eq. (5.15) indicates that the growth rate is concentrated at higher frequencies, which is in agreement with observations of a growing sea (for example, Hasselmann et al., 1973).

The Miles (1957) theoretical expression for μ (see Eq. (2.97) depends on the average velocity fluctuations normal to the sea surface, and on the gradients of the mean wind velocity and vorticity. Using the scaling in terms of the friction velocity u_* , Mitsuyasu and Honda (1982) present Miles' theoretical coupling coefficient μ in more compact form:

$$\mu = \frac{0.16}{2\pi} \left(\frac{u_*}{C} \right)^2. \quad (5.18)$$

In practice, the coefficient μ is determined directly from cross spectra between simultaneous measurements of the water-surface elevation and the near-surface atmospheric pressure (obtained from a wave follower). An extensive experiment was conducted

by Snyder et al. (1981) in the Bight of Abaco, Bahamas. Field hardware included a three-dimensional array of six wave sensors and seven air pressure sensors, one of which was mounted on a wave follower. Their measurements, together with a re-examination of earlier results, provide the following expression for the coupling coefficient μ :

$$\mu = \begin{cases} (0.2 \text{ to } 0.3) \frac{\rho_a}{\rho_w} \left(\frac{U_5 \cos(\phi - \Theta)}{C} - 1 \right), & \text{for } 1 < \frac{U_5 \cos(\phi - \Theta)}{C} < 3 \\ 0 & \text{for } \frac{U_5 \cos(\Theta - \phi)}{C} \leq 1, \end{cases} \quad (5.19)$$

in which U_5 is the mean wind speed at height 5m in the atmospheric boundary layer, ϕ is the wind direction, and Θ is the direction of the wave component. Equation (5.19) indicates that waves grow exponentially only when the component of the wind speed in the wave direction exceeds the phase speed of the wave component.

Expression (5.19) is in reasonable agreement with the Miles' theory (1957, 1959), redefined in terms of u_*/C , where the friction velocity u_* (equal to $(\tau_a/\rho_a)^{1/2}$) is determined by the wind shear stress τ_a . If the ratio of u_*/U_5 is constant, the scaling of wave growth with u_* is not necessary.

However, the discussion in Section 2.2 indicates that the drag coefficient $C_z = \frac{u_*^2}{U_z^2}$ is a function of the wind speed, at height z in the constant stress layer. In particular, the Wu (1982) relation shows that ratio u_*/U_{10} changes as much as by a factor of $\sqrt{2}$, if U_{10} varies from 5 to 25 m/s.

Following the dimensional arguments of Kitaigorodskii (1962) and others, we can argue that if u_* is the only external parameter, defining the structure of the atmospheric boundary layer and its coupling to the ocean, and the generating mechanism is linear, the source function Q_2 must be of the form $Q_2 = B(u_*/C) \hat{\Psi}(k)$ (Komen et al., 1984). Thus, using $U_5 \approx 0.94U_{10}$ and $C_{10} = 1.12 \cdot 10^{-3}$, we have $u_*/C \approx 28u_*/C$, and Eq. (5.19) can be rewritten as follows:

$$\mu = \max \left[0, 0.25 \frac{\rho_a}{\rho_w} \left(28\beta \frac{u_*}{C} \cos(\phi - \Theta) - 1 \right) \right], \quad (5.20)$$

in which β is an empirical factor of $O(1)$, due to some uncertainty in parameterization of U/C in terms of u_*/C .

In the Mitsuyasu and Honda (1982) scaling of the Snyder et al. (1981) data, a parameterization $U_5 = 23u_*$ was used. Thus, $\beta \approx 0.85$. As will be shown later, an increase in β tends to close the gap between the spectral peak and wind input maximum.

Equation (5.20) indicates that wind generates waves only when $28\beta \frac{u_*}{C} \cos \Theta > 1.0$ (for simplicity we assumed that the wind direction was angle $\phi = 0$). This condition

implies also the low-frequency limit for the wind input. To find this limit we use Eqs. (5.17) and (5.20), and write the one-dimensional generation term in the form:

$$\frac{\partial S(\omega)}{\partial t} = \frac{1}{2\pi} \frac{\rho_a}{\rho_w} \omega S(\omega) \int_{-\Theta_l}^{\Theta_l} \left(28\beta \frac{u_*}{C} \cos \Theta - 1 \right) \cos^2 \Theta d\Theta, \quad (5.21)$$

in which the direction spreading factor $D(\Theta)$ was assumed to take the simple form $D(\Theta) = \frac{2}{\pi} \cos^2 \Theta$. The limiting angle Θ_l is given by:

$$\Theta_l = \arccos \left[\left(28\beta \frac{u_*}{C} \right)^{-1} \right] = \arccos \left[\left(28\beta \frac{u_* \omega_p}{g} \frac{\omega}{\omega_p} \right)^{-1} \right]. \quad (5.22)$$

Using the Mitsuyasu and Honda (1982) scaling, i.e. $U_5 = 23u_*$ and $\beta = 0.85$, Eq. (5.22) becomes:

$$\Theta_l = \arccos \left[\left(\frac{U_5 \omega_p}{g} \frac{\omega}{\omega_p} \right)^{-1} \right]. \quad (5.23)$$

Integrating in Eq. (5.21) gives:

$$\begin{aligned} \frac{\partial S(\omega)}{\partial t} = & \frac{1}{2\pi} \frac{\rho_a}{\rho_w} \omega S(\omega) \left[\frac{U_5 \omega_p}{g} \frac{\omega}{\omega_p} \left(2 \sin \Theta_l - \frac{2}{3} \sin^3 \Theta_l \right) - \right. \\ & \left. - \frac{1}{2} (2\Theta_l + \sin 2\Theta_l) \right]. \end{aligned} \quad (5.24)$$

Table 5.1: Limiting low-frequency $\left(\frac{\omega}{\omega_p} \right)$ as a function of $\frac{U_5 \omega_p}{g}$

$\frac{U_5 \omega_p}{g}$	0.8	0.9	1.0	1.1	1.2	1.3	1.5	2.0
$\frac{\omega}{\omega_p}$	1.26	1.12	1.00	0.91	0.84	0.77	0.67	0.50

The limiting low-frequency $\left(\frac{\omega}{\omega_p}\right)$ corresponds to condition $\frac{\partial S(\omega)}{\partial t} \geq 0$. The values of $\left(\frac{\omega}{\omega_p}\right)$ are collected in Table 5.1 for a given non-dimensional peak frequency $\frac{U_5 \omega_p}{g}$.

The low-frequency limit of the wind input moves towards the higher frequency part of the spectrum with sea growth. When $\frac{U_5 \omega_p}{g} \leq 1$, the wind energy is not transferred to wave frequencies smaller than the peak frequency (see, for example, Fig. 5.3).

Response of waves to an opposing wind

Tropical cyclones and strong frontal systems are characterized by complex wind fields in which wave propagation against the wind is not uncommon. Accurate wave predictions in such situations require the understanding of the response of waves to an opposing wind.

Let us consider the conservation equation of momentum in tensor notation:

$$\rho_a \left[\frac{\partial u_i}{\partial t} + \frac{\partial}{\partial x_j} (u_i u_j) \right] = \rho_a g_i + \frac{\partial \sigma_{ij}}{\partial x_j}, \quad (5.25)$$

where $u_i(x_i, t)$ is the instantaneous velocity in the x_i direction and $\sigma_{ij}(x_i, t)$ is the instantaneous stress tensor. The velocities u_i are summation of various components, i.e.:

$$u_i = \bar{u}_i + \tilde{u}_i + u'_i, \quad (5.26)$$

in which the upper bar denotes the overall time average, the tilde indicates a wave-induced component and the prime denotes the uncorrelated turbulent residual. Substituting Eq. (5.26) into Eq. (5.25) gives:

$$\rho_a \left[\frac{\partial \bar{u}_i}{\partial t} + \frac{\partial}{\partial x_j} (\bar{u}_i \bar{u}_j) \right] = \rho_a g_i + \frac{\partial}{\partial x_j} \left(\sigma_{ij} - \overline{u'_i u'_j} \right), \quad (5.27)$$

where $u''_i = \tilde{u}_i + u'_i$. It should be noted that $-\rho_a \overline{u''_i u''_j}$ represents the Reynolds' stresses in conventional turbulence analysis and these stresses yield an energy flux to (or from) the waves.

The water surface is oscillatory and the effective stress component acts in the direction normal to the water surface. Transformation of the measured stress components into the orthogonal curvilinear system in the water surface yields the following

expression for the coupling coefficient μ (Young and Sobey, 1985):

$$\begin{aligned} \mu = & \left[-amp(\tilde{p}) \sin \varphi - amp \left(\frac{\partial \zeta}{\partial x} \right) \rho_a \overline{u'' u''} - \right. \\ & - amp \left(\frac{\partial \zeta}{\partial x} \right) \rho_a \overline{u'' w''} + amp \left(\frac{\partial \zeta}{\partial x} \right) 2\mu_a \frac{\partial \bar{u}}{\partial x} + \\ & \left. + amp \left(\frac{\partial \zeta}{\partial x} \right) \mu_a \left(\frac{\partial \bar{w}}{\partial x} + \frac{\partial \bar{u}}{\partial z} \right) \right] / \rho_w C^2 k a, \end{aligned} \quad (5.28)$$

where φ is the phase difference between \tilde{p} and ζ , μ_a is the dynamic viscosity of air, u and w are the velocities in the x and z directions, respectively, and \tilde{p} is a wave-induced pressure. In Eq. (5.28), the first term represents the energy flux contribution due to normal stresses, the second and third terms represent the effects of Reynolds' stresses while the two last terms are viscous stress contributions.

An extensive set of laboratory experiments by Young and Sobey (1985) showed that the wave-induced pressure above the waves is approximately in antiphase with the water surface, which is in agreement with the predictions of potential theory.

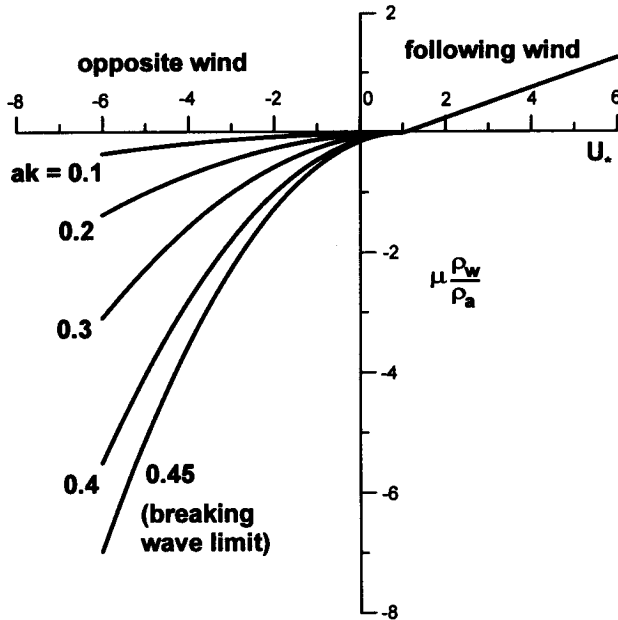


Figure 5.1: The wind-wave energy flux coefficient μ for following and opposite wind.

The wave-induced velocities follow the general trends expected for potential flow and the normal Reynolds stress is the dominant source of wind-wave energy flux in an opposing wind. The wave decay has a squared dependence in the wave slope and the ratio of the wind speed to the wave velocity. Therefore, the high-frequency waves attenuated much more rapidly than low-frequency waves. The resulting coupling coefficient μ takes the form (Young and Sobey, 1985):

$$\mu = (-0.7 \pm 0.2) \frac{\rho_a}{\rho_w} (ak)^2 \left(1 - \frac{U_{10} \cos(\phi - \Theta)}{C} \right)^2, \quad (5.29)$$

in which a is a local amplitude of the relevant wave component. The coupling coefficient μ , as a function of $U_* = \frac{U_{10} \cos(\phi - \Theta)}{C}$ and wave slope ak , is shown in Fig. 5.1 in conjunction with the following wind result of Snyder et al. (1981). The Figure shows strong dependence on the wave slope.

Steep waves (wind sea) attenuate rapidly, whereas less steep waves (swell) remain almost unaffected. Similar results were obtained by Tsuruya (1988). His experiments suggest, however, that μ is a factor of about 2 larger for higher wave steepness and almost an order of magnitude larger at very low wave steepness.

5.2.2 Nonlinear interaction between wave components

5.2.2.1 Evaluation of nonlinear energy transfer

The term $Q_5(Q_{nl})$ is probably the most debated term in all of the source set Q . Hasselmann's (1962, 1968) pioneering work established a theoretical framework for estimating the net transfer of energy among different frequency-direction components in a wave spectrum. He assumed that the probability density of the surface displacements is jointly normal, and calculated the net rate of energy transfer to any one wave number resulting from its interactions with all others. His result on the local rate of change of energy of the wave number spectrum $\hat{\Psi}(\vec{k})$ at the wave number \vec{k}_4 due to nonlinear wave-wave interactions, may be conveniently expressed in terms of the action density N (see Section 2.5) as:

$$\frac{\partial \hat{\Psi}(\vec{k})}{\partial t} = Q_5 = Q_{nl}, \quad (5.30)$$

in which:

$$Q_{nl}(\vec{k}_4) = \omega_4 \int \dots \int T(\vec{k}_1, \vec{k}_2, \vec{k}_3, \vec{k}_4) \{ [N_1 N_2 (N_3 + N_4) - N_3 N_4 (N_1 + N_2)] \cdot \\ \delta(\vec{k}_1 + \vec{k}_2 - \vec{k}_3 - \vec{k}_4) \delta(\omega_1 + \omega_2 - \omega_3 - \omega_4) \} d\vec{k}_1 d\vec{k}_2 d\vec{k}_3, \quad (5.31)$$

$N_i = N(\vec{k}_i, t)$, and \vec{k} is the two-dimensional wave number, related to the frequency ω by the dispersion relation $\omega_i = (g |\vec{k}_i|)^{1/2}$. The Dirac δ -function in Eq. (5.31) represents the resonant conditions. The coupling coefficient T is a complicated function of the wave numbers $\vec{k}_1, \dots, \vec{k}_4$, i.e.:

$$T = \frac{g\pi}{4} \frac{D^2(\vec{k}_1, \vec{k}_2, \vec{k}_3, \vec{k}_4)}{\omega_1 \omega_2 \omega_3 \omega_4}. \quad (5.32)$$

For the quantity D the reader can refer to Hasselmann (1962, 1963).

It should be noted that the wave action density spectrum $N(\vec{k})$ is directly related to the wave number spectrum $\hat{\Psi}(\vec{k})$ and frequency-directional spectrum $\hat{S}(\omega, \Theta)$ by:

$$N(\vec{k}, \vec{x}, t) = \frac{\hat{\Psi}(\vec{k}, \vec{x}, t)}{\sigma(\vec{k}, \vec{x})} = \frac{C_g}{k\sigma} \hat{S}(\omega, \Theta). \quad (5.33)$$

A non-trivial solution of the Hasselmann's six-dimensional Boltzmann type integral (5.31) has not yet been obtained. Early numerical integrations of this equation required very laborious efforts and were limited by computer systems available at that time.

However, Hasselmann (1963) gave a first insight into nonlinear energy transfer by calculating the energy transfer rate for the fully and partly developed Neumann spectrum. He showed that the peak of the spectrum gains energy from nonlinear interactions. The field measurements during the JONSWAP experiment (Hasselmann et al., 1973) indicate an opposite trend, namely, that the spectral peak tends to lose energy, especially to waves which frequencies are slightly below that of the peak.

Remarkable, yet simple theoretical advances in the calculation of the rate of energy transfer due to nonlinear interaction had been done by Longuet-Higgins (1976b). He used the evolution equation for three-dimensional packets of gravity waves, due to Davey and Stewartson (1974), and showed that the exchange of energy within the spectral peak itself is of dominant importance and that the energy from an isolated peak in the narrow spectrum tends to spread outwards.

If all of the wave numbers involved are nearly identical and equal to k_0 , then:

$$T(k_0, k_0, k_0, k_0) = 4\pi k_0^6. \quad (5.34)$$

The resonant interactions among the groups of four wave numbers conserve total wave action \mathcal{A} , energy E , and momentum M (Phillips, 1960a; Longuet-Higgins, 1976b):

$$\begin{aligned} \mathcal{A} &= \int \int N(\vec{k}) d\vec{k} = \text{const}, & E &= \int \int \omega(\vec{k}) N(\vec{k}) d\vec{k} = \text{const}, \\ M &= \int \int \vec{k} N(\vec{k}) d\vec{k} = \text{const}. \end{aligned} \quad (5.35)$$

In Fig. 5.2, the numerical result of Fox (1976), based on the Longuet-Higgins theory, is shown schematically for the symmetrical normal spectrum. Wave number k (horizontal axis) is measured from spectral peak, at which $k = 0$.

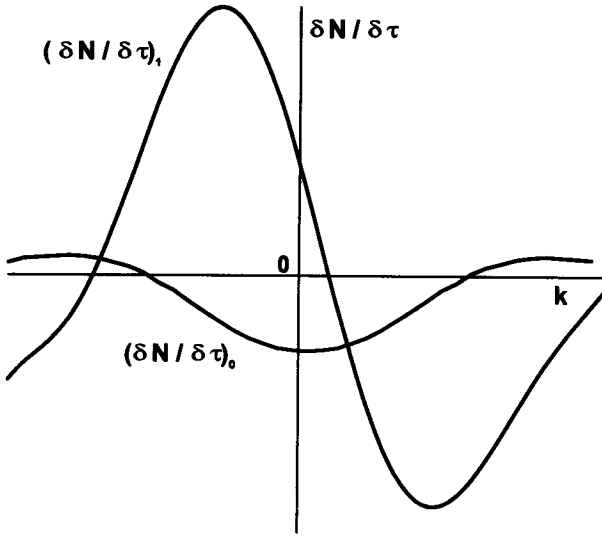


Figure 5.2: Resonant energy transfer rate $\frac{\partial N}{\partial \tau}$ as a function of wave number k :
 $\left(\frac{\partial N}{\partial \tau}\right)_0$ - spectral width is not included, $\left(\frac{\partial N}{\partial \tau}\right)_1$ - spectral width is included.

The Figure shows a negative minimum of $\left(\frac{\partial N}{\partial \tau}\right)_0$ at the origin (which corresponds to spectral peak) and two positive maxima, symmetrically situated to either side.

Dungey and Hui (1979) extended the work of Longuet-Higgins and Fox, including the effects of the width of a wave spectrum on the nonlinear energy transfer. The coupling coefficient T for a narrow spectrum was perturbed to the first order in a spectral width parameter ϵ . When a spectrum is represented as a sum of Gaussian curves, the one-dimensional energy transfer rate takes the form:

$$\frac{\partial N}{\partial \tau} = \left(\frac{\partial N}{\partial \tau}\right)_0 + \epsilon \left(\frac{\partial N}{\partial \tau}\right)_1 + O(\epsilon^2), \quad (5.36)$$

in which ϵ is a spectral width; $\left(\frac{\partial N}{\partial \tau}\right)_0$ is an energy transfer when spectral width is not included (Longuet-Higgins and Fox solution), and $\left(\frac{\partial N}{\partial \tau}\right)_1$ represents the influence of a spectral width.

Figure 5.2 indicates that the second term is skewed and causes energy to be pumped across the peak, from waves slightly shorter to waves slightly longer than

those at the peak. Thus, the effect of the width of a spectrum is to decrease the energy outflow from the peak. This is in agreement with numerical computations based on the JONSWAP spectrum. Simulations by Dungey and Hui also showed that the spectral width, the angular spreading, and the wave slope all have important effects on the energy transfer rate.

Although the above approximations to the exact nonlinear energy transfer term Q_5 reproduce many of the qualitative features of this term, they are not sufficiently accurate for typical wind-sea spectra. Hasselmann and Hasselmann (1985) introduced a more efficient method (the EXACT-NL scheme) of computing the nonlinear transfer in a surface wave spectrum by use of the symmetric properties of the integrand and discretizing the integral on a symmetrical five-dimensional integration grid. Further saving was achieved by precomputing the integration grid and the interaction coefficient T , and retaining only regions of phase space important for a given type of spectrum. Details on the calculation procedure are given in the Hasselmann and Hasselmann (1981, 1985) papers.

Snyder et al. (1993) proposed the hybrid integration scheme for the Hasselmann and Hasselmann (1985) model. This scheme combines the simplicity of earlier methods for computing the Boltzmann integral with the advantages of the EXACT-NL computation, accelerating this computation by about a factor of ten.

Resio and Perrie (1991) developed an economical method to evaluate the complete interaction integral. This method is based on the selected scaling properties and symmetries of the integrals to construct the integration grid. This study demonstrates the smoothing nature of the nonlinear terms, which effectively remove perturbations in the spectral shape at frequencies above the peak frequency. At these frequencies, the fluxes through the equilibrium range of a spectrum are approximately constant only for ω^{-4} type spectrum and are independent of peak frequency ω_p .

To summarize the principal properties of the nonlinear transfer we adopt some scale parameters for an initial surface wave spectrum and nonlinear transfer. For example, for a two-dimensional spectrum $\hat{S}(\omega, \Theta)$ we assume:

$$\hat{S}(\omega, \Theta) = \alpha g^2 \omega^{-5} F\left(\frac{\omega}{\omega_p}, \Theta\right), \quad (5.37)$$

and

$$\hat{Q}_5(\omega, \Theta) = \hat{Q}_{nl} = \alpha^3 g^2 \omega_p^{-4} F_Q\left(\frac{\omega}{\omega_p}, \Theta\right), \quad (5.38)$$

in which α is a Phillips constant, ω_p is a peak frequency, $F\left(\frac{\omega}{\omega_p}, \Theta\right)$ and $F_Q\left(\frac{\omega}{\omega_p}, \Theta\right)$ are the non-dimensional functions of $\frac{\omega}{\omega_p}$ and Θ .

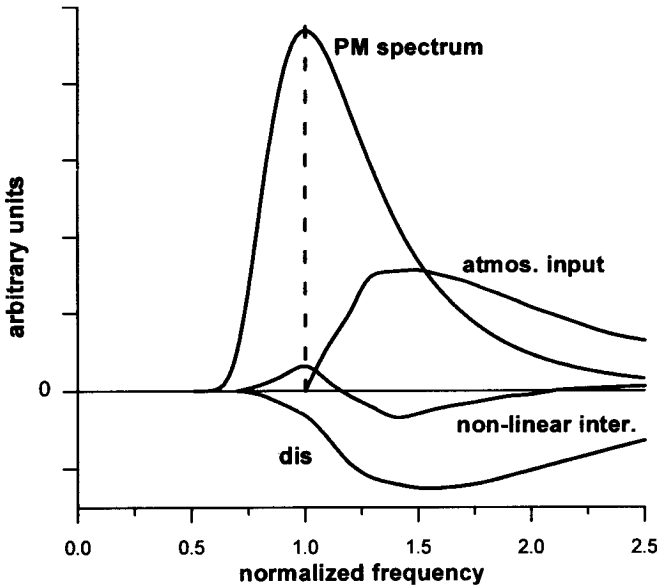


Figure 5.3: Scheme of atmospheric input, nonlinear interaction and dissipation terms for a fully developed Pierson-Moskowitz spectrum.

The source function expressing the nonlinear energy transfer Q_{nl} typically has a 3-lobed positive-negative-positive distribution. Extensive calculations by Hasselmann and Hasselmann (1985) showed that the low-frequency positive lobe for a fully developed Pierson-Moskowitz spectrum is located roughly at the spectral peak (see Fig. 5.3). For a growing wind-sea spectrum of the JONSWAP form, the low-frequency positive lobe lies slightly to the left of the peak on the forward face of the spectrum (Fig. 5.4). Also, the nonlinear transfer is approximately an order of magnitude larger than for the fully developed sea spectrum.

The nonlinear interactions are restricted to a relatively small range in wave number space. The strongest transfer rates are found close to the spectral peak. The high-frequency positive lobe has a broader directional distribution than the other two lobes, which results in observed broadening of the directional spreading function for higher frequencies.

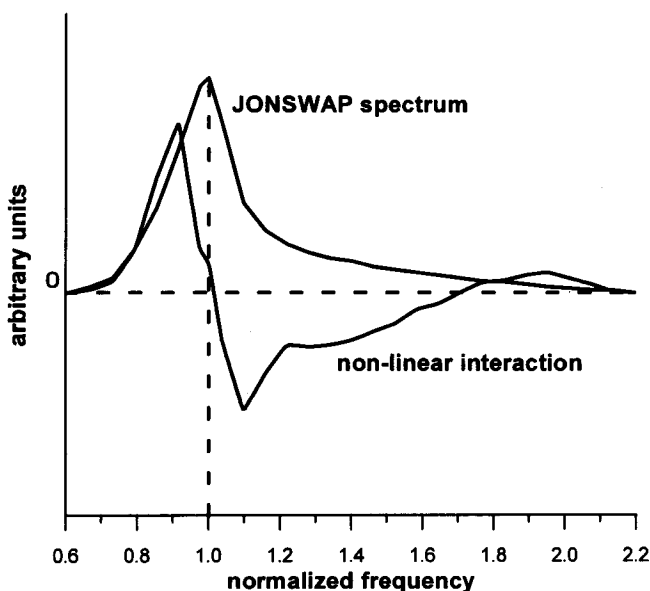


Figure 5.4: Scheme of atmospheric input, nonlinear interaction and dissipation terms for a growing sea spectrum (JONSWAP type).

5.2.2.2 Parameterization of nonlinear energy transfer

An evaluation of nonlinear energy transfer is a major computational task which cannot yet be undertaken within the framework of the spectral prediction models. The time needed to compute the exact source function greatly exceeds the practical limits of the operational wave models. Therefore, some parameterization of nonlinear energy transfer is needed. A given parameterization can be reliably tested by incorporating it into a wave model and verifying that the wave growth simulated by the model agrees in standard tests with the growth curves obtained with the same model when using exact computations of the nonlinear transfer.

Four different parameterizations of the nonlinear energy transfer Q_{nl} were proposed by Hasselmann et al. (1985). The first parameterization is based on the relation of Q_{nl} to different values of the peak-enhancement parameter γ . The dependence of Q_{nl} on γ explains the self-stabilization of the spectral shape and the shift of the peak to lower frequencies during the growth stage.

The second parameterization is based on the set of empirical orthogonal functions (EOFs) determined by the computed Q_{nl} ensemble itself. In particular, Hasselmann and Hasselmann (1981) used this technique to parameterize Q_{nl} in terms of two shape

parameters, i.e. the peak-enhancement factor γ and a directional spreading parameter s . The final form of the source function \hat{Q}_{nl} is (Hasselmann et al., 1985):

$$\hat{Q}_{nl}\left(\frac{\omega}{\omega_p}, \Theta\right) = E\left[\hat{Q}_{nl}\right] + \sum_{j=1}^5 C^{(i,j)} H_{nl}^{(j)}\left(\frac{\omega}{\omega_p}, \Theta\right), \quad i = 1, \dots, 18, \quad (5.39)$$

where $E\left[\hat{Q}_{nl}\right]$ is a mean value of a set of 18 exact computations for various JON-SWAP type spectra, with γ varying from 1 to 7, and a number of different directional spreading functions, $H_{nl}^{(j)}$ is a set of EOFs functions describing the variability of the ensemble relative to the mean. The expansion coefficients $C^{(i,j)}$ imply the dependence of the coefficients on the shape parameters γ and s . In the optional model, the five functions $H_{nl}^{(j)}$ and coefficients $C^{(i,j)}$ are stored in memory, resulting in the fast estimation of \hat{Q}_{nl} (see also Allender et al., 1985).

The above parameterizations techniques are limited to a relatively restricted class of spectra which are characterized by one or two shape parameters. They are unable to treat the wind sea-swell transition regime, as well as the rapidly changing wind field case where the spectral shape is not restricted *a priori* in the model. To overcome these limitations, the operator parameterization of Q_{nl} was introduced. This contains the same number of degrees of freedom as used to describe the spectrum. In particular, a cubic, fourth-order diffusion-operator expression was derived by Hasselmann et al. (1985). Such expansion is appropriate for interactions occurring in the vicinity of the central interaction point $\vec{k}_1 = \vec{k}_2 = \vec{k}_3 = \vec{k}_4 = \vec{k}$. This corresponds to the narrow-peak approximations of Longuet-Higgins (1976b), Fox (1976), and Dungey and Hui (1979), discussed above. However, the basis of the local-interaction approximation is different than the narrow-peak approximation in the sense that the diffusion-operator method assumes that the spectrum is smooth. The local-interaction expansion was found to be useful for understanding the mechanisms by which the nonlinear transfer generates and maintains the shape of the spectrum.

The fourth parameterization method also uses the fact that the interactions between closely neighbouring wave numbers reproduce the principal features of the nonlinear transfer. It was found that exact nonlinear transfer could be simulated by one mirror-image pair of intermediate-range interaction configurations. In each configuration, two wave numbers are taken as identical, $\vec{k}_1 = \vec{k}_2 = \vec{k}$. The wave numbers \vec{k}_3 and \vec{k}_4 are of different magnitude and lie at an angle to the wave number \vec{k} , as required by the eight-shape resonance curve. The second configuration is a mirror-image of the first one at the \vec{k} axis. The computations of the Q_{nl} source term are identical to the computation of the exact Boltzmann integral, but the integration is taken over a $2D$ -continuum and for two discrete interactions, instead of a $5D$ -interaction phase space. The particular interactions are summed up over the discretized \vec{k} -plane, and for each \vec{k} , over the pair of discrete-interactions, to yield the source function Q_{nl} . Hasselmann et al. (1985) calculated the spectra and energy balance using the method and the discrete interaction approximation method, and found a good agreement. The application of particular parameterizations in various prediction models will be discussed

in Section 5.3, and more information on parameterization techniques of Q_{nl} term can be found in a book by Komen et al. (1994).

5.2.2.3 Nonlinear coupling between swell and wind waves

In nature, the conditions of a uniform wind blowing over an ocean initially at rest occur very infrequently. Usually the local wind waves develop in the presence of a low-frequency swell that has radiated from a distant storm. The long waves can influence the shorter ones in various ways. For the shorter waves overtaken by the longer ones, the maximum unbroken wave height is less than it would be in the absence of the swell. Modulations of short surface waves by long waves play an important role in the remote imaging of the sea surface (see Section 9.4). On the other hand, it is well-known that the long swell is almost unaffected by local wind (Snodgrass et al., 1966).

Wave-wave nonlinear interactions provide another mechanism for coupling between swell and wind waves. As was shown above, they are local in wave number space. Therefore, if swell and a local wind sea are sufficiently separated in wave number, interactions between them will not exist. For a bimodal spectral distribution, in which the long wave and short wave components are very close, the nonlinear energy transfer is effective and can be described by Hasselmann's resonant third-order wave-wave interaction model (5.31). When the swell frequency ω_s is lower than the low-frequency cutoff of the local sea, the rate of change of swell energy E_s is (Hasselmann, 1963):

$$E_s(t) = E_s(t_0) \exp \left[-\frac{t - t_0}{\tau} \right], \quad (5.40)$$

in which τ is a time scale depending on the local sea spectral shape, and swell frequency and direction. The swell decay time scale increases as the swell frequency decreases away from the wind sea spectral peak ω_p .

An evaluation of the full nonlinear source Q_{nl} , given in Eq. (5.31), applied for the bimodal spectrum, consisting of a swell and a local sea component, demonstrates the difference between coupled and uncoupled systems (Masson, 1993). In Figure 5.5, the one-dimensional time rate of change of the spectrum due to nonlinear interactions is shown. The incident spectrum is composed of the JONSWAP spectrum and the narrow swell spectrum with peak frequency $\omega_s = 0.67\omega_p$ (ω_p is a peak frequency of the wind waves spectrum). For the single JONSWAP spectrum, the typical three-lobe shape is observed. Also, for the swell alone, Q_{nl} has a familiar shape associated with a narrow peak spectrum (not shown). However, for total bi-modal spectrum, the nonlinear source term Q_{nl} indicates that energy flows from the peak of the short waves to frequencies on each side of it. In the swell frequency range, the coupling transfers energy from the right of the narrow peak to its left. This is in agreement with Fox's (1976) calculations for the narrow asymmetric spectrum.

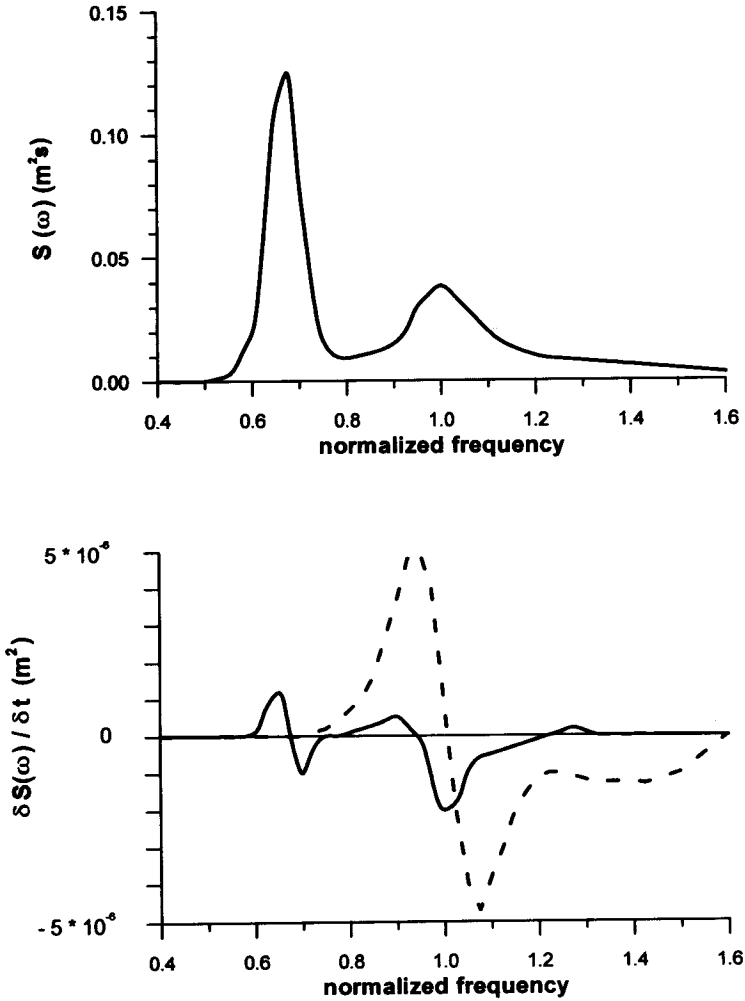


Figure 5.5: Bimodal frequency spectrum (a) and rate of change due to nonlinear interactions (b): — — — local sea only, — coupling between the two systems included (From Masson, 1993).

The numerical simulation of evolution in time of the bimodal spectrum indicates a gradual change into a unimodal distribution, when the local sea peak has completely disappeared and the swell component has broadened. However, when the two wave systems are decoupled, the short-wave system remains relatively unchanged and the sharp swell peak slowly spreads out over neighbouring frequencies.

It should be noted that nonlinear coupling decreases rapidly with the ratio of the swell and sea frequency; no coupling is observed for ratios less than ~ 0.6 . For such a value, the separation of the two peaks in frequency space is quite large for the high-frequency laboratory waves, but is rather small for lower frequency ocean waves. Therefore, it is reasonable to state that the coupling due to nonlinear interactions between swell and wind waves in ocean conditions occurs only when the two peaks are very close.

5.2.3 Energy dissipation due to white capping

The source term Q_7 in the radiation transfer equation (2.177), describes energy loss due to white capping, and belongs to so called strong nonlinear interactions. The actual threshold for breaking in a random field is still not well understood.

As was shown in Section 4.2.4, the vertical acceleration criterion may be an acceptable practical predictor of whitecap events. The appropriate threshold level appears to be approximately $0.4g$, as was suggested by Longuet-Higgins (1985).

The study of white capping in terms of the wave spectrum is usually concentrated on the concept of a high-frequency equilibrium range. For example, Phillips (1985) expressed the loss of energy due to breaking D in the equilibrium range in the form of the degree of saturation $B(\vec{k})$ as:

$$D = g\omega k^{-4} f(B(\vec{k})), \quad (5.41)$$

in which:

$$B(\vec{k}) = k^4 \hat{\Psi}(\vec{k}) = g^{1/2} k^{9/2} N(\vec{k}). \quad (5.42)$$

The form of function f should be found from the requirement of a balance among the three main processes, i.e. input from wind, the wave-wave interactions and wave breaking. The physics of energy dissipation suggests that the spectral dissipation of energy by wave breaking in the equilibrium range occurs at whatever rate is needed to accommodate the net input from the wind. As we will see in the next Section, the processes of wave-wave interaction and losses by wave breaking are not spectrally local. Therefore, all three physical processes should be taken into account in the equilibrium range and not only in this range.

For the purposes of prediction, wave energy dissipation due to breaking should be presented in the form of the source function (Q_7 component). If we do not go into detail on the white-capping process itself, and assume that white-capping is a process

strongly nonlinear locally, but still weak-in-the mean, we can write the Q_7 term as (Hasselmann, 1974):

$$Q_7 = Q_{dis} = -\gamma(\vec{k}) \hat{\Psi}(\vec{k}). \quad (5.43)$$

In order to evaluate the damping factor $\gamma(\vec{k})$, the internal fluid dynamic structure of a breaking wave must be known. The complete evaluation of $\gamma(\vec{k})$ is a very difficult problem, which is not yet solved. It requires both the detailed knowledge of hydrodynamics of breaking waves, and the representation of individual breaking events in a spectral form. For frequencies beyond the wind-sea peak, when the spectrum may be represented by the Phillips (1958) form:

$$\hat{\Psi}(\vec{k}) = \frac{\alpha}{2} k^{-4} D(\Theta), \quad (5.44)$$

the damping coefficient can be presented as:

$$\gamma = \eta \sigma_\zeta^2, \quad (5.45)$$

in which η is a function of the wave propagation direction and the overall statistical properties of the wave field. Thus, it is constant for a given sea state.

Some insight into the energy dissipation due to white capping can be obtained from an analysis of the spectrum which, when local, is stationary. For such a situation, the energy transfer equation (2.177) takes the form:

$$\frac{\partial \hat{\Psi}(\vec{k})}{\partial t} = Q_{in}^{(nl)} + Q_{nl} + Q_{dis} = 0, \quad (5.46)$$

or

$$Q_{dis} = -Q_{in}^{(nl)} - Q_{nl}. \quad (5.47)$$

Assuming that $Q_{in}^{(nl)}$ and Q_{nl} are known, the Q_{dis} can be obtained from this balance requirement. For example, for a stationary asymptotic spectrum, similar to the Pierson-Moskowitz spectrum, the best agreement was achieved with a dissipation term given by (Komen et al., 1984):

$$Q_7 = \hat{Q}_{dis} = -3.33 \cdot 10^{-5} \bar{\omega} \left(\frac{\omega}{\bar{\omega}} \right)^2 \left(\frac{\hat{\alpha}}{\hat{\alpha}_{PM}} \right)^2 \hat{S}(\omega, \Theta), \quad (5.48)$$

where:

$$\hat{\alpha} = \frac{\sigma_\zeta^2 \bar{\omega}^4}{g^2}, \quad \bar{\omega} = \frac{1}{\sigma_\zeta^2} \int \int \hat{S}(\omega, \Theta) \omega d\omega d\Theta, \quad (5.49)$$

and $\hat{\alpha}_{PM} = 4.57 \cdot 10^{-3}$. The dissipation source term Q_{dis} is very sensitive to the initial spectrum form.

5.2.4 Energy balance for fully-developed and growing seas

In wave prediction modelling practice, the source term Q in the radiative transfer equation (2.177) is usually restricted to the three terms $Q_{in}^{(nl)}$, Q_{nl} and Q_{dis} . Such representation is motivated for two main reasons. Firstly, these terms play a most important role in the overall balance of spectral energy, and they provide the situation where the predicted results are very close to observations. Secondly, present knowledge about the other source terms in Eq. (2.177) is still very limited, and the implementation of these terms into prediction wave models is not yet advanced.

Let us first discuss an application of such three terms representation for the simpler situation of a stationary asymptotic spectrum $\hat{\Psi}(\vec{k})$, which is a result of wind blowing over a fetch and a time duration sufficiently large to produce a stationary and homogeneous fully-developed wave state. This state is usually expressed by the Pierson-Moskowitz spectrum (3.78). Thus, the energy balance in terms of the two-dimensional spectrum $\hat{S}(\omega, \Theta)$ becomes:

$$\frac{\partial \hat{S}(\omega, \Theta)}{\partial t} = \hat{Q}_{in}^{(nl)} + \hat{Q}_{nl} + \hat{Q}_{dis} = 0, \quad (5.50)$$

in which:

$$\hat{S}(\omega, \Theta) = S_{PM}(\omega) D(\Theta; \omega), \quad (5.51)$$

where $S_{PM}(\omega)$ is given by Eq. (3.78) and the directional spreading function $D(\Theta; \omega)$ is given by Eqs. (3.143) and (3.147). In particular, Eq. (3.147) describes the dependence of angular distribution on wave frequency suggested by Hasselmann et al. (1980).

Using representation (5.51), all three terms in Eq. (5.50) can be evaluated. Komen et al. (1984) tested the existence of an equilibrium (5.50) with the wind input given by Eq. (5.17), and μ parameterization as in Eq. (5.20). The nonlinear energy transfer was calculated using the EXACT-NL scheme by Hasselmann and Hasselmann (1981). Finally, the dissipation term \hat{Q}_{dis} was parameterized, as in Eq. (5.43). When the Phillips constant α is slightly reduced, from $8.10 \cdot 10^{-3}$ to $5.0 \cdot 10^{-3}$, the Pierson-Moskowitz spectrum provides a balance of total rate of change for each frequency integrated over all directions. This is schematically shown in Fig. 5.3. Negative values of Q_{dis} balance both wind input $Q_{in}^{(nl)}$ and nonlinear transfer Q_{nl} terms. Thus, the Pierson-Moskowitz spectrum seems to represent a stationary solution of the energy balance equation.

However, the non-dimensional balance, in frequency space, does not necessarily imply balance in the two-dimensional frequency-angle space. The calculations by Komen et al. (1984) demonstrated a strong angular imbalance which yields a redistribution of energy in the spectrum. The two-dimensional balance can only be achieved by the appropriate modification of the input and dissipation source terms. Such a possibility was discovered by numerical asymptotic simulation.

To accelerate the computations, a field shape high-frequency spectral tail of the form $S(\omega) \sim \omega^{-5}$ was imposed for frequencies $\omega > 2.5\omega_p$. No explicit computations

were performed in this region and the results obtained were insensitive to the details of this high-frequency tail parameterization. However, Banner and Young recently (1994) discovered that the use of a constrained tail shape in computational models has fundamental implications in the total energy balance within the spectrum. In particular, the dissipation source term Q_{dis} strongly depends on the spectral tail shape. Moreover, they found that the evolution of total wave energy with fetch, the directional spreading function near the spectral peak, and the form of the high wave number tail region, cannot be satisfied with the Hasselmann type dissipation term Q_{dis} (5.43). An alternative form for Q_{dis} is required for more realistic modelling observational data.

It should be noted that Zakharov and Filonenko (1966) and Kitaigorodskii (1983) proposed an energy balance in which wind input dominates at low-frequencies and the dissipation is confined to high-frequencies. The energy within the spectrum is transformed from low to high-frequencies by a constant flux due to nonlinear interaction in analogy with Kolmogorov's theory of isotropic turbulence. However, calculations indicate that such a balance yields a spectrum that grows too rapidly and does not approach equilibrium.

If we restrict our attention to the high-frequency saturation range, the three physical processes, i.e. wind input, nonlinear wave-wave interaction and energy dissipation, take the form (Phillips, 1985):

$$\left. \begin{aligned} \text{wind input} &\approx m \cos^{2p} \Theta g k^{-4} \left(\frac{u_*}{C} \right)^2 \mathcal{B}(\vec{k}) \\ \text{nonlinear interaction} &\approx g k^{-4} \mathcal{B}^3(\vec{k}) \\ \text{energy dissipation} &\approx g k^{-4} f(\mathcal{B}(\vec{k})) \end{aligned} \right\}, \quad (5.52)$$

in which $\mathcal{B}(\vec{k})$ is the degree of saturation, mentioned in Section 5.2.3, i.e. $\mathcal{B}(\vec{k}) = k^4 \hat{\Psi}(\vec{k})$.

The balance of these processes inside the equilibrium range requires that the wave number spectrum should have the form:

$$\hat{\Psi}(\vec{k}) = k^{-4} \mathcal{B}(\vec{k}) = \beta_1 (\cos \Theta)^p u_* g^{-1/2} k^{-7/2}, \quad (5.53)$$

and the degree of saturation is (Phillips, 1985):

$$\mathcal{B}(\vec{k}) = \beta_2 \cos^p \Theta \left(\frac{u_*}{C} \right), \quad f(\mathcal{B}(\vec{k})) = \beta_2 \mathcal{B}^3(\vec{k}). \quad (5.54)$$

Accordingly, the corresponding frequency spectrum $S(\omega)$ becomes:

$$S(\omega) \approx \beta u_* g \omega^{-4}, \quad (5.55)$$

which is in agreement with the Toba (1973) prediction (see also Section 3.2.2).

For the case of duration-limited growth, the energy balance equation can be represented as:

$$\frac{\partial \hat{S}(\omega, \Theta)}{\partial t} = \hat{Q}_{in}^{(nl)} + \hat{Q}_{nl} + \hat{Q}_{dis} = \hat{Q}_{tot} \neq 0. \quad (5.56)$$

Numerical calculations by Young et al. (1985) indicate that in the earlier stage of growth (see Fig. 5.4), the form of \hat{Q}_{nl} has a strongly pronounced three-lobe structure which is also reflected in \hat{Q}_{tot} . The positive lobe of the transfer occurs slightly to the left of the spectral peak, which corresponds to the known fact of the migration of the spectral peak to lower frequencies.

When the spectrum approaches full development (see Fig. 5.3), the nonlinear transfer is reduced substantially, by almost an order of magnitude. The positive lobe is now situated under the peak and is balanced by dissipation. This yields an almost complete balance of the total source term \hat{Q}_{tot} across the entire spectrum for a fully-developed equilibrium state, as is expected.

The balance of the three mechanisms, particularly the stabilizing influence of the nonlinear wave-wave interaction, plays an important role in predicting the wave spectrum under non-stationary conditions, particularly when the wind suddenly changes its direction. For wind-direction changes of less than 60° , the wind-sea direction adjusts smoothly and the nonlinear interactions prevent the growth of a fresh secondary peak within the spectrum. The high-frequency components relax more rapidly to the new wind direction than the low-frequency components. When the wind-direction changes are greater than 60° , a second independent wind-sea spectrum is generated in the new wind direction, while the old wind-sea gradually decays as swell (Young et al., 1985).

5.3 Wave prediction models

For about 30 years, wind-driven numerical wave prediction models have proven useful for ship routing, offshore technology, and also more recently, for climate research. Since the pioneering model by Gelci et al. (1957), many wave models have been developed in which the complicated nature of wave generation, propagation and decay has been described. The basis for all numerical prediction models is a radiative transfer equation (2.177) with an appropriate source-sink term Q . However, except for this approach, the simpler semi-empirical methods, based on dimensional analysis, are still used. In the following, we first describe the models based on the radiative transfer equation, with special emphasis on the recent generation models. After that, a few of the most popular semi-empirical fetch-graph models will be discussed.

5.3.1 Wave models based on energy transfer equation

5.3.1.1 First generation wave models

The models based on the radiative-transfer equation are usually classified as models of first, second or third generation. At the end of the fifties, when the first model by Gelci et al. (1957) was developed, very little was known about the source function components. However, at about the same time, the publication of wave generation theories by Phillips (1957) and Miles (1957), and nonlinear energy transfer due to wave-wave interactions by Hasselmann (1962), provided a theoretical framework for wave generation modelling.

In the 1960s and 1970s several new models were developed (Pierson et al., 1966; Barnett, 1968; Gelci and Devillaz, 1970; Ewing, 1971; Gelci and Chavy, 1978). In these models the wind input terms Q_1 and Q_2 were represented by forms similar to Eqs. (5.10) and (5.16). The dissipation term $Q_7(Q_{dis})$ was used as a sort of limiter, which prevented the spectrum from exceeding the prescribed saturation level. When the wave components reached a universal saturation level, modelled by the ω^{-5} frequency spectrum, they suddenly stopped growing. The nonlinear interaction term $Q_5(Q_{nl})$ was either neglected or was simply parameterized, using the Hasselmann (1963) result for the fully-developed Neumann spectrum. This means that in the first generation wave models, each spectral component evolves essentially independently to all other components. Even if nonlinear transfer is considered, it represents a relatively small modification to the total energy balance.

The first generation models have been applied successfully for many years, and are still in operation. A typical operational first generation wave prediction model is the VENICE model, described by Cavaleri and Rizzoli (1981). The model is based on the ray technique, and is also suitable for shallow water applications (see next Chapter). In a coordinate system, moving along the rays with group velocity, the radiative-transfer energy equation takes a very simple form:

$$\frac{\partial \hat{S}}{\partial t} = \hat{Q}, \quad (5.57)$$

which is valid along each single ray. The two wind input source terms, \hat{Q}_1 and \hat{Q}_2 , correspond to the Phillips and Miles mechanisms in which the coupling coefficient μ is modelled according to Barnett (1968):

$$\mu = 5 \frac{\rho_a}{\rho_w} f \left(\frac{U \cos \Theta}{C} - 0.9 \right), \quad (5.58)$$

in which Θ is the angle between the wind and wave vectors. The term 0.9 allows for the experimental evidence of growing waves propagating faster than the wind.

In the model, which is basically uncoupled and linear, each energy component is evaluated independently of the other. Therefore, nonlinear interactions are not taken into account, but they are partly included in the μ value, as this value, being deduced

by direct fit to experimental data, implicitly contains all information on the physical processes involved.

Energy dissipation is modelled simply by establishing the limiting form of a saturation spectrum. The additional effects of white capping were not modelled explicitly, but it was believed that they were also implicitly included by the adopted μ value.

The second operational first generation model was developed by the Meteorological Research Institute (MRI) in Japan (The SWAMP Group, 1985). The wind input terms Q_1 and Q_2 were coupled with the dissipation term Q_7 , due to wave breaking, by putting the limit for wave growth in the form of the Pierson-Moskowitz spectrum. The forecasting procedure obeys three sea stages, i.e. the growing stage, decaying stage, and the case of opposing winds. As in the case of the VENICE model, the MRI model neglects the effects of nonlinear interactions between wave components.

The testing of the VENICE and MRI models program against the second generation models (see below) showed that they yield quite a different picture of the wave field. Generally, first generation models provide a wider variety of spectral distributions than second generation models. However, they are strongly dependent on the assumed directional spreading of the growth coefficients.

Besides some success in the forecasting of wave field, there was some doubt as to whether these models really represent explicitly and correctly the complete energy balance and physics of wave generation. The extensive field experimental studies in the 1970s (for example, Hasselmann et al., 1973) and wind-tank experiments (Mitsuyasu, 1968), provided a lot of information which led to a changed view of the spectral energy balance of a growing sea. It was found that the principal source of energy, during the main growth phase on the low-frequency forward face of the spectrum, is the nonlinear energy transfer from higher to lower frequencies.

The estimated wind input on the forward face of the spectrum was an order of magnitude smaller than that assumed in the first generation wave models. The enhancement of the spectral peak of a growing sea was equal to about 3 ($\gamma = 3.3$ in the JONSWAP experiment). This factor reflects the unexpectedly high nonlinear transfer rate and the importance of nonlinear wave-wave interaction for total energy balance.

At higher frequencies, an universal equilibrium range was not confirmed (see Chapter 3). The saturation law ω^{-4} , proposed by Toba (1973), fits better to the experimental data. As the nature of the spectral energy balance was changed, the wave prediction models required a basic restructuring. This restructuring resulted in the development of the second generation models.

5.3.1.2 Second generation wave models

Three distinctive approaches are commonly utilized in second generation wave models: discrete spectral models (DS), parametric models (P) and hybrid models (H).

Discrete spectral models (DS)

Discrete spectral models (DS) have been used since Gelci et al. (1957) and Pierson et al. (1966). The spectral density function $\hat{S}(\omega, \Theta; \vec{x}, t)$ is represented as a summation of separate frequency and direction bands, for each of the discrete mode points $(i\Delta x, j\Delta y)$ at times $t_0 + n\Delta t$. Then, the parabolic initial-value problem for radiative-transfer equation (2.177) or (2.185) is solved numerically. In typical applications, 10-15 frequencies and 12-16 directions have been adopted.

The SWAMP Group (1985) review presents three operational discrete spectral models and their intercomparison: The UK Meteorological Office Operational Wave Model (BMO), Atlantic Oceanographic and Meteorological Lab., NOAA Model (SAIL) and Scripps Institution of Oceanography Model (DNS).

Instead of comparing these prediction models against real data, a set of seven hypothetical wind fields were designed to focus separately on the various critical properties of the models:

- | | |
|----------|---|
| Case I | advection test:
a pure swell propagation experiment to compare the numerical advection schemes; |
| Case II | fetch - and duration limited growth:
a study of the wave growth for a uniform, stationary wind blowing orthogonally off a straight shore; |
| Case III | slanting fetch:
generalization of Case II to an offshore wind blowing at an angle of 45° to the coast; |
| Case IV | half-plane wind:
propagation of swell away from the side of a laterally bounded wind field into a neighboring calm region; |
| Case V | diagonal front:
propagation of wind waves across a diagonal front, where the wind turned suddenly by 90° from a parallel to a cross-wave direction; |
| Case VI | stationary and moving hurricane:
testing models under extreme wind conditions; |
| Case VII | 90° change in wind direction:
some simpler scenario of the Case V in which the advection effects were removed by considering a non-stationary wind field. |

The principal features of the models are listed in Table 5.2, based on the SWAMP (1985) study.

All models use a linear-feedback wind input function Q_2 with coupling coefficient μ , in accordance with the measurements of Snyder et al (1981). Moreover, some form of limiting saturation spectrum, depending on the stage of development of the sea, is adopted by all models.

The basic difference between models is related to the details of parameterization of the nonlinear transfer in the forward face and peak regions of the sea spectrum. In the BMO Model, at each growth step, the total energy input to the sea is computed by integrating the sum of Q_{in} and Q_{dis} over the spectrum (11 frequencies and 12 direction components). The net energy gain is then redistributed over the frequency and directional bands in accordance with the JONSWAP spectrum. The transformation into JONSWAP form is immediate and couples all components with frequency greater than 0.8 of the peak and direction within 90° of the wind.

Table 5.2: Source functions of discrete spectral models

Model	Linear growth	Nonlinear transfer	Saturation spectrum
BMO	$Q_{in}=Q_1 + Q_2$	Total net energy input computed from Q_{in} and Q_{dis} , then redistributed in accordance with JONSWAP form (Q_{dis} is based on Hasselmann's white-capping model (1974)).	JONSWAP spectrum; saturation is included in nonlinear transfer parameterization.
SAIL	$Q_{in}=Q_2$	Net source function inferred from JONSWAP growth curves is applied if greater than Q_{in} .	Modified JONSWAP-type distribution. Saturation is accompanied by directional energy redistribution.
DNS	$Q_{in}=Q_2$	Empirical orthogonal function representation of exact Q_{nl} computations as function of peak enhancement factor γ and directional spread $\Delta\Theta$.	Pierson-Moskowitz spectrum with sea-state-dependent saturation level.

The operational version of the SAIL Model has 24 directional bands and 15 frequency bands from 0.04 Hz to 0.22093 Hz. The growing sea spectrum is forced to conform closely to an empirical Pierson-Moskowitz type spectrum. The net incremental growth at each time step is taken from the empirical fetch-limited spectral growth data and does not depend on an explicit representation of Q_{nl} . A particular feature of the SAIL model is the treatment of the saturation region, which is not a simple cutoff limit approach. The energy in the saturation stage is also angularly distributed.

The DNS model is based on a parameterization of the Q_{nl} source term, depending on two spectral shape parameters (the peak enhancement factor γ and angular spread $\Delta\Theta$). This parameterization was obtained by Empirical Orthogonal Function (EOF) analysis of an ensemble of exact computations of Q_{nl} , made for a series of spectra with different values of γ and $\Delta\Theta$. The DNS limits the spectrum beyond the peak frequency by a Pierson-Moskowitz spectrum with variable saturation level depending on the stage of sea growth.

In fact, the BMO model is very similar, both in physics and in the numerics, to a one-parameter hybrid model (see below). On the other hand, the SAIL and DNS models possess some characteristics of parametrical models.

Parametric models

The fact that nonlinear energy transfer within the spectrum controls not only the rate of growth of the developing sea, but also the form of the spectrum, is significant both for proper description of the source function and for numerical technique. In particular, the assessment of the Boltzmann integral requires some form of parameterization. However, if nonlinear energy transfer is recognized as a controlling process, there appears little point in describing the remaining terms in the transfer equation in greater detail than the nonlinear terms.

This conclusion was the basis for a parametric wave model proposed by Hasselmann et al. (1976). In this model, the growth of the wind-sea spectrum is expressed in terms of a small set of coupled transport equations which describe the evolution of only a few characteristic spectral parameters (Hasselmann et al., 1973).

In the following, we describe briefly a simple version which is based on the observation that the growing sea spectra appear to have a rather similar shape, fairly close to the mean JONSWAP spectrum, i.e.:

$$\hat{S}(\omega, \Theta; x, y, t) = \hat{S}(\omega, \Theta; \omega_p, \alpha, \gamma, \sigma'_0, \sigma''_0). \quad (5.59)$$

The JONSWAP parameters $\omega_p, \alpha, \gamma, \sigma'_0, \sigma''_0$ are all functions of x, y and t . Therefore, at each mode we have 5 dependent variables. Note that for a discrete spectral model we typically have a few hundred variables (10-15 frequencies and 10-20 directions).

Representation of spectral energy density \hat{S} as $\hat{S}(a_i; i = 1, 2, \dots, 5)$, where a_i are the JONSWAP parameters, yields the radiative-transfer equation in the form (Has-

selmann et al., 1976):

$$\frac{\partial a_i}{\partial t} + \mathcal{D}_{ijk} \frac{\partial a_i}{\partial x_k} = T_i, \quad (5.60)$$

in which the propagation velocities \mathcal{D}_{ijk} and source terms T_i are determined by the advection and source terms in the original transport equation. Equation (5.60) gives a substantial reduction in the computational effort. Moreover, the parametric representation is now more consistent with parameterization of the nonlinear transfer which is only expressed in terms of the five JONSWAP parameters. Equation (5.60) still has the form of a radiative-transfer equation and is subject to numerical difficulties, as in the case of the discrete spectral approach. Let us assume the unidirectional wind as:

$$U = U_0 \left(\frac{gX}{U_0^2} \right)^p \quad \text{or} \quad U = U_0 \left(\frac{gt}{U_0^2} \right)^q, \quad (5.61)$$

in which U_0 is a constant. The solutions for JONSWAP parameters, resulting from Eq. (5.60), are:

$$\nu = \frac{\omega_p U_0}{2\pi g} = A_x \left(\frac{gX}{U_0^2} \right)^m \quad \text{or} \quad \nu = \frac{\omega_p U_0}{2\pi g} = A_t \left(\frac{gt}{U_0^2} \right)^n, \quad (5.62)$$

where:

$$m = \frac{3}{10} (2p - 1), \quad n = \frac{3}{7} (q - 1), \quad (5.63)$$

$$A_x = 2.84 (1 + 1.63p)^{3/10}, \quad A_t = 16.8 (1 + 1.51q)^{3/7}, \quad (5.64)$$

and

$$\alpha = \mathcal{B} \left(\frac{\omega_p U_0}{2\pi g} \right)^{2/3}, \quad E = \frac{\sigma_\zeta^2 g^2}{U_0^4} = \lambda \mathcal{B} \left(\frac{\omega_p U_0}{2\pi g} \right)^{-10/3}, \quad (5.65)$$

in which:

$$\lambda = \frac{\sigma_\zeta^2 g^2}{\alpha U_0^4} \left(\frac{\omega_p U_0}{2\pi g} \right)^4 = \frac{1}{(2\pi)^4 \alpha} \frac{\sigma_\zeta^2 \omega_p^4}{g^2} = 1.58 \cdot 10^{-4}. \quad (5.66)$$

Thus, we have:

$$\left. \begin{aligned} \alpha &= \mathcal{B} \nu^{2/3} \\ E &= C \nu^{-10/3} \end{aligned} \right\}, \quad (5.67)$$

where $C = \mathcal{B} \lambda$.

The power-law relations between α , E and ν are independent of the exponents p and q . Moreover, the coefficient \mathcal{B} (and C) varies by only a few percentages within a

wide range of these exponents. Therefore, for practical purposes, the wave field can be characterized by fetch or duration dependence on a single parameter ν . For the first order we obtain (Hasselmann et al., 1976):

$$\alpha \approx 0.032\nu^{2/3}, \quad (5.68)$$

$$E \approx 5.1 \cdot 10^{-6} \nu^{-10/3}. \quad (5.69)$$

Equations (5.67) and (5.68) lie within a few percentages of the exact solution. Physically, the quasi-equilibrium relations (5.68) and (5.69) express the fact that the dominant balance, determining the level of the spectrum, is between the atmospheric input and the nonlinear transfer of energy away from the central region of the spectrum.

Hybrid models

A parametrical description of the wave field is only appropriate for the wind-sea region of the spectrum in which nonlinear energy transfer is dominant. However, a wave spectrum consists of a superposition of a wind-sea spectrum and lower-frequency swell components which are no longer being actively generated by wind. The swell energy level is generally lower and the nonlinear coupling between swell components or bottom swell and wind-sea is negligibly small (see Section 5.2.2.3). Evolution of swell is controlled mainly by advection and can be represented by decoupled discrete spectral models.

To account for swell components, the parametrical wind-sea models are combined with a standard discrete spectral representation of the swell. Such combined models are known as coupled hybrid models (H). An example of this type of model is the Hybrid Parametrical (HYPA) wave prediction model for deep water, developed by Günther et al. (1979a,b). This model is an extension of the two-parametric model of Hasselmann et al. (1976), discussed above, to the full five JONSWAP parameters. The coefficients in the prognostic equation (5.60) now becomes:

$$a_1 = \omega_p, \quad a_2 = \alpha, \quad a_3 = \gamma, \quad a_4 = \sigma'_0 \quad \text{and} \quad a_5 = \sigma''_0. \quad (5.70)$$

Details of the generalized propagation velocity matrix \mathcal{D}_{ijk} are given in Günther et al. (1979a). The model is only valid in the wind-sea region of the energy spectrum and for wind speeds such that $\nu = \frac{\omega_p U}{2\pi g} \geq 0.13$ (value $\nu = 0.13$ corresponds to the fully-developed sea stage). When $\nu < 0.13$, the phase velocity of the waves exceeds the wind-speed and no energy is absorbed from the atmosphere. Waves propagate freely as swell and the problem is reduced to solving the radiative transfer equation (2.177) without a source function Q . The swell field is represented in a set of characteristics (rays). For each swell frequency ω , the model is covered with a mesh of rays at appropriate angles and spacing. Swell energy is represented as discrete energy packets, at points spaced along each ray at intervals of $\Delta s = \Delta t C_g$, where Δt is the model time step and C_g is the group velocity. It was assumed in the model

that the total energy (wind-sea + swell) is conserved in any exchange. Nonlinear interaction between swell and wind-sea is very weak unless the swell and wind-sea frequency domains overlap (see Section 5.2.2.3).

The overall model described here is thus, a hybrid model in which the wind-sea component of the energy spectrum is treated by a parametric approach, and the swell is treated by a characteristic ray method. Energy needs to be transferred between the two growing wind-seas in a rising wind, or energy from the wind-sea is lost to swell when the wind falls.

The hybrid parametrical wave model has been used to hindcast long-term wave height statistics in the northern North Sea (Ewing et al., 1979). It provides estimates of significant wave height without bias and with r.m.s. error of about 0.7 m, compared with wave recordings of a set of 40 storms. Moreover, the capability of a parametrical wave model to predict the sea state for highly variable wind fields was demonstrated by Günther et al. (1979b).

The intercomparison of various types of models by The SWAMP group (1985) yields the following conclusions:

1. The second generation (H) and (DS), based on a fundamentally different spectral energy balance, yield different relations between space and time variables in the development of a wind-sea.
2. All second generation models suffer from limitations in the parameterization of the nonlinear energy transfer Q_{nl} . They perform satisfactorily for the standard fetch- and duration-limited growth situation for which the parameterization was designed. However, under extreme conditions of rapidly changing winds, the parameterization of Q_{nl} generally contains far too many degrees of freedom to cope with the wide variety of spectral distributions which may arise.
3. A hybrid model (H) provides predictions comparable to discrete spectral (DS) models. DS models give not only the mean direction, but also the directional distribution.

Some of these limitations of the second generation models were removed in a third generation of DS models in which discretized continuous-operator parameterization of Q_{nl} was applied (see Section 5.2.2.2). On the other hand, the hybrid models (H), even with an extended number of parameters, are not able to compete with (DS) models for extreme, non-uniform wind field conditions. Their principal value lies in the computational economy for the large majority of wind fields for which the wind-sea spectrum is able to adjust to a local equilibrium in a time that is short compared with the wind field time scale.

In the next Section we will concentrate on the third generation DS type models, which also provide more reliable solutions for strongly varying wind fields.

5.3.1.3 Third generation wave models

In the mid-1980s, extensive numerical simulation studies, partly described in the previous Sections, showed that the first and second wave generation models cannot be applied for all wind fields, especially for extreme situations for which wave prediction is particularly needed. At the same time, numerical improvements in the computation of the Boltzmann-type integral had been developed by Hasselmann et al. (1985) and Snyder et al. (1993). These improvements overcame the basic numerical difficulties of the second generation wave models and were used in the third generation model which was developed within the framework of the WAM (Wave Modelling) program. The model was described in great detail in a book recently published by Komen et al. (1994).

The first implementation of a third generation wave model was published in 1988 (The WAMDI Group, 1988; The WAMDI denotes The Wave Model Development and Implementation group). The most important new features of the model are the following:

- A parameterization of the exact nonlinear transfer source function contains the same number of degrees of freedom as the spectrum itself. In the model, the discrete interaction approximation of Hasselmann et al. (1985) was used.
- The energy balance was closed by specifying the unknown dissipation source function. The function corresponds to the form proposed by Komen et al. (1984). The dissipation was tuned to reproduce the observed fetch-limited wave growth and the fully-developed Pierson-Moskowitz spectrum.

In the model, the evolution of the two-dimensional spectrum $\hat{S}(\omega, \Theta, \phi, \lambda, t)$ as a function of latitude ϕ and longitude λ on the spherical earth is governed by the radiative-transfer equation (The WAMDI Group, 1988; Komen et al., 1994):

$$\frac{\partial \hat{S}}{\partial t} + (\cos \phi)^{-1} \frac{\partial}{\partial \phi} (\dot{\phi} \cos \phi \hat{S}) + \frac{\partial}{\partial \lambda} (\dot{\lambda} \hat{S}) + \frac{\partial}{\partial \Theta} (\dot{\Theta} \hat{S}) = \hat{Q}, \quad (5.71)$$

in which:

$$\left. \begin{aligned} \dot{\phi} &= \frac{d\phi}{dt} = C_g R^{-1} \cos \Theta \\ \dot{\lambda} &= \frac{d\lambda}{dt} = C_g \sin \Theta (R \cos \phi)^{-1} \\ \dot{\Theta} &= \frac{d\Theta}{dt} = C_g \sin \Theta \tan \phi R^{-1} \end{aligned} \right\}, \quad (5.72)$$

C_g is a wave group and R is a radius of the earth.

The source function \hat{Q} contains the three basic terms $\hat{Q}_{in}^{(nl)}$, \hat{Q}_{nl} and \hat{Q}_{dis} . The wind input and dissipation source functions $\hat{Q}_{in}^{(nl)}$ and \hat{Q}_{dis} are based on the forms,

discussed in previous Sections, with small modification of term \hat{Q}_{dis} , i.e. the mean frequency $\bar{\omega}$ in the third generation wave model was replaced by the inverse of the mean period:

$$\hat{\omega} = \left[E^{-1} \int \hat{S}(\omega, \eta) \omega^{-1} d\omega d\Theta \right]^{-1}. \quad (5.73)$$

Therefore, the term \hat{Q}_{dis} takes the form:

$$\hat{Q}_{dis} = -2.33 \cdot 10^{-5} \hat{\omega} \left(\frac{\omega}{\bar{\omega}} \right)^2 \left(\frac{\hat{\alpha}}{\hat{\alpha}_{PM}} \right)^2 \hat{S}, \quad (5.74)$$

where:

$$\hat{\alpha} = E \hat{\omega}^4 g^{-2}, \quad \hat{\alpha}_{PM} = 0.66 \bar{\alpha}_{PM}. \quad (5.75)$$

The third source term, the nonlinear interaction term \hat{Q}_{nl} , is represented by the discrete interaction operator parameterization, suggested by Hasselmann et al. (1985). The basic advantage of such parameterization is reduction of the five-dimensional continuum of all resonant quadruplets (Eq. (5.31)) to a two-dimensional continuum (for more information see Section 5.2.2). The third generation wave model contains 25 frequency bands on a logarithmic scale with $\Delta\omega/\bar{\omega} = 0.1$, spanning a frequency range $\omega_{max}/\omega_{min} = 9.8$. The directional resolution is 30° . A high-frequency limit ω_{hf} of the prognostic region of the spectrum, was adopted as:

$$\omega_{hf} = \min \{ \omega_{max}, \max [2.5\bar{\omega}, 4\omega_{PM}] \}, \quad (5.76)$$

and beyond the high-frequency limit a tail ω^{-4} was added as:

$$\hat{S}(\omega, \Theta) = S(\omega_{hf}, \Theta) \left(\frac{\omega}{\omega_{hf}} \right)^{-4} \quad \text{for } \omega > \omega_{hf}. \quad (5.77)$$

Numerical tests showed that the model is not sensitive to the precise form of the tail. The WAM model utilizes a semi-implicit time integration scheme to calculate the change of energy density $\Delta\hat{S}$ in the time step Δt from the source terms Q , i.e.:

$$\Delta\hat{S}(\omega, \Theta) = \frac{\hat{S}(\omega, \Theta)}{1 - 0.5\mathcal{D}(\omega, \Theta)\Delta t} \Delta t, \quad (5.78)$$

in which \mathcal{D} is determined by the source terms $\hat{Q}_{in}^{(nl)}$, \hat{Q}_{nl} and \hat{Q}_{dis} .

Implementation of the model for some regions (the North Atlantic or the Gulf of Mexico) was done with a $1/4^\circ \times 1/2^\circ$ latitude-longitude resolution. The model was also implemented on the global scale with a $3^\circ \times 3^\circ$ resolution. For the numerical implementation of the model, we refer the reader to The WAMDI group (1988) and Komen et al. (1994).

The model was tuned to simulate the standard infinite-depth, fetch limited growth case. After tuning, the model was applied without further adjustments to a series of hindcast cases involving a strongly variable wind field. In particular, six windcast studies of North Atlantic-North Sea and three severe hurricanes (*Camille*, 1969; *Anita*, 1977; and *Frederick*, 1979) in the Gulf of Mexico were selected for comparison. The overall performance of the third generation wave model was good.

Though, the model was tuned to simple fetch and time-duration situations, it also provides better (than first and second generation models) representation of spectral details in the hurricane wave regime.

In Table 5.3, the predicted significant wave height is compared with the measured height during the peak sea states at the sites in the three hurricanes studied.

A hindcast study for wind derived from the entire 96-day global SEASAT scatterometer data was also carried out. The results were generally consistent with the wave height fields derived from the SEASAT altimeter data (see also Chapter 8).

Table 5.3: Comparison of the predicted significant wave height with measured height hurricanes in the Gulf of Mexico.

Storm	Site	Measured (m)	Hindcast (m)
<i>Camille</i>	ODGPSTN1	13.6	13.5
	ODGPSTN2	7.9	9.0
<i>Anita</i>	EB04	5.4	4.8
	EB71	6.6	7.7
	EI133	6.0	5.1
<i>Frederick</i>	42003	8.9	9.3
	Cognac	8.5	8.1

To illustrate a general feature of the global wave hindcast, more extensive verification of the third generation wave model WAM was reported by Romeiser (1993). The performance of the model on a global scale has been investigated using the GEOSAT radar altimeter data for the entire year of 1988. In general, the correlation between the model results and the GEOSAT data, for the entire year of 1988, is 0.98. The underestimation of WAM wave heights for the southern hemisphere and the tropical region varies with the season. An underestimation of up to about 30% is observed during May through September, while relatively good agreement is found for the rest of the year.

An opposite effect was observed in the North Pacific, where the WAM wave heights were overestimated by 10% to 40%. For the northern Indian Ocean, influenced by monsoons, the WAM wave heights were overestimated during the winter season.

In addition to testing of the WAM model on the global scale, this model was implemented for the Mediterranean Sea (Cavaleri et al., 1991; Dell'Osso et al., 1992). The Mediterranean basin has a complicated geometry and is almost completely surrounded by mountain ridges. Because of the complicated orography, the accuracy of the input wind fields plays a crucial role in wave model performance. Verification of the wind and wave forecast shows that, to obtain a realistic prediction of wave height, it is necessary to increase the horizontal resolution of the model of which the grid size should be smaller than 40 km.

Satellite measurements of wind and wave fields on the global scale provide wave modelers with a new and extensive set of data. As ocean wave prediction models are very sensitive to errors in the wind field, the question of the impact on wave predictions of wind measurements, obtained using satellite scatterometers, is also of interest. Conversely, since a wave model is such a sensitive measuring device for the wind field, the quality of scatterometer data may be checked using the satellite altimeter wave height data.

The mutual consistency of the satellite data of scatterometer winds and altimeter wave heights obtained from satellites is examined by assimilation analysis. As wind and waves form a coupled system, the simultaneous assimilation of wind and wave data is considered. Assimilation means finding those model results which best fit the observations and the first-guess fields. More information on assimilation techniques is given in the papers by Janssen et al. (1989), de Las Heras and Janssen (1992), Lionello et al. (1992), Bauer et al. (1992) and in Section 9.4.

The third generation wave model is heavily based on numerical manipulation and numerical errors are inseparable from wave forecasts. The most important sources of such errors and the methods of reducing or eliminating them are discussed by Tolman (1992).

5.3.2 Empirical prediction models

5.3.2.1 Fetch- and time-limited wave growth

In Section 2.2 we demonstrated the usefulness of dimensional analysis for evaluation of wave spectrum shape. Dimensional principles have also had a considerable impact on wind-wave predictions, when more sophisticated numerical models were not available. Relations (2.65) indicate that characteristic wave parameters in deep water depend on wind speed U , wind fetch X , and wind duration t . The wind fetch X is the distance over which the waves propagate under the sustained influence of wind. Wind fetch is limited by land boundaries, up-wind from the given point and by the extent of atmospheric systems. The definition of wind fetch should be modified if wind direction is changing along the path of wave propagation. Waves may propagate in all directions from the area of generation. The amount of wave energy propagated in a particular direction is described by the directional spreading function $D(\Theta)$. Usually the wave energy substantially decreases for waves propagating at angles greater than $\sim 30^\circ$ against the dominant wave direction.

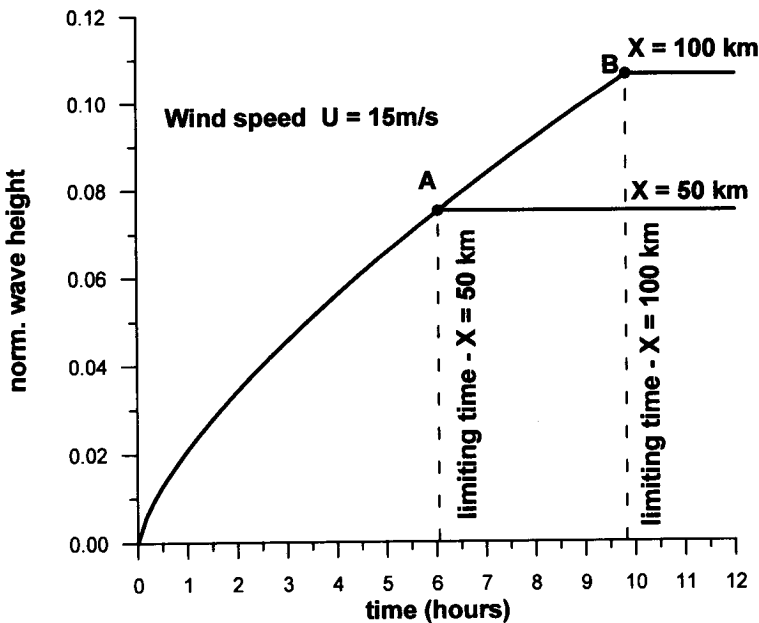


Figure 5.6: Duration-limited curves for points A and B.

The duration of wind t is a time during which the waves are propagated under the sustained influence of wind. Wave energy cannot grow infinitely even if the wind is maintained in the same direction as the wave propagation. At a particular fetch or at a particular time, waves reach a saturation level when wind input is balanced by energy dissipation due to bottom friction, breaking etc.

We now demonstrate the saturation stage in the simple case of waves induced by wind (wind speed $U = 15$ m/s), blowing offshore normally to an elongated straight shoreline. Two points, A and B , located at distances $X_A = 50$ km and $X_B = 100$ km, from the shoreline were selected.

Figure 5.6 illustrates wave height growth (in time) at points A and B . At point A waves grow till time $t_{Alim} = 6.04$ hours, when they reach the saturation stage. The time t_{Alim} is a time required for the wave field at fetch X_A to become fetch-limited if the wind has speed U . The continuing duration of the wind cannot generate further wave growth. Therefore, if $0 < t < t_{Alim}$, the wind field is duration-limited while for $t > t_{Alim}$, the wave field is fetch-limited. For point B , located at a distance of $X_B = 100$ km ($X_B > X_A$), the time of the approach of the wave field to saturation stage is equal to $t_{Blim} = 9.8$ hours.

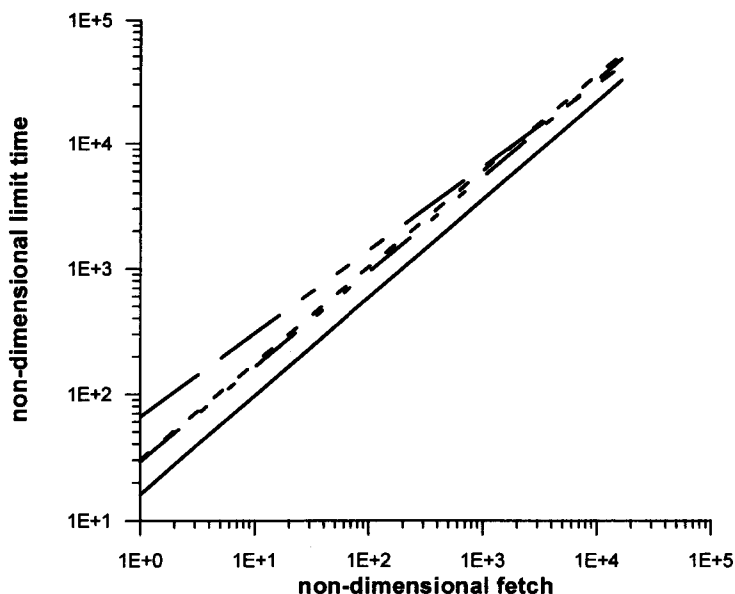


Figure 5.7: Simultaneous fetch-duration relationships: ——— Krylov's prediction model; - - - Donelan's model; - · - · SMB model; - - - JONSWAP model.

The relationships between distances X_A and X_B , and corresponding times $t_{A\lim}$ and $t_{B\lim}$, depend on the particular prediction model. In our case, the growth rates were calculated using relationships (5.84) and (5.86) (see below).

In general, the position of points A and B on the non-dimensional fetch duration plane results from the assumption that wave energy propagates at the group velocity. In the deep sea we have:

$$\frac{dx}{dt} = C_g, \quad (5.79)$$

in which x corresponds to sustained wind direction. Rewriting Eq. (5.79) as $dt = \frac{1}{C_g} dx$ and integrating it, we obtain:

$$\frac{gtX}{U} = \int_0^{gX/U^2} \frac{U}{C_g} d\left(\frac{gx}{U^2}\right) = F\left(\frac{gX}{U^2}\right). \quad (5.80)$$

The duration t_X and equivalent distance X correspond to the situation when the sea state is neither fetch nor duration-limited. Figure 5.7 shows the simultaneous fetch-duration relationship, predicted by some prediction models discussed below.

5.3.2.2 JONSWAP prediction graphs

The prediction formulas for a fetch-limited condition, resulting from the JONSWAP experiment (Hasselmann et al., 1973) are (see Eqs. (3.91) and (3.92)):

$$\frac{\sigma_\zeta^2 g^2}{U^4} = 1.6 \cdot 10^{-7} \left(\frac{gX}{U^2}\right), \quad (5.81)$$

$$\omega_p = \frac{2\pi}{T_p} = 7\pi \left(\frac{g}{U}\right) \left(\frac{gX}{U^2}\right)^{-0.33}. \quad (5.82)$$

In the earlier methods, the prediction graphs were presented in terms of the significant wave height H_s and corresponding period T_s . The significant wave period T_s is sometimes multiplied by a constant (1.06 or 1.05) to estimate T_p ; in practice, however, a value of unity is often used.

Using Eqs. (5.81) and (5.82), we obtain for H_{m0} and T_p as:

$$\frac{gH_{m0}^2}{16U^4} = 1.6 \cdot 10^{-7} \left(\frac{gX}{U^2}\right), \quad (5.83)$$

or

$$\frac{gH_{m0}}{U^2} = 1.6 \cdot 10^{-3} \left(\frac{gX}{U^2}\right)^{0.5}, \quad (5.84)$$

and

$$\frac{gT_p}{U} = 0.286 \left(\frac{gX}{U^2}\right)^{0.33}. \quad (5.85)$$

The time t_{lim} is required for the wave field at fetch X to become fetch-limited, if the wind having speed U is given by Eq. (5.80). Taking into account that in deep water $C_g = \frac{gT_p}{4\pi}$ and using Eq. (5.85), we obtain:

$$t_X = 65.9 \frac{U}{g} \left(\frac{gX}{U^2} \right)^{2/3}. \quad (5.86)$$

Equations (5.84), (5.85) and (5.86) provide an estimate of the significant wave height and significant wave period in a fetch-limited stage.

A measurement of fetch-limited wave growth is relatively straightforward. Measurement of the growth of waves with time is consequently more difficult, for there are widely differing estimates of the growth of waves with time. The parametric wave prediction model developed by Hasselmann et al. (1976), discussed above, also provides estimates of the significant wave height and peak periods over time. Assuming that the wind is constant in space and time ($p = g = 0$ in Eq. (5.61)), the model gives the following expressions for H_{m_0} and T_p :

$$\frac{gH_{m_0}}{U^2} = 8.033 \cdot 10^{-5} \left(\frac{gt}{U} \right)^{5/7}, \quad (5.87)$$

and

$$\frac{gT_p}{U} = 5.95 \cdot 10^{-2} \left(\frac{gt}{U} \right)^{3/7}. \quad (5.88)$$

The expression (5.87) follows from Eq. (5.65) in which $\mathcal{B} = 0.031$, i.e.:

$$\frac{\sigma_\zeta^2 g^2}{U_0^4} = 4.898 \cdot 10^{-6} \left[16.8 \left(\frac{gt}{U_0} \right)^{-3/7} \right]^{-10/3}, \quad (5.89)$$

or

$$\frac{\sigma_\zeta^2 g^2}{U_0^4} = 4.03 \cdot 10^{-10} \left(\frac{gt}{U_0} \right)^{10/7}. \quad (5.90)$$

Using $H_{m_0} = 4\sigma_\zeta$, we obtain Eq. (5.87). It should be noted that time t_{lim} can also be estimated through a comparison of Eqs. (5.84) and (5.87), i.e.:

$$t_X = 65.9 \frac{U}{g} \left(\frac{gX}{U^2} \right)^{7/10}, \quad (5.91)$$

which is in agreement with Eq. (5.86).

5.3.2.3 SPM prediction graphs

The JONSWAP prediction formulas are the basis for the prediction graphs, given in the 1984 version of the Shore Protection Manual (SPM, 1984). The Shore Protection Manual of the U.S. Army Coastal Engineering Research Center has been and continues to be a widely used guide in coastal engineering. For simplified wave predictions, the first three editions of SPM (1973, 1975, 1977) give graphs and formulas using the SMB (see below) formulation. In these editions, the wind speed recommended for use, is 'the mean surface wind speed'. There is almost no discussion of the wind-speed dependence on elevation or air-sea temperature difference.

In the latest edition of the SPM, the cosine-averaged fetch computation of the earlier editions is replaced with an arithmetically-averaged fetch over the wind direction $\pm 15^\circ$. Also, there is much more information on wind input. To adjust wind speed, measured at elevation z to a 10 m height, the following relationship is used:

$$U_{10} = U_z \left(\frac{10}{z} \right)^{1/7}, \quad z < 20m. \quad (5.92)$$

Moreover, two additional correction factors are proposed, i.e. factor R_L to compensate for overland (U_L) to overwater (U_W) wind-speed differences, and a factor R_T for stability effects of air-water temperature differences. To compensate for the observed nonlinear relationship between stress and wind speed, the SMP (1984) introduces an adjusted wind-speed factor U_A , where:

$$U_A = 0.71 U_\beta^{1.23} = 0.71 (R_T U)^{1.23}, \quad (5.93)$$

where $U_\beta = R_T U$.

The stability correction factor R_T as a function of air-sea temperature difference is given in Fig. 5.8.

The attempt of using an effective wind speed U_A is justified by two assumptions:

1. fetch-limited wave growth scales with friction velocity u_* rather than wind speed U_β , and
2. the relationship between u_* and U_β for open ocean data applies directly to fetch-limited conditions.

The prediction formulas are the same as the JONSWAP formulas, except that U_β is replaced by U_A , i.e.:

$$\frac{gH_{m0}}{U_A^2} = 1.6 \cdot 10^{-3} \left(\frac{gX}{U_A^2} \right)^{0.5}, \quad (5.94)$$

$$\frac{gT_p}{U_A} = 0.286 \left(\frac{gX}{U_A^2} \right)^{0.33}, \quad (5.95)$$

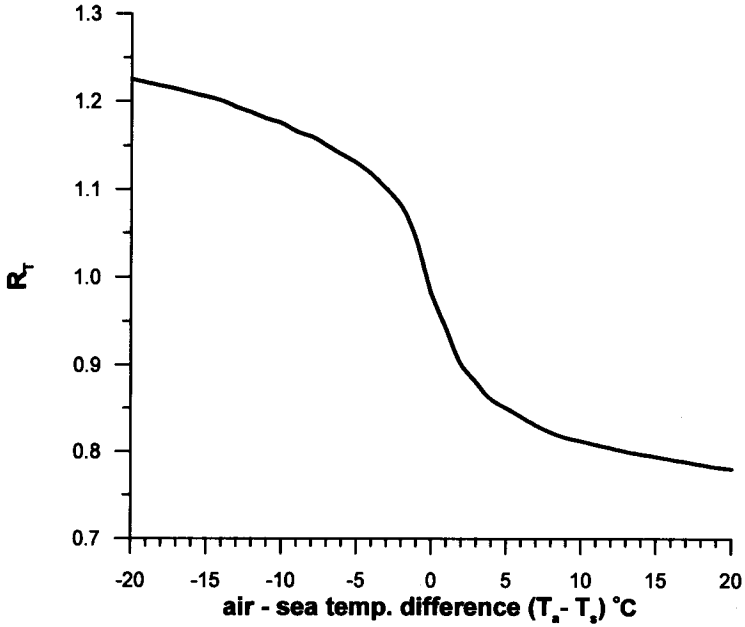


Figure 5.8: Stability correction factor R_T (from SPM, 1984).

and

$$\frac{gt_X}{U_A} = 68.8 \left(\frac{gX}{U_A^2} \right)^{2/3}. \quad (5.96)$$

Note that relationship (5.96) is slightly different from the original JONSWAP result (5.86).

If the duration of the storm is less than t_{lim} , the sea state is duration-limited and values of H_{m0} and T_p must be based on a modified fetch length calculated from Eq. (5.96).

When both $\left(\frac{gt}{U_A} \right)$ and $\left(\frac{gt_X}{U_A} \right)$ are greater than $\left(\frac{gt_{full}}{U_A} \right)$, the sea state is fully-developed and time t_{full} is given by:

$$\frac{gt_{full}}{U_A} = 7.15 \cdot 10^4. \quad (5.97)$$

For fully-developed conditions we have:

$$\frac{gH_{m0}}{U_A^2} = 0.243, \quad (5.98)$$

$$\frac{gT_p}{U_A} = 8.134. \quad (5.99)$$

Some inconsistencies in the SPM (1984) formulation were identified by Hurdle and Stive (1989). They also suggested an alternative formula.

5.3.2.4 SMB prediction graphs

This method was originally introduced by Sverdrup and Munk (1947). The wave forecasting parameters presented by them evolved from theoretical considerations (see for example, Kinsman, 1965), but the actual relationships required basic data for the determination of various constants and coefficients. The Sverdrup-Munk prediction curves were revised by Bretschneider (1958, 1970) using empirical data. This prediction system is therefore often called the Sverdrup-Munk-Bretschneider (SMB) method.

The SMB deep water hindcasting equations, as given by Bretschneider (1970), are:

$$\frac{gH_s}{U^2} = 0.283 \tanh \left[0.0125 \left(\frac{gX}{U^2} \right)^{0.42} \right], \quad (5.100)$$

$$\frac{gT_s}{U} = 7.54 \tanh \left[0.077 \left(\frac{gX}{U^2} \right)^{0.25} \right], \quad (5.101)$$

and

$$\frac{gt_x}{U} = K \exp \left\{ \left[A \left(\ln \left(\frac{gX}{U^2} \right) \right)^2 - B \ln \left(\frac{gX}{U^2} \right) + C \right]^{1/2} + D \ln \left(\frac{gX}{U^2} \right) \right\}, \quad (5.102)$$

where $K = 6.5882$, $A = 0.0161$, $B = 0.3692$, $C = 2.2024$, $D = 0.8798$.

5.3.2.5 Donelan method

In a series of papers Donelan and co-authors have developed and implemented a wave prediction method particularly suitable for fetch-limited conditions (Donelan, 1980; Schwab et al., 1984; Donelan et al., 1985; Bishop et al., 1992). Donelan's method does not assume coincident wind and wave directions ($\Theta = \psi - \phi \neq 0$; ψ is a wave direction and ϕ is a wind direction). If the gradient of fetch about the wind direction is large, one can expect the wave direction to be biased towards the longer fetches. Values of Θ up to 50 degrees have been observed in Lake Ontario.

For fetch-limited conditions, the ψ versus ϕ relation, for a point with known fetch distribution X_ψ , could be obtained by maximizing the expression ($X_\psi^{0.426} \cos \Theta$). A simple procedure for obtaining the ψ versus ϕ relation for any point can be formulated, as follows (Bishop and Donelan, 1989):

1. Starting in the wind direction and moving toward longer fetches, extend radials from the point of interest to the fetch boundary in the upwind direction. Radials should be at some convenient interval depending on the variability of fetch length.
2. Measure the fetch lengths and average them over 30° ($\pm 15^\circ$ from each radial).
3. Compute $(X_\psi^{0.426} \cos \Theta)$ for the average fetch centered in each radial.
4. The maximum value of the expression $(X_\psi^{0.426} \cos \Theta)$ for any particular wind direction gives the corresponding dominant wave direction ψ .

For a known angle difference Θ , the prediction expressions become:

$$\frac{gH_{m0}}{(U \cos \Theta)^2} = 0.00366 \left[\frac{gX_\psi}{(U \cos \Theta)^2} \right]^{0.38}, \quad (5.103)$$

$$\frac{gT_p}{U \cos \Theta} = 0.542 \left[\frac{gX_\psi}{(U \cos \Theta)^2} \right]^{0.23}, \quad (5.104)$$

$$\frac{gt_x}{U \cos \Theta} = 30.1 \left[\frac{gX_\psi}{(U \cos \Theta)^2} \right]^{0.77}, \quad (5.105)$$

in which X_ψ is the fetch in the dominant wave direction.

To avoid overdevelopment of the waves, the value of the X_ψ is subject to the criterion:

$$\frac{gX_\psi}{(U \cos \Theta)^2} \leq 9.47 \cdot 10^4. \quad (5.106)$$

If the geometric fetch from the wind direction exceeds that given by Eq. (5.106), the waves are fully-developed with the following height and period:

$$\frac{gH_{m0}}{U^2} = 0.285, \quad \frac{gT_p}{U} = 7.54. \quad (5.107)$$

The basic features of Donelan's method can be summarized as follows:

1. The model provides an estimate of the peak wave energy direction rather than simply assuming coincident wind and wave directions.
2. Wave direction is found by maximizing the expression $(X^{0.426} \cos \Theta)$.
3. The accuracy of the model is comparable with the JONSWAP and SPM (1977) models and is better than the SPM (1984) proposal; details of the comparison are given in Section 5.3.2.7.
4. The model is restricted to the deep sea and steady fetch-limited conditions.
5. The dependence of wave parameters on the wind and a directional wave energy spreading function are based on experiments in Lake Ontario.

5.3.2.6 Krylov method

All methods mentioned above are relatively widespread in Western literature. However, this is not the case with the method developed in the Soviet Union by Krylov (1966). Therefore, it will be useful to present this method in some detail.

The basis of the Krylov method is a two-dimensional spectrum of wind-induced waves $\hat{S}(\omega, \Theta)$. Let us consider the wave field in deep water induced by constant wind blowing offshore, normal to a straight coastline (Fig. 5.9). The mean wave height \bar{H}_0 , at a distance X_0 from the shoreline can be expressed as:

$$\bar{H}_0 = f(U, X_0). \quad (5.108)$$

Using the fact that $\bar{H} = \sqrt{2\pi}\sigma_\zeta$ we obtain:

$$\bar{H}_0^2(U, X_0) = 2\pi \int_0^\infty \int_{-\pi/2}^{\pi/2} \hat{S}(\omega, \Theta; U, X_0) d\omega d\Theta, \quad (5.109)$$

where Θ denotes the wave propagation angle.

Let us now introduce the directional spreading function $D(\Theta; X_0, U)$ as:

$$D(\Theta; X_0, U) = \int_0^\infty \hat{S}(\omega, \Theta; U, X_0) d\omega. \quad (5.110)$$

Therefore, Eq. (5.109) becomes:

$$\bar{H}_0^2(U, X_0) = 2\pi \int_{-\pi/2}^{\pi/2} D(\Theta; X_0, U) d\Theta. \quad (5.111)$$

As the technology of the directional wave spectra has not yet reached the point where the more complex directional spectra can be routinely used in an engineering design study, we assume that $D(\theta; X_0, U) \approx \cos^2 \theta$ can be frequently applied to many oceanographic and engineering applications.

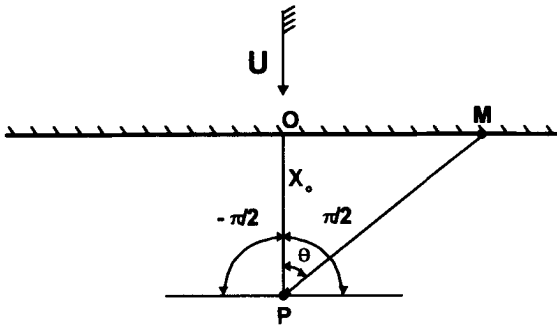


Figure 5.9: Definition scheme for straight coastline.

It should be pointed out that any directional spreading function can be used in this method. Therefore, Eq. (5.110) may be rewritten in a more convenient form:

$$D(\Theta; U, X_0) = f(U, X_0) \cos^2 \Theta, \quad (5.112)$$

and

$$\bar{H}_0^2(U, X_0) = 2\pi f(U, X_0) \int_{-\pi/2}^{\pi/2} \cos^2 \Theta d\Theta. \quad (5.113)$$

Hence:

$$D(\Theta; U, X_0) = \frac{\bar{H}_0^2(U, X_0)}{\pi^2} \cos^2 \Theta. \quad (5.114)$$

The value $Dd\Theta$ represents the energy of the spectral components propagating within the angle range $(\Theta, \Theta + d\Theta)$. This energy is totally defined by $X_0 = \overline{OP}$, which is a projection of the ray \overline{OP} on wind direction. The distance \overline{OP} is the so called effective fetch for point M (M is the point on the coastline associated with the angle Θ). The rate of energy growth of each component is different when we are moving along the radial MP but it is constant when we are moving along the wind direction. Thus, the coastline can be treated as a set of energy sources. In our particular case, the energy for each point (and wave) is the same, because the effective fetch X_0 and velocity U are constant.

In principle, we can extend the above idea for the case of an arbitrary coastline (Fig. 5.10). Thus, we have:

$$D[\Theta; U, r(\Theta)] = \frac{1}{\pi^2} \bar{H}_0^2[U, r(\Theta)] \cos^2 \Theta. \quad (5.115)$$

Using Eq. (5.111), the mean wave height at point P becomes:

$$\bar{H}_p^2 = \frac{2}{\pi} \int_{-\pi/2}^{\pi/2} \bar{H}_0^2[U, X = r(\Theta) \cos \Theta] \cos^2 \Theta d\Theta, \quad (5.116)$$

where: $\bar{H}_0(U, X)$ is a known function of U and X , and r is a radial distance from point P .

For a practical prediction, the integration should be replaced by a summation, i.e.:

$$\bar{H}_p^2 = \frac{2}{\pi} \sum_i \bar{H}_0^2(U, X_i) \cos^2 \Theta_i \Delta \Theta, \quad (5.117)$$

in which $X_i = r(\Theta_i) \cos \Theta_i$, $i = 1, 2, \dots, n$; n is a number of radials.

For later convenience Eq. (5.117) can be rewritten as:

$$\bar{H}_p^2 = \frac{2}{\pi} \sum_i \bar{H}_0^2(U, X_i) \Delta E_i, \quad (5.118)$$

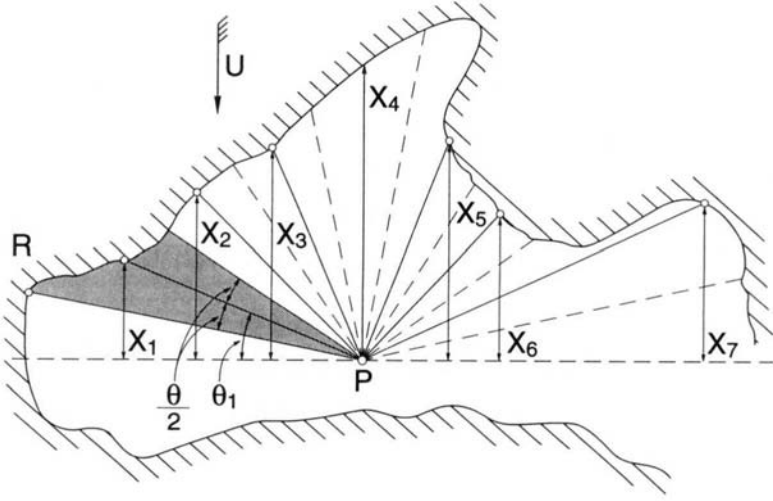


Figure 5.10: Definition scheme for arbitrary coastline.

where ΔE_i is part of the normalized energy, corresponding to the angle range $\Theta_i \pm \Delta\Theta/2$, i.e.:

$$\Delta E_i = E\left(\Theta + \frac{\Delta\Theta}{2}\right) - E\left(\Theta - \frac{\Delta\Theta}{2}\right), \quad (5.119)$$

in which:

$$E(\Theta) = \frac{\int_{\Theta}^{\pi/2} \cos^2 \Theta_1 d\Theta_1}{\int_{-\pi/2}^{\pi/2} \cos^2 \Theta_1 d\Theta_1} = \frac{1}{2} \left(1 - \frac{2\Theta}{\pi} - \frac{\sin 2\Theta}{\pi}\right). \quad (5.120)$$

It is clear that the elementary energy increment ΔE_i should satisfy the condition:

$$\sum_i \Delta E_i = 1. \quad (5.121)$$

According to Eq. (5.118), the wind transfers energy $\approx \bar{H}_0^2(U, X_i)$ to the water surface along the central radials of the particular subsectors of $\Delta\Theta$ in the amount proportional to ΔE_i (see Fig. 5.10).

Let us assume $n = 9$ ($\Delta\Theta = 20^\circ$) sectors within the sector $(-\pi/2, \pi/2)$, i.e. the central radials correspond to the following angles: $-80^\circ, -60^\circ, -40^\circ, -20^\circ, 0, +20^\circ, +40^\circ, +60^\circ$ and $+80^\circ$ against the wind direction. The number of subsectors depends on the variability of the coastline and the required accuracy.

Table 5.4: Elementary energy increments ΔE_i .

Angular sector width $\Delta\Theta = 20^\circ$									
i	-4	-3	-2	-1	0	+1	+2	+3	+4
Θ_i°	-80	-60	-40	-20	0	+20	+40	+60	+80
ΔE_i	0.0088	0.0567	0.1300	0.1945	0.2200	0.1945	0.1300	0.0567	0.0088

Angular sector width $\Delta\Theta = 22.5^\circ$									
i		-3	-2	-1	0	+1	+2	+3	
Θ_i°		-67.5	-45.0	-22.5	0	+22.5	+45.0	+67.5	
ΔE_i		0.0405	0.1250	0.2111	0.2468	0.2111	0.1250	0.0405	

The elementary energy increments ΔE_i for two different ΔE_i values are given in Table 5.4. Note that the radials at intervals $\Delta\Theta = 22.5^\circ$ are recommended by the Russian Standards (Const. Stand. & Regul., 2.06.04 -82).

To complete the prediction procedure, the specification of function $\bar{H}_0 = f(U, X)$, based on experimental data, is needed. Krylov et al. (1976) developed a special procedure for data preparation, where only the values lying within the confidence range, were taken into account. The experimental data corresponded to a wind velocity range from 7 m/s and 18 m/s and to wind fetch from 1 km to 560 km. The final formulas for mean wave parameters become (Krylov et al., 1976):

$$\frac{g\bar{H}}{U^2} = 0.16 \left\{ 1 - \left[1 + 6 \cdot 10^{-3} \left(\frac{gX}{U^2} \right)^{0.5} \right]^{-2} \right\}, \quad (5.122)$$

and

$$\frac{g\bar{T}}{U} = 19.478 \left(\frac{g\bar{H}}{U^2} \right)^{0.625}. \quad (5.123)$$

Using relationship (4.130) we get:

$$H_{m0} = 4.004 \sigma_\zeta = \frac{4.004}{\sqrt{2\pi}} \bar{H} = 1.6\bar{H}, \quad (5.124)$$

or

$$\frac{gH_{m0}}{U^2} = 0.256 \left\{ 1 - \left[1 + 6 \cdot 10^{-3} \left(\frac{gX}{U^2} \right)^{0.5} \right]^{-2} \right\}. \quad (5.125)$$

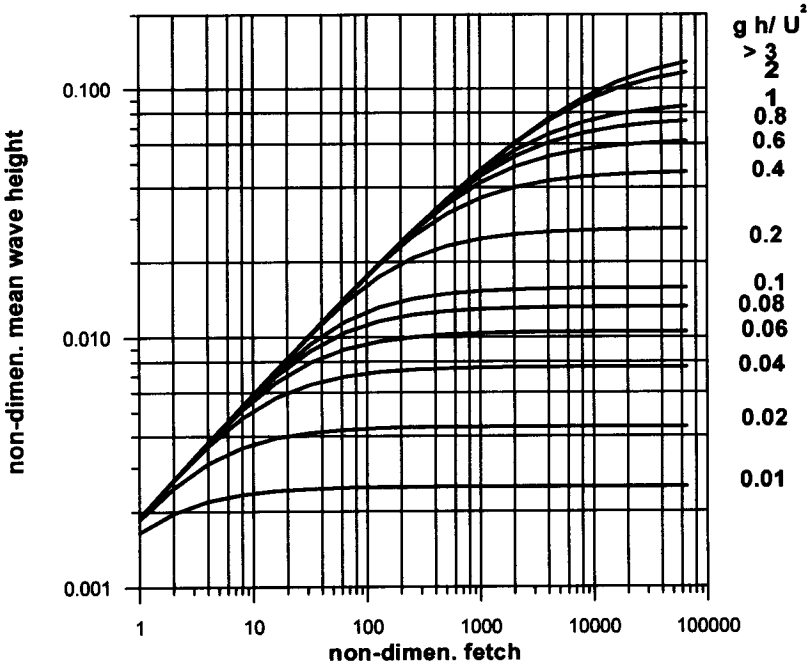


Figure 5.11: Dependence of mean wave height \bar{H} on non-dimensional fetch.

Function (5.125) is shown as an upper envelope in Fig. 5.11.

The wave period T_p , corresponding to the significant wave, is estimated as (Krylov, 1966):

$$T_p = 1.25 \bar{T}. \quad (5.126)$$

The Krylov's method is particularly suitable for prediction of waves in sea basins with a complicated shoreline and within an island presence. Water depth as well as wind speed and wind direction can vary along the wind fetch. As the Krylov method assumes that wave energy observed at a particular point is a superposition of energies coming from various directions, the resulting wave direction does not necessarily coincide with the wind-direction. The mean wave direction can be found as:

$$\bar{\Theta} = \frac{\sum_i \bar{H}_0^2(U, X_i) \Delta E_i \Theta_i}{\bar{H}_p^2}. \quad (5.127)$$

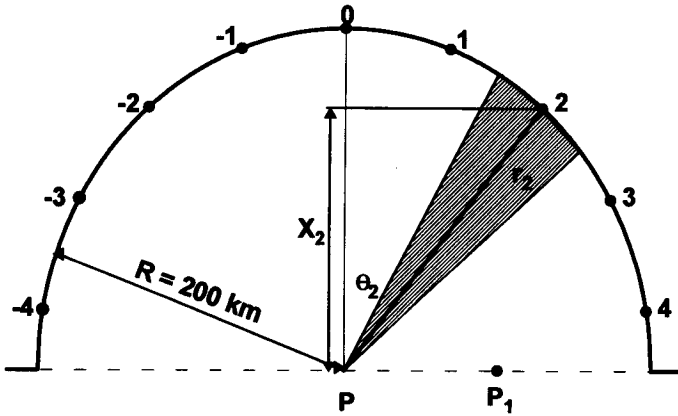


Figure 5.12: Wave prediction for semicircular bay.

The Donelan and Krylov methods are the only ones providing a distinction between wind and wave directions. However, the difference between angles is estimated in different ways in the two methods (see Section 5.3.2.7). In particular, in the Krylov method, the angle difference depends both on wind speed, wind direction and wind fetch, while in the Donelan method this difference is not dependent on wind speed.

Krylov's procedure can easily be computerized. To demonstrate the application of the Krylov method we consider the semicircular bay shown in Fig. 5.12. The radius of the bay is $R=200$ km and a wind with constant speed $U=20$ m/s is blowing along radius OP , where P is a point at which wave parameters are required. Assuming that fetch is partitioned on $n = 9$ sectors, we present wave height at point P in the form:

$$\bar{H}_p^2 = \sum_{i=1}^{i=9} \bar{H}_0^2(U, X_i) \Delta E_i = \sum_{i=1}^{i=9} \bar{H}_0^2(U, R \cos \Theta_i) \Delta E_i. \quad (5.128)$$

The values of function \bar{H}_0^2 for particular sectors are calculated using the relation (5.125) (or by graph in Fig. 5.11) and energy increments ΔE_i are given in Table 5.4. The resulting mean wave height \bar{H}_p and mean wave period \bar{T} are $\bar{H}_p = 3.04$ m and $\bar{T} = 7.75$ s. The corresponding significant wave height becomes $H_{m0} = 4.87$ m and $T_p = 9.69$ s.

For comparison, the wave parameters were also calculated by the JONSWAP, SMB and Donelan methods. In particular, the fetch was assumed to be an arithmetically-averaged fetch over wind direction $\pm 15^\circ$. Because of symmetry of fetch distribution, the expression $(X_\psi^{0.426} \cos \Theta)$ in the Donelan method reaches its maximum value at $\Theta = 0$, i.e. wind and wave directions are coincident. The results of comparison are summarized in Table 5.5.

Table 5.5: Wave parameters for semi-circular bay.

Method	\bar{H} (m)	\bar{T} (s)	H_{m0} (m)	T_p (s)
Krylov	3.04	7.75	4.87	9.69
JONSWAP	-	-	4.54	9.60
SMB	-	-	4.78	8.71
Donelan	-	-	3.75	7.78

The first three methods give very similar results; the Donelan method predicts smaller wave height and a shorter wave period.

The Krylov method can be easily extended to the case when both wind speed and wind direction vary in space (see Fig. 5.13). In this Figure, the U_1 , U_2 and U_3 denote wind-speed distributions and solid lines denote wind direction. To simplify prediction procedures, we assume that wind speed changes abruptly along lines (a) and (b). This means that between the (a) and (b) lines wind speed is constant and equal to U_2 and wind speed between line (a) and the coastline is equal to U_1 , while in the area between line (b) and point P, the wind speed is equal to U_3 .

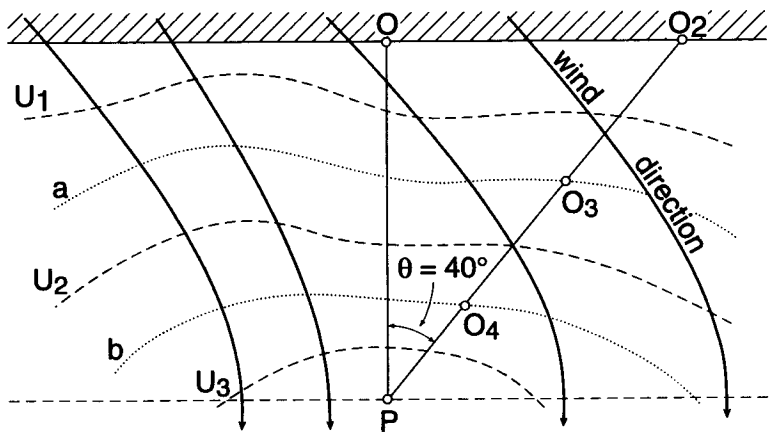


Figure 5.13: Wind direction and speed changing in space.

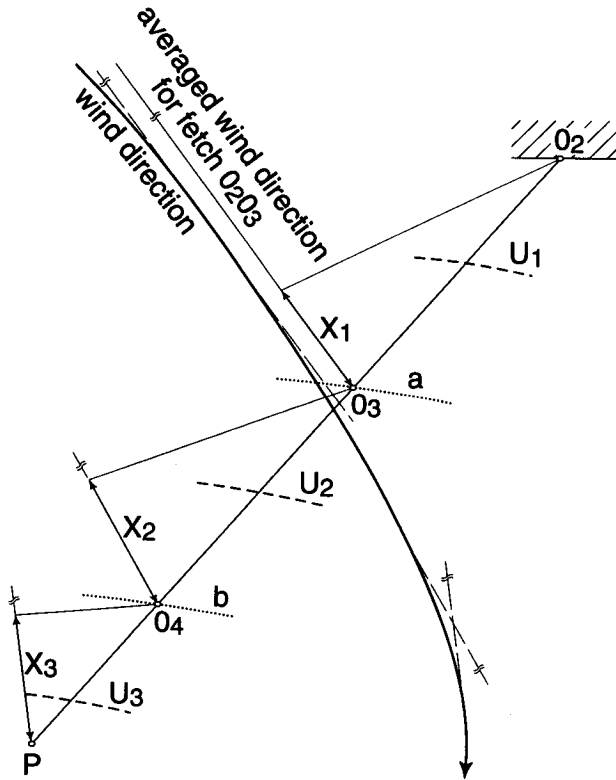


Figure 5.14: Calculation of effective fetch for radius PO_2 .

Equation (5.118) is still valid, however, due to the wind-speed variation in space the calculation procedure should be slightly modified. We demonstrate this modification for radius PO_2 corresponding to angle $\Theta = 40^\circ$ (see Fig. 5.14). In order to estimate the wave energy coming to point P from sector $(40^\circ \pm 10^\circ)$ additional intermediate points O_3 and O_4 , located on lines $(a-a)$ and $(b-b)$, are selected. The wave energy at point O_3 is a function of wind speed U_1 and effective local fetch X_1 which is a projection of distance $\overline{O_2O_3}$ on a direction parallel to the local wind direction.

Let the resulting wave height at O_3 be equal to \bar{H}_{O_3} . Along the radius section $\overline{O_3O_4}$, the wind speed is constant, but $U_2 \neq U_1$. Therefore, to calculate wave energy at point O_4 we first calculate the equivalent fetch X_{2eq} which is required to generate wave height \bar{H}_{O_3} by wind of speed U_2 .

For a given non-dimensional wave height $\frac{g\bar{H}_{O_3}}{U_2^2}$, from fetch graph (see Fig. 5.11)

we found $\frac{gX_{2eq}}{U_2^2}$. Thus, the total effective fetch at point O_4 is $X_{2sum} = X_2 + X_{2eq}$. Now the final wave height at point O_4 can easily be calculated by expression (5.122) or by using the fetch graph (Fig. 5.11). The above procedure should be repeated for the $\overline{O_4P}$ section of radius PO_2 .

In a similar way, we can calculate portions of wave energy propagated to point P from other sectors. It is clear that the resulting wave direction does not coincide with the wind direction.

5.3.2.7 Comparison of empirical prediction methods

All four presented empirical methods are strongly dependent on experimental data which served as a basis for determining of relationships between wind and wave parameters. Therefore, they probably have only a limited area of application. To obtain some idea about the validity of a particular method, the results of some comparisons are presented below.

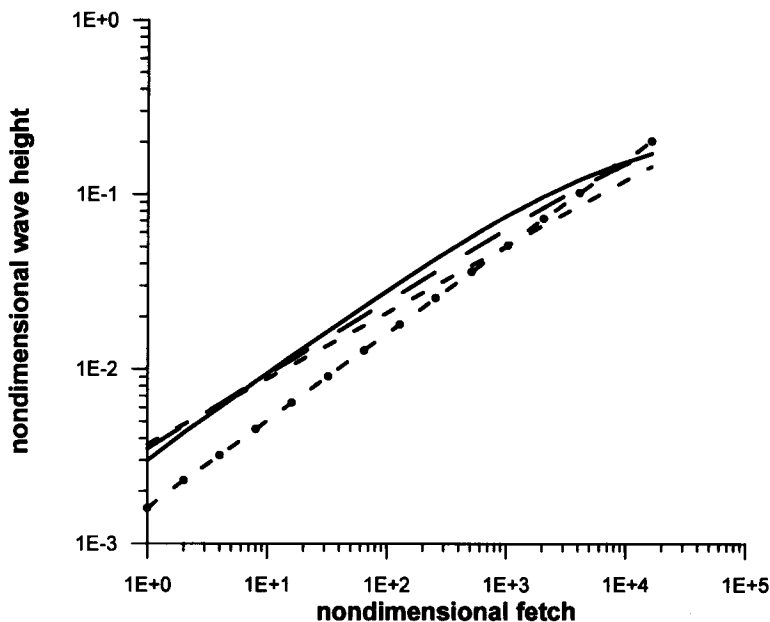


Figure 5.15: Comparison of empirical prediction methods for waves height: ——— Krylov's method; - - - Donelan's method; - · - SMB method and · · · JONSWAP method.

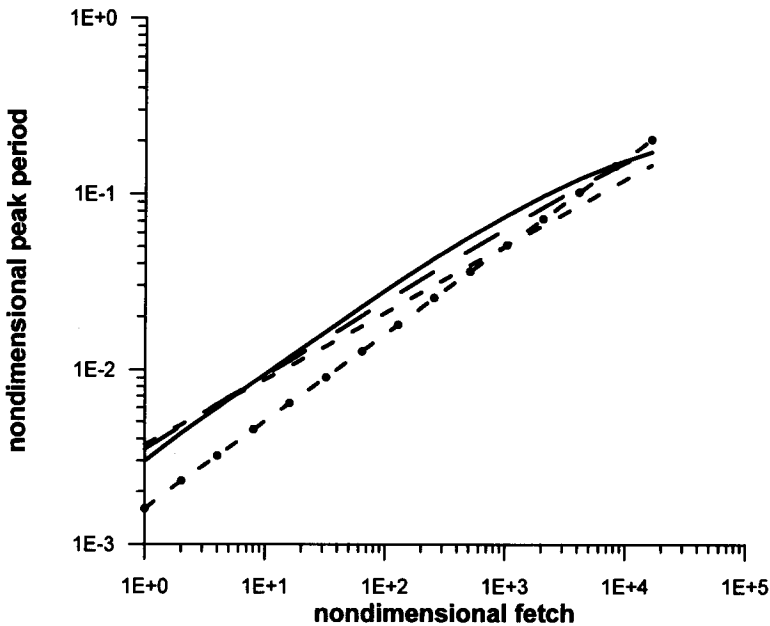


Figure 5.16: Comparison of empirical prediction methods for wave period: ——— Krylov's method; - - - Donelan's method; - - - SMB method and - . - JONSWAP method.

In Figure 5.15, the non-dimensional significant wave height resulting from Eqs. (5.84), (5.100), (5.103) and (5.125) is shown as a function of the non-dimensional fetch. For simplicity, the angle Θ in the Donelan expression (5.103) was assumed to be zero. The first three methods predict very similar results for small and large non-dimensional fetch ($\frac{gX}{U^2}$) values. The JONSWAP prediction is lower, especially for the small non-dimensional fetch. Similar results are obtained for wave period T_p (see Fig. 5.16).

Bishop et al. (1992) used data sets from various sources to examine the SPM (1984) formulas against others methods. A comparison showed that use of the adjusted wind-speed factor in the 1984 SPM prediction scheme yields the poorest statistical results of the four methods (SPM, SMB, JONSWAP and Donelan) relative to the measured data. The 1984 version of the SPM tends to overpredict wave height and period. Moreover, a comparison indicates that for steady state hindcasts, the omission of a stability correction is warranted.

It is of interest to compare the wave prediction methods for a more complicated shape of water basin when, however, all parameters can be easily controlled. Thus, consider a semi-circular bay as in Fig. 5.12.

Table 5.6: Comparison of wave parameters for asymmetric fetch in a semi-circular bay.

U (m/s)	Donelan			JONSWAP		Krylov		
	H_s (m)	T_p (s)	angle diff. (°)	H_s (m)	T_p (s)	H_s (m)	T_p (s)	angle diff. (°)
5	0.48	3.07	18.0	0.75	4.57	0.49	3.30	3.0
10	1.16	4.46	18.0	1.50	5.78	1.45	5.49	4.0
15	1.91	5.55	18.0	2.26	6.64	2.60	7.12	5.2
20	2.73	6.49	18.0	3.02	7.32	3.81	8.42	5.6

Wave parameters are required at point P_1 , situated at the entrance of the bay at the distance of half or bay radius from center point P . The bay radius is equal to 200 km and wind speed is constant and equal to U . The wind is blowing along radius OP .

The results of a calculation for the Donelan, JONSWAP and Krylov methods are summarized in Table 5.6. Both Donelan's and Krylov's methods predict the difference between wind and wave directions. With the Krylov method this difference is smaller than that predicted by Donelan's method and depends on wind speed U . As the Krylov method is also applicable for finite water depth, further discussion of that method will be given in the next Section.

This page is intentionally left blank

Chapter 6

Prediction of Ocean Waves in Shallow Water

6.1 Introduction

In this Chapter, the prediction methods described in the previous Chapter are extended to the case of ocean waves in shallow water. Due to bottom presence, the list of physical processes determining wave behaviour in finite depth is longer than in the case of deep water. The additional phenomena are: the wave refraction, wave diffraction, wave reflection, and energy dissipation due to depth controlled breaking and bottom friction.

The linear theory suggests that the bottom influences on the surface waves when the water depth is $h < \frac{L}{2}$ (L is a wavelength). Since the phase velocity of water waves increases with the local water depth, the part of a wave crest lying over deeper water travels faster than the part of the same wave crest lying over shallow water. In the course of crest propagation, a wave front turns gradually toward the shallows. This agrees with the common observation that on beaches the crests end up almost parallel to the shoreline, even when they approach the coast at an oblique angle from the sea.

The presence of islands, coastal headlands and various types of man-made structures induces wave diffraction. Wave diffraction is the process by which wave energy spreads laterally, perpendicular to the dominant direction of wave propagation. Due to diffraction waves are transmitted into the geometric shadow zone at the lee side of the obstacles. Diffraction mechanism also plays an important role for waves propagating across long distances by slowing the convergence of wave rays and preventing their intersection. Usually the diffraction and refraction processes act together. It is therefore desirable to obtain a solution which accounts for slow depth variations and which allows for rapid horizontal variations associated with diffraction.

As waves propagate through finite-depth region they are attenuated by bottom

friction. Within the boundary layer in the immediate vicinity of the bottom, the flow is strongly sheared, and associated with significant dissipation of energy. In the shallower coastal water zone wave energy is mostly controlled by water depth. At some water depth waves loose their stability and eventually break in the surf zone. They break in different ways, depending on the wave height, wave period and bottom slope.

There is no unified model which is able to predict spectra of the flow in breaking waves. This is partly due to the difficulties of finding a precise mathematical description of a fluid that is, in general, nonlinear and time-dependent. The fluid accelerations can no longer be assumed to be small compared to gravity, nor is the particle velocity any longer small compared to the phase velocity.

In the following, we will discuss the above processes for wind-induced waves using the concept of wave energy balance equation. As in Chapter 5, depending on the degree of complication, the three different types of wave prediction models are discussed. Moreover, the shallow water version of the empirical prediction models are described and compared.

6.2 Basic wave processes in shallow water

6.2.1 Wave refraction due to bottom shoaling

The simplest description of waves propagating over a slowly changing sea bottom is given by the so called geometrical optics approximation (Massel, 1989). A wave ray, being basic quantity in this approximation, is a curve which is tangent to the local wave number \vec{k} vector at every point along the curve. The wave number should satisfy the following conservation equation:

$$\frac{\partial (k \sin \Theta)}{\partial x} - \frac{\partial (k \cos \Theta)}{\partial y} = 0, \quad (6.1)$$

in which $k = |\vec{k}|$, and Θ is an angle between the normal to local bottom contours and wave direction.

For bottom contours parallel to the y direction, Eq. (6.1) reduces to:

$$k \sin \Theta = k_0 \sin \Theta_0 = \text{constant}. \quad (6.2)$$

Equation (6.2) expresses the known Snel's law.

Evolution of wave energy along wave rays for stationary motion and in an absence of currents is given by the law of wave energy conservation:

$$\nabla_h \cdot (E \vec{C}_g) = 0, \quad (6.3)$$

in which:

$$\nabla_h = \frac{\partial}{\partial x} \vec{i} + \frac{\partial}{\partial y} \vec{j}, \quad (6.4)$$

and \vec{C}_g is a group velocity vector.

It can be shown that the geometrical optics approximation is valid only if the bottom slope is small, with respect to kh , and the wave amplitude A variation in space is also small, with respect to the sea surface slope kA (Massel, 1989):

$$\frac{\nabla_h h}{kh} \frac{\nabla_h A}{kA} \ll 1. \quad (6.5)$$

To extend the geometrical optics approximation for random waves and to demonstrate an evolution of the two-dimensional spectrum $\hat{S}(\omega, \Theta)$ in space, due to refraction only, we consider Eq. (2.185) in which we assume a steady-state condition and $\hat{Q}(\omega, \Theta, \vec{x}, t) \equiv 0$. Thus, we have:

$$C_g \left[\cos \Theta \frac{\partial}{\partial x} (CC_g \hat{S}) + \sin \Theta \frac{\partial}{\partial y} (CC_g \hat{S}) + \frac{1}{C} \left(\sin \Theta \frac{\partial C}{\partial x} - \cos \Theta \frac{\partial C}{\partial y} \right) \frac{\partial}{\partial \Theta} (CC_g \hat{S}) \right] = 0. \quad (6.6)$$

Rewriting of Eq. (6.1) in the orthogonal coordinate system (\vec{s}, \vec{n}) , where \vec{s} is in the wave direction, while \vec{n} is normal to the ray, it can be shown that the wave ray equations are (Massel, 1989):

$$\frac{dx}{ds} = \cos \Theta; \quad \frac{dy}{ds} = \sin \Theta; \quad \frac{d\Theta}{ds} = \frac{1}{C} \left(\sin \Theta \frac{\partial C}{\partial x} - \cos \Theta \frac{\partial C}{\partial y} \right). \quad (6.7)$$

Substituting Eq. (6.7) into Eq. (6.6) yields (along wave ray):

$$C_g \frac{d}{ds} [CC_g \hat{S}(\omega, \Theta, \vec{x})] = 0, \quad (6.8)$$

or:

$$CC_g \hat{S}(\omega, \Theta, \vec{x}) = \text{constant}, \quad (6.9)$$

As was shown in Section 2.5, the wave frequency ω is constant along a wave ray. Thus, the condition (6.9) can be rewritten as:

$$\frac{C_g}{k} \hat{S}(\omega, \Theta, \vec{x}) = \text{constant} \quad (6.10)$$

or

$$\hat{S}(\omega, \Theta, \vec{x}) = \frac{k}{k_0} \frac{C_{g0}}{C_g} \hat{S}_0(\omega, \Theta_0, \vec{x}_0). \quad (6.11)$$

Let us now consider the simple case of waves arriving at an angle with a parallel bottom contour, i.e. $h = h(x)$. The Snel's law (6.2) is then:

$$\frac{\sin \Theta}{C} = \frac{\sin \Theta_0}{C_0}, \quad (6.12)$$

where phase speed C_0 and angle Θ_0 (with respect to the normal isobaths) correspond to a particular point on the ray. Using Eq. (6.12) we rewrite Eq. (6.11) as:

$$\hat{S}(\omega, \Theta, \vec{x}) = \frac{k}{k_0} \frac{C_{g0}}{C_g} \hat{S}_0 \left[\omega, \arcsin \left(\frac{k}{k_0} \sin \Theta \right), \vec{x}_0 \right]. \quad (6.13)$$

When the initial point is given in deep water, Eq. (6.13) takes the form:

$$\hat{S}(\omega, \Theta, \vec{x}) = \tanh^{-\frac{3}{2}}(kh) \left[1 + \frac{2kh}{\sinh 2kh} \right]^{-1} \hat{S}_0 \left[\omega, \arcsin \left(\frac{k}{k_0} \sin \Theta \right), \vec{x}_0 \right]. \quad (6.14)$$

Solution (6.13) is identical with the Krasitskii (1974) closed form solution obtained by the method of characteristics.

From Eq. (6.13) it follows that:

$$\left| \frac{k}{k_0} \sin \Theta \right| \leq 1, \quad (6.15)$$

in which the bottom contours perpendicular to the x axis are assumed. If the water depth decreases in the direction of the x -axis, the left-hand side of Eq. (6.15) increases and at a certain combination of ω, Θ and x , Eq. (6.15) is no longer valid. This means that a given spectral component (ω, Θ) could not have come from deep water. Therefore, it is necessary to put $S(\omega, \Theta, x) = 0$ for the combination of (ω, Θ, x) , for which Eq. (6.15) is no longer valid.

If waves propagate into deep water, the left-hand side of Eq. (6.15) decreases and that condition is still valid. The slope of wave rays, associated with particular spectral components, increases and at some point becomes infinite. The possibility therefore arises that wave rays may be turned back toward shallow water before they reach the deep sea. The envelope of all turning rays is called caustic, by analogy with optics (Massel, 1989). In the vicinity of the caustic line the wave rays approach each other closely and finally intersect. Thus, the energy flux increases infinitely and the geometrical optics approximation is no longer applied.

Generally, the linear approach to the refraction of the wave spectrum is based on the superposition of elementary spectral components. For each frequency, the energy level is treated as an invariant during the transformation. Therefore, the transformation of each spectral component is identical to the transformation of the monochromatic wave of the same amplitude and frequency. The energy contained in each frequency band and direction, travels along its corresponding wave ray at group velocity. The shallow water spectrum is then determined from the deep water spectrum by applying the shoaling (K_T) and refraction (K_R) coefficients squared to each frequency component, i.e. (Krylov et al., 1976; Le Mehaute and Wang, 1982; Massel, 1989):

$$\hat{S}(\omega, \Theta) = K_T^2 K_R^2 \frac{\partial \Theta_0}{\partial \Theta} \hat{S}(\omega, \Theta_0), \quad (6.16)$$

in which:

$$K_T^2 = \frac{C_{g0}}{C_g}, \quad (6.17)$$

$$K_R^2 = \frac{l_0}{l}, \quad (6.18)$$

in which l_0 and l are distances between adjacent wave rays.

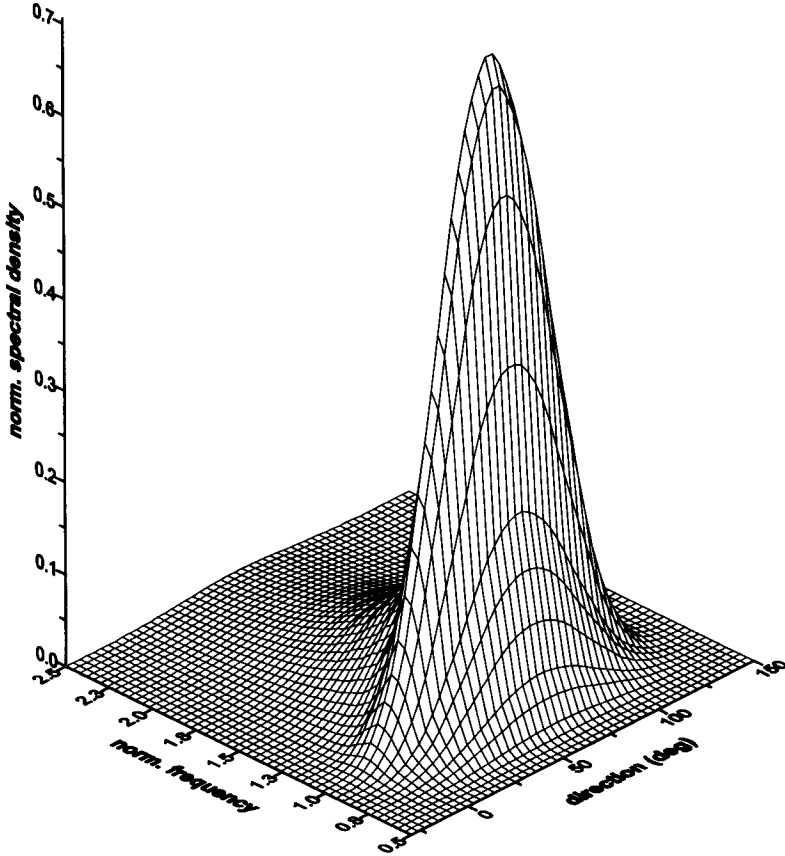


Figure 6.1: Two-dimensional incident wave spectrum $\hat{S}_0(\omega, \Theta)$.

It can be demonstrated that formulas (6.13) and (6.16) are identical. Particularly for parallel bottom contours the Snel's law gives:

$$\frac{\partial \Theta_0}{\partial \Theta} = \frac{k \cos \Theta}{k \cos \Theta_0}, \quad (6.19)$$

and

$$\frac{l_0}{l} = \frac{\cos \Theta_0}{\cos \Theta}. \quad (6.20)$$

Using Eqs. (6.19) and (6.20) in Eq. (6.16) gives:

$$\hat{S}(\omega, \Theta) = \frac{C_{g0}}{C_g} \frac{k}{k_0} \hat{S}(\omega, \Theta_0) = \frac{C_{g0}}{C_g} \frac{k}{k_0} \hat{S}_0 \left[\omega, \arcsin \left(\frac{k}{k_0} \sin \Theta_0 \right) \right], \quad (6.21)$$

which is Eq. (6.13).

To demonstrate the applicability of Eq. (6.13) we assume the incident spectrum $\hat{S}(\omega, \Theta_0, \vec{x})$ in the deep water, with mean wave direction $\bar{\Theta}_0 = 60^\circ$, with respect to the normal to parallel isobaths. Let us consider the spectrum $\hat{S}(\omega, \Theta_0, \vec{x})$ in the form:

$$\hat{S}_0(\omega, \Theta_0, x=0) = S_0(\omega, x=0) D(\Theta_0, \bar{\Theta}_0), \quad (6.22)$$

in which $S_0(\omega)$ is the JONSWAP spectrum and directional spreading $D(\Theta_0, \bar{\Theta}_0)$ takes the form:

$$D(\Theta_0, \bar{\Theta}_0) = \frac{8}{3\pi} \cos^4(\Theta_0 - \bar{\Theta}_0). \quad (6.23)$$

The following parameters are adopted in Eq. (6.22) and Eq. (6.23), i.e.: Phillips' constant $\alpha = 0.0136$ (wind speed $U = 20$ m/s and fetch $X = 100$ km), peak frequency $\omega_p = 0.82$ rad/s, enhancement factor $\gamma = 3.3$, and mean wave direction $\bar{\Theta}_0 = 60^\circ$.

In Fig. 6.1 the initial two-dimensional spectrum $\hat{S}(\omega, \Theta_0)$ is shown. The corresponding frequency spectrum $S_0(\omega)$ is given in Fig. 6.2. Results of calculation of shoaling of the initial spectrum, for water depth $h=10$ m are demonstrated in Figs. 6.2 and 6.3 for $S(\omega)$ and $\hat{S}(\omega, \Theta)$ spectra, respectively. The resulting two-dimensional spectrum $\hat{S}(\omega, \Theta)$ is much narrower than the initial one. Some spectral components cannot reach the isobath $h=10$ m. The main wave direction shifts towards the normal to the isobaths.

Let us now consider a more general case when isobaths are parallel to the y -axis, i.e. $h = h(x)$, but the wave motion is not uniform in the y direction. Now Eq. (2.184) takes the form:

$$\cos \Theta \frac{\partial f}{\partial x} + \sin \Theta \frac{\partial f}{\partial y} - \sin \Theta \frac{\partial (\ln k)}{\partial x} \frac{\partial f}{\partial \Theta} = 0, \quad (6.24)$$

in which f is given by Eq. (2.181).

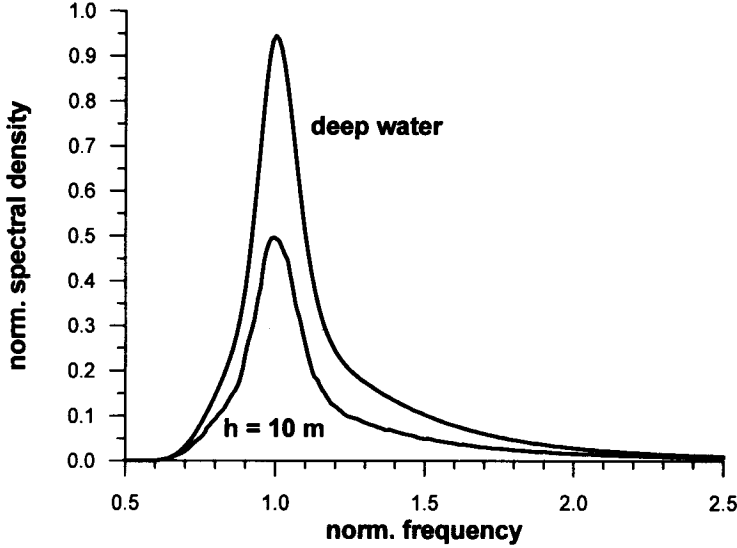


Figure 6.2: Frequency spectrum $S(\omega)$ in deep water and at $h = 10$ m.

To solve Eq. (6.24) we assume that in a plane (x, y) a curve $y_0 = y(x_0)$ is given, and the spectrum $\hat{S}(\omega, \Theta, x_0, y_0)$ on this curve is known. Therefore, the equation of characteristics has the following form (Krasitskii, 1974):

$$\frac{dy}{dx} = \tan \Theta, \quad \frac{d\Theta}{dx} = -\frac{\partial(\ln k)}{\partial x} \tan \Theta, \quad \frac{\partial f}{\partial x} = 0. \quad (6.25)$$

It can be verified by differentiating of Eq. (6.2), with respect to x , that the second equation in (6.25) represents the Snel's law, i.e.:

$$\frac{\partial \Theta}{\partial x} = -\frac{\sin \Theta}{k \cos \Theta} \frac{\partial k}{\partial x} = -\frac{\partial(\ln k)}{\partial x} \tan \Theta \quad (6.26)$$

Using Eq. (2.181), from the third equation we obtain:

$$\hat{S}(\omega, \Theta, x, y) = \frac{k}{k_0} \frac{C_{g0}}{C_g} \hat{S}(\omega, \Theta, x_0, y(x_0)), \quad (6.27)$$

in which $C_g = C_g(\omega, x)$. Finally, the first equation in (6.25) can be rewritten as:

$$\frac{dy}{dx} = \pm k_0 \sin \Theta_0 [k^2 - (k_0 \sin \Theta_0)^2]^{-1/2}, \quad (6.28)$$

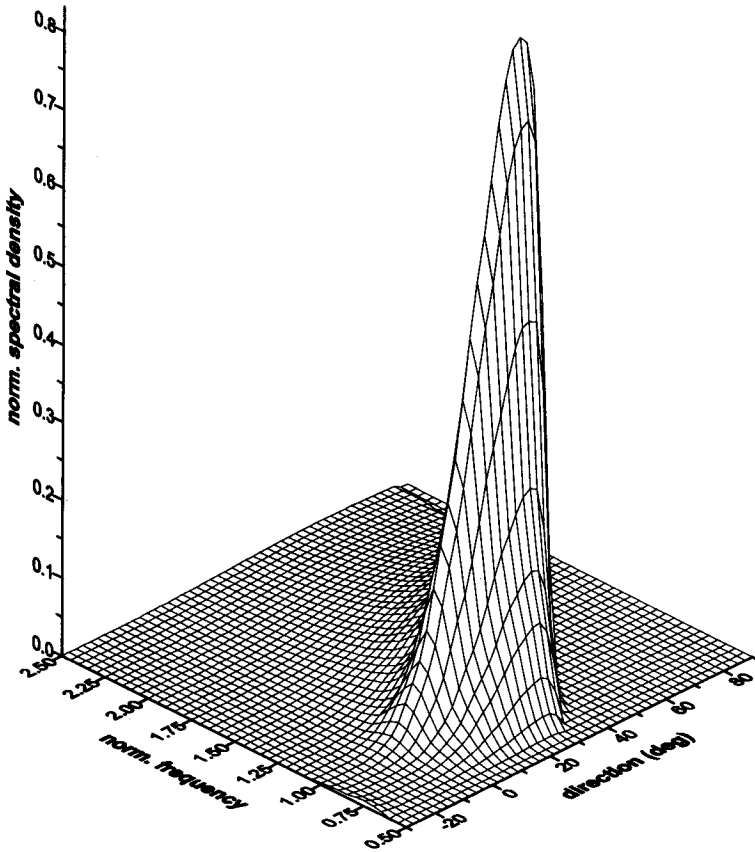


Figure 6.3: Two-dimensional spectrum $\hat{S}(\omega, \Theta)$ at $h = 10$ m.

and

$$y(x) = \pm k_0 \sin \Theta_0 \int_{x_0}^x \left[k^2 - (k_0 \sin \Theta)^2 \right]^{-1/2} dx + y(x_0). \quad (6.29)$$

When waves propagate into shallower water, i.e. when $\min k(x) > k_0 \sin \Theta_0$, the sign (+) in Eq. (6.29) should be used.

To find the spectrum $\hat{S}(\omega, \Theta, x, y)$ in the explicit form, the system of Eqs. (6.12) and (6.29) should be solved for x_0 and Θ_0 , and the result should be substituted into Eq. (6.27).

For water depth changing in both x and y directions, the basic formula (6.11) for $\hat{S}(\omega, \Theta, x, y)$ is still valid. The dispersive term $\left(\frac{k}{k_0} \right)$ and the shoaling term

$\left(\frac{C_{g0}}{C_g}\right)$ can be determined in a straightforward manner. However, the function $\Theta_0 = \arcsin\left(\frac{k}{k_0} \sin \Theta\right)$ requires a fan refraction diagram, or equivalent computer program, for all frequencies and directions. As was pointed out by Le Mehaute and Wang (1982), the complete determination of the $\hat{S}(\omega, \Theta)$ spectrum requires not much more additional work than determining the frequency spectrum only.

Shiau and Wang (1977) proposed a numerical scheme based on a square mesh instead of along a wave ray. To overcome the difficulties in defining the boundary conditions at the lateral boundaries, they assumed that at the boundary the bottom topography is defined by parallel bottom contours. They reported agreement of their numerical results with the Krasitskii's analytical solution. Other numerical schemes, for calculation of energy spectra due to wave refraction, will be discussed in the next Section.

The evolution of the energy spectrum due to refraction induces modifications of the statistical properties of shallow water waves. In Chapter 4, the basic statistical parameters and functions were described for deep and shallow water. However, the relationships between the statistical functions for deep and shallow water were not explicitly mentioned. In the following, we will discuss the transformation of the two-dimensional joint probability distribution of wave height and period $f_2(H, T)$ in shallow water zone. Analogous with directional energy spectrum, we assume that the joint probability of wave height ($H \approx 2a$), wave period T and angle Θ is given by a product of the joint probability distribution of wave height and period $f_2(H, T)$ and the directional spreading function $f(\Theta)$.

Following Longuet-Higgins (1975) we define two non-dimensional variables ξ and η as:

$$\xi = \frac{a}{\sqrt{m_0}}, \quad \eta = \frac{t - \bar{T}}{\nu \bar{T}}, \quad (6.30)$$

in which a is a wave amplitude, \bar{T} is mean wave period, t is a time, and ν is a spectral width parameter. By virtue of the rule in the change of variables we have (Le Mehaute et al., 1986):

$$f_2(\xi, \eta, \Theta) = f_0(\xi_0, \eta_0, \Theta_0) |J|^{-1}, \quad (6.31)$$

in which the Jacobian of transformation is:

$$|J| = \frac{\partial(\xi, \eta, \Theta)}{\partial(\xi_0, \eta_0, \Theta_0)}. \quad (6.32)$$

Taking into account that $\frac{\partial \Theta}{\partial \xi_0} = \frac{\partial \eta}{\partial \Theta_0} = 0$, and $\frac{\partial \eta}{\partial \xi_0} = 0$, since the wave period T is not a function of wave amplitude a , the Jacobian is reduced to:

$$J = \frac{\partial \xi}{\partial \xi_0} \frac{\partial \eta}{\partial \eta_0} \frac{\partial \Theta}{\partial \Theta_0}. \quad (6.33)$$

For the narrow-band spectrum we have $\frac{\partial \eta}{\partial \eta_0} \approx 1$, as in the case of monochromatic waves. Additionally, $\frac{\partial \xi}{\partial \xi_0} \approx \frac{\xi}{\xi_0} = K_T K_R$ (see, for example, Massel 1989). After substituting $\frac{\partial \xi}{\partial \xi_0}$ and $\frac{\partial \eta}{\partial \eta_0}$ values into Eq. (6.31), we obtain:

$$f_2(\xi, \eta, \Theta) = \frac{1}{K_T K_R} \frac{\partial \Theta_0}{\partial \Theta} f_0(\xi_0, \eta_0, \Theta_0). \quad (6.34)$$

Equations (6.13) and (6.16) indicate that $\frac{k}{k_0} = K_R^2 \left(\frac{\partial \Theta_0}{\partial \Theta} \right)$. Thus:

$$f_2(\xi, \eta, \Theta) = \frac{k}{k_0} \frac{1}{K_T K_R^3} f_0(\xi_0, \eta_0, \Theta_0). \quad (6.35)$$

In addition, Eq. (6.27) in Eq. (6.35) yields:

$$f_2(\xi, \eta, \Theta) = \frac{\hat{S}(\omega, \Theta)}{\hat{S}(\omega, \Theta_0)} \frac{1}{K_T^3 K_R^3} f_0(\xi_0, \eta_0, \Theta_0). \quad (6.36)$$

Eqs. (6.35) and (6.36) are universal since no hypothesis has been made on the form of wave spectrum or probability density distribution.

It can be shown that for a unidirectional spectrum the probability of wave height for a constant wave period is still the Rayleigh distribution. However, the probability density of wave period, at a specific wave height, is no longer Gaussian distribution because K_T is a function of the wave period. The calculations by Le Mehaute et al. (1986), who used the Pierson-Moskowitz spectrum with 20 m/s wind speed and main wave direction in deep water at 45° shorewards, indicate that the effects caused by shoaling and refraction result in asymmetric probability contours. When the water depth is greater than 20 m, the probability contours shift toward longer periods. Conversely, when the water depth is smaller than 20 m, they skew towards shorter periods. The longer wave period shift is attributed to the shoaling factor which causes more dispersion on shorter waves, whereas longer waves will refract seawards in shallow water. Also, the wave shoaling results in the decrease of probability for large wave heights in shallow water.

In general, the above analysis confirms the fact that the probability distribution of wave height in an intermediate and shallow water depth is no longer given by a Rayleigh distribution nor can the period distribution be considered as a Gaussian distribution.

6.2.2 Refraction by currents in a shoaling water depth

6.2.2.1 Propagation of random waves in an inhomogeneous region

It is a very common situation that the fluid upon which waves propagate is flowing and that the waves are modified by current. The transformation of sea waves by

currents is a significant physical process in many coastal areas, for instance: near river mouths and tidal inlets, in the surf zone along beaches under storm conditions, and where wind waves meet major ocean currents. The inclusion of the wave-current interaction is of great importance for phenomena such as sediment transport, ship navigation, and the forces on man-made structures.

The interaction between short waves and currents is a problem of wave propagation in an inhomogeneous, non-isotropic, dispersive and dissipative moving medium. When waves propagate in such a medium the kinematics and dynamics of the water particles are changed substantially in comparison with the absence of current. In particular, the spectral energy density is not conserved in contrast to the wave action density which remains conserved in a moving medium (see Eq. (2.186)). Other effects of moving medium on wave motion are discussed in detail, mostly for monochromatic waves, by Jonsson et al. (1970), Peregrine (1976) and Massel (1989).

In the following we consider a medium, with a non-uniform slowly varying still water depth h , moving with a velocity \vec{U} relative to fixed (\vec{x}, z) coordinate system. The observed frequency ω of surface waves propagating in such a medium is given by Eq. (2.170), i.e.:

$$\omega = \vec{U} \cdot \vec{k} + \sigma, \quad (6.37)$$

in which the intrinsic frequency σ is given by:

$$\sigma^2 = gk \tanh(kh). \quad (6.38)$$

If the dissipation, generation and wave-wave interactions are negligible, the conservation of the wave action density (2.186) reduces to:

$$\frac{\partial}{\partial t} \left(\frac{\hat{\Psi}}{\sigma} \right) + \nabla_h \cdot \left[(\vec{C}_g + \vec{U}) \frac{\hat{\Psi}}{\sigma} \right] = 0. \quad (6.39)$$

Equation (6.39) states that the local rate of change of a wave action is balanced by the divergence of the flux of action, a quantity that flows relative to the moving medium with the absolute group velocity C_g . The absolute group velocity C_g , i.e.:

$$C_g = \frac{\partial \omega}{\partial k} = \frac{\partial \sigma}{\partial k} + \vec{U} \cdot \frac{\vec{k}}{|\vec{k}|} > 0, \quad (6.40)$$

defines the wave ray direction. The local group velocity $\frac{\partial \sigma}{\partial k}$ is associated with the normal to wave front. In the extreme condition, when $\frac{\partial \sigma}{\partial k} = -\vec{U} \cdot \frac{\vec{k}}{|\vec{k}|}$, the spectral component no longer propagates against the current in that direction. Theoretically, the local spectral energy density $\hat{S}(\omega, \Theta, \vec{x})$ becomes infinite. This suggests that these components will tend to attenuate by wave breaking or by a lateral stretching in the crest direction, before this point is reached.

It should be noted that the local wave number vector is irrotational, i.e.:

$$\frac{\partial \vec{k}}{\partial t} + \nabla_h \omega = 0. \quad (6.41)$$

For a steady state, Eq. (6.41) reduces to:

$$\nabla_h \omega = 0. \quad (6.42)$$

This implies that the observed frequency ω is an invariant under a steady state and along wave rays we obtain:

$$\frac{\hat{\Psi}}{\sigma} = \frac{C_g}{k} \frac{\hat{S}(\omega, \Theta; \vec{x}, t)}{\sigma} = \text{constant}. \quad (6.43)$$

Equation (6.43), together with (2.170) and the initial values of $\hat{S}(\omega, \Theta)$, \vec{x} and Θ are sufficient to determine the spectral density $\hat{S}(\omega, \Theta; \vec{x}, t)$.

Let us apply the above formulas for the case of random waves propagating from a spatially homogeneous region, such as deep water, into an inhomogeneous region with a non-uniform depth profile $h = h(x)$ and traversing a steady non-uniform current field $\vec{U} = (0, U_2(x), 0)$. Under these conditions, the spatial inhomogeneity of the problem is restricted to the x -direction with the Snel's law in the form:

$$k \sin \Theta = \text{constant}, \quad (6.44)$$

where angle Θ is taken relative to the x -axis.

From Eqs. (6.37) and (6.43) we obtain:

$$\frac{C_g}{k} \frac{\hat{S}(\omega, \Theta; \vec{x})}{\omega - \vec{U} \cdot \vec{k}} = \text{constant}. \quad (6.45)$$

Let us assume that group velocity, wave number and two-dimensional spectral density in the deep water, in absence of current, are C_{g0} , k_0 and $\hat{S}_0(\omega, \Theta)$, respectively. Thus, Eq. (6.45) can be rewritten as:

$$\hat{S}(\omega, \Theta; \vec{x}) = \left(\frac{k}{k_0} \right) \left(\frac{C_{g0}}{C_g} \right) \frac{\omega - \vec{k} \cdot \vec{U}}{\omega} \hat{S}_0(\omega, \Theta). \quad (6.46)$$

As the two-dimensional spectral density functions $\hat{S}(\omega, \Theta; \vec{x})$ and $\hat{S}_0(\omega, \Theta)$ are both positive, the following condition should be satisfied:

$$\frac{\omega - \vec{k} \cdot \vec{U}}{\omega} \geq 0. \quad (6.47)$$

Locally the wave components must satisfy the condition (6.15) resulting from the Snel's law. To evaluate this condition for the case of a non-uniform current-depth interaction, we substitute Eq. (6.38) into Eq. (6.37) and obtain:

$$\left(1 - \frac{\vec{U} \cdot \vec{k}}{\omega} \right) = \left(\frac{k \tanh(kh)}{k_0} \right)^{1/2}, \quad (6.48)$$

in which $k_0 = \frac{\omega^2}{g}$.

Using the Snel's law (6.2) in Eq. (6.48) yields:

$$\left(1 - \frac{\vec{U} \cdot \vec{k}}{\omega}\right) = \left(\frac{\sin \Theta_0}{\sin \Theta} \tanh(kh)\right)^{1/2}. \quad (6.49)$$

Because $|\sin \Theta| \leq 1$, Eq. (6.49) can be rewritten in the form:

$$\left(1 - \frac{\vec{U} \cdot \vec{k}}{\omega}\right) \geq [|\sin \Theta_0| \tanh(kh)]^{1/2}. \quad (6.50)$$

When condition (6.50) becomes an equality, then $|\sin \Theta_0| = 1$. This case corresponds to total reflection of the associated spectral component.

While the spatial transformation of the two-dimensional spectrum $\hat{S}(\omega, \Theta; \vec{x})$ involves the combined current-depth effects, the transformation of the wave number spectrum $\hat{\Psi}(\vec{k})$ is entirely due to the current interaction.

Finally, following Tayfun et al. (1976), we list the most important relationships needed for the prediction of the two-dimensional spectrum $\hat{S}(\omega, \Theta; \vec{x})$ in the presence of a non-uniform current:

- dispersion relation:

$$\omega^2 \left[1 - \frac{U(x)}{C_0} \sin \Theta_0\right]^2 = gk \tanh(kh), \quad (6.51)$$

- wave number k and angle Θ :

$$k = k_0 \left(1 - \frac{U(x)}{C_0}\right)^2 (\tanh kh)^{-1}, \quad (6.52)$$

$$\sin \Theta = \left(\frac{k_0}{k}\right) \sin \Theta_0 = \left(1 - \frac{U(x)}{C_0} \sin \Theta_0\right)^{-2} \tanh(kh) \sin \Theta_0, \quad (6.53)$$

- phase speed relative to the current:

$$C_r = C_0 \left(\frac{k}{k_0}\right) \left(1 - \frac{U(x)}{C_0} \sin \Theta_0\right) = C_0 \left(1 - \frac{U(x)}{C_0} \sin \Theta_0\right)^{-1} \tanh(kh), \quad (6.54)$$

- group velocity C_g :

$$C_g = \frac{\partial \omega}{\partial k} = \frac{\omega}{k} \left[m + (1 - m) \frac{U(x)}{C_0} \sin \Theta_0 \right], \quad (6.55)$$

in which:

$$m = m(kh) = \frac{1}{2} \left(1 + \frac{2kh}{\sinh 2kh} \right), \quad (6.56)$$

- two-dimensional spectral density $\hat{S}(\omega, \Theta; \vec{x})$:

$$\hat{S}(\omega, \Theta; \vec{x}) = \frac{1}{2} \frac{k}{k_0} \frac{C_0}{C} \frac{\left(1 - \frac{U(x)}{C_0} \sin \Theta_0 \right)}{\left[m + (1 - m) \frac{U(x)}{C_0} \sin \Theta_0 \right]} \hat{S}(\omega, \Theta). \quad (6.57)$$

Let us now consider the simpler one-dimensional case. The conservation of wave action (6.39) for a steady wave train is:

$$\frac{\partial}{\partial x} \left\{ \left(U + \frac{d\sigma}{dk} \right) \frac{E}{\sigma} \right\} = 0, \quad (6.58)$$

in which $E = S(\omega)d\omega$ is wave energy. As the absolute frequency ω is invariant, Eq. (6.58) becomes (see also Hedges et al., 1985):

$$S(\omega) = \frac{m(k_0 h) \sigma}{k_0 \left[U + m(kh) \frac{\sigma}{k} \right]} S_0(\omega), \quad (6.59)$$

in which function $m = m(kh)$ is given in Eq. (6.56), and the intrinsic frequency σ is defined by Eq. (6.38).

In deep water $m(k_0 k) = m(kh) = \frac{1}{2}$, $\sigma = \frac{g}{C}$, and $k_0 = \frac{g}{C_0^2}$. Therefore, Eq. (6.59) takes the form:

$$S(\omega) = \frac{0.5 C_0^2}{(U + 0.5C) C} S_0(\omega). \quad (6.60)$$

6.2.2.2 Influence of uniform current on a saturation range spectrum

The shape of the frequency spectrum in the saturation range in deep water is defined by Phillips' formula (3.16). The extension of the saturation range approach to the finite water depth was proposed by Kitaigorodskii et al. (1975). We now extend the Kitaigorodskii et al. formula by including an uniform current. Let us first rewrite the dispersion relation (6.37) in the form:

$$\omega = kU \cos \Theta + [gk \tanh(kh)]^{1/2}, \quad (6.61)$$

in which Θ is an angle between the current vector and the normal to wave front for a given spectral component. Thus, for the non-dimensional wave number kh we obtain:

$$kh = \omega_*^2 \frac{\left(1 - kh \frac{\omega_U \cos \Theta}{\omega_*^2}\right)^2}{\tanh(kh)} = \omega_*^2 f, \quad (6.62)$$

in which:

$$f(\omega_*, \omega_U, \Theta) = \frac{\left(1 - kh \frac{\omega_U \cos \Theta}{\omega_*^2}\right)^2}{\tanh(kh)}, \quad (6.63)$$

$$\omega_*^2 = \frac{\omega^2 h}{g}, \quad \omega_U = \frac{\omega U}{g}. \quad (6.64)$$

Finally, rearranging Eq. (6.61) provides the transcendental equation for function f as:

$$f \omega_U \cos \Theta + [f \tanh(\omega_*^2 f)]^{1/2} = 1. \quad (6.65)$$

Using the function f , the group velocity C_g becomes:

$$C_g = \frac{\partial \omega}{\partial k} = \frac{1}{2} \frac{g}{\omega} f_1(\omega_*, \omega_U, \Theta), \quad (6.66)$$

where:

$$f_1(\omega_*, \omega_U, \Theta) = 2\omega_U \cos \Theta + \left(\frac{\tanh(\omega_*^2 f)}{f}\right)^{1/2} \left[1 + \frac{2\omega_*^2 f}{\sinh(2\omega_*^2 f)}\right]. \quad (6.67)$$

Eqs. (3.59) and (3.60) allow representation of the frequency spectrum in the form:

$$S(\omega) = \int_{-\pi}^{\pi} \left[\Psi(k, \Theta) \frac{k}{C_g} \right]_{k=k(\omega, \Theta)} d\Theta. \quad (6.68)$$

After substituting Eqs. (6.62) and (6.66) into (6.68), and using (3.60) and (3.62) we obtain:

$$S(\omega) = \alpha g^2 \omega^{-5} \int_{-\pi}^{\pi} \frac{D(\Theta)}{f^3 f_1} d\Theta, \quad (6.69)$$

where $D(\Theta)$ is a directional spreading function, and $\alpha = 2B$.

Without loss of generality, we assume the long-crested waves propagating at the angle Θ_0 with respect to current, i.e.:

$$D(\Theta) = \delta(\Theta - \Theta_0), \quad (6.70)$$

in which $\delta()$ is the Dirac delta. Substituting Eq. (6.70) into (6.69) gives:

$$S(\omega) = \alpha g^2 \omega^{-5} f^{-3}(\omega_*, \omega_U, \Theta_0) f_1^{-1}(\omega_*, \omega_U, \Theta_0). \quad (6.71)$$

When $U = 0$, ($\omega_U = 0$) and $\Theta_0 = 0$, functions f and f_1 simplify as (see also Eq. (3.65)):

$$1 = f \tanh(\omega_*^2 f), \quad (6.72)$$

and

$$f_1 = \left[\frac{\tanh(\omega_*^2 f)}{f} \right]^{1/2} \left[1 + \frac{2\omega_*^2 f}{\sinh(2\omega_*^2 f)} \right]. \quad (6.73)$$

Thus:

$$S(\omega) = \alpha g^2 \omega^{-5} f^{-2} \left[1 + \frac{2\omega_*^2 f}{\sinh(2\omega_*^2 f)} \right]^{-1}, \quad (6.74)$$

which is in agreement with the Kitaigorodskii et al. (1975) solution for a non-current case (see Eq. (3.67)).

When $\omega_* \rightarrow \infty$ (deep water) and $\omega_U \neq 0$, Eq. (6.65) yields:

$$f \omega_U \cos \Theta + f^{1/2} = 1, \quad (6.75)$$

with a solution:

$$f = \frac{(2a + 1) - \sqrt{4a + 1}}{2a^2}, \quad (6.76)$$

in which $a = \omega_U \cos \Theta$.

If current velocity U diminishes or $\Theta = 90^\circ$ (current vector is normal for wave vector), $a = \omega_U \cos \Theta \rightarrow 0$. Then, L'Hospital's Rule yields $f \rightarrow 1$, and from Eq. (6.67) we obtain $f_1 = 1$; thus $S(\omega) = \alpha g^2 \omega^{-5}$, which is expected.

For a non-zero current in the deep water Eq. (6.67) gives $f_1 = 2a + f^{-1/2}$ and:

$$S(\omega) = \alpha g^2 \omega^{-5} \frac{1}{(1 + a f^{1/2}) f^{5/2}}. \quad (6.77)$$

In the shallow water limit, i.e. when $\omega_* \rightarrow 0$, Eqs. (6.65), (6.67) and (6.71) become:

$$f = \frac{1}{\omega_* + \omega_U \cos \Theta}, \quad f_1 = 2(\omega_* + \omega_U \cos \Theta), \quad (6.78)$$

and

$$S(\omega) = \frac{1}{2} \alpha g^2 \omega^{-5} (\omega_* + \omega_U \cos \Theta)^2. \quad (6.79)$$

When $\omega_U \rightarrow 0$, Eq. (6.79) gives:

$$S(\omega) = \frac{1}{2} \alpha g h \omega^{-3}, \quad (6.80)$$

which is in agreement with the Kitaigorodskii et al. (1975) solution for a non-current case (see Eq. (3.69)).

Gadzhiyev et al. (1978) obtained an approximate expression for the spectrum $S(\omega)$ for three different directional distributions ($D_1(\Theta) = \delta(\Theta)$, $D_2(\Theta) = \frac{1}{\pi}$, and $D_3(\Theta) = \frac{2}{\pi} \cos^2 \Theta$), assuming the small current velocity U and expanding the function $\frac{1}{f^3 f_1}$ into a Taylor series in $(\omega_U \cos \Theta)$, and keeping only the linear term. Suk et al. (1994) found a good agreement of the approximate solution by Gadzhiyev et al. (1978) with their experimental data on a following and opposing current.

All of the above results are restricted to the currents assumed to be uniform over water depth. However, currents typically do not possess so simple a form, but instead have variations over depth. The problem for a random wave motion on arbitrarily varying currents still remains unsolved. The laboratory experiments on waves propagating on a shear current indicate that the power spectra of a combined wave-current motion are strongly dependent upon the depth variation in the current profile (Cummins and Swan, 1994).

6.2.3 Combined refraction and diffraction

The condition (6.5) imposes some restriction on the applicability range of the refraction solution. If the bottom slope becomes steeper, the ray method is no longer able to predict the wave parameters properly. This is especially true for sandy beaches where many longshore sandbars are observed. The local slopes in the vicinity of the underwater bars are sometimes substantial.

Other examples of steep bottom slopes are those at underwater shoals or coral reefs. Along the Norwegian coast there are many sea mounts like shoals. Water depth on the shoal is usually very small, but increases rapidly to 50 m and more out from the shoal (Lie and Torum, 1991).

The Great Barrier Reef (GBR), located off the eastern coastline of Australia, is composed of almost three thousands reefs. In the northern section of the GBR the

reefs are long, two-dimensional structures. Seaward of the reef the water depth rises very rapidly from approximately 1000 m to a shallow reef crest at the low tide level.

In all these situations, the refraction and diffraction effects are substantial and cannot be neglected. In order to account for these effects, an alternative approach, based on the so called mild-slope equation, is considered. This equation originally was introduced by Berkhoff (1972). In recent years, many papers on applicability of the mild-slope equation to many coastal problems have been published (e.g. Berkhoff et al., 1982; Mei, 1983; Dingemans, 1985; Massel, 1989, 1993a).

According to Booij (1983), the mild-slope equation gives accurate results even with a plane bottom slope up to 1:3. When the bottom profile is arbitrary, bottom curvature ($\approx \nabla^2 h$) and possibly higher orders of the bottom slope (e.g. $(\nabla h)^2$) cannot be omitted.

In this Section we discuss shortly properties of the mild-slope equation and methods of its solution. Let us assume for a moment a motion of the monochromatic wave with frequency ω . Hence, the velocity potential $\Phi(x, y, z, t)$ takes the form:

$$\Phi(x, y, z, t) = \Re \left\{ -\frac{ig}{\omega} \varphi(x, y) \frac{\cosh k(z+h)}{\cosh kh} e^{-i\omega t} \right\}, \quad (6.81)$$

in which $\varphi(x, y)$ is a complex wave amplitude, \Re is a real part of the complex function.

Berkhoff (1972) derived the following equation to describe the evolution of wave amplitude $\varphi(x, y)$ in the horizontal plane:

$$\nabla_h^2 \varphi + \frac{\nabla_h(CC_g)}{CC_g} \cdot \nabla_h \varphi + k^2 \varphi = 0. \quad (6.82)$$

Equation (6.82) is called the 'mild-slope' due to an inherent assumption that the bottom slopes are small. The first and third terms in Eq. (6.82) represent the diffraction effects, while the second term describes the influence of the refraction.

A number of monochromatic wave propagation models have been developed for simulating refraction-diffraction phenomena, and they have been applied successfully in a wide variety of situations (for example, De Girolamo et al., 1988; Massel and Belberova, 1990; Tsutsui and Lewis, 1991; Tsutsui and Zamami, 1993).

However, the wave heights resulting from the monochromatic models are only approximate estimations of the actual irregular sea state. Vincent and Briggs (1989) studied combined refraction-diffraction of wave transformations over a shoal in a hydraulic model and observed large differences between the actual irregular and representative regular conditions.

The representation of a wave field as a spectrum is not new, but has only recently become common place in engineering practice (e.g. Krylov et al., 1976; Druet, 1978; Goda, 1985); Briggs et al., 1987). The 'spectral model' essentially consists of decomposing a spectrum of the irregular sea into monochromatic components, and assembling the component results by linear superposition. The input wave amplitude for a particular frequency component with initial direction Θ is $[2S(\omega)D(\Theta)\Delta\omega\Delta\Theta]^{1/2}$.

The resulting wave heights H_i at any location are used to compute the characteristic wave height, for example, the significant wave height (H_s), as follows:

- elementary energy $\Delta E_i = 0.125 H_i^2$,
- total energy $E = \sum_i \Delta E_i = 0.125 \sum_i H_i^2 = \sigma_\zeta^2$,
- significant wave height $H_s^2 = 16\sigma_\zeta^2 = 2 \sum_i H_i^2$.

Assuming that the nonlinearities are not too strong and the linear superposition of the spectral components provides a satisfactory representation of the irregular wave field, the improvement in the modelling of an irregular sea strongly depends on the accuracy of numerical models of monochromatic wave refraction-diffraction.

The original mild-slope model is expressed by an inseparable elliptic partial differential equation. Due to the elliptical nature, Eq. (6.82) is difficult to implement for typical wave-propagation problems extending over many wavelengths. However, the finite-difference elliptic models for very large domains have recently been developed by Panchang et al. (1991), and Li and Anastasiou (1992).

The 'open' boundary (where the computational domain intersects the surrounding sea) need special treatment. This boundary contains, besides the incident waves, so called 'scattered' waves that arise from bathymetric effects and/or the presence of reflecting boundaries. The outgoing boundary conditions for elliptic-type models usually are developed as the various parabolic approximations for the scattered waves (Kirby, 1989), or by approximation of the bathymetry outside the computational domain by a constant water depth. The scattered wave potential in the open sea is described using a Fourier-Bessel series and the external and internal solutions are matched by minimizing the overall error functional along the boundary (Xu and Panchang, 1993).

Because of the difficulties with the solution of elliptic-type equations, the theory based on parabolic approximation has been developed and has emerged as a powerful tool for studying combined wave refraction and diffraction phenomena in shallow water (Radder, 1979; Kirby and Dalrymple, 1983). The practical advantages over more accurate elliptic equations are that numerical integration can be obtained by marching from a deep water region toward the shoreline. Although easy to use, the parabolic approximation has two important limitations, i.e. the waves must have a principal propagation direction, since diffraction effects are restricted to the perpendicular direction only, and the reflected components of the waves in the negative direction should be negligibly small. In order to satisfy this requirement, a curvilinear coordinate system is sometimes applied (Isobe, 1987). Panchang et al. (1990) applied the parabolic approximation model to simulate the irregular wave propagation over an underwater shoal. The comparison with experiments by Vincent and Briggs (1989) confirms the usefulness of the parabolic approximation.

It is known that the mild-slope equation satisfies the conservation law for the energy flux. Let us show now that the time-dependent mild-slope equation, governing

the propagation of waves in the presence of a varying depth and current, satisfies the conservation law for the wave action. In the presence of a large ambient current $\vec{U}(x, y, t)$, the velocity potential $\Phi(x, y, z, t)$ for a wave motion in the mild-slope approximation can be written as:

$$\Phi(x, y, z, t) = \Phi_0(x, y, t) + \epsilon Z(x, y, z) \varphi(x, y, t), \quad (6.83)$$

in which Φ_0 is the potential for the mean current,

$$\vec{U}(x, y, t) = \nabla_h \Phi_0, \quad (6.84)$$

and

$$Z(x, y, z) = \frac{\cosh k(z + h)}{\cosh kh}, \quad (6.85)$$

where ϵ is a small wave amplitude parameter. Potential $\Phi(x, y, t)$ should satisfy the following time-dependent mild-slope (Kirby, 1984):

$$\frac{D^2 \varphi}{Dt^2} + (\nabla_h \cdot \vec{U}) \frac{D\varphi}{Dt} - \nabla_h \cdot (CC_g \nabla_h \varphi) + (\sigma^2 - k^2 CC_g) \varphi = 0, \quad (6.86)$$

where:

$$\frac{D}{Dt} = \left(\frac{\partial}{\partial t} + \vec{U} \cdot \nabla_h \right), \quad (6.87)$$

and σ is the intrinsic frequency given by Eq. (6.38).

Let us define the potential φ in the wave form, i.e.:

$$\varphi(x, y, t) = \frac{-ig}{\sigma} A(x, y) e^{i\psi(x, y, t)} = -igR(x, y) e^{i\psi(x, y, t)}, \quad (6.88)$$

where $R = \sigma^{-1}A$ and ψ are taken to be purely real quantities.

After substituting Eq. (6.88) into Eq. (6.86), separating the real and imaginary parts in the resulting expression, and multiplying by R , we obtain (Kirby, 1984):

$$\frac{\partial}{\partial t} (\sigma R^2) + \sigma \vec{U} \cdot \nabla_h (R^2) + \sigma \vec{C}_g \cdot \nabla_h (R^2) + \nabla_h \cdot (\sigma \vec{U}) R^2 + \nabla_h \cdot (\sigma \vec{C}_g) R^2 = 0, \quad (6.89)$$

or:

$$\frac{\partial}{\partial t} (\sigma R^2) + \nabla_h \cdot [\sigma R^2 (\vec{C}_g + \vec{U})] = 0. \quad (6.90)$$

Using the fact that the wave action is defined as:

$$N = \frac{1}{2} \rho g \frac{A^2}{\sigma}, \quad (6.91)$$

Eq. (6.90) finally yields:

$$\frac{\partial N}{\partial t} + \nabla_h \cdot [N (\vec{C}_g + \vec{U})] = 0, \quad (6.92)$$

which is the required conservation law for wave action N .

6.2.4 Reflection of ocean waves

Ocean basins are very large, however, they are not unlimited. Waves approaching the coast undergo substantial modification due to reflection from beaches, cliffs or man-made structures. Wave reflection from beaches is a subject of major importance to understand the nearshore zone and to improve the coastal structure design. In particular, the level of energy dissipation on a beach depends on the magnitude of the wave reflection from the beach. Therefore, the wave reflection influences, in an indirect manner, many coastal processes, such as the longshore current and sediment transport, wave run-up, and others. All these processes are basic ones for the determination of the design criteria for coastal protection structures. The dependence of wave-induced forces on the rate of reflection is even more straightforward for such structures as breakwaters or offshore structures.

Most of the information on wave reflection comes from laboratory and theoretical studies based on the monochromatic wave theory. In such a situation, the reflection coefficient C_r is defined as the ratio of the amplitude of the reflected wave (A_{ref}) to the amplitude of the incident wave (A_{in}):

$$C_r = \frac{A_{ref}}{A_{in}}. \quad (6.93)$$

When waves reflect only partly from some boundary (beach slope, rubble-mound breakwater etc.), the phase shift φ between incident and reflected waves appears. Therefore, in general the reflection coefficient is the non-dimensional complex value:

$$C_r = |C_r| e^{i\varphi}. \quad (6.94)$$

The estimation of reflection coefficient on a slope was first introduced by Miche (1951). He empirically determined that the coefficient C_r for monochromatic waves, normally incident on a plane beach, is:

$$C_r^2 \approx \begin{cases} 1 & \text{for } M \geq 1, \\ M & \text{for } M < 1, \end{cases} \quad (6.95)$$

in which:

$$M = \frac{16g^2 \tan^5 \beta}{2\pi H_0^2 \omega}, \quad (6.96)$$

where β is the beach slope, H_0 and ω are the deep water wave height and wave frequency, respectively. A convenient representation of Miche's reflection coefficient is obtained in terms of similarity parameter ξ_0 (Battjes, 1974):

$$C_r \approx 0.1 \xi_0^2, \quad (6.97)$$

where:

$$\xi_0 = \frac{\tan \beta}{\sqrt{\frac{H}{L_0}}}, \quad (6.98)$$

β is a beach slope, H is the incident wave height at the toe of the slope, and $L_0 = \frac{gT^2}{2\pi}$ is the deepwater wavelength.

Seelig and Ahrens (1981) collected the experimental data from several sources and developed the curves to obtain an estimate of the reflection coefficient for smooth slopes, sand beaches, and rubble-mound breakwaters as a function of similarity parameter ξ_0 (see Fig. 6.4).

The reflection from natural beaches or man-made structures under irregular wave action is more complex. In general, the reflection coefficient is strongly dependent on wave frequency. The determination of the reflection coefficient basically involves separation of the incident and reflected waves from a given time series of surface elevation.

In the following, we present two different approaches to estimate the reflection coefficient. In the first, the Fourier series representation is used, while the second one is based on the solution of a corresponding boundary value problem.

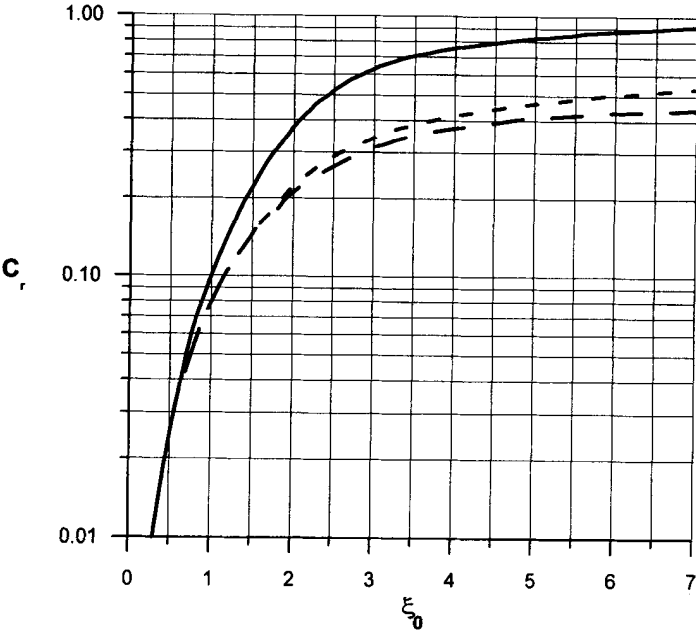


Figure 6.4: Reflection coefficient for slopes (—), beaches (---), rubble-mound breakwaters (- - -) as a function of similarity parameter ξ_0 (From SPM, 1984).

In order to define the reflection coefficient for irregular waves, according to the first method, we suppose that a one-dimensional wave field is observed by recording the surface elevation $\zeta_p(t)$ at locations x_p ($p = 1, 2, \dots, P$). The observed surface oscillation at the particular point x_p is a summation of the incident waves, travelling in the direction of the negative x -axis, and of the wave reflected from a beach or man-made structure, and travelling in the direction of the positive x -axis.

The incident wave train at location x_0 may be expressed in the form of the Fourier series:

$$\zeta(x_p, t) = \sum_{j=-\frac{N}{2}}^{j=\frac{N}{2}} a_j^{(in)} \exp[i(k_j x_p + \omega_j t)], \quad (6.99)$$

where $\omega_j = 2\pi j/T$, T is a length of the time series, and N is the maximum number of frequencies of interest. Under the assumption that dissipation and nonlinear interactions are negligible, the total surface elevation at a location x_p becomes:

$$\zeta(x_p, t) = \sum_{j=-\frac{N}{2}}^{j=\frac{N}{2}} \left\{ a_j^{(in)} \exp[i(k_j x_p + \omega_j t)] + a_j^{(ref)} \exp[i(-k_j x_p + \omega_j t)] \right\}. \quad (6.100)$$

The surface elevation Eq. (6.100) should be equal to the observed one, i.e.:

$$\begin{aligned} \sum_{j=-\frac{N}{2}}^{j=\frac{N}{2}} \left\{ a_j^{(in)} \exp(i\varphi_{j,p}) + a_j^{(ref)} \exp(-i\varphi_{j,p}) \right\} \exp(i\omega_j t) = \\ = \sum_{j=-\frac{N}{2}}^{j=\frac{N}{2}} A_{j,p} \exp(i\omega_j t), \end{aligned} \quad (6.101)$$

in which $\varphi_{j,p} = k_j x_p$; $A_{j,p}$ are the observed Fourier component amplitudes at the location of wave gauge p . Eq. (6.101) yields the following equations for each Fourier component j :

$$a_j^{(in)} \exp(i\varphi_{j,p}) + a_j^{(ref)} \exp(-i\varphi_{j,p}) = A_{j,p} \quad \text{for } p = 1, 2, \dots, P. \quad (6.102)$$

For example, for two wave gauges, Eq. (6.102) yields exact solution for $a_j^{(in)}$ and $a_j^{(ref)}$ amplitudes:

$$\left. \begin{aligned} a_j^{(in)} &= \frac{-A_{j,1} \exp(-i\varphi_{j,2}) + A_{j,2} \exp(-i\varphi_{j,1})}{\exp[i(-\varphi_{j,1} + \varphi_{j,2})] - \exp[i(\varphi_{j,1} - \varphi_{j,2})]} \\ a_j^{(ref)} &= \frac{A_{j,1} \exp(i\varphi_{j,2}) - A_{j,2} \exp(i\varphi_{j,1})}{\exp[i(-\varphi_{j,1} + \varphi_{j,2})] - \exp[i(\varphi_{j,1} - \varphi_{j,2})]} \end{aligned} \right\}. \quad (6.103)$$

When the number of gauges is greater than 2, Eq. (6.102) is over-determined and amplitudes $a^{(in)}$ and $a^{(ref)}$ must be estimated by an approximate technique. For

example, we can minimize a weighted sum of the squares of the errors for each wave gauge as follows (Zelt and Skjelbreia, 1992):

$$E_j = \sum_{p=1}^P W_{j,p} \epsilon_{j,p} \epsilon_{j,p}^* \quad (6.104)$$

in which $W_{j,p}$ is the weighting coefficient for wave gauge p at frequency ω_j , while $\epsilon_{j,p}$ represents the error in matching the j^{th} Fourier coefficient $A_{j,p}$ at the wave gauge p :

$$\epsilon_{j,p} = a_j^{(in)} e^{i\varphi_{j,p}} + a_j^{(ref)} e^{-i\varphi_{j,p}} - A_{j,p}. \quad (6.105)$$

The non-uniform weighting is used to enhance the wave gauges that provide more reliable estimates. The requirement of the minimum of function E_j yields the following solution for $a_j^{(in)}$ and $a_j^{(ref)}$:

$$\left. \begin{aligned} a_j^{(in)} &= \sum_{p=1}^P C_{j,p}^* A_{j,p} \\ a_j^{(ref)} &= \sum_{p=1}^P C_{j,p} A_{j,p} \end{aligned} \right\}, \quad (6.106)$$

where:

$$C_{j,p} = 2iW_{j,p} \frac{e^{i\varphi_{j,p}}}{D} \sum_{q=1}^P W_{j,q} \sin(\Delta\varphi_{j,pq}) \exp(i\Delta\varphi_{j,p}). \quad (6.107)$$

The $\Delta\varphi_{j,pq} = \varphi_{j,p} - \varphi_{j,q} = k_j(x_p - x_q)$ represents the phase difference between wave gauges p and q at frequency ω_j , and the denominator D is:

$$D = \left\{ \sum_{p=1}^P W_{j,p} \right\}^2 - \sum_{p=1}^P W_{j,p} e^{2i\Delta\varphi_{j,p}} \sum_{p=1}^P W_{j,p} e^{-2i\Delta\varphi_{j,p}}. \quad (6.108)$$

The solution (6.103) for $P = 2$, as well as the formulae of Mansard and Funke (1980) for $P = 3$, are the special cases of the general solution (6.106), when $W_{j,p} \equiv 1$.

The numerical simulation showed that a good accuracy is obtained if more than three wave gauges are used, especially for broadband wave spectra. Another way to improve the decomposition accuracy is the proper choice of the weighting coefficients.

Walton (1992), in his field experiments at natural beaches with an average slope of 1/15 to 1/10, found that the frequency dependent reflection coefficient was less than 10%, which suggests that reflected energy from the beach is less than 1% of the incident energy. Therefore, it seems that a reasonable first approximation for engineering coastal phenomena is to consider natural beaches to be effective energy dissipators at least in the cross-shore direction.

Elgar et al. (1994) observed that the ratio of seaward to shoreward propagating energy in the swell-sea frequency band (0.044-0.20 Hz) varies between 0.5 and 3, and

decreases with increasing beach slope. This conclusion is consistent with the Miche parameterization (6.95).

For waves at infragravity frequencies, corresponding to wave periods from about 30 seconds to 5 or 6 minutes, the reflection from exposed dissipative beach is much higher (Nelson and Gonsalves, 1990) and the degree of reflection depends on the frequency and tide level. Elgar et al. (1994) reported that there was more seaward than shoreward propagating energy in the frequency band (0.010–0.044 Hz).

When amplitudes $a_j^{(in)}$ and $a_j^{(ref)}$ are known, the reflection coefficient C_r for a frequency ω_j becomes:

$$C_r(\omega_j) = \frac{a_j^{(ref)}}{a_j^{(in)}}. \quad (6.109)$$

Let us now consider the reflection of wind-induced waves from man-made structures when only partial reflection occurs. Examples of such structures are the rubble-mound or other type of porous breakwaters. We consider the simple case of an homogeneous, porous rectangular breakwater subjected to normal wind-induced waves propagated in water of a constant depth h (Fig. 6.5). At the front of the breakwater the wave motion consists of incident and partly reflected waves. The resulting velocity potential takes the form (Massel and Butowski, 1982):

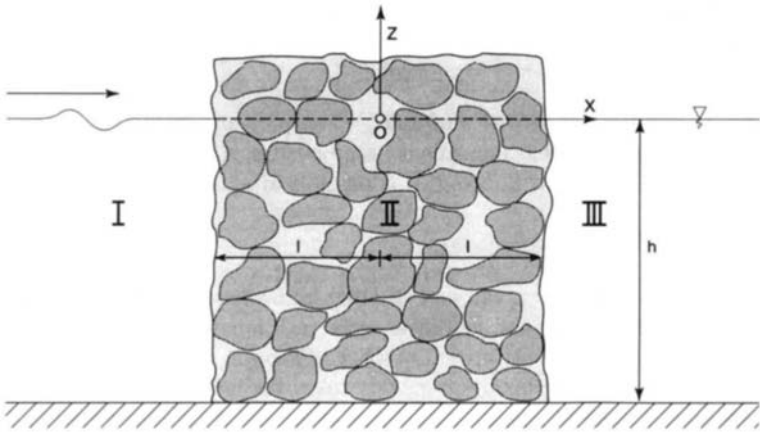


Figure 6.5: Cross-section of schematic porous breakwater.

$$\begin{aligned}\Phi_1(x, z, t) = & \Re \int_{-\infty}^{\infty} \frac{-ig}{\omega} e^{-i\omega t} \left\{ \left[e^{ik(x+l)} - e^{-ik(x+l)} \right] \frac{\cosh k(z+h)}{\cosh kh} + \right. \\ & \left. + \sum_{\alpha} R_{\alpha}(\omega) e^{\alpha(x+l)} \frac{\cos \alpha(z+h)}{\cos \alpha h} \right\} dA(\omega),\end{aligned}\quad (6.110)$$

in which the wave numbers α must satisfy the following dispersion relation:

$$\frac{\omega^2 h}{g} + (\alpha h) \tan(\alpha h) = 0. \quad (6.111)$$

Dispersion relation (6.111) has an infinite discrete set of real roots $\pm\alpha_n$ and a pair of imaginary roots $\alpha_0 = \pm ik$. In our notation, only the positive real roots α_n and negative imaginary root $\alpha_0 = -ik$ have a physical sense.

Behind the breakwater, the wave motion is a simply transmitted wave and the velocity potential becomes:

$$\Phi_3(x, z, t) = \Re \int_{-\infty}^{\infty} \frac{-ig}{\omega} e^{-i\omega t} \sum_{\alpha} \left\{ T_{\alpha}(\omega) e^{\alpha(l-x)} \frac{\cosh \alpha(z+h)}{\cosh \alpha h} \right\} dA(\omega). \quad (6.112)$$

The description of flow through the breakwater, consisting of a coarse, granular material, is a very difficult and tedious task. A more reasonable approach to the problem is to determine the physical and hydraulic properties of the media and then evaluate the macroscopic flow field in terms of these properties. The equation of motion within the breakwater body usually is presented in the form proposed by Forchheimer (Sollitt and Cross, 1972; Massel and Butowski, 1982):

$$\frac{\partial \vec{u}}{\partial t} = -\frac{1}{\rho} \nabla(p + \gamma z) - \frac{\nu n}{K} \vec{u} - \frac{C_f n^2}{\sqrt{K}} |\vec{u}| \vec{u}, \quad (6.113)$$

in which ν is a kinematic viscosity of fluid, n is a porosity, K is an intrinsic permeability, and C_f is a coefficient dependent on properties of porous media.

An analytical solution of Eq. (6.113) is possible after its linearization, i.e.:

$$\frac{\nu n}{K} \vec{u} + \frac{C_f n^2}{\sqrt{K}} |\vec{u}| \vec{u} \rightarrow f_e \omega_p n \vec{u}. \quad (6.114)$$

The linearization coefficient f_e can be evaluated from the minimalization of the mean square error between linear and nonlinear resistance forces, when the mean is taken over time in the stochastic sense as well as space. Thus, the resulting velocity potential for wave motion within the breakwater body takes the form:

$$\begin{aligned}\Phi_2(x, z, t) = & \Re \int_{-\infty}^{\infty} \frac{ge^{-i\omega t}}{\omega \left(i - n f_e \frac{\omega_p}{\omega} \right)} \sum_{\psi} \left\{ \left[P_{\psi} e^{-\psi(x+l)} + \right. \right. \\ & \left. \left. + Q_{\psi} e^{\psi(x-l)} \right] \frac{\cos \psi(z+h)}{\cos \psi h} \right\} dA(\omega),\end{aligned}\quad (6.115)$$

in which the complex wave number ψ is a solution of the following dispersion relation:

$$\left(1 + in f_e \frac{\omega p}{\omega}\right) \frac{\omega^2 h}{g} + (\psi h) \tan(\psi h) = 0. \quad (6.116)$$

To calculate the unknown coefficients R_α , T_α , P_ψ and Q_ψ , the boundary conditions at $x = \pm l$ are used.

The velocity potential of the waves reflected from the breakwater can be presented as:

$$\Phi_{1r}(x, t) = \Re \int_{-\infty}^{\infty} \frac{-ig}{\omega} e^{-i\omega t} \sum_{\alpha} \tilde{R}_{\alpha} e^{\alpha(x+l)} \frac{\cos \alpha(z+h)}{\cos \alpha h} dA(\omega), \quad (6.117)$$

in which:

$$\tilde{R}_{\alpha} = \begin{cases} R_k - 1 & \text{at } \alpha = ik, \\ R_{\alpha} & \text{at } \alpha \neq -ik. \end{cases} \quad (6.118)$$

Thus, the surface elevation of reflected waves is:

$$\zeta_{1r}(x, t) = \Re \int_{-\infty}^{\infty} e^{-i\omega t} \sum \tilde{R}_{\alpha} e^{\alpha(x+l)} dA(\omega), \quad (6.119)$$

and frequency spectrum $S_r(\omega)$ for waves reflected from the breakwater takes the form:

$$S_r(\omega, x) = \left| \sum_{\alpha} \tilde{R}_{\alpha} e^{\alpha(x+l)} \right|^2 S_{in}(\omega), \quad (6.120)$$

in which:

$$E \left[dA(\omega) dA^*(\omega') \right] = S_{in}(\omega) \delta(\omega - \omega') d\omega d\omega'. \quad (6.121)$$

Because of the presence of the evanescent modes (when $\alpha \neq -ik$), the spectrum $S_r(\omega, x)$ depends on the distance from a breakwater. However, at a sufficiently large distance from the breakwater, these modes disappear completely and only reflected progressive waves (when $\alpha = -ik$) are observed. Taking the limit $x \rightarrow -\infty$ in Eq. (6.120) gives:

$$S_r(\omega, x)|_{x \rightarrow -\infty} = |R_k(\omega) - 1|^2 S_{in}(\omega). \quad (6.122)$$

In a similar way we find that the spectrum of waves transmitted through the breakwater becomes:

$$S_t(\omega, x)|_{x \rightarrow \infty} = |T_k|^2 S_{in}(\omega). \quad (6.123)$$

The spectra (6.122) and (6.123) should be used to evaluate the reflection and transmission coefficients C_r and C_t . Taking the analogy to monochromatic waves we adopt

the following expressions for the global reflection coefficient C_r and transmission coefficient C_t :

$$C_r = \frac{\sigma_r}{\sigma_{in}} = \left\{ \frac{\int_0^\infty S_r(\omega) d\omega}{\int_0^\infty S_{in}(\omega) d\omega} \right\}^{1/2}, \quad (6.124)$$

and

$$C_t = \frac{\sigma_t}{\sigma_{in}} = \left\{ \frac{\int_0^\infty S_t(\omega) d\omega}{\int_0^\infty S_{in}(\omega) d\omega} \right\}^{1/2}, \quad (6.125)$$

in which $S_{in}(\omega)$, $S_r(\omega)$ and $S_t(\omega)$ are the incident, reflected and transmitted wave spectra, respectively. The σ_{in} , σ_r and σ_t are the corresponding standard deviations. Conservation of wave energy requires that the following energy balance should be satisfied:

$$E_{in} = E_{ref} + E_{tran} + E_{dis}, \quad (6.126)$$

or

$$\sigma_{in}^2 = \sigma_{ref}^2 + \sigma_{tran}^2 + \sigma_{dis}^2. \quad (6.127)$$

Thus:

$$C_r^2 + C_t^2 + C_d^2 = 1, \quad (6.128)$$

in which C_d is an energy dissipation coefficient.

In Fig. 6.6, an example of partition of the total energy is shown. The breakwater width is 15 m and the water depth 10 m. Incident wave spectrum is the JONSWAP spectrum with frequency $\omega_p = 0.81 \text{ rad/s}$ and significant wave height $H_s = 3.6 \text{ m}$. Breakwater body stones have a mean diameter $d_m = 1.5 \text{ m}$ and coefficient n , C_f and K are equal, correspondingly, to 0.44, 0.228 and $5.5 \cdot 10^{-4} \text{ m}^2$. The reflection and transmission coefficients, calculated according to Eqs. (6.124) and (6.125), are $C_r = 46\%$ and $C_t = 25\%$. This means that 85% of wave incident wave energy is dissipated within the breakwater body. Figure 6.6 indicates that the partition between reflected, transmitted and dissipated energy depends on wave frequency; a more energy is transmitted in the low-frequency band.

In principle, the sea spectrum contains all frequencies and wavelengths. However, most of the energy resides in a short range where the wavelength is quite long compared to the depth of the site of many breakwaters ($h < 20 \text{ m}$ say).

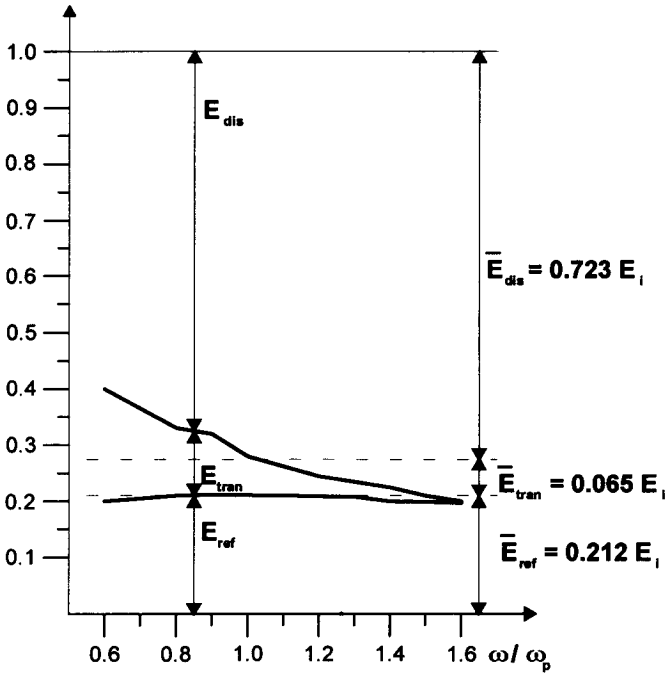


Figure 6.6: Partition of total energy incident on porous breakwater.

For the JONSWAP spectrum most of the energy lies in the frequency band $0.6 \leq \frac{\omega}{\omega_p} < 2.0$. Assuming that $kh < 0.5$, the long wave equations (Massel, 1989) are:

$$\frac{\partial \zeta}{\partial t} + h \frac{\partial u}{\partial x} = 0, \quad \frac{\partial u}{\partial t} + g \frac{\partial \zeta}{\partial x} = 0. \quad (6.129)$$

They are fairly good approximations for a sufficiently small amplitude. When $\frac{\omega}{\omega_p} < 2$, the long wave equations may be used if:

$$h < \frac{g}{(4\omega_p)^2}. \quad (6.130)$$

For instance, for wind fetch $X = 900$ km and wind speed $U = 20$ m/s, the peak frequency ω_p is 0.38 rad/s. Hence, the depth should be less than 14 m. Massel and Mei (1977) showed that under shallow water conditions, the determination of the reflection, transmission and dissipation of energy for waves impinging on a breakwater can be obtained in a simpler manner than for the full linear theory given above. In

particular, the reflection and transmission coefficients C_r and C_t are given explicitly as:

$$C_r = \frac{1 - i f_e \frac{\omega_p}{\omega} - n^2}{1 - i \frac{\omega_p}{\omega} - n - i \frac{n}{kl}}, \quad (6.131)$$

$$C_t = \frac{1}{1 + i \frac{kl}{n} \left(1 - i f_e \frac{\omega_p}{\omega} + n^2 \right)}. \quad (6.132)$$

Moreover, the stochastic equivalent linearization technique provides the linearization coefficient f_e in the following explicit compact form:

$$f_e = \frac{n}{2k_p l} \left[- \left(1 - \frac{la}{\sqrt{gh}} \right) + \sqrt{\left(1 + \frac{la}{\sqrt{gh}} \right)^2 + 8 \sqrt{\frac{2}{\pi}} \frac{bl\sigma_{in}}{h}} \right], \quad (6.133)$$

in which:

$$a = \frac{\nu n}{K}, \quad b = \frac{C_f n^2}{\sqrt{K}}. \quad (6.134)$$

It should be noted that reflected waves are introduced into particular boundary value problems through the boundary conditions. The reflective boundary is relatively easily implemented for the elliptic and hyperbolic partial differential equations (for example, the mild-slope equation). Although no approximation is necessary, an integration over a large area and a large number of wave periods is a difficult task.

However, if the parabolic approximation is applied, the waves must have a principal propagation direction and the reflected waves should be negligibly small. If the reflection cannot be neglected, the elliptic type boundary value problem must be solved. Recent developments by Panchang et al. (1991), and Li and Anastasiou (1992) considerably improve the efficiency of the solvers of elliptic type equations.

6.2.5 Nonlinear interaction between spectral wave components

6.2.5.1 Narrow-band spectrum approximation

The Boltzmann integral for the energy transfer, due to resonant third-order wave-wave interactions given in Eq. (5.31), is valid for any water depth, assuming that the interactions are still weak. The interacting wave components $\vec{k}_1, \vec{k}_2, \vec{k}_3$ should satisfy the resonance condition:

$$\vec{k}_1 + \vec{k}_2 = \vec{k}_3 + \vec{k}_4, \quad \omega_1 + \omega_2 = \omega_3 + \omega_4, \quad (6.135)$$

with wave frequencies ω_i given by the dispersion relation:

$$\omega_i^2 = gk_i \tanh(k_i h). \quad (6.136)$$

For the narrow spectrum, and for ocean depths greater than approximately one-tenth of the wavelength ($kh > 0.7$), the finite-depth case can be reduced to Longuet-Higgins' (1976b) result for an infinitely deep ocean by a similarity transformation (Herticher and Hasselmann, 1980). The magnitude and the two-dimensional frequency-directional distribution of the energy transfer do not differ significantly from the case of an infinitely deep ocean. The similar relationship between the finite-depth and infinite-depth energy transfer implies that the basic nonlinear mechanisms that control the evolution of an finite-depth wave spectrum are similar to those in deep water.

The exact calculations of the nonlinear transfer for the complete finite-depth spectrum confirmed the above conclusions for a narrow-band spectrum (Hasselmann and Hasselmann 1981, 1985). The three-lobe structure of the transfer function is retained for all $k_p h$ values (k_p is a wave number corresponding to the peak frequency ω_p). The finite-depth source function can be scaled by a depth-dependent factor R , i.e.,

$$\hat{Q}_{nl}(\omega, h) = R \left(\omega_p \sqrt{\frac{h}{g}} \right) \hat{Q}_{nl}(\omega; h = \infty), \quad (6.137)$$

in which:

$$R \left(\omega_p \sqrt{\frac{h}{g}} \right) = \frac{\chi^4}{\left[1 + \frac{\omega_p^2 h}{g} (\chi^2 - 1) \right]^2}, \quad (6.138)$$

and χ is the solution to the transcendental equation: $\chi \tanh \left(\frac{\omega_p h}{g} \chi \right) = 1$. For $k_p h > 0.8$, the shape of the finite-depth source function \hat{Q}_{nl} is very similar to the shape of the infinite-depth source function. However, at $k_p h = 0.8$, the magnitude of the source function is twice that of the infinite-depth case. For $k_p h \leq 0.4$, the nonlinear transfer exceeds the deep water values by more than an order of magnitude. In this small depth the theory is not valid because the nonlinear transfer becomes too strong for application of the weak interaction approximation.

6.2.5.2 Stokes' perturbation technique

Field experiments, as well as the theoretical models (Massel, 1973; Freilich and Guza, 1984; Liu et al., 1985; Freilich et al., 1990), suggest that wave transformation in shallow water results from both linear conservation of energy flux and nonlinear, near-resonant triad interactions. These nonlinear interactions are of a lower order than the fourth wave type interactions discussed above, and they cannot be neglected

in shallow water. To clarify the nature of the near-resonant triad interactions we first assume the velocity potential and surface elevation to the second order in the form (Massel, 1973):

$$\Phi(\vec{x}, z, t) = \Phi^{(1)}(\vec{x}, z, t) + \Phi^{(2)}(\vec{x}, z, t), \quad (6.139)$$

$$\zeta(\vec{x}, t) = \zeta^{(1)}(\vec{x}, t) + \zeta^{(2)}(\vec{x}, t), \quad (6.140)$$

in which:

$$\Phi^{(1)}(\vec{x}, z, t) = \int_{\omega} \int_{\Theta} \frac{g \cosh k(z+h)}{\omega \cosh kh} \sin[k(x \cos \Theta + y \sin \Theta) - \omega t + \epsilon] dA(\omega \Theta), \quad (6.141)$$

$$\zeta^{(1)}(\vec{x}, t) = \int_{\omega} \int_{\Theta} \cos[k(x \cos \Theta + y \sin \Theta) - \omega t + \epsilon] dA(\omega \Theta). \quad (6.142)$$

The perturbation method provides the following solution for the second order approximation of the velocity potential $\Phi^{(2)}(\vec{x}, z, t)$:

$$\begin{aligned} \Phi^{(2)}(\vec{x}, z, t) = & \Im \int_{\omega_1} \int_{\omega_2} \int_{\Theta_1} \int_{\Theta_2} \frac{g^2 k_1 k_2}{\omega_1 \omega_2} \left[\frac{P(t)}{R(t)} \right] \frac{\cosh[\gamma^{(\mp)}(z+h)]}{\cosh(\gamma^{(\mp)}h)} \cdot \\ & \cdot \exp\{i[x(k_1 \cos \Theta_1 \mp k_2 \cos \Theta_2) + y(k_1 \sin \Theta_1 \mp k_2 \sin \Theta_2) - \\ & - (\omega_1 \mp \omega_2) + (\epsilon_1 \mp \epsilon_2)]\} \cdot dA_1 dA_2, \end{aligned} \quad (6.143)$$

in which:

$$\gamma^{(\mp)} = [k_1^2 + k_2^2 \mp 2k_1 k_2 \cos(\Theta_1 - \Theta_2)]^{1/2}. \quad (6.144)$$

The signs \mp correspond to functions $\left[\frac{P(t)}{R(t)} \right]$, respectively. Function $R(t)$ is a solution of the following ordinary differential equation:

$$\frac{d^2 R}{dt^2} + \nu^2 R = F \exp(-i\mu t), \quad (6.145)$$

in which:

$$\nu^2 = g\gamma^{(-)} \tanh(\gamma^{(-)}h), \quad (6.146)$$

$$\mu = \omega_1 - \omega_2, \quad (6.147)$$

$$F = -(\omega_1 - \omega_2) [\cos(\Theta_1 - \Theta_2) + \tanh(k_1 h) \tanh(k_2 h)]. \quad (6.148)$$

The general solutions of Eq. (6.145) are:

$$R(t) = \frac{F}{\nu^2 - \mu^2} e^{-i\mu t} \quad \text{for } \nu^2 \neq \mu^2, \quad (6.149)$$

and

$$R(t) = \frac{iFt}{2\mu} e^{-i\mu t} \quad \text{for } \nu^2 = \mu^2. \quad (6.150)$$

When $\nu^2 \neq \mu^2$, the interaction produce a modification to the motion, which remains bounded in time. Assuming that $\nu^2 \approx \mu^2$, this modification may be substantial.

However, it is also possible for a transfer of energy to take place from two primary waves to a third wave, through the near-resonant triad interactions. The necessary requirements are that both the frequencies and the vector wave numbers of the interacting waves must make the sum of (nearly) zero; i.e.:

$$\omega_1 \pm \omega_2 \pm \omega_3 = 0, \quad (6.151)$$

$$\vec{k}_1 \pm \vec{k}_2 \pm \vec{k}_3 = \vec{k}_\delta, \quad \frac{|\vec{k}_\delta|}{|\vec{k}_{1,2,3}|} \ll 1. \quad (6.152)$$

Using the condition $\nu^2 = \mu^2$, these requirements yield:

$$g\gamma^{(\mp)} \tanh(\gamma^{(\mp)} h) \approx (\omega_1 \mp \omega_2)^2. \quad (6.153)$$

If we adopt the shallow water limit as $kh \leq \frac{1}{2} \left(\frac{L}{h} \geq 4\pi \right)$, then $\tanh(kh) \approx kh$, with error less than $\sim 7\%$, and Eq. (6.153) now becomes:

$$\omega_1 \mp \omega_2 = \sqrt{gh} [k_1^2 + k_2^2 \mp 2k_1 k_2 \cos(\theta_1 - \theta_2)]^{1/2}. \quad (6.154)$$

For collinear, interacting components, Eq. (6.154) simply is:

$$\omega_1 \mp \omega_2 = \sqrt{gh} (k_1 \mp k_2). \quad (6.155)$$

It should be noted that result (6.155) is equivalent to the zero value of mismatch in the wave number \vec{k}_δ .

The value of mismatch \vec{k}_δ can be calculated from Eq. (6.151) and the linear dispersion relation as (case of super harmonics for collinear motion was assumed):

$$\left. \begin{aligned} \omega_1 + \omega_2 &= \omega_3 \\ \left| 1 - \frac{k_3}{k_1 + k_2} \right| &= \frac{k_\delta}{k_1 + k_2} \end{aligned} \right\}. \quad (6.156)$$

The normalized mismatch wave number $\frac{k_\delta}{k_1 + k_2}$ (as a percentage) is given in Fig. 6.7 for water depth $h = 4.0\text{m}$ and $0.3 < \omega_1, \omega_2 < 1.30$. The adopted shallow water limit $kh = 0.5$ is also marked. This frequency range corresponds to a normalized mismatch in the wave number of, at most, 13%.

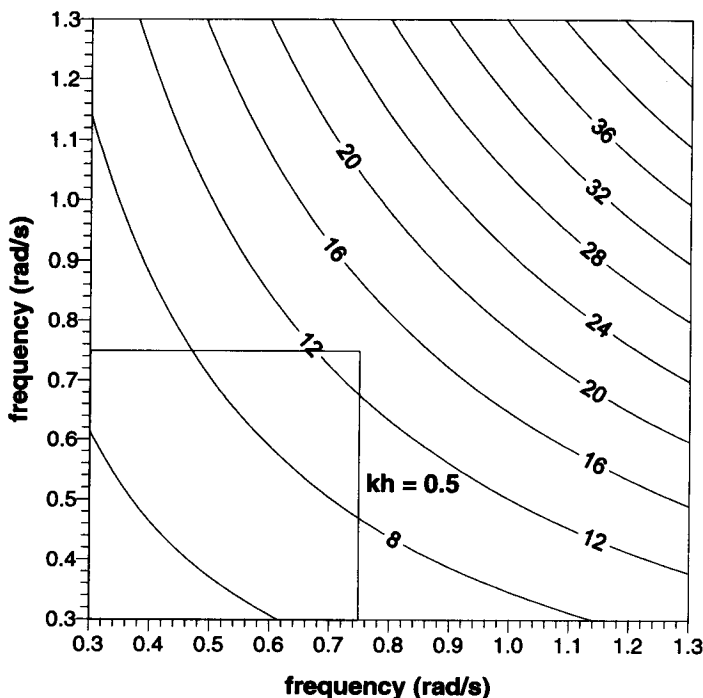


Figure 6.7: Normalized mismatch wave number (in percents) for water depth $h = 4.0\text{m}$ and frequency range $0.3 < \omega_1, \omega_2 < 1.3$ rad/s.

Using the shallow water approximation (6.155) of the resonance condition, the mismatch of wave numbers can be presented in another way as:

$$\left. \begin{aligned} \omega_1 + \omega_2 &= \omega_3 \\ \left| 1 - \frac{\omega_1 + \omega_2}{\sqrt{gh}(k_1 + k_2)} \right| &= \frac{k_\delta}{k_1 + k_2} \end{aligned} \right\}. \quad (6.157)$$

The normalized mismatch wave number $\frac{k_\delta}{k_1 + k_2}$ (as a percentage) for the shallow water approximation is illustrated in Fig. 6.8. The calculated mismatch in the wave number represents a departure from the strict shallow water conditions when it is simply equal to zero. The collinear interaction yields the minimum mismatch in a wave number resonance condition. When waves propagate in different directions, interaction results in large wave number mismatches, and hence, in less near-resonant energy transfer.

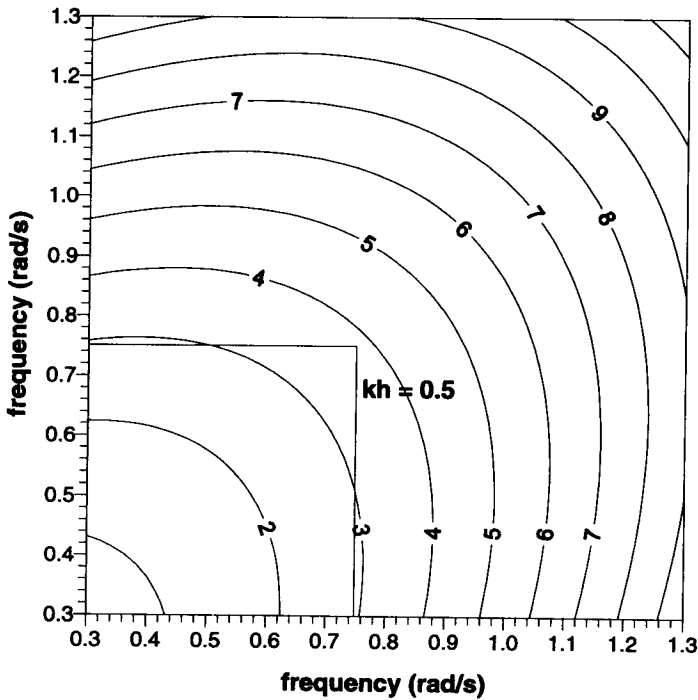


Figure 6.8: Normalized mismatch wave number (in percents) for shallow water approximation. Water depth $h = 4.0m$ and frequency range $0.3 < \omega_1, \omega_2 < 1.3$ rad/s.

In the last decade considerable progress has been made in the development of models based on the nonlinear Boussinesq equation (Freilich and Guza, 1984; Liu et al., 1985). Freilich and Guza developed a set of coupled evolution equations for the amplitudes and phases of the Fourier modes of the wave field. They showed that triad interactions across the entire wind wave frequency band provide the mechanism for cross spectral energy transfer and modal phase modifications as the waves propagate shoreward.

The Korteweg-de Vries equation (KdV) is consistent with the Boussinesq equation when considering only shoreward propagating waves. Mase and Kirby (1992) modified this equation to provide better representation of wave shoaling in the non-breaking region. Moreover, the formulation of the damping term in model equation was based on the measured spectral densities and the bore model of Thornton and Guza (1983). The resulting hybrid model predicts transformation of random waves satisfactorily, as indicated by comparison of energy spectra, representative wave heights, periods, and crest heights.

Madsen and Sorensen (1993) used the special form of the Boussinesq equations with improved linear dispersion characteristics, derived by Madsen et al. (1991), to formulate evolution equations for near-resonant interactions on a constant depth and on a mildly sloping bottom. For the one-dimensional propagation, they expanded the surface elevation $\zeta(t)$ at each location in a Fourier series as:

$$\zeta(t; x) = \sum_{p=-\infty}^{p=\infty} A_p \exp[i(\omega_p t - \varphi_p(x))], \quad (6.158)$$

where A_p denotes a complex amplitude, p indicates the rank of the harmonic ($\omega_p = p\omega_1$), and φ_p is a phase corresponding to the p harmonic.

By substituting Eq. (6.158) into the time-domain Boussinesq equations, Madsen and Sorensen (1993) obtained a set of coupled evolution equations, for the set of complex amplitudes A_p , in the form:

$$\frac{dA_p}{dx} = R_p \frac{dh}{dx} A_p + \sum_{m=1}^{p-1} Q_{m,p}^+ A_m A_{p-m} + \sum_{m=1}^{\infty} Q_{m,p}^- A_m^* A_{p+m}, \quad (6.159)$$

in which first-term represents a linear shoaling and the second- and third-terms are the interaction terms.

Complete expressions for the coefficients R_p , $Q_{m,p}^+$ and $Q_{m,p}^-$ can be found in Madsen and Sorensen (1993). The Boussinesq evolution equation, supplemented with a quasi-linear dissipation term to account for wave breaking, has recently been developed by Battjes et al. (1993) to study random waves passing over a shallow bar. The spectrum at an upwave location was discretized with a band width $\Delta\omega$. For each realization, a set of initial phases was drawn at random, assuming them to be uniformly distributed over 2π . After numerical integration of Eq. (6.159), the spectral energy densities at downwave locations were estimated as $2|A_p|^2/\Delta\omega$.

Numerical simulation and comparison with laboratory experiments showed that energy dissipation, due to wave breaking, reduces the total (spectrally integrated) energy without affecting the spectral shape. However, this formulation is rather a deterministic than a spectral one, depending on the initial phases.

Using a Hamiltonian formalism, Abreu et al. (1992) derived the evolution equation in terms of the spectral energy balance for a two-dimensional spectra in shoaling waters. The shoaling and refraction effects are considered through the application of the geometrical optics (i.e. diffraction effects are excluded), while the triad interactions are presented in the form of the Boltzmann equation. Thus, for a steady state we have:

$$\frac{d(CC_g \hat{S})}{ds} = \hat{Q}'_{nl}, \quad (6.160)$$

in which the length along the wave ray (s) satisfies Eqs. (6.7), and \hat{Q}'_{nl} is a source term due to the triad type interaction given by Abreu et al. (1992). The \hat{Q}'_{nl} should be distinguished from Q_{nl} (see Eq. (2.195)), representing the four-wave interaction.

The bispectra measured in shallow water at Torrey Beach in Southern California (Freilich et al., 1990) provide experimental evidence of nonlinear excitation of waves with frequencies and wave numbers satisfying triad near-resonance conditions (6.151) and (6.152). The linear, finite-depth theory does not predict the shoaling of the directional spectra properly, as do the Boussinesq models, based on triad nonlinear interactions. In conclusion, we can say, that in terms of the energy balance equation for shallow water, the source term Q_{nl} should comprise both triad and four-waves interactions.

6.2.6 The largest wave height in water of constant depth

6.2.6.1 Experimental data

A reliable estimation of the maximum wave height at a particular location is a fundamental requirement in the design of coastal or offshore structures. For structures located on the sea bottom of finite slope, the design criteria are based on the limiting wave height, resulting mostly from laboratory data. For example, the Shore Protection Manual (SPM, 1984) provides a family of curves for slopes between 0.2 and 0.02. For slopes less than 0.02, the interpolation is assumed to be consistent with the H/h ratio of 0.78 predicted for solitary waves over a horizontal bottom.

Nelson, in a series of papers (1985, 1987, 1994), showed that a significant discrepancy exists between the value 0.78 and that actually achieved in practice, when waves are propagating on water of a constant depth. In particular, in his paper of 1994, Nelson presents a review of existing laboratory and field data for shallow water waves and concludes that the upper limit value for the ratio H/h is 0.55, which is a value considerably less than 0.8. Using various data sets, he has proposed an envelope curve for both, transitional and shallow water waves, in the form (see Fig. 6.9):

$$\left(\frac{H}{h}\right)_{max} = \frac{F_c}{22 + 1.82F_c}, \quad (6.161)$$

in which F_c , discussed in next Section, is the so called non-linearity parameter after Swart and Loubser (1978).

From Eq. (6.161) it follows that the limiting value of $\frac{H}{h} = 0.55$ applies to shallow water waves for which $F_c \geq 500$.

All data sets collected by Nelson (1994) were shown in Fig. 6.9. They fall into two categories: sets with the points at, or near, the limit of stability (Le Mehaute et al., 1968; Keating and Webber, 1977; Riedel and Byrne, 1986; Nelson, 1994), and sets with unknown distance from stability limit (denoted by the shadow area in Fig. 6.9). (Keating and Webber (1977), who used a piston-type wave-maker to generate waves in shallow water, reported that the maximum achievable wave height was $H_{max} \approx 0.47h$. Tucker et al. (1983) measured waves, using two waverider buoys, seaward and landward of a relatively flat offshore bank of the east coast of England.

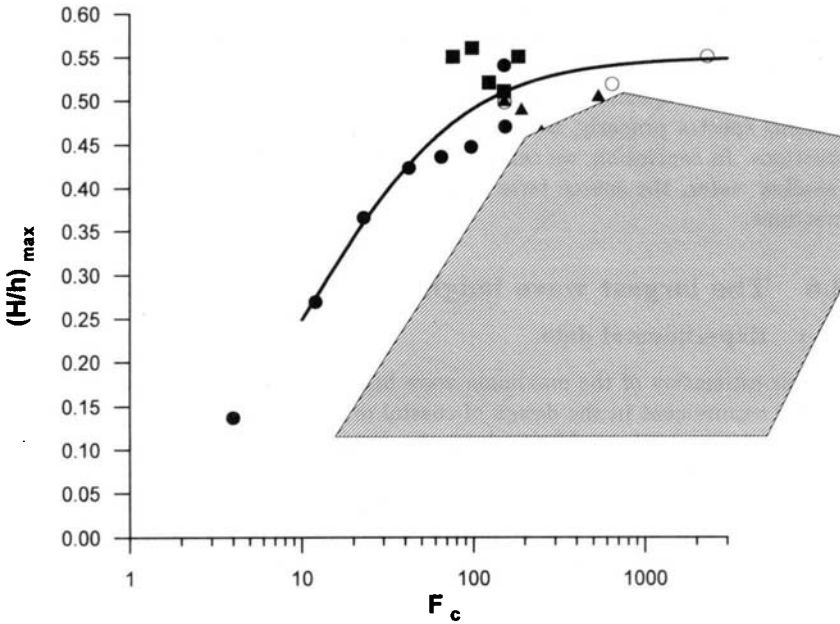


Figure 6.9: Experimental data on maximum wave height and envelope proposed by Nelson (1994) - solid line. Points indicate experimental data at or near the limit of breaking. Shadow area represents other data.

Minimum water depth over the bank was approximately 4.5 m at mid-tide level. The measured saturation level corresponding to a breaking wave showed the ratio of maximum wave height to water depth of about 0.5.

Laboratory experiments on random waves propagating over a horizontal bed, reported by Riedel and Byrne (1986), showed that the limiting ratio $(H/h)_{max}$ of 0.55 applies equally well to random and monochromatic waves. A Pierson-Moskowitz spectral form was adopted and modelled on measured wave spectra during cyclones off the north Australian coast, with peak period in the range 8 – 12 sec. The corresponding highest values of H/h ranged from 0.44 to 0.54, which is below the envelope given by Eq. (6.161).

6.2.6.2 Regular waves

It will be instructive to discuss the limiting wave height for regular waves which are frequently reproduced in the wave flumes. The results of regular wave tests can serve as some approximation for wind-induced wave train. However, prior to doing so, we must clarify the nature of the parameter F_c .

Nonlinearity parameter F_c

An Ursell-like parameter F_c was proposed to assist the evaluation of the application range of the various wave theories. This parameter depends solely on the measurable wave parameters H, T and h , i.e.:

$$F_c = \left(\frac{H}{h}\right)^{1/2} \left(T\sqrt{\frac{g}{h}}\right)^{5/2}, \quad (6.162)$$

in which H, T and h are wave height, wave period and water depth, respectively. Nelson (1994) found that waves with the same F_c value have approximately the same relative wave profile $\frac{\zeta(t)}{H}$. In the following, we examine the dependence of the parameter F_c on wave shape, using a more rigorous approach.

It should be noted that the parameter F_c provides the following classification of 'shallow', 'transitional' and 'deep' water waves :

deep water waves: $F_c < 10$,

transitional water waves: $10 < F_c < 500$,

shallow water waves: $F_c > 500$.

The most popular parameter for identification of shallow water waves is the Ursell parameter U (Ursell, 1953):

$$U = \left(\frac{H}{h}\right) \left(\frac{L}{h}\right)^2 = (2\pi)^2 \frac{\frac{H}{h}}{(kh)^2}, \quad (6.163)$$

in which L is a wavelength.

Combining Eqs. (6.162) and (6.163), and assuming that in shallow water phase velocity $C = \sqrt{gh}$, we obtain:

$$F_c = \left(\frac{H}{h}\right)^{1/2} U. \quad (6.164)$$

The Ursell parameter, U , represents the ratio of the wave nonlinearity and the rate of the dispersion. However, relationship (6.164) indicates that it is not true for the F_c parameter, which is not linearly proportional to the parameter U .

In fact, Eq. (6.161) is a transcendental equation for $\left(\frac{H}{h}\right)$ because parameter F_c also depends on $\frac{H}{h}$. For practical calculations, it will be more convenient to express the ratio $\frac{H}{h}$ as a function of some independent variable, say $\frac{h}{gT^2}$. The substitution of Eq. (6.162) into Eq. (6.161) gives:

$$\frac{H_{max}}{h} = \left[\frac{\sqrt{1 + 0.01504h_*^{-2.5}} - 1}{0.1654h_*^{-1.25}} \right]^2, \quad (6.165)$$

or:

$$\frac{H_{max}}{gT^2} = \left[\frac{\sqrt{1 + 0.01504h_*^{-2.5}} - 1}{0.1654h_*^{-1.25}} \right]^2 \left(\frac{h}{gT^2} \right), \quad (6.166)$$

in which:

$$h_* = \frac{h}{gT^2}. \quad (6.167)$$

The non-dimensional maximum wave heights (6.165) and (6.166) versus $\frac{h}{gT^2}$ are shown in Fig. 6.10. Lower values of $\frac{h}{gT^2}$ correspond to shallow water, while the higher values represent deep water.

With logarithmic axes, the function $\frac{H_{max}}{gT^2} = f\left(\frac{h}{gT^2}\right)$ is almost linear. In particular, for F_c values between 100 and 1000 we obtain:

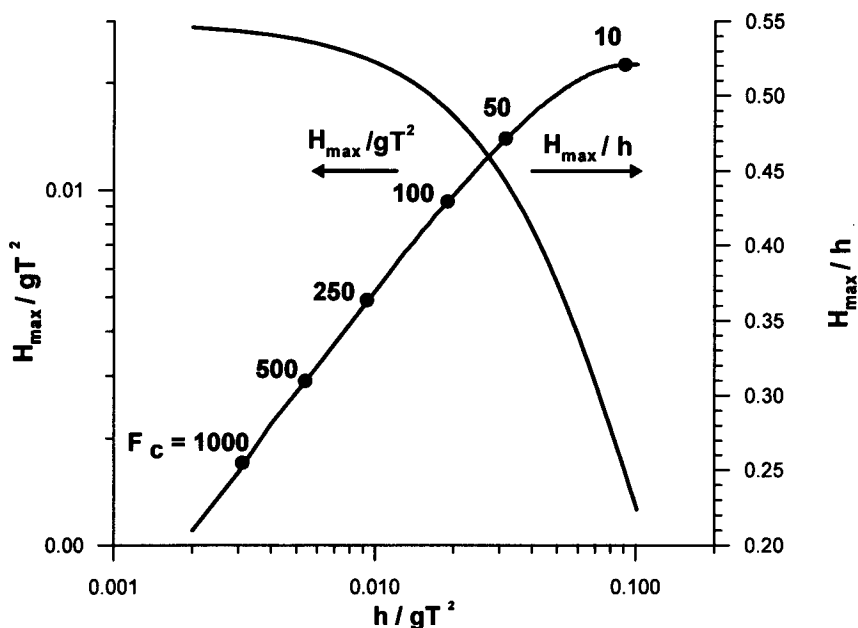


Figure 6.10: Normalized maximum wave height versus normalized water depth.

$$\frac{H_{max}}{gT^2} \approx 0.481 \frac{h}{gT^2}, \quad (6.168)$$

or $\frac{H_{max}}{h} \approx 0.481$, which is very close to the experimental estimation given by Keating and Webber (1977), who found $H_{max} \approx 0.47h$.

Let us now consider the dependence of F_c on a wave shape. For sinusoidal waves, F_c should be rather small and should increase with the departure of wave shape from the pure sinusoidal form. A simple measure of this departure is a skewness coefficient being a measure of asymmetry of wave profile, with respect to the mean water level. For small amplitude and low wave steepness, positive and negative amplitudes of waves are almost the same. For steep waves in shallow water, crests become sharper and the troughs are shallower and wider. Therefore, the resulting skewness is much higher.

Swart and Loubser (1978) found that the shallow water wave profile can be approximated using the so called vocoidal function:

$$\tilde{\zeta}(X) = \frac{\zeta(X)}{H} = [\cos^2(\pi X)]^P - \zeta_t, \quad (6.169)$$

in which $X = x/L$, ζ_t is the depth at the wave trough. Power P expresses the variation of wave profile from sinusoidal ($P = 1$) to the solitary wave profile ($P \gg 1$). It should be noted that parameter F_c was approximated to be linearly proportional to P (Swart and Loubser, 1978). We define the skewness coefficient γ_1 as:

$$\gamma_1 = \frac{m_3}{(m_2)^{3/2}}, \quad (6.170)$$

in which:

$$m_n = \int_0^1 [\tilde{\zeta}(X)]^n dX. \quad (6.171)$$

Using the tables given by Swart and Loubser (1978), the skewness γ_1 was calculated for given H/h and $T\sqrt{\frac{g}{h}}$ values (or F_c values). The result is illustrated in Fig. 6.11. The best fitting curve for the numerical results in the range $100 \leq F_c \leq 1000$ is given by:

$$\gamma_1 = -1.2120 + 0.0165F_c - 3.4943 \cdot 10^{-5}F_c^2 + 3.6460 \cdot 10^{-8} \cdot F_c^3 - 1.4223 \cdot 10^{-11}F_c^4. \quad (6.172)$$

Coefficient γ_1 is proportional to F_c , but the proportionality has a nonlinear character. As the skewness coefficient γ_1 is a function of F_c , waves of the same F_c possess approximately the same skewness, i.e. the same asymmetry with respect to the mean water level. Additionally, when we assume that waves are symmetric with respect to the vertical planes at the wave crests, we can say that wave profiles with the same F_c

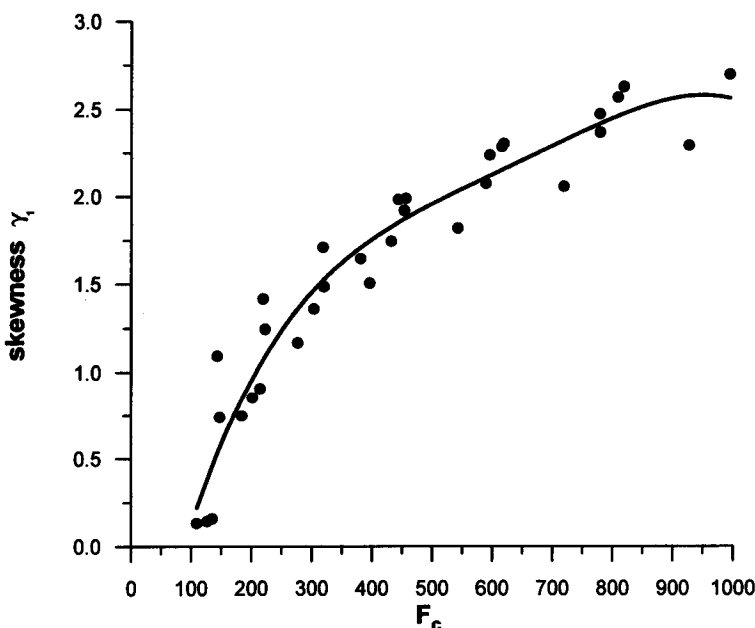


Figure 6.11: Skewness coefficient γ_1 as a function of parameter F_c .

are similar to each other. However, the similarity is only approximate because the skewness is an integral type quantity and its dependence on the details of wave profile is considered in the integral sense only.

Application of higher approximations of Stokes' and cnoidal theories

To clarify the discrepancy between the observed limiting wave height and that based on the theoretical considerations of solitary waves, we examine shortly an applicability of a few higher order theoretical solutions.

One of the most comprehensive studies related with the second Stokes' perturbation method was that by Cokelet (1977b). Following Stokes (1880), he used the inverse plane method in which the velocity potential ϕ and the stream function ψ were adopted as the dependent variables rather than (x, z) of the common physical plane method (Massel, 1989). In Cokelet's numerical terminology, the breaking condition corresponds to the so called stagnation point. Cokelet applied his method to full range of water depth and wave heights, and computed the wave profile, wave phase velocity and some integral properties. The function $\left(\frac{H}{h}\right)_{max} = f(F_c)$ based on the Cokelet solution is given in Fig. 6.12. It can be seen that a limiting breaking wave height

asymptotically approaches to the solitary wave limit. Various authors give disparate values of that limit (Table 5.2 by Massel, 1989). For example, the last calculations by Williams (1985) give 0.8332. In Fig. 6.12, the limit 0.78, recommended by SPM (1984), is also marked. Moreover, in the same figure, the Miche (1944) breaking limit is given, i.e.:

$$\frac{H}{h} = 0.142 \left(\frac{L}{h} \right) \tanh \left(\frac{2\pi h}{L} \right). \quad (6.173)$$

The limiting ratio H/h is of special importance for shallow water. Therefore, the shallow wave theory seems to be more appropriate than the higher approximations of the Stokes' theory for estimation of this limiting ratio. The first shallow water theory of periodic waves was given by Korteweg and de Vries (1885), who showed that the lowest approximation to the surface profile of steady progressive waves in shallow

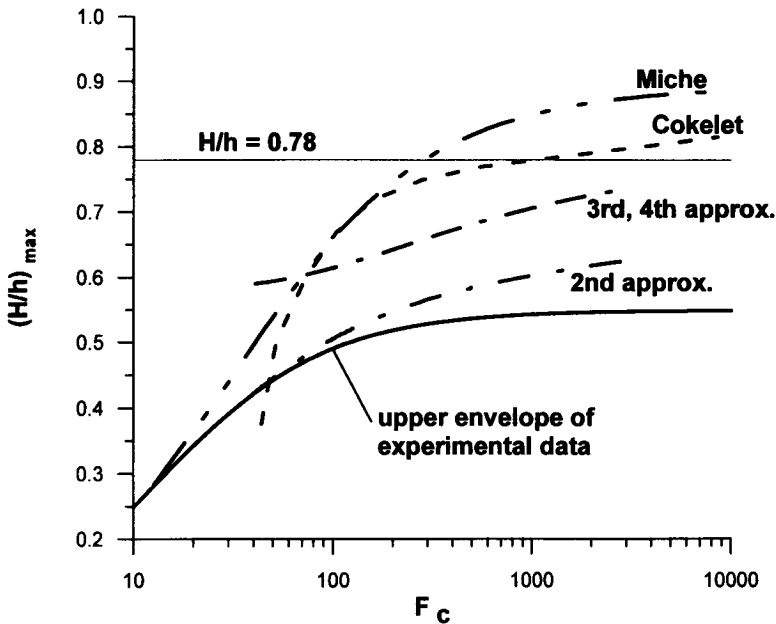


Figure 6.12: Comparison of various theoretical approximations with the upper envelope of experimental data.

water was given by the cnoidal function (Abramowitz and Stegun, 1975). The second order approximations for cnoidal waves were obtained by Laitone (1960, 1962), while fifth order approximation by Fenton (1979, 1990).

It will be convenient to introduce, in favour of the fixed coordinate system $(0, x, z)$, the system $(0, X, Z)$ moving with the same speed as the waves. In the moving coordinate system, the kinematic breaking criterion states that the horizontal component of orbital velocity at the wave crest should be equal to zero. Using Fenton's (1979, 1990) representations of the cnoidal wave theory, the limiting wave height was determined with the second, third and fourth order of approximation (difference between Fenton's third and fourth order approximation was negligible). The results of calculation, presented in Fig. 6.12, suggest that higher approximations of the Stokes' theory and cnoidal wave theory give much higher limiting waves than those observed in the experiments. Details of calculations can be found in another paper by the author (Massel, 1995a).

Influence of mechanical wave generation on the limiting wave height

Most of the experimental data reported by Nelson are the results of experiments in wave flumes. The utilization of laboratory wave channels to simulate ocean waves and their action on the sea bottom and man-made structures, has become standard practice. However, laboratory studies of surface waves are complicated due to the contamination contributed to the wave motion by wave-makers, as the simple harmonic motion produces a wave train not only with the wave-maker frequency but also with its higher harmonic (Galvin, 1970). The sinusoidal motion of the generator does not match the water particle motion required by the wave.

In this Section, an attempt is made to estimate the influence of the mechanical generation of waves on the limiting wave height in the wave flume. The theory of mechanically generated waves can be found elsewhere (Fontanet, 1961; Madsen, 1971; Massel, 1981b, 1982b; Bendykowska and Massel, 1988) and are only outlined here.

Let us consider a harmonic motion of the plain paddle wave-maker with horizontal displacement given by:

$$\xi(z, t) = \xi^{(0)} \frac{h + l_0 + z}{h + l_0} \sin \omega t, \quad (6.174)$$

in which ω is a frequency of paddle motion, $\xi^{(0)}$ is the maximum paddle displacement at the mean water level, l_0 is a vertical distance below the channel bottom of the point of rotation of the paddle, and z is a vertical axis directed upward from the mean water level. If $l_0 \rightarrow \infty$, Eq. (6.174) expresses the motion of a piston-type wave-maker.

We will restrict ourselves to the second order of approximation (the third order theory is outlined by Bendykowska and Massel, 1988). The velocity potential up to the second order of accuracy is (Massel, 1981b):

$$\begin{aligned}
\Phi(x, z, t) = & \frac{ga}{\omega} \frac{\cosh k(z+h)}{\cosh kh} \sin(kx - \omega t) + \\
& + \frac{3}{8} \omega a^2 \frac{\cosh 2k(z+h)}{\sinh^4 kh} \sin 2(kx - \omega t) + \\
& + A_F \frac{\cosh l(z+h)}{\cosh lh} \sin(lx - 2\omega t + \pi),
\end{aligned} \tag{6.175}$$

in which the first term represents the linear velocity potential and the second part is a potential of the Stokes second harmonic. Both these potentials satisfy the homogeneous form of the second order boundary value problem for surface waves, disregarding the conditions at the paddle. The remaining part of the second order solution (the third term in Eq. (6.175)) has to satisfy the homogeneous linearized equations of motion and the boundary conditions at the wave paddle, which states that mass flux through the paddle must vanish. The wave numbers k and l satisfy the following dispersion relations:

$$\omega^2 = gk \tanh kh \quad \text{and} \quad 4\omega^2 = gl \tanh lh. \tag{6.176}$$

The resulting surface elevation ζ takes the form:

$$\zeta(x, t) = a \cos(kx - \omega t) + a^{(2)S} \cos 2(kx - \omega t) + a^{(2)F} \cos(lx - 2\omega t + \pi), \tag{6.177}$$

in which:

$$a^{(2)F} = \frac{2\omega}{g} A_F. \tag{6.178}$$

It is most likely that waves start to break at the first point in which $\zeta(z, t) = \zeta_{max}$. To find the distance $x = x_{max}$ and time $t = t_{max}$, corresponding to the wave breaking, we adopt a coordinate system moving with waves with a speed of $C = \frac{\omega}{k}$. In this coordinate system Eq. (6.177) would be:

$$\zeta(x, t) = a + a^{(2)S} + a^{(2)F} \cos[(l - 2k)x + \pi]. \tag{6.179}$$

Thus:

$$x_{max} = \frac{(2n-1)\pi}{l-2k} \quad \text{and} \quad t_{max} = \frac{(2n-1)\pi k}{(l-2k)\omega}. \tag{6.180}$$

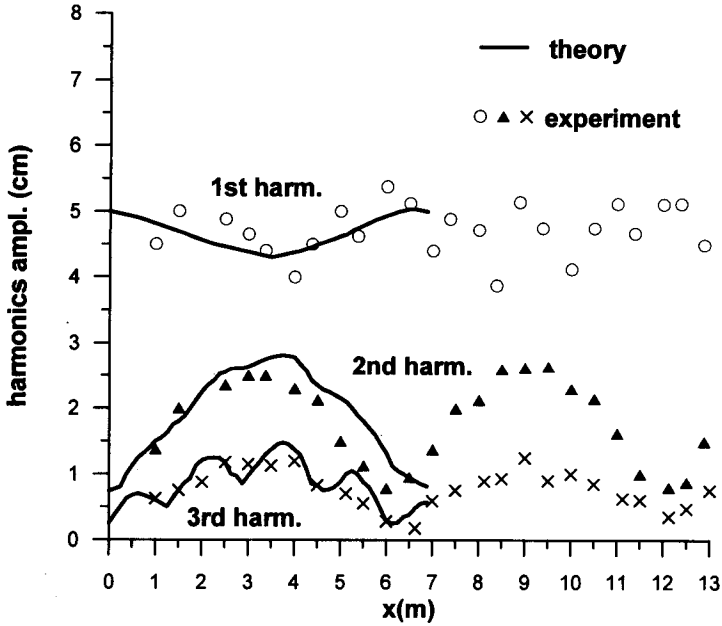


Figure 6.13: Higher harmonics evolution in space according Bendykowska and Massel (1988).

From Eq. (6.180) it is clear that the distance between two succeeding maxima of the wave profile is:

$$L_t = \frac{2\pi}{l - 2k}. \quad (6.181)$$

As was shown by Longuet-Higgins (1977), the distance L_t also depends slightly on wave amplitude. However, in this study this dependence is omitted.

To illustrate the periodic (in space) behavior of the higher harmonics amplitudes, in Fig. 6.13, taken from Bendykowska and Massel (1988), the comparison between observed and calculated harmonic amplitudes is given. The variation of first, second and third harmonics in space has a periodic character, with a repetition space distance given by Eq. (6.181).

From Eq. (6.177) it follows that an oscillation of the second harmonic is due to superposition of two second harmonic components with frequency 2ω , but with different speeds, i.e. $C_{2S} = \frac{k}{\omega}$ (Stokes component), and $C_{2F} = \frac{l}{2\omega}$ (free second harmonic). Both these harmonics are in phase at the repetition distance (6.181). In Fig. 6.13 a

small oscillation of the first harmonic is also observed. It can be shown that the basic mechanism responsible for this oscillation is the nonlinear interaction between the first harmonic (ω, k) and the second free harmonic $(2\omega, l)$ (see, for example, Massel, 1981b).

Taking into account the higher harmonics generation mechanism, we can determine the maximum wave height in a flume, applying the kinematic breaking condition at $x = x_{max}$ and $t = t_{max}$, i.e.:

$$u(x = x_{max}, z = \zeta_{max}, t = t_{max}) = C, \tag{6.182}$$

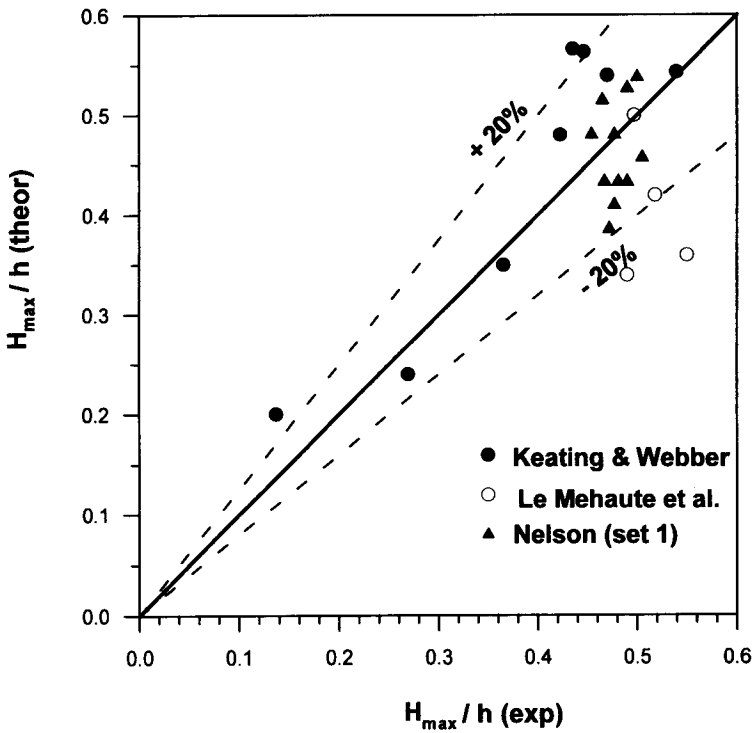


Figure 6.14: Comparison of theoretical and experimental normalized maximum wave height.

or:

$$\begin{aligned} \frac{gka}{\omega} \frac{\cosh k(\zeta_{max} + h)}{\cosh kh} + \frac{3}{4} \omega k a^2 \frac{\cosh 2k(\zeta_{max} + h)}{\sinh^4 kh} + \\ + \frac{gla^{(2)F}}{2\omega} \frac{\cosh l(\zeta_{max} + h)}{\cosh lh} = C. \end{aligned} \quad (6.183)$$

As the maximum elevation ζ_{max} is not known *a priori*, therefore, to solve Eq. (6.183), a recurrent procedure is needed. Accuracy of the prediction and range of applicability is discussed in another paper (Massel, 1995a).

Using the input data (water depth h and wave period T) from the sets of experiments described above, the kinematic breaking condition (6.182) was used to determine the possible maximum of the wave height over a horizontal bottom. The results of calculations are summarized in Fig. 6.14.

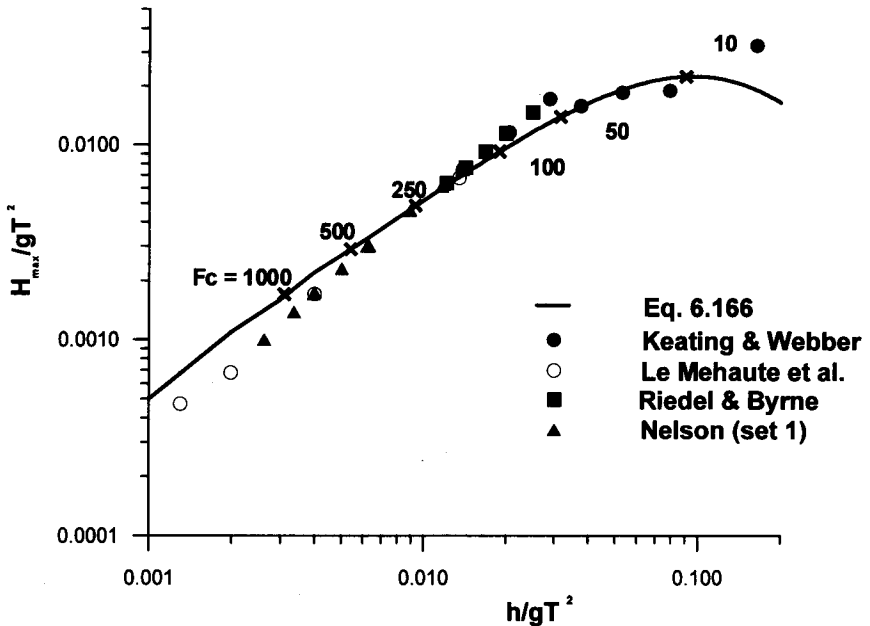


Figure 6.15: Comparison of computed normalized maximum wave height with upper experimental envelope.

The coincidence of the experimental and theoretical values of wave heights is good and the difference between experiments and theory is less than 20%. Two points with the highest error are based on input data from Le Mehaute et al. (1968), corresponding to extreme shallow water conditions ($F_c = 1403$ and 2314). They are clearly out of range of applicability of the second order wave generation theory. It should be also noted that the theoretical values correspond to a well-defined breaking condition, while the experimental values were described less precisely as 'near to breaking'. As was shown in Fig. 6.14, both the theoretical as well as the experimental non-dimensional maximum wave heights are smaller than ~ 0.6 .

In Fig. 6.15, the dependence of the normalized maximum wave height H_{max}/gT^2 on normalized water depth h/gT^2 is presented. The points in the figure denote the calculated values based on the input data from particular experiments, and the solid line is given according to experimental envelope Eq. (6.166). The coincidence is very close. However, the highest discrepancy is observed at the lowest values of $\frac{h}{gT^2}$ (shallow water), where the second order harmonics generation theory may not be applicable.

6.2.6.3 Irregular waves

The height of wind-induced irregular waves does not increase infinitely, being limited by breaking phenomena. Breaking is an intermittent process and its frequency depends on the severity of the sea. The experimental data on the maximum wave height in an irregular wave train, propagating over a horizontal bottom, are very limited. All data indicate that the ratio of maximum wave height to water depth is about 0.5, which is much smaller than value currently used in engineering practice.

In order to evaluate the probability that waves reach their limiting condition and start to break, the stability of waves is assumed to be controlled by the downwards vertical acceleration on the surface of the fluid, at the wave crests. In general, the probability that a crest of height ξ_l , or higher, will break, is given by Eq. (4.79), i.e.:

$$F_{br} = \int_{\xi_l}^{\infty} f_{br}(\xi_{max}) d\xi_{max}, \quad (6.184)$$

$$\text{where } \xi_{max} = \frac{\zeta}{\sqrt{m_0}} \quad \text{and} \quad \xi_l = \frac{\zeta_l}{\sqrt{m_0}}.$$

The question when positive wave crests will break, ($\zeta_l \gg 0$), is of special interest for engineers and oceanographers. Equation (4.79) and Fig. 4.10 indicate that the probability of such an event can be calculated approximately using Srokosz's formula (4.78) as:

$$F_{br} = \int_0^{\infty} f_{br}(\xi_{max}) d\xi_{max} \approx \exp\left(-\frac{\alpha^2 g^2}{2m_4}\right). \quad (6.185)$$

Let us assume a wave record with a time duration of t (for instance $t = 20$ min.). When waves are small (moment m_4 is small) then the downward acceleration at all wave crests is smaller than the threshold acceleration αg . The waves are stable and no breaking is observed. If wave energy increases, the vertical acceleration also increases, and eventually the threshold value is reached, at least at one wave crest, which starts to break. The probability $F_{br}^{(r)}$ that in a record of duration t one crest is breaking is:

$$F_{br}^{(r)} = \frac{1}{N} \approx \frac{\bar{T}}{t}, \quad (6.186)$$

where \bar{T} is a mean wave period. The equality:

$$F_{br} = F_{br}^{(r)}, \quad (6.187)$$

provides a moment m_4 necessary for breaking of at least one crest in a record of duration t , i.e.:

$$m_4 = -\frac{\alpha^2 g^2}{2 \ln F_{br}^{(r)}}, \quad (6.188)$$

or:

$$m_4 = \int_0^\infty \omega^4 S(\omega) d\omega = -\frac{\alpha^2 g^2}{2 \ln F_{br}^{(r)}}, \quad (6.189)$$

and

$$\int_0^\infty \omega^4 S(\omega) d\omega = -\frac{\alpha^2 g^2}{2 [\ln \bar{T} - \ln t]}. \quad (6.190)$$

Probability $F_{br}^{(r)}$ (see Eq. (6.186)) that in the record of duration t at least one wave becomes unstable, depends on spectral moments because the mean wave period \bar{T} is given by:

$$\bar{T} = 2\pi \frac{m_0}{m_1}. \quad (6.191)$$

Thus, the number of waves in a record becomes:

$$N = \frac{t}{\bar{T}} = \frac{m_1 t}{2\pi m_0}. \quad (6.192)$$

One of N crests in a record reaches the maximum value before breaking. The most probable height of the maximum wave \hat{H}_{max} is given by Eq. (4.199), i.e.:

$$\frac{\hat{H}_{max}}{\sigma_\zeta} = \frac{\hat{H}_{max}}{\sqrt{m_0}} = \frac{\hat{H}_{max}}{H_{rms}} \frac{H_{rms}}{\sqrt{m_0}} \approx 2\sqrt{2}\sqrt{\ln N}. \quad (6.193)$$

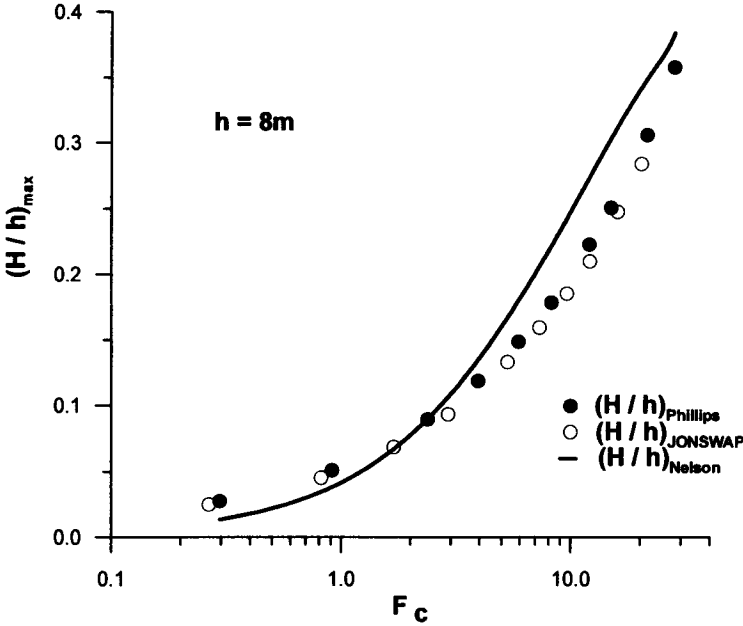


Figure 6.16: Maximum wave height for random waves versus parameter F_c .

It will be useful to determine the most probable wave period $T_{\max \text{ prob}}$ associated with wave height \hat{H}_{\max} . Using the two-dimensional distribution of wave heights and wave periods $f(T)$, we obtain:

$$T_{\max \text{ prob}} = \frac{2.0 \bar{T}}{1 + \sqrt{1 + 32\nu^2 \left(\frac{\hat{H}_{\max}}{\sigma_\zeta} \right)^{-2}}}. \quad (6.194)$$

Hence, the final ratio of the maximum possible wave height to water depth in a given wave record becomes:

$$\frac{H_{\max}}{h} = 2\sqrt{2}\sqrt{\ln N} \frac{\sqrt{m_0}}{h}, \quad (6.195)$$

in which moment m_0 is determined by the condition (6.187).

The results of calculations are illustrated in Fig. 6.16, for water depth $h = 8\text{ m}$. To calculate the spectral moment m_4 , two different spectral densities were adopted, i.e. the Phillips spectrum (3.16) and the JONSWAP spectrum (3.88) with threshold frequency $\omega = 3.5\omega_p$.

The finite water depth was modelled using the Kitaigorodskii et al. (1975) scaling. For comparison, the upper limit suggested by Nelson (1994) was added in Fig. 6.16. All details of evaluation of limiting wave height of wind-induced waves are given in another paper (Massel, 1995b).

6.2.7 Wave energy dissipation at sea bottom

6.2.7.1 A brief orientation

Energy balance of waves propagating in water of finite depth is affected by the energy dissipation at two boundary layers, i.e. sea surface and bottom boundary layers. Within the bottom boundary layer, with a thickness of a few centimeters, the flow is strongly sheared, generally turbulent, and associated with significant dissipation of energy. There are many possible mechanisms for the dissipation of wave energy. The most likely mechanisms are percolation and turbulent friction.

The percolation dominates when bottom sediment consists of coarse sand. When bottom material is finer, and low permeability prohibits percolation and granular friction prevents viscous flow behaviour, the friction is a dominant mechanism.

The special class of the interaction of oscillatory motion with the sea bottom is the interaction of surface waves with soft beds. The cohesive sediments usually demonstrate nonlinear behaviour, since their properties are functions of the state of strain. The measurements confirm that muds behave as elastic solids at low oscillatory strains, and as viscous fluids at high oscillatory strains. At intermediate strains the sediment may be described as viscoelastic material. The incorporation of these various rheological properties of the marine soft bed will be discussed in the next Sections.

6.2.8 Energy dissipation due to bottom friction

An empirical source function \hat{Q}_8 for energy dissipation due to bottom friction usually is written as (Bouws and Komen, 1983):

$$\hat{Q}_8(\omega, \Theta) = -\frac{C}{g^2} \frac{\omega^2}{\sinh^2 kh} \hat{S}(\omega, \Theta). \quad (6.196)$$

The JONSWAP experiment suggests that the mean value for C is $0.038 \text{ m}^2\text{s}^{-3}$. For later convenience we rewrite Eq. (6.196) in the form:

$$\hat{Q}_8(\omega, \Theta) = -\frac{2C}{g} \frac{k}{\sinh 2kh} \hat{S}(\omega, \Theta). \quad (6.197)$$

Dissipation coefficient is in fact a function of wave motion parameters and the bottom roughness (Young and Gorman, 1995; see also Eq. (6.208) below). Two different approaches are possible for evaluation of this functional dependence, i.e. a quadratic law approach and eddy-viscosity approach. The first one is based on the instantaneous values of the bottom stress and of the free stream velocity at the top of the boundary layer (Hasselmann and Collins, 1968). The drag-law expression is proportional to a friction factor f_r which has to be determined experimentally.

The eddy-viscosity approach (Madsen et al., 1988; Weber, 1991) is more fundamental in the sense that it does not contain free parameters. In the following, we will concentrate mostly on the eddy-viscosity model. The linearized boundary layer

approximation for the flow above a bottom located at $z = 0$ yields the following governing equation (Madsen et al., 1988):

$$\frac{\partial (\vec{u} - \vec{u}_\infty)}{\partial t} = \frac{\partial}{\partial z} \left[\kappa u_* z \frac{\partial (\vec{u} - \vec{u}_\infty)}{\partial z} \right], \quad (6.198)$$

in which $\vec{u} = (u, v)$, \vec{u}_∞ is a near-bottom orbital velocity, u_* represents the friction velocity and $\kappa = 0.4$ is a Karman constant.

The velocity \vec{u}_∞ can be specified in terms of the surface waves two-dimensional spectrum $\hat{S}(\omega, \Theta)$, i.e.:

$$\vec{u}_\infty(\omega, \Theta) = \frac{\omega}{\sinh kh} \sqrt{2\hat{S}(\omega, \Theta)} d\omega, d\Theta. \quad (6.199)$$

The solution of Eq. (6.198), written in terms of Kelvin functions of zeroth order $ker(\cdot)$ and $kei(\cdot)$ (Abramowitz and Stegun, 1975), takes the form:

$$\vec{u} - \vec{u}_\infty = - \frac{ker(2\sqrt{\xi}) + i kei(2\sqrt{\xi})}{ker(2\sqrt{\xi_0}) + i kei(2\sqrt{\xi_0})} \vec{u}_\infty, \quad (6.200)$$

in which $\xi = \frac{z\omega}{(\kappa u_*)}$.

In Eq. (6.200) no-slip conditions should be satisfied at $z = z_0 = k_b/30$, where k_b is the equivalent Nikuradse sand grain roughness of the bottom. For small values of the argument ξ , the Kelvin functions take a simpler form and the solution becomes:

$$|\vec{u} - \vec{u}_\infty| = \frac{|\vec{u}_\infty|}{\left\{ \left[\ln \left(\frac{\kappa u_*}{z_0 \omega} \right) + 1.15 \right]^2 + \left(\frac{\pi}{2} \right)^2 \right\}^{1/2}} \ln \left(\frac{z}{z_0} \right) \cos(\omega t + \phi), \quad (6.201)$$

where:

$$\tan \phi = \frac{\pi}{2 \left[\ln \left(\frac{\kappa u_*}{z_0 \omega} \right) - 1.15 \right]}. \quad (6.202)$$

The representative friction velocity u_* (not defined yet) is obtained by requiring the solution to reduce, in the limit, to that of a simple harmonic wave, i.e.:

$$u_* = \sqrt{\frac{\tau_b}{\rho}} = \sqrt{\frac{f_\tau}{2}} u_b, \quad (6.203)$$

or:

$$\tau_b = \frac{\rho \kappa u_*}{\ln \left(\frac{\kappa u_*}{z_0 \omega_r} - 1.15 \right)} u_b, \quad (6.204)$$

in which ω_r is a constant representative radian frequency.

The average rate of dissipation of wave energy in the bottom boundary layer can be expressed as (Madsen et al., 1988):

$$\hat{Q}_8 = E [\tau_b u_\infty] = -\frac{1}{2g} f_r u_b \hat{S}_{u_b}(\omega, \Theta), \quad (6.205)$$

in which:

$$u_b^2 = 2 \int \int \hat{S}_{u_b}(\omega, \Theta) d\omega d\Theta, \quad (6.206)$$

and

$$\hat{S}_{u_b}(\omega, \Theta) = \frac{\omega^2}{\sinh^2 kh} \hat{S}(\omega, \Theta). \quad (6.207)$$

The coefficient f_r is obtained from knowledge of the equivalent Nikuradse sand grain roughness of the bottom and an equivalent periodic wave, having the same root-mean-square orbital velocity and excursion amplitude as the specified directional wave spectrum.

Comparing Eqs. (6.197) and (6.205), we find the following expression for dissipation coefficient C :

$$C = \frac{1}{2} f_r g u_{br} = \frac{1}{2} f_r g \left\{ 2 \int \int \hat{S}_{u_b}(\omega, \Theta) d\omega d\Theta \right\}^{1/2}. \quad (6.208)$$

6.2.9 Energy dissipation due to bottom permeability

The energy dissipation due to bottom friction, discussed above, has been evaluated under the assumption of the non-permeability of the bottom. Generally, such an assumption generates correct representation of the surface geometry and simplifies calculations considerably. On the other hand, the wave motion percolated in a permeable bottom influences the wave forces on the hydraulic structures which have been founded on, or extended into, the bottom. Pipelines transporting oil from offshore terminals to the shore are usually laid on top of the seabed, if the water is deep, or buried in the seabed, if the water depth is small. Under a persistent attack of sea waves, not only the strength of the structure itself, but also the dynamic stability of the sea bed is of concern.

It is well known that realistic modelling of the nonlinear dynamic behaviour of soil, under the cyclic loading of ocean waves, is an extremely difficult task. This problem is out of the scope of this book. However, to provide some physical understanding of the dynamic interaction of surface waves with a permeable bottom, a description of the simplified models will be useful.

The simplest case of a permeable seabed is the bed with a fixed rigid grain skeleton. Let the origin of the two-dimensional Cartesian coordinates (x, z) be fixed on the mean free surface, $z = 0$, in which z is positive upwards. The depth of water is h and the

depth of the non-permeable bottom is h_n ; thus, the thickness of the permeable layer is $h_n - h$. We assume that the free surface may be represented as:

$$\zeta(x, t) = \frac{H}{2} \exp[i(kx - \omega t)] = \frac{H}{2} \exp(-k_i x) \exp[i(k_r x - \omega t)], \quad (6.209)$$

in which wave number k is a complex quantity, i.e. $k = k_r + ik_i$. From Eq. (6.209) it is evident that imaginary part of wave number is a damping factor.

For the porous media ($-h_n \leq z \leq -h$), we write the equation of motion in the form identical to that in Eq. (6.113), i.e. for the seepage velocity u_2 in the porous layer we have:

$$\frac{\partial \vec{u}_2}{\partial t} = -\frac{1}{\rho} \nabla(p + \gamma z) - \frac{\nu n}{K} \vec{u}_2 - \frac{C_f n^2}{\sqrt{K}} |\vec{u}_2| \vec{u}_2. \quad (6.210)$$

At the interface ($z = -h$) between the water and porous layers the following boundary conditions should be satisfied:

$$\left. \begin{aligned} p_{\text{water}} &= p_{\text{porous}} \\ \frac{\partial \Phi_1}{\partial z} &= n v_2 \end{aligned} \right\}, \quad (6.211)$$

in which p_{water} and p_{porous} represent pressure in water and porous layers, respectively, Φ is a velocity potential for the water layer, and v_2 is a vertical velocity of water motion in the porous layer.

The complete boundary value problem of motion in water and porous layers can be solved upon the linearization of the dissipative nonlinear stress term in Eq. (6.210) (for full details see Massel, 1976). In particular, the solution yields the following expression for the complex wave number k :

$$\frac{\omega^2 h}{g} = kh \frac{\tanh(kh) - inM \tanh[k(h_n - h)]}{1 - inM \tanh(kh) k(h_n - h)}, \quad (6.212)$$

in which:

$$M = \frac{m + im^2}{1 + m^2}, \quad m = \frac{1}{nf_e}, \quad (6.213)$$

where f_e is a dimensionless linearization coefficient (6.114). For a sandy bottom the permeability $K \sim 10^{-5} \text{ cm}^2$ and linearization coefficient $f_e \sim \frac{\nu}{\omega k} \sim 10^3$, when the wave frequency was assumed to be of the order of $O(1)$ (Massel, 1976). Therefore, $m \sim 10^{-3}$ and $M \sim m$.

Numerical calculations showed that the influence of the porous media permeability on the pressure distribution in water and porous domains is rather small. Let us assume, for example, that waves of frequency $\omega = 0.966 \text{ rad/s}$ propagate on the water depth $h = 8 \text{ m}$ and thickness of porous sand layer ($d_m = 1 \text{ mm}$) is $h_n - h = 3 \text{ m}$, and its porosity n and permeability K are $n = 0.35$ and $K = 1.59 \cdot 10^{-5} \text{ cm}^2$. The

resulting damping factor is $k_i = 2 \cdot 10^{-5} \text{m}^{-1}$. It means that the wave height decreases by one half of its initial value after a distance ≈ 2800 m. Very similar results are obtained for the rubble stone bottom ($d_m = 0.2$).

The mean rate of energy dissipation \hat{Q}_8 , due to percolation into the porous bed, is equivalent to the mean work done by the upper fluid on the fluid within the permeable layer, i.e.:

$$\hat{Q}_8 = -E[pv]_{z=-h}. \quad (6.214)$$

Substituting expressions for p and v , given in Massel (1976), into Eq. (6.214) gives the dissipation rate for a given frequency ω as:

$$E[pv]_{z=-h} = \frac{gKA^2k}{\nu} \tanh[k(h_n - h)] \cdot \frac{E[\cos(kx - \omega t - \varphi_1) \cos(kx - \omega t - \varphi_1 - \varphi_2)]}{\left\{ \cosh(kh) + \frac{\omega K}{\nu} \frac{k(h_n - h) \sinh(kh)}{\cosh^2[k(h_n - h)]} \right\}^2}, \quad (6.215)$$

in which:

$$\tan \varphi_1 = \frac{\left\{ k_i h - \frac{\omega K}{\nu} \tanh[k(h_n - h)] \right\} \tanh(kh)}{1 + \frac{\omega K}{\nu} k(h_n - h) \frac{\tanh(kh)}{\cosh^2[k(h_n - h)]}}, \quad (6.216)$$

and

$$\tanh \varphi_2 = \frac{k_i}{k} + \frac{2k(h_n - h)}{\sinh 2k(h_n - h)}; \quad (6.217)$$

A is the wave amplitude and pressure is expressed in the water column.

As the damping factor $k_i \sim 10^{-5} \div 10^{-4} \text{m}^{-1}$ for the most sandy bottom, the $k \approx k_r$. Equations (6.216) and (6.217) suggest that velocity v and pressure p are slightly out of phase with each other and with the sea surface. In the following, we neglect this phase difference. Therefore, the final expression for wave energy dissipation in terms of the sea surface spectral energy $\hat{S}(\omega, \Theta)$ becomes:

$$\hat{Q}_8 = \frac{-gKk}{\nu} \frac{\tanh[k(h_n - h)]}{\left\{ \cosh(kh) + \frac{\omega K}{\nu} \frac{k(h_n - h) \sinh(kh)}{\cosh^2[k(h_n - h)]} \right\}^2} \hat{S}(\omega, \Theta). \quad (6.218)$$

When the thickness of the porous layer is infinite ($(h_n - h) \rightarrow \infty$), Eq. (6.218) simplifies as:

$$\hat{Q}_8 = \frac{-2K\omega^2}{\nu \sinh(2kh)} \hat{S}(\omega, \Theta). \quad (6.219)$$

Comparisons by Shemdin et al. (1978) showed that percolation is most effective in coarse sand (mean diameter $d_m \geq 0.5mm$). In fine sand ($d_m \leq 0.4mm$) bottom friction becomes more important than percolation.

However, the assumption of the rigid and non-deformable bottom material is not quite realistic. Observations showed that porewater flow, volume change and deformation occur simultaneously in the real soil beds. While the fluid motion is fairly well described by Darcy's law, the solid skeleton requires different constitutive equations for different soils. The simplest approach is to describe the water waves by the linear potential wave theory, while the soil is modelled by equations developed by Biot (1941). Those equations, which model the soil skeleton as an elastic continuum, can be applied for a wide range of soils. For example, the granular seabeds, which have negligible deformation, are modelled by the Darcy flow equation, while for soft marine sediments, when elastic effects are more important than porosity, the equations reduce to the linear elastic model (Yamamoto et al., 1978; Dalrymple and Liu, 1979; Mei and Foda, 1981). The effects on the waves, due to the presence of a permeable bottom have been modelled in the paper by Dalrymple and Liu (1979). Yamamoto et al. (1978) simply assumed that wave number in the water layer is not affected by bottom permeability, and that dynamic pressure at the interface between water and soil is given by the linear wave theory. The imaginary part of wave number k_i , which is equal to zero in the Yamamoto et al. (1978) solution, is one of several unknowns in the Dalrymple and Liu (1979) method.

6.2.9.1 Energy dissipation due to soft mud

Accumulations of fluid mud front many coastlines around the world. Most muds occur as intertidal and subtidal mud shoals near major rivers. For example, the Mississippi River supplies muds to the coast of Louisiana, the Amazon River supplies mud to the shorelines of Guyana and Surinam, and mud flats of the Yellow Sea and Gulf of Po Hai are derived from both the Yangtze and Hwangho rivers in China. Soft muddy bottoms have significant effects on properties of water waves which propagate over them. The attenuation rates of surface waves propagated over a muddy bottom are much greater than normally attributed to bottom friction dissipation (see for example, Tubman and Suhayda, 1976). Hurricane-generated waves were reported by Bea (1974) to have wave heights about 22 m in deep water and to be reduced in heights to 3.5 m in water depths of 12-20 m.

Experiments on the rate of wave energy loss over a fluid mud in Surinam showed that 88% of wave energy was dissipated between the outer (water depth $h = 7.1$ m) and intermediate stations (water depth $h = 4.7$ m), in a distance of 11 km. Although the water depth at the inner station was less than 1.5 m, waves did not break, nor did they undergo the transformation, but were completely attenuated (Wells, 1983). Sylwester (1974) describes a location where waves are attenuated after propagating only several wavelengths.

In the past various theories have been proposed to describe the interaction between water waves and a soft bed. Depending on the representation of physical characteristics of bed material we can group them into a few classes (Table 6.1).

In all these models, the rate of the wave energy damping is not readily available and can be obtained only after the corresponding boundary value problem is solved.

In the following, we discuss in some detail the viscoelastic model which provides more straightforward information on dispersion relation and wave attenuation. The model conveniently combines the viscosity and elasticity of the bed. Let assume that wave propagates in x direction in water of depth h over a viscoelastic layer of thickness $(h_n - h)$ – see Fig. 6.17 for notation. The free surface displacement is denoted by $\zeta(x, t)$ and the interface between the two media is $\eta(x, t)$. These displacements are given by $\zeta(x, t) = a \exp[i(kx - \omega t)]$ and $\eta(x, t) = b \exp[i(kx - \omega t)]$. To simplify the boundary value problem, the displacement $\eta(x, t)$ was assumed to be small with a comparison to water depth and thickness of viscoelastic layer. Thus, the matching conditions are applied at $z = -h$. Following Hsiao and Shemdin (1980) we assume the velocity potential in the water layer as:

Table 6.1: Theoretical models for a soft bed.

Model	Description
Viscous fluid model	Muddy bed behaves like a very viscous fluid. The wave attenuation is mostly due to pressure of the surface waves working on the lower fluid (Gade, 1958; Dalrymple and Liu, 1978; Liu and Dalrymple, 1984).
Linear viscoelastic model	Viscous and elastic aspects of bottom motion are considered (muddy bottom is a ‘Voigt type body’ or ‘Maxwell type body’) (Hsiao and Shemdin, 1980; MacPherson, 1980; Maa and Mehta, 1988).
Poro-elastic model with the Coulomb friction	Sea bottom is modelled as a homogeneous medium which satisfies poro-elastic theory by Biot (1941) and constant Coulomb damping (Yamamoto and Takahashi, 1985).
A Bingham plastic bed model	Muddy bed with high concentration is treated as a Bingham-type plastic bed (Liu and Mei, 1987).
Mud fluidization model with rheological properties	Viscoelastic properties of the mud depend on a wave-induced strain inside the bed (Foda et al., 1993).

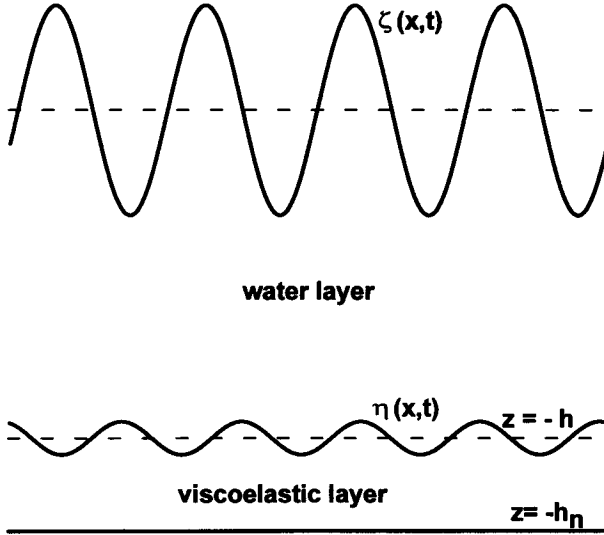


Figure 6.17: Definition scheme for surface waves propagated over viscoelastic bed.

$$\phi = \frac{-iag}{\omega} \left[\cosh(kz) + \frac{\omega^2}{gk} \sinh(kz) \right] \exp[i(kx - \omega t)]. \quad (6.220)$$

The stress-strain relationship for a muddy bottom is considered to have the property of a 'Voigt body', i.e.:

$$\tau = G\epsilon + \mu\dot{\epsilon}, \quad (6.221)$$

in which τ is shear stress, G is a shear modulus of elasticity, μ is a dynamic viscosity, ϵ is a shear strain, and $\dot{\epsilon}$ is a rate of change of shear strain. The Voigt body is based on the analogy of a spring-dashpot system. The spring is taken to obey Hooke's law and the dashpot can be considered as a piston being drawn through a Newtonian fluid. For the Voigt element, the response of elastic shear strain is delayed, but it finally reaches the value $\frac{\tau}{G}$, which the spring alone (representing a purely elastic response) would reach.

For small disturbances of an incompressible viscoelastic medium, the linear two-dimensional equations of motion are:

$$\left. \begin{aligned} \frac{\partial^2 u}{\partial t^2} &= J\nabla^2 u + \nu \nabla^2 \left(\frac{\partial u}{\partial t} \right) - \frac{1}{\rho_m} \frac{\partial^2 p}{\partial x \partial t} \\ \frac{\partial^2 w}{\partial t^2} &= J\nabla^2 w + \nu \nabla^2 \left(\frac{\partial w}{\partial t} \right) - \frac{1}{\rho_m} \frac{\partial^2 p}{\partial x \partial t} \end{aligned} \right\}, \quad (6.222)$$

where u and w are the horizontal and vertical velocity components, respectively, ρ_m is the density of mud, $J = G/\rho_m$ and $\nu = \mu/\rho_m$.

The solution of the boundary value problem provides the following expression for the dispersion relation:

$$k = k_r + ik_i = \frac{\omega^2}{g} \frac{1 + \tanh(\alpha kh)}{\alpha + \tanh(kh)}, \quad (6.223)$$

where:

$$\alpha = r \frac{(m^2 - k^2) \left[s_1 - \frac{k}{m} c_1 \right]}{(m^2 + k^2) \left[c_2 - \frac{k}{m} s_2 \right] - 2k^2}, \quad (6.224)$$

in which:

$$m = k \left[1 - \frac{\omega^2}{k^2 (J - i\omega\nu)} \right]^{1/2}, \quad (6.225)$$

$$s_1 = \sinh k (h_n - h) \cosh m (h_n - h),$$

$$s_2 = \sinh k (h_n - h) \sinh m (h_n - h),$$

$$c_1 = \cosh k (h_n - h) \sinh m (h_n - h),$$

$$c_2 = \cosh k (h_n - h) \cosh m (h_n - h),$$

and ν is a kinematic viscosity and r is the ratio of water density to mud density.

If the shear modulus $G \rightarrow \infty$ or when $\nu \rightarrow \infty$ (excessively viscous mud retards motion), wave number (6.223) reduces to the rigid-bottom dispersion relation:

$$\omega^2 = gk \tanh(kh). \quad (6.226)$$

The same conclusion is true for a very large mud density.

The numerical calculations using Eq. (6.223) indicate that the mud effect on waves decreases with increasing water depth and mud stiffness. Higher dissipation rates are observed in the thicker mud layer. The dissipation rate increases with mud viscosity, but high viscous mud attenuates motion very strongly and causes a decrease in the total rate of energy dissipation. The measured damping rate of waves reported by Tubman and Suhaya (1976) is consistent with the viscoelastic model, using estimates of mud viscosity given for the area. The decay rate due to bottom motion, is at least two orders of magnitude greater than estimated rates, based either on friction or the percolation mechanism.

6.2.10 Energy dissipation due to wave breaking

In the previous Section it was shown that outside the surf zone, the wave decay due to bottom friction or percolation in a porous bottom is rather weak, and may be so except on very muddy beds. However, inside the surf zone, the dissipation of wave energy due to wave breaking is much stronger. The flow in breaking random waves is highly complex and does not lead itself to a detailed deterministic treatment. Partly this is due to the difficulty of finding a precise mathematical description of a fluid that is, in general, nonlinear and time-dependent. The fluid accelerations no longer can be assumed to be small compared to gravity, nor is the particle velocity any longer small compared to the phase velocity.

Waves break in a different way, depending on wave height, wave period and beach slope. Laboratory studies (Galvin, 1972; Peregrine, 1983; Wiegell, 1964) have shown that breakers can be classified into four principle types:

- *Spilling*: White water appears at the wave crest and spills down the front face of the wave. The upper 25% of the front face may become vertical before breaking.
- *Plunging*: The whole front face of the wave steepens until vertical; the crest curls over the front face and falls into the base of the wave, sometimes preceded by the projection of a small jet.
- *Collapsing*: The lower part of the front face of the wave steepens until vertical, and this front face curls over as an abbreviated plunging wave. Minimal air pocket and usually no splash-up is observed.
- *Surging*: The wave slides up the beach with little or no bubble production. The water surface remains almost plane, except where ripples may be produced on the beach face.

Many properties of the surf zone appear to be governed by the parameter ξ_0 , defined by Eq. (6.98). In particular, the parameter ξ_0 is also used for classification of various breaker types:

- *surging and collapsing* if $3.3 < \xi_0$,
- *plunging* if $0.5 < \xi_0 < 3.3$,
- *spilling* if $\xi_0 < 0.5$.

A transformation of ξ_0 into the so called inshore parameter $\xi_b = \left(\frac{H_b}{L_0}\right)^{-0.5} \tan \beta$ yields:

- *surging or collapsing* if $2.0 < \xi_b$,
- *plunging* if $0.4 < \xi_b < 2.0$,

- *spilling* if $\xi_b < 0.4$.

It should be noted that parameters ξ_0 and ξ_b are equivalent to the parameter $\chi_0 = \frac{2\omega^2 a_0}{g \tan \beta}$ which is also used in literature (Battjes, 1988).

The modelling of energy dissipation, due to breaking in the wave train, is usually based on four main assumptions:

- dissipation is equivalent to dissipation in a bore connecting two regions of uniform flow (Battjes and Janssen, 1978),
- dissipation is proportional to the difference between the local energy flux and the stable energy flux (Dally et al., 1985),
- the breaking wave height is saturated, i.e. the wave height is proportional to the local water depth and the proportionality coefficient is assumed to be constant across the surf zone,
- dissipation is controlled by the presence of a surface roller (Svendsen, 1984).

6.2.10.1 Periodic bore approach

The power dissipated in a bore (per unit span) is (Lamb, 1932; Massel and Belberova, 1990):

$$D' = \frac{1}{4} \rho_w g (Y_2 - Y_1)^3 \left\{ \frac{g (Y_1 + Y_2)}{2Y_1 Y_2} \right\}^{1/2}, \quad (6.227)$$

where depths Y_1 and Y_2 are given in Fig. 6.18. Therefore:

$$\left. \begin{aligned} Y_2 - Y_1 &= \alpha H, \\ Y_1 &= h - (1 - \beta) \alpha H \\ Y_2 &= h + \alpha \beta H \end{aligned} \right\}. \quad (6.228)$$

The coefficient α is of an order one and expresses the influence of turbulence and presence of foam on the face of the wave. The coefficient β ($0.5 \leq \beta \leq 1.0$) is related to the wave steepness and the peakness of the crests and flatness of the troughs; for a sinusoidal wave $\beta = 0.5$.

Using Eqs. (6.228) we get:

$$\frac{Y_1 + Y_2}{2Y_1 Y_2} = \frac{1 + \frac{\alpha(2\beta - 1)}{2} \left(\frac{H}{h}\right)}{1 + \alpha(2\beta - 1) \left(\frac{H}{h}\right) - \alpha^2 \beta (1 - \beta) \left(\frac{H}{h}\right)^2} \frac{1}{h}. \quad (6.229)$$

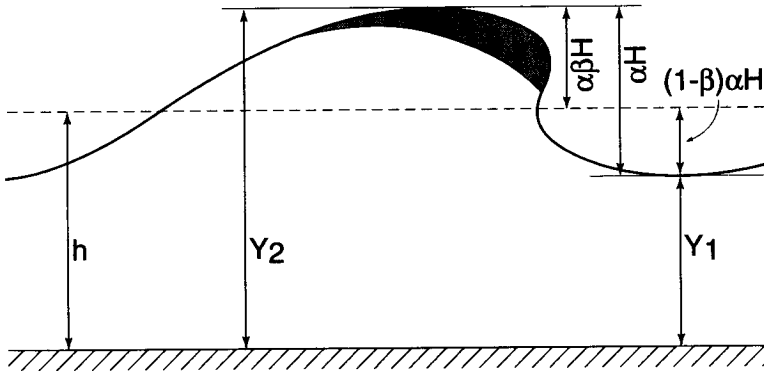


Figure 6.18: Periodic bore model. Definition scheme.

The coefficient α can be found only from experiments. Moreover, an estimation of β results from the nonlinear wave theories. As a first approximation we assume that $\alpha \approx 1.0$ and $\beta \approx 0.5$. Thus, Eq. (6.229) yields:

$$\frac{Y_1 + Y_2}{2Y_1Y_2} \approx \frac{1}{1 - \frac{1}{4}\left(\frac{H}{h}\right)^2} \frac{1}{h}. \quad (6.230)$$

Substitution of Eq. (6.230) into Eq. (6.227) yields:

$$D' = \frac{\alpha^3}{4} \rho_w g H^3 \left\{ \frac{g}{h \left[1 - \frac{1}{4}\left(\frac{H}{h}\right)^2 \right]} \right\}^{1/2}. \quad (6.231)$$

For waves with frequency ω , the power dissipated per unit area can be expressed as:

$$D = \frac{D'}{L} = \frac{\omega}{2\pi C} D', \quad (6.232)$$

and

$$D = \frac{\alpha_0 \rho_w g \omega}{8\pi} \frac{H^3}{h} \left(\frac{\sqrt{gh}}{C} \right) \psi', \quad (6.233)$$

in which $\alpha_0 = \alpha^3$ and

$$\psi' = \left[1 - \frac{1}{4}\left(\frac{H}{h}\right)^2 \right]^{-1/2}. \quad (6.234)$$

In the surf zone $\frac{H}{h} \approx 1.0$ and $\psi' \approx 1.15$. The influence of term ψ' is to increase the dissipation when comparing with the classical bore model in which $\psi' = 1$. In fact, Stive (1984) showed that the classical bore model underestimates the dissipation in breaking waves. Therefore, inclusion of the term ψ' and coefficient α_0 is to compensate this underestimation. When $\psi' = 0$ and $C \approx \sqrt{gh}$, Eq. (6.233) becomes:

$$D = \frac{\alpha_0 \rho g \omega}{8\pi} \frac{H^3}{h}, \quad (6.235)$$

which is in agreement with the Battjes and Janssen (1978) expression. Here, the underestimation of wave breaking is compensated by adjusting the α_0 coefficient.

In order to implement the dissipation rate (6.233) to the random wave train we assume that the heights of all waves which are breaking or broken at a given water depth h are equal to H_m . This is equivalent to the sharp cutoff in the probability density function $f(H)$ at wave height H_m :

$$fH = \begin{cases} \frac{H}{\hat{H}^2} \exp \left[-\frac{1}{2} \left(\frac{H}{\hat{H}} \right)^2 \right] & \text{for } 0 \leq H \leq H_m \\ \frac{Q_b}{H_m} \delta \left(\frac{H}{H_m} - 1 \right) & \text{for } H > H_m \end{cases}, \quad (6.236)$$

in which:

$$Q_b = Prob(H > H_m) = \exp \left[-\frac{1}{2} \left(\frac{H_m}{\hat{H}} \right)^2 \right], \quad (6.237)$$

is a fraction of waves which are breaking or broken at a given point, \hat{H} is a modal value which will be specified later, and $\delta(\cdot)$ is a delta function. Note, that for a non-dissipative system, $\hat{H} = \frac{1}{\sqrt{2}} H_{rms}$, $H_m \rightarrow \infty$ and the Rayleigh distribution is obtained.

All statistics of wave height can be expressed in terms of H_m and \hat{H} . In particular, the root-mean-square wave height H_{rms} becomes:

$$\begin{aligned} H_{rms}^2 &= \int_0^\infty H^2 f(H) dH = \frac{1}{\hat{H}^2} \int_0^{H_m} H^3 \exp \left[-\frac{1}{2} \left(\frac{H}{\hat{H}} \right)^2 \right] dH + \\ &+ \frac{Q_b}{H_m} \int_{H_m}^\infty H^2 \delta \left(\frac{H}{H_m} - 1 \right) dH, \end{aligned} \quad (6.238)$$

and:

$$H_{rms}^2 = 2 \left\{ 1 - \exp \left[-\frac{1}{2} \left(\frac{H_m}{\hat{H}} \right)^2 \right] \right\} \hat{H}^2, \quad (6.239)$$

or:

$$H_{rms}^2 = 2(1 - Q_b) \hat{H}^2. \quad (6.240)$$

From the physical point of view it will be more convenient to express the fraction Q_b in terms of H_{rms} and H_m . Eliminating \hat{H} from Eqs. (6.237) and (6.240) gives:

$$\frac{1 - Q_b}{\ln Q_b} = - \left(\frac{H_{rms}}{H_m} \right)^2, \quad (6.241)$$

or

$$Q_b = \exp \left(- \frac{1 - Q_b}{b^2} \right), \quad (6.242)$$

in which: $b = \frac{H_{rms}}{H_m}$. In relatively deep water, waves propagate almost without dissipation. When $\left(\frac{H_{rms}}{H_m} \right)$ increases, a fraction of broken waves Q_b also increases. In very shallow water virtually all the waves are breaking and $Q_b \rightarrow 1$, and wave height is now controlled by local depth ($H_{rms} \rightarrow H_m \rightarrow \gamma h$).

To apply the above results to the dissipation model we assume that the dissipation is due to breaking waves which have a height equal to H_m and that the probability of occurrence of these waves is Q_b . Moreover, the wave spectrum is narrow with the peak frequency $\omega = \omega_p$. Thus, Eq. (6.233) gives:

$$D = \frac{\alpha_0 \rho_w g \omega_p}{8\pi} \left(\frac{H_m^3}{h} \right) \left(\frac{\sqrt{gh}}{C} \right) \psi' Q_b, \quad (6.243)$$

or when $C \approx \sqrt{gh}$, $\psi' \approx 1$:

$$D = \frac{\alpha_0 \rho_w g \omega_p}{8\pi} \left(\frac{H_m^3}{h} \right) Q_b. \quad (6.244)$$

In the Battjes and Janssen (1978) model, the depth-limited height is given by a Miche type expression (Eq. (4.220)), adopted for the peak wave number k_p , i.e.:

$$H_m = \frac{0.88}{k_p} \tanh \left(\frac{\gamma}{0.88} k_p h \right). \quad (6.245)$$

To close the model, dissipation rate D is used as a sink term in the wave energy balance equation (the one-dimensional case is considered):

$$\frac{\partial (EC_g)}{\partial x} = -D, \quad (6.246)$$

in which:

$$E = \frac{1}{8} \rho_w g H_{rms}^2 = \rho_w g \int_{\omega} \int_{\Theta} \hat{S}(\omega, \Theta) d\omega d\Theta, \quad (6.247)$$

is a total wave energy and C_g is a group velocity associated with peak frequency ω_p , i.e.:

$$C_g = \frac{\omega_p}{2k_p} \left(1 + \frac{2k_p h}{\sinh 2k_p h} \right). \quad (6.248)$$

For a given bottom profile $h(x)$ and incident wave parameters, Eq. (6.246) can be integrated to find root-mean-square wave height H_{rms} .

The water depth h , used in the model, is the sum of the bottom depth below still water level (h_0) and a wave-induced set-up ($\bar{\zeta}$). The latter is usually calculated through the simultaneous integration of the energy balance equation (6.246) and the mean momentum balance given in the form:

$$\frac{\partial S_{xx}}{\partial x} + \rho g (h_0 + \bar{\zeta}) \frac{\partial \bar{\zeta}}{\partial x} = 0, \quad (6.249)$$

in which the radiation stress component S_{xx} is (Longuet-Higgins and Stewart, 1964; Massel, 1989):

$$S_{xx} = \left(\frac{1}{2} + \frac{2k_p h}{\sinh 2k_p h} \right) E. \quad (6.250)$$

In fact, the bore type dissipation model predicts the attenuation of some characteristic wave height (i.e. H_{rms}) but it does not give any information on the evaluation of the spectrum itself. Generally, little is known about the spectral representation of wave energy dissipation. In all existing models, the dissipation rate depends on the total wave energy (H_{rms} value) at a given point rather than on the individual spectral component. However, if we assume for a moment that the dissipation does not influence the shape of the spectrum, we can rewrite Eq. (6.246) approximately as:

$$\frac{\partial S(\omega)}{\partial t} \approx -\frac{\alpha_0 \omega_p}{\pi} \left(\frac{H_m^3}{h} \right) Q_b \frac{S(\omega)}{H_{rms}^2}. \quad (6.251)$$

The verification of the Battjes and Janssen (1978) model against the empirical data indicates that the model predicts well the root-mean-square wave height evolution due to breaking in a wide range of conditions, as far as bottom profiles and incident waves are concerned (Derks and Stive, 1984; Battjes and Stive, 1985).

Rather than use the single maximum wave height H_m in the dissipation rate (6.244) Thornton and Guza (1983) calculated the average rate of energy dissipation by multiplying the dissipation for a single broken wave of height H by the probability of the wave breaking at each height, i.e. instead of Eq. (6.244) we have:

$$D = \frac{\alpha_0 \rho_w g \bar{\omega}}{8\pi} \frac{H^3}{h}, \quad (6.252)$$

in which $\bar{\omega}$ is a mean wave frequency, and mean dissipation rate is:

$$E[D] = \frac{\alpha_0}{8\pi} \rho_w g \frac{\bar{\omega}}{h} \int_0^\infty H^3 f_{br}(H) dH. \quad (6.253)$$

Substituting Eq. (4.224) with weighting functions (4.226) and (4.227) for $n = 4$, we correspondingly obtain:

$$E[D] = \frac{3\sqrt{\pi}\alpha_0}{16} \rho_w g \frac{\bar{\omega}}{\gamma^4 h^5} H_{rms}^7, \quad (6.254)$$

and

$$E[D] = \frac{3\sqrt{\pi}\alpha_0}{16}\rho_w g \frac{\bar{\omega} H_{rms}^5}{\gamma^2 h^3} \left\{ 1 - \left[1 + \left(\frac{H_{rms}}{\gamma h} \right)^2 \right]^{-5/2} \right\}. \quad (6.255)$$

The sensitivity analysis yields the optimal value of $\alpha_0 = 1.54^3$. The numerical integration of the energy balance equation (6.246) indicates that, with the optimal choice of parameter α_0 , the model predicts a root-mean-square wave height within a standard error of 9% throughout the region from offshore to the beach.

6.2.10.2 Energy flux difference model

Many laboratory and field observations yield the conclusion that when waves start to break at some point, the breaking would continue with various intensity until some stable wave height H_{st} is attained. Horikawa and Kuo (1966), Thornton and Guza (1983), and Nelson (1994) found that a stable wave criterion can be expressed as:

$$H_{st} = \Gamma h, \quad (6.256)$$

in which H_s is the stable wave height and Γ is a dimensionless coefficient the value of which appears to be 0.35 - 0.60. Therefore, the rate of energy dissipation per unit area can be intuitively presented as (Dally et al., 1985):

$$\frac{\partial (EC_g)}{\partial x} = \frac{-K}{h} [EC_g - (EC_g)_{st}], \quad (6.257)$$

where K is an attenuation coefficient.

After using the linear wave theory for shallow water and substituting Eq. (6.256), Eq. (6.257) becomes:

$$\frac{\partial (H^2 h^{1/2})}{\partial x} = \frac{-K}{h} [H^2 h^{1/2} - \Gamma^2 h^{5/2}], \quad (6.258)$$

or:

$$\frac{\partial G}{\partial x} + \frac{K}{h} G = K \Gamma^2 h^{3/2}, \quad (6.259)$$

in which:

$$G = H^2 h^{1/2}. \quad (6.260)$$

For simpler shapes, the closed form solutions of Eq. (6.259) exist. In particular, the analytical solution for the breaker on a plane beach is given by:

$$\frac{H}{H_b} = \left[\left(\frac{h}{h_b} \right) \left(\frac{K}{\beta} - \frac{1}{2} \right) (1 + \alpha) - \alpha \left(\frac{h}{h_b} \right)^2 \right]^{1/2}, \quad (6.261)$$

where $\alpha = \alpha_* \left(\frac{h}{H} \right)_b^2$ and α_* is defined by Eq. (4.242). The subscript 'b' denotes the values at breaking point. Solution (6.261) was also rewritten in terms of $\left(\frac{H}{h_b} \right)$ in Eq. (4.241), where the energy flux difference model was used for determination of the probability density function $f(H)$ in the surf zone.

In order to facilitate the physical interpretation of the energy dissipation in terms of the radiative-transfer equation, we rewrite Eq. (6.257) as follows:

$$C_g \frac{\partial E}{\partial x} = -\frac{1}{2} \sqrt{\frac{g}{h}} \frac{dh}{dx} E - \left(\sqrt{\frac{g}{h}} E - \Gamma^2 h \sqrt{gh} \right) K. \quad (6.262)$$

For uniform depth Eq. (6.262) becomes:

$$\frac{\partial E}{\partial x} = -\frac{K}{h} E + K \Gamma^2 h, \quad (6.263)$$

with the solution in the form:

$$E(x) = (E_b - \Gamma^2 h^2) \exp \left(-\frac{K}{h} x \right) + \Gamma^2 h^2. \quad (6.264)$$

Note that wave energy is expressed in terms of a square of wave height, i.e. it has dimension $[m^2]$ and E_b denotes the energy at the breaking point ($x = 0$).

The solution for wave energy E on a plane beach, corresponding to Eq. (6.261), takes the form:

$$E = E_b \left[\left(\frac{h}{h_b} \right) \left(\frac{K}{\beta} - \frac{1}{2} \right) (1 + \alpha) - \alpha \left(\frac{h}{h_b} \right)^2 \right]. \quad (6.265)$$

When $K = 0$, Eq. (6.265) reduces to the Green's law of the wave shoaling without dissipation.

As in a periodic bore model, Eq. (6.262) predicts the attenuation of the monochromatic wave energy, not the spectral component attenuation.

6.2.10.3 Local water depth model

The simplest formulation of the dissipation rate is possible through determination of the limiting wave height. Slightly rearranging the Miche (1944) breaking condition (4.220), we present the limiting steepness of waves as (Chen and Wang, 1983):

$$\frac{H_s}{L_b} = 0.12 \tanh(k_b h_b), \quad (6.266)$$

in which $k_b = \frac{2\pi}{L_b}$ and $L_b = 7.72 \sigma_\zeta^{1/2} \sqrt{gh}$ is an empirical relationship of significant wavelength.

Using the linear dissipation relation we rewrite Eq. (6.266) as:

$$H_s = 0.12 \frac{2\pi}{g} \left(\frac{L_b}{T_b} \right)^2 = 0.12 \frac{2\pi C_b^2}{g}. \quad (6.267)$$

Substituting Eq. (6.267) into Eq. (4.130) yields:

$$E_{max} = \sigma_\zeta^2 = \frac{1}{16} H_s^2 = 0.0355 \frac{C_b^4}{g^2}. \quad (6.268)$$

Equation (6.268) imposes a limit on the growth of the spectrum but no information is provided on the limiting form of the spectrum.

It should be noted that at the very shallow water ($C_p \approx \sqrt{gh}$), Eq. (6.268) yields:

$$E_{max} = 0.0355 h^2. \quad (6.269)$$

6.2.10.4 Surface roller concept

In any type of breaking (spilling or plunging) there is a rapid change in the shape of the wave immediately following the initiation of breaking. This region is commonly called the *outer* or *transition region*, which covers a distance of, say 8 – 10 water depths, after the breaker point (Svendsen et al., 1978; Basco and Yamashita, 1986, 1988; Nairn et al., 1990). Shoreward of the transition region, the wave shape changes much more slowly. This is the so called *inner* or *bore region*, as the broken waves have many features in common with bores. The important feature dominating the wave motion in this region is the surface roller which is a passive volume of water carried shoreward with the wave speed. The generation of surface rollers due to wave breaking introduces a non-uniform velocity profile, which strongly influences the convective terms in the momentum equation. The resulting excess momentum effect can be defined as (Schäffer et al., 1993):

$$R = \delta_r \left(C - \frac{P}{d} \right)^2 \left(1 - \frac{\delta}{d} \right)^{-1}, \quad (6.270)$$

in which $P \equiv \int_{-h}^{\zeta} u dz$, $d = h + \zeta$ and δ_r is a roller thickness, i.e. a vertical distance between the free surface and the streamline (in a coordinate system following the wave; see Fig. 6.19).

Including the excess momentum R into the classical Boussinesq equation yields:

$$\frac{\partial P}{\partial t} + \frac{\partial}{\partial x} \left(\frac{P^2}{d} \right) + \frac{\partial R}{\partial x} + g d \frac{\partial \zeta}{\partial x} + \frac{h^3}{6} \frac{\partial^3}{\partial x^2 \partial t} \left(\frac{P}{h} \right) - \frac{h^2}{2} \frac{\partial^3 P}{\partial x^2 \partial t} = 0, \quad (6.271)$$

and

$$\frac{\partial \zeta}{\partial t} + \frac{\partial P}{\partial x} = 0. \quad (6.272)$$

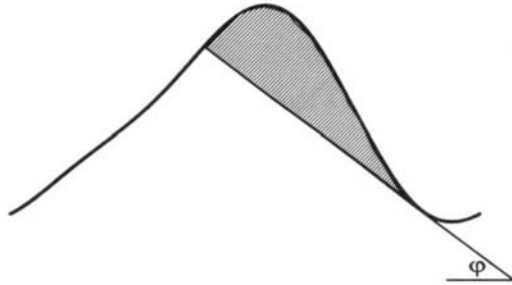


Figure 6.19: Surface roller in breaking wave.

At the stage of incipient breaking, the local steepness of the front reaches some maximum, say $\tan \varphi$ (see Fig. 6.19). When this gradient is exceeded, waves break. Schäffer et al. (1993) assumed that the water above the tangent of slope $\tan \varphi$, to the water surface, belongs to the roller. If the local slope becomes less than $\tan \varphi$, the breaking ceases. The angle φ was assumed to be of the order of 10° and typical value of maximum angle at the breaking stage $\varphi_b \approx 20^\circ$.

Numerical simulation of the irregular wave train propagating over a bar by Eqs. (6.271) and (6.272), with excess momentum R due to non-uniform velocity distribution caused by wave breaking, showed a satisfactory agreement with the laboratory data despite such a crude description of the energy dissipation due to the surface roller.

6.3 Wave prediction models

6.3.1 Models based on energy transfer equation

6.3.1.1 First generation wave models

In this Section we apply the same classification system for wave prediction models as in the case of deep water. Thus, we discuss the three basic generations of wave prediction models, starting from the simplest to the recent sophisticated models.

As waves propagate from deep water into shallow water they are modified by their interaction with the bottom topography. The processes involved in that interaction were discussed above. Depending on the model complexity, it includes all processes or only some of them. The simplest prediction models are so called first generation prediction models. The corresponding radiative transfer equation in the finite water

depth can be rewritten as:

$$\frac{\partial \hat{\Psi}(\vec{k})}{\partial t} + \nabla \cdot (\hat{\Psi} \vec{C}_g) = Q, \quad (6.273)$$

in which source term Q usually comprises the generation terms Q_1 and Q_2 , dissipation term Q_7 due to white capping and term Q_8 due to bottom friction. The term Q_{nl} , due to nonlinear interaction, is usually omitted in the first generation wave models.

Collins (1972) developed a prediction model capable of reproducing the wave propagation and shoaling for a simple bottom contour. A ray technique was applied to account for refraction and shoaling.

The same technique was used by Cavaleri and Rizzoli (1981) to hindcast storms in the Northern Adriatic Sea. All the considered physical processes (refraction, shoaling, generation and dissipation) have been introduced in the original formulation given in the literature and no model calibration has been made. Their computations follow a wave packet along a single wave ray, thus avoiding the troublesome convective term. Comparison with observations at the oceanographic tower, situated at the distance of 15 km from Venice at the water depth 16 m, showed that refraction and shoaling are well-handled by the model. The rms error of the significant wave height is of the order of 10 - 20%. It was pointed out that the largest source of error is associated with the determination of the wind field. Especially in the Northern Adriatic Sea, the strong orographic effects lead to wind fields rapidly varying both in time and in space.

In the Chen and Wang (1983) non-stationary numerical model for wind-induced waves transformed in a shallow water zone, a square mesh instead of wave rays was used. In a model, the usual wave refraction and shoaling effects as well as some parameterization of the nonlinear dissipative processes have been included. In particular, an empirical criterion Eq. (6.268), based upon total wave energy in terms of significant wave height, was employed. This equation imposes a limit on the growth of the variance. When the computed significant wave height H_s exceeds the limiting value, all the low-frequency components are decreased by a proportional amount. The governing equations of the model were solved using an explicit two-step Lax-Wendroff scheme.

6.3.1.2 Second generation wave models

As for deep water, the second generation wave models for shallow waters are presented in a discrete spectral space or in a parametric space. The governing equation for evolution of the two-dimensional spectrum $\hat{S}(\omega, \Theta)$ in the physical space is given by Eq. (2.185). Additionally, the kinematics of wave propagation are usually described by ray theory. In the net source term Q , a number of physical processes are included, i.e. atmospheric input, nonlinear interaction within the spectrum, white capping, bottom friction and wave breaking.

The formulation of the atmospheric input is similar to that given for deep water. The nonlinear interaction term \hat{Q}_{nl} is included in the wave prediction procedure through some parameterization. As was pointed out in the previous Chapter, the forward lobe (see Fig. 5.4) of the nonlinear transfer plays a vital role in the evolution of the spectrum. The negative lobe has much less significant role, restricted mainly to the maintaining of the spectral balance in the region to the right of the spectral peak. Young (1988) found that a triangle approximation of the forward lobe of the spectral transfer is sufficiently accurate to produce suitable results. The magnitude of the nonlinear transfer was scaled from the results of the mean JONSWAP spectrum. The energy dissipation terms due to white capping and bottom friction were parameterized in some way. In particular, the white capping dissipation was modelled by the inclusion of a saturation spectrum as an upper level to growth rather than specifying an analytical form for \hat{Q}_7 . The similar upper limit is also placed on the total energy of the spectrum, due to depth-limited breaking (see Eq. (6.268)).

The parametric alternative of the second generation wave model was developed by Graber and Madsen (1988). In the model an attempt was made to modify the lower limit of the peak frequency due to finite depth as:

$$\frac{U\omega_p}{g \tanh(kh)} = 0.879, \quad (6.274)$$

in which U is a mean wind speed parallel to the wave direction.

In the deep water this expression reduces to original Eq. (3.77). In the shallow water limit, the fully developed conditions would not be reached if $U > 0.82\sqrt{gh}$. To parameterize the nonlinear interaction term \hat{Q}_5 , the results of Herterich and Hasselmann (1980) were applied after some scaling by a depth-dependent factor R (see Eq. (6.137)).

Special attention in the Graber and Madsen (1988) model was paid to the influence of bottom friction on the spectral dynamics. The numerical study showed that bottom friction is an effective process attenuating wave energy for the space and time scales applicable to continental shelves and the interactions of waves, and that rough bottom plays an equally important role to that of nonlinear wave-wave interactions in the evolution of the spectrum. The net effect of these two processes controls the migration of the spectral peak. As was indicated in the previous Chapter, the spectral peak shifts towards lower frequencies as a consequence of the nonlinear energy transfer. When surface waves propagate into shallow water, the low-frequency spectral components interact with the bottom first. This interaction rapidly increases until all spectral components feel the bottom. The interaction with the bottom absorbs part of the energy transferred by the wave-wave interaction. This is reflected in the slower migration of the spectral peak towards lower frequencies. When the bottom friction dominates, the trend of the spectral peak shift along the frequency axis reverses. The parametric model allows the following equation for time gradient of the

peak frequency (Graber and Madsen, 1988):

$$\frac{\partial \omega_p}{\partial t} = Q_{nl}^{(1)} + Q_{bf}^{(1)}, \quad (6.275)$$

where $Q_{nl}^{(1)}$ and $Q_{bf}^{(1)}$ are the source terms corresponding to the nonlinear wave-wave interaction and the bottom friction, respectively. The particular formulation for $Q_{nl}^{(1)}$ and $Q_{bf}^{(1)}$ results from the projection of the source terms into parametric space - see Eq. (5.60) (Günther et al., 1979a,b). The numerical study showed that the bottom friction factor $f_r \leq 0.01$ would slow down the shift of the peak towards lower frequencies but would not completely stop this trend. However, when $f_r \geq 0.01$, the bottom friction dominates the low-frequency balance and spectral peak immigrates towards higher frequencies. At some frequencies, the bottom friction and non-linear transfer balance each other.

Observations near the Lightship *Texel*, 25 km west of the Dutch coast, during a storm with wind speed $U \approx 25 \text{ m/s}$ showed that the wave height (significant wave height $H_s \approx 6.8 \text{ m}$) remained at a constant level for approximately 12 hours, which seems to indicate that the spectrum is approximately in equilibrium (Bouws and Komen, 1983). The dominant source term was the wind input which was strongly balanced by dissipation due to white capping and bottom friction. The nonlinear transfer was found to be much smaller than in the deep sea.

6.3.1.3 Third generation wave models

The third generation wave model itself and the physical processes involved were described in the previous Chapter. They are also discussed extensively in the book by Komen et al. (1994). In this Section we only consider the implementation of the model for a shallow water basin. The WAM (Wave Model) Group selected the Adriatic Sea for testing. In this almost enclosed basin, the meteorological conditions are well-defined and large shallow areas provide opportunities for testing of the dissipation processes.

The full source term \hat{Q} comprises three main parts:

$$\hat{Q} = \hat{Q}_{in}^{(nl)} + \hat{Q}_{nl} + (\hat{Q}_{br} + \hat{Q}_{bf})_{dis}. \quad (6.276)$$

There are two main corrections in \hat{Q} when compared with the deep water case. The first is the scaling factor, due to shallow water applied for the discrete interaction operator parameterization (see Section 5.2.2.2). In the Adriatic Sea, where the peak period of storm spectra is about 10 s, the scaling allows use of the model down to a 16 m water depth (Cavaleri et al., 1989). Moreover, the dissipation processes, due to white capping and bottom friction, are modelled by expressions given in Eqs. (5.48) and (6.196), respectively. In the discrete spectral model of Cavaleri et al. (1989), 25 frequencies in the geometric progression ($\omega_1 = 0.262 \text{ rad/s}$, $\omega_{n+1} = 1.1\omega_n$) and a 15 min. time step has been used for the integration. The initial conditions are taken as

a uniform JONSWAP spectrum with the significant wave height $H_s = 0.25$ m and mean period $\bar{T} = 3$ s.

Three different storms were selected for hindcasting (*bora*, with a very active generation condition, *scirocco* with swell, and *scirocco* with cross-sea conditions). *Bora* is a strong and dry northerly wind in the northern part of the Adriatic Sea, generated when a northerly inflow of cold air takes place at its front edge. The *scirocco* (or *sirocco*) is a warm wind, usually damp after having crossed the sea. It is generated when the eastern motion of the low is impeded by the Russian winter high. *Scirocco* is responsible for many floods in Venice. The comparison of experiments with model results shows a good coincidence for all these different meteorological situations.

In the open sea, as well in shallow water, waves propagate over moving water due to large oceanic currents or tides. The Gulf Stream, the Agulhas Current, the Kuroshio or tides over the North Sea are good examples of such situations. For waves propagated on currents, the radiative transfer equation should be replaced by the wave action balance equation. The numerical tests (Tolman, 1991a,b) showed that tides and storm surges in shelf seas should be treated as an unsteady medium for wind wave propagation if wave-current interactions are assessed. Tides mainly result in oscillations of mean wave parameters, whereas surges result in their systematic variations. Due to accumulations of effects, small wind-induced currents may have a larger impact on a wave parameter than oscillating tidal currents. In North Sea conditions, the modification of the significant wave height or the mean wave period, due to relatively small tides, is of the order of 5 - 10%. Modulations of the spectral density can be of the order of 50-100%. Such high modification of the spectral density has straightforward implications for the dynamic analysis of offshore structures (Peters and Boanstra, 1988).

6.3.1.4 Wave prediction in very shallow water

Coastal engineers regularly require an estimation of wave conditions in coastal regions, up to the waterline and at the front of coastal structures. A fully discrete spectral model accounting for all processes of generation and dissipation and wave-current interaction implemented on a fine grid, usually demands excessive computer requirements. Therefore, some simplifications are needed. Probably the most obvious simplification is an assumption of stationary motion. It is justified by the short time of wave travel in coastal zone in comparison with the time scale of the local wind and current fields.

The second possible simplification is to parameterize the initial wave action balance equation (2.186). Therefore, instead of the full wave action function $N(\vec{k}, \vec{x})$, the directional action spectrum $A_o(\Theta)$ and the directional mean wave frequency $\omega_o(\Theta)$ can be defined. These simplifications are basic ones in a numerical model for the hindcasting of waves in shallow-water (HISWA) developed by Holthuijsen et al. (1989).

The $A_o(\Theta)$ and $\omega_o(\Theta)$ are defined as follows:

$$A_o(\Theta) = \int_0^\infty N(\omega, \Theta) d\omega = \hat{m}_0(\Theta), \quad (6.277)$$

and

$$\omega_o(\Theta) = \frac{1}{A_o(\Theta)} \int_0^\infty \omega N(\omega, \Theta) d\omega = \frac{\hat{m}_1(\Theta)}{\hat{m}_0(\Theta)}, \quad (6.278)$$

in which $\hat{m}_n = \int_0^\infty \omega^n N(\omega, \Theta) d\omega$.

After substituting Eqs. (6.277) and (6.278) into Eq. (2.177) and changing the variables (\vec{k}, \vec{x}) into $(\omega, \Theta, \vec{x})$, two evolution equations are obtained:

$$\frac{\partial}{\partial x} (C_{gx} \hat{m}_0) + \frac{\partial}{\partial y} (C_{gy} \hat{m}_0) + \frac{\partial}{\partial \Theta} (C_\Theta \hat{m}_0) = \tilde{Q}_0, \quad (6.279)$$

$$\frac{\partial}{\partial x} (\tilde{C}_{gx} \hat{m}_1) + \frac{\partial}{\partial y} (\tilde{C}_{gy} \hat{m}_1) + \frac{\partial}{\partial \Theta} (\tilde{C}_\Theta \hat{m}_1) = \tilde{Q}_1, \quad (6.280)$$

in which C_{gx}, C_{gy}, C_Θ and $\tilde{C}_{gx}, \tilde{C}_{gy}$, and \tilde{C}_Θ , are the propagation speed through (x, y, Θ) space of quantities m_0 and m_1 , respectively. In particular, C_{gx} and C_{gy} are the x - and y -components, respectively, of the group velocity \vec{C}_g associated with the mean-frequency ω_0 :

$$\vec{C}_g = \frac{\partial \sigma_0}{\partial k_0} \frac{\vec{k}_0}{k_0} + \vec{U}, \quad (6.281)$$

in which:

$$\omega_0 = \sigma_0 + \vec{k}_0 \cdot \vec{U}, \quad (6.282)$$

and

$$\sigma_0^2 = g k_0 \tanh(k_0 h), \quad (6.283)$$

and \vec{U} is the current vector.

The speed C_Θ represents the refraction at the mean-frequency ω_0 . The linear wave theory gives:

$$C_\Theta = -\frac{1}{k_0} \frac{\partial \sigma_0}{\partial h} - \frac{\vec{k}_0}{k_0} \frac{\partial \vec{U}}{\partial n}, \quad (6.284)$$

in which h is the local water depth and n is the vector normal to the path.

The source functions \tilde{Q}_0 and \tilde{Q}_1 are expressed in terms of functions which can more readily be estimated from information given in professional literature, i.e. wave energy and the mean-frequency of energy spectrum.

In the HISWA model the following physical processes are included: shoaling, refraction, generation by wind, bottom dissipation, wave breaking (surf zone) and wave blocking due to an opposing current. To implement the HISWA model, the computations are carried out in a regular grid using finite different methods. The diffraction is not incorporated and no artificial cap in the energy is utilized. Therefore, the question arises about the model ability to adequately predict wave properties in regions with complex bathymetry where diffraction effects are likely to be important (for example, underwater elliptic or circular shoals).

A comparison with the combined refraction-diffraction models (Panchang et al., 1990) and results of hydraulic tests for an elliptic shoal (Vincent and Briggs, 1989) showed that HISWA provides almost identical results. The degree of energy spreading considerably affects the performance of HISWA. The errors are small when compared with data and a combined refraction-diffraction model for broad input spectra. As the input spreading decreases, larger errors are observed (Bondzie and Panchang, 1993). It appears that HISWA simulates wave propagation under conditions similar to a realistic sea much better than for 'special' conditions. A comparison of the numerical results with observations in the mouth of the river Rhine showed that the rms errors of the significant wave height and the mean wave period are of the order of 10-20%.

6.3.2 Empirical prediction models

6.3.2.1 SPM prediction method

The origin and the basic properties of the empirical prediction models were discussed extensively in a previous Chapter. In this Section, some supplements relating to finite water depth are added. The fetch-limited shallow-water forecasting curves given in the last edition of the Shore Protection Manual (SPM, 1984), result from the following formulas:

$$\frac{gH_{m0}}{U_A^2} = 0.283 \tanh \left[0.530 \left(\frac{gh}{U_A^2} \right)^{3/4} \right] \cdot \tanh \left\{ \frac{0.00565 \left(\frac{gX}{U_A^2} \right)^{1/2}}{\tanh \left[0.530 \left(\frac{gh}{U_A^2} \right)^{3/4} \right]} \right\}, \quad (6.285)$$

and

$$\frac{gT_p}{U_A} = 7.54 \tanh \left[0.833 \left(\frac{gh}{U_A^2} \right)^{3/8} \right] \cdot \tanh \left\{ \frac{0.0379 \left(\frac{gX}{U_A^2} \right)^{1/3}}{\tanh \left[0.833 \left(\frac{gh}{U_A^2} \right)^{3/8} \right]} \right\}, \quad (6.286)$$

and

$$\frac{gt_X}{U_A} = 537 \left(\frac{gT_p}{U_A} \right)^{7/3}. \quad (6.287)$$

If the duration of the storm is less than t_X , the sea state is duration limited and values of H_s and T_p must be calculated using a modified fetch length calculated from Eq. (6.287).

At the deep water limit, when $h \rightarrow \infty$, expressions (6.285) and (6.286) are not exactly identical with the deep water formulas (5.94) and (5.95); there is a step change in the results in the transition between both formulations. Hurdle and Stive (1989) proposed an alternative formulation which asymptotically matches the SPM expressions in deep and shallow waters, for small and large fetch lengths.

The revised equations are:

$$\frac{gH_{m0}}{U_A^2} = 0.25 \tanh \left[0.6 \left(\frac{h}{gU_A^2} \right)^{0.75} \right] \cdot \tanh^{0.5} \left\{ \frac{4.3 \cdot 10^{-5} \left(\frac{gX}{U_A^2} \right)}{\tanh^2 \left[0.6 \left(\frac{h}{gU_A^2} \right)^{0.75} \right]} \right\}, \quad (6.288)$$

$$\frac{gT_p}{U_A} = 8.3 \tanh \left[0.76 \left(\frac{gh}{U_A^2} \right)^{0.375} \right] \cdot \tanh^{1/3} \left\{ \frac{4.1 \cdot 10^{-5} \left(\frac{gX}{U_A^2} \right)}{\tanh^3 \left[0.76 \left(\frac{gh}{U_A^2} \right)^{0.375} \right]} \right\}. \quad (6.289)$$

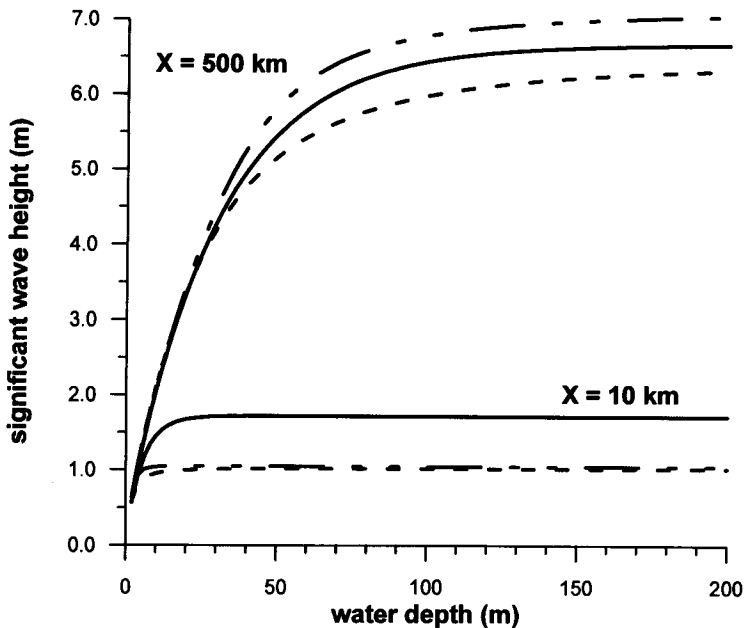


Figure 6.20: Comparison of significant wave height resulting from empirical prediction formulas: — SPM method, - - - revised SPM method, - . - . - Krylov's method.

If $\left(\frac{gh}{U_A^2}\right) \gg 1$ and $\left(\frac{gX}{U_A^2}\right) \ll 10^4$, Eqs. (6.288) and (6.289) give:

$$\frac{gH_{m0}}{U_A^2} \approx 1.6 \cdot 10^{-3} \left(\frac{gX}{U_A^2}\right)^{1/2}, \quad (6.290)$$

$$\frac{gT_p}{U_A} \approx 0.286 \left(\frac{gX}{U_A^2}\right)^{1/3}, \quad (6.291)$$

which is in agreement with Eqs. (5.94) and (5.95) for a deep water fetch limited case. When fetch becomes longer, Eqs. (6.290) and (6.291) become:

$$\frac{gH_{m0}}{U_A^2} \approx 0.25 \quad \text{and} \quad \frac{gT_p}{U_A} \approx 8.3, \quad (6.292)$$

which should be compared with Eqs. (5.98) and (5.99). For the extreme case of shallow water ($\frac{gh}{U_A^2} \ll 1$, $\frac{gX}{U_A^2} \gg 1$), Eqs. (6.288) and (6.289) yield:

$$\frac{gH_{m0}}{U_A^2} \approx 0.15 \left(\frac{gh}{U_A^2} \right)^{0.75} \quad \text{and} \quad \frac{gT_p}{U_A} \approx 6.31 \left(\frac{gh}{U_A^2} \right)^{0.375} \quad (6.293)$$

Again, the above relationships are in good agreement with the asymptotic shallow water behaviour of SPM formulas (6.285) and (6.286). In Fig. 6.20 and 6.21, the dependence of the significant wave height H_{m0} and period of peak spectral energy T_p on the water depth are shown for two wind fetches: $X = 10$ km and 500 km, and for various water depths. For comparison, the original SPM formulas, as well as revised graphs due to Hurdle and Stive (1989), and those due to Krylov (see below), were plotted.

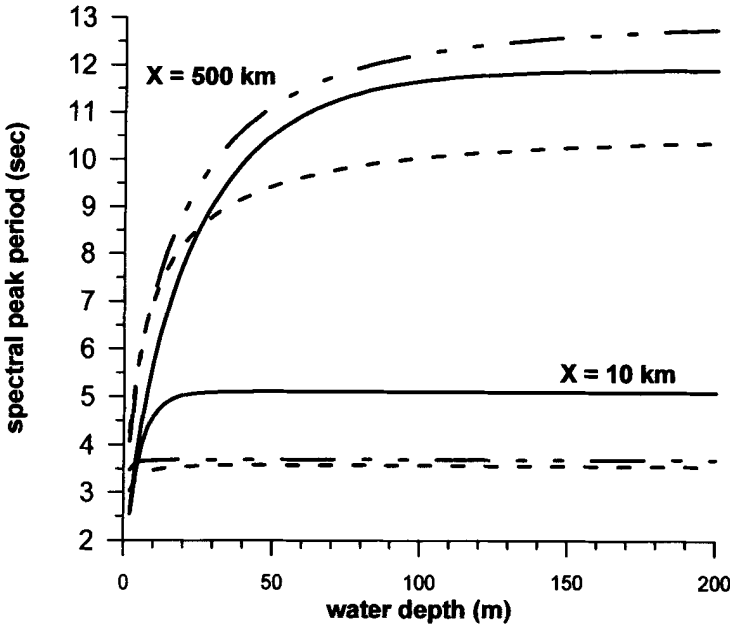


Figure 6.21: Comparison of spectral peak period resulting from empirical prediction formulas: — SPM method, - - - revised SPM method, - . - . Krylov's method.

6.3.2.2 Krylov prediction method

The basic philosophy of the Krylov's wave prediction model was presented in Section 5.3.2.6. Here we consider the extension of the Krylov's approach for finite water depth. Using the observations in many water basins of moderate and small depths, Krylov et al. (1976) proposed the following fetch graphs for the mean wave height \bar{H} and arbitrary water depth:

$$\frac{g\bar{H}}{U^2} = 0.16 \left\{ 1 - \left[1 + 6 \cdot 10^{-3} \left(\frac{gX}{U^2} \right)^{0.5} \right]^{-2} \right\} \cdot \tanh \left\{ 0.625 \left(\frac{gh}{U^2} \right)^{0.8} \left[1 - \left(1 + 6 \cdot 10^{-3} \left(\frac{gX}{U^2} \right)^{0.5} \right)^{-2} \right]^{-1} \right\}. \quad (6.294)$$

Equation (6.294) is shown in Fig. 5.11 for various water depths. When $h \rightarrow \infty$ (deep water), Eq. (6.294) yields the formula (5.122).

For very shallow waters when the wave motion is totally depth-controlled and independent in the wind speed, the mean and maximum wave periods become:

$$\bar{T} = 4.6 \sqrt{\frac{h}{g}} \quad \text{and} \quad T_{max} \approx 5.5 \sqrt{\frac{h}{g}}. \quad (6.295)$$

Using the linear dispersion relation in Eq. (6.295) gives:

$$\frac{\bar{L}}{h} \approx 3.2 \quad \text{and} \quad \frac{L_{max}}{h} \approx 4.3. \quad (6.296)$$

After substituting Eq. (6.295) into Eq. (5.123), the relationship between the non-dimensional mean wave height and the non-dimensional water depth takes the form:

$$\frac{g\bar{H}}{U^2} = 0.099 \left(\frac{gh}{U^2} \right)^{0.8}. \quad (6.297)$$

Vincent and Hughes (1985) argue that the maximum wave period at which the growth of shallow water waves would stop is determined by:

$$\frac{gT_{max}}{U} = 6.98 \left(\frac{gh}{U^2} \right)^{0.5}. \quad (6.298)$$

Rewriting the second relationship in Eq. (6.295) as:

$$\frac{gT_{max}}{U} \approx 5.5 \left(\frac{gh}{U^2} \right)^{0.5}, \quad (6.299)$$

we find the same functional dependence of both formulas.

According to Vincent and Hughes (1985), the significant wave height in the depth-controlled wave train is given by:

$$\frac{gH_{m0}}{U^2} = 0.210 \left(\frac{gh}{U^2} \right)^{0.75}. \quad (6.300)$$

Assuming that $H_{m0} \approx 1.5\bar{H}$ (see Chapter 4), from Eq. (6.297) we get:

$$\frac{gH_{m0}}{U^2} \approx 0.158 \left(\frac{gh}{U^2} \right)^{0.8}, \quad (6.301)$$

which can again be compared with Eq. (6.300).

The significant wave height H_{m0} and spectral peak period T_p , resulting from Krylov's methods, are compared with the SPM prediction in Fig. 6.20 and 6.21.

This page is intentionally left blank

Chapter 7

Waves at Islands and Coral Reefs

7.1 Introduction

Wave mechanics and wave forecasting techniques for island archipelagoes and coral reefs are still rather poorly known. This is due mostly to steep (and sometimes vegetated) bottom slopes and complicated scattering of waves on islands or reef matrix. Basically, the problem of wave prediction in such an environment can be formulated as a local problem for one island or reef or as a regional problem for all island archipelagoes. Both approaches are applied in this Chapter.

In the first Sections, the wave climate at a single island (or reef) is discussed. The extended refraction-diffraction equation is applied to study the wave propagation, wave refraction and diffraction, and dissipation at the islands (or reefs). These processes are complicated due to the fact that coral reefs are densely populated by flora and fauna. A correlation between wave motion and coral zonation has long been recognized by reef ecologists as one of the most important factors determining reef growth. To illustrate this correlation, in Section 7.6 an example of impact of wave motion on massive corals is discussed in detail.

Due to the presence of numerous islands (reefs), only a few gaps are open at a given location. It was shown below that although such gaps may appear large in comparison to the size of individual island (reef), wave attenuation is still significant.

7.2 Propagation of waves over steep bottom slopes

7.2.1 Geometrical optics and mild-slope approximations

In a previous Chapter, we described wave refraction over a shoaling bottom, under the assumption that diffraction effects, if any, are small. For refracting waves, the variations of phase are governed primarily by variations of wave number k , induced by a variable depth. The resulting wave amplitude variations serve as additional corrections which can be called diffraction effects.

In order to clarify the effect of diffraction on wave propagation, a solution of the mild-slope equation (6.82) is considered in a wave form:

$$\varphi(x, y) = B(x, y) \exp(iS(x, y)). \quad (7.1)$$

By substituting into Eq. (6.82) and separating the real and imaginary parts, we obtain:

$$(\nabla_h S)^2 = k^2 + \frac{\nabla_h(CC_g)}{CC_g} \cdot \frac{\nabla_h B}{B} + \frac{\nabla_h^2 B}{B}, \quad (7.2)$$

and

$$\nabla_h \cdot (CC_g B^2 \nabla_h S) = 0, \quad (7.3)$$

where the potential amplitude $B = \frac{gA}{\omega}$, and A is a wave amplitude.

Equations (7.2) and (7.3) can be rewritten as:

$$(\nabla_h S)^2 = k^2 + \frac{\nabla_h(CC_g)}{CC_g} \cdot \frac{\nabla_h A}{A} + \frac{\nabla_h^2 A}{A}, \quad (7.4)$$

and

$$\nabla_h \cdot (CC_g A^2 \nabla_h S) = 0, \quad (7.5)$$

in which (Dingemans, 1985; Massel, 1993a):

$$\frac{\nabla_h CC_g}{CC_g} = \frac{G(kh)}{h} \nabla_h h, \quad (7.6)$$

and

$$G(kh) = \frac{kh}{T + kh(1 - T)^2} \left[1 - 3T^2 + \frac{2T}{T + kh(1 - T^2)} \right], \quad (7.7)$$

are $T = \tanh(kh)$. Thus, the eikonal equation (7.4) becomes:

$$(\nabla_h S)^2 = k^2 + \frac{G(kh)}{h} \nabla_h h \cdot \frac{\nabla_h A}{A} + \frac{\nabla_h^2 A}{A}. \quad (7.8)$$

For constant water depth, the right-hand side of Eq. (7.8) is $\left(k^2 + \frac{\nabla_h^2 A}{A} \right)$. At a maximum wave crest, the diffraction term is negative. Therefore, the phase gradient $|\nabla_h S|$ is smaller and the wave speed is larger than at other locations. The opposite is true for a minimum in wave amplitude. In general, variations of amplitude along the wave crest cause variations in wave speed, which lead to changes in wave direction.

When the second and third terms on the right-hand side of Eq. (7.8) are smaller than k^2 , the geometrical optics approximation is valid. This means that the approximation can only be used when:

$$\frac{\nabla_h h}{kh} \cdot \frac{\nabla_h A}{A} \ll 1 \quad \text{and} \quad \frac{\nabla_h^2 A}{A} \ll k^2, \quad (7.9)$$

i.e. when the bottom slope is small with respect to (kh) , wave amplitude variation in space is also small with respect to surface slope kA , and diffraction effects are negligible.

For steeper slopes, the refraction and diffraction effects are substantial and cannot be neglected. In order to account for these effects, an alternative approach, based on the mild-slope equation, is usually considered (see Section 6.2.3). According to Booij (1983), this equation can give accurate results, even for a plane bottom slope up to 1:3. When a bottom slope is steeper, higher order terms in the bottom slope, as well as bottom curvature and evanescent modes should be taken into account. However, in the mild-slope equation (6.82), all of these terms are omitted.

7.2.2 Application of extended refraction-diffraction equation

7.2.2.1 Non-breaking waves

One way in which the accuracy of the mild-slope equation can be improved, is to define the water depth $h(x, y)$ as a summation of the slowly varying depth and rapid undulations about this depth. Using Green's identity method, Kirby (1986) developed a time-dependent extension of the mild-slope equation, under the assumption that deviations from the mean, slowly varying depth must be small, but may be of any arbitrary form.

To extend the mild-slope equation, Massel (1993a) has developed another approach, based on the Galerkin–Eigenfunction Method (Fletcher, 1984). The resulting equation consists of all wave modes, i.e. the propagation and evanescent modes. Additionally, it is assumed that the amplitudes of bottom undulations are not necessarily small. This method is only outlined here, but the full derivation is given by Massel (1993a).

Let us assume that the wave motion, if originally irrotational, remains irrotational, and the velocity potential $\Phi(x, y, z, t)$ is written as:

$$\Phi(x, y, z, t) = \Re \left\{ \frac{-igH}{2\omega} \phi(x, y, z) \exp(-i\omega t) \right\}. \quad (7.10)$$

Linearizing the free-surface boundary conditions we obtain the following boundary value problem for the non-dimensional wave height $\phi(x, y, z)$:

$$\mathcal{L}\phi = \nabla_h^2 \phi + \frac{\partial^2 \phi}{\partial z^2} = 0, \quad (7.11)$$

$$\frac{\partial \phi}{\partial z} - \lambda \phi = 0 \quad \text{at} \quad z = 0, \quad (7.12)$$

$$\frac{\partial \phi}{\partial z} + \nabla_h \phi \cdot \nabla_h h = 0 \quad \text{at} \quad z = -h(x, y), \quad (7.13)$$

in which $\lambda = \omega^2/g$ is a wave number in deep water, and g is the acceleration due to gravity. Considering the solution of Eqs. (7.11)–(7.13), we expand the $\phi(x, y, z)$ in terms of N depth-dependent functions $Z_n(x, y, z)$. We choose the functions $Z_n(x, y, z)$ which are continuously differentiable and which satisfy the boundary conditions of our problem, exactly as possible. Moreover, they should form a complete orthogonal set of Eigenfunctions in the domain $(-h(x, y), 0)$. Thus, let:

$$Z_n(x, y, z) = \frac{\cos[\alpha_n(z + h)]}{\cos(\alpha_n h)}, \quad (7.14)$$

in which $h(x, y)$ is the local water depth, and wave numbers α_n are the solution of the following dispersion relation:

$$\lambda + \alpha_n \tan(\alpha_n h) = 0. \quad (7.15)$$

Dispersion relation (7.15) has an infinite discrete set of real roots $\pm\alpha_n$ and a pair of imaginary roots $\alpha_0 = \pm ik$. Function $Z_0(x, y, z)$ represents the free wave mode, while the functions $Z_n(x, y, z)$ with $(n \geq 1)$ correspond to non-propagating (evanescent) wave modes.

Let us define now an inner product of functions f and g in the following manner:

$$\langle f, g \rangle = \int_{-h(x, y)}^0 f g \, dz. \quad (7.16)$$

In particular, for orthogonal functions $f = Z_m(x, y, z)$ and $g = Z_n(x, y, z)$, an inner product is:

$$\langle Z_m, Z_n \rangle = \begin{cases} \frac{h}{2\cos^2(\alpha_m h)} \left(1 + \frac{\sin(2\alpha_m h)}{2\alpha_m h} \right) & \text{if } m = n, \\ 0 & \text{if } m \neq n. \end{cases} \quad (7.17)$$

The Galerkin approach assumes that function $\phi(x, y, z)$ can be approximated by an expansion:

$$\phi(x, y, z) = \sum_{n=0}^N \varphi_n(x, y) Z_n(x, y, z), \quad (7.18)$$

in which the functions $\varphi_n(x, y)$ are found from the condition of orthogonality of functions $Z_n(x, y, z)$ and the left-hand side of Eq. (7.11), after the substitution of

Eq. (7.18) for $\phi(x, y, z)$. The orthogonality condition yields the following matrix equation for unknown functions $\varphi_n(x, y)$:

$$\mathbf{A} \nabla_{\mathbf{h}}^2 \varphi + \mathbf{B} \cdot \nabla_{\mathbf{h}} \varphi + \mathbf{C} \varphi = 0, \quad (7.19)$$

where the elements of \mathbf{A} , \mathbf{B} and \mathbf{C} are:

$$a_{mn} = \langle Z_m, Z_n \rangle = \begin{cases} \frac{h}{2\cos^2(\alpha_m h)} \left(1 + \frac{\sin(2\alpha_m h)}{2\alpha_m h} \right) & \text{if } m = n, \\ 0 & \text{if } m \neq n, \end{cases} \quad (7.20)$$

$$b_{mn} = 2\langle Z_m, \nabla_h Z_n \rangle + (Z_m Z_n)_{z=-h(x,y)} \nabla_h h, \quad (7.21)$$

$$c_{mn} = \lambda - \left\langle \frac{\partial Z_m}{\partial z}, \frac{\partial Z_n}{\partial z} \right\rangle + \langle Z_m, \nabla^2 Z_n \rangle + (Z_m \nabla_h Z_n)_{z=-h(x,y)} \cdot \nabla_h h. \quad (7.22)$$

By neglecting all evanescent modes ($m \geq 1, n \geq 1$) and keeping only free propagating waves ($m = n = 0$) in Eqs. (7.20)–(7.22) we obtain:

$$\nabla^2 \varphi + \frac{\nabla(CC_g)}{CC_g} \cdot \nabla \varphi + k^2(1 + \psi)\varphi = 0, \quad (7.23)$$

in which:

$$\psi = E_1(kh) (\nabla h)^2 + E_2(kh) \frac{\nabla^2 h}{\lambda}, \quad (7.24)$$

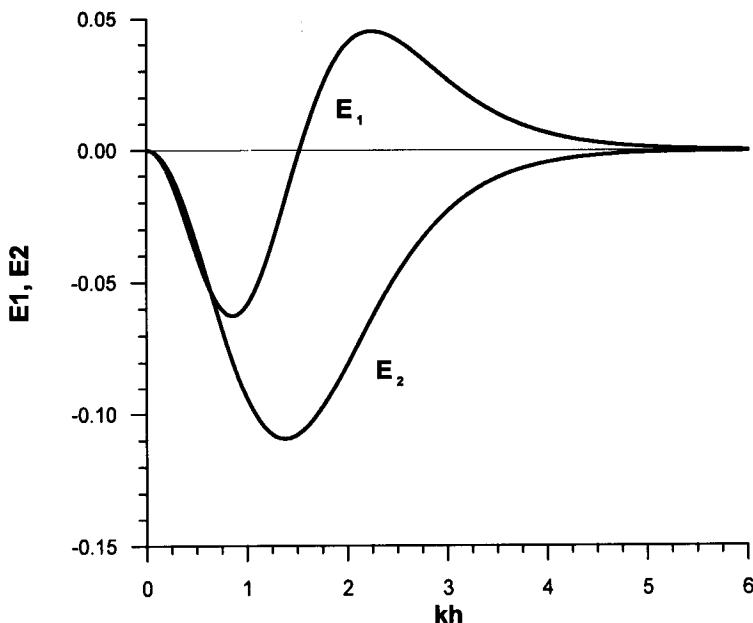
$$E_1(kh) = \frac{1}{p \tanh kh} \frac{1}{24(2kh + \sinh 2kh)^2 \cosh^3 kh}. \quad (7.25)$$

$$\begin{aligned} & \left\{ kh[12 + 16(kh)^2] \cosh kh + 6kh [\cosh 3kh + \cosh 5kh] + \right. \\ & \left. + [12 + 84(kh)^2] \sinh kh + 3[1 - 4(kh)^2] \sinh 3kh - 9 \sinh 5kh \right\}, \end{aligned}$$

and

$$\begin{aligned} E_2(kh) &= \frac{1}{p} \left\{ \frac{-4kh \cosh kh + \sinh kh + (kh)^2 \sinh kh + \sinh 3kh}{8(2kh + \sinh 2kh) \cosh^3 kh} + \right. \\ & \left. - \frac{kh \tanh kh}{2 \cosh^2 kh} \right\}, \end{aligned} \quad (7.26)$$

$$p = \frac{1}{2} \left(1 + \frac{2kh}{\sinh 2kh} \right). \quad (7.27)$$

Figure 7.1: Functions $E_1(kh)$ and $E_2(kh)$.

The functions $E_1(kh)$ and $E_2(kh)$ are shown in Fig. 7.1. In the case of constant water depth, the Helmholtz equation is obtained immediately:

$$\nabla^2 \varphi + k^2 \varphi = 0. \quad (7.28)$$

For the shallow water limit, when $kh \rightarrow 0$, from dispersion relation we have $\omega^2/gk^2 = h$. Thus, Eq. (7.23) yields:

$$\nabla^2 \varphi + \frac{\nabla h}{h} \cdot \nabla \varphi + k^2 \varphi = 0. \quad (7.29)$$

Result (7.29) is in full agreement with the long wave theory. It should be noted that for shallow water the validity of the extended refraction-diffraction equation does not depend upon the actual slope.

For slowly varying bottom topography with small amplitudes, both the $\nabla^2 h$ and $(\nabla h)^2$ can be omitted and Eq. (7.23) takes the form:

$$\nabla^2 \varphi_0 + \frac{\nabla(CC_g)}{CC_g} \cdot \nabla \varphi_0 + k^2 \varphi_0 = 0, \quad (7.30)$$

which is in full agreement with Berkhoff's solution (6.82).

The theoretical results were verified against the experimental results by Davies and Heathershaw (1984) on plane waves propagating over a patch of sinusoidal ripples, varying in one direction (see Massel, 1993a). Moreover, the arbitrary incident wave case was compared favourably with the theoretical result of Mei et al. (1988).

7.2.2.2 Breaking waves

Waves shoaling over a steep slope eventually lose their stability and break. Once the waves start to break, the breaking processes dominate wave transformation. To introduce the dissipation into Eq. (7.23), we use the representation suggested by Booij (1981). He found that in the shallow water limit, when only dissipation due to bottom friction is taken into account, the mild-slope equation becomes:

$$\nabla_h^2 \varphi + \frac{\nabla_h(CC_g)}{CC_g} \cdot \nabla_h \varphi + k^2 \left[1 + i \frac{W}{k\sqrt{gh}} \right] \varphi = 0, \quad (7.31)$$

in which:

$$W = \frac{4}{3\pi} \frac{f_r}{h} \frac{\hat{u}}{\cosh^2 kh}, \quad (7.32)$$

and \hat{u} is an amplitude of the horizontal bottom velocity.

For the shallow water $CC_g = gh$, and because of the close resemblance between Eqs. (7.23) and (7.31), we can assume that the extended refraction-diffraction equation with dissipation takes the form:

$$\nabla_h^2 \varphi + \frac{\nabla_h(CC_g)}{CC_g} \cdot \nabla_h \varphi + \left[k^2(1 + \psi) + i\gamma k \right] \varphi = 0, \quad (7.33)$$

in which γ is the unknown damping factor and ψ is given by Eq. (7.24).

The total energy flux on the slope is properly described by using an energy density spectrum with group velocity integrated over all frequencies and directions. Unfortunately, knowledge of the evolution of energy fluxes for a broad band nonlinear wave field in shallow water, particularly in a surf zone, is still very poor. Therefore, we restrict our analysis to the transformation of non-dimensional root-mean-square wave height, using the fact that the incident wave spectrum is very narrow and the incident wave train can be represented as a regular wave train with the wave height H_{rms0} and frequency ω_p .

The effect of the dissipation term ($i\gamma k$) in Eq. (7.33) becomes more evident when this equation is presented in the form of an energy transport equation. Hence, the complex non-dimensional wave height φ can be written as:

$$\varphi(x) = \hat{\varphi}(x) \exp[iS(x)] \quad \text{and} \quad \hat{\varphi} = \frac{H_{rms}}{H_{rms0}}. \quad (7.34)$$

Substituting Eq. (7.34) into Eq. (7.33) and the separation of real and imaginary terms, yields the wave energy transport equation in the form (one-dimensional case is assumed):

$$\frac{d}{dx} \left[\left(\frac{dS}{k dx} \right) C_g \varphi^2 \right] = -\gamma C_g \varphi^2, \quad (7.35)$$

or

$$\frac{d}{dx} \left[\left(\frac{dS}{k dx} \right) C_g E \right] = \frac{-1}{8} \rho g \gamma C_g H^2_{rms} = - \langle \epsilon \rangle, \quad (7.36)$$

in which:

$$E = \frac{1}{8} \rho g H^2_{rms}. \quad (7.37)$$

The phase $S(x)$ in Eq. (7.34) is a solution of the eikonal equation (7.8). The term $\langle \epsilon \rangle = -\frac{1}{8} \rho g \gamma C_g H^2_{rms}$ represents the average rate of energy dissipation (per unit area) due to wave breaking and bottom friction, i.e. $\langle \epsilon \rangle = \langle \epsilon_b \rangle + \langle \epsilon_f \rangle$. Using this representation in Eq. (7.36), we obtain:

$$\gamma = \gamma_b + \gamma_f, \quad (7.38)$$

in which:

$$\gamma_b = \frac{8 \langle \epsilon_b \rangle}{\rho g C_g H^2_{rms}} \quad \text{and} \quad \gamma_f = \frac{8 \langle \epsilon_f \rangle}{\rho g C_g H^2_{rms}}. \quad (7.39)$$

To determine the quantity γ_b , the similarity between a breaking wave and the phenomenon of a bore is utilized as a basis for the analysis. Therefore, the rate of energy dissipated per unit area for each bore is given by Eq. (6.252), i.e.:

$$\langle \epsilon_b \rangle = \frac{\alpha_0 \rho g \omega_p}{8\pi} \frac{\sqrt{gh}}{C} \frac{H^3}{h}, \quad (7.40)$$

in which α is a coefficient of $O(1)$. The average rate of energy dissipation is obtained by multiplying the dissipation for a single broken wave of height H by the probability of wave breaking at each height $f_{br}(H)$ (see Eq (4.224). Thus, we have:

$$\langle \epsilon_b \rangle = \frac{\alpha_0 \rho g \omega_p}{8\pi} \frac{\sqrt{gh}}{Ch} \int_0^\infty H^3 f_{br}(h) dH. \quad (7.41)$$

After using the weighting function $W(H)$, given in Eq. (4.226) with $n = 4$, and substituting Eq. (4.224) into Eq. (7.41), we obtain (Massel, 1992):

$$\langle \epsilon_b \rangle = \frac{3\alpha_0 \rho g \omega_p}{32\sqrt{\pi}} \frac{\sqrt{gh}}{C} \frac{H^3_{rms}}{h} \left(\frac{H_{rms}}{\Gamma h} \right)^4. \quad (7.42)$$

The experimental data reported by Hardy et al. (1990) showed $\Gamma \approx 0.3 - 0.5$. Now Eq. (7.39) yields:

$$\gamma_b = \frac{3\alpha_0\omega_p}{4\sqrt{\pi}} \frac{\sqrt{gh}}{CC_g} \frac{H_{rms}}{h} \left(\frac{H_{rms}}{\Gamma h} \right)^4. \quad (7.43)$$

The simple representation of the dissipation rate ϵ_f in the bottom boundary layer is given by (see also Section 6.2.7):

$$\epsilon_f = \frac{2}{3\pi} \rho f_r u_b^3, \quad (7.44)$$

where f_r is the friction factor, and u_b is the velocity amplitude at the bed. Substituting Eq. (7.44) into Eq. (7.39) gives:

$$\gamma_f = \frac{16f_r}{3\pi} \frac{u_b^3}{gC_g H_{rms}^2}. \quad (7.45)$$

On a reef coefficient f_r is much higher than that on a beach. Gerritsen's field experiments (Gerritsen, 1981) suggest that on the reef slope and reef flats $f_r \approx 0.1 - 1.0$.

Finally, after substituting Eqs. (7.38), (7.43) and (7.45) into Eq. (7.33), we obtain a differential equation for transformation of wave height H_{rms} over the bottom contour. To solve this equation, boundary conditions for H_{rms} at certain water depths should be prescribed. The possible formulation of these conditions is as follows: The surrounding bathymetry can be set to a constant depth $h = h(0)$, which is the depth of the continental shelf. In this area, a superposition of incident waves, which are prescribed as plain waves with known wave height and frequency, and waves reflected from a reef, is assumed. On the reef platform, at some distance from the reef edge, the water depth is constant and reformed, oscillatory, outgoing progressive waves are observed. For an arbitrary bottom profile, Eq. (7.33) is solved numerically.

7.2.2.3 Wave set-down and set-up

So far, the water depth $h(x)$ was described as a depth of the bottom below some reference plane, i.e. still water level. However, the spatial changes in the radiation stress due to shoaling, refraction, diffraction and dissipation, result in changes of sea level $\bar{\eta}$, according to the following momentum balance (Longuet-Higgins and Stewart, 1964):

$$\frac{dS_{xx}}{dx} + \rho g (h + \bar{\eta}) \frac{d\bar{\eta}}{dx} = 0, \quad (7.46)$$

in which:

$$S_{xx} = \left(\frac{3}{2}p - \frac{1}{2} \right) E + \frac{1}{2} Ep \cos 2\Theta, \quad (7.47)$$

where E and p are given by Eqs. (7.37) and (7.27), respectively, and Θ is a wave direction. After substituting Eq. (7.47) into Eq. (7.46) we obtain:

$$\frac{d\bar{\eta}}{dx} = \frac{-1}{8(h + \bar{\eta})} R(x), \quad (7.48)$$

in which:

$$R(x) = [(3 + \cos \Theta)p - 1] H_{rms} \frac{dH_{rms}}{dx} + \frac{1}{2}(3 + \cos 2\Theta) H_{rms}^2 \frac{dp}{dx} - p H_{rms}^2 \sin 2\Theta \frac{d\Theta}{dx}. \quad (7.49)$$

Equations (7.33) and (7.48) form a final system of two equations for unknown root-mean-square wave height H_{rms} and mean water level $\bar{\eta}$.

7.2.2.4 Numerical examples and comparison with experiments

Consider now an elongated reef situated in unrestricted open water. The cross-section of such a reef is given in Fig. 7.2. The incident water depth is $h_i = 32m$ and the water depth on the reef flat is $h_p = 2m$. The depth on the reef slope is changing according to the formulas:

$$h(x) = \frac{h_i + h_p}{2} - \frac{h_i - h_p}{2} \tanh[p(x)], \quad (7.50)$$

$$p(x) = \frac{2}{n(h_i - h_p)} \left\{ x - \left[x_0 + \frac{n(h_i - h_p)}{2} \right] \right\}, \quad (7.51)$$

in which $(1/n)$ is a tangent of a maximum slope (in our case: $1/n = 1/1$) at the abscissa $x = x_0 + \frac{n(h_i - h_p)}{2}$; x_0 is an adjusting parameter. It should be mentioned that this reef configuration is very similar to that considered by Nelson and Lesleighter (1985) in their physical model. However, a more realistic inclined slope is adopted instead of their vertical reef edge model.

Let us now select the incident wave height H_{rms0} to be 4.0 m and peak period $T_p = 8$ s. The results of calculations are presented in Fig. 7.2 in the form of functions $H_{rms} = H_{rms}(x)$, $\bar{\eta} = \bar{\eta}(x)$ and $A_b = A_b(x)$. The quantity A_b is defined by Eq. (4.226) as a fraction of all waves which are breaking at a given location. At the front of reef the wave height H_{rms} oscillates due to interference of incident waves and waves reflected from the reef edge. The calculations show that the reflection coefficient $K_R = 18.8\%$ and transmission coefficient $K_T = 29\%$. This means that $\approx 88\%$ of energy is dissipated. Waves start to break at water depth $h \approx 7$ m. The breaker index $\xi_b = \frac{1}{n} \left(\frac{H_b}{L_0} \right)^{-\frac{1}{2}} \approx 5$; thus, breakers belong to plunging and collapsing types of breakers. The full breaker ($A_b = 100\%$) was developed at abscissa $x \approx 67$ m, and was continued along the distance less than one wave length.

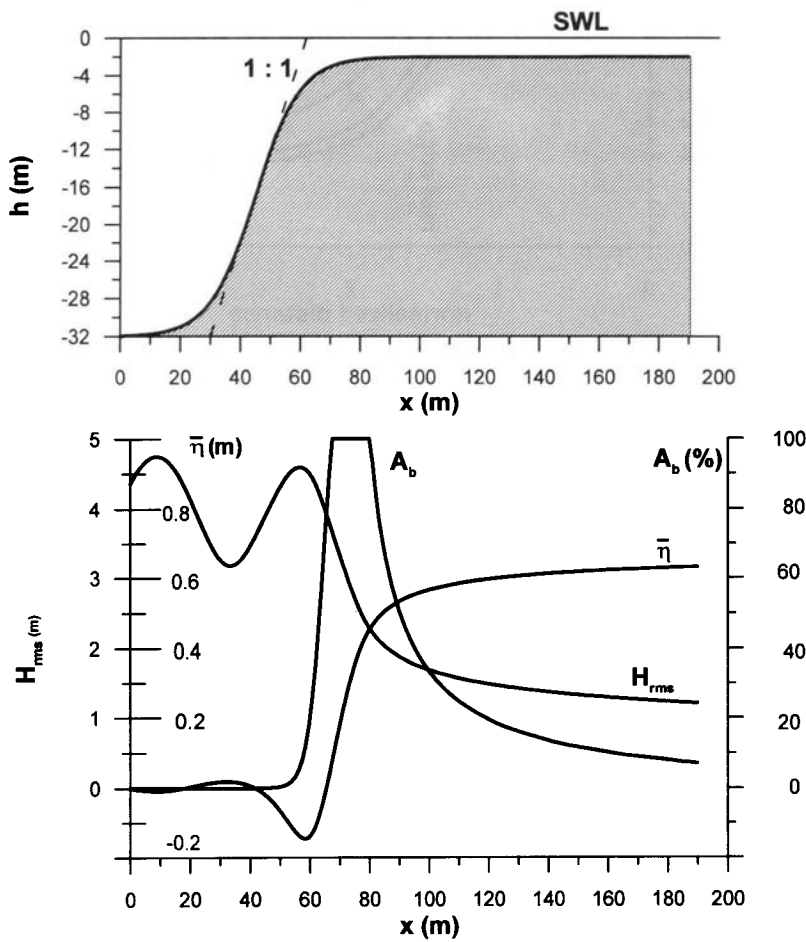


Figure 7.2: Wave transformation on reef: a) Cross-section, b) Variation of root-mean-square wave height H_{rms} , set-up $\bar{\eta}$, and fraction of breaking waves A_b .

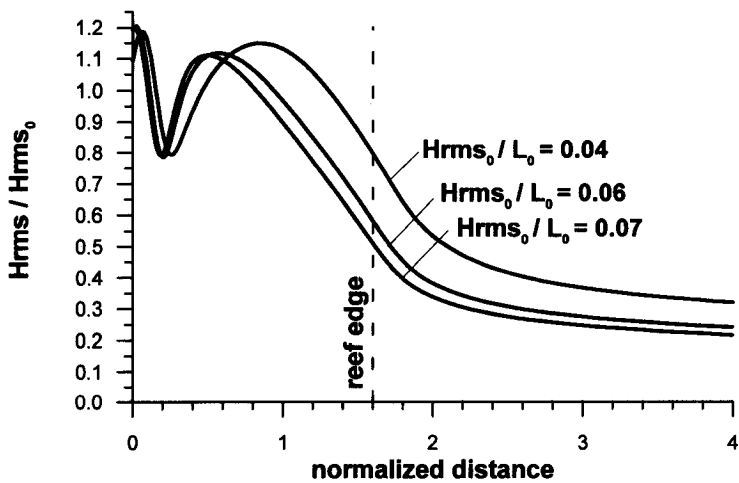


Figure 7.3: Influence of initial wave steepness on wave height decaying.

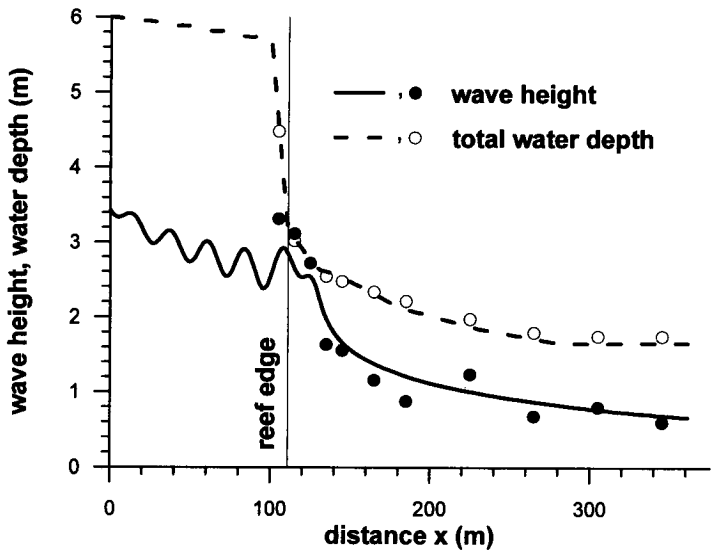


Figure 7.4: Comparison of numerical calculations and laboratory experiments for fringing reef with front face slope 1/4.5; wave height: ——— numerical calculations, ● experimental data; total water depth: - - - numerical calculation, ○ experimental data.

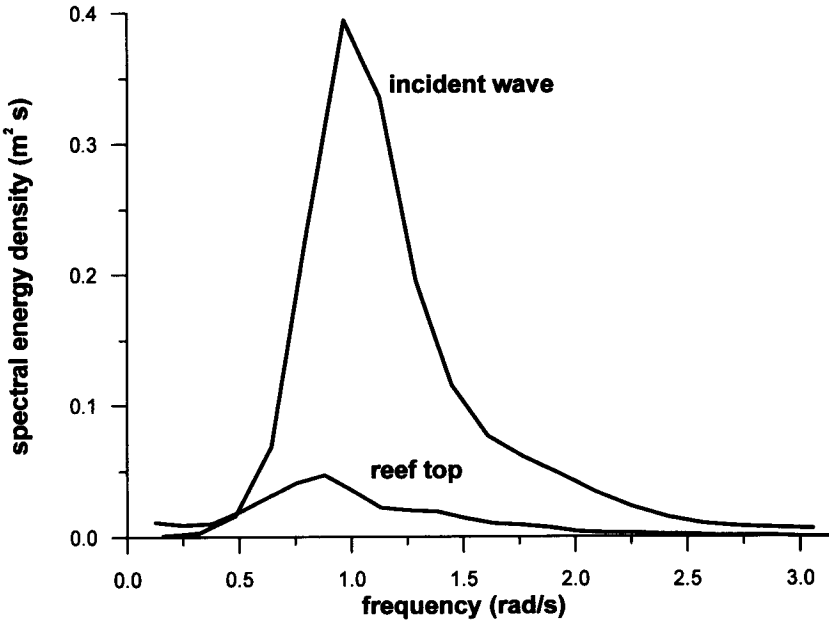


Figure 7.5: Frequency spectra for incident waves and for waves on reef top.

Afterwards the intensity of breaking decreases. At $x \approx 190$ m, the percentage of broken waves is $\approx 1.8\%$ and the waves are again reformed as oscillatory waves.

The evolution of wave height results in a change of the mean water level $\bar{\eta}$. On the reef top the wave set-up $\bar{\eta}$ is equal to $\approx 16.8\%$ of the incident wave height.

Figure 7.3 demonstrates the influence of the initial wave steepness on wave transformation and dissipation. The steeper waves start to break early, at a greater distance from the reef edge, and their breaking intensity is higher than that of smaller waves. Waves of a low steepness lose their stability closer to the reef edge and dissipate energy mostly on the reef platform. These results are in agreement with Nelson and Lesleighter's (1985) and Gourlay's (1994) observations.

In Fig. 7.4 comparison of theoretical and experimental wave height attenuation over a steep reef slope is given. The experimental values are the results of laboratory experiments on wave transformation over a natural reef profile (Gourlay, 1994). The prototype reef is a fringing reef located at Hayman Island on the east coast of Australia. The reef face, with a slope of 1 to 4.5, rises from a depth of 14 – 15 m to the reef edge where the water depth varies from 3 to 5 m, depending on tides.

The figure shows a case where the deep water wave height is equal to 3.39 m and the incident wave period is 6.75 s. At the reef front, the wave height gradually de-

creases over an almost horizontal sea bottom (slope $\sim 1/280$) due to bottom friction. Small wave height oscillations are due to reflection from a reef front. Over the reef edge waves start to break, constantly decreasing their height. In Fig. 7.4, the total water depth is indicated, rather than a set-up component to facilitate comparison with experiments.

Experimental field data on wave transformation over reef structure was reported by Young (1989), Massel (1994), and Massel and Steinberg (1994). The observed significant wave attenuation was found to be a function of both the deepwater incident wave height and the depth of reef submergence. The spectral shape also changed very significantly on the reef. Wave spectra on a reef top are very flat, with energy distributed across all frequencies (see Fig. 7.5). Such spectral modifications are caused by wave breaking and nonlinear generation of higher harmonics in the shallow water on the reef top.

7.3 Maximum wave height on shoal (reef) flat

The maximum possible wave height over the water of constant depth was discussed in Chapter 6. In particular, theoretical proof and experimental evidence demonstrated that the ratio of maximum wave height to water depth is smaller than 0.8 which is often used in engineering practice.

Similar behaviour is observed for waves propagating over the reef top. Coral reefs commonly grow to about the mean low tide level, and in their mature form, are planar reefs with extremely flat, solid and quite smoothly cemented surfaces. However, at high tide, depth-limited waves are able to propagate across the reef top. In the Great Barrier Reef region, tide ranges may be as great as 3 to 4 m, and water depths of 2 to 3 m over reefs at high tide are common. During the passage of a cyclone storm surge these depths could increase by 0.3 to 0.5 m, or much more, depending upon the intensity and path of the cyclone.

Since wave heights are governed by prevailing water depths, depth limited wave height criteria are essential for determining design wave heights for structures, and of sedimentological and geomorphological processes on coral reefs. A field experiment known as REEF88 was undertaken in 1988 at John Brewer Reef on the Great Barrier Reef (Australia). One objective of this experiment was to study the maximum height of stable oscillatory random waves, propagating in depth-limited conditions over a horizontal bed (Hardy et al., 1990; Nelson, 1994). Waves propagate from the deep ocean onto the reef slope, break on the reef as plunging breakers and then propagate over the reef top as a succession of bores, before reforming into stable oscillatory waves at some distance from the reef edge. Data collected during the experiment indicate that the largest stable $H_s/h \approx 0.4$ value, achieved by an individual wave in a random wave train propagating over a horizontal bed, is considerably lower than the usual engineering criterion. Taking into account that $H_{max} = \frac{\sqrt{2}}{2} \sqrt{\ln N} H_s$, we obtain

$$\frac{H_{max}}{h} \approx 0.6.$$

Recently Gourlay (1994) has published the results of laboratory experiments on wave transformation over a natural reef profile and provided further evidence that maximum depth-limited wave heights on a horizontal reef are consistent with the REEF88 experiment results. Sulaiman et al. (1994) has reported the results of experiments on maximum wave heights on the horizontal reef flat at Sanur Beach in Bali. For a non-dimensional water depth range $1.7 \cdot 10^{-4} < \frac{h}{gT^2} < 0.17$, the ratio of maximum wave height to water depth is always smaller than 0.6, except for a very few cases when it is about 0.65.

It is important to note that the lower limit of $(H/h)_{max}$ ratio is applicable to those locations on coral reef platforms where the distance from the reef edge is sufficient for waves to reform into oscillatory waves, after dissipating energy due to breaking. The breaking is initiated by the sudden depth change at the reef edge. Close to the reef edge waves with larger $(H/h)_{max}$ ratio can exist, but these would be turbulent breaking waves attenuating rapidly with distance from the reef edge.

In the previous Section, the extended refraction-diffraction equation with dissipation was used to predict the wave height on a steep reef slope. In that solution the attenuation of waves after breaking is controlled by coefficient Γ , which was chosen to be of order 0.3 - 0.5. This value results from experiments in the laboratory and in the field. In fact, the origin of the coefficient Γ can be explained using the same arguments as for waves propagating over a constant water depth (see Section 6.2.6). Many reef shoals can be presented schematically as steep underwater structures on which the water depth changes rapidly from tenths of a meter to a few meters on the reef top. In such situation, a formation of secondary crests in troughs of the main waves is observed. Harmonic analysis of simultaneous measurements in an incident region and on a step demonstrates a substantial growth of the higher harmonics in shallow water areas. A complete, second-order theory for generation of higher harmonics by an underwater step with a horizontal bottom has been developed in another paper (Massel, 1983). Using the amplitudes of both the first and second harmonics (bound harmonic and free harmonic), resulting from that theory, the kinematic breaking criterion (6.182) can be applied to determine the maximum height of reformed, oscillatory waves on the reef top.

In the case of irregular waves, the threshold downward vertical acceleration, together with Srokosz's formula (4.78), probably offers a more convenient approach for the determination of maximum wave height on the reef platform.

Real shoals or coral reefs are three-dimensional, and diffraction effects play a significant role in the wave climate in the vicinity of a reef. These effects are discussed in the next Section.

7.4 Sheltering of surface waves by islands

7.4.1 A brief orientation

In many of the world's ocean regions, the presence of island archipelagoes provide shelter and this effect has an influence on the wave climate for coasts or ocean basins located in the 'shadow' zones behind islands. The Great Barrier Reef along the eastern coast of Australia is not one solid barrier, but a matrix of almost 2900 separate reefs of various shapes and dimensions, covering the distance of about 3000 km. The Great Barrier Reef is a dominant factor in determining the north-east Australian coastal wave climate. Along the Norwegian coast there are also many areas with shoals and islands protecting the coast against the stormy North Sea (Lie and Torum, 1991). Another example are the offshore islands (Channel Islands) of the Southern Californian region (Pawka, 1983).

Waves incident from the deep ocean are blocked by the island boundaries and are refracted over the island shoals. The wave energy is partly dissipated in surf zones or reflected back out into the deep ocean. However, many other mechanisms, such as wave diffraction, wave scattering and wave-current interactions spread wave energy into the island lee regions.

It is convenient to consider modelling of wave motion in the island matrix from both the local and regional perspectives. In the local perspective, a particular island or shoal is considered under the assumption that waves incident on the island are known. From the regional perspective, the main objective is to assess the sheltering effect of a group of islands on the particular coastline or ocean region. Considering first the local field we use for simplicity a circular island (or shoal) as a model.

7.4.2 Scattering of waves by an isolated steep conical island

Let the origin of a polar coordinate system $O(r, \Theta, z)$ be taken in the mean free surface of the fluid, and the axes be chosen so that the r coordinate is horizontal and the z -coordinate is vertical and increasing upwards. An idealized cylindrical island with toe radius b is situated in an ocean of constant depth h_0 (see Fig. 7.6). The water depth over the shoal can be an arbitrary function of the distance r only, i.e. $h = h(r)$. To evaluate wave height evolution, we use the fact that the incident wave spectrum is very narrow and the incident wave train can be represented as a regular wave with the wave height H_{rms0} and frequency ω_p .

The complex velocity potential $\Phi(r, \Theta, z, t)$ should satisfy the following set of equations:

$$\mathcal{L} = \nabla^2 \Phi + \frac{\partial^2 \Phi}{\partial z^2} = 0, \quad a \leq r \leq \infty, \quad -h_0 \leq z \leq -h_p, \quad (7.52)$$

$$\frac{\partial^2 \Phi}{\partial t^2} + g \frac{\partial \Phi}{\partial z} = 0 \quad \text{at } z = 0, \quad r \geq a, \quad (7.53)$$

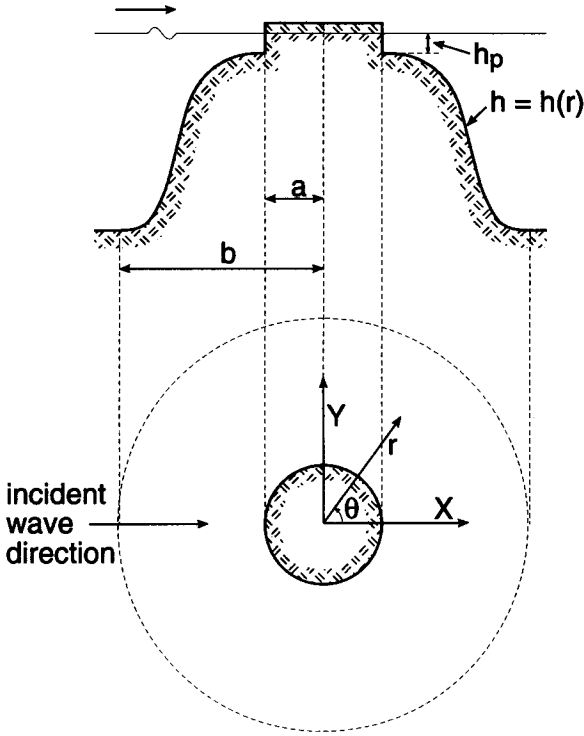


Figure 7.6: Circular reef. Definition scheme.

$$\frac{\partial \Phi}{\partial r} = 0 \text{ at } r = a \quad (\text{for island}), \quad (7.54)$$

$$\frac{\partial \Phi}{\partial z} + \nabla \Phi \cdot \nabla h = 0 \text{ at } z = -h(r, \theta), \quad a \leq r \leq b, \quad (7.55)$$

$$\frac{\partial \Phi}{\partial z} = 0 \text{ at } r \geq b. \quad (7.56)$$

The above boundary value problem should be supplemented by Sommerfeld's radiation condition, which states that as $r \rightarrow \infty$, only outgoing progressive waves are observed.

7.4.2.1 Pure refraction solution

To facilitate the interpretation of numerical results it will be useful to summarize briefly the pure refraction solution of surface waves around a circular reef. By Fermat's principle, the differential equation for a ray approaching an island is (Mei, 1983):

$$\frac{d\Theta}{dr} = \frac{\pm\chi}{r\sqrt{(kr)^2 - \chi^2}}, \quad (7.57)$$

where:

$$\chi = k_0 b \sin \alpha_0. \quad (7.58)$$

The α_0 , being an angle between the ray and the normal radius to the depth contour intersected by the ray, is the incident angle of the ray at $r = b$. The upper (lower) sign is taken for rays leaving (approaching) the reef. Upon entering the reef toe at $r = b$, all rays first bend toward the center of the reef. The final destination of a ray depends strongly on the variation of kr versus r . If $h(r)$ decreases monotonically from h_0 to h_p , the corresponding k must increase monotonically from k_0 to k_p . However, kr increases monotonically only if a is sufficiently large. Conversely, kr has a minimum within $a < r < b$, if the minimum of kr satisfies the condition $(kr)_{\min} < \chi < k_0 b$. Then, the incident ray (characterized by angle α_0) cannot pass a critical radius r_* at which the square root in Eq. (7.57) vanishes, and bends away from an island. The angle α_{0cr} , corresponding to the critical ray, is given by:

$$\sin^2 \alpha_{0cr} = \frac{(kr)_{\min}^2}{(k_0 b)^2}. \quad (7.59)$$

If $\alpha_0 < \alpha_{0cr}$, rays eventually intersect the shore at $r = a$. Such a case is illustrated in Fig. 7.7, where the incident wave period $T = 14$ s, the water depth at the continental shelf is $h_0 = 32$ m, and water depth at the reef edge is $h_e = 2.0$ m. The depth on the reef slope is assumed to be changing as:

$$h(r) \approx \frac{h_0 + h_e}{2} - \frac{h_0 - h_e}{2} \tanh[p(r)], \quad (7.60)$$

in which the reef radius is $a = 2000.0$ m and the reef edge is $r_e = 2120.0$ m. From the reef edge to the island coastline the water depth is given by:

$$h(r) = h_e - \frac{(h_e - h_p)}{2} \left(1 + \cos \left(\frac{\pi(r - a)}{r_e - a} \right) \right), \quad (7.61)$$

where the water depth h_p was adopted to be of 0.3 m.

Fig. 7.7 shows that all rays incident on the reef slope with angle $\alpha_0 > \alpha_{0cr} = 96^\circ$ intersect the shore. For all cases where $\alpha_0 \leq \alpha_{0cr}$ there is a region in the lee of the reef which is not reached by any incident ray. This means that in this region wave energy at the reef shoreline is theoretically equal to zero. In Fig. 7.7, the angle range

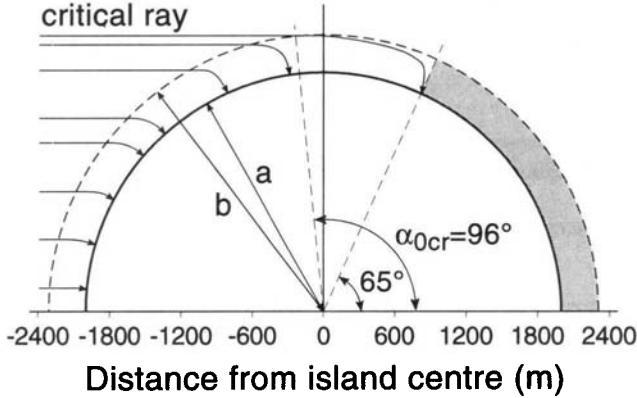


Figure 7.7: Wave rays refracting around the circular island.

$\Delta\theta$, corresponding to the zero wave energy at the shoreline, is $(-65^\circ, 65^\circ)$. However, this result is valid only if the diffraction effects are totally neglected. To improve the refraction pattern and develop a more realistic solution, we apply the extended refraction-diffraction equation, discussed in Section 7.2.2.

7.4.2.2 Refraction-diffraction solution with dissipation

Let us consider an idealized cylindrical island, shown in Figure 7.6. In order to solve the boundary value problem, defined by Eqs. (7.52)–(7.56), we divide the calculation area into two regions and then match the solutions at the boundary $r = b$ using continuity of the surface profile and of velocity.

Region 1 (constant water depth): $r \geq b$, $-h_0 \leq z \leq 0$, $0 \leq \Theta \leq 2\pi$

In this region the velocity potential $\Phi_1(r, \Theta, z, t)$ consists of the velocity potential of incident waves $\Phi_i(r, \Theta, z, t)$, and the velocity potential of scattering waves $\Phi_s(r, \Theta, z, t)$. Thus, we have:

$$\Phi_1(r, \Theta, z, t) = \Phi_i(r, \Theta, z, t) + \Phi_s(r, \Theta, z, t). \quad (7.62)$$

We represent a solution for scattering waves in the form of the Hankel function of the first kind $H_m^{(1)}(r)$. Following Morse and Feshbach (1953), and Massel (1981a), we pose the final expression for the potential Φ_1 in the form:

$$\Phi_1(r, \Theta, z, t) = \frac{-gH}{2\omega} \Re \left\{ e^{-i\omega t} \frac{\cosh k_0(z + h_0)}{\cosh k_0 h_0} \sum_{m=0}^{\infty} \epsilon_m i^{m+1} \cdot \left[\left(J_m(k_0 r) - \frac{J_m(k_0 b)}{H_m^{(1)}(k_0 b)} H_m^{(1)}(k_0 r) \right) + B_m \frac{H_m^{(1)}(k_0 r)}{H_m^{(1)}(k_0 b)} \right] \cos(m\Theta) \right\} \quad (7.63)$$

in which $J_m(kr)$ is a Bessel function of the first kind, $H_m^{(1)}$ is a Hankel function of the first kind, B_m is an unknown coefficient, and \Re is a real part of the complex quantity.

Region 2 (varying water depth): $a \leq r \leq b$, $-h_0 \leq z \leq -h_p$, $0 \leq \Theta \leq 2\pi$

When a reef top is covered totally by water, the distance a denotes the reef top radius. For $r < a$, the water depth is constant and equal to h_t . At very low tide, the reef top is dry and a conical island is formed; consequently, at $r = a$ a total reflection is assumed.

On the reef slope, the gradient of water depth is large. Therefore, the classical refraction solution given above is approximate only. To include the diffraction effects, the extended refraction-diffraction equation (7.23) is used. Thus, (Massel, 1993b):

$$\Phi_2(r, \Theta, z, t) = \frac{-gH}{2\omega} \Re \left\{ e^{-i\omega t} \frac{\cosh k(z + h)}{\cosh kh} \sum_{m=0}^{\infty} \epsilon_m i^{m+1} \Phi_m(r, \Theta) \right\}, \quad (7.64)$$

where:

$$\Phi(r, \Theta) = R_m(r) \cos(m\Theta). \quad (7.65)$$

The function $R_m(r)$ is a solution of the following equation:

$$\frac{d^2 R_m}{dr^2} + \left[\frac{1}{r} + \frac{\nabla C C_g}{C C_g} \frac{dh}{dr} \right] \frac{dR_m}{dr} + \left[k^2(1 + \psi) - \frac{m^2}{r^2} \right] R_m = 0, \quad (7.66)$$

where m is a separation constant ($m = 0, 1, 2, \dots$), and ψ is a function of kh , given by Eq. (7.24). For a dry reef top we assume that the island coastline ($r = a$) is fully reflecting, and at $r = b$ continuity in potential Φ and its first derivative with respect to r , is applied.

In the underwater shoal case, for $r < a$ and $h = h_t$, the solution takes the form:

$$\Phi_3(r, \Theta, z, t) = \frac{-gH}{2\omega} \Re \left\{ e^{-i\omega t} \frac{\cosh k_t(z + h_t)}{\cosh k_t h_t} \sum_{m=0}^{\infty} \epsilon_m i^{m+1} A_m \frac{J_m(k_t r)}{J_m(k_t a)} \cos(m\Theta) \right\}. \quad (7.67)$$

At $r = a$ and $r = b$, the continuity in potential Φ and its first derivative with respect to r , are used.

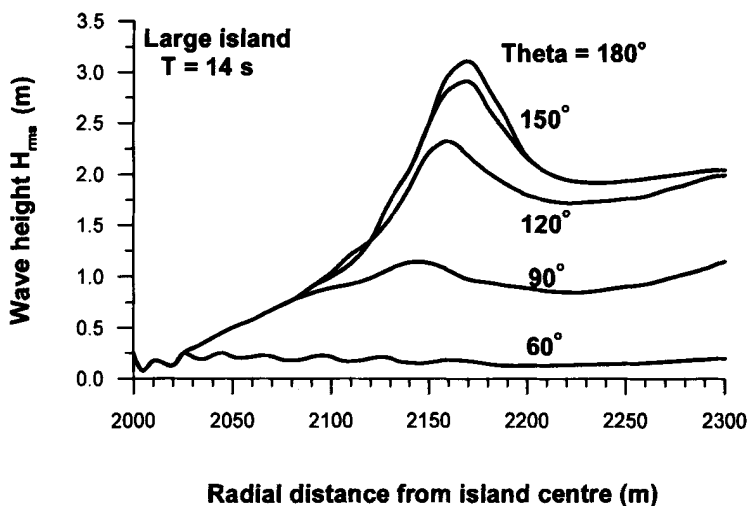


Figure 7.8: Attenuation of waves along various radii for island given in Fig. 7.7.

Using the results of Section 7.2.2.2, we adopt an equation governing also the wave breaking as:

$$\frac{d^2 R_m}{dr^2} + \left[\frac{1}{r} + \frac{\nabla C C_g}{C C_g} \frac{dh}{dr} \right] \frac{dR_m}{dr} + \left[k^2 (1 + \psi) - \frac{m^2}{r^2} + i\gamma k \right] R_m = 0. \quad (7.68)$$

An example of the calculation, for the same reef as in Fig. 7.7, is shown in Fig. 7.8 for several azimuths and incident wave height $H_{rms0} = 2.0$ m.

7.4.3 Scattering of waves by a group of islands

The basic effect of islands bordering the coastline is a blockage of certain directions of the possible wave approach in the lee of the islands. In some cases, due to the presence of numerous islands (reefs) with complicated cross sections, only a few 'windows' of exposure to deep ocean waves are open at a given coastal location.

In the simpler case of an ocean of constant water depth having arbitrary distributed circular islands with vertical bottom slopes, the sheltering problem reduces to the diffraction problem for a system of circular contours.

Observations of wave shadows induced by islands of arbitrary shape are not numerous. The most comprehensive are probably these obtained in the field experiment, carried out in the Southern California region, to evaluate a numerical model of the sheltering of gravity waves by offshore islands (Pawka, 1983; Pawka et al., 1984). The frequency and directional spectra measured in the deep ocean were used as input to the sheltering model and the results were compared with coastal observations.

The model employs the method of refraction of a continuous spectrum when (see Eq. (6.9)):

$$C^2 C g \hat{S}(\omega, \Theta) = \text{constant along a ray.} \quad (7.69)$$

The ray path is constructed from coastal sites through the island shoals into the deep ocean. The resulting two-dimensional spectrum at a given location $\hat{S}_l(\omega, \Theta_l)$ can be written as follows:

$$\hat{S}_l(\omega, \Theta_l) = \frac{1}{2\Delta_l} \int_{f(\Theta_l - \Delta\Theta_l)}^{f(\Theta_l + \Delta\Theta_l)} \hat{S}_0(\omega, \Theta_0) \frac{d\Theta_l}{d\Theta_0} d\Theta_0, \quad (7.70)$$

in which $\hat{S}_0(\omega, \Theta_0)$ is a deep ocean spectrum, the angles Θ_l and Θ_0 are related by the transformation $\Theta_0 = f(\Theta_l)$, and $2\Delta_l$ is the fine resolution bandwidth. If $d\Theta_l/d\Theta_0$ is relatively constant over the integration range, Eq. (7.70) simplifies as:

$$\hat{S}_l(\omega, \Theta_l) \approx \frac{1}{\Delta_l} \int_{f(\Theta_l - \Delta\Theta_l)}^{f(\Theta_l + \Delta\Theta_l)} \hat{S}_0(\omega, \Theta_0) d\Theta_0. \quad (7.71)$$

The application of Eq. (7.71) assumes that the singularities in $d\Theta_l/d\Theta_0$ are localized and integrable. The fine scale (0.1 to 0.2°) values of spectrum $\hat{S}(\omega, \Theta_l)$ are averaged into 1° directional bands. Rays which intercept the islands are terminated, leaving gaps in the coastal directional spectra. The model predictions well agree with data at Torrey Pines Beach in a limited frequency range where the unimodal deep ocean spectrum is appropriate. However, strongly bimodal directional spectra at a low frequency can occur in the coastal zone in response to a deep ocean swell.

For the Great Barrier Reef, the 'porosity' of the reef matrix or density of reefs varies, from almost complete barrier sections to wave penetration in the northern sections, to more porous in the central section, where the distances between individual reefs are quite substantial. The Seasat altimeter data (Young, 1989) shows that isolated reefs cause a significant reduction in wave height for many kilometers on either side of the reef itself. Hence, the Great Barrier Reef which appears quite porous, still acts as a very effective wave barrier.

7.5 Prediction of waves on island (reef) archipelagoes

At present, the predictions of the interaction of waves and coral reef or island archipelagoes are still mostly based on observations. Lee and Black (1978), and Gerritsen (1981), reported on the wave-induced processes dominated by a longer period swell occurring on a fringing reefs in Hawaii. The most of the experimental data of waves on island (reef) archipelagoes has been collected in the Great Barrier Reef area (Wolanski, 1986; Young, 1989; Hardy et al., 1990; Massel, 1994). These observations provide information on wave climate only at some individual points. More comprehensive

information may be obtained by the use of numerical wave prediction models. Such models must be quite sophisticated to be capable of accurately representing the complex bathymetry of the GBR, strong nonlinear effects which may occur in the shallow water over reefs and the temporal and spatial changes of a tropical cyclone wind field.

A tropical cyclone is a large scale atmospheric disturbance, having an organized horizontal motion over an area of more than a thousand kilometers in diameter, but significant vertical motion only in the lowest few kilometers. Tropical cyclones develop from tropical depressions which occur during middle to late summer in the equatorial regions of both hemispheres. Globally, just over 60% of these tropical depressions become tropical cyclones, to make an average of about fifty such cyclones annually (Fendell, 1974). Seventy-five per cents of these cyclones occur in the Northern Hemisphere.

Usually a cyclonic wind is represented in the form of a two-dimensional vortex, characterized by the central pressure, radius to maximum wind, velocity of forward movement, direction of forward movement, and the position of the storm center. The position of a tropical cyclone is usually known approximately only, with an accuracy of ~ 25 km.

Young and Hardy (1993) used the second generation spectral model (Sobey and Young, 1986) to predict the wave parameters during the passage across the Great Barrier Reef, of tropical cyclone *Aivu* in April 1989. The model is based on the radiative transfer equation (2.185). The source function \hat{Q} is a sum of atmospheric input from wind \hat{Q}_2 , nonlinear interaction between spectral components \hat{Q}_{nl} , dissipation due to white capping and bottom friction \hat{Q}_{dis} . The processes of propagation, shoaling, and refraction, are included in the left-hand side of the equation (2.185). However, the diffraction of waves around the particular reefs and nonlinear processes of wave transformation over the reefs are omitted. Therefore, the model is better for predicting wave fields in larger scale, inter-reef regions rather than in the vicinity of reefs.

In order to assess the influence of the reef matrix on the wave field, two independent hindcasts were performed. In the first run, all individual reefs were represented by land, while in the second run all reefs were removed. The comparison of these two runs with recorded data indicates that individual reefs appear to represent an almost complete barrier to wave penetration, even at high tides. However, wave energy penetrates through the inter-reef gaps. Although such inter-reef gaps may appear large in comparison to the size of individual reefs, wave attenuation is still significant.

7.6 Interaction of waves with coral reef bottoms

In contrast to sandy coasts, coral reef slopes and reef platforms are densely populated by flora and fauna. The various species of coral predominate. Correlations between water motion and coral zonation on reef slopes have long been recognized by reef scientists. Recent studies have also identified wave climates associated with coral

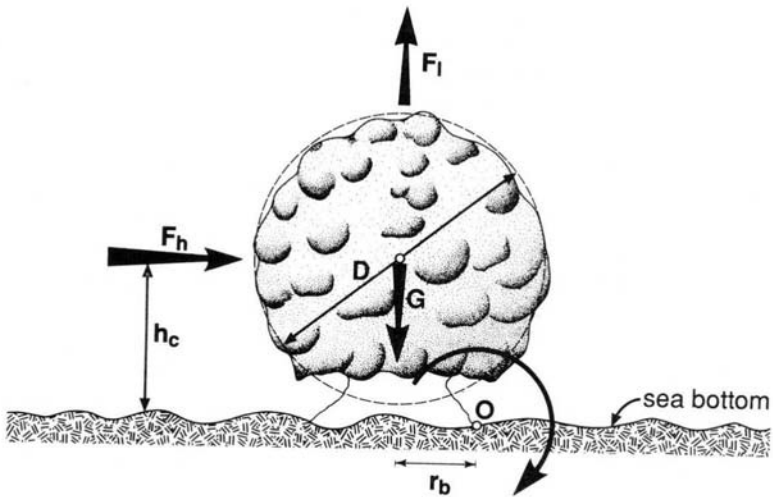


Figure 7.9: Wave forces on a massive coral.

community structures, and some demographic implications of cyclones on localized coral populations have been investigated (Massel and Done, 1993).

In general, the forces transmitted by waves onto the reefs and corals are a function of horizontal components of orbital velocity u and acceleration a , induced by waves of height H and period T , at given depth of z . Therefore, the magnitude and frequency of wave forces depend strongly on the wave regime on the reef slope and the coral's response depends on its weight, size and shape. To illustrate the modelling of the impact of cyclone waves on coral stability we assume that an individual massive coral is of genus *Porites*, with an idealized spherical shape (see Fig 7.9). We also adopt average density and annual radial growth rate values as reported by Lough and Barnes (1992), i.e., mean skeletal density $\rho_s = 1.45 \text{ g/cm}^3$ and mean coral annual radial growth rate $= 0.011 \text{ m/year}$.

7.6.1 Forces on coral

For objects such as corals that are small compared to the incident wave length, it may be assumed that the presence of the object has no substantial effect on the wave, and that the flow field at the center of the object extends to infinity. The total force vector can then be represented as the sum of three components: inertia, drag and lift:

$$\vec{F} = \vec{F}_i + \vec{F}_d + \vec{F}_l, \quad (7.72)$$

in which \vec{F}_i is an inertia force acting in the horizontal direction, \vec{F}_d is a drag force, directed horizontally, and \vec{F}_l is a lift force acting vertically. The component due to

inertia is proportional to the local fluid acceleration, while the components due to drag and lift are proportional to the square of velocity of the fluid (Milne-Thomson, 1960). If a coral is to remain stationary and attached to the surface plane, the force \vec{F} must be resisted by the coral's weight and adhesion to the substratum.

Inertia force

The inertia component is obtained as a product of water mass $\rho_w V$ (where ρ_w is the density of water, and V is the displaced volume of the body) and the fluid acceleration a . Therefore, we have:

$$\vec{F}_i = C_m \rho_w V a \vec{i}_x, \quad (7.73)$$

in which \vec{i}_x is a unit vector in the x direction, and the proportionality coefficient C_m is called *the inertia coefficient*. The empirical coefficient C_m depends on the body shape and the Reynolds number $\text{Re} = \frac{uD}{\nu}$. For a sphere subjected to unbounded accelerating fluid, $C_m = 1.5$. However, because coral heads rest on the reef which influences the streamline pattern around them, we adopt a more fundamental approach based on the kinetic energy concept. Therefore, we represent the inertia force \vec{F}_i as a summation of two components, viz.: the product of the displacement volume and the pressure gradient of the incident wave, and $\Delta \vec{F}_i$ due to the mass of the sphere. Thus, we obtain:

$$\vec{F}_i = \frac{4}{3} \pi \rho_w \left(\frac{D}{2} \right)^3 a \vec{i}_x + \Delta \vec{F}_i. \quad (7.74)$$

To calculate $\Delta \vec{F}_i$ in Eq. (7.74), we first evaluate the kinetic energy of fluid acting on a sphere as (Milne-Thomson, 1960):

$$E_k = \frac{\pi}{3} \rho_w \left(\frac{D}{2} \right)^3 \left(1 + \frac{3}{16} \frac{\left(\frac{D}{2} \right)^3}{h_c^3} \right) u^2, \quad (7.75)$$

in which h_c is the distance of the center of the sphere from the reef surface, i.e. $h_c = \frac{D}{2}$. The component ΔF_i is related to kinetic energy in the following way (Kochin et al., 1963):

$$\Delta F_i = \frac{\partial^2 E_k}{\partial u \partial t} = \frac{19}{24} \pi \rho_w \left(\frac{D}{2} \right)^3 a \vec{i}_x. \quad (7.76)$$

The acceleration a is calculated at the point corresponding to the center of the sphere. Substituting Eq. (7.76) into Eq. (7.74) we finally obtain:

$$\vec{F}_i = \frac{51}{24} \pi \rho_w \left(\frac{D}{2} \right)^3 a \vec{i}_x = 1.57 \rho_w V a \vec{i}_x. \quad (7.77)$$

Thus, the proximity of the bottom causes only a slight change of C_m .

Drag force

The drag force \vec{F}_d , due to a wave-induced flow, is usually represented as:

$$\vec{F}_d = \frac{1}{2} \rho_w C_d \pi \left(\frac{D}{2} \right)^2 |u| u \vec{i}_x. \quad (7.78)$$

The *drag coefficient* C_d depends on the flow regime past a sphere, indicated by the Reynolds number \mathbf{Re} . For typical storm conditions ($T \approx 8s$, $H \approx 2$ m) and for a sphere of diameter $D = 2$ m, we obtain $\mathbf{Re} \approx 1.5 \cdot 10^6$. Experiments indicate that for this Reynolds number, $C_d \approx 0.45$ (Newman, 1977).

Lift force

Water flowing around a sphere speeds up as it passes along the sides and creates areas of low pressure. The flow around a sphere lying on a reef is not exactly symmetrical and a net force arises perpendicular to the flow. We represent it in a way similar to the drag force:

$$\vec{F}_l = \frac{1}{2} \rho_w C_l \pi \left(\frac{D}{2} \right)^2 u^2 \vec{i}_z, \quad (7.79)$$

in which \vec{i}_z is the unit vector in the z -axis direction, i.e. vertical to the reef surface. The experimental value $C_l \approx 0.15$ was found for spheres by Hoerner (1965). The adopted values of C_d and C_l do not include the influence of coral roughness, which is very difficult to assess under natural conditions. However, experiments with rough cylinders indicate that roughness of surface does not change the C_d and C_l values dramatically (Sarpkaya and Isaacson, 1981).

Total force

After substituting Eqs. (7.77), (7.78) and (7.79) into Eq. (7.72), we obtain the total force vector:

$$\begin{aligned} \vec{F} = & \left[\frac{51}{24} \pi \rho_w \left(\frac{D}{2} \right)^3 a + \frac{1}{2} \pi \rho_w C_d \left(\frac{D}{2} \right)^2 |u| u \right] \vec{i}_x + \\ & + \frac{1}{2} \pi \rho_w C_l \left(\frac{D}{2} \right)^2 u^2 \vec{i}_z. \end{aligned} \quad (7.80)$$

A trade-off associated with the growth of the coral head may be quantified as the relative importance (β) of the drag force and the inertia force:

$$\beta = \frac{|\vec{F}_d|}{|\vec{F}_i|} \approx 0.034 K, \quad (7.81)$$

in which $K = \frac{uT_s}{D}$ is the Keulegan–Carpenter number (Sarpkaya and Isaacson, 1981). For storm conditions ($H \approx 2$ m) and a large coral diameter ($D \approx 2$ m), the ratio $\beta \approx 0.1$ and the drag force is thus only a small percentage of the inertia force. A similar conclusion is true for the ratio of the lift force to the inertia force. However, for small corals, the drag and lift forces constitute a substantial part of the total force and cannot be neglected. For example, if $D = 0.2$ m, we obtain $K \approx 10\pi$ and $\beta \approx 1.0$.

Resistance forces

Resistance forces are due to coral weight and its adhesion to the substratum. Attachment strength depends on both the area and the strength of the adhesion. For massive *Porites* corals, the ratio of basal area to maximum cross-section of area δ , varies with coral diameter. Assuming that the basal area is a circle of radius r_b , and using data on colony forms reported by Done and Potts (1992), we obtain the following relationship:

$$\delta = \frac{2r_b}{D} \approx \exp(-1.083 D^{0.9}). \quad (7.82)$$

Multiplying the attachment area A_b by the breaking shear strength of the skeleton, σ_s , we obtain the force that must be exceeded by wave-induced horizontal forces to dislodge the coral from the substratum:

$$\frac{4}{3} \frac{F_i + F_d}{A_b} \geq \sigma_s \quad \text{or} \quad F_i + F_d \geq \frac{3}{4} A_b \sigma_s. \quad (7.83)$$

The coefficient $4/3$ reflects the non-uniform distribution of shear stress across the basal area (Timoshenko and Gere, 1972). Experimental data on the breaking strength in shear σ_s are very rare and uncertain and depend on the porosity of material. We use an empirical formula from Ryskewitch (Wainwright et al., 1976) to obtain:

$$\sigma_s = \sigma_{s_0} \exp(-np), \quad (7.84)$$

in which σ_{s_0} is the strength of the non-porous matrix, p is the porosity and n is an empirical exponent. For our purposes we adopt the value $\sigma_{s_0} \approx 200$ MN/m², obtained by Chamberlain (1978). Assuming that the mean porosity of the skeleton is $\approx 60\%$, we obtain $\sigma_s \approx 10$ MN/m². Examination of the breaking condition (7.83) indicates that these shear forces alone cannot break the adhesion and that they are too small to dislodge the coral head, even when the basal area is only 1% of the maximum cross-sectional area (Massel and Done, 1993).

However, forces F_i and F_d also act above the base to induce an overturning moment about the neutral axis, which is perpendicular to flow direction and which passes through the center of the base (Fig. 7.9). The lift force F_l , and the weight of the coral head G , do not contribute to the overturning moment because they act in the vertical

plane through this center. However, the overturning moment lifts the upstream edge of the basal area, and forces down the downstream edge. This tendency creates tension at the upstream edge ($x = -r_b$) and compression at the downstream edge ($x = r_b$), which are superimposed on the compression stresses induced by the coral weight G and the lift force F_l . The resulting overturning moments, needed to break the coral head from the substratum, are:

$$\frac{G + F_l}{A_b} - \frac{\frac{1}{2}(F_i + F_d)D r_b}{I} \geq \sigma_t, \quad (7.85)$$

or

$$\frac{G + F_l}{A_b} + \frac{\frac{1}{2}(F_i + F_d)D r_b}{I} \geq \sigma_c, \quad (7.86)$$

in which σ_t is the breaking strength in tension, σ_c is the breaking strength in compression, I is the second moment of area for the base, i.e.

$$I = \frac{1}{4}\pi r_b^4, \quad (7.87)$$

G is the weight of the coral head, i.e.:

$$G = \frac{4}{3}\pi(\rho_s - \rho_w)g\left(\frac{D}{2}\right)^3, \quad (7.88)$$

in which ρ_w is the density of water and ρ_s is skeletal density.

Equation (7.85) expresses the failure condition due to an excess of coral strength in tension, and Eq. (7.86) gives the corresponding condition for compression. Conditions (7.85) and (7.86) were examined for water depths from 3 m to 12 m and for corals up to 3 m in size, under the assumption that the coral is attacked by waves of maximum height at a given water depth. The basal area was reduced by 20% and 75% for possible boring due to bioerosion. In each case, the calculations showed that such waves could not break massive coral from the substratum through the exceedance of coral strength in either tension or compression. It therefore appears that even a small amount of adhesion to a consolidated substratum is sufficient to prevent dislodgement. Therefore, it can be concluded that corals which are dislodged by storms are either unattached, or attached only to unconsolidated or weak substratum (Massel and Done, 1993).

Total force balance

For unattached corals, coral heads will overturn about point O (Fig. 7.9), and dislodge from substratum when:

$$F_x(t) \frac{D}{2} \geq F_v(t) r_b, \quad (7.89)$$

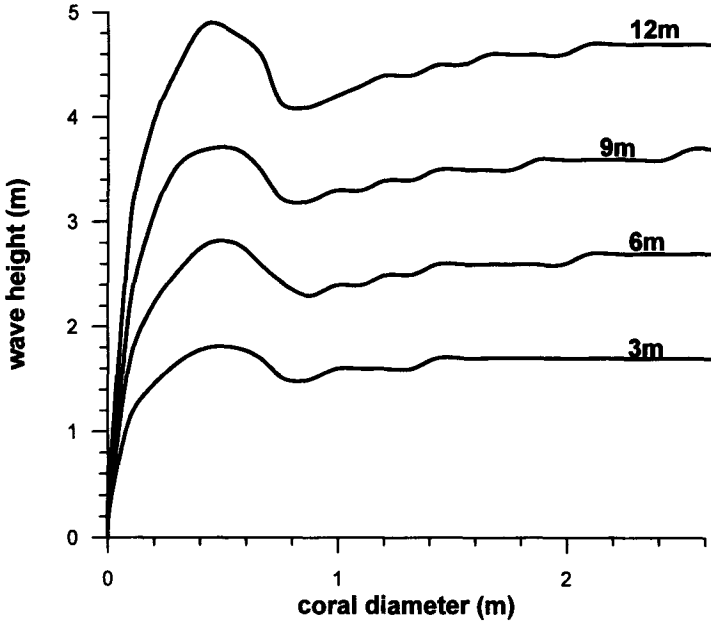


Figure 7.10: Threshold wave height versus coral diameter for various water depths.

where $F_x(t)$ is the total horizontal force, $F_v(t)$ is the total vertical force and r_b is an arm of the vertical force with respect to point O . Substituting all forces into Eq. (7.89) we obtain an equation for the threshold wave height H , which creates sufficient force to overturn the coral head, in a form:

$$\begin{aligned} \frac{1}{2} U_1^2 [C_d |\cos(\omega t)| \cos(\omega t)] + \delta C_l \cos^2(\omega t) H^2 - \\ - \left[\frac{51\pi}{24} \frac{D U_1}{T_p} \sin(\omega t) \right] H - \frac{2}{3} \frac{\rho_s - \rho_w}{\rho_w} g \delta D = 0, \end{aligned} \quad (7.90)$$

in which:

$$U_1 = \frac{\pi}{T_p} \frac{\cosh(kD/2)}{\sinh(kh)}. \quad (7.91)$$

An example of the dependence of threshold wave height on coral diameter for various water depths is given in Fig. 7.10.

As shown above, for larger coral heads and typical storm conditions, the inertia force is predominant and drag lift forces can be neglected. Thus, Eq. (7.90) can be

simplified considerably:

$$H \geq \frac{16\delta}{51\pi^2} \frac{\rho_s - \rho_w}{\rho_w} \frac{\sinh(kh)}{\cosh(kD/2)} g T_p^2. \quad (7.92)$$

Expression (7.92) indicates that for the threshold wave height, H depends only on parameter δ (see Eq. (7.82)) and on the coral head diameter through the function:

$$\frac{\sinh(kh)}{\cosh(kD/2)} \approx \frac{\sinh(kh)}{\left[1 + \frac{1}{2!} \left(\frac{kD}{2}\right)^2 + \dots\right]}, \quad (7.93)$$

However, the non-dimensional coral diameter $k\frac{D}{2} = \frac{\pi D}{L}$ is usually of a small quantity, much less than one. Therefore, we have:

$$\frac{\sinh(kh)}{\cosh(kD/2)} \approx \sinh(kh). \quad (7.94)$$

Thus, the height of an unbroken wave needed to dislodge an unattached coral is almost independent of the coral diameter. This rather unexpected result can be explained as follows: the inertia force depends on the product of coral mass (volume), which is proportional to the cube of its diameter, and water acceleration. Because coral weight is also proportional to the cube of diameter, the balance of the overturning and stabilizing forces involves only water acceleration at the coral center, parameter δ , which is weakly dependent on the coral diameter.

In another extreme case, if we neglect totally the inertia force, we obtain:

$$(C_d + \delta C_l) \frac{\pi^2 H^2}{T_p^2} \frac{\cosh^2 k(z+h)}{\sinh^2(kh)} \geq \frac{4}{3} \frac{\rho_s - \rho_w}{\rho_w} \delta g D. \quad (7.95)$$

7.6.2 Velocity field around coral

Let us consider the velocity potential Φ , close to the coral head, in the form (Milne-Thomson, 1960):

$$\Phi(x, y, z) = U x \left\{ 1 + \frac{D^3}{16} \left(\frac{17}{16} \frac{1}{r^3} + \frac{1}{r_1^3} \right) \right\}, \quad (7.96)$$

in which r and r_1 are the distances from the center of the sphere and its image in the bottom, respectively. Hence:

$$r = \sqrt{x^2 + y^2 + \left(z - \frac{D}{2}\right)^2} \quad \text{and} \quad r_1 = \sqrt{x^2 + y^2 + \left(z + \frac{D}{2}\right)^2}. \quad (7.97)$$

For simplicity, the origin of a coordinate system is taken as the point in which the sphere touches the bottom. There is only a weak dependence on the vertical coordinate, so the ambient velocity U is calculated at a level corresponding to the sphere center, i.e.:

$$U = \frac{\pi H}{T_p} \frac{\cosh\left(k\frac{D}{2}\right)}{\sinh(kh)}. \quad (7.98)$$

Velocity at the bottom is found simply by differentiation of the velocity potential $\Phi(x, y, z)$. In particular, for maximum velocity at the sea bottom, in the cross-section perpendicular to direction of flow, we obtain:

$$u_{max}(y) = \frac{\pi H}{T_p} \frac{\cosh\left(k\frac{D}{2}\right)}{\sinh(kh)} \left\{ 1 + \frac{33}{32} \left(1 + \left(\frac{2y}{D} \right)^2 \right)^{-\frac{3}{2}} \right\}, \quad (7.99)$$

in which y is a distance from the plane of symmetry of flow. The term in brackets represents the enhancement of wave-induced velocity due to the presence of the sphere. For wave height $H = 2.0$ m, wave period $T_p = 7.0$ s, water depth $h = 6.0$ m, coral diameter $D = 1.5$ m, the ambient velocity is ≈ 1.05 m/s, while the velocity at the coral base edge is ≈ 1.77 times higher, and the velocity at a distance equal to the coral radius is 1.38 times higher than the ambient velocity.

7.6.3 Probability of coral dislodgement or persistence

The threshold wave height H , needed to overturn a coral of a given diameter, is associated with the specific return period $T_R(H)$ (or average time between storms) of storm or cyclone conditions, which induce waves of this height. If a coral occupies a location for L years, the *encounter probability* $E(L, T_R)$ for a wave exceeding height H , during the L years of coral life (Borgman, 1963), is:

$$E(L, T_R) = 1 - \left(1 - \frac{1}{T_R} \right)^L. \quad (7.100)$$

The encounter probability E is the probability that the design wave is equalled or exceeded during a period L . Thus, the probability of survival of a massive coral to a given age at a given water depth P can be defined as:

$$P = 1 - E = \left(1 - \frac{1}{T_R} \right)^L. \quad (7.101)$$

In habitats exposed to both short period waves and swell, survival probability generally decreases with increasing coral age and the rate of this decrease depends strongly on the water depth. An example of probability of survival of massive corals situated on the exposed reef slope, at various water depths, is given in Fig. 7.11.

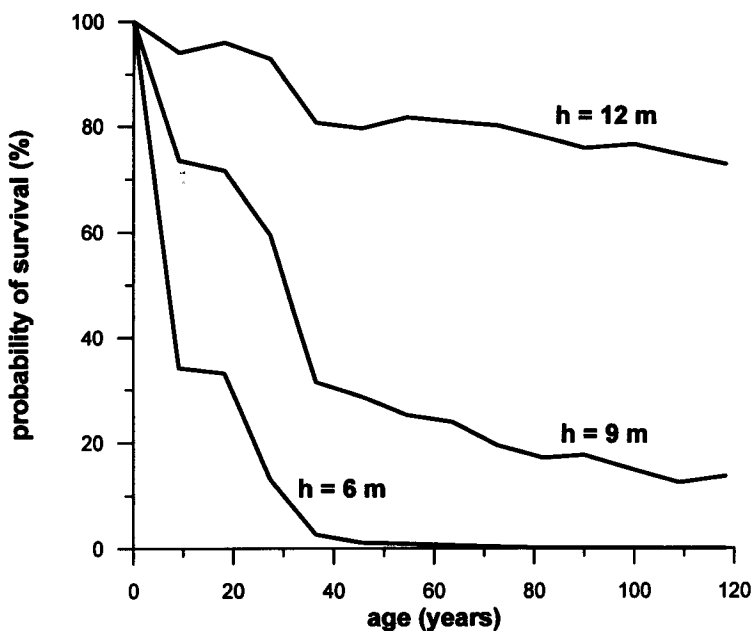


Figure 7.11: Probability of survival as a function of coral age for three water depths.

For corals of 20 years of age, the probability of survival is equal to $\sim 95\%$ at water depth $h = 12$ m and only $\sim 30\%$ at water depth $h = 6$ m.

Chapter 8

Long-Term Statistics for Ocean Surface Waves

8.1 Introduction

A key step in establishing the structural loading on offshore and coastal structures is the proper estimation of design wave parameters. These parameters should be related to the extreme waves in a longer period of time (50 or 100 years) rather than to waves observed on a daily base. Unfortunately, the experimental data on wave heights and periods are available only for a much shorter duration. Thus, some extrapolation techniques are indispensable.

In the first Sections we review visual and instrumental wave data and then discuss the three different prediction procedures for long-term statistics of ocean waves.

In the second part of the Chapter, variability of ocean waves in various regions of the World Ocean is presented. Fortunately at present, the satellite measurements provide detailed information on waves also in areas where surface observations are not available (for example, the southern part of the World Ocean).

8.2 Visual observations of wave heights

Historically visual observations of waves and wind were the first basic source of ocean wave statistics. Although another type of wave data is now available, visual observations are still the source which covers most of the ocean areas. Initially, the state of the sea was represented using the Beaufort scale. In fact the Beaufort scale, with a grading from 0 to 12, gives the gradation of wind speed associated with some description of the sea state. However, there is not a straightforward relationship between wind speed and wave height. Only in 1947 did the World Meteorological Organisation introduce the international code for the observation of wind and waves.

There are two main sources of visual data of waves, i.e. data from merchant ships

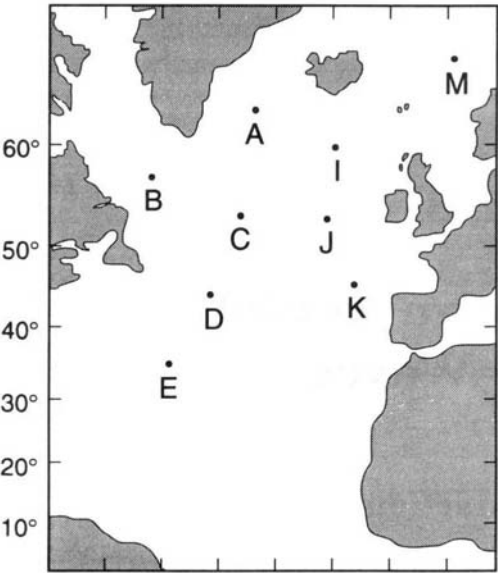


Figure 8.1: Weather ships in the North Atlantic.

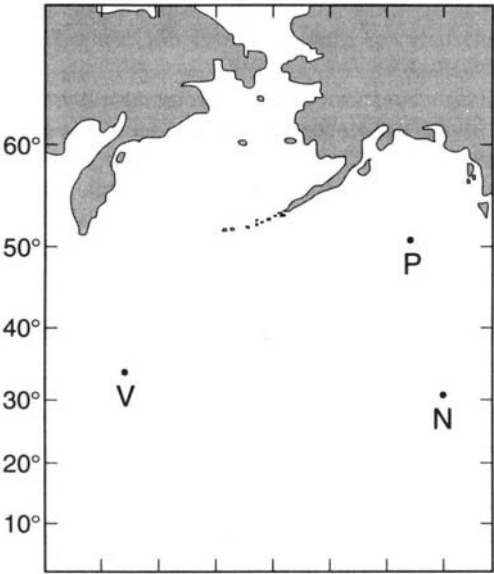


Figure 8.2: Weather ships in the Pacific.

and observations in weather ships (Ocean Weather Stations – OWS). Merchant ships are generally expected to avoid bad weather, thus being subjected to less severe wave conditions than weather ships. A map of the weather ship stations in the North Atlantic is shown in Fig. 8.1. The stations cover most of the ship routes between Europe and North America. The Pacific Ocean is not so well documented and only a few stations operate in the northern part of the Pacific (Fig. 8.2). Major sources of visual data are the compilations made by Hogben and Lumb (1967), Hogben et al. (1986), and Hogben (1988). The book *Global Wave Statistics* by Hogben et al. (1986) contains wave data covering a global grid of 104 sea areas. This provides a very large number of visual observations of both waves and wind reported from ships in service all over the world.

In the analysis of experimental data two parametric models with a relevant statistical relationship have been used. The first of these is of the joint frequency distribution of wave height and wind speed. The second synthesizes the joint frequency distribution of wave height and period. The modelling of joint frequency distribution is based on two formulas, each containing three parameters which are determined by best fitting of the joint wave height and wind speed statistics, i.e.

$$\bar{H} = (H_1^2 + H_2^2)^{1/2} = [(aU^n)^2 + H_2^2]^{1/2}, \quad (8.1)$$

in which \bar{H} is a mean wave height observed in each of the 12 classes of the Beaufort scale, used for observing wind speed U ; and H_2 is a mean swell height, while a and n are coefficients in a formula for the mean height of a wind generated waves $H_1 = aU^n$.

The modelling of the wave height and period statistics is based on a 'bivariate log-normal' distribution and involves five modelling parameters, two depending only on wave height and the others having dependence on wave period.

The final results of the analysis of visual wave and wind data, for each of the 104 sea areas, are presented in tables corresponding to the data covering the whole year and four seasons (Hogben et al., 1986). Each table contains data in the form of nine probability distributions of wave height and period, corresponding to all 45° sectors.

There are two sets of visual observations, i.e. those reported by voluntary ships and those collected on weather ships. The voluntary ships collect data along the trade routes used by merchant ships, where the need for information is the greatest. Because observations are made in many different ship types and sizes, there is a large degree of variability. This variability leads to a randomization of the error and results in a lack of bias of mean values. The comparison of visual wave heights at weather ships with visual wave height at voluntary observing ships, collected in the vicinity of given weather ships, yields the relationship in the form (Soares, 1986a):

$$H_{OWS} = 1.02 + 0.89 H_{vos} \text{ (m)}, \quad (8.2)$$

in which H_{OWS} is a wave height visually observed in weather ships (OWS) and H_{vos} is a wave height provided by voluntary observing ships.

8.3 Visual observations versus instrumental data

Comparative studies between visual observations and instrumental wave data have been reported since the weather ships were equipped with shipborn wavemeters. Most of these studies are related to the North Atlantic. In Table 8.1 the resulting regression equations between measured (H_s) and visual significant wave height (H_v) are summarized (Soares, 1986a).

Since these equations were obtained from data belonging to the same population, they can be combined together to produce a final equation in the form:

$$H_s = 1.47 + 0.84H_v \quad (\text{m}), \quad (8.3)$$

in which H_s is a measured significant wave height. Compiling a data base of 3901 simultaneous wave measurements and observations at OWS (*India*) in the North Atlantic, yields regression line in the form (Jardine, 1979):

Table 8.1: Regression equations between measured (H_s) and visual wave heights (H_v).

Source of data	$H_s = AH_v + B$		Number of observations	Correlation coefficient
	A	B		
Cartwright (1964)	0.88	1.28	892	0.86
Hogben and Lumb (1967)	0.88	1.23	317	0.86
Nordstrom (1969)	0.85	1.51	269	0.83
Data: Hogben and Lumb (1967)				
Hoffman and Miles (1976)	0.89	1.25	323	-
Soares (1986a)	0.85	1.62	323	0.76
Data: Hoffman and Miles (1976)				
Soares (1986a)	0.62	2.22	93	0.39
Data: Hoffman (1980)				
Soares (1986a)	0.82	1.72	416	0.72
Data: two above data sets				
Jardine (1979)	0.89	0.50	3901	
Hoffman and Walden (1977)	0.78	2.13	660	-
Hogben (1970)	0.52	1.19	527	0.73
Quayle and Changery (1982)	1.38	-0.1	58	0.94
Final results (Soares, 1986a)	0.84	1.47	1577	
(all data)				

$$H_v = 0.22 H_s^2 + 0.78 H_s + 0.83. \quad (8.4)$$

Instead of using a maximum of the observed sea and swell significant wave heights, Jardine determined the observed wave height as the square root of the sum of the squares of the two components, whenever they existed. Regression equation (8.4) is in agreement with that obtained by Davidan et al. (1985) using the 1968 and 1969 year data from weather ships I, J, K (total number of observations: 2149).

In addition to those North Atlantic and Pacific OWS studies a few other comparisons between observed and measured wave heights in coastal waters or small seas are available. In particular, Wahl (1974) reported data from three lightships stationed in Swedish coastal waters. As all wave heights were smaller than 3 m, therefore, his regression lines may be of interest for areas of very small wave heights only. Other relationships between observed and measured wave heights are published for the Great Lakes (Liu and Kessenich, 1976), Mediterranean Sea (Bowman, 1979), and the east coast of the Baltic Sea (Davidan et al., 1985).

8.4 Visual observations of wave periods

Wave period is another wave parameter of which knowledge is required in ocean engineering and oceanography. The average period of a sea state governs the response of ocean structures to wave excitation through the relationship between the average wave period and the natural period of the structural response. Even a slight change of wave period is enough to make a structure very sensitive, or almost insensitive to wave excitation. The data on wave periods are very few and the degree of confidence of the data is usually unknown.

A summary of regression equations, between measured an average wave period (T_a) and visual period (T_w), is given in Table 8.2 (Soares, 1986 b). The T_w denotes the visually observed period in weather ships. Although the final regression line:

$$T_a = 0.31 T_w + 5.61, \quad (8.5)$$

is applicable to any of the ocean weather stations, one should be aware that this calibration relation represents only predominant weather conditions. There are indications that systematic differences may exist between the observations made at the various ocean stations (Dorrestein, 1955).

An examination of data, published by Hogben and Lumb (1967), provides an additional relationship between wave period (T_v), resulting from visual observations at voluntary observing ships, and wave period observed at ocean weather stations (T_w) (Soares, 1986 b), as:

$$T_w = 0.20 T_v + 6.58. \quad (8.6)$$

Substituting Eq. (8.6) into Eq. (8.5) gives:

$$T_a = 0.06 T_v + 7.56. \quad (8.7)$$

Table 8.2: Regression equations between measured average wave period (T_a) and visual period (T_w).

Source of data	$T_a = AT_w + B$		Correlation coefficient	Number of obs.	Standard error
	A	B			
Cartwright (1964)	0.37	5.19	0.48	834	1.12
Hogben and Lumb (1967)	0.32	4.70	0.50	294	1.00
Soares (1986b) Data: Hoffman (1980)	0.21	6.15	0.38	75	1.24
Soares (1986b) (Data: <i>Famita</i>)	1.17	1.30	0.75	1931	
Final results (Soares, 1986b)	0.31	5.61	0.42	1203	1.18

The average period T_a is practically insensitive to the visually observed period T_v , reflecting the cumulative effect of two poorly correlated data sets. This effect can probably be attributed to poor data quality. On the other hand, the visually observed period should, in principle, be more accurate than wave height because the former is determined by a stopwatch, while the other is only estimated. Therefore, the lack of correlation in the data sets might not be representative of the general situation. Soares (1986b) examined this conclusion using the simultaneous measurements and observations at the rescue vessel *Famita* in the North Sea. The resulting regression equation is:

$$T_a = 1.7 T_v + 1.30, \tag{8.8}$$

with a correlation coefficient of 0.75. The above correlation indicates that observed wave periods can be as reliable as observed wave heights.

Davidan et al. (1985) compared the visual observation of wave period T_v with mean period resulting from measurements by Russian pressure-type GM-46 wavemeters. For $T_v \leq 7$ s, the ratio $\frac{T_a}{T_v} \approx 1.0$, but for longer periods this ratio decreases and at $T_v = 13$ s and $T_v = 15$ s is equal to 0.78 and 0.73, accordingly. The standard deviation is equal to ± 1 s, for short waves, and ± 2.5 s for longer waves.

8.5 Long-term distributions of wave heights

The design of marine structures requires a detailed knowledge of extreme wave or sea state, corresponding to a chosen return period (for instance 50, 100 or 1000 years). In

an ideal situation, we should be able to use the data within such a time which include variations of possible periodic climate. However, usually only the time series of much shorter duration are available. The general procedure for estimating extreme values may be grouped into three categories, depending on available initial data (Ochi, 1990): a) the initial probability distribution is known, b) the initial probability distribution is unknown, and c) the largest wave heights (periods), regularly sampled during a certain period of time, are available. A typical example of the first category is the wave height in deep water for which the Rayleigh probability distribution is usually considered. In such a case, the probability distribution of the extreme values can be found by applying the analytical formulations given in Section 4.3.

8.5.1 The initial probability distribution is unknown

There is no theoretical basis for selecting any particular probability distribution to represent the observed data. Therefore, the estimation of the extreme values is

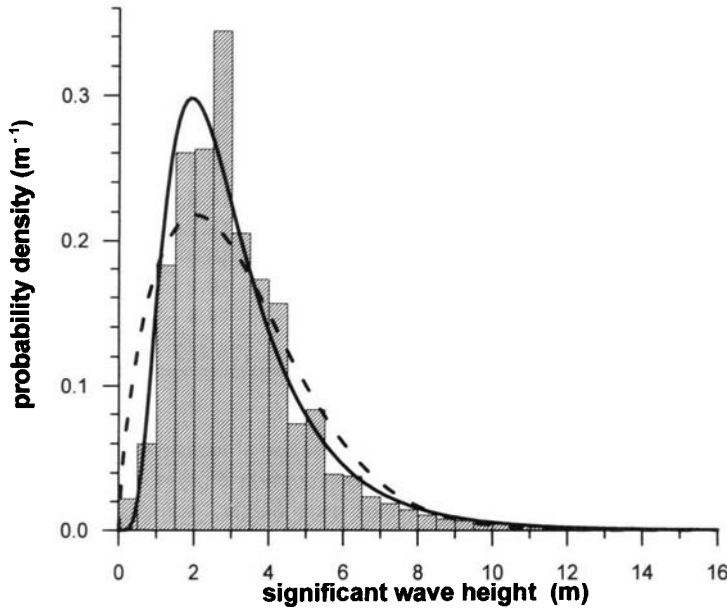


Figure 8.3: Probability density distributions for wave heights observed in the North Atlantic; bar graph denotes experimental data, ——— log-normal distribution, - - - Weibull distribution.

Table 8.3: Significant wave height data for period 1949–1982 observed in the North Atlantic (sector: 30°N–60°N, 3°W–30°W). Data from Hogben (1988).

Significant wave height (m)	Number of observations	Significant wave height (m)	Number of observations
0 – 0.5	1930	10.1 – 10.5	392
0.6 – 1.1	5253	10.6 – 11.0	295
1.1 – 1.5	16032	11.1 – 11.5	183
1.6 – 2.0	22824	11.6 – 12.0	75
2.1 – 2.5	23036	12.1 – 12.5	101
2.6 – 3.0	30161	12.6 – 13.0	87
3.1 – 3.5	18032	13.1 – 13.5	76
3.6 – 4.0	15158	13.6 – 14.0	15
4.1 – 4.5	13692	14.1 – 14.5	30
4.6 – 5.0	6425	14.6 – 15.0	19
5.1 – 5.5	7306	15.1 – 15.5	26
5.6 – 6.0	3420	15.6 – 16.0	13
6.1 – 6.5	3295	16.1 – 16.5	8
6.6 – 7.0	2063	16.6 – 17.0	8
7.1 – 7.5	1637	17.1 – 17.5	4
7.6 – 8.0	1258	17.6 – 18.0	0
8.1 – 8.5	940	18.1 – 18.5	1
8.6 – 9.0	709	18.6 – 19.0	1
9.1 – 9.5	594	19.1 – 19.5	0
9.6 – 10.0	356	19.6 – 20.0	3
Total number of observations 175,459			

carried out by approximate methods, through the use of measured (or observed) data. First of all, the initial probability distribution function $F(x)$ is constructed from the observed data. Then, the probable extreme wave height, expected to occur in large number of observations, N , is given as:

$$Q(x) = 1 - F(x) = \frac{1}{N}, \quad (8.9)$$

The extreme value in a desired period of time can be determined by extending the probability distribution function. At the same time it is worthwhile examining the coincidence of the observational data with some known, theoretical distribution functions, such as the log-normal or the Weibull distribution. To illustrate the extreme

wave height distribution we use the data reported by Hogben (1988) in his Table 1. Significant wave heights were observed in the North Atlantic in the sector: 30°N–60°N, 3°W–30°W, during the period 1949–1982. The sample of data is shown in Table 8.3, and the experimental probability density distribution is given in Fig. 8.3. The mean significant wave height for a period of observation, is equal to 3.17 m, and the standard deviation of scatter around this value is 1.78 m. Using these two values, the shape parameters A and B (see Table 8.4) of the log-normal distribution were determined to be $A = 0.999$ and $B = 0.341$. Comparison shows that the log-normal distribution provides a satisfactory approximation of the visually observed data, except near the peak where the theoretical value is strongly affected by a high occurrence of waves in the range 2.5 – 3.0 m. However, from this figure it is impossible to make any conclusions on the behaviour of wave height in the extreme range.

To estimate the parameters of extreme waves, the extrapolation of the instrumental or visually observed data beyond the observation range is usually needed. The extrapolation procedure is carried out in the following steps:

- a) A plotting formula is used to reduce the data to a set of points describing the long-term probability distribution.
- b) The points are plotted on an extreme value probability paper, corresponding to a chosen probability distribution function.
- c) A straight line is fitted through the points, and extrapolated to a design value corresponding to a chosen return period or a chosen encounter probability.

Various probability papers are available with scales constructed to meet the requirement of a straight line. In these scales, the y is related to the probability distribution function $F(x)$, and the linear abscissa scale x is related to the variate H . Scale relationships for the long-term probability distribution were listed by Isaacson and Mackenzie (1981). For illustration, we apply log-normal scale relationships to data listed in Table 8.3. Thus, we plot the experimental probability distribution function on a log-normal grid and compare it with the log-normal distribution, which is represented on this grid as a straight line (Fig. 8.4). As can be seen in this figure, the data appear to follow the log-normal distribution for the probability distribution function approximately up to 0.99. For larger wave heights, the log-normal distribution underestimates the cumulative distribution (or overestimates the probability of exceedance of large wave heights). In particular, the probability of exceedance of the significant wave height $H_s = 18$ m, resulting from experimental data, is equal to $2.6 \cdot 10^{-5}$, while the probability predicted using the log-normal distribution is equal to $5.9 \cdot 10^{-4}$. When the wave height increases, the gap between experimental probabilities resulting from log-normal distribution increases too.

Experimental data were also plotted on the Weibull grid, as shown in Fig. 8.5, using the scale relationships given in Table 8.4. It can be seen that data are not

Table 8.4: Properties of some probability distributions.

Lognormal	
Distribution function $F(H)$	$\frac{1}{\sqrt{2\pi}B} \int_0^H \frac{1}{H} \exp \left[-\frac{1}{2} \left(\frac{\ln H - A}{B} \right)^2 \right] dH$
Probability density function $f(H)$	$\frac{1}{\sqrt{2\pi}BH} \exp \left[-\frac{1}{2} \left(\frac{\ln H - A}{B} \right)^2 \right]$
Mean \bar{H}	$\exp \left[A + \frac{B^2}{2} \right]$
Variance σ_H^2	$\exp(2A + B^2) [\exp(B^2) - 1]$
Range	$0 < H < \infty; -\infty < A < \infty; 0 < B < \infty$
Fisher - Tippet (FT I)	
Distribution function $F(H)$	$\exp \left[-\exp \left(\frac{x-A}{B} \right) \right]$
Probability density function $f(H)$	$\frac{1}{B} \exp \left[\left(\frac{x-A}{B} \right) - \exp \left(\frac{x-A}{B} \right) \right]$
Mean \bar{H}	$A + \gamma B \ (\gamma = 0.5772 \dots)$
Variance σ_H^2	$\frac{\pi^2}{6} B^2$
Range	$-\infty < H < \infty; -\infty < A < \infty; 0 < B < \infty$
Fisher - Tippet (FT II)	
Distribution function $F(H)$	$\exp \left[-\left(\frac{x}{B} \right)^{-A} \right]$
Probability density function $f(H)$	$\frac{A}{B} \left(\frac{x}{B} \right)^{-(A+1)} \exp \left[-\left(\frac{x}{B} \right)^{-A} \right]$
Mean \bar{H}	$B \Gamma \left(1 - \frac{1}{A} \right)$
Variance σ_H^2	$B^2 \left[\Gamma \left(1 - \frac{2}{A} \right) - \Gamma^2 \left(1 - \frac{1}{A} \right) \right]$
Range	$0 < H < \infty; 0 < A < \infty; 0 < B < \infty$
Fisher - Tippet (FT III) (lower bound)	
Distribution function $F(H)$	$\exp \left[-\left(\frac{x-A}{B} \right)^C \right]$
Probability density function $f(H)$	$\frac{C}{B} \left(\frac{x-A}{B} \right)^{C-1} \exp \left[-\left(\frac{x-A}{B} \right)^C \right]$
Mean \bar{H}	$A + B \Gamma \left(1 + \frac{1}{C} \right)$
Variance σ_H^2	$B^2 \left[\Gamma \left(1 + \frac{2}{C} \right) - \Gamma^2 \left(1 + \frac{1}{C} \right) \right]$
Range	$A < H < \infty; 0 < A < \infty; 0 < B < \infty$
Weibull	
Distribution function $F(H)$	$1 - \exp \left[-(BX)^C \right]$
Probability density function $f(H)$	$CB^C X^{C-1} \exp \left[-(BX)^C \right]$
Mean \bar{H}	$\frac{1}{B} \Gamma \left(1 + \frac{1}{C} \right)$
Variance σ_H^2	$B^{-2} \left[\Gamma \left(1 + \frac{2}{C} \right) - \Gamma^2 \left(1 + \frac{1}{C} \right) \right]$
Range	$0 \leq H < \infty;$

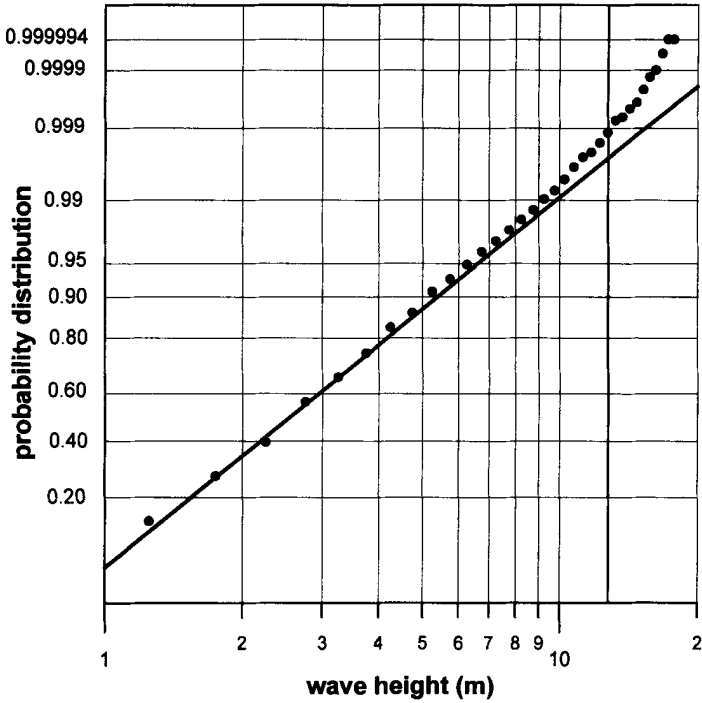


Figure 8.4: Fit of the experimental data to the log-normal distribution.

satisfactorily represented over the entire range of significant wave height. The Weibull distribution provides the proper rate of growth of probability distribution function of extreme waves, but the absolute values of the probability are greater than observed. This means that the Weibull distribution gives a smaller probability of exceedance of extreme wave height than observed values. For example, the probability of exceedance of wave height $H_s = 18$ m, predicted by the Weibull distribution, is equal to $4 \cdot 10^{-5}$.

It should be pointed out that experimental data toward the extreme values are very sparse. For example, Table 8.3 indicates that only five of observed waves were higher than 18 m. Hence, the question remains as to how reliable the prediction procedure is if we estimate the extreme significant wave heights using a very small number of observations, in the situation when theoretical distributions for extreme large wave heights substantially differ from experimental ones. Finally, it should be noted that data collected in Table 8.3 are the raw data, provided by various ships in various conditions and using various methods of observation. Therefore, we cannot expect a better agreement with some model distributions as in the case of the measured data.

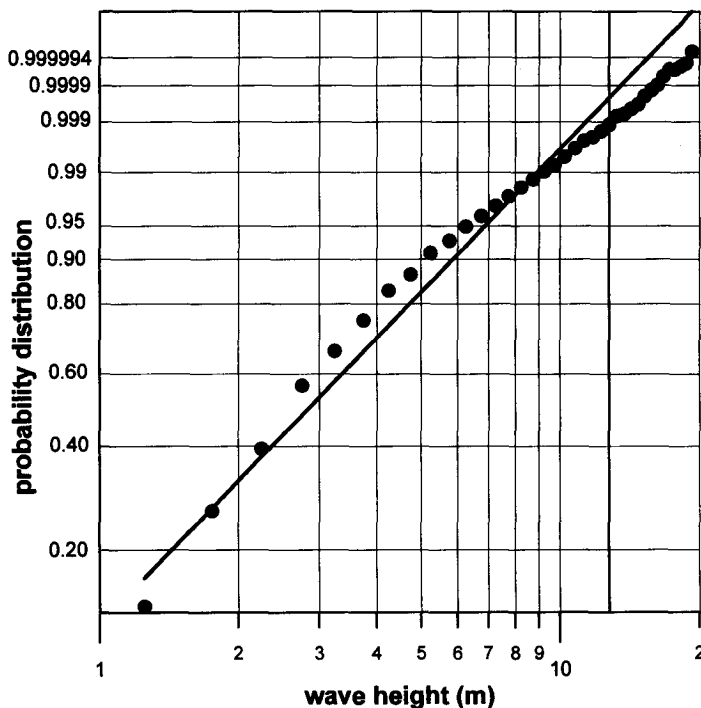


Figure 8.5: Fit of the experimental data to the Weibull distribution.

One way to improve the estimation of the extreme values is to use a combination of log-normal and Weibull distributions. Davidan et al. (1985) proposed using the log-normal distribution for $\frac{H_s}{H_{s50\%}} \geq 1.0$, and the Weibull distribution when $\frac{H_s}{H_{s50\%}} \leq 1.0$ ($H_{s50\%}$ denotes a median of distribution). In similar way the distribution of wave periods can be described. In particular, the log-normal distribution should be used for long periods ($T > T_{50\%}$), while the Weibull distribution is useful for shorter periods ($T < T_{50\%}$).

Another way is to express the probability distribution function $F(x)$ in the form (Ochi and Whalen, 1980):

$$F(x) = 1 - \exp[-q(x)], \quad (8.10)$$

in which:

$$q(x) = ax^m \exp(-px^k). \quad (8.11)$$

The parameters involved in $q(x)$ should be determined numerically by a minimalization procedure.

8.5.2 Probability distributions of extreme waves

The third category of prediction procedure is related to the situation in which the largest wave heights (periods), regularly sampled (monthly or yearly) during a certain period of time, are available. If the number of measured data is large then it is possible to estimate the extreme wave height (wave period) expected to occur in, for example, 50 or 100 years. The basis for the extreme value prediction methods is the asymptotic behaviour of the probability distribution function for the maxima of the relevant random variable. Distribution functions of extreme wave heights, in a sample of N waves, were given in Chapter 4. However, for long-term of prediction of wave heights, when number of wave $N \rightarrow \infty$, the asymptotic behaviour of these distributions should be known. Thus, let us rewrite Eq. (4.193) as:

$$F_{H_{max}}(H_{max}) = [F_H(H_{max})]^N = \exp[N \ln F_H(H_{max})]. \quad (8.12)$$

When $N \rightarrow \infty$, $\ln F_H(H_{max}) \rightarrow 0$, then the probability $F_{H_{max}}(H_{max})$ entirely depends on the asymptotic behaviour of the probability distribution function $F_H(H_{max})$ at $N \rightarrow \infty$.

It was shown by Fisher and Tippet (1928) and by Gnedenko (1943) that, for independent and identically distributed data, there are purely three limiting distributions for their maxima, i.e.:

- Fisher–Tippett I distribution (also known as the double exponential, the FT-I, the Gumbel, or the extreme value distribution),
- Fisher–Tippett II distribution (also termed the FT-II, or Frechet distribution), and
- Fisher–Tippett III distribution (also termed the FT-III).

The basic properties of these probability distributions are listed in Table 8.4.

When all positive moments of the distribution exist, then the distribution has the FT-I distribution at its limit. If some positive moments do not exist, then the distribution has the FT-II or FT-III form as its limit, depending upon whether or not it is bounded above (Muir and El-Shaarawi, 1986). The extreme value distributions are related to each other, for example, the transformation $y = \ln(x - D)$ will transform an FT-II distribution into an FT-I, provided that D is known.

All of the above extreme value distributions have been applied to ocean wave data. Petruskas and Aagaard (1971), Forristall (1978), and Carter and Challenor (1983) used the FT-I distribution. The FT-II distribution has been applied by Thom (1971, 1973), while Readshaw and Baird (1981), Battjes (1972b) and Borgman (1975)

Table 8.5: Maximum significant wave heights at weather ships in the Atlantic Ocean and Pacific Oceans (according Thom, 1971).

Weathership	Latitude	Longitude	Probabilities			
			$F = 0.50$	$F = 0.90$	$F = 0.96$	$F = 0.98$
Atlantic Ocean						
A	62°00' <i>N</i>	33°00' <i>W</i>	10.7	14.3	16.5	18.6
B	56°30' <i>N</i>	51°00' <i>W</i>	10.4	13.3	14.6	16.2
C	22°45' <i>N</i>	35°30' <i>W</i>	10.4	12.5	13.4	14.3
D	44°00' <i>N</i>	41°00' <i>W</i>	10.4	12.5	13.4	14.3
E	35°00' <i>N</i>	48°00' <i>W</i>	9.1	11.0	12.2	13.1
I	59°00' <i>N</i>	19°00' <i>W</i>	12.2	17.1	20.4	23.2
J	52°30' <i>N</i>	20°00' <i>W</i>	12.2	17.1	20.1	22.9
K	45°00' <i>N</i>	16°00' <i>W</i>	11.0	14.9	17.1	19.2
M	66°00' <i>N</i>	02°00' <i>W</i>	7.3	11.6	14.9	17.7
Pacific Ocean						
N	30°00' <i>N</i>	140°00' <i>W</i>	6.1	8.2	9.8	11.3
P	50°00' <i>N</i>	145°00' <i>W</i>	11.0	14.9	17.7	19.8
V	34°00' <i>N</i>	164°00' <i>E</i>	9.8	13.4	15.5	17.4

applied the FT-III distribution. Moreover, the log-normal distribution was used by Draper (1963, 1966), and later by Earle and Bear (1982), and by Davidan et al. (1985), while the Weibull distribution has been applied by Petrauskas and Aagaard (1971), Carter and Challenor (1983), and Davidan et al. (1985).

Kerstens et al. (1988) proposed another method of estimating the extreme values of wave height based on Bayesian statistics. This method has significant advantages over the classical method, since it enables all types of uncertainty associated with the design wave prediction to be handled in a consistent manner.

It should be stressed that the extreme value distributions are applicable to regularly sampled data only, such as annual or monthly maxima. These distributions are not suitable for data sets containing all of the maxima above a certain level. For such data sets the compound distributions should be used (Muir and El-Shaarawi, 1986; The-fu and Feng-shi, 1980).

Let us now illustrate extreme wave height distributions with some examples. As was mentioned above, Thom (1971) has applied the FT-II distribution to annual significant wave height, observed by the weather ships located in the Atlantic Ocean (ships A, B, C, D, E, I, J, K, M), and Pacific Ocean (ships N, P, V). The results are shown in Table 8.5. Here, the probabilities 0.50, 0.90, 0.96 and 0.98 correspond to 2, 10, 25 and 50 year mean occurrence interval waves. In order to find the extreme wave heights, Thom applied the rounded ratio of 1.8 as a scale change to the FT-II

extreme value distribution. This approximate ratio of the extreme wave height to the significant wave height was obtained theoretically by Longuet-Higgins (1952), and experimentally by Wiegel (1949). Therefore, at weather ship P in the Pacific Ocean, the highest wave in a 50 year period is equal to about 36 m. Moreover, in Fig. 8.6, the directional distribution of the maximum wave heights, observed at the rescue ship *Famita* located in the North Sea ($57^{\circ}30'N$, $3^{\circ}E$), is shown (Massel, 1981a).

The highest waves correspond to the NW and SE directions, which is related to the location of the ship between the British Isles and Scandinavia. Studies comparing of various probability distributions of extreme waves are not numerous. In one of the latest and most comprehensive analyses, Vledder et al. (1994) used three-hourly records, collected during a 9-year period at Haltenbanken off the Norwegian coast ($65^{\circ}05'N$, $7^{\circ}34'E$), and a 20-year period of storm peak wave heights resulting from a numerical hindcast of historical data in the Kodiak area in the North Pacific ($51^{\circ}50'N$, $148^{\circ}78'W$). Several probability distributions have been tried for comparison tests. They include: FT-I, FT-II, log-normal, two- and three-parameter Weibull distribution being truncated, having the following form:

$$F(x) = 1 - \exp \left[- \left(\frac{x - x_0}{\sigma} \right)^k + \left(\frac{x_c - x_0}{\sigma} \right)^k \right] \quad \text{for } x > x_c, \quad (8.13)$$

in which σ is the scale parameter, k is the shape parameter, x_0 is the location parameter, and x_c is the threshold level at which the distribution is truncated.

Despite the variety of probability distributions applied and the various data selection method and fitting techniques, the estimated 100-year return wave heights differ less than 10%. In particular, for Haltenbanken they obtained $14.2 \text{ m} < H_{100\text{year}} < 15.8 \text{ m}$, with the mean value $H_{100\text{year}} = 15.0 \text{ m}$, while for Kodiak the corresponding values are $12.1 \text{ m} < H_{100\text{year}} < 12.8 \text{ m}$, with the mean value $H_{100\text{year}} = 12.5 \text{ m}$. The half-widths of 90% confidence intervals are of the order of 1.5 m.

Recently, simulation data were used to evaluate the performance of various probability distributions in the estimation of extreme wave heights (Goda et al., 1994). The Weibull distribution with the shape parameter $C = 1.4$ was selected as the parent population. The mean value of the estimated return wave heights was almost the same as the true value, but their statistical deviations were large, depending on sampling variability.

All methods for determining the probability of extreme waves assume that the highest wave in 50 (or 100) years occurs during the most severe storm in 50 (or 100) years. However, there is a significant possibility that it will occur in the second highest storm, or even in other storms. In order to take account of this it would be desirable, in principle, to measure every individual wave occurring over one, or preferably more, complete years and to extrapolate the probability of these to the height exceeded on the average of one in 50 (or 100) years. Such continuous records of individual wave heights are not generally available. Battjes (1972b) proposed a method in which the

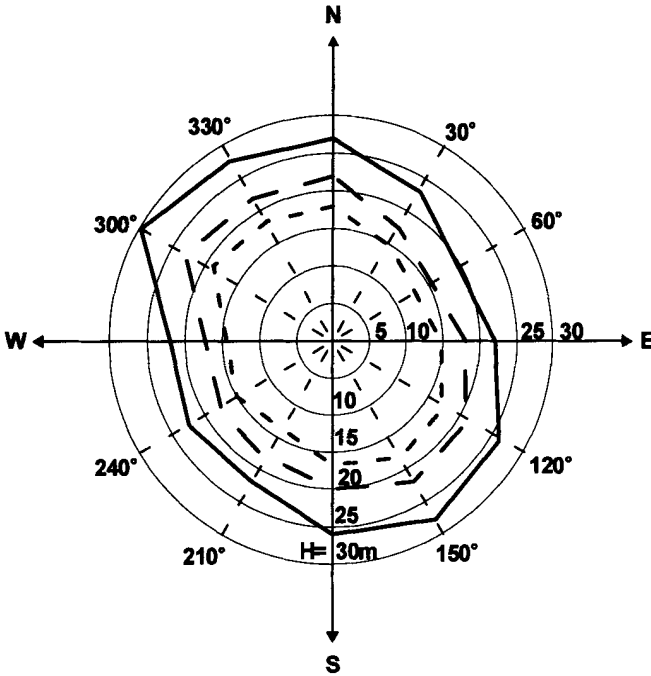


Figure 8.6: Directional distribution of the maximum wave heights observed at the rescue ship *Famita*: ——— 100 years period; - - - 1 year period; - · - 1 month period.

required distribution is estimated from measured 3-hourly significant wave heights H_s and zero-crossing period T_z .

To calculate the probability of exceedance in N years, a calculation of the number of waves in N years is required. This also involves the waves in periods of low sea state and those recorded as calms. From a physical point of view, the probability of extreme waves should not depend on assumptions about the wave period in calms. Therefore, Tucker (1989a) developed a method which improved Battjes' method, and calculated the expected number of individual waves exceeding H_0 in a year. The value H_0 for which the expected number is $1/N$ is the N -year return value of an individual wave height.

In Tucker's concept, each storm is considered as one event, but still takes account of the possibility of the highest wave in 50 (100) years not coming from the most severe storm. Let the number of waves with particular values of H_s and T_z , during a year, be $N(H_s, T_z)$, while the expected number of waves exceeding height H_0 in 3

hours will be defined as:

$$N_3 = \text{Prob}(H > H_0 \parallel H_s) 10800/T_z, \quad (8.14)$$

in which $\text{Prob}(H > H_0 \parallel H_s)$ is the probability that, for a given significant wave height H_s , a randomly chosen wave of height H , will exceed H in height.

Adding the wave numbers for all 3 hours intervals in a year gives the expected total number $M(H_0)$, exceeding level H_0 in a year as:

$$M(H_0) = 10800 \sum_{H_s} \text{Prob}(H > H_0 \parallel H_s) \sum_{T_z} N(H_s, T_z) / T_z. \quad (8.15)$$

For convenience later we will define the mean frequency $\bar{\Omega}(H_s)$ as:

$$\bar{\Omega}(H_s) = \frac{\sum_{T_z} N(H_s, T_z) / T_z}{N(H_s)}, \quad (8.16)$$

in which $N(H_s)$ is the total number of measurements at H_s . The substitution of Eq. (8.16) into Eq. (8.15) gives:

$$M(H_0) = 10800 \sum_{H_s} \text{Prob}(H > H_0 \parallel H_s) N(H_s) \bar{\Omega}(H_s). \quad (8.17)$$

Using the fact that the total number of measurements at H_s can be expressed as:

$$N(H_s) \approx f(H_s) \Delta H_s \times \text{number of three - hour periods in a year}, \quad (8.18)$$

we finally obtain (Tucker, 1989a):

$$\begin{aligned} M(H_0) &= 10800 \cdot 2922 \sum_{H_s} \text{Prob}(H > H_0 \parallel H_s) f(H_s) \bar{\Omega}(H_s) \Delta H_s = \\ &= 3.16 \cdot 10^7 \int_0^\infty \text{Prob}(H > H_0 \parallel H_s) f(H_s) \bar{\Omega}(H_s) dH_s. \end{aligned} \quad (8.19)$$

Tucker provided two examples of calculations and compared the results with the conventional computation based on FT-I distribution. For data recorded in the *Seven Stone Light Vessel* off the west coast of Britain ($50^\circ 04' N, 06^\circ 04' W$) he obtained the highest wave in a 50-year period equal to $H_{50} = 30.38$ m, while the FT-I distribution gives $H_{50} = 26.95$ m. The ratio of the values from both methods is 1.127. A similar ratio (1.113) was found for data from the *Dowsing Light Vessel* in the North Sea ($53^\circ 34' N, 50^\circ 02' E$). Carter and Challenor (1989) showed that this ratio varies from 1.12 by a maximum of only $\pm 1\%$ for a wide range of values of the parameters A and B in the FT-I formula, and for practical purposes it can therefore be assumed to be constant.

8.6 Estimation of distribution parameters

The extreme value distributions considered here present a family of distributions whose properties depend upon the parameter values assigned to them. The parameter values should be determined to provide the best empirical fit between the distribution and the data. The simplest approach is to plot the individual data points on the selected probability paper and draw a straight line through these points. More precisely, the best fit line may be derived using one of the following methods: the method of least squares, the method of moments and the method of maximum likelihood. The values of distribution parameters, resulting from these methods, will be different for the same sample of data.

The method of least squares provides the best line fit to the data plotted on the pertinent probability paper. The resulting distribution parameters correspond to the minimum quadratic difference between the data points and a theoretical straight line. In method of moments, the equality of the first two or three moments of the distribution to those of the data is used. This method was applied above to determine the values of parameters in the log-normal and Weibull distributions. Finally, the maximum likelihood method provides the estimated parameters which give the data sample the highest probability of being observed. The data sample is considered to consist of a series of independent observations from the same distribution. The method of maximum likelihood selects values of each parameter which maximizes the so called likelihood function L :

$$L(H_1, H_2, \dots, H_n) = \prod_{i=1}^n f(H_i), \quad (8.20)$$

in which f is a probability density of the chosen distribution and H_i are the measured wave heights. Since most of the common density functions have an exponential form, the maximum likelihood estimator is obtained by maximizing the logarithm of L . The method of maximum likelihood provides estimated parameters which are unbiased and possess the smallest variance of the estimator (Isaacson and Mackenzie, 1981; Muir and El-Shaarawi, 1986; Ochi, 1990)

8.7 Goodness of fit tests and confidence intervals

The different probability distributions result in very different estimates of extreme wave parameters and are usually very difficult to check the goodness-of-fit. A number of quantitative tests are in use to quantify the goodness-of-fit, to reject or accept distributions and to choose between various fitted distributions. The most important are: Kolmogorov-Smirnov, Anderson-Darling, Chi-square, correlation coefficient, residue of correlation coefficient, and minimum ratio of residual correlation coefficient.

If a simple numerical goodness-of-fit test is required, either the correlation coefficient or chi-squared test could be used between the computed and observed heights

(Bendat and Piersol, 1986). More sophisticated numerical methods of fit tests are discussed by Lawless (1982).

The closeness of fit of the data points to the fitted distribution is described in terms of confidence limits on either side of the fitted line. The particular confidence limits determine the confidence bands within which data are expected to lie with corresponding probabilities. (The complete derivation of confidence bands, as applied to any chosen distribution, is described by Borgman, 1961). For given sample size N , and chosen confidence probability level, a pair of height limits for the particular statistics is provided. This method assumes the residuals are normally distributed and is appropriate for the range of data that was used in the fit. It cannot be extrapolated beyond the observed data, and therefore cannot be used for prediction.

An alternative approach is to use the Monte Carlo simulation to generate random sets of data which are derived from the best-fit distribution that has been obtained (Petrauskas and Aagaard, 1971). The spread of this simulated data can then be used to describe the confidence or uncertainty attached to any chosen value. The major advantage of this approach is that it can be used for any values of height, including predicted values.

8.8 Design wave selection

The selection procedure of the design wave height is usually described in terms of the return period and encounter probability. The non-dimensional form of the return period is known as the expected waiting time, i.e. T_R/r , in which r is the recording interval associated with each data point (in the case where each data point corresponds to the largest year value, r would be equal to one year). Using Eq. (8.9), we can relate the waiting time T_R/r directly to the probability distribution $F(H)$:

$$\frac{T_R}{r} = \frac{1}{1 - F(H)}. \quad (8.21)$$

If $\frac{T_R}{r} > 7$, the relationship with the probability distribution $F(H)$ can be simplified as (Isaacson and Mackenzie, 1981):

$$\frac{T_R}{r} \approx \frac{1}{2} + \exp(y), \quad (8.22)$$

in which $y = -\ln[-\ln(F)]$.

In design considerations an additional factor, i.e. the time in which the structure is exposed to the hazard (the so called life-time of a structure L), should be taken into account. Therefore, the probability that the design wave height is equalled or exceeded during the life of the structure L is:

$$E = 1 - \left(1 - \frac{r}{T_R}\right)^{L/r}. \quad (8.23)$$

When r is associated with the largest wave height during a year, and T_R and L are expressed in years, Eq. (8.23) takes the form:

$$E = 1 - \left(1 - \frac{1}{T_R}\right)^L, \quad (8.24)$$

which is in agreement with the definition of E given in Eq. 7.100. For example, a structure with a life of 50 years has a 63.6% chance of encountering a 50 year wave during its life. If the acceptable risk of encountering waves is only 10%, the design waves should be associated with a return period of 475 years.

8.9 Geography of waves

8.9.1 A brief orientation

Wind and wave climate varies considerably between various regions of the World Ocean. Peak wave conditions occur at high latitudes ($\pm 50^\circ$). In the Southern Ocean, the almost constant strong winds acting along large fetches generate consistently large waves, which propagate over very large distances. In contrast, the North Atlantic Ocean has a more variable sea state.

The amount of energy which is available in the wave field is prodigious. In Fig. 8.7, the relationship between the average wave power density (in kW/m of wave frontage) over a whole year and the wave period for three observing stations is given (Salter, 1974). They are: in the Atlantic Ocean - weather ship 'I' (*India*) and Light Vessel *Seven Stones*, and Rescue Ship *Famita* in the North Sea. The total annual mean power density 77 kW/m occurs at Station 'I', and values of 36.8 kW/m and 25.8 kW/m are observed at the rescue ship *Famita* and the *Seven Stones* Light Vessel, respectively.

In all oceans, the intensity of wave motion decreases from high latitudes towards the Equator. In the tropical zones, the frequency of storm winds is 2-3 times smaller than in high latitudes. However, the tropical regions are the locations where cyclones (or hurricanes or typhoons) are generated. Due to the complicated pattern of wind field, the resulting storm waves are superimposed upon swell propagating from various directions. Some parameters of extreme wind speed and wave heights, in various regions of the World Ocean, are given in Table 8.6, based on data reported by Davidan et al. (1985). The wind speed denotes the mean value during 100 s. However, the wind speed during tropical cyclones was omitted from the Table. Confidence intervals with confidence level of 95% are added in parenthesis. A lot of detailed information on the extreme historical and present wave events and damage to ships are also given in a book by Davidan and Lopatukhin (1978).

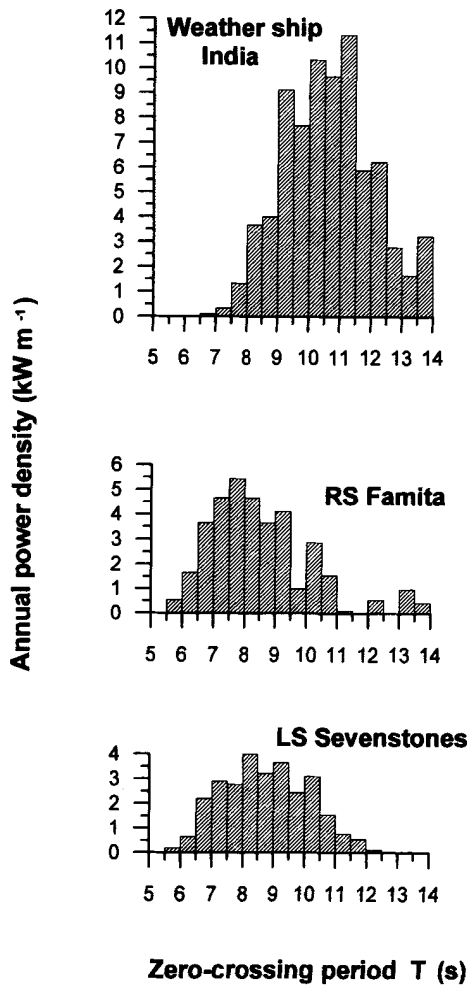


Figure 8.7: Wave power in KW per meter of wave frontage as a function of wave period for three various locations.

Table 8.6: Extreme wind speed and wave heights in various regions of the World Ocean.

Region	Extreme value		
	Wind speed (m/s)		Wave height (m)
	$T_R = 30 \text{ y}$	$T_R = 50 \text{ y}$	$T_R = 30 \text{ y}$
Midlatitude zones of the North Atlantic Ocean	48 (42–54)	53 (44–62)	20 (17–23)
Midlatitude zones of the South Atlantic and Indian Ocean	50 (42–58)	55 (43–67)	23 (19–27)
Midlatitude and subtropical Pacific; midlatitude south Pacific	48 (40–56)	55 (43–67)	21 (18–24)
Tropical zone of the North Atlantic Ocean	39 (31–47)	44 (34–54)	16 (13–19)
Tropical zone of the South Atlantic and Indian Ocean	32 (28–36)	36 (30–42)	14 (12–16)
Tropical zone of Pacific and tropical monsoon zone in Indian Ocean	33 (29–37)	36 (30–42)	12 (10–14)
Equatorial zone	32 (28–36)	35 (29–41)	12 (10–14)

8.9.2 Atlantic Ocean

The Atlantic Ocean extends from north to south through all climatic zones. The number of atmospheric depressions in the Atlantic Ocean is higher during winter (October – March) and decreases during summer (Massel, 1982a). During tropical cyclones the wind speed exceeds 40 m/s, reaching 70 m/s and more, and waves can be as high as 20 m. During tropical cyclone *Camille* (1969) in the Mexican Gulf, a wave height of 23.6 m was recorded. The S.S. *Majestic*'s officers observed waves from 18.3 m to 27.4 m near 48°30'N and 21°05'W on December 29, 1922. The passenger ship *Michelangelo*, during a North Atlantic crossing, was struck by a wave that collapsed the superstructure and broke heavy windows at 24.6 m above the water line (James, 1966).

An observation of waves with heights of 19.6–20.0 m is also given in Table 8.3. These observations were made in the sector (30°N – 60°N, 3°W – 30°W) in the Atlantic Ocean.

The data collected from weather ships shows that the yearly mean duration of constant presence of wind with speed > 25 m/s, in the northern part of ocean in January, can reach 15 hours (Birman et al., 1980). Once in 10 years, this duration

is equal to 36 hours, and once in 50 years it can be equal to 40 hours. The wave intensity also varies substantially between years. For example, at the weather ship 'A' in January 1955, the percentage of occurrence of wave heights bigger than 7.5 m was 2.5%, but in 1961 it was 40%. On weather ship 'D', in January 1952, wave heights bigger than 5 m occurred at 3% of the time, but in January 1959, the occurrence of such waves was about 30% (Davidan et al., 1985).

The mean monthly significant wave heights, obtained recently from the three-year GEOSAT radar altimeter measurements, confirm the high seasonal variability of wave climate in the Atlantic Ocean. For example, the maximum significant wave height H_s of 6 m occurs at latitude 50° in January, while at the same latitude in June the significant wave height is equal to only 1.8 m (Young, 1994a). In the North Atlantic Ocean, values of H_s bigger than 6–7 m can be expected 10% of the time and wave heights of 1–2 m occur 90% of the time. On the other hand, visual observations collected in Table 8.3 indicate that the mean significant wave height, observed during 34 years in the sector ($30^\circ N - 60^\circ N$, $3^\circ W - 30^\circ W$), is equal to 3.17 m. During 12% of the time, waves are bigger than 5 m and significant wave heights of 1 m can be expected 91% of the time. Note a close coincidence of both estimations.

In the South Atlantic, 2–3 m seas in December–January were replaced by waves of a 4–5 m height during September–November.

8.9.3 Pacific Ocean

The Pacific Ocean is the largest ocean with the greatest average, as well as the greatest observed depth. Especially, in the Southern Pacific, the large, almost unlimited wind fetches create conditions for generation of large waves. For example, on April 2, 1966, the S.S. *Ob's* officers measured a wave of 24.9 m using the stereophotogrammetry method. In 1921 Captain Wilson of the Blue Funnel Line, while en route from Yokohama to Puget Sound, Washington, recorded waves that were higher than 21.3 m. The U.S.S. *Ramapo*, a navy tanker, encountered a wave of 33.5 m on February 7, 1933, between Manila and San Diego. The mean monthly wave heights obtained by Young (1994a) from the GEOSAT data shows a seasonal variability, but it is less pronounced than in the Atlantic Ocean. For example, at Hawaii ($22^\circ N$, $198^\circ E$), the mean significant wave height varies from ~ 2.8 m in January to ~ 1.8 m in summer (June–July).

The southern Pacific has a higher mean annual wave climate with its maximum in May–November. In the northern Pacific, the strongest waves occur in January–February and the smallest waves are observed in June–August. The difference between the maximum and minimum wave heights is bigger in the northern part than in the southern part. Moreover, in the Pacific yearly variations are substantial. For example, in the northeast part of the ocean, usually 15 hurricanes are observed per year; however, in 1964 only 6 such hurricanes occurred (Davidan et al., 1985).

In Fig. 8.8, the probability distribution and the exceedance probability of a given

significant wave height H_s at Macquarie Island ($-54^{\circ}30'S$, $159^{\circ}E$) is shown. Buoy data were obtained from measurements between November 1988 and October 1989 (Steedman, 1993). The mean value of a significant wave height is about 4.0 m. During 25% of the time, the significant wave is higher than 4.5 m, while during 10% of the time it is higher than 5.5 m.

8.9.4 Indian Ocean

There are two distinctive regions of the Indian Ocean, characterized by different climates. The northern part is dominated by the Asian summer monsoon, while in the southern part, between $40^{\circ}S$ and the Antarctic continent, the powerful Westerlies are located.

The swell generated in the southern Ocean propagates towards lower latitudes, resulting in a more energetic wave climate in the Indian Ocean. The waves are consistently larger than those in either the South Pacific or South Atlantic Oceans.

Significant monthly variations are observed in the Westerlies. The highest wind speeds are found in a broad band between Africa and Australia, where the largest waves also occur (Mognard et al., 1983; Young, 1994a). A maximum appears in this region during July. At the latitude -50° , the maximum significant wave height H_s is equal to 6 m in July–August. During the southern Hemisphere summer, H_s wave height falls to 3.1 m. In that season there is a relatively uniform wave climate in the region between Africa and Australia. The influence of New Zealand and South America is mostly the reduction of the wave climate during winter.

In the western region of the Indian Ocean, close to the African coastline, between Durban and Port Elizabeth, giant waves (freak waves) sometimes occur, even during relatively calm weather. Their front slope is very steep and heights of the waves are typically 15–18 m. During a 22 year period (1952–1973), in this region eleven ships were sunk or seriously damaged (Davidan and Lopatukhin, 1978). Two particularly unfortunate cases were the *World Glory*, which broke in two and sank in June 1968, and the *Neptune Sapphire*, which lost 60 m of its bow section in August 1973. It can only be speculated that giant waves may account for many of the ships which have been lost without trace off this coast.

All except one of the eleven incidents involved vessels riding on the rapid Agulhas Current. This current, generated in the Passat region of the Indian Ocean, flows in a southwest direction along the African coast. The typical current speed is of the order 2.0–2.5 m/s, and its width is about 90–170 km. Energetic swell, generated at higher latitudes, propagates against this current. The swell is particularly intensive from May to October. Waves generated by local winds and superimposed on the swell are much shorter than it (a typical swell wavelength is equal to about 200 m, and wave steepness is about 0.08). The kinematics of waves propagating in the current in deep ocean is governed by the equation (Massel, 1989):

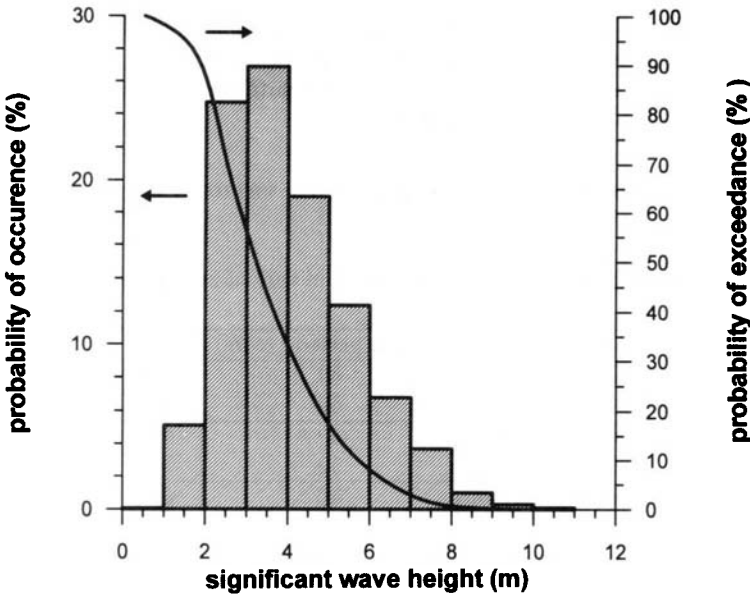


Figure 8.8: Probability distribution and exceedance probability of a given significant wave height H_s at the Macquarie Island.

$$\frac{C}{C_0} = \frac{1}{2} + \frac{1}{2} \left(1 + \frac{4U}{C_0} \right)^{1/2}, \quad (8.25)$$

in which C_0 corresponds to the phase velocity without current. When $U = -\frac{1}{4}C_0 = -\frac{1}{2}C = -C_g$ (i.e. if the current velocity is greater and opposite to the local group velocity of the waves), the energy can no longer be propagated. The wave action conservation law (Massel, 1989) also implies that when the waves are opposed by the current, the wave height will be large, as not only is the group velocity reduced, but also the waves receive energy from the current. This can be expressed in terms of spectral density functions, as in Eq. (6.60). The monochromatic wave analog takes the form:

$$\frac{A}{A_0} = \frac{C_0}{[(2U + C)C]^{1/2}}, \quad (8.26)$$

in which A and A_0 are the amplitudes of waves with and without current, respectively.

Equation (8.26) implies that if the opposing current velocity is equal only to 20% of the wave speed without current ($U = -0.2C_0$), the amplification of wave amplitude is equal to ~ 2.1 . When $U = -0.25C_0$, the amplitude increases theoretically to infinity (caustic line is formed). Of course, the waves break before this point.

A more detailed analysis, using the nonlinear Schrödinger equation, showed that the giant waves occupy a tiny fraction of the Agulhas Current width but that the wave height amplification could exceed a factor of 4 (Smith, 1976), which agrees with the conditions when giant waves are encountered.

8.9.5 Examples of wave climate in various seas

Table 8.7: Significant wave height H_s expected in various smaller seas in the Northern Hemisphere.

Sea	Return period (years)	H_s (m)
Kaspiyan Sea	30	9.6
	50	10.4
Barents Sea	30	12.8
	50	15.2
Sea of Okhotsk	30	12.8
	50	15.2
Baltic Sea	30	9.2
	50	9.6

Due to smaller wind fetches, depth limitations and presence of ice cover, the wave climate in smaller seas is less severe than in the oceans. However, the Barents Sea and North Sea are two of the most severe sea regions. Regular hydro-meteorological observations are not available for many seas. One well documented sea is the North Sea. The data recorded at the *Frigg* platform ($59^{\circ}53'N$, $2^{\circ}3'E$) indicate that for 25% of the time values of $H_s \geq 2.5$ m can be expected, while significant wave height of 3.75 m and higher can be expected 10% of the time. Extreme statistics, based on the FT-I distribution, gives the significant wave height with a 50-year return period equal to about 16 m (Tournadre and Ezraty, 1990). In a region 300 km south of the *Frigg* platform, data recorded by the rescue ship *Famita* (see Fig. 8.6) indicated that a maximum wave height, with a 100-year return period, is equal to 27 m. Cavaleri et al. (1986) reported the results of a hindcast study of extreme waves in the Tyrrhenian Sea, which is in the northern part of the Mediterranean basin. Seventy-one storms were chosen, all dated between 1960 and 1980. Calculations showed that there is a 10% probability that during 50 years the extreme wave height will be 12.8 m. In the Baltic Sea, the highest waves occur during September–March in northern part, and during November–February in the central and southern part. It is estimated that in winter, the probability of waves greater than 8 m is equal to 1.5–2.0%.

In Table 8.7, significant wave heights expected in various seas in the northern Hemisphere are listed. The values are based on data given by Davidan et al. (1985).

Chapter 9

Measurement, Simulation and Data Processing

9.1 Introduction

The final Chapter deals with measurements techniques, data processing and simulation methods which apply to ocean surface waves. The measurements and theory are complementary rather in competition. Peregrine (1990b) mentioned few examples of interactions between theory and measurements which are fully applicable for ocean waves, namely: a) observations in nature or laboratory lead to theory being developed to explain it, b) new phenomena predicted by theory lead to experiments being made to verify the prediction, and c) discrepancies between theory and measurements stimulate further development of both.

The ideal data base to study particular wave phenomenon would be a number of actual measurements taken preferably during major storms at the site of interest. However, in most cases this is unavailable. Simulated data provide an artificial substitute for such records. Usually the simulated wave data are based on the assumption that the wave properties follow a Gaussian distribution with zero mean and variances consistent with the wave spectra.

The Chapter is rather short and provides only brief review of these subjects. However, many cross-references provide the reader with additional sources of information.

9.2 A single point wave data

9.2.1 Measurement techniques

9.2.1.1 Laboratory wave measurement

The bulk of the available information on surface waves has come as a result of laboratory and field experiments. Laboratory methods were recently extensively reviewed

by Hughes (1993). In this Section, therefore, these methods will be outlined only.

Wave measurements at a point have been made since the time when laboratory flumes first featured mechanically generated wave motion. At present, such wave measurements are considered a routine laboratory capability. The variety of instruments (wave gauges) used to obtain information on surface waves can be grouped into resistance, capacitance and pressure type gauges.

Resistance wave gauges

Resistance wave gauges are usually formed from two parallel wires, separated by a fixed distance. During gauge operation, the conductance between the wires is recorded. The measured conductance is proportional to the length of wire beneath the wave surface. This means that changes in sea surface elevation, change the recorded conductance. The gauge exhibits good linear response and possesses a resolution of about ± 0.1 mm.

Capacitance wave gauges

In the capacitance wave gauge, the principle of linear variation of capacitance with sea surface elevation change is used. The capacitor is formed from insulated wire held taut by a supporting rod, with water serving as a 'ground'. The single-wire capacitance wave gauge demonstrates good linearity and dynamic response over a reasonable length, and is stable over a sufficiently long time.

Pressure transducers

Measurement of surface waves with pressure transducers has been practiced since 1947. Although measuring subsurface pressure for evaluation of the wave height is practically feasible, an explicit transfer relationship between the wave pressure and the wave height is necessary. Unfortunately, some controversy over the adequacy of the transfer function still exists.

The first-order expression for wave pressure head $H_p = p/\rho g$ is related to the surface wave height, H , by:

$$H = \frac{H_p}{K_p}, \quad (9.1)$$

where K_p is the pressure response factor.

The linear wave theory gives:

$$K_p = \frac{\cosh k(h - z)}{\cosh kh}, \quad (9.2)$$

where z is the depth of the pressure sensor under the still water level, and h is the water depth.

To account for the difference between theory and observation, an empirical correction factor, N , is usually introduced:

$$H = N \frac{H_p}{K_p}. \quad (9.3)$$

In an engineering application a typical value of N is equal to 1.25. However, a recent review by Bishop and Donelan (1987) showed a considerable difference of opinions on this issue. To attempt to resolve discrepancies, tests were conducted by Bishop and Donelan (1987), Kuo and Chiu (1994), and Townsend and Fenton (1995). Results of the first series of experiments indicated that the linear theory is adequate to compensate pressure records to give surface wave heights to within five per cent. However, only spectral analysis of the data, not a wave-by-wave analysis, can give adequate results. Thus, the relationship between surface wave elevation ζ and subsurface pressure p can be treated in terms of the single-input/output relationship:

$$H(\omega) = \frac{|S_{p\zeta}(\omega)|}{S_\zeta(\omega)}, \quad (9.4)$$

where $H(\omega)$ is a frequency response function, $S_\zeta(\omega)$ is a frequency spectrum of surface elevation, and $S_{p\zeta}(\omega)$ is the cross-spectrum of surface elevation and wave pressure.

Equation (9.4) implies that the relationship between frequency spectra for surface elevation ζ and pressure p takes the form:

$$S_p(\omega) = |H(\omega)|^2 S_\zeta(\omega) \quad \text{or} \quad S_\zeta(\omega) = |H(\omega)|^{-2} S_p(\omega). \quad (9.5)$$

Kuo and Chiu (1994) showed that the frequency response function depends on two non-dimensional parameters $\frac{\omega^2 z}{g}$ and kh , i.e.:

$$H(\omega) = \exp\left(-0.905 \frac{\omega^2 z}{g} - 0.027\right) \quad \text{for } 0.1 \leq \frac{\omega^2 z}{g} \leq 5.0, \quad \text{and } kh \geq 0.44. \quad (9.6)$$

Formula (9.6) appears to provide a good coincidence with laboratory and field experiments by Cavaleri et al. (1978) and Bishop and Donelan (1987). However, as was pointed out by Townsend and Fenton (1995), this method is only valid at or below $\frac{L}{h} \approx 14$.

More recent local methods provide greater accuracy over a wide range of waves. In particular, Nielsen's methods (Nielsen, 1986; 1989) predict wave heights well but they do not estimate the wave profile accurately. The local polynomial approximation, introduced by Fenton (1986), does not perform as well as Nielsen's methods when predicting wave heights from pressure readings close to the sea bottom but generally describes the wave profile with better accuracy than all other methods.

9.2.1.2 Field wave measurements

In wave experiments under field conditions, three groups of instruments are used: wave staffs, wave buoys, and pressure gauges. Pressure gauges were described in the previous Section, so in this Section we describe wave staffs and wave buoys only.

Wave staffs

For the wave staff, other principles, besides resistance and conductance principles, are used. One of them is the so called contact wave staff where the set of contacts is distributed along a vertical pole. The contacts are closed when they are covered by water.

Zwarts (1974) proposed a different wave staff, based on a principle commonly used in the telephone industry to detect the location of faults in coaxial cables. The wave measuring staff consists of two pipes, one inside the other, forming a coaxial cable. Slots in the outer pipe allow the movement of water into the space between the outer and inner pipes. The configuration of the pipes in a coaxial cable form acts as the tuning element of an electronic oscillator. An electromagnetic wave, propagating down the pole, is generated by electronics located at the head of the pole. This wave reflects off the discontinuity (in the dielectric contact) at the air-water interface. The length of the unimmersed section of the staff is directly proportional to the period of the oscillation of the electronic signal. The output of the system is a number of reflections of the signal during a very small time interval.

Wave buoys

In deeper water, where the supporting structures for wave staffs are not available, wave buoys are used. They usually are a small sphere, or small platform, which follow the movements of the water surface. In the simplest case, the internal sensor measures a vertical acceleration of the buoy. The acceleration is integrated twice with respect to time, to produce a measure of the instantaneous wave height profile about the still water level. The response of the buoys varies with wave frequency. For the most popular wave rider buoy manufactured by Datawell bv, Haarlem, Netherlands, the transfer function shows that the buoy response is essentially flat for wave periods between 5 and 10 s. Some attenuation is observed for periods between 10 and 25 s.

When a moored wave rider follows the waves, the force of the mooring line will change. This force is produced by change in buoy's immersion. The wave rider buoy does not follow the wave surface if the wavelength is less than 5 m (the wave period is less than 1.8 s). To avoid measurement of unwanted accelerations due to roll and pitch of the buoy, the sensitive axis of the accelerometer is mounted on a stabilized platform. To keep a moored wave rider at the correct position, a rubber cord is used as a part of the mooring system. The stiffness of the rubber cord allows the buoy to follow waves up to 20 m. A buoyancy of approximately 900N keeps the wave rider from submerging under the combined action of a 18 m wave height and a 1m/s

current.

A comprehensive comparison of various types of wave buoy is given by Allender et al. (1989). During the WADIC Project (Wave Direction Measurement Calibration Project) which was held at or in the vicinity of the *Edda* platform in the Ekofisk field in the North Sea during winter 1985-1986, several wave buoys, platforms and wave staffs were intercalibrated. Authors compared the performance of a particular buoy against the best estimated data set obtained from the platform-based measurements. Although differences in accuracy have been found, comparisons for the most important engineering parameters, significant wave height, mean wave period and wave direction at the spectral peak are satisfactory. Most of the buoys were directional (WAVETRACK, USA; WAVEC, Netherlands; WADIBUOY, France; NORWAVE, Norway; MAREX, England) and they measure the surface elevation and surface slopes along two perpendicular directions. Processing of the directional buoy data provides information on wave directionality (see Section 9.3).

For large wave buoys, the response of the buoy itself must be taken into account when calculating the wave parameters, especially those related to directional spreading. The buoy response depends on mooring constraints which are varied by a number of factors, including current and wind speed. Therefore, a data processing method which does not assume a constant response is desired. Methods for determining the total sensor-hull response for the U.S. National Oceanic and Atmospheric Administration (NOAA) network of environmental data buoys were reported by Steele et al. (1992), by Tucker (1989b) for U.K. data buoys DB1 and DB2, and by Gnanadesikan and Terray (1994) for three buoys deployed in the Gulf of Alaska.

9.2.2 Determination of spectral characteristics of surface waves

In Chapter 3, basic ideas on the spectral description of the ocean surface were given and some comparisons of experimental and theoretical spectra were shown. In this Section we summarize briefly practical methods for evaluation of experimental frequency spectra.

9.2.2.1 Data sampling

Let us assume that a record of sea surface oscillation is of duration t . The digital data consists of N data values with an equally spaced sampling interval of Δt . Thus:

$$\zeta_n = \zeta(t_0 + n\Delta t) \quad n = 1, 2, \dots, N, \quad (9.7)$$

where t_0 is an arbitrary initial time and Δt is a sampling interval. During the wave experiment planning stage, particular care should be taken in the adoption of the Δt value. Let us assume that the frequency band of interest ranges from 0 to f_c (H_z) ($\omega_c = 2\pi f_c$ rad/s).

The number N of discrete samples, required to describe $\zeta(t)$, should satisfy the following relationship:

$$N = \frac{t}{1/2f_c} = 2f_c t = \frac{\omega_c t}{\pi}, \quad (9.8)$$

or

$$\Delta t = \frac{t}{N} = \frac{1}{2f_c} = \frac{\pi}{\omega_c}. \quad (9.9)$$

The fundamental increment $\Delta t = 1/2f_c = \left(\frac{\pi}{\omega_c}\right)$ is called the Nyquist sampling interval, and f_c or ω_c is called the Nyquist frequency. For example, a typical wave rider buoy records the surface elevation with sampling interval $\Delta t = 0.3906$ s. Therefore, the corresponding frequency band is $(0, 1.2801)$ Hz or $(0, 8.043)$ rad/s.

The sampling interval (9.9) is the maximum interval required to properly describe the data $\zeta(t)$. Frequencies in the original data above ω_c will lead to aliasing error, which is inherent in all digital processing, but not present in direct analog data processing. The use of discrete data points introduces a cut-off frequency in the spectrum, at frequency ω_c . This means that all variance in the data which must be accounted for, must be distributed amongst the bands below ω_c .

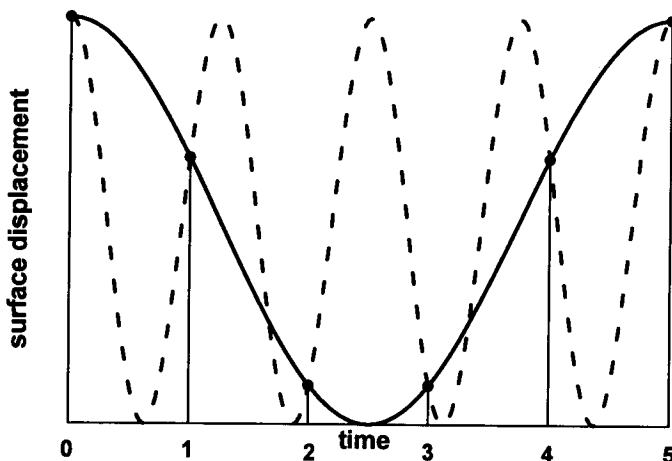


Figure 9.1: Illustration of an aliasing phenomenon.

However, some of this variance may come from the higher unresolvable frequencies. Such situation is illustrated in Fig. 9.1, in which two curves of different frequencies have been fitted to the same data. Only the continuous curve may be resolved, and the variance must be attributed to that, yet the data may be generated completely by the dashed curve. For any frequency f in the range $0 \leq \omega \leq \omega_c$, the higher frequencies which are aliased with ω_c are defined by:

$$(2\omega_c \pm \omega), (4\omega_c \pm \omega), \dots, (2n\omega_c \pm \omega), \dots \quad (9.10)$$

If $t = \frac{\pi}{\omega_c}$, the harmonic with frequency ω becomes:

$$\cos(\omega t) = \cos\left[(2n\omega_c \pm \omega) \frac{\pi}{\omega_c}\right] = \cos\left(\frac{\pi\omega}{\omega_c}\right). \quad (9.11)$$

Thus, all data at frequencies $(2n\omega_c \pm \omega)$ have the same cosine function as data at frequency ω , when sampled at points $\frac{\pi}{\omega_c}$ apart. For example, the wave rider buoy data ($\Delta t = 0.3906$ s, $\omega_c = 8.043$ rad/s) at frequency $\omega = 6$ rad/s would be aliased with data at the frequencies 10.086 rad/s, 22.086 rad/s, 26.172 rad/s, and so forth. Similarly, the power at these higher frequencies is aliased with the power in the lower frequencies. Thus, the true spectrum would be folded into the aliased spectrum.

9.2.2.2 Standardization of data, trend removal and filtering

Prior to calculating the frequency spectrum of surface elevation ζ , various preliminary operations are usually applied to the data, i.e. data standardization, trend removal and filtering. To standardize the ζ values we present them in a non-dimensional form:

$$\xi_n = \frac{\zeta_n - \bar{\zeta}}{\sigma_\zeta}, \quad (9.12)$$

where:

$$\bar{\zeta} = \frac{1}{N} \sum_{n=1}^N \zeta_n. \quad (9.13)$$

For a stationary ergodic process, the quantity $\bar{\zeta}$ is an unbiased estimate of the true mean value. The unbiased estimate of the standard deviation of data ζ_n is given by:

$$\sigma_\zeta = \left[\frac{1}{N-1} \sum_{n=1}^N (\zeta_n - \bar{\zeta})^2 \right]^{1/2}. \quad (9.14)$$

Especially in the case of wave orbital velocity measurements in a coastal zone, in regions with a large tidal motion, removal of the spurious trend or low frequency components, with a wavelength longer than the record length, is usually required. The most common technique for trend removal is to fit a low-order polynomial to the

data using the least square method. Thus, we assume that the original wave data $\{\zeta_n\}$ can be approximated by a polynomial of order K :

$$\tilde{\zeta}_n = \sum_{k=0}^K b_k (n\Delta t)^k \quad n = 1, 2, \dots, N. \quad (9.15)$$

A 'least squares' fit provides a system of equations for unknown coefficients b_k as (Bendat and Piersol, 1986):

$$\sum_{k=0}^K b_k \sum_{n=1}^N (n\Delta t)^{k+m} = \sum_{n=1}^N \zeta_n (n\Delta t)^m, \quad m = 0, 1, 2, \dots, K. \quad (9.16)$$

Assuming that $K = 1$, we obtain:

$$b_0 = \frac{2(2N+1) \sum_{n=1}^N \zeta_n - 6 \sum_{n=1}^N n \zeta_n}{N(N-1)}, \quad (9.17)$$

$$b_1 = \frac{12 \sum_{n=1}^N n \zeta_n - 6(N+1) \sum_{n=1}^N \zeta_n}{\Delta t N(N-1)(N+1)}. \quad (9.18)$$

The corrected time series $\hat{\zeta}_n$ now becomes:

$$\hat{\zeta}_n(n\Delta t) = \zeta_n(n\Delta t) - \sum_{k=0}^K b_k (n\Delta t)^k. \quad (9.19)$$

Filtering of wave data prior to a detailed analysis is desirable for various reasons. If we are particularly interested in wind-induced waves, the swell component should be filtered out. On the other hand, if we concentrate on the most energetic part of the wave spectrum only, the high frequency components with negligible energy should be removed by filtering.

Digital filtering can be performed in either the time domain or the frequency domain. A detailed description of those filtering procedures can be found elsewhere, so they are not repeated here (Otnes and Enochson, 1972).

9.2.2.3 Calculation of frequency spectra

Frequency spectra are usually estimated by either of two methods. The first one is based on the Wiener-Khinchine theorem (1.45) and is called the Blackman-Tukey procedure. In the second method, called the Cooley-Tukey method, the direct Fast Fourier Transformation is used. In the following, we briefly discuss both methods.

Blackman-Tukey method

The Blackman-Tukey procedure requires calculations in the following steps:

1. Subtracting a mean value from digital data $\{\hat{\zeta}_n\}$, trend removing and filtering (if necessary).
2. Calculating of the autocorrelation function:

$$K(r\Delta t) = \frac{1}{N-r} \sum_{n=1}^{N-r} \hat{\zeta}_n \hat{\zeta}_{n+r}, \quad r = 0, 1, 2, \dots, m, \quad (9.20)$$

where r is called the lag number and m is the maximum lag number ($m < N$). Selection of the m value, which provides the optimum estimate for the autocorrelation function, will be discussed later. A finite value of m implies that surface elevations $\zeta(t)$, at times $t > m\Delta t$ are uncorrelated.

3. Suppression of the spectrum leakage using a window for the autocorrelation function. Such window tapers the autocorrelation function to eliminate the discontinuity at the end of function K . There are numerous such windows in use. A typical window is the Hanning window:

$$u_{hr} = \frac{1}{2} \left(1 + \cos \frac{\pi r}{m} \right). \quad (9.21)$$

The modified autocorrelation function becomes:

$$\tilde{K}(r\Delta t) = K(r\Delta t)u_{hr}. \quad (9.22)$$

4. Calculating of the frequency spectral density by numerical integration of the autocorrelation function $\tilde{K}(r\Delta t)$:

$$S(\omega_k) = \frac{\Delta t}{\pi} \left\{ \tilde{K}(0) + 2 \sum_{r=1}^{m-1} \tilde{K}(r\Delta t) \cos \left(\frac{\pi r k}{m} \right) + \tilde{K}(m\Delta t) \cos(\pi k) \right\}, \quad (9.23)$$

for frequencies $\omega_k = k \Delta \omega = \frac{K\pi}{m\Delta t}$, $k = 0, 1, 2, \dots, m$.

The estimate $S(\omega)$ describes the time average of $[\hat{\zeta}(t)]^2$ in terms of its frequency components laying inside the frequency band: $\omega - \left(\frac{B_e}{2}\right), \omega + \left(\frac{B_e}{2}\right)$, divided by the resolution bandwidth B_e (rad/s). Equation (9.23) gives $\frac{1}{2}m$ independent estimates of the spectrum. The estimates separated by frequency increments smaller than $\frac{2f_c}{m}$ are correlated.

For a given bandwidth B_e , the required maximum lag number m is:

$$m = \frac{2\pi}{B_e \Delta t}. \quad (9.24)$$

The standard error ϵ of the spectrum estimation is usually presented as a function of the number of degrees of freedom n :

$$\epsilon = \sqrt{\frac{2}{n}} = \sqrt{\frac{m}{N}}, \quad (9.25)$$

where

$$n = \frac{nN}{m}. \quad (9.26)$$

It should be noted that, for given N , when the maximum lag number m is small, then the error is also small. The minimum total record length t , required to achieve a desired error ϵ in terms of other parameters, is given by:

$$t = \frac{2\pi}{B_e \epsilon^2} = \frac{m \Delta t}{\epsilon^2}. \quad (9.27)$$

Typical parameters for the measurement of surface waves, using the wave rider buoy, are:

$$\Delta t = 0.3906s, \quad N = 3072, \quad m = 30,$$

$$n = \frac{2N}{m} = 205, \quad \epsilon = \sqrt{\frac{2}{n}} = 9.8\%, \quad B_e = \frac{2\pi}{m \Delta t} = 0.534 \text{ rad/s}.$$

Method based on Fast Fourier Transform of original data

The direct transform of the data is an alternative method calculating the frequency spectra. We first assume that the wave record $\zeta(t)$ is given for a finite time interval $(0, t)$ and is sampled at N equally spaced points a distance Δt apart. The Fourier representation of the $\zeta(t)$ record is:

$$X(\omega, t) = \Delta t \sum_{n=0}^{N-1} \zeta_n \exp[-i\omega n \Delta t]. \quad (9.28)$$

The usual selection of discrete frequency values for the computation of $X(\omega, t)$ is:

$$\omega_k = \frac{2\pi k}{t} = \frac{2\pi k}{N \Delta t}, \quad k = 0, 1, 2, \dots, N-1. \quad (9.29)$$

Fast Fourier Transform techniques are designed to compute the quantities $X(\omega, t)$ and publications on FFT algorithms are very numerous. For example, the popular algorithm, appropriate for binary digital computers, was introduced by Cooley and Tukey (1965). This algorithm applies when the number of data samples N is a power of 2, i.e. $N = 2^p$. If necessary, zero is added to the data sequence to satisfy this requirement. The iterative procedure to determine quantities $X(\omega, t)$ requires the sum of p terms, where every term involves $(N/2)$ Fourier transforms, requiring 4

operations each. This gives a total of $2Np$ complex multiply-add operations. A full discussion of these matters is given by Cooley and Tukey (1965), Otnes and Enochson (1972), Bendat and Piersol (1986), and many others.

In practical calculations, the record $\zeta(t)$ is usually divided into K segments, each of length $L\Delta t$. The Fourier Transform of $\zeta(t)$ for each segment can then be viewed as the Fourier Transform of an unlimited time history record multiplied by a rectangular data window:

$$\tilde{\zeta}(t) = \zeta(t)v(t), \quad (9.30)$$

where:

$$v(t) = \begin{cases} 1 & \text{for } 0 \leq t \leq L\Delta t, \\ 0 & \text{otherwise.} \end{cases} \quad (9.31)$$

Fourier analysis of finite length records results in inherent side lobes in the spectral domain. The large side lobes allow leakage of energy at frequencies well separated from the main lobe. To reduce the leakage problem, it is common practice to introduce a time window that tapers the time-history data, to eliminate the discontinuities at the beginning and end of the records to be analysed. There are numerous such windows in current use. For example, the Hanning data window has the form:

$$v(t) = \begin{cases} \frac{1}{2} \left[1 - \cos \left(\frac{2\pi t}{L\Delta t} \right) \right] = 1 - \cos^2 \left(\frac{\pi t}{L\Delta t} \right) & \text{for } 0 \leq t \leq L\Delta t, \\ 0 & \text{otherwise.} \end{cases} \quad (9.32)$$

If the total number of points, N , cannot be made arbitrarily large to get better accuracy spectrum estimation, then a reasonable procedure is to overlap the segments by one half their length. The number of overlapping segments now becomes:

$$K_1 = \frac{2N}{L} - 1 = 2K - 1, \quad (9.33)$$

in which K is the number of non-overlapped segments.

The final estimate of the one-sided spectral density $S(\omega)$ becomes:

$$\tilde{S}(\omega_k) = \frac{2}{K_1 L \Delta t} \sum_{i=1}^{K_1} |X(\omega_k)|^2, \quad k = 0, 1, 2, \dots, \frac{L}{2}, \quad (9.34)$$

in which $\omega_k = \frac{2\pi k}{L\Delta t}$.

Similarly, the bispectrum $B(\omega_1, \omega_2)$ is estimated as:

$$B(\omega_1, \omega_2) = \frac{1}{K_1} \sum_{p=1}^{K_1} X_p(\omega_1) X_p(\omega_2) X_p^*(\omega_1 + \omega_2). \quad (9.35)$$

9.2.3 Calculation of statistical characteristics of waves

The basic statistical wave parameters, namely surface displacement, wave-induced orbital velocities and pressure at a given time, wave height, wave amplitude, and wave period, are the random variables subjected to various statistics which can be evaluated using experimental data.

Let us consider the N digital data values $\{x_n\}$, $n = 1, 2, \dots, N$ of surface elevation or orbital velocity (or pressure) with an equally spaced sampling interval of Δt seconds. We assume that record $x(t)$ is stationary with $\bar{x} = 0$. The estimate of the probability density function of $x(t)$ can be expressed as:

$$\tilde{f}(x) = \frac{N_x}{\Delta x N}, \quad (9.36)$$

where Δx is a narrow interval centered at x , and N_x is the number of data values that fall within the range $x \pm \frac{1}{2}\Delta x$. To find the number N_x , the full range of x is divided into a number of classes with intervals of equal widths. The number of data in each class is then tabulated. This procedure implies that the estimate $\tilde{f}(x)$ is dependent on the number of class intervals and their width Δx . In an analysis of wave data the number of class intervals is about 10–20.

The similar procedure is applied to estimate of the probability density function for a wave height or wave period. Assuming that the total number of waves in a record is N , the estimate of the probability density function for wave height or wave period takes the form of Eq. (9.36), in which Δx now denotes the width of class intervals for a wave height or wave period.

In addition to the estimation of the probability density function, estimates of statistical moments are also required. Eqs. (9.13) and (9.14) provide estimates of the first two moments. The estimates for the third and fourth central moments can be written as:

$$\mu_3 = E \left[(x - \bar{x})^3 \right] = \frac{N^2}{(N-1)(N-2)} m_3, \quad (9.37)$$

$$\mu_4 = E \left[(x - \bar{x})^4 \right] = \frac{N(N^2 - 2N + 3)m_4 - 3N(2N - 3)m_2^2}{(N-1)(N-2)(N-3)}, \quad (9.38)$$

where:

$$m_n = \frac{1}{N} \sum_{k=1}^N (x - \bar{x})^n. \quad (9.39)$$

Eqs. (9.37) and (9.38) are unbiased and consistent estimates of true central moments.

9.3 Measurement of wave directionality

In the past, various techniques have been used to measure the wave directionality. These included arrays of wave gauges (Barber, 1963; Krylov et al., 1966; Panicker and Borgman, 1970; Borgman, 1979; Krogstad, 1988; Nwogu, 1989; Young, 1994b), pitch-roll and cloverleaf buoys (Longuet-Higgins et al., 1961b; Mitsuyasu et al., 1975; Ewing and Laing, 1987; Tucker, 1989b; Brissette and Tsanis, 1994), and two-dimensional current meters (Simpson, 1969; Kobune and Hashimoto, 1986). Recently, completely new methods have become available, namely: stereophotogrammetry (Simpson, 1969; Holthuijsen, 1983; Davidan et al., 1985), marine radar (Young et al., 1985), HF radar (Tyler et al., 1974; Trizna et al., 1977, 1980), side-looking airborne radar (McLeish et al., 1981), and Synthetic Aperture Radar-SAR (Beal, 1986; Alpers and Bruening, 1986). In this Section, sea surface techniques are described, while remote sensing techniques are discussed, in a more general context, in the next Section.

9.3.1 Measurement techniques

As was mentioned in Chapter 3, the directional frequency spectrum $\hat{S}(\omega, \Theta)$ is commonly presented in terms of the one-dimensional spectrum $S(\omega)$:

$$\hat{S}(\omega, \Theta) = S(\omega) D(\Theta; \omega). \quad (9.40)$$

The directional spreading function $D(\omega, \Theta)$ satisfies the normalization condition:

$$\int_{-\pi}^{\pi} D(\Theta; \omega) d\Theta = 1. \quad (9.41)$$

Three main analytical forms for $D(\Theta; \omega)$ have been proposed by Longuet-Higgins et al. (1961), Mitsuyasu et al. (1975), Hasselmann et al. (1980), and Donelan et al. (1985) – see Eqs. (3.143), (3.146), (3.147) and (3.154). On the other hand, the most directional wave measurements consist of a time series of various wave parameters, e.g. surface elevation, water velocity, surface slope, dynamic pressure etc. There are two basic systems for measurement of wave directionality, i.e. the single point system and the spatial system. The most common are the following single point triples, which record three wave properties situated at the same location:

- the heave–pitch–roll buoy triplet $\left(\zeta, \frac{\partial \zeta}{\partial x}, \frac{\partial \zeta}{\partial y} \right)$,
- the pressure gauge–horizontal current triplet (p, u, v) .

An analysis of the resolving power of pitch–roll buoy systems shows that, although such instruments can provide an accurate measurement of the mean wave direction, directional spectra will be broader, compared with those of spatial array data.

The pressure–horizontal current triplet is recorded by some commercially manufactured current meters, for example, by the Inter Ocean' S4 current meter or the

Woods Hole directional current meter. The S4 current meter, due to its simplicity and efficiency, is commonly used for coastal and offshore oceanographic measurements. The instrument is spherical in shape with a diameter of 25 cm. Electrodes are located on the surface of the sphere; the compass and all electronics, including data storage as well as the power supply, are located within the sphere. The current meter measures the voltage, resulting from the motion of water, through a magnetic field generated by the instrument. At very low speeds, flow around a sphere is laminar and separation from the rear of the sphere does not occur. At higher speeds, the flow becomes turbulent. In order to avoid separation from the sphere, the spherical surface is vertically grooved.

The spatial array system is usually arranged in a linear or polygonal array. Wave direction is determined from the time series of wave elevation simultaneously measured by array gauges. The performance of a spatial array is determined by the number of array elements and their geometry (Davis and Regier, 1977). If there are n_e array elements there are at most $\frac{1}{2}n_e(n_e - 1) + 1$ truly distinct lags in the co-array. Other lags will be redundant, due to array symmetry. For optimum performance, an array should have as many non-redundant spatial lags between elements as possible (Young, 1994b).

The design of a directional wave gauge, based on pressure sensors arranged in an equilateral triangle array, was recently reported by Howell (1994). The system records directional spectra hourly, during a 13-month deployment period. If desired, the system can provide real-time data simultaneously with internal analysis and recording.

9.3.2 Determination of directional wave spectra

There is a number of possible analysis techniques for experimental data on directional spreading of wave energy. All techniques can be classified into two groups. In the first group, the directional spreading function has a predetermined form (for example, a Fourier series). The formulations within second group are independent models and are applicable when the direction spreading form is not prescribed in advance.

9.3.2.1 Fourier Expansion Method

To illustrate the Fourier Expansion Method (FEM), we consider data from pitch-roll buoys. The buoy measures a vertical displacement of the sea surface and its slope in coordinate directions, i.e. $\zeta(x, y, t)$, $\frac{\partial \zeta(x, y, t)}{\partial x}$ and $\frac{\partial \zeta(x, y, t)}{\partial y}$. Using the Fourier–Stieltjes integral representation of the sea surface, in space (ω, Θ) , we obtain:

$$\zeta(x, y, t) = \zeta_0 = \int_{-\infty}^{\infty} \int_{-\pi}^{\pi} \exp[ik(x \cos \Theta + y \sin \Theta) - i\omega t] dA(\omega, \Theta). \quad (9.42)$$

The relationship between wave amplitude $dA(\omega, \Theta)$ and two-dimensional energy spectrum $\hat{S}(\omega, \Theta)$ is given by:

$$E[dA(\omega, \Theta) dA^*(\omega', \Theta')] = \hat{S}(\omega, \Theta) \delta(\omega - \omega') \delta(\Theta - \Theta') d\omega d\omega' d\Theta d\Theta'. \quad (9.43)$$

The sea surface slopes $\frac{\partial \zeta}{\partial x}$ and $\frac{\partial \zeta}{\partial y}$ at point (x, y) become:

$$\frac{\partial \zeta}{\partial x} = \zeta_1 = \int_{-\infty}^{\infty} \int_{-\pi}^{\pi} ik \cos \Theta \exp[ik(x \cos \Theta + y \sin \Theta) - i\omega t] dA(\omega, \Theta), \quad (9.44)$$

$$\frac{\partial \zeta}{\partial y} = \zeta_2 = \int_{-\infty}^{\infty} \int_{-\pi}^{\pi} ik \sin \Theta \exp[ik(x \cos \Theta + y \sin \Theta) - i\omega t] dA(\omega, \Theta). \quad (9.45)$$

Covariance functions and corresponding co- and quadrature spectra can be calculated for any of the data pairs (ζ_j, ζ_k) ($j, k = 0, 1, 2$). Using the method described in Section 1.3.3, we obtain:

$$S_{jk}(\omega) = C_{jk}(\omega) + iQ_{jk}(\omega), \quad (9.46)$$

where:

pair (ζ_0, ζ_0) :

$$\left. \begin{aligned} C_{00}(\omega) &= \int_{-\pi}^{\pi} \hat{S}(\omega, \Theta) d\Theta \\ Q_{00}(\omega) &= 0 \end{aligned} \right\}, \quad (9.47)$$

pair (ζ_0, ζ_2) :

$$\left. \begin{aligned} C_{02}(\omega) &= 0 \\ Q_{02}(\omega) &= \int_{-\pi}^{\pi} k \sin \Theta \hat{S}(\omega, \Theta) d\Theta \end{aligned} \right\}, \quad (9.48)$$

pair (ζ_1, ζ_1) :

$$\left. \begin{aligned} C_{11}(\omega) &= \int_{-\pi}^{\pi} k^2 \cos^2 \Theta \hat{S}(\omega, \Theta) d\Theta \\ Q_{11}(\omega) &= 0 \end{aligned} \right\}, \quad (9.49)$$

pair (ζ_2, ζ_2) :

$$\left. \begin{aligned} C_{22}(\omega) &= \int_{-\pi}^{\pi} k^2 \sin^2 \Theta \hat{S}(\omega, \Theta) d\Theta \\ Q_{22}(\omega) &= 0 \end{aligned} \right\}, \quad (9.50)$$

pair (ζ_1, ζ_2) :

$$\left. \begin{aligned} C_{12}(\omega) &= \int_{-\pi}^{\pi} k^2 \sin \Theta \cos \Theta \hat{S}(\omega, \Theta) d\Theta \\ Q_{12}(\omega) &= 0 \end{aligned} \right\}. \quad (9.51)$$

We can now assume that the two-dimensional spectrum $\hat{S}(\omega, \Theta)$ is expanded in the Fourier series:

$$\hat{S}(\omega, \Theta) = \frac{1}{2}a_0 + \sum_{n=1}^M a_n(\omega) \cos(n\Theta) + b_n(\omega) \sin(n\Theta), \quad (9.52)$$

or:

$$\hat{S}(\omega, \Theta) = \sum_{n=-M}^M q_n(\omega) \exp(in\Theta). \quad (9.53)$$

In our case $M = 2$. The q_n values are related to a_n and b_n as follows:

$$\left. \begin{aligned} q_0(\omega) &= \frac{1}{2}a_0 \\ q_n(\omega) &= \frac{1}{2}(a_0 - ib_n) \\ q_{-n}(\omega) &= \frac{1}{2}(a_0 + ib_n) \end{aligned} \right\}. \quad (9.54)$$

Thus:

$$\left. \begin{aligned} a_0(\omega) &= 2q_0(\omega) \\ a_n(\omega) &= q_n(\omega) + q_{-n}(\omega), \quad n = 1, 2 \\ b_n(\omega) &= \frac{1}{i} [q_{-n}(\omega) - q_n(\omega)], \quad n = 1, 2 \end{aligned} \right\}. \quad (9.55)$$

The $q_n(\omega)$ functions can be written as one integral:

$$q_n(\omega) = \frac{1}{2\pi} \int_{-\pi}^{\pi} \hat{S}(\omega, \Theta) \exp(-in\Theta) d\Theta \quad \text{for } n = 0, \pm 1, \pm 2. \quad (9.56)$$

Comparing Eqs. (9.55) with (9.47) – (9.51), and using Eq. (9.56), we obtain the first five coefficients as follows:

$$a_0(\omega) = \frac{1}{\pi} \int_{-\pi}^{\pi} \hat{S}(\omega, \Theta) d\Theta = \frac{1}{\pi} C_{00}(\omega), \quad (9.57)$$

$$a_1(\omega) = \frac{1}{\pi} \int_{-\pi}^{\pi} \cos \Theta \hat{S}(\omega, \Theta) d\Theta = \frac{1}{\pi k} Q_{01}(\omega), \quad (9.58)$$

$$\begin{aligned} a_2(\omega) &= \frac{1}{\pi} \int_{-\pi}^{\pi} \cos 2\Theta \hat{S}(\omega, \Theta) d\Theta = \\ &= \frac{1}{\pi} \int_{-\pi}^{\pi} (\cos^2 \Theta - \sin^2 \Theta) \hat{S}(\omega, \Theta) d\Theta = \frac{1}{\pi k^2} (C_{11}(\omega) - C_{22}(\omega)), \end{aligned} \quad (9.59)$$

and

$$b_1(\omega) = \frac{1}{\pi} \int_{-\pi}^{\pi} \sin \Theta \hat{S}(\omega, \Theta) d\Theta = \frac{1}{\pi k} Q_{02}(\omega), \quad (9.60)$$

$$b_2(\omega) = \frac{1}{\pi} \int_{-\pi}^{\pi} \sin 2\Theta \hat{S}(\omega, \Theta) d\Theta = \frac{2}{\pi k^2} C_{12}(\omega). \quad (9.61)$$

The series must be truncated at $M = 2$. This results in development of the negative lobes for spectrum $\hat{S}(\omega, \Theta)$. The negative lobes can be eliminated by using a special weighting function, which results as the spectrum $\hat{S}(\omega, \Theta)$ in the form (Longuet-Higgins et al., 1961b):

$$\hat{S}(\omega, \Theta) \approx \frac{a_0(\omega)}{2} + \frac{2}{3} [a_1(\omega) \cos \Theta + b_1(\omega) \sin \Theta] + \frac{1}{6} [a_2(\omega) \cos 2\Theta + b_2(\omega) \sin 2\Theta]. \quad (9.62)$$

As the spectrum is essentially non-negative, Longuet-Higgins et al. (1961b) suggested to constrain the directional spreading function to the parametric form given in Eq. (3.143). Thus, we have:

$$\hat{S}(\omega, \Theta) = S(\omega) D(\Theta; \omega), \quad (9.63)$$

in which:

$$D(\Theta; \omega) = \frac{2^{2s-1} \Gamma^2(s+1)}{\pi \Gamma(2s+1)} \cos^{2s} \left(\frac{\Theta - \Theta_0}{2} \right). \quad (9.64)$$

Using the coefficients a_n and b_n , given above, the parameters Θ_0 and s can be determined to first order approximation as:

$$\Theta_0 = \arctan \left(\frac{b_1}{a_1} \right), \quad (9.65)$$

$$S = \frac{\sqrt{a_1^2 + b_1^2}}{a_0 - \sqrt{a_1^2 + b_1^2}}. \quad (9.66)$$

This approach was applied by Mitsuyasu et al. (1975) and Hasselmann et al. (1980).

9.3.2.2 Maximum Entropy Method

In Section 4.2.5 the Maximum Entropy Method (MEM) was applied for determining the probability density function of surface displacements in finite water depth. The MEM is the independent method, used when the function which has to be approximated has no prescribed form. In this Section we use the MEM for determining the directional spreading function. We consider a single point system which measures underwater pressure and two orbital velocity components. An example of such a system is the popular S4 current meter, mentioned above.

Wave pressure (expressed in the water column) at a given level z below the mean water level is:

$$p = -\frac{1}{\rho g} \left(\rho \frac{\partial \Phi}{\partial t} \right) = \int_{-\infty}^{\infty} \int_{-\pi}^{\pi} \frac{\cosh k(z+h)}{\cosh kh} \exp [ik(x \cos \Theta + y \sin \Theta) - i\omega t] dA(\omega, \Theta), \quad (9.67)$$

or:

$$p(x, y, z, t) = \int_{-\infty}^{\infty} \int_{-\pi}^{\pi} \exp [ik(x \cos \Theta + y \sin \Theta) - i\omega t] dP(\omega, \Theta), \quad (9.68)$$

in which the spectral pressure amplitude is:

$$dP(\omega, \Theta) = \frac{\cosh k(z + h)}{\cosh kh} dA(\omega, \Theta). \quad (9.69)$$

Therefore, the two-dimensional spectrum for dynamic pressure becomes:

$$\overline{dP(\omega, \Theta) dP^*(\omega_1, \Theta_1)} = \hat{S}_{pp}(\omega, \Theta) \delta(\omega - \omega_1) \delta(\Theta - \Theta_1) d\omega d\omega_1 d\Theta d\Theta_1. \quad (9.70)$$

It should be noted from Eq. (9.69), that the directional properties of the dynamic pressure are the same as for the surface waves, because the transfer function $\frac{\cosh k(z + h)}{\cosh kh}$ does not depend on the direction Θ . Therefore, the directional spreading function, defined on the basis of S4 current meter measurements, reflects the directional spreading function of the surface waves too.

In a similar way, the orbital velocity components become:

$$u = \int_{-\infty}^{\infty} \int_{-\pi}^{\pi} \frac{gk \cos \Theta}{\omega} \exp [ik(x \cos \Theta + y \sin \Theta) - i\omega t] dP(\omega, \Theta), \quad (9.71)$$

and:

$$v = \int_{-\infty}^{\infty} \int_{-\pi}^{\pi} \frac{gk \sin \Theta}{\omega} \exp [ik(x \cos \Theta + y \sin \Theta) - i\omega t] dP(\omega, \Theta). \quad (9.72)$$

Let us formulate the cross-correlation and cross-spectral functions for pressure and velocities. For convenience later we can assume that velocities and pressure are recorded at the origin of the coordinate system, i.e. $x = y = 0$. Thus, for the cross-correlation of pressure $p(t)$ and velocity $u(t)$, we obtain:

$$K_{pu}(\tau) = \int_{-\infty}^{\infty} \left\{ \frac{gk}{\omega} S_{pp}(\omega) \int_{-\pi}^{\pi} \cos \Theta D(\Theta; \omega) d\Theta \right\} e^{i\omega\tau} d\omega, \quad (9.73)$$

and

$$S_{pu}(\omega) = C_{pu}(\omega) + iQ_{pu}(\omega), \quad (9.74)$$

in which:

$$C_{pu}(\omega) = \frac{gk}{\omega} S_{pp}(\omega) \int_{-\pi}^{\pi} \cos \Theta D(\Theta; \omega) d\Theta, \quad (9.75)$$

$$Q_{pu}(\omega) = 0. \quad (9.76)$$

The vanishing of the quadrature spectral density $Q_{pu}(\omega)$ is a consequence of the assumption that pressure p and velocity u are given at the same point, and that there is no time delay between them.

For convenience later, we rewrite Eq. (9.75) as:

$$\int_{-\pi}^{\pi} D(\Theta; \omega) \cos \Theta d\Theta = \frac{C_{pu}(\omega)}{S_{pp}(\omega)} \frac{\omega}{gk}. \quad (9.77)$$

In a similar way we have:

$$\int_{-\pi}^{\pi} D(\Theta; \omega) \sin \Theta d\Theta = \frac{C_{pv}(\omega)}{S_{pp}(\omega)} \frac{\omega}{gk}, \quad (9.78)$$

and

$$\int_{-\pi}^{\pi} D(\Theta; \omega) \sin 2\Theta d\Theta = 2 \frac{C_{uv}(\omega)}{S_{pp}(\omega)} \left(\frac{\omega}{gk} \right)^2, \quad (9.79)$$

in which C_{pv} and C_{uv} are the co-spectra for pressure p and velocity v , and for velocities u and v , respectively.

It can be shown that the autocorrelation function $K_{pp}(\tau)$, for pressure $p(t)$, takes the form:

$$K_{pp}(\tau) = \frac{1}{2} \int_{-\infty}^{\infty} \left\{ S_{pp}(\omega) \int_{-\pi}^{\pi} D(\Theta; \omega) d\Theta \right\} e^{i\omega\tau} d\omega = \frac{1}{2} \int_{-\infty}^{\infty} S_{pp}(\omega) e^{i\omega\tau} d\omega. \quad (9.80)$$

Thus:

$$\int_{-\pi}^{\pi} D(\Theta; \omega) d\Theta = 1. \quad (9.81)$$

The spectra $S_{uu}(\omega)$ and $S_{vv}(\omega)$ are given by the following relationships:

$$S_{uu}(\omega) = \left(\frac{gk}{\omega} \right)^2 S_{pp}(\omega) \int_{-\pi}^{\pi} \cos^2 \Theta D(\Theta; \omega) d\Theta, \quad (9.82)$$

and

$$S_{vv}(\omega) = \left(\frac{gk}{\omega} \right)^2 S_{pp}(\omega) \int_{-\pi}^{\pi} \sin^2 \Theta D(\Theta; \omega) d\Theta. \quad (9.83)$$

Equations (9.82) and (9.83) can be combined to give:

$$\int_{-\pi}^{\pi} D(\Theta; \omega) \cos 2\Theta d\Theta = \frac{C_{uu}(\omega) - C_{vv}(\omega)}{S_{pp}(\omega)} \left(\frac{\omega}{gk} \right)^2, \quad (9.84)$$

in which $C_{uu}(\omega) = S_{uu}(\omega)$ and $C_{vv}(\omega) = S_{vv}(\omega)$.

For convenience later we can rewrite Eqs. (9.77), (9.78), (9.79), (9.81) and (9.84) in a more compact form:

$$\int_{-\pi}^{\pi} D(\Theta; \omega) \alpha_i(\Theta) d\Theta = \beta_i, \quad i = 0, 1, \dots, 4, \quad (9.85)$$

in which:

$$\alpha_0 = 1; \quad \alpha_1 = \cos \Theta; \quad \alpha_2 = \sin \Theta; \quad \alpha_3 = \cos 2\Theta; \quad \alpha_4 = \sin 2\Theta, \quad (9.86)$$

$$\beta_0 = 1; \quad \beta_1 = \frac{C_{pu}(\omega)}{S_{pp}(\omega)} \frac{\omega}{gk}; \quad \beta_2 = \frac{C_{pv}(\omega)}{S_{pp}(\omega)} \frac{\omega}{gk}, \quad (9.87)$$

$$\beta_3 = \frac{C_{uu}(\omega) - C_{vv}(\omega)}{S_{pp}(\omega)} \left(\frac{\omega}{gk} \right)^2, \quad (9.88)$$

$$\beta_4 = 2 \frac{C_{uv}(\omega)}{S_{pp}(\omega)} \left(\frac{\omega}{gk} \right)^2. \quad (9.89)$$

Equation (9.85) forms a system of basic equations for the unknown directional spreading function $D(\Theta; \omega)$. The directional spreading $D(\Theta; \omega)$ is a non-negative function, defined within the range $(-\pi, \pi)$ and the restriction (9.81), imposed on the directional spreading function $D(\Theta; \omega)$, is the same as that imposed in the probability density function. Thus, it is expected that the directional spreading function can be obtained through a similar procedure as the probability density function given in Section 4.2.5.

Equation (9.85) is generally insufficient to define $D(\Theta; \omega)$ uniquely, but may delineate a set of feasible directional spreading functions. These functions contain a certain amount of uncertainty which can be expressed by employing the concept of entropy. The entropy is a numerical measure of uncertainty associated with $D(\Theta; \omega)$. In particular, the entropy functional in terms of the directional spreading $D(\Theta; \omega)$ can be written as (Kobune and Hashimoto, 1986):

$$E = - \int_{-\pi}^{\pi} D(\Theta; \omega) \ln [D(\Theta; \omega)] d\Theta. \quad (9.90)$$

The principle of the maximum entropy states that the minimally prejudiced assignment of directional spreading is that which maximizes the entropy E subject to given constraints (9.85). In order to maximize the entropy functional E by the method of Lagrange multipliers we introduce parameters $(1 - \lambda_0), \lambda_1, \dots, \lambda_4$, which are chosen such that variations in a functional of $D(\Theta; \omega)$ vanish, i.e.:

$$E = - \int_{-\pi}^{\pi} D(\Theta; \omega) \left\{ [\ln [D(\Theta; \omega)]] + (\lambda_0 - 1) + \sum_{i=1}^4 \lambda_i \alpha_i \right\} d\Theta. \quad (9.91)$$

This gives:

$$D(\Theta; \omega) = \exp \left\{ - \left[\lambda_0 + \sum_{i=1}^4 \lambda_i \alpha_i(\Theta) \right] \right\}. \quad (9.92)$$

The function $D(\Theta; \omega)$ is the MEM estimate of the true directional spreading function, based on knowledge of the α_i and β_i functions. After substituting Eq. (9.92) into Eq. (9.85), we obtain:

$$\int_{-\pi}^{\pi} \exp \left\{ - \left[\lambda_0 + \sum_{i=1}^4 \lambda_i \alpha_i(\Theta) \right] \right\} \alpha_i(\Theta) d\Theta = \beta_i. \quad (9.93)$$

In particular, for $i = 0$ we get:

$$\lambda_0 = \ln \left\{ \int_{-\pi}^{\pi} \exp \left[- \sum_{j=1}^4 \lambda_j \alpha_j(\Theta) \right] d\Theta \right\}. \quad (9.94)$$

Finally, using Eq. (9.94) in Eq. (9.93), we can represent the set of nonlinear equations for unknown Lagrange multipliers λ_i as:

$$\int_{-\pi}^{\pi} [\beta_i - \alpha_i(\Theta)] \exp \left\{ - \sum_{j=1}^4 \lambda_j \alpha_j(\Theta) \right\} d\Theta = 0 \quad i = 1, 2, 3, 4. \quad (9.95)$$

To solve a nonlinear system of equations (9.95), the Newton-Raphson method is used, i.e.:

$$\sum_{j=1}^4 A_{ij} \epsilon_j = B_i, \quad (i = 1, 2, 3, 4), \quad (9.96)$$

in which:

$$A_{ij} = \int_{-\pi}^{\pi} [\alpha_i(\Theta) - \beta_i] \alpha_j(\Theta) \exp \left[- \sum_{l=1}^4 \lambda_l \alpha_l(\Theta) \right] d\Theta, \quad (9.97)$$

$$B_i = \int_{-\pi}^{\pi} [\alpha_i(\Theta) - \beta_i] \exp \left[- \sum_{l=1}^4 \lambda_l \alpha_l(\Theta) \right] d\Theta, \quad (9.98)$$

and

$$\epsilon_j = \lambda_j^{(k+1)} - \lambda_j^{(k)}.$$

The $\lambda_j^{(k)}$ denotes the value of multiplier λ_j in the k -th iteration, while $\lambda_j^{(k+1)}$ is the value of this multiplier in the $(k+1)$ -th iteration.

The Newton-Raphson method converges rapidly if the starting values are sufficiently close to the exact solution. In order to generate the 'proper' starting values for λ_j we assume that the first approximation for the directional spreading function $D(\Theta; \omega)$ will be a cosine-type spreading:

$$D(\Theta; \omega) = \frac{4}{3\pi} \cos^4 \left(\frac{\Theta - \Theta_0}{2} \right). \quad (9.99)$$

Assuming that the directional spreading function (9.99) is a first approximation for function (9.92), we obtain the following first approximations for the unknown Lagrange multipliers:

$$\lambda_0 = \frac{1}{2} \left[\ln \left(\frac{3\sqrt{3}}{2} \pi^{3/2} \right) + \frac{\xi}{2} \right], \quad (9.100)$$

$$\lambda_1 = \frac{1}{2} \left[\ln \left(\frac{3\pi}{4} \right) - \xi \right] \cos \Theta_0(\omega), \quad (9.101)$$

$$\lambda_2 = \frac{1}{2} \left[\ln \left(\frac{3\pi}{4} \right) - \xi \right] \sin \Theta_0(\omega), \quad (9.102)$$

$$\lambda_3 = [\lambda_0 - \ln(3\pi)] \cos 2\Theta_0(\omega), \quad (9.103)$$

$$\lambda_4 = [\lambda_0 - \ln(3\pi)] \sin 2\Theta_0(\omega), \quad (9.104)$$

in which $\xi \approx 5.0$ is a best fit parameter.

The main direction $\Theta_0(\omega)$ is simply estimated as:

$$\Theta_0(\omega) \approx \arctan \left(\sqrt{\frac{C_{vv}(\omega)}{C_{uu}(\omega)}} \right). \quad (9.105)$$

9.3.2.3 Maximum Likelihood Method

The Maximum Likelihood Method (MLM) is another procedure which belongs to the class of independent formulation models. This method provides the directional spectrum which has the maximum likelihood of conforming to the limited number of cross-spectral estimates. As a first step in the procedure, the estimated wave number-frequency spectrum $\tilde{\Psi}(k, \omega)$ is expressed as a linear combination of the cross-spectra (Isobe et al., 1984):

$$\tilde{\Psi}(\vec{k}, \omega) = \sum_m \sum_n \alpha_{mn}^{(\vec{k})} S_{mn}(\omega), \quad (9.106)$$

in which summation is extended over all measured wave properties, and α_{mn} are coefficients. Using the arguments given in Chapter 3, the cross-spectra $S_{mn}(\omega)$ can be represented as:

$$S_{mn}(\omega) = \int_{\vec{k}} e^{-i\vec{k}(\vec{x}_n - \vec{x}_m)} \Psi(\vec{k}, \omega) d\vec{k}, \quad (9.107)$$

where \vec{x}_n are the locations of the particular wave gauges. After substituting Eq. (9.107) into Eq. (9.110) we obtain:

$$\tilde{\Psi}(\vec{k}, \omega) = \int_{\vec{k}'} \Psi(\vec{k}', \omega) w(\vec{k}, \vec{k}') d\vec{k}', \quad (9.108)$$

in which:

$$w(\vec{k}, \vec{k}') = \sum_m \sum_n \alpha_{mn}(\vec{k}) e^{-i\vec{k}'(\vec{x}_n - \vec{x}_m)}. \quad (9.109)$$

Equation (9.108) indicates that the estimate of the wave number-frequency spectrum can be determined as a convolution of the true wave number-frequency spectrum and the window function $w(\vec{k}, \vec{k}')$. The best approximation of the true wave number-frequency spectrum $\Psi(\vec{k}, \omega)$ can be achieved when the function $w(\vec{k}, \vec{k}')$ is very close to Dirac's delta form.

As both the true wave number-frequency spectrum $\Psi(\vec{k}, \omega)$ and function $w(\vec{k}, \vec{k}')$ are non-negative functions, with the best approximation being associated with minimizing the $\Psi(\vec{k}, \omega)$ spectrum, i.e.:

$$\sum_m \sum_n \gamma_m(\vec{k}) S_{mn}(\omega) \gamma_n^*(\vec{k}) \rightarrow \text{minimum}, \quad (9.110)$$

in which $\gamma_m(\vec{k})$ and $\gamma_n^*(\vec{k})$ are given by:

$$\alpha_{mn}(\vec{k}) = \gamma_m(\vec{k}) \gamma_n^*(\vec{k}). \quad (9.111)$$

The minimizing procedure, based on the Lagrange multiplier theory (see Isobe et al., 1984 for details), yields the following final expression for estimate $\tilde{\Psi}(\vec{k}, \omega)$:

$$\tilde{\Psi}(\vec{k}, \omega) = \frac{A(\omega)}{\sum_m \sum_n S_{mn}^{-1}(\omega) e^{i\vec{k}(\vec{x}_n - \vec{x}_m)}}. \quad (9.112)$$

The normalization factor $A(\omega)$ should be determined from the relationship between the wave number-frequency spectrum and the frequency spectrum $S(\omega)$, i.e. $\Psi(\vec{k}, \omega)$:

$$S(\omega) = \int_{\vec{k}} \tilde{\Psi}(\vec{k}, \omega) d\vec{k}. \quad (9.113)$$

It should be noted that the Maximum Likelihood Method (MLM) may be applied to spatial arrays of any wave instruments (wave meters, accelerometers, current meters, pressure sensors, etc.) and pitch-roll buoys, by adopting the appropriate cross-spectral function $S_{mn}(\omega)$ (Isobe et al., 1984) and (Young, 1994b).

9.3.2.4 Comparison of various analytical techniques

Besides the Fourier Expansion Method (FEM), Maximum Entropy Method (MEM), and Maximum Likelihood Method (MLM), several other methods are also used. Long and Hasselmann (1979) proposed a variational fitting technique in which the initial estimate is subsequently modified to minimize a 'nastiness' function, depending on various properties related to the directional spreading function $D(\Theta; \omega)$. Haug and Krogstad (1994) derived a combined Maximum Likelihood – Maximum Entropy

Method which has been shown to have superior properties compared to the MLM. Also in use is a Maximum Entropy Method, based on the autoregressive process of directional waves (Kim et al., 1994). Hashimoto et al. (1987) introduced a Bayesian Directional Method (BDM) to assess the directional spreading function $D(\Theta; \omega)$. No *a priori* assumption is made on the function $D(\Theta; \omega)$ which is considered a piecewise constant function over band $[0, 2\pi]$. The values of $D(\Theta; \omega)$, on each segment, are obtained from the constraints of the spectral cross-correlation coefficients, when the measurement errors are taken into account.

A comparison of various analysis methods yields the following conclusions (Kim et al., 1994; Benoit, 1994; Young, 1994b):

1. The Fourier Expansion Method (FEM) can be very easily implemented, but it often has the shortcoming of producing a negative spectral value.
2. Although the MLM produces a superior representation of the directional spreading, when applied to pitch-roll buoy data, the improvement is only marginal.
3. The MEM, based on a probability density distribution of directional waves, shows an overall better performance than the MEM based on autoregressive processes and FEM. The MEM is able to describe asymmetric, multiple-peaked spectra.
4. The combined MLM/MEM has superior properties, compared to MLM.
5. Although rather difficult to implement, the BDM provides a very accurate estimate of the true directional spreading function, without any side lobes. This applies even when the distance between the wave gauges is twice that of the wavelength. It is the preferred method when at least four wave properties are simultaneously recorded. When only three elements are measured, the MLM or MEM are recommended.
6. Improved instrument performance can be achieved by increasing the number of measurement elements in the measurement system, which can be achieved with a spatial array of wave gauges.

9.4 Remote sensing techniques

9.4.1 A brief orientation

The launch of oceanographic satellites has provided a new and extensive set of data on the state of the ocean surface. These measurements are of special importance in a study of the deep oceans, which comprise the vast majority of the globe, where reliable observations are almost nonexistent.

As was shown in Chapter 8, ship observations are not accurate and their spatial coverage is non-uniform. Furthermore, the operation of conventional buoys in deep regions is expensive.

At present, in terms of ocean surface waves, the most important satellite remote sensing systems are: SEASAT, GEOSAT, TOPEX-POSEIDON, RADARSAT, ERS-1 and ERS-2. An overview of all satellites deploying instruments detecting the ocean surface is given by Komen et al. (1994). There are three standard active microwave instruments of principal interest for surface wave detection; namely, the altimeter, the Synthetic Aperture Radar (SAR) and scatterometer. These instruments can provide global, all weather, day and night data coverage.

A typical polar orbiting satellite orbits the earth once every 100 min, which corresponds to a spacing of 2800 km at the Equator and a mean equatorial separation of all ascending and descending orbits within one day of 1400 km. As the grid fills in, the spacing is reduced. For example, GEOSAT which was launched in March 1985 and operated till January 1990 (however, quantity of usable data gradually started to decline in early 1989), was placed in a 17-day repeat pattern, corresponding to ground track spacing of 1.475° , i.e. 163 km at the Equator and 82 km at a latitude of 60° (Tournadre and Ezraty, 1990). This data coverage is still not sufficient for the computation of wind and wave fields on the typical synoptic scale of weather variability. Therefore, to interpolate the wind and wave fields in an optimal way, the data must be assimilated with available data from conventional observations or numerical models.

9.4.2 Application of satellite altimetry

In order to provide some understanding of the relationship between the signal measured by the instrument and the physical characteristics of the medium from which the signal backscatters, we must first provide some information on the satellite altimeter's operation. However, we will concentrate only on surface wave detection. The derivation of wind speed at the ocean surface from the altimeter backscatter is described elsewhere (for example, Dobson et al., 1987).

The radar altimeter is a nadir-looking instrument. The measurement of the travel time of the reflected microwave pulse yields the position of the sea surface relative to the orbit of the satellite. The distortion of the mean shape of the return pulse provides an estimate of the sea surface variance m_0 , and hence of significant wave height $H_{m_0} = 4\sqrt{m_0}$. In particular, the earlier return from the wave crest and the retarded return from the wave troughs leads to a broadening of the return pulse, which can be directly related to the significant wave height. The shape of the return pulse depends upon the statistics of the reflecting surface. For a Gaussian sea surface, the relation between pulse shape and the root mean square value of the surface displacement can be computed theoretically (Brown, 1977). To determine a mean pulse shape, several

hundred pulses need to be averaged, resulting in one significant wave height estimate about every 7 km along the satellite track.

The comparison of GEOSAT estimates of significant wave height H_{m0} against values from buoys, in NOAA's National Data Buoy Center network, showed that GEOSAT underestimated the significant wave height by 13% (Carter et al., 1992), i.e.:

$$H_{m0}^{(buoy)} = 1.13H_{m0}^{(alt)}. \quad (9.114)$$

The correction factor introduced by Hayne and Hancock (1990), to the procedure used on board GEOSAT, reduced the excess of the buoy data over the GEOSAT values to 6%.

Recent studies for the ERS-1 altimeter showed a satisfactory agreement for wave heights up to 4 m. The higher waves are underestimated by the altimeter, relative to the buoy data. When compared with the WAM numerical prediction model, the altimeter wave height measurements showed the best agreement in the Northern Hemisphere. In the Southern Hemisphere, the WAM model predicts wave heights lower than the altimeter wave heights (Komen et al., 1994).

As was mentioned in Chapter 8, mean monthly significant wave height climatologies for the globe, based on 3-year GEOSAT radar altimeter data, were reported by Young (1994a).

9.4.3 Application of satellite Synthetic Aperture Radar

Synthetic Aperture Radar (SAR) is a high resolution imaging system. It is based on the emission of short pulses at an incidence angle of 20° to 25° . The amplitude and phase histories of the returned signals, from a large number of pulses, are collected to simulate the signal from a large antenna. The typical swath scanned by SAR is of the order of 100 km, with a resolution of $20 \text{ m} \times 20 \text{ m}$.

The reflectivity of a moving, random backscattering sea surface is regarded as spatially uncorrelated (a white noise process) within the spatial resolution of a SAR. The variance spectrum of such a backscattering surface is a function of position in the wave field. When this spectrum is known, the imaging problem is reduced to a typical mapping procedure. For the linear small-wave limit, the mapping can be represented in terms of the linear transfer function, relating the wave and image spectra.

The dominant backscattering process is Bragg scattering for which the incident electromagnetic waves interact resonantly with short ripple waves. The resonant condition is:

$$\vec{k}_b = \pm 2\vec{k}_0, \quad (9.115)$$

in which \vec{k}_0 is the projection of the incident wave number onto the facet plane. Thus:

$$\vec{k}_b = (0, 2k_0 \sin \phi), \quad (9.116)$$

where ϕ is the angle of incidence. This Bragg scattering is the same as, for example, the scattering of surface waves incident in a region of undulating seabed topography (Mei, 1985; Massel, 1989).

The two-dimensional, instantaneous ocean surface images contain information on the two-dimensional wave spectrum (Beal et al., 1986). Extraction of the wave spectra from SAR image spectra is a complicated procedure, due to processes modulating the backscattering signal. The most important processes are:

1. Variation in the local angle of incidence associated with variation in the facet orientation and position.
2. Variation in the energy of Bragg scattering, caused by interactions between the short ripples and longer waves.
3. Oscillation of the Doppler shift of the return signal which results in variations of the apparent facet density in the SAR image plane.

A full discussion of the extraction processes and comparison with the WAM model can be found in the book by Komen et al. (1994). The comparison of spectral peak wavelength and wave direction obtained from the SAR image with a surface buoy is reported by Rufenach et al. (1991).

Usefulness of SAR data can be substantially upgraded by using model spectra as a first-guess input. The combination of using model results and observations to create an optimal estimate of the sea state is known as the data assimilation process. However, the description of this process is beyond the scope of this book. A full explanation of data assimilation can be found elsewhere (Komen et al., 1994).

9.5 Numerical simulation techniques

Marine engineers and oceanographers are becoming more and more concerned with applying the concept of a directional wave spectrum $S(\omega\Theta)$. The preferred data base for such an application is a number of actual measurements of spectra taken during major storms at the site of interest. However, in most cases this is unavailable. Directional buoys are deployed in some restricted waters where the data are needed for ship routing and general ocean engineering. Remote sensing techniques are very expensive and still far from being routinely applicable. In such a situation, simulated data provide an alternative solution.

In simulation, the common assumption is that the water level elevations take the form:

$$\zeta(x, y, t) = 2 \sum_{m=1}^{M_\omega} \sum_{n=1}^{N_\Theta} A_{nm} \cos(k_m x \cos \Theta_n + k_m y \sin \Theta_n - \omega_m t + \epsilon_{nm}), \quad (9.117)$$

in which:

$$A_{nm}^2 = \hat{S}(\omega_m, \Theta_n) \Delta\omega_m \Delta\Theta_n, \quad (9.118)$$

$\hat{S}(\omega_m, \Theta_n)$ is the directional spectrum, ω_m and Θ_n are the central frequency and angle in the (m, n) cell of the frequency-angle plane; $\Delta\omega_m$ and $\Delta\Theta_n$ are the dimensions of the cell and the phase ϵ_{nm} is an independent random variable uniformly distributed in the interval $(0, 2\pi)$.

Equation (9.117) is an extension of Eq. (1.21) for the two-dimensional plane (ω, Θ) . The assumption of random phase leads to the same behaviour as the assumption of Gaussian distribution of the sea surface when N_Θ is relatively large. For small N_Θ , some modification is needed, i.e. (Borgman, 1982):

$$\begin{aligned} \zeta(x, y, t) = & 2 \sum_{m=1}^{M_\omega} \sum_{n=1}^{N_\Theta} \sum_{r=1}^R \left(\frac{A_{nm}}{\sqrt{R}} \right) \cos(k_{nmr} x \cos \Theta_{nmr} + \\ & + k_{nmr} y \sin \Theta_{nmr} - \omega_{nmr} t + \epsilon_{nmr}). \end{aligned} \quad (9.119)$$

The values ω_{nmr} and Θ_{nmr} (for $r = 1, 2, \dots, R$) are randomly selected from the (m, n) cell. When R is four or larger, the surface elevation $\zeta(x, y, t)$ will behave approximately as a normal, even if N is unity.

There are two main simulation concepts, i.e. time domain simulation and frequency domain simulation. In the first procedure, the values of $\zeta(x, y, t)$ for each time step are simulated one after the other. In second, the discrete Fourier transform of the time series is simulated first. Then, the FFT method is used to revert to the time domain. As this procedure exploits the speed of the FFT method, it is much faster than time domain simulation. The various techniques of time domain and frequency domain simulation have been described by Borgman (1982).

9.5.1 Time domain simulation with a random-phase structure

This method proceeds through the following steps:

1. The $N \times M \times R$ random phases ϵ_{nmr} are determined by generating uniform, independent pseudorandom numbers and multiplying them by 2π . Various pseudorandom number generators were reviewed by Borgman (1982). Useful computer codes can be found in the book by Press et al. (1986) or in mathematical tables by Abramowitz and Stegun (1975).
2. The $N_\Theta \times M_\omega \times T$ uniform, independent pseudorandom numbers U_{nmr} are generated and the frequency ω_{nmr} is computed as:

$$\omega_{nmr} = \omega_m + (U_{nmr} - 0.5) \Delta\omega_m. \quad (9.120)$$

3. In a similar way, the directions Θ_{nmr} are determined as:

$$\Theta_{nmr} = \Theta_n + (U_{nmr} - 0.5) \Delta \Theta_n. \quad (9.121)$$

The wave numbers k_{nmr} are related to the frequencies ω_{nmr} by a linear dispersion relationship (1.20).

4. For a known set of k_{nmr} , ω_{nmr} , Θ_{nmr} and ϵ_{nmr} , the sea surface elevation $\zeta(x, y, t)$ can be calculated from Eq. (9.119).

If a time domain simulation of various wave properties (wave orbital velocities, accelerations or dynamic pressure) must be determined for various locations within the wave, random-phase simulation is particularly useful.

9.5.2 Frequency domain simulation by a random-phase structure

The simulation of random surface waves in the frequency domain can be based on two different representations of the linear, Gaussian process, which is continuous in time; namely (for simplicity a wave train propagating along the x axis is considered):

$$\zeta(t) = \frac{a_0}{2} + \sum_{n=1}^{\frac{1}{2}N} (a_n \cos \omega_n t + b_n \sin \omega_n t), \quad (9.122)$$

or:

$$\zeta(t) = \frac{c_0}{2} + \sum_{n=1}^{\frac{1}{2}N} c_n \cos(\omega_n t - \Theta_n). \quad (9.123)$$

In the first representation, coefficients a_n and b_n are independent random variables, normally distributed with zero mean and with a standard deviation given by:

$$\sigma_n = [S(\omega_n) \Delta \omega]^{\frac{1}{2}}. \quad (9.124)$$

In the second representation, the deterministic amplitudes c_n are given by:

$$c_n = [2S(\omega_n) \Delta \omega]^{\frac{1}{2}}. \quad (9.125)$$

However, the phases Θ_n are random and uniformly distributed in the interval $(0, 2\pi)$. To evaluate the realizations simulated by the first representation (9.122), we express sea surface elevation (9.122) as a discrete Fourier sum. Thus, the corresponding FFT pair takes the form (Tuah and Hudspeth, 1983):

$$\zeta(j \Delta t) = \frac{1}{N} \sum_{n=1}^N A_n \exp \left[\frac{2\pi i(n-1)(j-1)}{N} \right], \quad j = 1, 2, \dots, N, \quad (9.126)$$

and

$$A_n = \sum_{j=1}^N \zeta(j\Delta t) \exp \left[\frac{-2\pi i(n-1)(j-1)}{N} \right], \quad n = 1, 2, \dots, N. \quad (9.127)$$

The inverse Fourier transform will be exact when $\Delta t \Delta \omega = \frac{2\pi}{N}$; N must be equal to the integer 2 raised to an integer power. The complex Fourier amplitude coefficients, A_n , represents a discrete two-sided Fourier amplitude spectrum.

The procedure for simulation in the frequency domain is as follows:

1. Generate a sequence of paired random numbers, α_n and β_n , which are normally distributed with zero mean and unit variance, $N(0, 1)$.
2. Calculate the random amplitudes:

$$\left\{ a_n \right\} = \left\{ \begin{array}{c} \alpha_n \\ \beta_n \end{array} \right\} [S(\omega_n) \Delta \omega]^{\frac{1}{2}}. \quad (9.128)$$

The spectrum $S(\omega)$ is a target spectrum which should be known from theory or from measurements.

3. Calculate R_n and Θ_n values as:

$$R_n \sqrt{a_n^2 + b_n^2}, \quad \Theta_n = \arctan \left(\frac{b_n}{a_n} \right). \quad (9.129)$$

4. Calculate amplitudes A_n (which are random):

$$A_n = N \left(\frac{R_{n-1}}{2} \right) \exp(i\Theta_{n-1}), \quad n = 1, 2, \dots, \frac{N}{2} + 1. \quad (9.130)$$

5. Synthesize the sequence A_n by inverse FFT, to obtain a discrete time sequence for random simulation, $\zeta(j\Delta t)$.

The corresponding procedure for the second representation (9.123) is given by the following:

1. Generate a sequence of uniform random numbers which are uniformly distributed in the interval $(0, 1)$.
2. Multiply these numbers by 2π , to obtain a sequence of random phase Θ_n , uniformly distributed in the interval $(0, 2\pi)$.
3. Compute amplitude A_n as:

$$A_n = N \left[\frac{1}{2} S(\omega) \Delta \omega \right]^{\frac{1}{2}} \exp(i\Theta_n). \quad (9.131)$$

4. Synthesize the sequence A_n by inverse FFT, to obtain a discrete time sequence for random simulation, $\zeta(j\Delta t)$.

Simulation procedures for nonlinear ocean waves are discussed by Hudspeth and Chen (1979), Dean and Sharma (1981) and Tuah and Hudspeth (1982), while for wave kinematics and wave forces they are given by Borgman (1990).

This page is intentionally left blank

Chapter 10

References

- Abramowitz, M. and Stegun, I.A., 1975. *Handbook of Mathematical Functions*. Dover Publ., 1045 pp.
- Abreu, M., Larraza, A. and Thornton, E., 1992. Nonlinear transformation of directional wave spectra in shallow water. *Jour. Geoph. Res.*, 97: 15579–15589.
- Allender, J.H., Barnett, T.P. and Lybanon, M., 1985. An improved spectral model for ocean wave prediction. In: *Ocean Wave Modeling. The SWAMP Group*, Plenum Press, New York, 256 pp.
- Allender, J., Andunson, T., Barstow, S.F., Bjerken, S., Krogstad, H.E., Steinbakke, P., Vartdal, L., Borgman, L.E. and Graham, C., 1989. The WADIC project: A comprehensive field evaluation of directional wave instrumentation. *Ocean Eng.*, 16: 505–536.
- Alpers, W.R. and Bruening, C., 1986. On the relative importance of motion-related contribution to the SAR mechanism of ocean surface waves. *IEEE Trans.*, G24: 873–885.
- Anastasiou, K., Tickell, R.G. and Chaplin, J.R., 1982. Measurements of particle velocities in laboratory-scale random waves. *Coastal Eng.*, 6: 233–254.
- Antsyferov, S.M., Belberov, Z.K. and Massel, S.R. (Eds.), 1990. *Dynamical Processes in Coastal Regions*. Publ. House of Bulgarian Academy of Sciences, Sofia, 190 pp.
- Banner, M.L., 1990. Equilibrium spectra of wind waves. *Jour. Phys. Ocean.*, 20: 966–984.
- Banner, M.L. and Phillips, O.M., 1974. On the incipient breaking of small scale waves. *Jour. Fluid Mech.*, 65: 647–656.

- Banner, M.L., Jones, I.S.F. and Trinder, J.C., 1989.** Wave number spectra of short gravity waves. *Jour. Fluid Mech.*, 198: 321–344.
- Banner, M.L. and Peregrine, D.H., 1993.** Wave breaking in deep water. *Ann. Rev. Fluid Mech.*, 22: 373–397.
- Banner, M.L. and Young, I.R., 1994.** Modeling spectral dissipation in the evolution of wind waves. Part I: Assessment of existing model performance. *Jour. Phys. Oceanogr.*, 84: 1550–1571.
- Barber, N.F., 1963.** The directional resolving power of an array of wave recorders. In: *Ocean Wave Spectra.*, Prentice-Hall, Englewood Cliffs, N.J., 137–150.
- Barnett, T.P., 1968.** On the generation, dissipation and prediction of ocean wind waves. *Jour. Geoph. Res.*, 73: 513–530.
- Barnett, T.P. and Wilkerson, J.C., 1967.** On the generation of ocean wind waves as inferred by airborne radar measurements of fetch-limited spectra. *Jour. Mar. Res.*, 25: 292–328.
- Basco, D.R. and Yamashita, T., 1986.** Toward a simple model of the wave breaking transition region in surf zones. *Proc. 20th Coastal Eng. Conf.*, 1: 955–970.
- Basco, D.R. and Yamashita, T., 1988.** On the partition of horizontal momentum between velocity and pressure components through the transition region of breaking waves. *Proc. 21st Coastal Eng. Conf.*, 1: 682–697.
- Battjes, J.A., 1972a.** Set-up due to irregular waves. *Proc. 13th Conf. Coastal Eng.*, 3: 1993–2004.
- Battjes, J.A., 1972b.** Long-term height distributions at seven stations around the British Isles. *Deutsches. Hydr. Zeit.*, 25: 180–189.
- Battjes, J.A., 1974.** *Computation of Set-Up, Longshore Currents, Run-Up and Overtopping due to Wind-generated Waves.* Communications on Hydraulics, Delft Univ. of Technology, Rep. 74-2, 244 pp.
- Battjes, J.A., 1988.** Surf-zone dynamics. *Ann. Rev. Fluid Mech.*, 20: 257–293.
- Battjes, J.A. and Janssen, J.P.F.M., 1978.** Energy loss and set-up due to breaking of random waves. *Proc. 16th Coastal Eng. Conf.*, 1: 563–587.
- Battjes, J.A. and Stive, M.J.F. 1985.** Calibration and verification of a dissipation model for random breaking waves. *Jour. Geoph. Res.*, 90: 9159–9167.
- Battjes, J.A., Zitman, T.J. and Holthuijsen, L.H., 1987.** A reanalysis of the spectra observed in JONSWAP. *Jour. Phys. Oceanogr.*, 17: 1288–1295.

- Battjes, J.A., Eldeberky, Y. and Won, Y., 1993.** Spectral Boussinesq modelling of breaking waves. In: Magoon, O.T and Hemsley, J.M. (Editors), *Proc. 2nd Inter. Symposium Ocean Wave Measurement and Analysis*, New Orleans, 813–820.
- Bauer, E., Hasselmann, S. and Hasselmann, K., 1992.** Validation and assimilation of Seasat altimeter wave heights using the WAM wave model. *Jour. Geoph. Res.*, 97: 12671–12682.
- Bea, R.G., 1974.** Gulf of Mexico hurricane wave heights. *Proc. 6th Offshore Techn. Conf., Dallas*, 1: 791–810.
- Beal, R.C., Monaldo, F.M., Tilley, D.G., Irvine, D.E., Walsh, E.J., Jackson, F.C., Hancock III, D.W., Hines, D.E., Swift, R.N., Gonzalez, F.I., Lyzenga, D.R. and Zambresky, L.F., 1986.** A comparison of SIR-B directional ocean wave spectra with aircraft scanning radar spectra. *Science*, 232: 1531–1535.
- Belberova, D.Z., Zaslavskii, M.M. and Soloviev, J.P., 1990.** O potoke volnovo go deystviya (On the flux of wave action). *Okeanologiya*, 30: 365–370.
- Bendat, J.S. and Piersol, A.G., 1986.** *Random Data. Analysis and Measurement Procedures*. John Wiley & Sons, New York, 566 pp.
- Bendykowska, G. and Massel, S.R., 1988.** On the theory and experiment of mechanically generated waves. *Proc. Inter. Symp. Wave Research and Coastal Eng., Hannover*, 1:401–413.
- Bendykowska, G. and Werner, G., 1989.** *Shallow Water Wave Spectra; their Dispersion, Transformation and Spectral Characteristics*. The Royal Inst. of Techn., Stockholm/Inst. of Hydroeng., Gdańsk, Report TRITA-VBI-142, 59 pp.
- Benoit, M., 1994.** Extensive comparison of directional wave analysis methods from gauge array data. *Proc. of Inter. Symposium Ocean Wave Measurement and Analysis*, New Orleans, July 25–28, 1993: 740–754.
- Berge, B. and Penzien, J., 1974.** Three-dimensional stochastic response of offshore towers to wave forces. *Proc. 6th Annual Techn. Conf.*, 173–190.
- Berkhoff, J.C.W., 1972.** Computation of combined refraction-diffraction. *Proc. 13th Coastal Eng. Conf.*, 1: 471–490.
- Berkhoff, J.C.W., Booij, N. and Radder, A.C., 1982.** Verification of numerical wave propagation models for simple harmonic linear water waves. *Coastal Eng.*, 6: 255–279.

- Biot, M.A., 1941. General theory of three-dimensional consolidation. *Jour. Applied Phys.*, 12: 155-164.
- Birman, B.A., Klen, L.A. and Parmuzina, T.A., 1980. Veroyatnost i prodolzhitel'nost opasnykh dla navigatsiy skorosti vetra v Severnoy Atlantike (Probability and duration of wind speeds danger for navigation in the North Atlantic). *Trudy VNIIGMI*, 64: 14-37.
- Bishop, C.T. and Donelan, M.A., 1987. Measuring waves with pressure transducers. *Coastal Eng.*, 11: 309-328.
- Bishop, C.T. and Donelan, M.A., 1989. Wave prediction models. In: Lakhan, V.C. and Trenhaile, A.S. (Editors), *Applications in Coastal Modeling*, Elsevier Science Publ., 75-106.
- Bishop, C.T., Donelan, M.A. and Kahma, K.K., 1992. Shore protection manual's wave prediction reviewed. *Coastal Eng.*, 17: 25-48.
- Bitner, E.M., 1978. Statystyczny model falowania wiatrowego na małych głębokościach (Statistical model of wind waves in shallow water). *Hydrot. Trans.*, 39: 25-67.
- Bitner, E.M., 1980. Nonlinear effects of the statistical model of shallow-water wind waves. *Appl. Ocean Res.*, 2: 63-73.
- Boccotti, P., 1981. On the highest waves in a stationary Gaussian process. *Atti. Acc. Lig.*, 38: 45-73.
- Boccotti, P., 1989. On mechanics of irregular gravity waves. *Atti. Acc. Naz. Lincei Mem.*, 19: 109-170.
- Bondzie, C. and Panchang, V.G., 1993. Effects of bathymetric complexities and wind generation in a coastal wave propagation model. *Coastal Eng.*, 21: 333-360.
- Booij, N., 1981. *Gravity Waves with Non-Uniform Depth and Current*. Ph.D. Thesis, Delft Univ. of Technology, 130 pp.
- Booij, N., 1983. A note on the accuracy of the mild-slope equation. *Coastal Eng.*, 7: 191-203.
- Borgman, L.E., 1961. The frequency distribution of near extremes. *Jour. Geoph. Res.*, 66: 3295-3307.
- Borgman, L.E., 1963. Risk criteria. *Jour. of Waterways and Harbors Div.*, 89: 1-35.

- Borgman, L.E.**, 1972. Statistical models for ocean waves and wave forces. *Advances in Hydrosience*, 8: 139–181.
- Borgman, L.E.**, 1975. Extremal statistics in ocean engineering. *Proc. Civil Eng. in the Oceans*, ASCE, 1: 111–117.
- Borgman, L.E.**, 1979. Directional wave spectra from wave sensors. In: *Ocean Wave Climate*, Plenum, New York, 269–300.
- Borgman, L.E.**, 1982. Techniques for computer simulation of ocean waves. In: Osborne, A.R. and Rizzoli, P.M. (Eds), *Proc. Inter. School of Physics 'Enrico Fermi', Course LXXX: Topics in Ocean Physics*. North-Holland, Amsterdam, 387–417.
- Borgman, L.E.**, 1990. Irregular ocean waves: kinematics and forces. In: Le Méhauté, B. and Hanes, D.M. (Eds), *Ocean Engineering Science*, 9: 121–168.
- Bouws, E. and Komen, G.J.**, 1983. On the balance between growth and dissipation in an extreme depth-limited wind-sea in the southern North Sea. *Jour. Phys. Oceanogr.*, 13: 1653–1658.
- Bouws, F., Günther, H., Rosenthal, W. and Vincent, C.L.**, 1985. Similarity of the wind wave spectrum in finite depth water: 1. Spectral form. *Jour. Geoph. Res.*, 90: 975–986.
- Bowman, D.**, 1979. Validity of visual estimated wave parameters. *Jour. Earth Science*, 28: 94–99.
- Bretherton, F.P. and Garrett, C.J.R.**, 1969. Wavetrains in homogeneous moving media. *Proc. Roy. Soc.*, A302: 529–554.
- Bretschneider, C.L.**, 1958. Revisions in wave forecasting deep and shallow water. *Proc. 6th Conf. on Coastal Eng. Conf.*, 1: 30–67.
- Bretschneider, C.L.**, 1970. Wave forecasting relations for wave generation. *Look Lab.*, Hawaii, 1, No. 3.
- Briggs, M.J., Borgman, L.E. and Outlaw, D.G.**, 1987. Generation and analysis of directional spectral waves in a laboratory basin. *Proc. 19th Annual Offshore Techn. Conf.*; 495–502.
- Brissette, F.P. and Tsanis, I.K.**, 1994. Estimation of wave directional spectra from pitch-roll buoy data. *Jour. Waterway, Port, Coastal and Ocean Eng.*, 120: 93–115.
- Brown, G.S.**, 1977. The average impulse response of a rough surface and its applications. *IEEE Trans. Antennas Propag.*, AP-25: 67–74.

- Carter, D.J.T. and Challenor, P.G., 1983. Methods of filling the Fisher-Tippett Type I extreme value distribution. *Ocean Eng.*, 10: 191-199.
- Carter, D.J.T. and Challenor, P.G., 1989. Metocean parameters. Vol. 1. Waves. Department of Energy Offshore Technology. Rep. No. OTH 89300, Her Majesty's Stationary Office, London.
- Carter, D.J.T., Challenor, P.G. and Srokosz, M.A., 1992. An assessment of GEOSAT wave height and wind speed measurements. *Jour. Geoph. Res.*, 97: 11383-11392.
- Cartwright, D.E. and Longuet-Higgins, M.S., 1956. The statistical distribution of the maxima of a random function. *Proc. Roy. Soc.*, A237: 212-232.
- Cavaleri, L., Ewing, J.A. and Smith, N.D., 1978. Measurement of the pressure and velocity field below surface waves. In: Favre, A. and Hasselmann, K. (Editors), *Turbulent Fluxes Through the Sea Surface, Wave Dynamics, and Prediction*, Plenum Press, New York & London, 257-272.
- Cavaleri, L. and Rizzoli, P.M., 1981. Wind wave prediction in shallow water: theory and applications. *Jour. Geoph. Res.*, 86: 10961-10973.
- Cavaleri, L., De Filippi, P.L., Grancini, G.F., Ioveniti, G.L. and Tosi, R., 1986. Extreme wave conditions in the Tyrrhenian Sea. *Ocean Eng.*, 13: 157-180.
- Cavaleri, L., Bertotti, L. and Lionello, P., 1989. Shallow water application of the third-generation WAM Wave Model. *Jour. Geoph. Res.*, 94: 8111-8124.
- Cavaleri, L., Bertotti, L. and Lionello, P., 1991. Wind wave cast in the Mediterranean Sea. *Jour. Geoph. Res.*, 96: 10739-10764.
- Cavanie, A., Arhan, M. and Ezraty, R., 1976. A statistical relationship between individual heights and periods of storm waves. *Proc. Symp. Behaviour of Offshore Structures*, 2: 354-360.
- Chakrabarti, S.K., 1986. Unification of two-parameter energy spectrum models. *Jour. Waterway, Port, Coastal, and Ocean Eng.*, 112: 173-176.
- Chalikov, D.V. and Makin, V.K., 1991. Models of the wave boundary layer, *Boundary Layer - Meteorology*, 56: 83-99.
- Chamberlain, J.A., 1978. Mechanical properties of coral skeleton: compressive strength and its adaptive significance. *Paleobiology*, 4: 419-435.
- Chen, Y.H. and Wang, H., 1983. Numerical model for non stationary shallow water wave spectral transformation. *Jour. Geoph. Res.*, 88: 9851-9863.

- Cieřlikiewicz, W., 1985. Nonlinear approach to the problem of probability distributions of the orbital velocities and pressures for wind-induced waves. *Arch. Hydrot.*, 32: 192–220.
- Cieřlikiewicz, W., 1990. Determination of the surface elevation probability distribution of wind waves using maximum entropy principle. In: Torum, A. and Gudmestad, O.T. (Editors), *Proc. Res. Workshop on Water Wave Kinematics*, Molde (Norway), Kluwer Academic Publ., Amsterdam, 345–348.
- Cieřlikiewicz, W. and Massel, S.R., 1988. Interaction of wind waves with vertical wall. *Jour. Waterway, Port, Coastal and Ocean Eng.*, 114: 653–672.
- Cieřlikiewicz, W. and Thai, N.H., 1991. Probabilistyczne własnořci wzniesieñ swobodnej powierzchni silnie niegaussowskich fał wiatrowych (Probability distribution of non-Gaussian wind waves). *Rozpr. Hydrot.*, 54: 3–16.
- Cieřlikiewicz, W. and Gudmestad, O.T., 1993. Stochastic characteristics for orbital velocities of random water waves. *Jour. Fluid Mech.*, 255: 285–2993.
- Cieřlikiewicz, W. and Gudmestad, O.T., 1994a. Mass transport within the free surface zone of water waves. *Wave Motion*, 19: 145–158.
- Cieřlikiewicz, W. and Gudmestad, O.T., 1994b. Random water waves kinematics. Part 2. Experiment. *Arch. Hydroeng. and Environ. Mech.*, 41: 37–84.
- Cokelet, E.D., 1977a. Breaking waves. *Nature*, 267: 769–774.
- Cokelet, E.D., 1977b. Steep gravity waves in water of arbitrary uniform depth. *Phil. Trans. of Royal Soc.*, A286: 183–230.
- Collins, J.I., 1970. Probabilities of breaking wave characteristics. *Proc. 12th Conf. Coastal Eng.*, 1: 399–412.
- Collins, J.I., 1972. Prediction of shallow-water spectra. *Jour. Geoph. Res.*, 77: 2693–2701.
- Cooley, J.W. and Tukey, J.W., 1965. An algorithm for machine calculation of complex Fourier series. *Math. Comput.*, 19: 297–301.
- Creamer, D.B. and Wright, J.A., 1992. Surface films and wind wave growth. *Jour. Geoph. Res.*, 97: 5221–5229.
- Cummins, I. and Swan, C., 1994. Vorticity effects in combined waves and currents. *24th Conf. Coastal Eng.*, (Abstracts).
- Dally, W.R., 1990. Random breaking waves: a closed-form solution for planar beaches. *Coastal Eng.*, 14: 233–263.

- Dally, W.R., Dean, R.G. and Dalrymple, R.A., 1985. Wave height variation across beaches of arbitrary profile. *Jour. Geoph. Res.*, 90: 10,917–11,927.
- Dalrymple, R.A. and Liu, P.L.F., 1978. Waves over soft muds: a two-layer fluid model. *Jour. Phys. Oceanogr.*, 8: 1121–1131.
- Dalrymple, R.A. and Liu, P.L.F., 1979. Gravity waves over a poro-elastic sea bed. *Proc. Conf. Coastal Sediments*, 1: 181–195.
- Davey, A. and Stewartson, K., 1974. On three-dimensional packets of surface waves. *Proc. Roy. Soc.*, A338: 101–110.
- Davidan, I.N., 1969. Model formirovaniya spektralnoy struktury vetrovogo volneniya i ego sopostavleniye s naturalnymi dannymi (Model of spectral structure of wind waves and its comparison with experimental data). *Trudy Koord. Soveshchaniy po Gidrotekhnike*, 50: 139–157.
- Davidan, I.N., and Lopatukhin, L.I., 1978. *Na Vstrechu so Shtormami* (Towards the storms). Gidrometeoizdat, Leningrad, 135 pp.
- Davidan, I.N., Lopatukhin, L.I. and Rozhkov, W.A., 1978. *Vetrovoye Volneniye kak Veroyatnostnyy Gidrodinamicheskiy Process* (Wind Waves as a Stochastic Hydrodynamic Process). Gidrometeoizdat, Leningrad, 287 pp.
- Davidan, I.N., Lopatukhin, L.I. and Rozhkov, W.A., 1985. *Vetrovoye Volneniye v Mirovom Okeane* (Wind Waves in the Ocean). Gidrometeoizdat, Leningrad, 256 pp.
- Davies, A.G. and Heathershaw, A.D., 1984. Surface-waves propagation over sinusoidally varying topography. *Jour. Fluid Mech.*, 192: 33–50.
- Davis, R.E. and Regier, L.A., 1977. Methods for estimating directional wave spectra from multi-element arrays. *Jour. Marine Res.*, 35: 453–477.
- Dean, R.G., 1968. Breaking wave criteria: A study employing a numerical wave theory. *Proc. 11th Conf. Coastal Eng.*, 1: 108–123.
- Dean, R.G. and Sharma, J.N., 1981. Simulation of wave systems due to nonlinear directional spectra. *Proc. Inter. Symp. on Hydrodynamics in Ocean Eng.*, 2: 1211–1222.
- De Girolamo, P., Kostense, J.K. and Dingemans, M.W., 1988. Inclusion of wave breaking in a mild-slope model. *Proc. Conf. on Computer Modelling in Ocean Eng.*, 221–229.
- de Las Heras, M.M. and Janssen, P.A.E.M., 1992. Data assimilation with a coupled wind-wave model. *Jour. Geoph. Res.*, 97: 20261–20270.

- Dell'Osso, L., Bertotti, L. and Cavaleri, L., 1992. The Gorbush Storm in the Mediterranean Sea: atmospheric and wave simulation. *Monthly Weather Rev.*, 120: 77-90.
- Dera, J., 1992. *Marine Physics*. Elsevier – PWN, Amsterdam – Warszawa, 516 pp.
- Derks, H. and Stive, M.J.F., 1984. Field investigations in the TOW study programme for coastal sediment transport in The Netherlands. *Proc. 19th Coastal Eng. Conf.*, 2: 1830-1845.
- Dingemans, M.W., 1985. *Evaluation of Two-Dimensional Horizontal Wave Propagation Models*. Delft Hydr. Lab. Rep. W301, 117 pp.
- Dobson, E., Monaldo, F., Goldhirsh, J. and Wilkerson, J., 1987. Validation of Geosat altimeter-derived wind speeds and significant wave heights using buoy data. The Johns Hopkins APL Tech. Dig., 8: 222-233.
- Doering, J.C. and Donelan, M.A., 1993. The joint distribution of heights and periods of shoaling waves. *Jour. Geoph. Res.*, 98: 12543-12555.
- Done, T.J. and Potts, D.C., 1992. Influences of habitat and natural disturbances on contributions of massive *Porites* corals to reef communities. *Mar. Biology*, 114: 479-493.
- Donelan, M.A., 1980. Similarity theory applied to the sea forecasting of wave heights, periods and directions. *Proc. Canadian Coastal Conf.*, 47-61.
- Donelan, M.A., 1982. The dependence of the aerodynamic drag coefficient on wave parameters. *Proc. 1st Inter. Conf. on Meteorological and Air/Sea Interaction in the Coastal Zone*, 1: 381-387.
- Donelan, M.A., Hamilton J. and Hui, W.H., 1985. Directional spectra of wind-generated waves. *Phil. Trans. Roy. Soc.*, A315: 509-562.
- Donelan, M.A., 1990. Air-sea interaction. In: Le Mehaute, B. and Hanes, D.M. (Editors), *Ocean Engineering Science*, Vol. 9, A Wiley-Interscience Publ., New York, 9: 239-292.
- Donelan, M.A., Anctil, F. and Doering, J.C., 1992. A simple method for calculating the velocity field beneath irregular waves. *Coastal Eng.*, 16: 399-424.
- Dorrestein, R., 1955. On the wave observations by weather ships in the Eastern North Atlantic. *Deutsches Hydr. Zeit.*, 8: 177-186.
- Draper, L., 1963. Derivation of a design wave from instrumental records of sea waves. *Proc. Inst. Civil Eng.*, 26: 291-304.

- Draper, L.**, 1966. The analysis and presentation of wave data - a plea for uniformity. *Proc. 10th Coastal Eng. Conf.*, 1: 1-11.
- Druet, C.**, 1978. *Hydrodynamika Morskich Budowli i Akwenów Portowych* (Hydrodynamics of Marine Structures and Harbour Basins). Wydawnictwo Morskie, Gdańsk, 390 pp.
- Dungey, J.C. and Hui, W.H.**, 1979. Nonlinear energy transfer in a narrow gravity-wave spectrum. *Proc. Roy. Soc.*, A368: 239-265.
- Earle, M.D. and Baer, L.**, 1982. Effects of uncertainties on extreme wave heights. *Jour. Waterways, Port, Coastal and Ocean Div.*, 108: 456-478.
- Ebersole, B.A. and Hughes, S.A.**, 1987. DUCK'85 photopole experiment. U.S. Army Corps Eng., WES, Misc. Papers, CERC-87-18.
- Efimov, V.V.** (Editor), 1985. *Volny v Pogranichnykh Oblastyakh Okeana* (Ocean Boundary Waves). Gidrometeoizdat, Leningrad, 280 pp.
- Efimov, V.V., Soloviev, J.P. and Khristoforov, G.N.**, 1972. Eksperimentalnoye opredeleniye fazovoy skorosti rozprostraneniya spektralnykh sostavlyayushchikh morskogo vetrovogo volneniya (Experimental determination of phase velocity of spectral components of wind waves). *Izv. Akad. Nauk SSSR, Ser. Fizika Atm. i Okeana*, 8: 435-446.
- Elgar, S. and Guza, R.T.**, 1985. Observations of bispectra of shoaling surface gravity waves. *Jour. Fluid Mech.*, 161: 425-448.
- Elgar, S., Herbers, T.H.C. and Guza, R.T.**, 1994. Reflection of ocean surface gravity waves from a natural beach. *Jour. Phys. Oceanogr.*, 24: 1503-1511.
- Epstein, B.**, 1949. The distribution of extreme values in sample whose members are subject to a Markov chain condition. *Ann. Mathematical Stat.*, 20: 590-594.
- Ewing, J.A.**, 1971. A numerical wave prediction method for the North Atlantic Ocean. *Deutsches Hydr. Zeit.*, 24: 241-261.
- Ewing, J.A. and Laing, A.K.**, 1987. Directional spectra for seas near full development. *Jour. Phys. Oceanogr.*, 17: 1696-1706.
- Ewing, J.A., Weare, T.J. and Worthington, B.A.**, 1979. A hindcast study of extreme wave conditions in the North Sea. *Jour. Geoph. Res.*, 84: 5739-5747.
- Fendell, F.E.**, 1974. Tropical cyclones. *Adv. in Geophysics*, 17: 1-100.
- Fenton, J.D.**, 1979. A high-order cnoidal wave theory. *Jour. Fluid Mech.*, 94: 129-161.

- Fenton, J.D., 1986. Polynomial approximation and water waves. *Proc. 20th Coastal Eng. Conf.*, 1: 193-207.
- Fenton, J.D., 1990. Nonlinear wave theories. In: Le Mehaute, B. and Hanes, D.M. (Editors), *Ocean Engineering Science*, 9: 3-25.
- Fisher, R.A. and Tippett, L.C.H., 1928. Limiting forms of the frequency distribution of the largest or smallest member of a sample. *Proc. Camb. Phil. Soc.*, 24: 180-190.
- Fletcher, C.A.J., 1984. *Computational Galerkin Methods*, Springer-Verlag, Berlin, 309pp.
- Foda, M.A., Hunt, J.R. and Chou, H.T., 1993. A nonlinear model for the fluidization of marine mud by waves. *Jour. Geoph. Res.*, 88: 7039-7047.
- Fontanet, P., 1961. Theorie de la generation de la houle cylindrique par un batteur plan. *La Houille Blanche*, 16: 3-31.
- Forristall, G.Z., 1978. On the statistical distribution of wave heights in a storm. *Jour. Geoph. Res.*, 83: 2353-2358.
- Forristall, G.Z., 1982. Kinematics of directionally spread waves. In: Wiegel, R.L. (Editor), *Int. Proc. Conf. on Directional Wave Spectra Applications*, ASCE, 129-146.
- Forristall, G.Z., 1984. The distribution of measured and simulated wave heights as a function of spectral shape. *Jour. Geoph. Res.*, 89: 10547-10552.
- Forristall, G.Z., Ward, E.G., Cardone V.J. and Borgman, L.E., 1978. The directional spectra kinematics of surface gravity waves in Tropical Storm Delta. *Jour. Phys. Oceanogr.*, 8: 888-909.
- Fox, M.J.H., 1976. On the nonlinear transfer of energy peak of a gravity-wave spectrum. II. *Proc. Roy. Soc.*, A348: 467-483.
- Freilich, M.H. and Guza, R.T., 1984. Nonlinear effects in shoaling surface gravity waves. *Phil. Trans. Royal Soc.*, A 311: 1-41.
- Freilich, M.H., Guza, R.T. and Elgar, S.L., 1990. Observations of nonlinear effects in directional spectra of shoaling gravity waves. *Jour. Geoph. Res.*, 95: 9645-9656.
- Gade, H.G., 1958. Effects of non-rigid, impermeable bottom on plane surface waves in shallow water. *Jour. Mar. Res.*, 16: 61-82.

- Gadzhiev, Y.Z., Kitaigorodskii, S.A. and Krasitskii, V.P., 1978.** O ravno-vesnom intervale v spektrakh vetrovykh voln v more konetchnoy glubiny pri prisudstvii techeniy (On the saturation range in wind waves spectra for finite water depth and currents). *Okeanologiya*, 18: 267–270.
- Galvin, C.J., 1970.** Finite-amplitude, shallow water waves of periodically recurring form. *Proc. of the Symp. on Long Waves*, Delaware.
- Galvin, C.J., 1972.** Wave breaking in shallow water. In: Meyer, R.E. (Editor), *Waves on Beaches and Resulting Sediment Transport*, Academic Press, London, 413–456.
- Garratt, J.R., 1977.** Review of drag coefficients over oceans and continents. *Monthly Review*, 105: 915–929.
- Gastel, K.van, Janssen, P.A.E.M. and Komen, G.J., 1985.** On phase velocity and growth rate of wind-induced gravity-capillary waves. *Jour. of Fluid Mech.*, 161: 199–216.
- Gelci, R., Cazalé, H. and Vassal, J., 1957.** Prévision de la houle. La méthode des densités spectroangulaires (Prediction of waves. The method of frequency-directional spectral densities). *Bull. Infor. Comité Central Oceanogr. d'Etude Côtes*, 9: 416–435.
- Gelci, R. and Devillaz, E., 1970.** La calcul numérique de l'état de la mer (Numerical prediction of the sea state). *La Houille Blanche*, 25: 117–131.
- Gelci, R. and Chavy, P., 1978.** Seven years of numerical wave prediction with the DSA5 model. In: Favre, A. and Hasselmann, K. (Editors), *Turbulent Fluxes Through the Sea Surface, Wave Dynamics, and Prediction*, Plenum Press, New York, 565–591.
- Gerritsen, F., 1981.** Wave attenuation and wave set-up on a coastal reef. *Look Laboratory Techn. Rep. No. 48*, Univ. of Hawaii, 415 pp.
- Glukhovskiy, B.H., 1966.** *Issledovaniye Morskogo Vetrovogo Volnieniya* (Study of Sea Wind Waves), Gidrometeoizdat, Leningrad, 284 pp.
- Gnanadesikan, A. and Terray, E.A., 1994.** A comparison of three wave-measuring buoys. *Proc. of Inter. Symp. Ocean Wave Measurement and Analysis*, New Orleans, July 25–28, 1993, 287–301.
- Gnedenko, B.V., 1943.** Sur la distribution limite du terme maximum d'une série aleatoire (On the limiting distributions of random data). *Ann. Math.*, 44: 423–430.

- Goda, Y.**, 1975. Irregular wave deformation in the surf zone. *Coastal Eng. in Japan*, 18: 13–26.
- Goda, Y.**, 1985. *Random Sea and Design of Maritime Structures*, Univ. Tokyo Press, 323 pp.
- Goda, Y., Hawkes, P., Mansard, E., Martin, M.J., Mathiessen, M., Peltier, E., Thompson, E. and Vledder, G.Ph.van**, 1994. Intercomparison of extremal wave analysis methods using numerically simulated data. *Proc. 2nd Inter. Symp. on Ocean Wave Measurement and Analysis*, New Orleans, July 25–28, 1993, 963–977.
- Gourlay, M.R.**, 1994. Wave transformation on a coral reef. *Coastal Eng.*, 23: 17–42.
- Graber, H.C. and Madsen, O.S.**, 1988. A finite-depth wind-wave model. Part I: Model description. *Jour. Phys. Oceanogr.*, 18: 1465–1483.
- Gradshteyn, I.S. and Ryzhik, I.M.**, 1980. *Table of Integrals, Series and Products*, Academic Press, New York, 1160 pp.
- Greenhow, M.**, 1989. A probability distribution of breaking wave crest height based on a crest-acceleration threshold method. *Ocean Eng.*, 16: 537–544.
- Günther, H., Rosenthal, W., Weare, T.J., Worthington, B.A., Hasselmann, K. and Ewing, J.A.**, 1979a. A hybrid parametrical wave prediction model. *Jour. Geoph. Res.*, 84: 5727–5738.
- Günther, H., Rosenthal, W. and Richter, K.**, 1979b. Application of the parametrical surface wave prediction model to rapidly varying wind fields during JONSWAP 1973. *Jour. Geoph. Res.*, 84: 4855–4864.
- Hardy, T.A., Young, I.R., Nelson, R.C. and Gourlay, M.R.**, 1990. Wave attenuation on an off-shore coral reef. *Proc. 22nd Coastal Eng. Conf.*, 1: 330–344.
- Hashimoto, N., Kobune, K. and Kameyama, Y.**, 1987. Estimation of directional spectrum using the Bayesian approach and its application to field data analysis. *The Port and Harbour Res. Inst.*, Rep. 26: 57–100.
- Hasselmann, D., Dunkel, M. and Ewing, J.A.**, 1980. Directional wave spectra observed during JONSWAP 1973. *Jour. Phys. Oceanogr.*, 10: 1264–1280.
- Hasselmann, K.**, 1962. On the nonlinear energy transfer in a gravity wave spectrum. Part 1. General theory. *Jour. Fluid Mech.*, 12: 481–500.
- Hasselmann, K.**, 1963. On the nonlinear energy transfer in a gravity wave spectrum. Part 2 and 3. *Jour. Fluid Mech.*, 15: 273–281 and 385–398.

- Hasselmann, K., 1968. Weak-interaction theory of ocean waves. In: Holt, M., (Editor), *Basic Developments in Fluid Dynamics*, Academic Press, 2: 117–182.
- Hasselmann, K., 1974. On the spectral dissipation of ocean waves due to white capping. *Boundary-Layer Meteorology*, 6: 107–127.
- Hasselmann, K., Munk, W. and MacDonald, G., 1963. Bispectra of ocean waves. In: Rosenblatt, M. (Editor), *Time Series Analysis*, John Wiley, New York, 125–138.
- Hasselmann, K. and Collins, J.I., 1968. Spectral dissipation of finite-depth gravity waves due to turbulent bottom friction. *Jour. Mar. Res.*, 26: 1–12.
- Hasselmann, K., Barnett, T.P., Bouws, E., Carlson, H., Cartwright, D.E., Enke, K., Ewing, J.A., Gienapp, H., Hasselmann, D.E., Kruseman, P., Meerburg, A., Müller, P., Olbers, D.J., Richter, K., Sell, W. and Walden, H., 1973. Measurements of wind-wave growth and swell decay during the Joint North Sea Wave Project (JONSWAP), *Deutsches Hydr. Zeit.*, A12: 1–95.
- Hasselmann, K., Ross, D.B., Müller, P. and Sell, W., 1976. A parametric wave prediction model. *Jour. Phys. Oceanogr.*, 6: 200–228.
- Hasselmann, S. and Hasselmann, K., 1981. A symmetrical method of computing the nonlinear transfer in a gravity-waves spectrum. *Hamb. Geophys. Einzelschriften*, Reihe A, 52: 138 pp.
- Hasselmann, S. and Hasselmann, K., 1985. Computations and parameterization of the nonlinear energy transfer in a gravity-wave spectrum. Part I: A new method for efficient computations of the exact nonlinear transfer integral. *Jour. Phys. Oceanogr.*, 15: 1369–1377.
- Hasselmann, S., Hasselmann, K., Allender, J.H. and Barnett, T.P., 1985. Computations and parameterization of the nonlinear energy transfer in a gravity-wave spectrum. Part II: Parameterization of the nonlinear energy transfer for application in wave models. *Jour. Phys. Oceanogr.*, 15: 1378–1391.
- Haug, O. and Krogstad, H.E., 1994. Estimation of directional spectra by ML/ME-methods. *Proc. Conf. Ocean Wave Measurement and Analysis*, New Orleans, July 25–28, 1993, 394–405.
- Hayne, G.S. and Hancock III, D.W., 1990. Corrections for the effect of significant wave height and attitude on GEOSAT radar altimeter measurements. *Jour. Geoph. Res.*, 95: 2837–2842.

- Hedges, T.S., Anastasiou, K. and Gabriel, D., 1985. Interaction of random waves and current. *Jour. Waterways, Port, Coastal and Ocean Eng.*, 111: 275-288.
- Herterich, K. and Hasselmann, K., 1980. A similarity relations for the nonlinear energy transfer in a finite depth gravity-wave spectrum. *Jour. Fluid Mech.*, 97: 215-235.
- Hoerner, S.F., 1965. Fluid-dynamic drag. Practical information on aerodynamic drag and hydrodynamic resistance. Hoerner Dynamics Drag, Bricktown, New York.
- Hogben, N., 1988. Experience from compilation of global wave statistics. *Ocean Eng.*, 15: 1-31.
- Hogben, N. and Lumb, F.E., 1967. *Ocean Wave Statistics*, Her Majesty's Stationery Office, London.
- Hogben, N., Dacunka, N.M.C. and Olliver, G.F., 1986. *Global Wave Statistics*, Unwin Brothers, London.
- Holthuijsen, L.H., 1983. Observations of the directional distribution of ocean-wave energy in fetch-limited conditions. *Jour. Phys. Oceanogr.*, 13: 191-207.
- Holthuijsen, L.H., and Herbers, T.H.C., 1986. Statistics of breaking waves observed as whitecaps in the open sea. *Jour. Physical Oceanogr.*, 16: 290-297.
- Holthuijsen, L.H., Booij, N. and Herbers, T.H.C., 1989. A prediction model for stationary, short crested waves in shallow water with ambient currents. *Coastal Eng.*, 13: 23-54.
- Horikawa, K. and Kuo, C.T., 1966. A study of wave transformation inside surf zone. *Proc. 10th Coastal Eng. Conf.*, 1: 217-233.
- Houmb, O.G. and Overvik, T., 1976. Parameterization of wave spectra and long term joint distribution of wave height and period. *Proc. Conf. Behaviour of Offshore Structures, BOOS'76*, Trondheim, 1: 144-169.
- Howell, G.L., 1994. Design of an in-situ directional wave gauge for one year deployments. *Proc. Inter. Symp. Ocean Wave Measurement and Analysis*. July 25-28, 1993, New Orleans, 264-276.
- Hsiao, S.V. and Shemdin, O.H., 1980. Interaction of ocean waves with a soft bottom. *Jour. Phys. Oceanogr.*, 10: 605-610.
- Hsu, S.A., 1974. A dynamic roughness equation and its application to wind stress determination at the air-sea interface. *Jour. Phys. Oceanogr.*, 4: 116-120.

- Huang, N.E. and Tung, C.C., 1976. The dispersion relation for a nonlinear random gravity wave field. *Jour. Fluid Mech.*, 75: 337-345.
- Huang, N.E. and Tung, C.C., 1977. The influence of the directional energy distribution on the nonlinear dispersion relation in a random gravity wave field. *Jour. Phys. Oceanogr.*, 7: 403-414.
- Huang, N.E., Long, S.R., Tung, C.C., Yuen, Y. and Bliven, L.F., 1981. A unified two-parameter wave spectral model for a general sea state. *Jour. Fluid Mech.*, 112: 203-224.
- Huang, N.E., Wang, H., Long, S.R. and Bliven, L.F., 1983a. A study on the spectral models for waves in finite water depth. *Jour. Geoph. Res.*, 88: 9579-9587.
- Huang, N.E., Long, S.R., Tung, C.C., Yuen, Y. and Bliven, L.F., 1983b. A non-Gaussian statistical model for surface elevation of nonlinear random wave fields. *Jour. Geoph. Res.*, 88: 7597-7597.
- Hudspeth, R.T. and Chen, M.C., 1979. Digital simulation of nonlinear random waves. *Jour. Waterway, Port, Coastal and Ocean Div.*, 105: 67-85.
- Hughes, S.A., 1993. *Physical Models and Laboratory Techniques in Coastal Engineering*. World Scientific, Singapore, 568 pp.
- Hunt, J.N., 1979. Direct solution of wave dispersion equation. *Jour. Waterway, Port, Coastal and Ocean Eng.*, 105: 457-459.
- Hurdle, D.P. and Stive, M.J.F., 1989. Revision of SPM 1984 wave hindcast model to avoid inconsistencies in engineering applications. *Coastal Engineering*, 12: 339-357.
- Inter. Assoc. for Hydraulic Res. (IAHR) , 1989. List of sea-state parameters. *Jour. Waterway, Port, Coastal, and Ocean Eng.*, 115: 793-808.
- Isaacson, M. and Mackenzie, N.G., 1981. Long-term distributions of ocean waves: a review. *Jour. Waterway, Port, Coastal and Ocean Div.*, 107: 93-109.
- Isobe, M., 1987. A parabolic equation model for transformation of irregular waves due to refraction, diffraction and breaking. *Coastal Eng. in Japan*, 30: 121-135.
- Isobe, M., Kondo, K. and Horikawa, K., 1984. Extension of MLM for estimating directional wave spectrum. Symp. *Description and Modelling of Directional Seas*, Copenhagen, 1-15.
- Jacobs, S.J., 1987. As asymptotic theory for the turbulent flow over a progressive water wave. *Jour. Fluid Mech.*, 174: 69-80.

- Jähne, B. and Riemer, K.S., 1983. Two-dimensional wave number spectra of small-scale water surface waves. *Jour. Geoph. Res.*, 95: 11531-11546.
- James, R.W., 1966. The hazard of giant waves. *Mariners Weather Log*, ESSA, 10: 115-117.
- Janssen, P.A.E.M., 1989. Wave-induced stress and the drag of air flow over sea waves. *Jour. Phys. Oceanogr.*, 19: 745-754.
- Janssen, P.A.F.M., 1991. Quasi-linear theory of wind generation applied to wave forecasting. *Jour. Phys. Oceanogr.*, 21: 1631-1642.
- Janssen, P.A.E.M., Lionello, P., Reistad, M. and Hollingsworth, A., 1989. Hindcast and data assimilation studies with the WAM model during the Seasat period. *Jour. Geoph. Res.*, 94: 973-993.
- Jardine, T.P., 1979. The reliability of visual observed wave heights. *Coastal Eng.*, 3: 33-38.
- Jaynes, E.T., 1982. On the rationale of entropy methods. *Proc. of IEEE*, 70: 939-952.
- Jeffreys, H., 1925. On the formation of waves by wind. II. *Proc. Roy. Soc.*, A110: 341-347.
- Jonsson, I.G., Skovgaard, C. and Wang, J.D., 1970. Interaction between waves and currents. *Proc. 12th Coastal Eng. Conf.*, 1: 489-507.
- Kawai, S., 1979. Generation of initial wavelets by instability of a coupled shear flow and their evolution to wind waves. *Jour. Fluid Mech.*, 93: 661-703.
- Kawai, S., Okuda, K. and Toba, Y., 1977. Field data support of three-seconds power law and $gu_*\sigma^{-4}$ spectral form for growing wind waves. *Jour. Oceanogr. Soc. Japan*, 33: 137-150.
- Keating, T. and Webber, N.B., 1977. The generation of laboratory waves in a laboratory channel. A comparison between theory and experiment. *Proc. Inst. Civil Eng.*, 63: 819-832.
- Kerstens, J.G.M., Pacheco, L.A. and Edwards, G., 1988. A Bayesian method for the estimation of return values of wave heights. *Ocean Eng.*, 15: 153-170.
- Kim, Y.K. and Powers, E.J., 1979. Digital bispectral analysis and its applications to nonlinear wave interactions. *IEEE Trans. on Plasma Science*, 7: 120-131.

- Kim, T., Liu, L. and Wang, H., 1994. Comparison of directional wave analysis methods. *Proc of Inter. Symp. Ocean Wave Measurement and Analysis*, New Orleans, July 25-28, 1993, 554-568.
- Kimura, A., 1980. Statistical properties of random wave groups. *Proc. 17th Coastal Eng. Conf.*, 3: 2955-2973.
- Kinsman, B., 1965. *Wind Waves, their Generation and Propagation on the Ocean Surface*. Prentice-Hall, Inc., Englewood Cliffs, 676 pp.
- Kirby, J.T., 1984. A note on linear surface wave-current interaction over slowly varying topography. *Jour. Geoph. Res.*, 89: 745-747.
- Kirby, J.T., 1986. A general wave equation for waves over rippled beds. *Jour. Fluid Mech.*, 162: 171-186.
- Kirby, J.T., 1989. A note on parabolic radiation boundary conditions for elliptic wave calculations. *Coastal Eng.*, 13: 211-218.
- Kirby, J.T. and Dalrymple, R.A., 1983. A parabolic equation for the combined refraction-diffraction of Stokes waves by mildly varying topography. *Jour. Fluid Mech.*, 136: 453-466.
- Kitaigorodskii, S.A., 1962. Nekotoryye prilozheniya metodov teorii podobiya pri analize vetrovogo volnieniia (Application of similarity methods to the analysis of wind waves). *Izv. Akad. Nauk, Ser. Geophys.*, 1: 105-117.
- Kitaigorodskii, S.A., 1970. *Fizika Vzaimodeystviya Atmosfery i Okieana* (Physics of Air-Sea Interaction), Gidrometeoizdat, Leningrad, 284 pp.
- Kitaigorodskii, S.A., 1983. On the theory of the equilibrium range in the spectrum of wind-generated gravity waves. *Jour. Phys. Oceanogr.*, 13: 816-827.
- Kitaigorodskii, S.A., Krasitskii, V.P. and Zaslavskii, M.M., 1975. On Phillips' theory of equilibrium range in the spectra of wind-generated gravity waves. *Jour. Phys. Oceanogr.*, 5: 410-420.
- Kobune, K. and Hashimoto, N., 1986. Estimation of directional spectra from maximum entropy principle. *Proc. 5th Intern. Conf. on Offshore Mechanics and Arctic Engineering*, Tokyo, 80-85.
- Kochin, N.J., Kibiel, I.A. and Roze, N.V., 1963. *Teoreticheskaya Gidromekhanika* (Theoretical Hydromechanics), Gos. Izdat. Fiz.-Mat. Lit., Moscow, 583 pp.
- Komen, G.J., Hasselmann, S. and Hasselmann, K., 1984. On the existence of a fully developed wind-sea spectrum. *Jour. Phys. Oceanogr.*, 14: 1271-1285.

- Komen, G.J., Cavaleri, L., Donelan, M., Hasselmann, K., Hasselmann, S. and Janssen, P.A.E.M., 1994. *Dynamics and Modelling of Ocean Waves*, Cambridge Univ. Press, Cambridge, 532 pp.
- Kononkova, G.E., 1969. *Dinamika Morskikh Voln* (Dynamics of Sea Waves), Izd. Mosk. Gosud. Univ., Moscow, 206 pp.
- Korteweg, D.J. and de Vries, G., 1895. On the change of form of long waves advancing in a rectangular canal and on a new type of long stationary wave. *Phil. Mag.*, 39: 422–443.
- Kostichkova, D.P. and Polyakov, J.P., 1980. Analiticheskaya approksimatsiya chastotnogo spektra vetrovogo volnieniya na glubokoy vode (Analytical approximation of frequency spectrum of wind waves in deep water). *Okeanologiya*, 7: 9–17.
- Krasitskii, V.P., 1974. K teorii transformatsii spektra pri refraktsii vetrovykh voln (On the wind waves spectrum transformation due to refraction). *Izv. Akad. Nauk SSSR, Ser. Fiz. Atm. i Okeana*, 10: 72–82.
- Krasitskii, V.P., 1980. O generatsii vetrovykh voln na nachalnoy stadii (On the generation of wind waves on the initial stage). *Izv. Akad. Nauk SSSR, Ser. Fiz. Atm. i Okeana*, 11: 1214–1217.
- Krasitskii, V.P. and Zaslavskii, M.M., 1978. Comments on the Phillips-Miles' theory of wind generated waves. *Boundary Layer Meteorology*, 14: 199–215.
- Krivitskii, S.V. and Strekalov, S.S., 1985. Sherokhovatost podstilyayushchey po-verkhnostii i struktura vetrovogo potoka v otkrytoy i pribrezhnoy zone morya (Roughness of sea surface and structure of wind flow in open sea and in coastal zone). In: *Razvite Metodov Razcheta Morskikh Sooruzheniy* (On the Methods of Designing of Marine Structures), Min. Transport, Moscow, 75–85.
- Krogstad, H.E., 1988. Maximum likelihood estimation of ocean wave spectra from general arrays of wave gauges. *Modeling, Identification and Control*, 9: 81–97.
- Krylov, Y.M., 1966. *Spektralnyye Metody Issledovaniya i Razcheta Vetrovykh Voln* (Spectral Methods of Studying and Predicting of Wind Waves). Gidrometeoizdat, Leningrad, 256 pp.
- Krylov, Y.M., Strekalov, S.S. and Tsyplukhin, V.F., 1966. Issledovaniye uglovogo energeticheskogo spektra vetrovykh voln (Study on directional spectrum of wind waves). *Izv. Akad. Nauk SSSR, Ser. Fiz. Atm. i Okeana*, 7: 729–739.
- Krylov, Y.M., Strekalov, S.S. and Tsyplukhin, W.F., 1976. *Vetrovyye Volny i ikh Vozdeystviye na Sooruzheniya* (Wind Waves and their Interaction with Structures), Gidrometeoizdat, Leningrad, 255 pp.

- Krylov, Y.M. (Editor), Duginov, B.A., Galenin, B.G., Krivitskii, S.W., Podmogilnyj, I.A., Polyakov, J.P., Popkov, R.A. and Strekalov, S.S., 1986. *Veter, Volny i Morskiye Porty* (Wind, Waves and Marine Harbors), Gidrometeoizdat, Leningrad, 264 pp.
- Kunishi, H., 1963. An experimental study on the generation and growth of wind waves. *Disaster Prev. Res. Inst., Kyoto Univ., Bulletin No. 61*: 1-41.
- Kuo, C.T. and Kuo, S.T., 1974. Effect of wave breaking on statistical distribution of wave heights. *Proc. Civil Eng. in Oceans*, 3: 1211-1231.
- Kuo, Y.Y. and Chiu, Y.F., 1987. Transfer function between wave height and wave pressure for progressive waves. *Coastal Eng.*, 23: 81-93.
- Kuznetsov, P.I., Stratonovitch, R.L. and Tikhonov, W.I., 1954. O dlitelnosti vibrosov sluchaynoy funktsii (On the duration of high runs of random functions). *Zhurnal Tekhnicheskoy Fiziki*, 24: 103-112.
- Kuznetsov, P.I., Stratonovitch, R.L. and Tikhonov, W.I., 1960. Quasi-momentnyye funktsii v teorii sluchaynykh processov (Quasi-moments functions in theory of random processes). *Teoriya Veroyatnostey i Primeneniya*, 1.
- Lamb, H., 1932. *Hydrodynamics*, Dover Publ., New York, 738pp.
- Laitone, E.V., 1960. The second approximation to cnoidal and solitary waves. *Jour. Fluid Mech.*, 9: 430-444.
- Laitone, E.V., 1962. Limiting conditions for cnoidal and Stokes waves. *Jour. Geoph. Res.*, 67: 1555-1564.
- La Thi Cang, 1987a. Wpływ skorelowania wysokości fal na charakterystyki grup falowych (Influence of correlation of wave heights on wave group statistics). *Arch. Hydrot.*, 34: 3-21.
- La Thi Cang, 1987b. Prognozowanie parametrów charakterystycznych grup fal (Forecasting of wave group parameters). *Arch. Hydrot.*, 34: 23-33.
- Lawless, J.F., 1982. *Statistical Models and Methods for Lifetime Data*, John Wiley & Sons, New York
- Lee, T. and Black, K.P., 1978. The energy spectra of surf waves on a coral reef. *Proc. 16th Coastal Eng. Conf.*, 1: 588-608.
- LeBlond, P.H. and Mysak, L.A., 1978. *Waves in the Ocean*, Elsevier, Amsterdam, 602 pp.

- Le Mehaute, B. and Koh, R.C.Y.**, 1967. On the breaking of waves arriving at an angle to the shore. *Jour. Hydraulic Res.*, 5: 541-549.
- Le Mehaute, B., Divoky, D., Liu, A.**, 1968. Shallow water waves: a comparison of theories and experiments. *Proc. Coastal Eng. Conf.*, 1: 86-107.
- Le Mehaute, B. and Wang, J.D.**, 1982. Wave spectrum changes on sloped beach. *Jour. Waterway, Port, Coastal and Ocean Div.*, 108: 33-47.
- Le Mehaute, B., Liu, C.C. and Ulmer, E.W.**, 1986. Transformation of statistical properties of shallow-water waves. In: Phillips, O.M. and Hasselmann, K. (Editors), *Wave Dynamics and Radio Probing of the Ocean Surface*. Plenum Press, New York, 181-191.
- Lewis, A.W. and Allos, R.N.**, 1990. JONSWAP parameters: sorting out the inconsistencies. *Ocean Eng.*, 17: 409-415.
- Li, B. and Anastasiou, K.**, 1992. Efficient elliptic solvers for the mild-slope equation using the multi grid method. *Coastal Eng.*, 16: 245-266.
- Lie, V. and Torum, A.**, 1991. Ocean waves over shoals. *Coastal Eng.*, 15: 545-562.
- Lighthill, M.J.**, 1975. *Fourier Analysis and Generalized Functions*. Cambridge Univ. Press, Cambridge, 79 pp.
- Lindgren, G. and Rychlik, I.**, 1982. Wave characteristic distribution for Gaussian waves-wavelength, amplitude and steepness. *Ocean Eng.*, 9: 411-432.
- Lionello, P., Günther, H. and Janssen, P.A.E.M.**, 1992. Assimilation of altimeter data in a global third-generation wave model. *Jour. Geoph. Res.*, 97: 14453-14474.
- Liu, P.**, 1989. On the slope of the equilibrium range in the frequency spectrum of wind waves. *Jour. Geoph. Res.*, 94: 5017-5023.
- Liu, P.C. and Kessenich, T.A.**, 1976. IF4GL shipboard visual wave observations vs. wave measurements. *Jour. Great Lakes Res.*, 2: 33-42.
- Liu, P.C. and Green, A.W.**, 1978. Higher order wave spectra. *Proc. 16th Coastal Eng. Conf.*, 1: 360-371.
- Liu, P.L.F. and Dalrymple, R.A.**, 1984. The damping of gravity water-waves due to percolation. *Coastal Eng.*, 8: 33-49.
- Liu, P.L.F., Yoon, S.B. and Kirby, J.T.**, 1985. Nonlinear refraction-diffraction of waves in shallow water. *Jour. Fluid Mech.*, 153: 185-201.

- Liu, K. and Mei, C.C., 1987. Solitary waves over a Bingham-plastic sea bed. *Proc. Specially Conf. Coastal Sediments'87, ASCE*, 1: 324-347.
- Lo, J.M. and Dean, R.G., 1986. Evaluation of a modified stretched linear wave theory. *Proc. 20th Conf. Coastal Eng.*, 1: 522-536.
- Long, R.B. and Hasselmann, K., 1979. A variational technique for extracting directional spectra from multicomponent wave data. *Jour. Phys. Ocean.*, 9: 373-381.
- Longuet-Higgins, M.S., 1952. On the statistical distribution of heights of sea waves. *Jour. Mar. Res.*, 11: 245-266.
- Longuet-Higgins, M.S., 1962. Resonant interactions between two trains of gravity waves. *Jour. Fluid Mech.*, 12: 321-332.
- Longuet-Higgins, M.S., 1963. The effect of nonlinearities on statistical distributions in the theory of sea waves. *Jour. Fluid Mech.*, 17: 459-480.
- Longuet-Higgins, M.S., 1969a. On wave breaking and equilibrium spectrum of wind-generated waves. *Proc. Roy. Soc.*, A310: 151-159.
- Longuet-Higgins, M.S., 1969b. Action of variable stress at the surface of water waves. *The Physics of Fluids.*, 12: 737-740.
- Longuet-Higgins, M.S., 1973. A model of flow separation at a free surface. *Jour. Fluid Mech.*, 57: 129-148.
- Longuet-Higgins, M.S., 1974. Breaking waves-in deep or shallow water. *Proc. 10th Symp. Naval Hydrol.*, pp. 597-605.
- Longuet-Higgins, M.S., 1975. On the statistical distribution of the periods and amplitudes of sea waves. *Jour. Geoph. Res.*, 80: 2688-2694.
- Longuet-Higgins, M.S., 1976a. Recent development in the study of breaking waves. *Proc. 15th Conf. Coastal Eng.*, 1: 441-460.
- Longuet-Higgins, M.S., 1976b. On the nonlinear transfer of energy in a peak of a gravity-wave spectrum: a simplified model. *Proc. Roy. Soc.*, A347: 311-328.
- Longuet-Higgins, M.S., 1977. On the nonlinear transformation of wave train in shallow water. *Archiv. Hydrot.*, 24.
- Longuet-Higgins, M.S., 1980. On the distribution of the heights of sea waves: some effects of nonlinearity and finite band width. *Jour. Geoph. Res.*, 85: 1519-1523.

- Longuet-Higgins, M.S.**, 1983. On the joint distribution of wave periods and amplitudes in a random wave field. *Proc. Roy. Soc.*, A389: 241–258.
- Longuet-Higgins, M.S.**, 1984. Statistical properties of wave groups in a random sea state. *Phil. Trans. Roy. Soc.*, A312: 219–250.
- Longuet-Higgins, M.S.**, 1985. Acceleration in steep gravity waves. *Jour. Phys. Oceanogr.*, 15: 1570–1579.
- Longuet-Higgins, M.S. and Stewart, R.W.**, 1961a. The changes in amplitude of short gravity waves on steady nonuniform currents. *Jour. Fluid Mech.*, 10: 529–549.
- Longuet-Higgins, M.S., Cartwright, D.E. and Smith, N.D.**, 1961b. Observations of the directional spectrum of sea waves using the motions of a floating buoy. In: *Ocean Wave Spectrum*, Prentice-Hall Inc., 111–136.
- Longuet-Higgins, M.S. and Stewart, R.W.**, 1964. Radiation stresses in water waves: a physical discussion with applications. *Deep Sea Research*, 11: 529–562.
- Longuet-Higgins, M.S. and Fox, M.J.H.**, 1977. Theory of the almost-highest wave: the inner solution. *Jour. Fluid Mech.*, 80: 721–741.
- Lough, J.M. and Barnes, D.L.**, 1992. Comparison of skeletal density variations in *Porites* from the Central Barrier Reef. *Jour. Exper. Mar. Ecology*, 155: 1–25.
- Maa, P.Y. and Mehta, A.J.**, 1988. Soft mud properties: Voight model. *Jour. Waterway, Port, Coastal and Ocean Eng.*, 114: 765–770.
- MacPherson, H.**, 1980. The attenuation of water waves over a non-rigid bed. *Jour. Fluid Mech.*, 97: 721–742.
- Madsen, O.S.**, 1971. On the generation of long waves. *Jour. Geoph. Res.*, 76: 8672–8683.
- Madsen, O.S., Poon, Y. and Graber, H.C.**, 1988. Spectral wave attenuation by bottom friction: theory. *Proc. 21st Coastal Eng. Conf.*, 1: 492–504.
- Madsen, P.A., Murray, R. and Sorensen, O.R.**, 1991. A new form of the Boussinesq equations with improved linear dispersion characteristics. *Ocean Eng.*, 15: 371–388.
- Madsen, P.A. and Sorensen, O.R.**, 1993. Bound waves and triad interactions in shallow water. *Ocean Eng.*, 20: 359–388.
- Mansard, E.P.D. and Funke, E.R.**, 1980. The measurement of incident and reflected spectra using a least squares method. *Proc. 17th Inter. Conf. Coastal Eng.*, 1: 154–172.

- Mardia, K.V., 1972. *Statistics of Directional Data*. Academic Press, London, 239 pp.
- Mase, H. and Kirby, J.T., 1992. Hybrid frequency-domain KdV equation for random wave transformation. *Proc. 23th Coastal Eng. Conf.*, 1:474-487.
- Massel, S.R., 1973. Falowanie wiatrowe na ograniczonych głębokościach; jego struktura i procesy współoddziaływania z budowlami hydrotechnicznymi (Wind waves in shallow water; their structure and interactions with engineering structures). *Hydrot. Trans.*, 32, Supplement: 3-105.
- Massel, S.R., 1976. Gravity waves propagated over permeable bottom. *Jour. Waterways, Harbors and Coastal Eng. Div.*, 102: 111-121.
- Massel, S.R., 1980. Związek dyspersyjny dla fal wiatrowych (Dispersion relation for wind waves). *Archives of Hydrot.*, 27: 151-170.
- Massel, S.R., 1981a. *Hydrodynamiczne Problemy Budowli Półmorskich* (Hydrodynamical Problems of Offshore Structures), Państwowe Wydawnictwo Naukowe, Warszawa, 155 pp.
- Massel, S.R., 1981b. On the nonlinear theory of mechanically generated waves in laboratory channels. *Mitteil. der Techn. Univ. Braunschweig*, 70: 333-376.
- Massel, S.R., 1982a. Falowanie wód atlantyckich (Waves in the Atlantic Ocean). In: Rühle, E. and Zaleski, J. (Editors), *Ocean Atlantycki* (Atlantic Ocean), Państwowe Wydawn. Naukowe, Warszawa, 388-414.
- Massel, S.R., 1982b. Mechaniczna generacja falowania wodnego w kanale hydraulicznym w świetle teorii nieliniowej (Nonlinear theory of paddle generated waves). *Arch. Hydrot.*, 29: 183-208.
- Massel, S.R., 1983. Harmonic generation by waves propagating over a submerged step. *Coastal Eng.*, 7: 357-380.
- Massel, S.R., 1985. Rozkład prawdopodobieństwa wysokości fal powierzchniowych wzbudzanych wiatrem (On the distribution of wave heights in a random wave field). *Archives of Hydrot.*, 32: 343-360.
- Massel, S.R., 1989. *Hydrodynamics of Coastal Zones*, Elsevier Science Publ. Comp., Amsterdam, 336 pp.
- Massel, S.R., 1992. Wave transformation and dissipation on steep reef slopes. *Proc. 11th Australasian Fluid Mech. Conf.*, 1: 319-322.
- Massel, S.R., 1993a. Extended refraction-diffraction equation for surface waves. *Coastal Eng.*, 19: 97-126.

- Massel, S.R., 1993b. Scattering of surface waves by a conical coral. *Proc 11th Australasian Conf. on Coastal and Ocean Eng.*, 2: 467-471.
- Massel, S.R., 1994. Measurement and modelling of waves incident on steep islands or shoals. *Proc. Inter. Symp.: Waves - Physical and Numerical Modelling*, 2: 982-9991.
- Massel, S.R., 1995a. On the largest wave height in water of constant depth. *Ocean Eng.*, (in press).
- Massel, S.R., 1995b. The limiting wave height in wind-induced wave train. *Ocean Eng.*, (submitted).
- Massel, S.R. and Mei, C.C., 1977. Transmission of random wind waves through perforated or porous breakwaters. *Coastal Eng.*, 1:63-78.
- Massel, S.R. and Butowski, P., 1980. Transmission of wind waves through porous breakwater. *Proc. 17th Coastal Eng. Conf.*, 3: 333-346.
- Massel, S.R. and Chybicki, W., 1983. Nieliniowy związek dyspersyjny dla fal wiatrowych na ograniczonych głębokościach. Analiza teoretyczna (Nonlinear dispersion relation for wind surface waves at limited water depths. Theoretical analysis). *Studia i Mater. Oceanol.*, 40: 47-71.
- Massel, S.R. and Robakiewicz, M., 1986. Osobliwości charakterystyk statystycznych falowania wiatrowego w strefie brzegowej morza (On the statistical characteristics of wind waves in the coastal zone). *Rozpr. Hydrot.*, 48: 21-51.
- Massel, S.R. and Belberova, D.Z., 1990. Parameterization of the dissipation mechanism in the surface waves induced by wind. *Arch. Mech.*, 42: 515-539.
- Massel, S.R., Belberov, Z.K., Kostichkova, D.P. and Cherneva, Z.I., 1990. Distinctive features of wind waves in coastal zone. In: Antsyferov, S.M., Belberov, Z.K. and Massel, S.R., (Editors), *Dynamical Processes in Coastal Regions*. Publ. House of the Bulgarian Academy of Science, Sofia.
- Massel, S.R. and Done, T.J., 1993. Effects of cyclone waves on massive coral assemblages on the Great Barrier Reef: meteorology, hydrodynamics and demography. *Coral Reefs*, 12: 153-166.
- Massel, S.R. and Steinberg, C.R., 1994. Basic properties of wave motion in coastal and reef environment. *Inter. Symp. Ecology and Engineering*, Kuala Lumpur, 2: 1-18.
- Masson, D., 1993. On the nonlinear coupling between swell and wind waves. *Jour. Phys. Oceanogr.*, 23: 1249-1258.

- Masuda, A. and Kuo, Y.Y., 1981. A note on the imaginary part of bispectra. *Deep-Sea Research*, 28A: 213-222.
- McLeish, W.D., Swift, J.P., Long, R.B., Ross, D. and Merrill, G., 1981. Ocean surface patterns above sea-floor bedform as recorded by radar, Southern Bight of North Sea. *Marine Geology*, 43: 1-8.
- Mei, C.C., 1983. *The Applied Dynamics of Ocean Surface Waves*. World Scientific, Singapore, 734 pp.
- Mei, C.C., 1985. Resonant reflection of surface water waves by periodic sandbars. *Jour. Fluid Mech.*, 152: 315-335.
- Mei, C.C., Hara, T. and Naciri, M., 1988. Note on Bragg scattering of water waves by parallel bars on the seabed. *Jour. Fluid Mech.*, 186: 147-162.
- Mei, C.C. and Foda, M.A., 1981. Wave-induced responses in a fluid-filled poro-elastic solid with a free surface - a boundary layer theory. *Geophys. Jour. Royal Astr. Soc.*, 66: 597-631.
- Memos, C.D., 1994. On the theory of the joint probability of heights and periods of sea waves. *Coastal Eng.*, 22: 201-215.
- Miche, R., 1944. Mouvements ondulatoires de la mer eu profondeur constante ou décroissante (Breaking wave motion in water of constant water depth). *Ann. Ponts et Chaussees*, 121: 285-318.
- Miche, R., 1951. Le pouvoir reflechissant des ouvrages maritimes exposes a l'action de la houle (Reflectivity of marine structures exposed to action of waves). *Ann. des Ponts et Chaussees*, 121: 285-319.
- Middleton, D., 1960. *Introduction to Statistical Communication Theory*. Mc Graw-Hill, New York, 650 pp.
- Miles, J.W., 1957. On the generation of surface waves by shear flows. *Jour. Fluid Mech.*, 3: 185-204.
- Miles, J.W., 1959. On the generation of surface waves by shear flows. Part 2. *Jour. Fluid Mech.*, 6: 568-582.
- Miles, J.W., 1962. On the generation of surface waves by shear flows. Part 4. *Jour. Fluid Mech.*, 13: 433-448.
- Miles, J.W., 1965. A note on the interaction between surface waves and wind profiles. *Jour. Fluid Mech.*, 22: 823-827.

- Milne-Thomson, L.M.**, 1960. *Theoretical Hydrodynamics*, Mac Millan Press Ltd., London, 743 pp.
- Mitsuyasu, H.**, 1968. A note on the nonlinear energy transfer in the spectrum of wind generated waves. *Rep. Res. Inst. Appl. Mech. Kyushu Univ.*, 16: 251-264.
- Mitsuyasu, H., Nakayama, R. and Komori, T.**, 1971. Observations of the wind and waves in Hakata Bay. *Rep. Res. Inst. Appl. Mech., Kyushu Univ.*, 19: 37-74.
- Mitsuyasu, H., Suhaya, T., Mizuno, S., Ohkuso, M., Honda T. and Rikiishi, K.**, 1975. Observations of the directional spectrum of ocean waves using a cloverleaf buoy. *Jour. Phys. Oceanogr.*, 5: 750-760.
- Mitsuyasu, H., Suhaya, T., Mizuno, S., Ohkuso, M., Honda, T. and Rikiishi, K.**, 1980. Observations of the power spectrum of waves using a cloverleaf buoy. *Jour. Phys. Oceanogr.*, 10: 286-296.
- Mitsuyasu, H. and Honda, T.**, 1982. Wind-induced growth of water waves. *Jour. Fluid Mech.*, 123: 425-442.
- Mognard, N.M., Campbell, W.J., Cheney, R.E. and Marsh, J.G.**, 1983. Southern Ocean mean monthly waves and surface winds for winter 1978 by Seasat radar altimeter. *Jour. Geoph. Res.*, 88: 1736-1744.
- Monin, A.S. and Yaglom, A.M.**, 1965. *Statisticheskaya Gidromekhanika* (Statistical Fluid Mechanics), Vol. 2, Izdatelstvo Nauka, Moscow, 720 pp.
- Monin, A.S. and Krasitskii, V.P.**, 1985. *Yavleniya na Poverkhnosti Okeana* (Phenomena on the Ocean Surface). Gidrometeoizdat, Leningrad, 375 pp.
- Morison, J.R., O'Brien, M.P., Johnson, J.W. and Schaaf, S.A.**, 1950. The force exerted by surface waves on piles. *Petroleum Trans., AIME*, 189: 149-154.
- Morse, P.M. and Feshbach, H.**, 1993. *Methods of Theoretical Physics*. Vol. 2. Mc Graw-Hill, 1929 pp.
- Muir, L.R. and El-Shaarawi, A.H.**, 1986. On the calculation of extreme wave heights: a review. *Ocean Eng.*, 13: 93-118.
- Myrhaug, D. and Kjeldsen, S.P.**, 1986. Steepness and asymmetry of extreme waves and the highest waves in deep water. *Ocean Eng.*, 13: 549-568.
- Naess, A.**, 1984. The effect of the Markov chain condition on the prediction of extreme values. *Jour. Sound and Vibration*, 94: 87-103.

- Naess, A., 1985a. On the distribution of crest to trough wave heights. *Ocean Eng.*, 12: 221-234.
- Naess, A., 1985b. The joint crossing frequency of stochastic processes and its application to wave theory. *Applied Ocean Res.*, 7: 35-50.
- Nairn, R.B., Roelvink, J.A. and Southgate, H.N., 1990. Transition zone width and implications for modeling surf zone hydrodynamics. *Proc. 22nd Coastal Eng. Conf.*, 1: 68-81.
- Nath, J.H. and Ramsey, F.L., 1976. Probability distributions of breaking wave heights emphasizing the utilization of the JONSWAP spectrum. *Jour. Phys. Oceanogr.*, 6: 316-323.
- Nelson, R.C., 1985. Wave heights in depth limited conditions. *Civil Eng. Trans.*, 27: 210-215.
- Nelson, R.C., 1987. Design wave heights on very mild slopes. *Civil Eng. Trans.*, 29: 157-161.
- Nelson, R.C., 1994. Depth limited design wave heights in very flat regions. *Coastal Eng.*, 23: 43-59.
- Nelson, R.C. and Lesleighter, E.J., 1985. Breaker height attenuation over platform coral reefs. *Proc. 7th Australian Conf. on Coastal and Ocean Eng.*, 1: 9-16.
- Nelson, R.C. and Gonsalves, J., 1990. A field study of wave reflections from an exposed dissipative beach. *Coastal Eng.*, 14: 457-477.
- Newman, J.N., 1977. *Marine Hydrodynamics*, The Mass. Inst. Techn. Press, Cambridge.
- Niedzwecki, J.M. and Whatley, C.P., 1991. A comparative study of some directional sea models. *Ocean Eng.*, 18: 111-128.
- Nielsen, P., 1986. Local approximation: a new way of dealing with irregular waves. *Proc. 20th Coastal Eng. Conf.*, 1: 633-646.
- Nielsen, P., 1989. Analysis of natural waves by local approximations. *Jour. Waterway, Port, Coastal and Ocean Div.*, 115: 384-397.
- Nwogu, O., 1989. Maximum entropy estimation of directional wave spectra from an array of wave probes. *Applied Ocean Research*, 11: 176-182.
- Ochi, M.K., 1990. *Applied Probability and Stochastic Processes in Engineering and Physical Sciences*. John Wiley & Sons., New York, 499 pp.

- Ochi, M.K. and Hubble, E.N., 1976. On six-parameter wave spectra. *Proc. 15th Coastal Eng. Conf.*, 1: 301–328.
- Ochi, M.K. and Whalen, J.E., 1980. Prediction of the severest significant wave height. *Proc. 17th Coastal Eng. Conf.*, 1: 669–688.
- Ochi, M.K. and Tsai, C.H., 1983. Prediction of occurrence of breaking waves in deep water. *Jour. Phys. Oceanogr.*, 13: 2008–2019.
- Ochi, M.K. and Wang, W.C., 1984. Non-gaussian characteristics of coastal waves. *Proc. 19th Coastal Eng. Conf.*, 1: 516–531.
- Ochi, M.K. and Sahinoglou, I.I., 1989. Stochastic characteristics of wave groups in random seas. Part 1: Time duration of and number of waves in a wave group. *Applied Ocean Res.*, 11: 39–50.
- Osborne, A.R., 1982. The simulation and measurement of random ocean wave statistics. In: Osborne, A.R. and Rizzoli, P.M., (Editors), *Proc. Inter. School of Physics: Topics in Ocean Physics*, North-Holland, Amsterdam, 515–550.
- Otnes, R.K. and Enochson, L., 1972. *Digital Time Series Analysis*. John Wiley & Sons, New York, 388 pp.
- Panchang, V.G., Ge, W., Pearce, B.R. and Briggs, M.J., 1990. Numerical simulation of irregular wave propagation over a shoal. *Jour. Waterways, Port, Coastal and Ocean Eng.*, 116: 324–340.
- Panchang, V.G., Pearce, B.R., Wei C.C. and Cushman-Roisin, B., 1991. Solution of the mild-slope wave problem by iteration. *Appl. Ocean Res.*, 13: 187–199.
- Panicker, N.N. and Borgman, L.E., 1970. Directional spectra from wave-gage arrays. *Proc. 12th Coastal Eng. Conf.*, 1: 117–136.
- Papoulis, A., 1965. *Probability, Random Variables, and Stochastic Processes*. McGraw-Hill Book Comp., New York, 583 pp.
- Pawka, S.S., 1983. Island shadows in wave directional spectra. *Jour. Geoph. Res.*, 88: 2579–2591.
- Pawka, S.S., Juman, D.L. and Guza, R.T., 1984. Island sheltering of surface gravity waves: model and experiment. *Continental Shelf Research*, 3: 35–53.
- Pedlosky, J., 1979. *Geophysical Fluid Dynamic*. Springer Verlag, New York, 624 pp.
- Peregrine, D.H., 1976. Interaction of water waves and currents. *Adv. Appl. Mech.*, 16: 9–117.

- Peregrine, D.H., 1983. Breaking waves on beaches. *Ann. Rev. Fluid Mech.*, 15: 149-178.
- Peregrine, D.H., 1990a. Report from the working group on breaking and freak waves. In: Torum, A. and Gudmestad, O.T., (Editors) *Water Wave Kinematics*. Kluwer Academic Publ., 17-20.
- Peregrine, D.H., 1990b. Theory versus measurements. In: Torum, A. and Gudmestad, O.T., (Editors) *Water Wave Kinematics*. Kluwer Academic Publ., 89-101.
- Peters, H.C. and Boanstra, H., 1988. Fatigue loading on a single pile platform due to combined action of waves and currents. *Proc. 5th Inter. Conf. on the Behaviour of Offshore Structures*, 1: 1015-1034.
- Petrauskas, C. and Aagaard, P.M., 1971. Extrapolation of historical storm data for estimating design-wave heights. *Trans. Soc. Petrol Eng.*, 251: 23-37.
- Phillips, O.M., 1957. On the generation of waves by turbulent wind. *Jour. Fluid Mech.*, 2: 417-445.
- Phillips, O.M., 1958. The equilibrium range in the spectrum of wind-generated waves. *Jour. Fluid Mech.*, 4: 426-434.
- Phillips, O.M., 1960a. The mean horizontal momentum and surface velocity of finite-amplitude random gravity waves. *Jour. Geoph. Res.*, 65: 3473-3476.
- Phillips, O.M., 1960b. On the dynamics of unsteady gravity waves of finite amplitude. Part 1. *Jour. Fluid Mech.*, 9: 193-217.
- Phillips, O.M., 1966. *The Dynamics of the Upper Ocean*, Cambridge Univ. Press, 265 pp.
- Phillips, O.M., 1977. *The Dynamics of the Upper Ocean. Second Edition*, Cambridge Univ. Press, 336 pp.
- Phillips, O.M., 1985. Spectral and statistical properties of the equilibrium range in wind-generated gravity waves. *Jour. Fluid Mech.*, 156: 505-531.
- Phillips, O.M. and Katz, E.J., 1961. The low frequency components of the spectrum of wind generated waves. *Jour. Marine Res.*, 19: 57-69.
- Phillips, O.M. and Banner, M.L., 1974. Wave breaking in the presence of wind drift and swell. *Jour. Fluid Mech.*, 66: 625-640.
- Phillips, O.M., Gu, D. and Donelan, M., 1993a. Expected structure of extreme waves in a Gaussian sea. Part I: Theory and SWADE buoy measurements. *Jour. Phys. Ocean.*, 23: 992-1000.

- Phillips, O.M., Gu, D. and Wash, E.J., 1993b. On expected structure of extreme waves in a Gaussian sea. Part II: SWADE scanning radar altimeter measurements. *Jour. Phys. Ocean.*, 23: 2297–2309.
- Pierson, W.J., Neumann, G. and James, R.W., 1955. Practical methods for observing and forecasting ocean waves by means of wave spectra and statistics. Publ. No. 603, U.S. Naval Hydrographic Office.
- Pierson, W.J. and Moskowitz, L., 1964. A proposed spectral form for fully developed wind seas based on the similarity theory of S.A. Kitaigorodskii. *Jour. Geoph. Res.*, 69: 5181–5190.
- Pierson, W.J., Tick, L.J. and Baer, L., 1966. Computer based procedure for preparing global wave forecasts and wind field analysis capable of using wave data obtained from a spacecraft. *Proc. 6th Symp. Naval Hydrodynamics*, Washington, D.C.
- Press, W.H., Flannery, B.P., Teukolsky, S.A. and Vetterling, W.T., 1986. *Numerical Recipes. The Art of Scientific Computing*, Cambridge Univ. Press, Cambridge, 818 pp.
- Puzyrewski, R. and Sawicki, J., 1987. *Podstawy Mechaniki Płynów i Hydrauliki* (Basic Fluid Mechanics and Hydraulics). Państwowe Wydawn. Naukowe, Warszawa, 332 pp.
- Radder, A.C., 1979. On the parabolic equation method for water-wave propagation. *Jour. Fluid Mech.*, 95: 159–176.
- Ramamonjiarisoa, A. and Coantic, M., 1976. Loi exp'imentale de dispersion des vagues par le vent sur une faible longueur d'action (Experimental dispersion relation for fetch limited wind waves). *C. R. Acad. Sci. Paris*, B282: 111–114.
- Readshaw, J.S. and Baird, W.F., 1981. A discussion of procedures to estimate extreme wave heights over the Canadian Atlantic continental shelf. *MEDS Contractor Rep. No. 3*, Ottawa, 73 pp.
- Resio, D. and Perrie, W., 1991. A numerical study of nonlinear energy fluxes due to wave-wave interactions. Part I. Methodology and basic results. *Jour. Fluid Mech.*, 223: 603–629.
- Rice, O., 1944. Mathematical analysis of random noise. *Bell. Syst. Tech. Jour.*, 23: 282–332.
- Rice, O., 1945. Mathematical analysis of random noise. *Bell. Syst. Tech. Jour.*, 24: 46–156.

- Riedel, H.P. and Byrne, A.P., 1986. Random breaking waves – horizontal seabed. *Proc. 12th Coastal Eng. Conf.*, 1: 903–908.
- Riley, D.S., Donelan, M.A. and Hui, W.H., 1982. An extended Miles' theory for wave generation by wind. *Boundary Layer - Meteorology*, 22: 209–225.
- Romeiser, R., 1993. Global validation of the wave model WAM over a one-year period using Geosat wave height data. *Jour. Geoph. Res.*, 98: 4713–4726.
- Rufenach, C.L., Olsen, R.B., Shuchman, R.A. and Russel, C.A., 1991. Comparison of aircraft synthetic aperture radar and buoy spectra during the Norwegian Continental Shelf Experiment of 1988. *Jour. Geoph. Res.*, 96: 10423–10441.
- Salter, S.H., 1974. Wave power. *Nature*, 249: 720–724.
- Sarpkaya, T. and Isaacson, M.St.Q., 1981. *Mechanics of Wave Forces on Offshore Structures*. Van Nostrand Reinold, New York, 651 pp.
- Schäffer, H.A., Madsen, P.A. and Deigaard, R., 1993. A Boussinesq model for wave breaking in shallow water. *Coastal Eng.*, 20: 185–202.
- Schwab, D.J., Benett, J.R., Liu, P.C. and Donelan, M.A., 1984. Application of a simple numerical wave prediction model to Lake Erie. *Jour. Geoph. Res.*, 89: 3586–3592.
- Seelig, W.N., 1980. *Maximum wave heights and critical water depths for irregular waves in the surf zone*. U.S. Army Corps of Eng. CERC, Rep. 80-1, 11pp.
- Seelig, W.N. and Ahrens, J.P., 1981. *Estimation of Wave Reflection and Energy Dissipation Coefficients for Beaches, Revetments, and Breakwaters*. Techn. Paper 81-1 U.S. Army Corps of Engineers, CERC.
- Shannon, C.E., 1948a. The mathematical theory of communications, Part I and II. *Bell System Tech. Jour.*, 27: 379–423.
- Shannon, C.E., 1948b. The mathematical theory of communications, Part III and IV. *Bell System Tech. Jour.*, 27: 623–656.
- Shemdin, O., Hasselmann, K., Hsiao, S.V. and Herterich, K., 1978. Nonlinear and linear bottom interaction effects in shallow water. In: Favre, A. and Hasselmann, K. (Editors), *Turbulent Fluxes through the Sea Surface, Wave Dynamics, and Prediction*, Plenum Press, New York, 347–372.
- Shiau, J.C. and Wang, H., 1977. Wave energy transformation over irregular bottom. *Jour. Waterway, Port, Coastal and Ocean Div.*, 103: 57–68.

- Shore Protection Manual (SPM)**, 1973, 1975, 1977, 1984. U.S. Army Coastal Engineering Research Center, Fort Belvoir, Vol. I-III.
- Simpson, J.H.**, 1969. Observations of the directional characteristics of sea waves. *Geoph. Jour. Roy. Astr. Soc.*, 17: 93-120.
- Smith, R.**, 1976. Giant waves. *Jour. Fluid Mech.*, 77: 417-431.
- Snodgrass, F.E., Groves, G.W., Hasselmann, K., Miller, G.R., and Munk, W.H., Powers, W.H.**, 1966. Propagation of ocean swell across the Pacific. *Phil. Trans. Roy. Soc.*, A249: 431-497.
- Snyder, R.L.**, 1974. A field study of wave-induced pressure fluctuations above surface gravity waves. *Jour. Marine Res.*, 32: 497-531.
- Snyder, R.L., Dobson, F.W., Elliott, J.A. and Long, R.B.**, 1981. Array measurements of atmospheric pressure fluctuations above surface gravity waves. *Jour. Fluid Mech.*, 102: 1-59.
- Snyder, R.L. and Kennedy, R.M.**, 1983a. On the formation of whitecaps by a threshold mechanism. Part I: Basic formalism. *Jour. Phys. Oceanogr.*, 13: 1482-1492.
- Snyder, R.L. and Kennedy, R.M.**, 1983b. On the formation of whitecaps by a threshold mechanism. Part II: Monte Carlo experiments. *Jour. Phys. Oceanogr.*, 13: 1493-1504.
- Snyder, R.L., Thacker, W.C., Hasselmann, K., Hasselmann, S. and Barzel, G.**, 1993. Implementation of an efficient scheme for calculating nonlinear transfer from wave-wave interactions. *Jour. Geoph. Res.*, 98: 14507-14525.
- Soares, C.G.**, 1984. Representation of double-peaked sea wave spectra. *Ocean Eng.*, 11: 185-207.
- Soares, C.G.**, 1986a. Assessment of the uncertainty in visual observations of wave height. *Ocean Eng.*, 13: 37-56.
- Soares, C.G.**, 1986b. Calibration of visual observations of wave period. *Ocean Eng.*, 13: 539-547.
- Soares, C.G.**, 1991. On the occurrence of double peaked wave spectra. *Ocean Eng.*, 18: 17-171.
- Sobey, R.J.**, 1992a. The distribution of zero-crossing wave heights and periods in a stationary sea state. *Ocean Eng.*, 19: 101-118.

- Sobey, R.J., 1992b. A local Fourier approximation method for irregular wave kinematics. *Applied Ocean Res.*, 14: 93-105.
- Sobey, R.J., 1992c. Estimation of irregular wave kinematics from a measured record. *Proc. 23th Coastal Eng. Conf.*, 1: 644-657.
- Sobey, R.J. and Young, I.R., 1986. Hurricane wind waves - a discrete spectral model. *Jour. Waterway, Port, Coastal and Ocean Eng.*, 112: 370-388.
- Sobey, R.J., Chandler, B.D. and Harper, B.A., 1990. Extreme waves and wave counts in a hurricane. *Proc. 22nd Coastal Eng. Conf.*, 1: 358-370.
- Sollitt, C.K. and Cross, R.H., 1972. *Wave Reflection and Transmission at Permeable Breakwaters*, Ralph M. Parsons Lab., Mass. Inst. Techn., Techn. Rep., No. 147.
- Soulsby, R.L., 1987. Calculating bottom orbital velocity beneath waves. *Coastal Eng.*, 11: 371-380.
- Srokosz, M.A., 1986. On the probability of wave breaking in deep water. *Jour. Phys. Oceanogr.*, 16: 382-385.
- Srokosz, M.A. and Longuet-Higgins, M.S., 1986. On the skewness of sea-surface elevation. *Jour. Fluid Mech.*, 164: 487-497.
- Srokosz, M.A. and Challenor, P.G., 1987. Joint distributions of wave heights and period: a critical comparison. *Ocean Eng.*, 14: 295-311.
- Starr, V.P., 1947. A momentum integral for surface waves in deep water. *Jour. Marine Res.*, 6: 126-135.
- Steedman, R.K., 1993. Data report on Southern Ocean surface wave climate adjacent Macquarie Island, Nov. 1988 - Oct. 1989. Steedman Science & Eng., Rep. R594, Perth, Australia.
- Steele, K.E., Teng, C.C. and Wang, D.W.C., 1992. Wave direction measurements using pitch-roll buoys. *Ocean Eng.*, 19: 349-375.
- Stive, M.J.F., 1984. Energy dissipation in wave breaking on gentle slopes. *Coastal Eng.*, 8: 99-127.
- Stokes, G.G., 1847. On the theory of oscillatory waves. *Trans. Camb. Phil. Soc.*, 8: 441-455.
- Stokes, G.G., 1880. Considerations relative to the greatest height of oscillatory waves which can be propagated without change of form. *Mathematical and Physical Papers*, 1: 225-228.

- Strekalov, S.S. and Massel, S.R.**, 1971. Niektore zagadnienia widmowej analizy falowania wiatrowego (On the spectral analysis of wind waves). *Arch. Hydrot.*, 18: 457-485.
- Strekalov, S.S. and Krivitskii, S.V.**, 1983. O kharakteristikakh slabostratsirovanovo vetrovogo potoka nad vodnoy poverkhnosti (Characteristics of weakly stratified wind layer over water surface). *Izv. Akad. Nauk, Fizika Atmosfery i Okeana*, 19: 100-102.
- Suk, K.D., Kim, Y.Y. and Lee, D.Y.**, 1994. Equilibrium-range spectrum of waves propagating on currents. *Jour. Waterways, Port, Coastal and Ocean Eng.*, 120: 434-450.
- Sulaiman, D.M., Tsutsui, S., Yoshioka, H., Yamashita, T., Oshiro, S. and Tsuchiya, Y.**, 1994. Prediction of the maximum wave on the coral flat. *Proc. 24th Coastal Eng. Conf., Kobe* (in press).
- Sultan, N.J. and Hughes, S.A.**, 1993. Irregular wave-induced velocities in shallow water. *Jour. Waterway, Port, Coastal, and Ocean Eng.*, 119: 429-447.
- Svendsen, I.A.**, 1984. Wave heights and set-up in a surf zone. *Coastal Eng.*, 8: 303-329.
- Svendsen, I.A., Madsen, P.A. and Hansen, J.B.**, 1978. Wave characteristics in the surf zone. *Proc. 16th Coastal Eng. Conf.*, 1: 520-539.
- Sverdrup, H.U. and Munk, W.H.**, 1947. Wind, sea, and swell; theory of relations for forecasting. *U.S. Navy Hydrographic Office, H.O.*, Publ. No. 601.
- Sveshnikov, A.A.**, 1965. *Podstawowe Metody Funkcji Losowych* (Basic Methods of Random Functions.) Polish Science Publ., Warsaw, 292 pp.
- The SWAMP Group**, 1985. *Ocean Wave Modeling*. Plenum Press, New York, 256 pp.
- Swart, D.H. and Loubser, C.C.**, 1978. Vocoidal theory for all non-breaking waves. *Proc. 16th Coastal Eng. Conf.*, 1: 467-486.
- Sylwester, R.**, 1974. *Coastal Engineering, I*. Elsevier Science Publ., Amsterdam, 457 pp.
- Tayfun, M.A.**, 1981a. Breaking-limited wave heights. *Jour. Waterway, Port, Coastal and Ocean Eng.*, 107: 59-69.
- Tayfun, M.A.**, 1981b. Distribution of crest-to-trough wave height. *Jour. Waterway, Port, Coastal and Ocean Eng.*, 107: 149-158.

- Tayfun, M.A.**, 1990. Distribution of large wave heights. *Jour. Waterway, Port, Coastal and Ocean Eng.*, 116: 686-707.
- Tayfun, M.A.**, 1993. Joint distribution of large wave heights and associated periods. *Jour. Waterway, Port, Coastal and Ocean Eng.*, 119: 261-273.
- Tayfun, M.A., Dalrymple, R.A. and Yang, C.Y.**, 1976. Random wave-current interactions in water of varying depth. *Ocean Eng.*, 3: 403-420.
- Tayfun, M.A. and Lo, J.M.**, 1989. Envelope, phase, and narrow-band models of sea waves. *Jour. Waterway, Port, Coastal and Ocean Eng.*, 115: 594-613.
- Teh-fu, L. and Feng-shi, M.**, 1980. Prediction of extreme wave heights and wind velocities. *Jour. Waterway, Port, Coastal and Ocean Div.*, 106: 469-479.
- Thom, H.C.S.**, 1971. Asymptotic extreme-value distribution of wave heights in the open ocean. *Jour. of Mar. Res.*, 29: 19-27.
- Thom, H.C.S.**, 1973. Distribution of extreme winds over oceans. *Jour. Waterway, Harbors and Coastal Eng. Div.*, 99: 1-17.
- Thornton, E.B. and Guza, R.T.**, 1983. Transformation of wave height distribution. *Jour. Geoph. Res.*, 88: 5925-5938.
- Tikhonov, W.I.**, 1966. *Statisticheskaya Radiotekhnika* (Statistical Radiotechnics), Sov. Radio Publ., Moscow, 678 pp.
- Timoshenko, S.P. and Gere, J.M.**, 1972. *Mechanics of Materials*, van Nostrand Reinhold, New York.
- Toba, Y.**, 1973. Local balance in the air-sea boundary process. III: On the spectrum of wind waves. *Jour. Oceanogr. Soc. Japan*, 29: 209-220.
- Tolman, H.L.**, 1991a. Effects of tides and storm surges on North Sea wind waves. *Jour. Phys. Oceanogr.*, 21: 766-781.
- Tolman, H.L.**, 1991b. A third-generation model for wind waves on slowly varying unsteady, and inhomogeneous depths and currents. *Jour. Phys. Oceanogr.*, 21: 782-797.
- Tolman, H.L.**, 1992. Effects of numeric on the physics in a third-generation wind-wave model. *Jour. Phys. Oceanogr.*, 22: 1095-1111.
- Tournadre, J. and Ezraty, R.**, 1990. Local climatology of wind and sea state by means of satellite radar altimeter measurements. *Jour. Geoph. Res.*, 95: 18255-18268.

- Townsend, M. and Fenton, J.D.**, 1995. Numerical comparison of wave analysis methods. *Proc. 12th Australasian Coastal and Ocean Eng. Conf.*, 1:169-173.
- Trizna, D.B., Moore, J.C., Headrick, J.M. and Bogle, R.W.**, 1977. Directional sea spectrum determined using HF Doppler radar techniques. *IEEE Trans.*, AP25: 4-11.
- Trizna, D.B., Bogle, R.W., Moore, J.C. and Howe, M.C.**, 1980. Observations by H.F. radar of the Phillips resonance mechanism for generation of wind waves. *Jour. Geoph. Res.*, 85: 4946-4956.
- Tsuruya, H.**, 1988. Experimental study on the wave decay in an opposing wind. *Coastal Eng. in Japan*, 30: 25-43.
- Tsutsui, S. and Lewis, D.P.**, 1991. Wave height prediction in unbounded coastal domains with bathymetric discontinuity. *Coastal Eng. in Japan*, 34: 145-158.
- Tsutsui, S. and Zamami, K.**, 1993. Jump condition of energy flux at the line of bathymetric discontinuity and wave breaking on the reef flat. *Coastal Eng. in Japan*, 36: 155-175.
- Tuah, H. and Hudspeth, R.T.**, 1982. Comparison of numerical random sea simulations. *Jour. Waterway, Port, Coastal and Ocean Div.*, 108: 569-583.
- Tubman, M.W. and Suhayda, J.N.**, 1976. Wave action and bottom movements in fine sediments. *Proc. 15th Coastal Eng. Conf.*, 2: 1168-1183.
- Tucker, M.J.**, 1989a. An improved 'Battjes' method for predicting the probability of extreme waves. *Applied Ocean Research*, 11: 212-218.
- Tucker, M.J.**, 1989b. Interpreting directional data from large pitch-roll-heave buoys. *Ocean Eng.*, 16: 173-192.
- Tucker, M.J., Car, A.P. and Pitt, E.G.**, 1983. The effect of an off-shore bank in attenuating waves. *Coastal Eng.*, 7: 133-144.
- Tulin, M.P. and Li, J.J.**, 1992. On the breaking of energetic waves. *Jour. Offshore and Polar Eng.*, 2: 46-53.
- Tung, C.C.**, 1975. Statistical properties of the kinematics and dynamics of a random gravity wave field. *Jour. Fluid Mech.*, 70: 251-255.
- Tung, C.C. and Huang, N.E.**, 1985. Peak and trough distributions of nonlinear waves. *Ocean Eng.*, 12: 201-209.
- Tyler, G.L., Teague, C.C., Stewart, R.H., Peterson, A.M., Munk, W.H. and Joy, J.W.**, 1974. Wave directional spectra from synthetic aperture observations of radio scatter. *Deep-Sea Res.*, 21: 989-1016.

- Ursell, F., 1953. The long wave paradox in the theory of gravity waves. *Proc. Cambridge Phil. Soc.*, 46: 685-694.
- Ursell, F., 1956. Wave generation by wind. In: Batchelor, G. (Editor) *Survey in Mechanics*, Cambridge Univ. Press, 216-249.
- Valenzuela, G.R., 1976. The growth of gravity-capillary waves in the coupled shear flow. *Jour. Fluid Mech.*, 76: 229-250.
- Vincent, C.L. and Hughes, S.A., 1985. Wind wave growth in shallow water. *Jour. Waterways, Port, Coastal and Ocean Eng.*, III: 765-770.
- Vincent, L. and Briggs, M.J., 1989. Refraction-diffraction of irregular waves over a mound. *Jour. Waterways, Port, Coastal and Ocean Eng.*, 115: 269-284.
- Vinje, T., 1989. The statistical distribution of wave heights in a random seaway. *Applied Ocean Res.*, 11: 143-152.
- Vladder, G.Ph.van, Goda, Y., Hawkes, P., Mansard, E.P.D., Martin, M.J., Mathiessen, M., Peltier, E. and Thompson, E., 1994. Case studies of extreme wave analysis: a comparative analysis. *Proc. 2nd Inter. Symp. on Ocean Wave Measurement and Analysis*, New Orleans, July 25-28, 1993, 978-992.
- Wahl, G., 1974. Wave statistics from Swedish coastal waters. *Proc. of Inter. Symp. on Dynamics of Marine Vehicles and Structures in Waves*, Inst. Mech. Eng., London, 33-40.
- Wainwright, S.A., Biggs, W.D., Currey, J.D., and Gosline, J.M., 1976. *Mechanics Design in Organisms*, Edward Arnold, London.
- Walton, T.L., 1992. Wave reflection from natural beaches. *Ocean Eng.*, 19: 239-258.
- The WAMDI Group, 1988. The WAM model - a third generation ocean wave prediction model. *Jour. Phys. Oceanogr.*, 18: 1775-1810.
- Weber, N., 1991. Bottom friction for wind sea and swell in extreme depth-limited situations. *Jour. Phys. Oceanogr.*, 21: 149-172.
- Wehausen, J.V. and Laitone, E.V., 1960. Surface waves. In: Flugge, W. (Editor), *Handbuch der Physik*. Springer-Verlag, Berlin, pp. 446-778.
- Wells, J.T., 1983. Dynamics of coastal fluid muds in low-, moderate- and high-tide-range environments. *Can. Jour. Fish. Aquat. Science*, 40 (suppl.): 130-142.
- Wheeler, J.D., 1969. Method for calculating forces produced by irregular waves. *Proc. 1st Annual Offshore Techn. Conf.*, 1: 71-82.

- Whitham, G.B., 1974. *Linear and Nonlinear Waves*. A Wiley Interscience Publ., New York, 636 pp.
- Wiegel, R.L., R.L., 1949. An analysis of data from wave recorders on the Pacific coast of the United States. *Trans. Amer. Geoph. Union*, 30: 700-704.
- Wiegel, R.L. (Editor), 1982. *Directional Wave Spectra Applications*, ASCE, Berkeley, 495 pp.
- Willebrand, J., 1975. Energy transport in a nonlinear and inhomogeneous random gravity wave field. *Jour. of Fluid Mech.*, 70: 113-126.
- Williams, J.W., 1985. Near-limiting waves in water of finite depth. *Phil. Trans. Roy. Soc.*, A314: 353-377.
- Wolanski, E., 1986. Observations of wind-driven surface gravity waves offshore from the Great Barrier Reef. *Coral Reefs*, 4: 213-219.
- Wu, J., 1982. Wind-stress coefficients over sea surface from breeze to hurricane. *Jour. Geoph. Res.*, 87: 9704-9706.
- Xu, B. and Panchang, V.C., 1993. Outgoing boundary conditions for finite-difference elliptic water-wave models. *Proc. Roy. Soc.*, 441: 575-588.
- Yaglom, A.M., 1962. *Stationary Random Functions*, Prentice-Hall, Englewood Cliffs, 262 pp.
- Yamamoto, T., Koning, H.L., Sellmeijer, H. and Hijum, E.van, 1978. On the response of the poro-elastic bed to water waves. *Jour. Fluid Mech.*, 87: 193-206.
- Yamamoto, T. and Takahashi, S., 1985. Wave damping by soil motion. *Jour. Waterway, Port, Coastal and Ocean Eng.*, III: 62-77.
- Young, I.R., 1988. A shallow water spectral wave model. *Jour. Geoph. Res.*, 93: 5113-5129.
- Young, I.R., 1989. Wave transformation over coral reefs. *Jour. Geoph. Res.*, 94: 9779-9789.
- Young, I.R., 1992. The determination of spectral parameters from significant wave height and peak period. *Ocean Eng.*, 19: 497-508.
- Young, I.R., 1994a. Global ocean wave statistics obtained from satellite observations. *Applied Ocean Res.*, 16: 235-248.
- Young, I.R., 1994b. On the measurement of directional wave spectra. *Applied Ocean Res.*, 16: 283-294.

- Young, I.R., Rosenthal, W. and Ziemer, F., 1985. A three-dimensional analysis of marine radar images for determination of ocean wave directionality and surface currents. *Jour. Geoph.*, 90: 1049-1068.
- Young, I.R. and Sobey, R.J., 1985. Measurements of the wind-wave energy flux in an opposing wind. *Jour. Fluid Mech.*, 151: 427-442.
- Young, I.R. and Hardy, T.A., 1993. Measurements and modelling of tropical cyclone waves in the Great Barrier Reef. *Coral Reefs*, 12: 85-95.
- Young, I.R., Verhagen, L.A. and Banner, M.L., 1995. A note on the bimodal directional spreading of fetch limited wind waves. *Jour. Geoph. Res.*, 100: 773-778.
- Young, I.R. and Gorman, R.M., 1995. Measurements of the evolution of ocean wave spectra due to bottom friction. *Jour. Geoph. Res.*, 100: 10987-11004.
- Zakharov, V.E. and Filonenko, N.N., 1966. Energeticheskiy spektr stokhasticheskikh kolebaniy poverkhnosti zhidkosti (The energy spectrum of stochastic oscillations of a fluid surface). *Dokl. Akad. Nauk SSSR*, 170: 1292-1295.
- Zakharov, V.E. and Shrira, V.I., 1990. O formirovaniy uglovogo spektra vetrovykh voln (On the formation of directional spectrum of wind waves). *Zhurnal Eksp. i Teor. Fiziki*, 98: 1941-1958.
- Zaslavskii, M.M., 1982. Odnoparametricheskaya aproksimatsiya energeticheskoy chasti chastotnogo spektra (One-parametric approximation of the energetic range of frequency spectra). *Okeanologiya*, 22: 916-921.
- Zaslavskii, M.M. and Krasitskii, V.P., 1976. O generatsii vetrovykh voln v more konechnoy glubiny (On the generation of wind waves in water of finite depth). *Okeanologiya*, 16: 207-211.
- Zaslavskii, M.M. and Zakharov, V.E., 1982. K teorii prognoza vetrovykh voln (On the theory of prediction of wind waves). *Dok. Akad. Nauk SSSR*, 265: 567-571.
- Zelt, J.A. and Skjelbreia, J.E., 1992. Estimating incident and reflected wave fields using an arbitrary number of wave gauges. *Proc. 23th Inter. Conf. Coastal Eng.*, 1: 777-789.
- Zwarts, C.M.G., 1974. Transmission line wave height transducer. *Proc. Inter. Symp. Ocean Wave Measurement and Analysis*, New Orleans, 1: 605-620.

Appendix A

Symbols and Notation

a	wave amplitude.
a_{rms}	root mean square wave amplitude.
A	wave amplitude.
A_b	fraction of broken waves.
A_0	directional action spectrum.
B	bispectrum.
B_e	resolution bandwidth.
c_p	specific heat at constant pressure.
c_r	resistance coefficient.
C	co-spectrum.
C	wave phase velocity.
C_g	wave group velocity.
C_r	reflection coefficient.
C_t	transmission coefficient.
C_x	drag coefficient.
D	directional spreading function
\mathcal{D}_w	wave diffusion coefficient.
erf	error function.
$erfc$	supplemented error function.
E	encounter probability.
$E[x]$	average value of the random variable x .
\mathcal{E}_w	non-dimensional wave energy.
f	probability density function of variable x .
f_2	two-dimensional probability density function.

f_3	three-dimensional probability density function.
f_{max}	probability density function of extreme values.
f_c	Coriolis parameter.
f_c	Nyquist frequency.
f_e	linearization coefficient.
f_r	friction coefficient.
$f(x y)$	conditional probability density function.
F	probability (cumulative) distribution.
F_{br}	probability of breaking.
F_c	non-linearity parameter after Swart.
F_d	drag force.
F_i	inertia force.
F_l	lift force.
g	gravity acceleration.
G	shear modulus of elasticity.
h	water depth.
h_b	water depth at incipient breaking.
H	wave height.
H	frequency response function.
\bar{H}	mean wave height.
H_b	wave height at breaking.
H_{m0}	significant wave height (spectral formulation).
H_{rms}	root mean square wave height.
H_s	significant wave height (statistical formulation).
H_v	visually observed significant wave height.
H_1	smudged Heaviside's function.
$H[z]$	Hermite polynomial of degree n .
i	imaginary unit, $i = \sqrt{-1}$.
\vec{i}	unit vector in x direction.
I	entropy functional.
I_0	modified Bessel function of zero order.
\vec{j}	unit vector in y direction.
J	Jacobian of transformation.
J_m	Bessel function of m order.
k	wave number.
k_{cr}	critical wave number.
k_p	wave number corresponding to peak frequency.

\vec{k}	vertical unit vector.
kei	Kelvin function of zero order.
ker	Kelvin function of zero order.
K	autocorrelation function.
K	intrinsic permeability.
K	Dally's attenuation coefficient.
K_r	refraction coefficient.
K_s	shoaling coefficient.
l_0	mixing length.
L	wave length.
L_{min}	minimum wave length.
L	likelihood function.
L	Monin-Obukhov length.
L_t	repetition distance.
\mathcal{L}	Laplace operator.
m_n	spectral moments of order n .
\tilde{m}_n	central spectral moments of order n .
\hat{m}_n	moments of standardized Gaussian distribution.
n	porosity.
n	degree of freedom.
\vec{n}	unit vector.
N	wave action density.
N	number of waves in a sample.
N_h	sequence of waves the heights of which exceed a certain level.
N_t	number of waves in a total run.
\mathcal{O}	order of
p	pressure.
p	flux of wave action.
p_a	turbulent atmospheric pressure.
q	magnitude of the surface drift.
q_θ	vertical heat flux.
Q	quadrature spectrum.
Q_b	fraction of broken waves.
Q_7, Q_{dis}	energy dissipation term.
Q_1, \hat{Q}_1	atmospheric input term (Phillips mechanism).
$Q_{in}^{(P)}, \hat{Q}_{in}^{(P)}$	atmospheric input term (Phillips mechanism).

Q_2, \hat{Q}_2	atmospheric input term (Miles mechanism).
$Q_{in}^{(M)}, \hat{Q}_{in}^{(M)}$	atmospheric input term (Miles mechanism).
$Q_{in}^{(nl)}, \hat{Q}_{in}^{(nl)}$	atmospheric input term (Miles mechanism).
Q_5, \hat{Q}_5	non-linear wave-wave interaction term.
Q_{nl}, \hat{Q}_{nl}	non-linear wave-wave interaction term.
r_0	correlation coefficient.
s	sheltering coefficient.
s	spreading factor.
sl	significant slope.
S	phase.
S	frequency spectrum.
S_r	frequency spectrum of reflected waves.
S_t	frequency spectrum of transmitted waves.
\tilde{S}	symmetric frequency spectrum.
\hat{S}	two-dimensional spectrum.
S_J	JONSWAP spectrum.
S_{xx}	radiation stress component.
t	time.
t_X	equivalent duration time.
T	wave period.
T_a	measured average wave period.
T_p	peak wave period.
T_v	visually observed wave period.
\bar{T}	mean wave period.
\bar{T}_0	average wave period.
$T_{max,prob}$	the most probable wave period.
T	surface tension.
U	Ursell number.
\vec{U}	wind velocity vector, $\vec{U} = (U, V, W)$.
\vec{U}	current velocity vector, $\vec{U} = (U, V, W)$.
\vec{u}	wave velocity vector, $\vec{u} = (u, v, w)$.
u'	random component of u .
u_*	friction velocity.
v'	random component of v .
w'	random component of w .
x	horizontal coordinate.
X	wind fetch.

X_{eq}	equivalent wind fetch.
y	horizontal coordinate perpendicular to the x - direction.
z	vertical coordinate from undisturbed sea, pointed upwards.
z_0	roughness length.
α	Phillips' constant.
α_{cr}	critical angle.
β	nondimensional Miles' pressure coefficient.
β	attenuation coefficient.
β	constant in the Toba's spectrum.
β	bottom slope.
γ	proportionality coefficient at incipient breaking.
γ	peakedness parameter in JONSWAP spectrum.
γ_1	skewness.
γ_2	kurtosis.
Γ	gamma function.
Γ	dimensionless coefficient of breaking waves recovery.
δ	boundary layer thickness.
δ	roller thickness.
δ	Dirac's delta.
ϵ	random phase shift.
ϵ	spectral width parameter.
ϵ	shear strain.
$< \epsilon_f >$	rate of energy dissipation due to bottom friction.
$< \epsilon_b >$	rate of energy dissipation due to breaking.
ζ	sea surface displacements.
ζ	Monin-Obukhov parameter.
ζ_{max}	local maximum of surface displacements.
$\dot{\zeta}$	vertical velocity of sea surface changes.
$\ddot{\zeta}$	vertical acceleration of sea surface changes.
$\bar{\zeta}$	mean of sea surface displacements.
$\bar{\eta}$	wave set-up, set-down.
θ, Θ	angle of wave propagation.

Θ	absolute temperature.
κ	von Karman constant.
λ	Ochi's spectrum shape parameter.
λ	longitude.
λ	wave number in deep water.
λ	Lagrangian multipliers.
μ	coupling coefficient.
μ	dynamic viscosity coefficient.
μ_n	nth central statistical moment.
ν	spectral width parameter.
ν	kinematic viscosity coefficient (molecular).
ν	non-dimensional peak frequency.
ν_T	turbulent viscosity coefficient.
$\nu + i\mu$	complex coupling coefficient.
ξ	dimensionless sea surface displacements.
ξ	non-dimensional fetch.
ξ_b	inshore similarity parameter.
ξ_0	similarity parameter.
Π	turbulent stresses at sea surface.
ρ	normalized wave height.
ρ_a	density of air.
ρ_w	density of water.
σ	intrinsic frequency.
σ_ζ^2	variance of surface displacement.
σ_ζ	standard deviation of surface displacement.
σ_0	peak width parameter.
σ_0	peak width parameter.
ϕ	wind direction.
ϕ	latitude.
Φ	velocity potential.
φ	wave phase.
χ	normalized vertical component of wave-induced air velocity.

ψ	stream function.
Ψ	wave number spectrum.
$\hat{\Psi}$	wave number-frequency spectrum of the surface displacement.
Ψ_a	wave number-frequency spectrum of the atmospheric turbulent stress.
ω	radian frequency.
ω_0	directional mean wave frequency
ω_c	Nyquist frequency.
ω_p	peak frequency.
ω_*	non-dimensional water depth.
$\bar{\omega}$	mean frequency.
$\bar{\omega}_0$	average frequency.
Ω	radian frequency.
\approx	approximately equals.
\sim	proportional to.
∂	partial differential operator.
∇	gradient operator in three-dimensional space.
∇_h	horizontal gradient operator.
∇^2	Laplace operator in three-dimensional space.
∇_h^2	horizontal Laplace operator.
$-$	time average.
\sim	normalized value.
$*$	complex conjugate quantity.
\Im	imaginary part of complex quantity.
\Re	real part of complex quantity.

This page is intentionally left blank

Author index

- Aagaard, P.M., 381, 382, 387, 456
Abramowitz, M., 20, 79, 101, 104, 121,
125, 138, 146, 298, 307, 422,
427
Abreu, M., 290, 427
Ahrens, J.P., 276, 458
Allender, J.H., 215, 399, 427, 440
Allos, R.N., 83, 447
Alpers, W.R., 407, 427
Anastasiou, K., 166, 190, 273, 284, 427,
441, 445
Anctil, F., 435
Andunson, T., 427
Antsyferov, S.M., 75, 89, 427
Arhan, M., 432
Baer, L., 457
Baird, W.F., 457
Banner, M.L., 21, 70, 78, 106, 127, 427,
428, 456, 466
Barber, N.F., 407, 428
Barnes, D.L., 360, 449
Barnett, T.P., 204, 223, 427, 428, 440
Barstow, S.F., 427
Barzel, G., 459
Basco, D.R., 323, 428
Battjes, J.A., 83, 164, 165, 275, 290,
316, 318, 319, 320, 381, 383,
428
Bauer, E., 234, 429
Bea, R.G., 311, 429
Beal, R.C., 407, 429
Bear, L., 382, 436
Belberov, Z.K., 427, 457
Belberova, D.Z., 75, 272, 316, 429, 451
Bendat, J.S., 20, 387, 402, 405, 429
Bendykowska, G., 98, 298, 300, 429
Benett, J.R., 458
Benoit, M., 418, 429
Berge, B., 104, 429
Berkhoff, J.C.W., 272, 429
Bertotti, L., 432, 435
Biot, M.A., 311, 312, 430
Birman, B.A., 390, 430
Bishop, C.T., 241, 252, 397, 430
Bitner, E.M., 131, 135, 143, 144, 160,
179, 430
Bjerken, S., 427
Black, K.P., 358, 446
Bliven, L.F., 442
Boanstra, H., 328, 456
Boccotti, P., 124, 430
Bogle, R.W., 463
Bondzie, C., 330, 430
Booij, N., 272, 339, 343, 429, 430, 441
Borgman, L.E., 12, 367, 381, 387, 407,
422, 425, 427, 430, 431, 437,
455
Bouws, E., 91, 306, 327, 431, 440
Bowman, D., 373, 431
Bretherton, F.P., 60, 431
Bretschneider, C.L., 241, 431
Briggs, M.J., 104, 272, 273, 330, 431,
455, 464
Briggs, W.D., 464
Brisette, F.P., 407, 431
Brown, G.S., 419, 431
Bruening, C., 407, 427
Butowski, P., 279, 280, 451
Byrne, A.P., 291, 292, 458
Campbell, W.J., 453

- Car, A.P., 463
 Cardone, V.J., 437
 Carlson, H., 440
 Carter, D.J.T., 381, 382, 385, 420, 432
 Cartwright, D.E., 67, 118, 121, 122, 432, 440, 449
 Cavaleri, L., 223, 234, 325, 327, 394, 397, 432, 435, 445
 Cavanie, A., 130, 174, 175, 432
 Cazalé, H., 438
 Chakrabarti, S.K., 183, 432
 Chalikov, D.V., 22, 53, 432
 Challenor, P.G., 174, 178, 381, 382, 385, 432, 460
 Chamberlain, J.A., 363, 432
 Chandler, B.D., 460
 Chaplin, J.G., 427
 Chavy, P., 223, 438
 Chen, Y.H., 322, 325, 425, 432
 Cheney, R.E., 453
 Cherneva, Z.I., 451
 Chiu, Y.F., 397, 446
 Chou, H.T., 437
 Chybicki, W., 98, 99, 451
 Cieřlikiewicz, W., 131, 133, 190, 192, 433
 Coantic, M., 98, 457
 Cokelet, E.D., 127, 296, 433
 Collins, J.I., 164, 165, 306, 325, 433, 440
 Cooley, J.W., 7, 404, 405, 433
 Creamer, D.B., 57, 433
 Cross, R.H., 280, 460
 Cummins, I., 271, 433
 Currey, J.D., 464
 Cushman-Roisin, B., 455
 Dacunka, N.M.C., 441
 Dally, W.R., 166, 167, 316, 321, 433, 434
 Dalrymple, R.A., 273, 311, 312, 434, 444, 462, 447
 Davey, A., 210, 434
 Davidan, I.N., 87, 89, 92, 103, 177, 373, 374, 380, 382, 388, 391, 392, 394, 407, 434
 Davies, A.G., 343, 434
 Davis, R.E., 408, 434
 De Filippi, P.L., 432
 Dean, R.G., 154, 187, 425, 434, 448
 De Girolamo, P., 272, 434
 Deigaard, R., 458
 de Las Heras, M.M., 234, 434
 de Vries, G., 297, 445
 Dell'Osso, L., 234, 435
 Dera, J., 5, 435
 Derks, H., 320, 435
 Devillaz, E., 223, 438
 Dingemans, M., 272, 338, 434, 435
 Divoky, D., 447
 Dobson, F.W., 419, 435, 459
 Doering, J.C., 175, 435
 Done, T.J., 360, 363, 364, 435, 451
 Donelan, M.A., 25, 32, 75, 83, 84, 104, 105, 175, 187, 241, 397, 407, 430, 434, 435, 445, 456, 458
 Dorrestein, R., 373, 435
 Draper, L., 382, 435, 436
 Druet, Cz., 272, 436
 Duginov, B.A., 446
 Dunkel, M., 439
 Dungey, J.C., 211, 215, 436
 Earle, M.D., 382, 436
 Ebersole, B.A., 166, 436
 Edwards, G., 443
 Efimov, V.V., 3, 99, 436
 Eldeberky, Y., 429
 Elgar, S., 95, 278, 279, 436, 437
 Elliott, J.A., 459
 El-Shaarawi, A.H., 381, 382, 386, 453
 Enke, K., 440
 Enochson, L., 402, 405, 455
 Epstein, B., 159, 436
 Ewing, J.A., 88, 223, 230, 407, 432, 436, 439, 440

- Ezraty, R., 394, 419, 432, 462
Fendell, F.E., 359, 436
Feng-shi, M., 382, 462
Fenton, J.D., 188, 298, 397, 436, 437, 463
Feshbach, H., 355, 453
Filonenko, N.N., 221, 466
Fisher, R.A., 381, 437
Flannery, B.P., 457
Fletcher, C.A.J., 339, 437
Foda, M.A., 311, 312, 437, 452
Fontanet, P., 298, 437
Forristall, G.Z., 103, 144, 149, 158, 163, 187, 381, 437
Fox, M.J.H., 127, 210, 211, 215, 216, 437, 449
Freilich, M.H., 285, 289, 291, 437
Funke, E.R., 278, 449
Gabriel, D., 441
Gade, H.G., 312, 437
Gadzhiyev, Y.Z., 271, 438
Galenin, B.G., 446
Galvin, C.J., 298, 315, 438
Garratt, J.R., 26, 27, 60, 438
Garrett, C.J.R., 60, 431
Gastel, K.van, 155, 157, 438
Ge, W., 455
Gelci, R., 222, 223, 225, 438
Gere, J.M., 363, 462
Gerritsen, F., 345, 358, 438
Gienapp, H., 440
Glukhovskiy, B.M., 160, 438
Gnanadesikan, A., 399, 438
Gnedenko, B.V., 381, 438
Goda, Y., 165, 272, 383, 439, 464
Goldhirsh, J., 435
Gonsalves, J., 279, 454
Gonzalez, F.I., 429
Gorman, R.M., 466
Gosline, J.M., 464
Gourlay, M.R., 349, 351, 439
Grabner, H.C., 326, 327, 439, 449
Gradshteyn, I.S., 161, 439
Graham, C., 427
Grancini, G.F., 432
Green, A.W., 447
Greenhow, M., 130, 439
Groves, G.W., 459
Gu, D., 456, 457
Gudmestad, O.T., 190, 192, 433
Günther, H., 229, 230, 327, 431, 439, 447
Guza, R.T., 95, 160, 165, 285, 289, 320, 321, 436, 437, 455, 462
Hamilton, J., 435
Hancock III, D.W., 420, 429, 440
Hansen, J.B., 461
Hara, T., 452
Hardy, T.A., 345, 350, 358, 359, 439, 466
Harper, B.A., 460
Hashimoto, N., 407, 414, 418, 439, 444
Hasselmann, D., 102, 103, 106, 220, 439, 440
Hasselmann, K., 21, 61, 72, 81, 82, 83, 89, 92, 204, 209, 210, 212, 213, 214, 215, 216, 219, 220, 223, 224, 227, 229, 231, 232, 237, 238, 285, 306, 326, 407, 411, 417, 429, 439, 440, 441, 444, 445, 448, 458, 459
Hasselmann, S., 42, 212, 213, 215, 220, 231, 232, 285, 429, 440, 444, 445, 459
Haug, O., 417, 440
Hawkes, P., 439, 464
Hayne, G.S., 420, 440
Headrick, J.M., 463
Heathershaw, A.D., 343, 434
Hedges, T.S., 268, 441
Herbers, T.H.C., 436, 441
Herterich, K., 285, 326, 441, 458
Hijum, E.van, 465
Hines, D.E., 429

- Hoerner, S.F., 362, 441
 Hogben, N., 371, 373, 376, 377, 441
 Hollingsworth, A., 443
 Holthuijsen, L.H., 107, 328, 407, 428, 441
 Honda, T., 204, 205, 206, 453
 Horikawa, K., 321, 441, 442
 Howe, M.C., 463
 Howell, G.L., 408, 441
 Hsiao, S.V., 312, 441, 458
 Hsu, S.A., 32, 441
 Huang, N.E., 86, 96, 98, 115, 135, 152, 442, 463
 Hubble, E.N., 90, 455
 Hudspeth, R.T., 423, 425, 442, 463
 Hughes, S.A., 166, 183, 187, 334, 335, 396, 436, 442, 461, 464
 Hui, W.H., 211, 215, 435, 436, 458
 Hunt, J.N., 59, 442
 Hunt, J.R., 437
 Hurdle, D.P., 241, 331, 333, 442
 IAHR, 141, 442
 Ioveniti, G.L., 432
 Irvine, D.E., 429
 Isaacson, M.St.Q., 99, 362, 363, 377, 386, 387, 442, 458
 Isobe, M., 273, 416, 417, 442
 Jähne, B., 107, 443
 Jackson, F.C., 429
 Jacobs, S.J., 22, 442
 James, R.W., 390, 443, 457
 Janssen, J.P.F.M., 165, 316, 318, 319, 320, 428
 Janssen, P.A.E.M., 22, 32, 54, 234, 434, 438, 443, 445, 447
 Jardine, T.P., 372, 373, 443
 Jaynes, E.T., 133, 443
 Jeffreys, H., 36, 443
 Johnson, J.W., 453
 Jones, I.S.F., 428
 Jonsson, I.G., 265, 443
 Juman, D.L., 455
 Joy, J.W., 463
 Kahma, K.K., 430
 Kameyama, Y., 439
 Katz, E.J., 43, 456
 Kawai, S., 57, 75, 443
 Keating, T., 291, 295, 443
 Kennedy, R.M., 127, 130, 459
 Kerstens, J.G.M., 382, 443
 Kessenich, T.A., 373, 447
 Khristoforov, G.N., 436
 Kibiel, I.A., 444
 Kim, T., 418, 444
 Kim, Y.K., 95, 443, 461
 Kimura, A., 198, 444
 Kinsman, B., 9, 10, 22, 37, 41, 241, 444
 Kirby, J.T., 273, 274, 289, 339, 444, 447, 450
 Kitaigorodskii, S.A., 21, 24, 25, 31, 33, 72, 76, 78, 79, 91, 205, 221, 269, 270, 271, 305, 438, 444
 Kjeldsen, S.P., 158, 453
 Klen, L.A., 430
 Kobune, K., 407, 414, 439, 444
 Kochin, N.J., 361, 444
 Koh, R.C.Y., 164, 447
 Komen, G.J., 22, 202, 205, 216, 219, 220, 231, 232, 306, 327, 419, 420, 421, 431, 438, 444, 445
 Komori, T., 453
 Kondo, K., 442
 Koning, H.L., 465
 Kononkova, G.E., 50, 445
 Korteweg, D.J., 297, 445
 Kostense, J.K., 434
 Kostichkova, D.P., 89, 445, 451
 Krasitskii, V.P., 3, 22, 31, 43, 50, 51, 60, 258, 261, 438, 444, 445, 453, 466
 Krivitskii, S.V., 31, 445, 446, 461
 Krogstad, H.E., 407, 417, 427, 440, 445
 Kruseman, P., 440
 Krylov, J.M., 22, 26, 27, 28, 29, 30, 44,

- 49, 72, 80, 87, 88, 89, 101, 103,
243, 246, 247, 248, 258, 333,
334, 407, 445, 446
- Kunishi, H., 29, 446
- Kuo, C.T., 164, 321, 441, 446
- Kuo, S.T., 164, 397, 446
- Kuo, Y.Y., 99, 446, 452
- Kuznetsov, P.I., 143, 179, 195, 446
- La Thi Cang, 200, 446
- Laing, A.K., 407, 436
- Laitone, E.V., 95, 298, 446, 464
- Lamb, H., 316, 446
- Larrazza, A., 427
- Lawless, J.F., 387, 446
- Le, D.Y., 461
- LeBlond, P.H., 3, 446
- Lee, T., 358, 446
- Le Mehaute, B., 164, 258, 263, 264,
291, 303, 447
- Leslighter, E.J., 346, 349, 454
- Lewis, A.W., 83, 272, 447
- Lewis, D.P., 463
- Li, B., 273, 284, 447
- Lie, V., 271, 352, 447
- Lighthill, M.J., 12, 14, 48, 76, 447
- Lindgren, G., 174, 447
- Lionello, P., 234, 432, 443, 447
- Liu, A., 447
- Liu, C.C., 447
- Liu, K., 448
- Liu, L., 444
- Liu, P., 76, 447
- Liu, P.C., 95, 373, 447, 458
- Liu, P.L.-F., 285, 289, 311, 312, 434,
447
- Lo, J.M., 151, 152, 187, 448, 462
- Long, S.R., 442
- Long, R.B., 417, 448, 452, 459
- Longuet-Higgins, M.S., 39, 61, 67, 70,
96, 101, 115, 117, 118, 121, 122,
127, 144, 154, 155, 158, 172,
174, 175, 194, 196, 198, 210,
211, 215, 218, 263, 285, 300,
320, 345, 383, 407, 411, 432,
448, 449, 460
- Lopatukhin, L.I., 388, 392, 434
- Loubser, C.C., 291, 295, 461
- Lough, J.M., 360, 449
- Lumb, F.E., 371, 372, 373, 441
- Lybanon, M., 427
- Lyzenga, D.R., 429
- Maa, P.Y., 312, 449
- MacDonald, G., 440
- Mackenzie, N.G., 377, 386, 387, 442
- MacPherson, H., 312, 449
- Madsen, O.S., 298, 306, 308, 326, 327,
439, 449
- Madsen, P.A., 290, 449, 458, 461
- Makin, V.K., 22, 53, 432
- Mansard, E.P.D., 278, 439, 449, 464
- Mardia, K.V., 278, 450
- Marsh, J.G., 453
- Martin, M.J., 439, 464
- Mase, H., 289, 450
- Massel, S.R., 21, 37, 58, 61, 63, 88, 95,
98, 99, 131, 139, 145, 163, 165,
166, 178, 179, 192, 256, 267,
258, 264, 265, 272, 279, 280,
283, 285, 286, 296, 297, 298,
300, 301, 302, 305, 309, 310,
316, 320, 338, 339, 343, 344,
350, 351, 355, 356, 358, 360,
363, 364, 383, 390, 392, 393,
421, 427, 429, 433, 450, 451, 461
- Masson, D., 216, 451
- Masuda, A., 95, 452
- Mathiesen, M., 439, 464
- McLeish, W.D., 407, 452
- Mehta, A.J., 312, 449
- Meerburg, A., 440
- Mei, C.C., 272, 283, 311, 312, 343, 354,
421, 448, 451, 452
- Memos, C.D., 175, 452
- Merrill, G., 452

- Miche, R., 164, 275, 297, 322, 452
 Middleton, D., 118, 146, 452
 Miles, J.W., 22, 34, 38, 39, 42, 54, 57,
 204, 205, 223, 452
 Miller, G.R., 459
 Milne-Thomson, L.M., 361, 366, 453
 Mitsuyasu, H., 30, 83, 89, 101, 204, 205,
 206, 224, 407, 411, 453
 Mizuno, S., 453
 Mognard, N.M., 392, 453
 Monaldo, F.M., 429, 435
 Monin, A.S., 3, 24, 453
 Moore, J.C., 463
 Morison, J.R., 186, 453
 Morse, P.M., 355, 453
 Moskowitz, L., 21, 35, 79, 457
 Muir, L.R., 381, 382, 386, 453
 Munk, W.H., 33, 37, 139, 241, 440, 459,
 461, 463
 Murray, R., 449
 Müller, P., 440
 Myrhaug, D., 158, 453
 Mysak, L.A., 3, 446
 Naess, A., 145, 158, 453, 454
 Naciri, M., 452
 Nairn, R.B., 323, 454
 Nakayama, R., 453
 Nath, J.H., 154, 454
 Nelson, R.C., 279, 291, 293, 321, 346,
 349, 350, 454
 Neumann, G., 457
 Newman, J.N., 362, 454
 Niedzwecki, J.M., 100, 103, 104, 454
 Nielsen, P., 397, 454
 Nwogu, O., 407, 454
 O'Brien, M.P., 453
 Ochi, M.K., 20, 90, 93, 111, 118, 125,
 130, 131, 134, 145, 154, 163
 195, 375, 380, 386, 454, 455
 Ohkuso, M., 453
 Okuda, K., 443
 Olbers, D.J., 440
 Olliver, G.F., 441
 Olsen, R.B., 458
 Osborne, A.R., 149, 455
 Oshiro, S., 461
 Otnes, R.K., 402, 405, 455
 Outlaw, D.G., 431
 Overvik, T., 84, 441
 Pacheco, L.A., 443
 Panchang, V.G., 273, 284, 330, 430,
 455, 465
 Panicker, N.N., 407, 455
 Papoulis, A., 116, 455
 Parmuzin, T.A., 430
 Pawka, S.S., 352, 357, 455
 Pearce, B.R., 455
 Pedlosky, J., 3, 455
 Peltier, E., 439, 464
 Penzien, J., 104, 429
 Peregrine, D.H., 21, 118, 127, 265, 315,
 395, 428, 455, 456
 Perrie, W., 212, 457
 Peters, H.C., 328, 456
 Peterson, A.M., 463
 Petrauskas, P., 381, 382, 387, 456
 Phillips, O.M., 3, 22, 34, 39, 41, 43,
 44, 47, 48, 69, 75, 78, 79, 89,
 96, 124, 125, 126, 127, 192, 210,
 218, 219, 427, 456, 457
 Piersol, A.G., 120, 387, 402, 405, 429
 Pierson, W.J., 21, 35, 79, 100, 103, 223,
 225, 457
 Pitt, E.G., 463
 Podmogilnyj, I.A., 446
 Polyakov, J.P., 89, 445, 446
 Poon, Y., 449
 Popkov, R.A., 446
 Potts, D.C., 363, 435
 Powers, E.J., 95, 443
 Powers, W.H., 95, 459
 Press, W.H., 422, 457
 Puzyrewski, R., 4, 457
 Radder, A.C., 273, 429, 457

- Ramamonjariisoa, A., 98, 457
Ramsey, F.L., 154, 454
Readshaw, J.S., 381, 457
Regier, L.A., 408, 434
Reistad, M., 443
Resio, D., 212, 457
Rice, O., 66, 118, 145, 172, 457
Richter, K., 439, 440
Riedel, H.P., 291, 292, 458
Riemer, K.S., 107, 443
Rikiishi, W.J., 453
Riley, D.S., 22, 52, 458
Rizzoli P.M., 223, 325, 432
Robakiewicz, M., 163, 451
Roelvink, J.A., 454
Romeiser, R., 234, 458
Rosenthal, W., 431, 439, 466
Ross, D.B., 440, 452
Roze, N.V., 444
Rozhkov, W.A., 434
Rufenach, C.L., 421, 458
Russel, C.A., 458
Rychlik, J., 174, 447
Ryzhik, I.M., 161, 439
Sahinoglou, I.I., 195, 455
Salter, S.H., 388, 458
Sarpkaya, T., 362, 363, 458
Sawicki, J., 4, 457
Schaaf, S.A., 453
Schäffer, 323, 324, 458
Schuchman, R.A., 458
Schwab, D.J., 241, 458
Seelig, W.N., 165, 276, 458
Sellmeijer, H., 465
Sell, W., 440
Shannon, C.E., 132, 458
Sharma, J.N., 425, 434
Shemdin, O., 311, 312, 441, 458
Shiau, J.C., 263, 458
Shrira, V.I., 106, 466
Simpson, J.H., 407, 459
Skjelbreia, J., 278, 466
Skovgaard, C., 443
Smith, N.D., 432, 449
Smith, R., 394, 459
Snodgrass, F.E., 216, 459
Snyder, D.L., 30, 42, 127, 130, 205, 209, 212, 226, 231, 459
Soares, C.G., 88, 371, 372, 373, 374, 459
Sobey, R.J., 158, 175, 188, 208, 209, 359, 459, 460, 466
Sollitt, C.K., 280, 460
Soloviev, J.P., 429, 436
Sorensen, O.R., 290, 449
Soulsby, R.L., 183, 186, 460
Southgate, H.N., 454
SPM, 239, 241, 330, 331, 332, 333, 459
Srokosz, M.A., 117, 128, 174, 178, 460
Starr, V.P., 192, 460
Steedman, R.K., 392, 460
Steele, K.E., 399, 460
Stegun, I.A., 20, 79, 101, 104, 121, 125, 138, 146, 298, 307, 422, 427
Steinbakke, P., 427
Steinberg, C.R., 350, 451
Stewart, R.H., 463
Stewart, R.W., 61, 320, 345, 449
Stewartson, K., 210, 434
Stive, M.J.F., 241, 318, 320, 331, 333, 428, 435, 442, 460
Stokes, G.G., 115, 296, 460
Stratonovitch, R.L., 446
Strekalov S.S., 31, 88, 89, 90, 445, 446, 461
Suhaya, T., 311, 314, 453, 463
Suk, K.D., 271, 461
Sulaiman, D.M., 351, 461
Sultan, N.J., 183, 187, 461
Svendsen, I.A., 316, 323, 461
Sverdrup, H.U., 33, 37, 139, 241, 461
Sveshnikov, A.A., 178, 461
Swan, C., 271, 433
Swart, D.H., 291, 295, 461

- Swift, R.N., 429, 452
 Sylwester, R., 311, 461
 Takahashi, S., 312, 465
 Tayfun, M.A., 146, 147, 148, 151, 152,
 155, 158, 177, 178, 167, 461,
 462
 Teague, C.C., 463
 Terray, E.A., 399, 438
 Thai, N.H., 131, 433
 Teh-fu, L., 382, 462
 Teng, C.C., 460
 Teukolsky, S.A., 457
 Thom, H.C.S., 381, 382, 462
 Thornton, E.B., 160, 165, 289, 320,
 321, 427, 462
 Tick, L.J., 457
 Tickell, R.G., 427
 Tikhonov, W.I., 10, 118, 143, 151, 446,
 462
 Tilley, D.G., 429
 Timoshenko, S.P., 363, 462
 Tippett, L.C.H., 381, 437
 Thacker, W.C., 459
 Thompson, E., 439, 464
 Toba, Y., 75, 221, 224, 443, 462
 Tolman, H.L., 234, 328, 462
 Torum, A., 271, 352, 447
 Tosi, R., 432
 Tournadre, J., 394, 419, 462
 Townsend, M., 397, 463
 Trinder, J.C., 428
 Trizna, D.B., 407, 462
 Tsai, C.H., 130, 154, 455
 Tsanis, I.K., 407, 431
 Tsuchiya, Y., 461
 Tsuruya, H., 209, 463
 Tsutsui, S., 272, 461, 463
 Tsyplukhin, W.F., 445
 Tuah, H., 423, 425, 463
 Tubman, M.W., 311, 314, 463
 Tucker, M.J., 291, 384, 385, 399, 407,
 433, 463
 Tukey, J.W., 7, 404, 405,
 Tung, C.C., 96, 98, 152, 189, 190, 442,
 463
 Tyler, G.L., 407, 463
 Ulmer, E.W., 447
 Ursell, F., 22, 293, 464
 Valenzuela, G.R., 55, 57, 464
 Vartdal, L., 427,
 Vassal, J., 438
 Verhagen, L.A., 466
 Vetterling, W.T., 457
 Vincent, C.L., 272, 273, 330, 334, 335,
 431, 464
 Vinje, T., 144, 464
 Vledder, G., Ph.van, 383, 439, 464
 Wahl, G., 373, 464
 Wainwright, S.A., 363, 464
 Walden, H., 440
 Walsh, E.J., 429
 Walton, T.L.Jr., 278, 464
 Wang, D.W.C., 460
 Wang, H., 263, 322, 325, 432, 442, 444,
 458
 Wang, J.D., 258, 443, 447
 Wang, W.C., 131, 134, 455
 Ward, E.G., 437
 Wash, E.J., 457
 Weare, T.J., 436, 439
 Webber, N.B., 291, 295, 443
 Weber, N., 396, 464
 Wehausen, J.V., 95, 464
 Wei, C.C., 455
 Wells, J.T., 311, 464
 Werner, G., 98, 429
 Whalen, J.E., 380, 455
 Whatley, C.P., 100, 103, 104, 454
 Wheeler, J.D., 187, 464
 Whitham, G.B., 58, 465
 Wiegel, R.L., 99, 315, 383, 465
 Wilkerson, J.C., 204, 428, 435
 Willebrand, J., 61, 96, 465
 Williams, J.W., 128, 297, 465

- Wolanski, E., 358, 465
Won, Y., 429
Worthington, B.A., 436, 439
Wright, J.A., 57, 433
Wu, J., 26, 205, 465
Xu, B., 273, 465
Yaglom, A.M., 13, 14, 24, 453, 465
Yamamoto, T., 311, 312, 465
Yamashita, T., 428, 461
Yang, C.Y., 462
Yoon, S.B., 447
Yoshioka, H., 461
Young, I.R., 84, 107, 208, 209, 221, 222,
326, 350, 358, 359, 391, 392,
407, 408, 417, 418, 420, 428,
439, 460, 465, 466
Yuen, Y., 442
Zakharov, V.E., 74, 106, 221, 466
Zamami, K., 272, 463
Zambresky, L.F., 429
Zaslavskii, M.M., 22, 43, 73, 74, 429,
444, 445, 466
Zelt, J.A., 278, 466
Ziener, F., 466
Zitman, T.J., 428
Zwarts, C.M.G., 398, 466

This page is intentionally left blank

Subject index

- Adriatic Sea 325, 327
- Agulhas Current 328
- air flow over waves 23, 52, 53
- aliasing effect 400
- altimeter 126
- assimilation techniques 234, 421
- Atlantic Ocean 232, 233, 371
- atmospheric boundary layer 23, 24
- atmospheric forcing 203
 - following wind 206
 - opposing wind 207
- autocorrelation function 6, 15, 18, 40, 64, 92, 126, 144, 403
- Baltic Sea 5, 90, 131, 163
- Beaufort scale 370
- Bight of Abaco 205
- Bingham body 313
- bispectrum 64, 92, 93, 405
- Blackman-Tukey method 402
- Boltzmann integral 210, 212
- bora 328
- bottom friction 306, 326, 345
- bottom permeability 308
- boundary layer
 - atmospheric 23
 - sea bottom 5, 306
 - sea surface 5
- Bragg scattering 420
- caustic lines 258
- Charnock's formula 27
- cnoidal function 298
- coastal zone 2
- combined refraction and diffraction 271
- complementary error function 125, 141
- continuous fluid 3
- convolution integral 146
- Coriolis parameter 23
- correlation coefficient 146, 198
- correlation scale 15, 64
- coupling coefficient 42, 54, 204, 205, 208, 209, 223
- cross-correlation function 14, 19, 20, 412
- cross-spectrum 19, 409, 412
- cumulative distribution function 121
- data assimilation 421
- data processing
 - autocorrelation windowing 403
 - data window 405
 - sampling 399
 - standardization 401
 - trend removal 401
- density
 - of air 23
 - of water 5
- depth dependent factor 285
- design wave selection 387
- Dirac delta function 12
- directional mean wave frequency 328
- directional action spectra 328
- directional spreading function 20, 64, 99, 206, 243, 260, 407
 - cosine-power type 100, 101, 260
 - double peak type 106
 - hyperbolic type 104
 - wrapped-around Gaussian type 103
 - von Mises type 104

- directionality estimation methods
 - Bayesian Directional Method 418
 - Fourier Expansion Method 408
 - Maximum Entropy Method 411
 - Maximum Likelihood Method 416
- dispersion relation 10, 13, 58, 59, 95, 111, 280, 281, 340
 - deep water waves 18, 96
 - in porous media 267
 - mud waves 314
 - shallow water waves 95
 - waves on current 267
- dissipation coefficient 306, 308
 - waves on current 267
- drag coefficient 21, 26, 28
- duration-limited graph 36, 239, 330
- elliptic type equation 273
- entropy functional 133, 414
- ergodic theorem 9
- error function 121
- equation
 - Boussinesq 289, 290, 323
 - continuity 5
 - eikonal 338, 344
 - energy transport 344
 - extended mild-slope equation 339, 343, 356
 - Forchheimer 280
 - Hamilton 58
 - Helmholtz 342
 - kinematical conservation 58
 - kinetic 59
 - Korteweg-de-Vries 289
 - Laplace 6, 38
 - long waves 283
 - mean horizontal momentum 207, 320, 345
 - mild-slope 272, 338
 - Orr-Sommerfeld 55
 - radiative transfer 59, 74, 202, 227, 231, 322, 359
 - Rayleigh 42
 - time-dependent mild slope 274
- evanescent modes 281
- fetch-limited graphs 35, 238, 330
- first generation models: *see* wave prediction
- fluid particle 4
- forces on corals 360
 - drag 362
 - inertia 301
 - lift 362
 - resistance 363
 - total 364
- Fourier integral 51
- Fourier series 188, 277, 423
- Fourier-Stieltjes integral 14, 38, 44, 48, 408
- Fourier transform 12, 15
 - Fast Fourier Transform 7, 404, 423
- fraction of broken waves 319
- freak waves 392
- frequency
 - average 66
 - cut-off 80
 - infragravity 279
 - intrinsic 49, 58, 60, 75, 265
 - mean 66
 - Nyquist 400
 - observed (apparent) 58, 265
- frequency response function 397
- friction velocity 24, 35, 69, 204, 307
- Froude number 27
- Galerkin-Eigenfunction Method 339
- geometrical optics approximation 256, 337, 339
- goodness of fit tests 386
- Great Barrier Reef 271, 352
- Green's law 166, 322
- group velocity 58, 265, 268, 269, 319
- growth rates 42
- Gulf of Mexico 163, 232, 233

- Hanning window 403
- Heaviside's function 74
- Hermite polynomials 114
- higher harmonic generation 299, 300, 351
- Hilbert transform 151, 196
- HISWA model 328
- incompressible fluid 5
- Indian Ocean 234
- inner product 340
- intermittence effect 188
- intrinsic permeability 280
- inviscid fluid 4
- irrotational motion 6, 38
- Jacobian transformation 60, 116, 138, 151, 263
- Jeffreys' mechanism 36
- JONSWAP experiment 72, 81, 210, 227
- Kamchiya experiment 74
- Karman constant 24
- Kaspiyan Sea 88
- Kelvin function 307
- Keulegan-Carpenter number 303
- Knudsen number 4
- kurtosis coefficient 113, 131, 183
- Lagrange theorem 6
- Lagrangian multipliers 133, 414
- level crossing 193, 194
- likelihood function 386
- linearization coefficient 280, 284, 309
- Markov chain 159, 193, 198
- maximum entropy principle 133, 414
- wave measurement techniques
 - heave-pitch-roll buoy 407
 - laboratory techniques 395
 - pressure transducers 396
 - SAR 407, 420
 - satellite altimetry 419
 - spatial array 407
 - two-dimensional current meter 407
 - wave gauges 396
 - wave rider buoy 398
 - wave staffs 398
- Mediterranean Sea 234, 373
- Miles' theory of wave generation 39
- mixing length 53
- moments
 - spectral 66
 - statistical 111, 112, 138, 406
- momentum balance 23, 320
- momentum flux 24
- Monin-Obukhov similarity theory 24
- Monin-Obukhov length 24
- nonlinear interactions 209, 284
- nonlinearity parameter 291, 293
- old sea 32, 53
- Pacific Ocean 197, 234, 371
- parabolic approximation 273
- peak enhancement parameter 81, 82, 214
- peak frequency 35, 64, 72, 80
- percolation 306
- Phillips constant 70, 260
- Phillips' theory of wave generation 39
- Phillips-Miles model 38
- polynomial series 188
- porosity 280
- porous breakwater 279
- pressure fluctuations 38, 43, 48
- pressure response factor 396
- probability density function 8, 128
 - breaking wave 128, 153, 169, 170
 - conditional 125, 145, 177
 - crest-to-trough wave height 145, 146
 - extreme crests 121, 122
 - extreme wave heights 155, 156
- Glukhovskiy 161
- Gram-Charlier series 114, 131, 183

- joint distribution 115, 125, 137, 143, 146, 151, 172, 174, 178, 189, 263
- large wave height 148
- modified Rayleigh 144, 145
- nonlinear Stokes' type wave 115, 135, 150
- normal (Gaussian) 8, 111
- orbital velocities 180, 190
- positive and negative maxima 118
- pressure 180
- Rayleigh 70, 121, 138, 198
- standardized Gaussian 112
- three-dimensional 118
- total run 198
- truncated 122
- two-dimensional 137, 146, 154
- wave amplitude 138, 152
- wave crest 152
- wave height in surf zone 164, 166, 167
- wave period 80, 146, 176
- wave phase 138, 152
- wave trough 153
- Weibull 163
- probability distribution 123, 375
 - breaking waves 128, 130, 154, 155
 - extreme wave height 156
 - Fisher-Tippett 378, 381
 - Frechet 378, 381
 - Gumbel 381
 - large wave height 149
 - log-normal 376, 377, 378, 380
 - long-term 374
 - Rayleigh 70
 - Weibull 376, 378, 379, 380, 383
- probability
 - coral dislodgement 367
 - encounter 367
 - exceedance 377, 378
 - survival 368
- radiation stress 320
- random process 8
 - ergodic 8
 - Gaussian 8, 16, 17
 - Markov 16, 17, 198
 - non-stationary 8
 - stationary 8
 - white noise 16, 17
- remote sensing techniques 418
 - satellite altimetry 419
 - Synthetic Aperture Radar (SAR) 420
- repetition distance 300
- resolution bandwidth 403
- resonance mechanism 39, 41, 43, 285
- resonant wave number locus 46
- Reynolds number 4, 27, 28, 29
- roughness length 21, 26, 27, 28, 30, 32
- resistance coefficient 37
- response function 397
- run of high waves 195
- sampling interval 399
- saturation range 63, 218, 269
 - finite water depth 76
 - influence of surface drift 78
 - influence of uniform current 269
 - Phillips representation 69
 - Toba representation 75, 78
 - Zaslavskii and Zakharov representation 73
- seawater
 - density 5
 - salinity 5
- second generation models: *see* wave prediction
- set-up and set-down
- shear modulus of elasticity 313
- sheltering coefficient 37
- sheltering of surface waves by islands 352
- shoaling coefficient 258, 259
- similarity laws 21, 33
- similarity parameter 275

- simulation techniques 421
 - time domain simulation 422
 - frequency domain simulation 423
- sirocco 328
- skewness coefficient 113, 117, 131, 183, 295
- Snel's law 256, 257, 260
- soft mud bottom 311
 - viscous fluid model 312
 - viscoelastic model 312
 - Coulomb friction model 312
 - Bingham model 312
 - rheological model 312
- source terms
 - definition 59, 61, 62
 - bottom friction 306
 - bottom permeability 310
 - nonlinear interaction 209, 284
 - whitcapping dissipation 218, 219
 - wind input 203
- spectral width parameter 67, 121, 144
- spectrum
 - amplitude 19
 - broad 67
 - co-spectrum 7, 19, 409
 - cross-spectrum 19, 397, 416
 - Davidan 87
 - directional 99
 - Donelan 84
 - equilibrium range 69, 75
 - frequency 7, 15, 18, 33, 43, 74, 79, 403, 405
 - higher order 92
 - JONSWAP 81
 - Kolmogorov 74
 - Krylov 87
 - low-frequency 90
 - multipeak 88
 - narrow 67
 - non-symmetric 18
 - phase 19
 - Pierson-Moskowitz 35, 79
 - quadrature 7, 19, 20, 409
 - Strekalov-Massel 88
 - swell 92
 - symmetric 15
 - TMA 91
 - Toba 75
 - two-dimensional 14, 212, 266, 268, 409, 410
 - Wallops 86
 - wave number 14, 18, 41, 49, 57, 69, 75
 - wave number-frequency 41, 47, 97, 416, 417
- stability correction factor 239
- standard deviation 26, 32, 282
- standard error 404
- stochastic process 8
 - ergodic 8, 13
 - stationary 8, 13
 - non-stationary 8
- Stokes breaking criteria 127
- stratification parameter 25, 27
- stream function 55
- stress
 - tangential 39, 50, 52
 - turbulent 39, 41, 54
 - viscous 4, 54
 - wave-induced 23, 39, 53
- stretching method 187
- structure of extreme waves 124
- surface contaminants 57
- surface drift 78
- surface tension 33, 43, 56
- SWADE 126
- swell 92
- swell-wind waves coupling 216, 229
- third generation models: *see* wave prediction
- time-limited graphs 238
- total run 194
- transmission coefficient 282, 284
- tropical cyclones 359

- Ursell parameter 175, 293
- variance 15, 25, 66, 72, 111, 182
- velocity field around coral 366
- velocity potential 6, 38, 43, 339
- viscosity
 - dynamic coefficient 4, 37, 56, 208
 - kinematic coefficient 5, 24, 27, 33, 280
 - molecular 50
 - turbulent 50
- vocoidal function 295
- Voigt body 312, 313
- wave
 - capillary 1, 69
 - cnoidal 297
 - deterministic representation 10
 - internal 3
 - planetary 1
 - random representation 13
 - sinusoidal 37
 - solitary 297
 - sound 1
- wave action 60, 210, 269
 - conservation law 60, 75, 265, 268, 274
 - flux 74, 75
- wave amplitude 137
- wave breaking 127
 - breaking criteria 127, 301
 - breakers types 315
 - energy flux difference model 321
 - inner region 323
 - local water depth model 322
 - outer region 323
 - periodic bore approach 316, 344
 - surface roller concept 323
- wave diffraction 255, 272, 337
- wave energy
 - balance 57, 59, 220, 319
 - flux 37, 61, 256
 - dissipation 306, 308, 310, 311
- wave generation 36
 - wind generation 36
 - mechanical generation 298
- wave geography 388
 - Atlantic Ocean 370, 372, 376, 382, 383, 388, 390, 391
 - Baltic Sea 373, 394
 - Barents Sea 394
 - Great Lakes 373
 - Indian Ocean 390, 392
 - Kaspiyan Sea 394
 - Mediterranean Sea 373, 394
 - North Sea 383, 385, 388, 394
 - Pacific Ocean 370, 382, 383, 390, 391
 - Sea of Okhotsk 394
- wave groups 192
 - level-crossing problem 194
 - Markov chain representation 198
- wave height
 - crest-to-trough 145
 - depth-controlled 334, 335
 - largest 155, 291, 350
 - mean 139, 143, 156
 - most probable 156
 - root mean square 139, 144, 318
 - significant 35, 139
 - visual observed 371, 372, 377
- wave-induced stress 53
- wavelength 47
- wave number 46, 267
 - conservation law 58, 256
- wave period 172
 - average 66, 177
 - mean 66, 177
 - visual observed 373, 374
- wave prediction 222
 - empirical models 235
 - Donelan method 241
 - JONSWAP prediction graphs 237
 - Krylov method 334, 243
 - SMB method 241, 330

- SPM method 239, 330
 - first generation models 223, 324
 - second generation models 225, 325, 326, 359
 - third generation models 231, 327
- wave pressure 180
- wave reflection 275
 - reflection coefficient 275, 282, 284
- wave refraction 255, 354
 - refraction coefficient 258
 - due to bottom shoaling 256
 - due to current 264
- wave set-down 345
- wave set-up 345
- wave slope 86, 117
- wave velocity 180
 - bottom orbital velocity 183
 - group velocity 54, 58, 265, 268, 319
 - phase velocity 32, 45, 47, 99, 267, 300
 - velocity close to surface (intermittency effect) 186, 188
- Wiener-Khinchine Theorem 7, 15, 93
- wind
 - duration 33, 35
 - fetch 33, 35
 - logarithmic profile 25, 57
- Young modulus of water 5
- young sea 32, 53, 54

OCEAN SURFACE WAVES: THEIR PHYSICS AND PREDICTION

This book is intended as a handbook for professionals and researchers in the areas of Physical Oceanography, Ocean and Coastal Engineering and as a text for graduate students in these fields.

It presents a comprehensive study on surface ocean waves induced by wind, including basic mathematical principles, physical description of the observed phenomena, practical forecasting techniques of various wave parameters and applications in ocean and coastal engineering, all from the probabilistic and spectral points of view.

The book commences with a description of mechanisms of surface wave generation by wind and its modern modeling techniques. The stochastic and probabilistic terminology is introduced and the basic statistical and spectral properties of ocean waves are developed and discussed in detail.

The bulk of material deals with the prediction techniques for waves in deep and coastal waters for simple and complex ocean basins and complex bathymetry. The various prediction methods, currently used in oceanography and ocean engineering, are described and the examples of practical calculations illustrate the basic text.

An appendix provides a description of the modern methods of wave measurement, including the remote sensing techniques. Also the wave simulation methods and random data analysis techniques are discussed. In the book a lot of discoveries of the Russian and East European scientists, largely unknown in the Western literature due to the language barrier, are referred to.

"The range of topics and applications is far more extensive; there is much more to tie together. The treatment is less discursive and somewhat more demanding, but always clear to a technically-trained reader ... should be available to all physical and dynamical oceanographers interested in applications, and should be close at hand to graduate students and practitioners of ocean and coastal engineering."

Appl. Mech. Rev.

Cover photo courtesy of the Commonwealth Scientific and Industrial Organization (CSIRO)

www.worldscientific.com

2285 sc

ISBN 981-02-2109-6(pbk)



9 9810221096